



Provided by the author(s) and University of Galway in accordance with publisher policies. Please cite the published version when available.

Title	Experimental characterisation and computational constitutive modelling of high temperature degradation in 9Cr steels including microstructural effects
Author(s)	Barrett, Richard A.
Publication Date	2016-04-20
Item record	http://hdl.handle.net/10379/5700

Downloaded 2024-04-25T11:21:29Z

Some rights reserved. For more information, please see the item record link above.



Experimental Characterisation and Computational Constitutive Modelling of High Temperature Degradation in 9Cr Steels Including Microstructural Effects

Richard A. Barrett B.E. (2011)

Supervisors: Prof. Sean Leen and Prof. Padraic
O'Donoghue



A thesis submitted to the National University of Ireland, Galway
as fulfilment of the requirements for the Degree of Doctor of Philosophy

Mechanical Engineering, National University of Ireland, Galway

April, 2016

Table of Contents

Abstract	vii
Acknowledgements	ix
List of Publications	x
Nomenclature	xi
1. Introduction.....	1
1.1. General	1
1.2. The Changing Landscape of Power Generation.....	2
1.3. Materials for High Temperature Applications	6
1.4. A multi-scale approach for the design and assessment of 9Cr steels..	9
1.5. Aims and Objectives	12
1.6. Thesis Overview and Scope of Research Work.....	13
2. Background and Literature Review	15
2.1. Introduction.....	15
2.2. Creep of steel alloys	16
2.2.1. Mechanisms of creep deformation	21
2.2.2. Creep testing of power plant materials.....	24
2.3. Fatigue of steel alloys	26
2.3.1. Fatigue testing of 9Cr steels	31
2.3.2. Influence of strain-rate	33
2.4. Modelling inelastic deformations in materials.....	35
2.4.1. Phenomenological models for high temperature fatigue.....	36
2.4.2. Simulating inelastic deformations from a physical basis	42
2.5. Strengthening mechanisms in steel alloys.....	49
2.5.1. Dislocation strengthening.....	51
2.5.2. Precipitate strengthening	52
2.5.3. Solid-solution strengthening.....	53

2.5.4.	Grain boundary strengthening	54
2.6.	Microstructure of 9-12Cr steels	55
2.6.1.	Chemical composition and effect of element content	57
2.6.2.	Heat treatment	63
2.6.3.	Cracking of welded connections	69
2.6.4.	Microstructural evolution in 9-12Cr steels.....	73
2.6.4.1.	Precipitate and solute strengthening in 9-12Cr steels.....	73
2.6.4.2.	Martensitic lath growth and subgrain formation	79
2.6.4.3.	Evolution of dislocation density	83
2.7.	Summary and conclusions.....	86
3.	High Temperature Experimental Testing of 9Cr steels	90
3.1.	Introduction	90
3.2.	High temperature experimental programs.....	92
3.3.	Chemical Composition and heat treatment	98
3.4.	High temperature fatigue of ex-service P91 steel	101
3.4.1.	Effect of temperature on P91 steel	101
3.4.2.	High temperature fatigue tests at varying strain-ranges	104
3.4.3.	Cyclic softening behaviour.....	107
3.4.4.	The strain-rate effect in ex-service P91 steel	110
3.4.5.	Stress relaxation behaviour in 9Cr steels.....	116
3.5.	Thermo-mechanical fatigue testing.....	117
3.6.	High temperature fatigue testing of MarBN	124
3.7.	High temperature fatigue life of 9Cr steels	127
3.7.1.	Failure of 9Cr steels under high temperature fatigue	127
3.7.2.	Microstructural analysis	131
3.7.3.	Fatigue scatter.....	135
3.7.4.	High temperature fatigue comparison of 9Cr steels.....	137

3.8.	Discussion	142
3.8.1.	HTLCF and TMF test results	142
3.8.2.	Effect of chemical composition.....	143
3.8.3.	Potential of MarBN for next generation power plant.....	145
3.8.4.	Cyclic softening behaviour.....	147
3.8.5.	Failure of 9Cr steels.....	147
3.9.	Conclusions	151
4.	A Unified Cyclic Viscoplastic Modelling Framework for Strain-Rate Dependent Materials	153
4.1.	Introduction	153
4.2.	Benefits of a hyperbolic sine modelling framework.....	156
4.3.	A strain-rate sensitive unified cyclic viscoplastic model.....	158
4.3.1.	Model development	159
4.3.2.	Cyclic softening.....	161
4.3.3.	Kinematic hardening	163
4.4.	Implementation of the model within the FE method	163
4.4.1.	Material Jacobian and the consistent tangent stiffness matrix	167
4.5.	Material parameter identification process.....	171
4.5.1.	Elastic material parameters.....	173
4.5.2.	Cyclic softening material constants.....	175
4.5.3.	Back-stress material parameters	176
4.5.4.	Identification of cyclic viscoplasticity parameters	180
4.6.	Validation of material model against experimental data.....	184
4.6.1.	Modelling of 'as received' P91 under HTLCF and TMF.....	185
4.6.1.1.	Model calibration for 'as received' P91 steel	185
4.6.1.2.	Validation against HTLCF experimental data.....	188
4.6.1.3.	Modelling TMF deformation in 'as received' P91 steel	192

4.6.2.	Application of material model to ex-service P91 steel.....	193
4.6.2.1.	Identification of parameters for ex-service P91.....	193
4.6.2.2.	Strain-range validation for ex-service P91 steel.....	201
4.6.2.3.	Prediction of cyclic softening.....	203
4.6.2.4.	Capturing strain-rate effects in ex-service P91 steel.....	204
4.6.3.	Application of the material model to MarBN.....	206
4.7.	Life prediction.....	212
4.8.	Discussion.....	213
4.9.	Conclusions.....	220
5.	Application of a Unified Cyclic Viscoplastic Material Model to Thermo-mechanical and Multi-Axial Fatigue.....	223
5.1.	Introduction.....	223
5.2.	Simulating thermo-mechanical fatigue in ex-service P91.....	224
5.3.	Multi-axial modelling of notched specimens.....	227
5.3.1.	Notched specimen experiments.....	227
5.3.2.	Application of material model to notched geometry.....	229
5.3.3.	Multi-axial validation of the UMAT subroutine.....	236
5.4.	Modelling of thin-walled tubes.....	239
5.5.	Discussion.....	242
5.6.	Conclusions.....	245
6.	A dislocation-based model for high temperature cyclic deformation of 9-12Cr steels.....	246
6.1.	Introduction.....	246
6.2.	Strengthening mechanisms of 9-12Cr steels.....	246
6.2.1.	Cyclic softening.....	249
6.3.	Dislocation-based material model.....	250
6.3.1.	Precipitate Hardening.....	253
6.3.2.	Dislocation strengthening and evolution of dislocation density.....	254

6.3.3.	Evolution of the lath microstructure.....	257
6.4.	Results.....	257
6.4.1.	Parameter identification.....	258
6.4.2.	Calibration of micro-structural parameters	263
6.4.3.	Validation against high temperature fatigue data.....	264
6.4.4.	Effects of micro-structural parameters	266
6.5.	Discussion	268
6.6.	Conclusions.....	271
7.	An improved dislocation-mechanics model for microstructural evolution and degradation in 9-12Cr steels.....	273
7.1.	Introduction.....	273
7.2.	A dislocation-mechanics framework for 9Cr steels.....	274
7.2.1.	Precipitate hardening in 9-12Cr steels.....	277
7.2.2.	Back-stress at high angle grain boundaries	280
7.2.3.	A model for dislocation density evolution	283
7.2.4.	Simulating the martensitic lath microstructure.....	288
7.3.	Results.....	293
7.3.1.	Material parameter identification	293
7.3.2.	Validation for 9Cr steel cyclic plasticity.....	299
7.3.3.	Effect of microstructure on constitutive behaviour.....	301
7.3.4.	Initial modelling of creep deformation.....	307
7.3.5.	Limitations of the current model for creep deformation	309
7.4.	Discussion	311
7.5.	Conclusions.....	313
8.	Conclusion and Recommendations.....	315
8.1.	Conclusions.....	315
8.2.	Recommendations for Future Work.....	319

Appendix A: Thermodynamic Framework	325
Appendix B: Material Jacobian for Viscoplastic Deformation.....	329
Bibliography.....	333

Abstract

The transition from base-load to intermittent power plant operation has led to the requirement for increased knowledge and more accurate prediction of the effects of flexible loading on plant components. This thesis is concerned with the experimental characterisation and novel computational modelling, including dislocation-mechanics based modelling, of high temperature cyclic plasticity and fatigue for current and next generation power plant materials. The modelling is designed to capture the constitutive behaviour of 9Cr steels across a range of operating conditions, calibrated and validated via measured test data. Phenomenological and microstructurally-based models are developed at the continuum level and applied to isothermal fatigue, thermo-mechanical fatigue and multi-axial loading conditions relevant to next generation power plant.

High temperature low cycle fatigue test programmes are conducted on P91 steel and MarBN, a new high temperature alloy currently in development. The results illustrate cyclic softening due to dynamic recovery and dependent on the initial microstructure. A program of thermo-mechanical fatigue experiments is presented for P91 steel across a range of strain-rates, with a significant reduction in fatigue life observed for out-of-phase loading. This highlights the effect of thermal transients on the material performance.

The observed strain-rate effect is incorporated within a phenomenological material model via a hyperbolic sine constitutive equation. The hyperbolic sine framework enables variable strain-rate sensitivity in the model and the successful prediction of the strain-rate effect at higher and intermediate strain-rates. A phenomenological kinematic hardening model enables prediction of the effect of the various strengthening mechanisms, with isotropic softening included to predict the cyclic softening behaviour. The material model is implemented in a UMAT user material subroutine, including consistent tangent stiffness, for use with the commercial finite element code Abaqus and calibrated using a step-by-step parameter identification methodology. The material model is successfully validated

against isothermal fatigue, thermo-mechanical fatigue and stress relaxation behaviour via comparison with experimental data, and demonstrated for multi-axial applications to notched specimen geometries and thin-walled pipes.

A novel dislocation-mechanics based constitutive model is developed, including mean values of microstructural parameters related to the key strengthening mechanisms in 9-12Cr steels. This model includes kinematic hardening based on back-stresses developed due to the presence of precipitates, as well as the pile-up of dislocations at high-angle grain boundaries. A dislocation-mechanics approach is implemented to predict recovery in the material. The novel material model is applied to high temperature fatigue of P91 steel and successfully compared to experimental test data and measured evolutions of key microstructural parameters, viz. dislocation density and martensitic lath width. These results illustrate the ability of the microstructure-sensitive framework to capture both the constitutive behaviour and mean microstructural evolutions of 9Cr steels. This model enables successful advancement of the microstructure under flexible operation within a wider creep-fatigue modelling methodology at the macro-scale and component levels.

The microstructure-sensitive material model developed in this work will allow for more accurate simulations of the constitutive behaviour of complex 9Cr welded connections in power plant components. This will, in turn, enable power plant designers to account for microstructural degradation during cyclic viscoplastic deformation.

Acknowledgements

Firstly and foremost, I would like to thank my supervisors Prof Sean Leen and Prof Padraic O'Donoghue for their support, enthusiasm and expertise over the past four years.

I would like to acknowledge Science Foundation Ireland (SFI) for funding this research as part of the SFI METCAM project under grant number SFI/10/IN.1/I3015. I would like to acknowledge the contribution made by its members, Dr Rory Monaghan, Dr Tadhg Farragher, Dr Dongfeng Li, Dr Noel Harrison, Mr Conor O'Hagan and Mr Ming Li of NUI Galway, Prof Noel O'Dowd, Dr Peter Tiernan and Mr Brian Golden from University of Limerick, and Mr Stephen Scully and Ms Adelina Adams of ESB Energy International.

I would like to thank the technical staff at NUI Galway, Mr Patrick Kelly, Mr Bonaventure Kennedy, Mr William Kelly and Mr Gerry Hynes for their help with specimen manufacture and testing equipment. Thanks to Dr Barry O'Brien for his discussions on material microstructure and to Ms Eimear O'Hara for carrying out the SEM analysis. Thanks also to the IMPACT and IMPEL group members from E-ON UK, Alstom, Doosan Power, Goodwin Steel Castings, IMPACT Power Tech Ltd. and Loughborough University. I would like to thank Dr Chris Hyde at the University of Nottingham for carrying out the TMF testing.

I would like to thank my friends and colleagues in the NUI Galway research suites, including James, Oliver, Evelyn, Ciaran, Teng, Claire, Heather, Caoimhe, Neil, Donnacha, Tarek, David, Brendan and Sinead.

Finally, and most importantly, I would like to thank my wife, Lisa, my parents, Mary and Michael, my siblings, John, Cathal, Helen and Brian and extended family and friends for all of their support during the last four years.

List of Publications

The work presented in this thesis has resulted in the following publications:

- Barrett, R.A., O'Donoghue, P.E., Leen, S.B. An improved unified viscoplastic constitutive model for strain-rate sensitivity in high temperature fatigue. *International Journal of Fatigue*, **48** (2013), pp. 192-204. (**Chapter 4**)
- Barrett, R.A., O'Donoghue, P.E., Leen, S.B. Finite element modelling of the thermo-mechanical behaviour of a 9Cr martensitic steel. In: Altenbach, H., Kruch, S. (Eds.), *Advanced Materials Modeling for Structures*. New York: Springer (2013), pp. 31-42. (**Chapter 4**)
- Barrett, R.A., Farragher, T.P., Hyde, C.J., O'Dowd, N.P., O'Donoghue, P.E., Leen, S.B. A unified viscoplastic model for high temperature low cycle fatigue of service-aged P91 steel. *Transactions of the ASME Journal of Pressure Vessel Technology*, **136** (2014), pp. 021402. (**Chapter 3, Chapter 4**)
- Barrett, R.A., O'Hara, E., O'Donoghue, P.E., Leen, S.B. High temperature low cycle fatigue behaviour of MarBN at 600 °C. *Transactions of the ASME Journal of Pressure Vessel Technology*, (2015) In Press. (**Chapter 3, Chapter 4**)
- Barrett, R.A., Farragher, T.P., O'Dowd, N.P., O'Donoghue, P.E., Leen, S.B. Multiaxial cyclic viscoplasticity model for high temperature fatigue of P91 steel. *Materials Science and Technology*, **30** (2014), pp. 67-74. (**Chapter 5**)
- Barrett, R.A., O'Donoghue, P.E., Leen, S.B. Multi-axial application of a hyperbolic sine unified viscoplasticity constitutive model to P91 steel. *9th International Conference on Creep and Fatigue at High Temperature*, 25-27th September 2012, London, UK. (**Chapter 5**)
- O'Donoghue, P.E., Barrett, R.A., Reape, S., Scully, S., Hyde, C.J., Leen, S.B. Thermo-mechanical fatigue in power plant steels: Enhanced numerical modelling with experimental validation. *Civil Engineering Research Association of Ireland (CERAI) 2014*, 28-29th August 2014 (S. Nanukuttan and J. Goggins, Editors), pp.167-172, Belfast, Northern Ireland. (**Chapter 5**)
- Barrett, R.A., O'Donoghue, P.E., Leen, S.B. A dislocation-based model for high temperature cyclic viscoplasticity of 9-12Cr steels. *Computational Materials Science*, **92** (2014), pp. 286-297. (**Chapter 6**)

Nomenclature

Symbol	Definition
a	Interatomic spacing of solutes
A_0	Norton power law creep constant
A_w	Area of LAB region
b	Basquin exponent
b	Isotropic hardening rate exponent
b	Magnitude of Burgers vector
B	Solute strengthening material constant
B^a	Micromechanical back-stress
c	Fatigue ductility exponent
c	Atomic concentration of solutes
C	Hardening modulus (Frederick Armstrong)
C	Creep damage constant (Hayhurst model)
C	Precipitate strengthening constant (FHP)
C_∞	Particle solubility
d	Grain size
d_{dip}	Critical distance dipole dislocation formation
d_e	Critical distance for mutual annihilation (edge)
d_g	Block width
d_j	Precipitate diameter
$d_{j,0}$	Initial precipitate diameter
d_l	Critical distance for locked dislocation formation
d_s	Critical distance for mutual annihilation (screw)
D	Diffusion coefficient
D	PAG size
D	Material Jacobian
D_{Fe}	Diffusion coefficient for Fe
D_{GB}	Grain boundary diffusion
D_v	Volume diffusivity
E	Young's modulus
f	Plastic yield function
f_g	HAGB volume fraction
f_j	Precipitate volume fraction
f_w	LAB volume fraction
F	Viscous network contribution (two layer model)
F	Thermal activation energy (micromechanical model)
F	Force
h	Primary creep constant (Hayhurst model)
H	Primary creep (Hayhurst model)
H^*	Primary creep saturation value (Hayhurst model)
$h(p)$	Isotropic hardening function
I	Identity matrix

k	Cyclic yield stress
k_B	Boltzmann constant
k_{sol}	Solute atom parameter
k_y	Hall-Petch constant
k_1	Dislocation growth constant (Kocks Mecking model)
k_2	Dislocation consumption constant (Kocks Mecking model)
K_c	Carbide coarsening rate (Hayhurst model)
K_i	Ostwald ripening precipitate coarsening rate
K_p	Elastic-plastic network modulus (two layer model)
K_v	Viscous network modulus (two layer model)
L_e	Mean free path travelled by a dislocation
L_i	Martensitic lath dimension
m_{cl}	Climb mobility rate
M	Taylor factor
n	Norton creep exponent
n	Number of active slip systems
\mathbf{n}	Normal tensor
n_g	Number of dislocations in a pile-up
n_g^*	Number of sites for dislocation pile-ups
N	Cycle number
N_f	Number of cycles to failure
N_r	Number of cycles to failure by ratchetting
Q	Saturated isotropic stress
Q_{cr}	Creep activation energy
p	Accumulated effective plastic strain
P_w	Martensitic lath perimeter
r	Isotropic hardening state variable
R	Isotropic hardening
\bar{R}	Universal gas constant
s	LAB dislocation spacing
\mathbf{s}	Deviatoric stress tensor
\mathbf{s}^{tr}	Deviatoric trial stress tensor
s_0	Initial LAB dislocation spacing
S^α	Micromechanical slip resistance
t	Time
T	Temperature
T	Dislocation line tension
T_H	Temperature (high)
T_L	Temperature (low)
\mathbf{x}	Deviatoric back-stress tensor
v	Dislocation velocity
v	Molar volume
V_l	Martensitic lath volume
V_w	LAB volume

w	Martensitic lath width
Z	Chaboche cyclic viscoplastic material constant
Z_k	Consistent tangent stiffness constants
α	Cyclic viscoplastic material parameter
\mathbf{a}	Kinematic hardening state variable
α_{coe}	Coefficient of thermal expansion
α_{cr}	Creep material parameter
α_g	HAGB material constant
$\alpha_{w,0}$	Static lath growth constant
α_1	Material constant
α_2	Martensitic lath material constant
β	Cyclic viscoplastic material parameter
$\beta_{w,0}$	Dynamic lath growth constant
γ	NLKH back-stress material parameter
γ	Surface energy
$\dot{\gamma}^{\text{pl}}$	Plastic slip-rate
γ_w	Lath growth constant
ΔH	Helmholtz free energy
$\Delta \varepsilon^{\text{pl}}$	Plastic strain-range
$\Delta \varepsilon_{\text{r}}$	Ratchet strain-range
ε	Total strain
ε_c	Material ductility
ε^{cr}	Creep strain
ε^{el}	Elastic strain
ε_f'	Fatigue ductility coefficient
ε^{in}	Inelastic strain
ε^{pl}	Plastic strain
ε^{th}	Thermal strain
ε^{vp}	Viscoplastic strain
$\dot{\varepsilon}_{\text{min}}^{\text{cr}}$	Minimum creep strain-rate
ζ	HAGB growth constant
η	Thermal efficiency
η_1	Static block growth material constant
η_2	Dynamic block growth material constant
θ	Angle of misorientation
λ	Precipitate spacing
λ	Lamé's constant
λ_g	Mean spacing between slip lines
A	Number of LAB dislocations per metre of boundary
$\mathbf{\Lambda}$	Elasticity tensor
μ	Shear modulus
ν	Poisson's ratio
ρ	Mass density

ρ	Dislocation density
$\bar{\rho}$	Mobile dislocation density
ρ_i	Lath interior dislocation density
ρ_g	Grain boundary dislocation density
ρ_{GND}	Geometrically necessary dislocation density
ρ_{SSD}	Statistically stored dislocation density
ρ_w	Lath boundary dislocation density
σ	Stress
σ_b	Back-stress
σ_d	Dislocation back-stress
σ_e	Equivalent stress
σ_e^{tr}	Equivalent trial stress
σ_f'	Fatigue strength coefficient
σ_g	HAGB back-stress
σ_h	Hydrostatic stress
σ_{Or}	Orowan stress
σ_p	Precipitate back-stress
σ_v	Viscous stress
σ_y	Yield stress
$\sigma_{y,0}$	Initial yield stress
τ	Shear stress
τ_c	Critical resolved shear stress
τ_0	Critical shear stress
τ_0	Friction stress
Φ	Carbide coarsening damage variable (Hayhurst model)
χ	Kinematic back-stress
Ψ	Specific free energy
Ψ	Isotropic hardening modulus
Ψ_{el}	Elastic specific free energy
Ψ_{pl}	inelastic specific free energy
ω	Creep damage (Hayhurst model)
Ω	Dissipation potential
Ω_g	HAGB hardening modulus
Ω_p	Precipitate hardening modulus

1. Introduction

1.1. General

Deformation of materials via microstructural degradation remains a key limiting factor to more sustainable energy production. In terms of fossil fuel based electrical power generation, the current demand for improved plant efficiency and reduced emissions via increased plant operating temperatures (e.g. towards ultra-supercritical operation) is concomitant with a shift to intermittent mode operation to accommodate renewable sources of energy. This combination of more severe loading conditions (e.g. increased steam temperature and pressure) under flexible operation has led to expanding and increasing complexity in the mechanisms of deformation of advanced alloys for high temperature power generation.

To facilitate the successful development of advanced high temperature materials for next generation power plants, it is important to characterise and understand interactions of creep, fatigue and oxidation loading in candidate materials. Although the creep response of the current state-of-the-art materials is relatively well understood, the high temperature fatigue and thermo-mechanical loading of such materials has not received as much attention. Coupled with the need to characterise the next generation of materials for higher temperature applications, improvements to macro-scale material models for high temperature fatigue are required to capture adjustments to the mechanisms of deformation in light of recent changes and future challenges in electricity generation.

The focus of this chapter is to highlight recent developments in electrical power generation and the requirement for advanced materials development. In particular, this chapter deals with the background and motivation for this research, including an overview of recent changes in power generation and the requirement for materials with improved high temperature fatigue and creep resistance in Section 1.2. Section 1.3 discusses the benefits of using 9Cr steels for high temperature applications in current and next generation

1. Introduction

power plants, and the concept of a design tool for the improvement of such steels is presented in Section 1.4. The main motivations for conducting this research, including the primary aims and objectives are outlined in Section 1.5 and Section 1.6 summaries the scope of work presented in the thesis.

1.2. The Changing Landscape of Power Generation

Modern and next generation power plants are currently (i) in transition from base-load (continuous operation under constant load between standard scheduled maintenance with a design life of approximately 200,000 hrs) to intermittent-mode operation to accommodate renewable sources of energy and continuous mixing of energy sources, and (ii) seeking to improve efficiency and reduce emissions via increased steam temperatures and pressures.

These changes are required to meet regulations such as the European Union Directive 2009/28/EC. Under this directive, for example, Ireland has set out targets of generating at least 16 % of its electrical power from renewable sources by the year 2020. As illustrated in Figure 1.1, it is proposed to achieve these goals predominantly using wind power generation, which is by nature an unpredictable source. Thus, conventional power plant, designed for long-term operation under constant load, must now be capable of starting and shutting down much more frequently. This involves complex attemperation cycles during start-up, where the temperature varies as per the measured data of Figure 1.2a, which shows a typical start-up attemperation cycle in Lough Ree power plant (Ireland). These complex start-up cycles induce thermal gradients, which in turn cause thermo-mechanical fatigue (TMF) of plant components. TMF is a simultaneous cyclic variation of temperature and pressure, leading to continuous microstructural degradation and deformation of materials and hence, reduction of plant life. Particularly susceptible to TMF are heavy wall header units, which comprise of complex geometrical cylinders with many welded connections as illustrated in Figure 1.2b.

1. Introduction

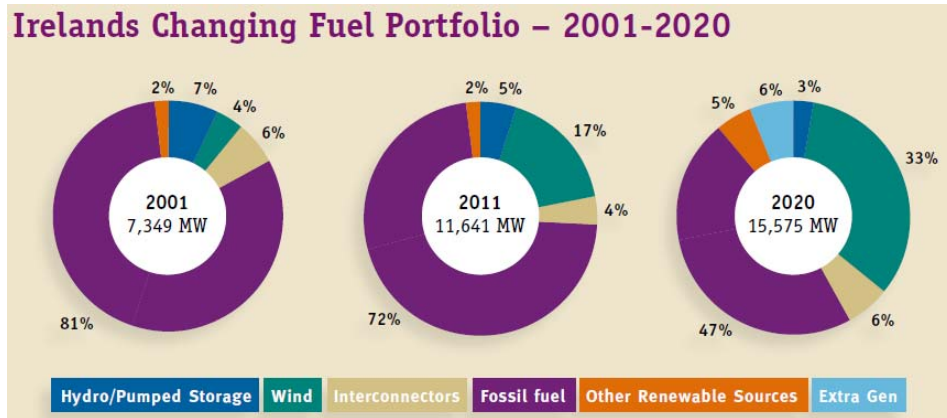


Figure 1.1: Measured and predicted breakdown of the energy mix in Ireland (courtesy of EirGrid).

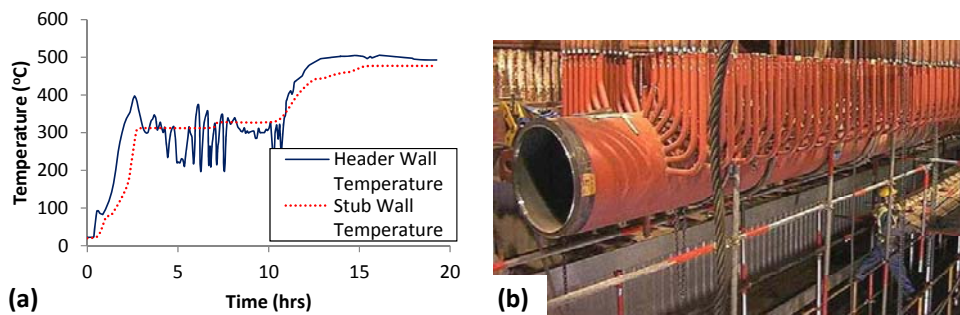


Figure 1.2: Lough Ree power station (a) measured steam histories during a start-up cycle and (b) installation of a branched header [Courtesy of Stephen Scully, ESB Energy International].

The requirement to improve plant efficiency is related to (i) more sustainable and cleaner energy production and (ii) the requirement to reduce the economic cost of fossil fuel energy production. The efficiency of a power plant can most simply be described in terms of Carnot efficiency, which states that the thermal efficiency of a fully reversible heat engine with no losses is:

$$\eta = 1 - \frac{T_L}{T_H} \quad (1.1)$$

where T_L and T_H are the lowest and highest plant temperatures, respectively. Hence, under the assumption that T_L is a constant of approximately 293 K, significant gains in thermal efficiency can be achieved by raising the maximum plant operating temperature. Coupled with an increase in plant

1. Introduction

operating pressures, current power plant components are subjected to increased creep deformation. Creep is time-dependent high temperature deformation under an applied stress in metallic materials, where the dominant mechanism of deformation is dependent on the material microstructure, loading conditions and operating temperature.

The current generation of materials, namely the 9Cr family of steels, are designed for safe operation at temperatures of less than 550 °C [*Fournier et al., 2009b*]. At temperatures above this, rapid degradation of the microstructure occurs. As it is not economically feasible to manufacture the majority of plant components from expensive Ni-based superalloys, there is a requirement to enhance the capability of 9Cr steels and develop new metallic materials capable of withstanding high temperature creep-TMF deformation.

An additional and possibly more important reason for improving plant efficiency relates to the potential for reducing CO₂ emissions. Operating power plant at higher temperatures ensures more complete combustion of fossil fuels, reducing the level of CO₂ emitted. As illustrated in Figure 1.3, a 2 % increase in net plant efficiency can also lead to a 5 % reduction in CO₂ emissions. However, to prolong the life of components, many plant operators run their plants at subcritical loading conditions (lower temperatures), with plant efficiencies on the order of 38 % or less and operating temperatures below 550 °C. As a typical power plant outage can cost more than €500,000 per day [*Scully, 2013*], and with many outages requiring a significant lead time to resolve failures, the financial benefit of operating at higher temperatures is not clear. However, there are potential financial savings, efficiency gains and emission reductions to be made if suitable materials can be found or developed in conjunction with an accurate life prediction methodology, to allow safer, more reliable operation under ultra-supercritical conditions (i.e. plant operating temperatures in excess of 615 °C and pressures up to 30 MPa). The requirement for improved materials and wider maintenance schedules is the driver for more accurate computational models and enhanced life prediction methodologies,

1. Introduction

potentially resulting in a reduction in the number of plant outages and microstructural degradation during start-up cycles.

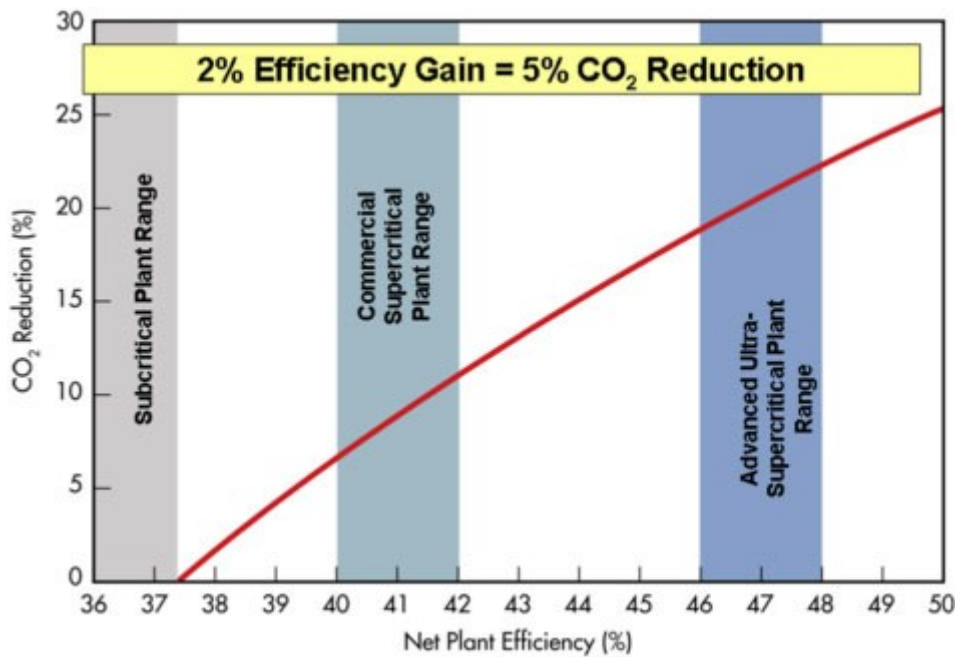


Figure 1.3: The effect of increasing plant efficiency on the level of CO₂ emissions [Abson and Rothwell, 2013].

A further trend for power plants is a transition to biomass co-firing to reduce CO₂ emissions. Coupled with the higher firing temperatures however, biomass co-firing leads to a considerable increase in corrosion of plant components as illustrated on the thin-walled tubes in Figure 1.4. Coupled with oxidation in components, the effect of corrosion manifests itself in the form of a net loss of material and hence, a reduction in effective wall thickness. Oxidation and corrosion in candidate materials also lead to a depletion of the strengthening mechanisms [O'Hagan et al., 2015a], resulting in a further reduction of component life.

1. Introduction



Figure 1.4: Corrosion of steam tubes due to ash deposits [O'Hagan *et al.*, 2015a].

Thus, material performance and degradation remains a key limiting factor to achieving more sustainable energy production with reduced CO₂ emissions. As a consequence, there is a continuing need for advanced materials in the power generation industry. The development of such materials is the focus of the next section. Coupled with this is the requirement for the development of an advanced materials capability for high temperature interactions of fatigue, creep and oxidation and identification of the primary mechanisms of deformation and degradation in candidate materials.

1.3. Materials for High Temperature Applications

Since the start of the 1990's, most large scale high temperature power plant components are manufactured from 9Cr steels. Compared to their CrMoV predecessors, the 9Cr family of steels has improved creep strength, enhanced corrosion resistance and reduced cost. Originally developed at Oakridge National Laboratory, the inherent high creep strength of 9-12Cr martensitic steels is attributed to the complex hierarchical microstructure, which consists of prior austenite grains, packets, blocks and martensitic laths as illustrated schematically in Figure 1.5. This precipitate strengthened microstructure enables improved creep strength via grain boundary, precipitate and solid solution strengthening mechanisms. Since the original development of Grade 91 steel, many modifications and improvements, due

1. Introduction

to the incorporation of additional precipitates and solutes have been made. Each of these strengthening mechanisms is discussed in detail in Chapters 2 and 3.

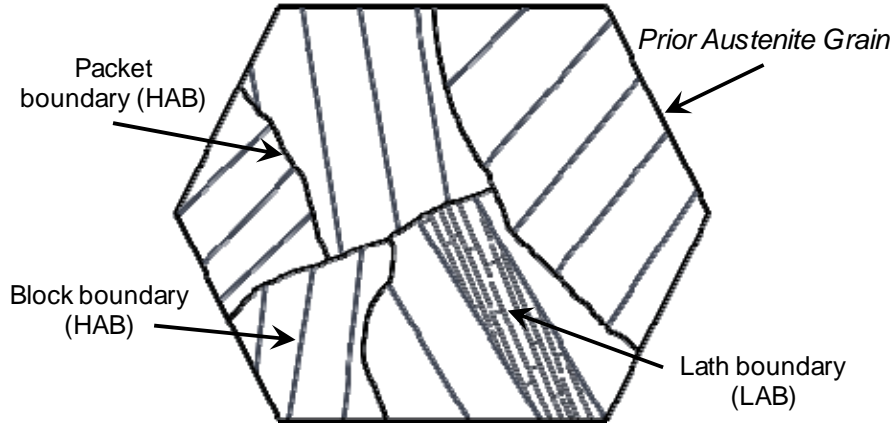


Figure 1.5: Schematic representation of the hierarchical microstructure of 9-12Cr steels.

The maximum operating temperatures of various power plant materials are summarised in Figure 1.6. As is evident from this comparison, the 9Cr steels (e.g. P91, E911 and P92 steels) and the stainless steels (AISI 316, 321 and 347) demonstrate excellent high temperature properties. Figure 1.6 also highlights the importance of chemical composition – the primary difference between P91 and P92 steels, for example, is the presence of 1.8 wt.% tungsten in P92 steel. Thus, small variations in composition can have a substantial impact on the high temperature strength of candidate materials. However, Figure 1.6 only highlights the high strength performance of candidate materials and does not account for oxidation and corrosion performance, cost, flexible operation and thermal expansion of candidate materials.

1. Introduction

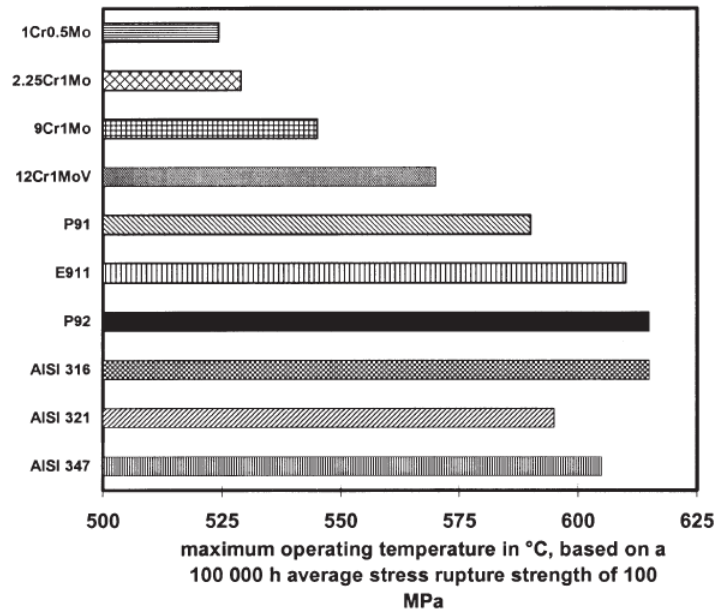


Figure 1.6: Maximum operating temperatures of various power plant steels [Ennis and Czyrska-Filemonowicz, 2003].

Due to the large cost associated with commissioning new plant and retrofitting old power plants, material amounts for large-scale components such as plant header and piping systems must be kept at a minimum. Figure 1.7a compares the cost of a variety of steels for high temperature applications. The material cost increases, almost exponentially, with increasing allowable temperature. For example, the inclusion of nickel, which can be beneficial for material toughness, significantly increases cost. As highlighted in Figure 1.7b, the use of 9Cr steels when compared with low alloy CrMoV steels enables the pipe wall thickness to be reduced by up to 50 %, reducing the relative cost of commissioning a power plant.

1. Introduction

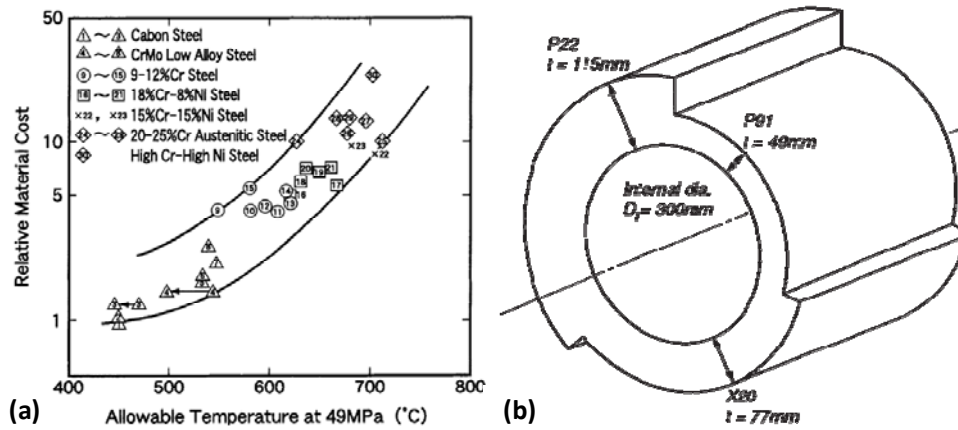


Figure 1.7: The dependence of material choice on (a) cost as a function of allowable temperature for various materials at a load of 49 MPa [Masuyama, 2001] and (b) potential reduction in wall thickness available using 9-12Cr steels [Abson and Rothwell, 2013].

Hence, due to their high creep strength, excellent oxidation performance and relative expense, 9-12Cr steels are used extensively for plant header and piping systems. However, as power plants move to flexible operation at higher temperatures, premature failures of components have been observed, sometimes at as little as 5 % of the design life. Hence, the thermo-mechanical fatigue (TMF) and fatigue-creep performance of candidate materials must be investigated in detail. The complexity of the microstructure and the variations in mechanisms of deformation under different loading conditions for next generation power plants requires advanced materials modelling techniques to carefully assess the challenges faced.

1.4. A multi-scale approach for the design and assessment of 9Cr steels

The transition to flexible plant operation at high temperatures has resulted in the requirement for analysis of a much broader range of loading scenarios, pushing the current generation of materials to their limits. Due to the large cost and duration involved in high temperature creep-fatigue and TMF tests, particularly under realistic loading conditions (e.g. slow strain-rates), a multi-scale modelling methodology, calibrated and validated against relevant test data, can facilitate the characterisation of new candidate

1. Introduction

materials and reduce the experimental costs involved with the verification process. The concept of a materials design tool (MDT) for creep-fatigue-corrosion resistant materials and components is introduced here, as depicted in the flowchart of Figure 1.8. The various elements of this design tool are now briefly outlined and it should be noted that this thesis will focus on a number of key aspects; namely macro-scale model development and experimental testing.

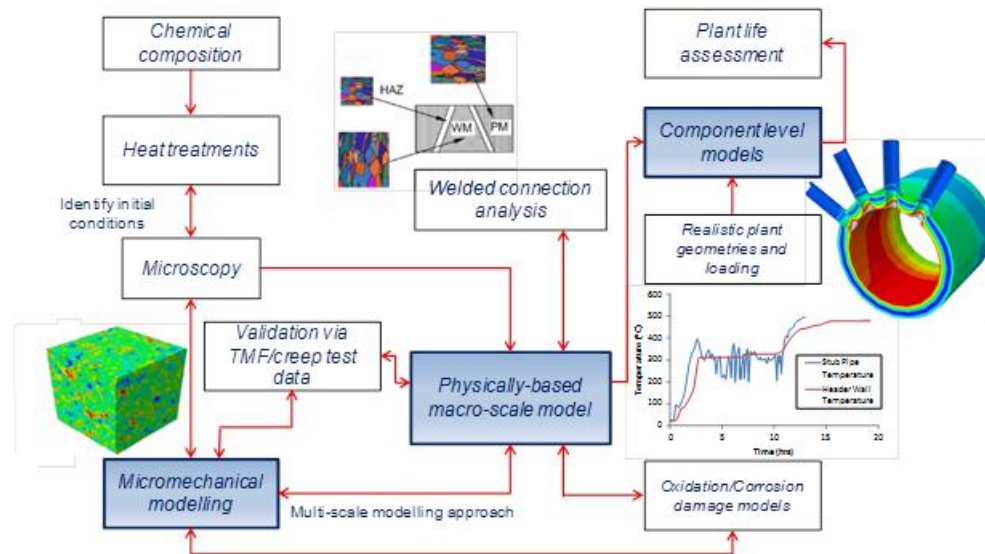


Figure 1.8: Proposed materials design tool for the development of advanced alloys for next generation power plants.

Chemical composition and heat treatment have a significant effect on the performance of the material due to the complex hierarchical microstructure of 9Cr steels. For example, the inclusion of small amounts of boron can provide thermal stability with respect to precipitates [Abe *et al.*, 2008] and more severe heat treatments can result in a coarser microstructure [Ennis and Czyska-Filemonowicz, 2003], which may prove beneficial to high temperature creep, while hindering the fatigue performance. Thus, these effects must be addressed during the design of the materials to ensure optimum material performance for the potentially broad set of loading conditions.

In order to characterise the material behaviour for next generation loading conditions, a wide range of high temperature testing is required, including

1. Introduction

fatigue, fatigue-creep and corrosion testing. There is also a requirement for microstructural analysis including optical microscopy at the grain level, scanning electron microscopy (SEM) to characterise the block structure and fractography and transmission electron microscopy (TEM) studies to achieve high resolution at the martensitic lath level and to acquire critical information on nano-scale precipitates in the material.

Micromechanical modelling, at the block (meso-scale) and lath (micro-scale) levels, is important for developing physically-based models to simulate the microstructural degradation mechanisms in 9Cr steels. These models can establish a microstructure from electron backscatter diffraction (EBSD) measurements, for example, and can be validated against monotonic and fatigue tests from the experimental program. Such micromechanical models should be based on a set of primary microstructural variables, including martensitic lath width, dislocation density and precipitate spacing and must be capable of operating through the range of strain-rates observed in modern power plant.

Central to the successful development of a materials design tool is a macro-scale material model which provides a mechanistic link between micromechanical modelling and simulations at the component level. Such a material model is required to simulate large-scale realistic geometries efficiently (e.g. welded, multi-tube, heavy-wall section headers), whilst at the same time, be capable of predicting (i) the constitutive behaviour observed in mechanical tests, (ii) the effects of microstructural degradation and (iii) the salient mechanisms of deformation. Thus, this thesis develops a macro-scale material model with variable strain-rate sensitivity, as well as identification, incorporation and evolution of a set of key microstructural variables which can be implemented in the macro-scale model. The set of key microstructural variables will also be determined based on the primary strengthening mechanisms under creep and cyclic loading, in such a manner to advance the microstructure under fatigue loading and through the development of a parallel microstructure-sensitive creep model, provide creep deformation based on the cyclically-degraded microstructure.

1. Introduction

The development of a multi-scale materials design tool is intended to have important applications to welded connections. As failures of power plant components typically occur in welded connections, the development of a microstructure-sensitive modelling approach at the macro-scale will enable more accurate modelling of the heterogeneous microstructure of welded connections. It is not typically possible, for computational overhead reasons, to simulate the weld-induced heterogeneity using micromechanical models due to the small length-scales associated with the latter. Hence, a microstructure-sensitive macro-scale material model is required for welded analysis and design. Furthermore, the advanced material modelling capability developed as part of the multi-scale materials design tool will also enable key microstructural parameters, such as grain size and precipitate spacing, to be optimised for creep-fatigue deformation under realistic loading conditions. Through the development of a microstructure-sensitive model for creep-fatigue deformation and subsequent macro-scale simulations of realistic geometries, the key microstructural parameters can be achieved via careful consideration of (i) chemical composition and (ii) heat treatment.

1.5. Aims and Objectives

The aim of this thesis is to characterise, understand and simulate the complex high temperature cyclic plasticity behaviour of 9Cr steels and to investigate the primary factors affecting the performance and structural integrity of such alloys, with particular attention focused on current and next generation power plant loading conditions. There are four key elements to the work:

1. The development of a unified cyclic viscoplastic modelling framework for variable strain-rate sensitivity for extrapolation from short-term tests to longer-term (realistic plant) operating conditions and implementation within the commercial finite element code Abaqus are key objectives of this thesis. The material model needs to be calibrated and validated across a broad range of loading conditions, including varying strain-ranges, strain-rates and

1. Introduction

temperatures, for application to realistic geometries under flexible loading conditions.

2. Another objective is the experimental characterisation of the high temperature low cycle fatigue (HTLCF) and TMF behaviour of P91 steel. This thesis will also seek to investigate and understand the mechanisms of deformation under high temperature fatigue loading.
3. This research characterises, for the first time, the HTLCF performance of MarBN (9Cr-3W-3Co-V-Nb) steel. MarBN is a new 9Cr steel with 3 % tungsten (by weight) and small amounts of boron included to improve creep strength. The high temperature cyclic plasticity performance of MarBN is compared with that of existing 9Cr steels, to comparatively assess the potential for MarBN to operate under high temperature creep-fatigue-corrosion loading conditions.
4. A dislocation-mechanics based high temperature microstructure-sensitive modelling framework will also be developed and this can act as an interface between the physical mechanisms at the micro-scale and the macro-scale. This will allow robust, effective and efficient modelling of the effects of microstructural variables on the mechanical behaviour of realistic component geometries. This is achieved through the identification, inclusion and evolution of a set of key microstructural parameters. This approach will also enable optimisation of initial values of the microstructural variables and can be potentially combined with existing creep models to allow microstructure-sensitive creep-fatigue life prediction of components using a consistent set of microstructural variables.

1.6. Thesis Overview and Scope of Research Work

Chapter 2 contains a detailed background and review of the literature relevant to this research work, incorporating descriptions of fatigue and creep testing and numerical modelling, as well as microstructural investigations of 9Cr steels. Chapter 2 also discusses the microstructure, strengthening mechanisms and mechanisms of deformation for 9Cr steels.

1. Introduction

Chapter 3 presents the results of high temperature fatigue test programs on two 9Cr steels, P91 and MarBN, including HTLCF and TMF testing across a range of temperatures, strain-rates and strain-ranges. Chapter 3 also includes discussion on the effect of chemical composition and heat treatment on the fatigue performance of 9Cr steels.

In Chapter 4, a novel unified cyclic viscoplastic material model, specifically designed for strain-rate independent material parameters is developed, and implemented in a UMAT user material subroutine. The UMAT is subsequently applied to isothermal fatigue and TMF loading conditions and successfully compared to P91 test data available in the literature. A step-by-step parameter identification methodology is also presented in Chapter 4, including calibration and validation of the unified cyclic viscoplastic modelling framework against the HTLCF test results of Chapter 3.

Chapter 5 focuses on applications of the material model to (i) TMF and (ii) multi-axial loading conditions, to verify the use of the UMAT user material subroutine for such complex situations and explore some key issues for next generation plant components.

A new microstructure-sensitive unified cyclic viscoplastic modelling framework is presented in Chapter 6, based on a dislocation-mechanics framework. This model includes microstructural parameters for evolution of martensitic lath width, dislocation density and precipitate radii and volume fraction. This model is calibrated and validated against (i) experimental data from Chapter 3 and (ii) measured microstructural evolution data from the literature. Significant modifications to this model are presented in Chapter 7, most notably, a dislocation-mechanics framework for low-angle boundary dislocation annihilation and the inclusion of a back-stress for dislocation pile-up formation at grain boundaries.

Chapter 8 presents the main conclusions, outlines the limitations of the work presented and includes a set of recommendations for future work.

2. Background and Literature Review

2.1. Introduction

The design and characterisation of candidate materials for high temperature applications is a multi-scale process involving (i) microstructural analysis, (ii) experimental programs and (iii) computational constitutive and failure models. The type of loading and service history to which the material is subjected can have significant implications for the material performance and primary mechanisms of deformation. Furthermore, small changes to chemical composition or heat treatment can have a dramatic effect on the performance of materials.

Due to the complex precipitate-strengthened hierarchical microstructure of 9-12Cr steels and associated microstructural evolution and degradation during loading, a detailed understanding of the strengthening mechanisms is required, as well as knowledge of the controlling mechanism of deformation for a given loading condition. Such information is also required to improve upon the current state-of-the-art materials and hence to provide component and equipment designers with adequate materials knowledge for harsh and complex loading conditions. A comprehensive experimental program, including tensile testing, thermal aging and oxidation, fatigue, creep, fatigue-creep and creep-fatigue testing is required to obtain the information necessary to identify the controlling mechanisms of deformation.

Furthermore, to complement this, there is a requirement to be able to simulate (i) the constitutive behaviour of candidate materials and (ii) the failure behaviour of realistic components. The development of material models from a mechanistic and physical viewpoint is crucial to generating more accurate simulations of realistic loading conditions and associated microstructural degradation. The generation of such models should consider effects such as heat treatment to aid with identification of optimum initial material microstructures to withstand complex creep-fatigue-corrosion loading histories.

2. Background and Literature Review

The following review and discussion of the literature focuses on the primary factors affecting material performance as highlighted above. In particular, this chapter presents a theoretical background for the material models developed in the thesis and a review of the literature relevant to the high temperature degradation of 9-12Cr steels and associated mechanisms of deformation in such materials. Firstly, the creep of metals is reviewed in Section 2.2, including the primary mechanisms of creep deformation, with the fatigue of metals reviewed in Section 2.3. The testing and modelling of 9-12Cr steels are reviewed in Sections 2.2.2, 2.3.1 and 2.4, including thermal ageing, creep, fatigue and various interactions of these conditions. Section 2.5 reviews the primary methods of strengthening in steels and Section 2.6 highlights the contribution of chemical composition and heat treatment on the high temperature performance of 9-12Cr steels and the role of microstructure on high temperature deformation. Section 2.7 highlights how this thesis builds upon the current literature to improve understanding of 9Cr steels under flexible operation.

2.2. Creep of steel alloys

Creep is the time-dependent accumulation of strain under a constant applied load. Creep of metals typically occurs at 0.3 to 0.4 of the melt temperature, T_m , with the melt temperature in Kelvin [Ashby and Jones, 2012]. For 9-12Cr steels, the melt temperature is in excess of 1800 K [Yaghi et al., 2005] and hence, viscous effects are expected to be important at operating temperatures in excess of 700 K. When viscous effects are important, the strain becomes a function of the applied stress, σ , time, t , and temperature, T :

$$\varepsilon = f(\sigma, t, T) \quad (2.1)$$

For a uniaxial constant load test, with an applied stress of σ , the resulting time-strain response is illustrated schematically in Figure 2.1. The total strain is the sum of the elastic and creep strain components, such that:

2. Background and Literature Review

$$\varepsilon = \varepsilon^{\text{el}} + \varepsilon^{\text{pl}} \quad (2.2)$$

where ε^{el} is elastic strain and ε^{cr} is creep strain. The elastic contribution is simply defined using Hooke's law ($\varepsilon^{\text{el}} = \sigma/E(T)$, where $E(T)$ is temperature-dependent Young's modulus). However, the creep strain is more complex, as it is made up of three main strain contributions, namely (i) primary creep, (ii) secondary or steady-state creep and (iii) tertiary creep, as highlighted in Figure 2.1.

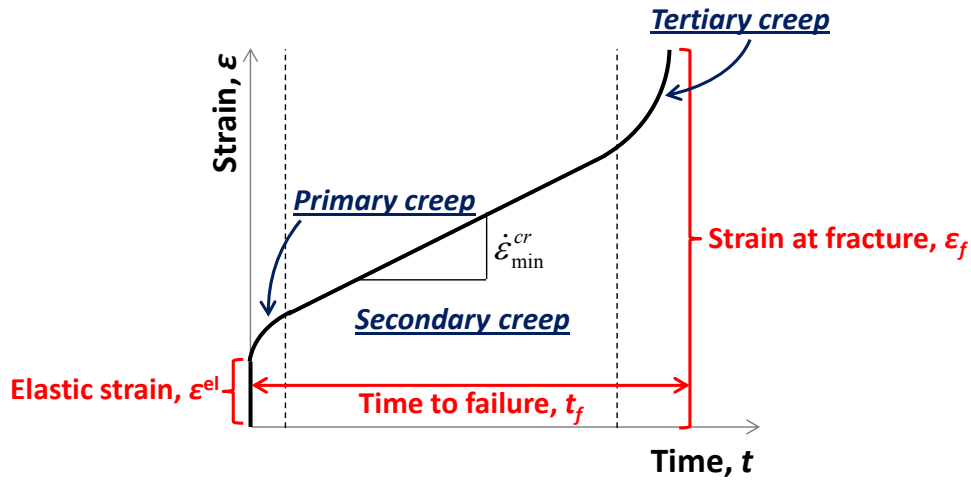


Figure 2.1: Time-strain response of a metal subjected to a constant load test.

The level and duration of the primary creep stage is related to hardening of the material due to mechanisms such as precipitate and solid solution strengthening, as discussed in more detail in later sections. This results in a deceleration of the creep strain-rate, as shown in Figure 2.2a. The duration of the primary creep stage is material dependent and can be quite long for 9Cr steels due to the complex nature and evolution of the microstructure [Abe, 2015]. As such, the steady-state creep region is typically of short duration compared to other materials.

As highlighted in Figure 2.2a, the steady-state creep region corresponds to the region of minimum creep strain-rate (MSR). Figure 2.2b plots the typical MSR-stress response observed for metals on a log-log plot. For most metals, two distinct linear regions (on the log-log plot) are observed, one region with a slope of approximately unity and the other with a slope of

2. Background and Literature Review

between 3 and 12. Thus, the constitutive relationship between the steady-state creep strain-rate, $\dot{\epsilon}_{\min}^{\text{cr}}$, and the applied stress, σ , can be defined using the Norton steady-state creep law [Norton, 1929], presented here with an Arrhenius term included to provide temperature-dependence:

$$\dot{\epsilon}_{\min}^{\text{cr}} = A_0 e^{-(Q_{\text{cr}}/\bar{R}T)} \sigma^n \quad (2.3)$$

where A_0 is a material constant, Q_{cr} is creep activation energy, \bar{R} is the universal gas constant, T is temperature in Kelvin and n is the Norton creep exponent, the slope of the (corresponding) linear region of the $\log(\text{MSR})$ - $\log(\sigma)$ plot. The creep activation energy, Q_{cr} , and material constant A_0 can be identified from the slope and intercept of the natural logarithm of MSR plotted as a function of the inverse of temperature (see inset of Figure 2.2b).

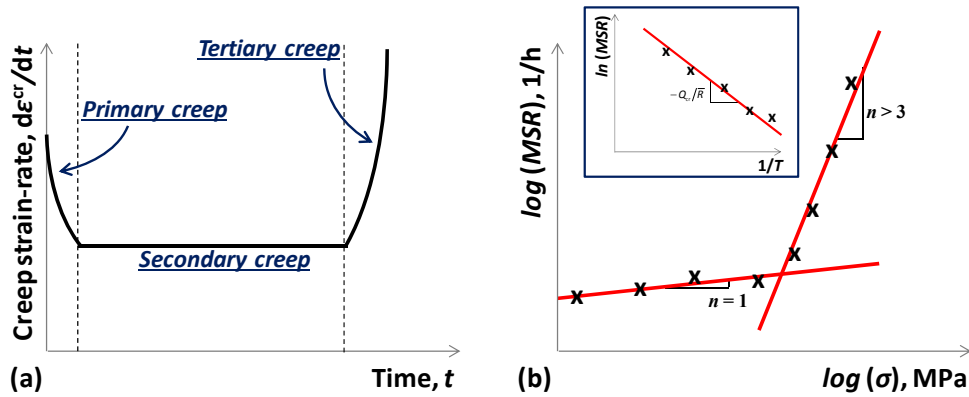


Figure 2.2: Schematic representation of (a) the variance in creep strain-rate as a function of time and (b) the effect of applied stress on the minimum creep strain-rate (MSR). The inset includes a schematic representation of the variation of MSR with the inverse of temperature.

As creep deformation continues, creep voids and cavities begin to appear along grain boundaries, as shown schematically in Figure 2.3. Creep voids typically initiate at the point of intersection of three grains (triple point) or at inclusions such as precipitates distributed along grain boundaries. The formation of voids results in a reduced effective cross sectional area, leading to a decrease in material strength and therefore structural integrity of the component. As the time increases, these voids begin to coalesce and form small cracks (across a number of grains within the material), leading to the

2. Background and Literature Review

development of a macroscopic crack and eventually resulting in rapid failure of the specimen (i.e. due to tensile overload of the specimen as a result of a reduced load-bearing area). The formation of voids is termed creep damage and occurs alongside microstructural degradation in a given material. As voids usually form at grain boundaries, a larger grain size (and, hence, a reduced number of locations for voids to initiate) is just one method for improving the creep strength of a given material. Other methods include (i) adding favourable alloying elements and (ii) careful choice of heat treatment procedures to retard microstructural degradation and hence, improve the materials resistance to creep deformation.

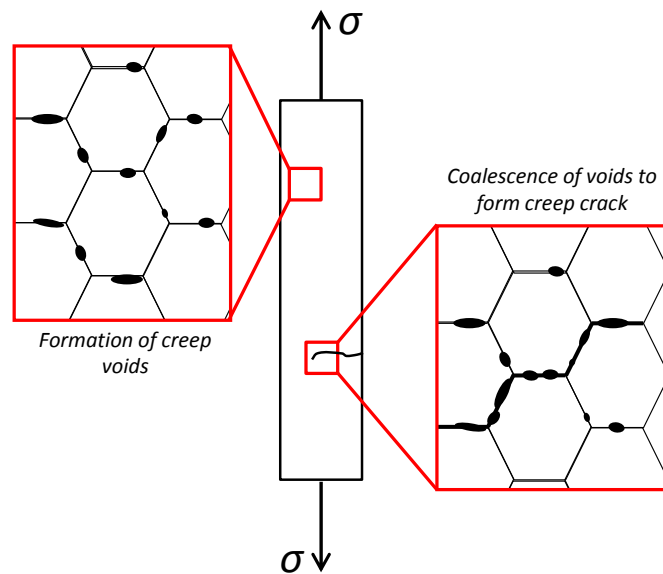


Figure 2.3: Creep void formation and coalescence of voids to form a creep crack in a creep test specimen.

It is evident from Equations (2.1) and (2.3) that both temperature and stress play a pivotal role in creep deformation. As expected, increasing the stress or temperature leads to increased strain and hence, reduced life, as illustrated from the measured data in Figure 2.4 for P91 steel. Figure 2.4a illustrates the effect of varying the stress applied at a constant temperature of 600 °C, where a wide range of time to failure is observed across a stress range from 80 MPa to 175 MPa. An even more detrimental effect is observed when investigating the effect of temperature on the strain produced, as presented in Figure 2.4b. The data acquired at 600 °C [*Panait*

2. Background and Literature Review

et al., 2010b] indicate a creep life of approximately 113,000 hrs, whereas the data at 650 °C [Hyde *et al.*, 2006] show that the creep life has reduced to just over 400 hrs. It is this inability to withstand increased temperatures which proves to be the key limiting factor in achieving increased plant operating temperatures and hence, improved plant efficiencies. The reason for decreased performance is related to (i) microstructural instabilities and degradation and (ii) the mechanisms of creep deformation at varying stresses and temperatures. However, it should be noted that the P91 material presented in Figure 2.4 is a significantly weaker grade of P91 material (defined as Bar 257) and estimated to be approximately 6 to 10 times weaker than conventional P91 piping steels [Hyde *et al.*, 2006; Magnusson and Sandström, 2009]. Figure 2.5 presents a comparison of Bar 257 with a conventional P91 material from the literature at a temperature of 650 °C and applied stress of 70 MPa. Taking this reduced performance of Bar 257 into account, a creep strength reduction factor in excess of 25 exists for increasing the operating temperature from 600 °C to 650 °C. The comparison of Figure 2.5 highlights the effect of chemical composition on the performance of 9Cr steels. Bar 257 has increased Al content compared with conventional P91 steel, resulting in reduced MX precipitate strengthening due to the formation of AlN nitrides [Magnusson and Sandström, 2009]. This result also highlights the importance of MX precipitates to the creep strength of 9Cr steels. The microstructure of 9Cr steels is discussed in more detail in Section 2.6.

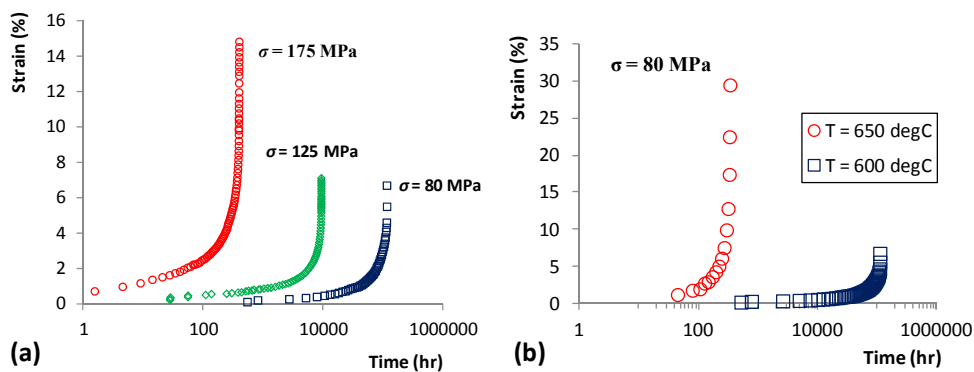


Figure 2.4: The effect of varying (a) applied stress at 600 °C (175 MPa and 125 MPa – [Orlová *et al.*, 1998], 80 MPa – [Panait *et al.*, 2010b]) and (b) temperature

2. Background and Literature Review

at a constant applied stress of 80 MPa at 600 °C [Panait *et al.*, 2010b] and 650 °C [Hyde *et al.*, 2006].

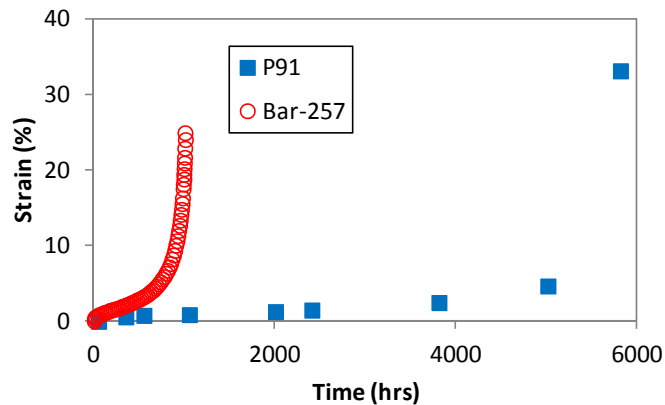


Figure 2.5: Comparison of the effect of chemical composition (Al content) on the creep strength of Bar 257 P91 steel [Hyde *et al.*, 2006] and conventional P91 pipe material [Abd El-Azim *et al.*, 2013] for an applied stress of 70 MPa at a temperature of 650 °C.

2.2.1. Mechanisms of creep deformation

As illustrated in the results presented in Figure 2.4, stress and temperature play an important role in material degradation due to creep deformation. Various combinations of stress and temperature will activate different creep mechanisms of deformation, which can be summarised using deformation mechanisms maps [Ashby, 1972]. A deformation mechanisms map presents the stress-temperature relationship in metals via plotting the ratio of shear stress to shear modulus (τ/μ) against the homologous temperature (T/T_m). Figure 2.6 presents a schematic representation of a typical deformation mechanisms map for a steel alloy, with bulk and grain boundary diffusion processes corresponding to deformation with a creep exponent, n , of approximately unity and dislocation creep corresponding to a material response with an exponent of greater than 3 (see Figure 2.2b). The primary mechanisms of creep deformation are described in the following sections.

2. Background and Literature Review

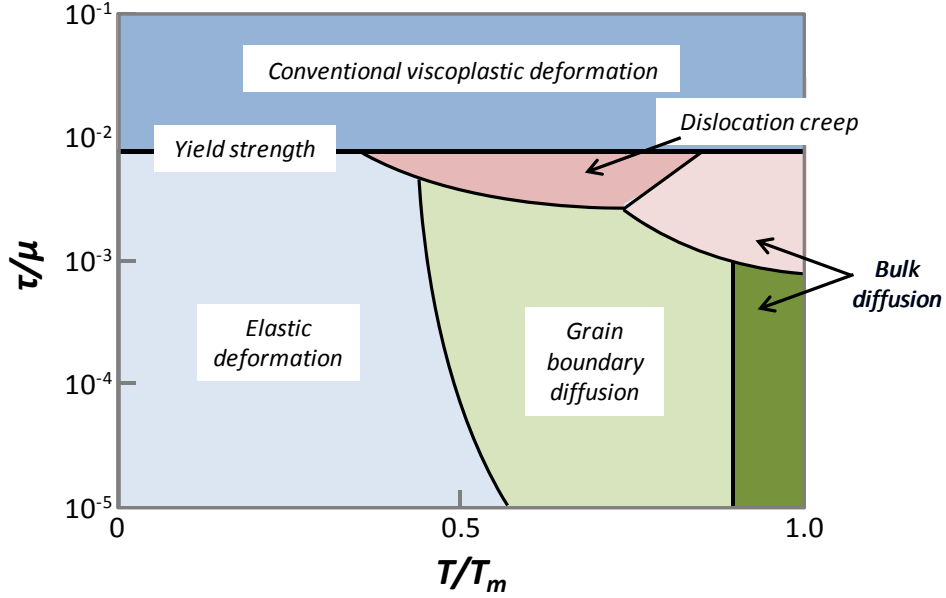


Figure 2.6: Deformation mechanisms map.

Diffusion-based creep mechanisms: For low stress regimes and intermediate to high temperatures, the primary mechanism of creep deformation is Coble creep [Coble, 1963], in which grain-boundary diffusion occurs under a constant stress, σ , i.e. atoms diffuse along one region of interfaces such as grain boundaries to other regions of the grain boundary. This creep mechanism is illustrated schematically in Figure 2.7 and the minimum creep strain-rate is given as [Hertzberg, 1996]:

$$\dot{\epsilon}_{\min}^{cr} = \frac{50\sigma D_{GB} b^4}{k_B T d^3} \quad (2.4)$$

where D_{GB} is grain boundary diffusivity, b is the magnitude of Burger's vector, k_B is Boltzmann's constant and d is grain size.

At higher temperatures, the diffusion of atoms occurs within the grain (crystal) due to bulk diffusion, as illustrated schematically in Figure 2.7. Atoms will diffuse through the material from boundaries experiencing tensile loading, via a vacancy migration process, to a boundary under compressive loading [Herring, 1950; Nabarro, 1948]. This is Nabarro-Herring creep, with a minimum creep strain-rate defined as [Hertzberg, 1996]:

2. Background and Literature Review

$$\dot{\epsilon}_{\min}^{cr} = \frac{7\sigma D_v b^3}{k_B T d^2} \quad (2.5)$$

where D_v is volume diffusivity through the grain interior.

Nabarro-Herring and Coble creep are both mass transport (diffusion) creep mechanisms in which deformation occurs due to the presence of point defects, such as vacancies, in the material. From Equation (2.4) and Equation (2.5), both of these mechanisms of creep deformation are strongly dependent on the grain size, d , with an increased grain size also reducing the steady-state creep strain-rate at low stresses in conjunction with decreasing the number of potential sites for void formation. This highlights the importance of microstructure on material deformation and the need to account for evolving microstructures during high temperature deformation. Coble type creep is also more sensitive to varying grain size than Nabarro-Herring creep, such that the control of grain size during heat treatment is extremely important for components operating in the low stress and intermediate-to-high temperature regime, an important regime for power plant components. Furthermore, as grain boundaries have a disordered crystal structure, grain boundary diffusion (i.e. Coble creep) occurs at a much quicker rate than bulk diffusion as the activation energy barrier is much lower at the boundaries.

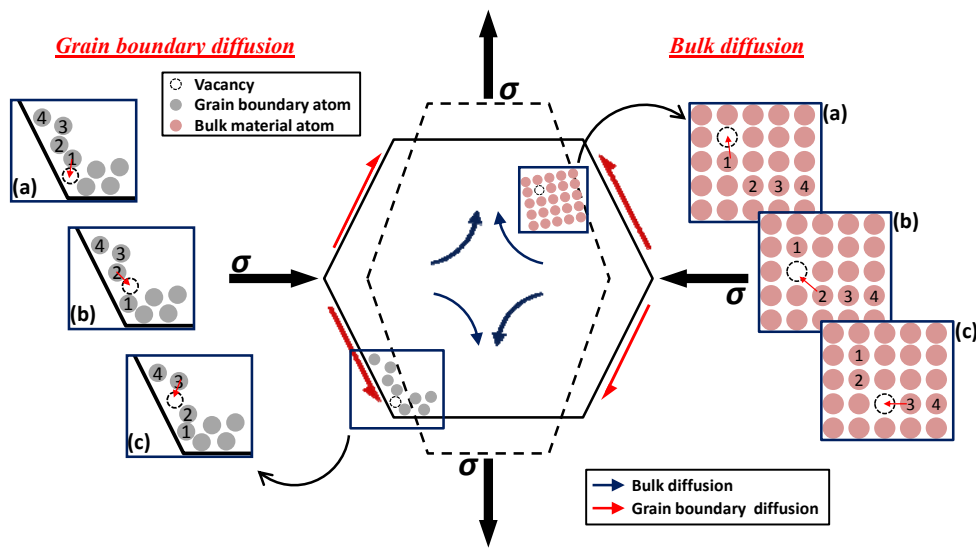


Figure 2.7: Grain boundary diffusion and bulk diffusion processes during creep deformation with an applied stress, σ , in steels.

2. Background and Literature Review

Dislocation-based creep mechanisms: At higher stresses, dislocation creep is the dominant mechanism of creep deformation. Under conventional viscoplastic deformation, a dislocation will normally glide through the material until it becomes immobilised by interacting with obstacles such as precipitates, solutes or other dislocations. Due to the diffusion of atoms (away from the bottom of the dislocation) at high temperatures, dislocations can move upward off their glide path due to a climb process, as illustrated schematically in Figure 2.8, resulting in further viscoplastic slip. Dislocation creep can be modelled using the Norton creep law of Equation (2.3) and represents a key mode of deformation for plant components at stress concentrations such as welded connections with the transition to flexible plant operating at high strain-rates.

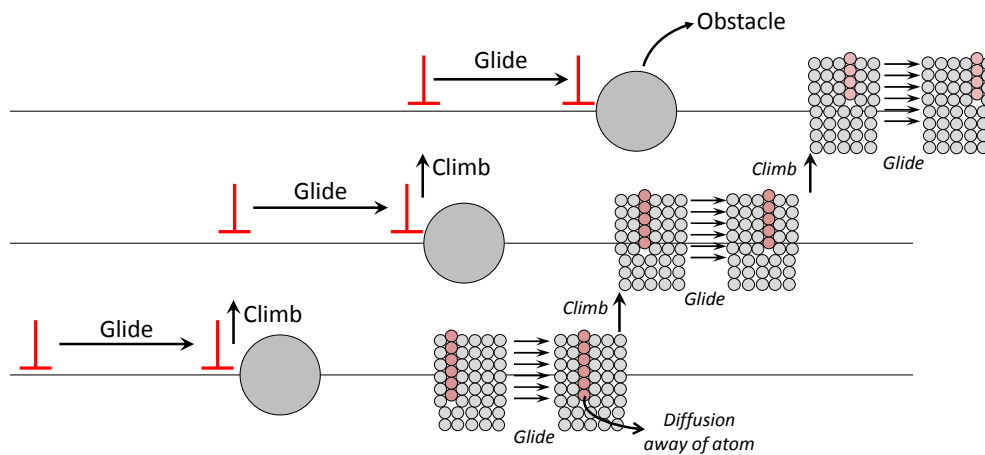


Figure 2.8: Dislocation glide and dislocation climb processes in metals under high temperature deformation.

2.2.2. Creep testing of power plant materials

Extensive studies on creep testing of 9-12Cr steels have been carried out to date, e.g. Abe and co-workers [2004; 2008], Hyde and co-workers [2006], Orlová *et al.* [1998] and Panait *et al.* [2010a; 2010b] have all conducted creep tests under various loads and temperatures on 9Cr steels. As can be seen from the creep test results of Figure 2.4, temperature and stress have a large effect on the mechanism, with increasing stress and temperature resulting in more rapid microstructural degradation of components and hence, shorter creep rupture times. Due to the combination of strengthening

2. Background and Literature Review

mechanisms within the microstructure of 9Cr steels, a long primary creep stage is a characteristic of such steels, as can be seen in Figure 2.9a for MarBN steels and Figure 2.9b presents the creep rupture data for a variety of 9Cr steels. The wide variation in time to rupture is due to variations in microstructure, with the inclusion of tungsten and boron contributing significantly to the differences between T91 and the 9Cr-3W-3Co-VNb steels. Under constant strain conditions, stress relaxation occurs in 9Cr steels, as highlighted in Figure 2.10. Following the initial relatively rapid decrease in stress, a steady-state value is obtained and as illustrated in Figure 2.10, the relaxation behaviour is temperature-dependent.

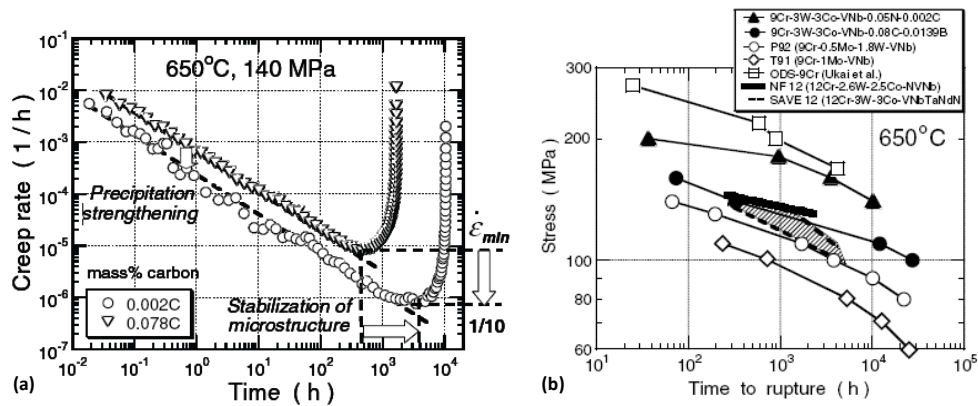


Figure 2.9: Creep testing of 9Cr steels for (a) strain-rate versus time for a MarBN steel with varying carbon compositions for an applied stress of 140 MPa at a temperature of 650 °C [Abe, 2008] and (b) creep rupture data for various high temperature power plant steels [Abe, 2004].

2. Background and Literature Review

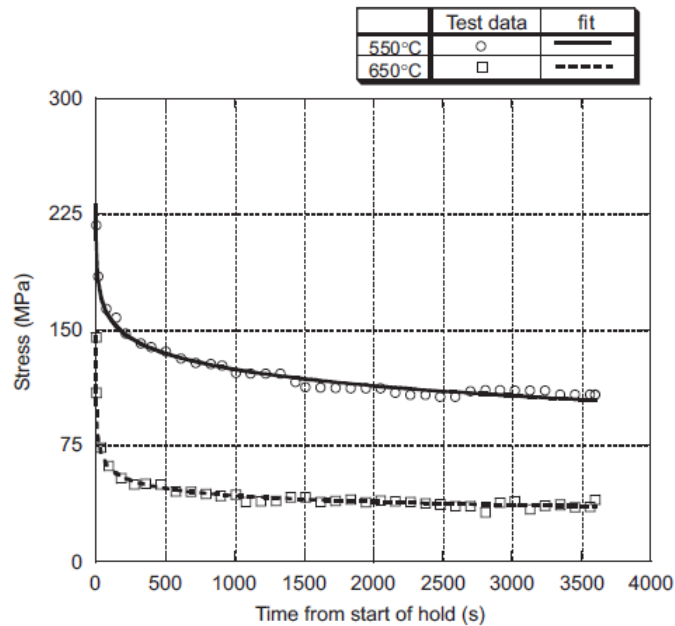


Figure 2.10: Stress relaxation behaviour in P91 steel [Takahashi, 2008].

2.3. Fatigue of steel alloys

Fatigue is the progressive degradation of a material subjected to cyclic loading, leading to the generation of micro-cracks and ultimately fatigue crack growth, until failure by fatigue occurs. Normally, these fatigue cracks lead to a brittle-like failure, necking does not typically occur in cyclic deformation due to the strains being much lower than the material ductility. The two primary classifications of fatigue are high cycle fatigue (HCF) and low cycle fatigue (LCF). These fatigue classifications are shown schematically in Figure 2.11, with HCF normally constituting at least 10,000 cycles to failure. The primary difference between high and low cycle fatigue failure relates to crack initiation and crack growth. Typically for LCF conditions, crack initiation occurs quite early in the fatigue life, sometimes as low as 3 to 10 % of the fatigue life, with a long crack growth (or propagation) period [Stephens *et al.*, 2001]. On the other hand, HCF failures are normally characterised by a long fatigue crack initiation period. Furthermore, LCF tests illustrate both elastic and plastic (or viscoplastic) behaviour, where the LCF process can be divided into four main stages, (i) cyclic hardening (or softening), (ii) crack initiation, (iii) crack propagation and (iv) final fracture [Hertzberg, 1996]. As illustrated in Figure 2.11b, the

2. Background and Literature Review

number of reversals, $2N_f$, to failure under fatigue loading can be approximated by combining the strain-based fatigue life methods of Basquin [1910] for HCF and Coffin-Manson [Coffin, 1954; Manson, 1953] for LCF:

$$\frac{\Delta\varepsilon}{2} = \frac{\sigma_f'}{E}(2N_f)^b + \varepsilon_f'(2N_f)^c \quad (2.6)$$

where $\Delta\varepsilon$ is total strain range, σ_f' is the fatigue strength coefficient, ε_f' is material ductility and b and c are material constants.

As modern plant components are subjected to viscoplastic deformation at welded connections and regions of stress concentrations, LCF characterisation represents a key step in the assessment of candidate materials for power plant applications. Furthermore, although a fatigue crack leading to zero load-bearing capability may render the component failed due to fatigue, shorter-term fatigue loading can also have a major impact on microstructural evolution and degradation of the material, leading to significant implications, and possibly detrimental effects, for interactions with other loading mechanisms such as creep and corrosion.

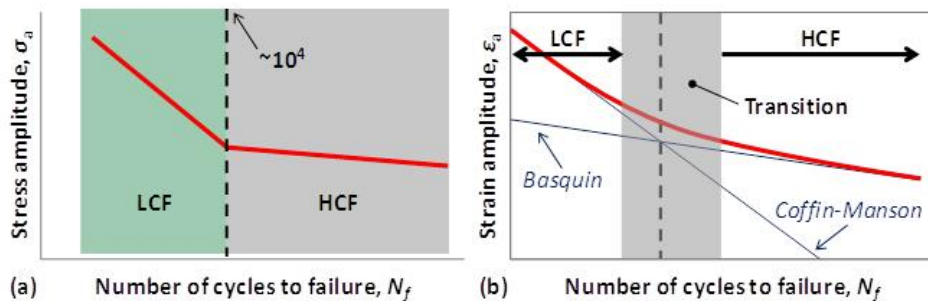


Figure 2.11: Representation of LCF and HCF regimes as a function of (a) stress amplitude and (b) strain amplitude.

Thus, there is a requirement to understand and characterise the fatigue behaviour of materials subjected to either full or partial cyclic loading. To achieve such characterisation, a wide range of fatigue tests are available, including but not limited to stress relaxation, thermo-mechanical fatigue (TMF) and creep-fatigue tests. A fatigue test is defined in terms of its R -ratio, the ratio of minimum to maximum strain ($R_e = \varepsilon_{\min}/\varepsilon_{\max}$) for a strain-

2. Background and Literature Review

controlled test and the ratio of minimum to maximum stress for a stress-controlled test ($R_\sigma = \sigma_{\min}/\sigma_{\max}$).

The fractography of fatigue failures typically highlights fatigue striations in materials with secondary phase particles and is illustrated on the fracture surface of a Chinese Low Activation Martensitic (CLAM) 9Cr steel in Figure 2.12a. A single striation is indicative of a localised crack during one cycle of loading and the distance, Δa , between striations is representative of fatigue crack growth during that cycle. Beach marks are another common observation during fractography of fatigue tested specimens and represent variations in loading of the system. They are caused by variations in the stress intensity factor range, ΔK , i.e. acceleration or deceleration of the crack front [Reardon, 2011]. An example of beach marks is shown in Figure 2.12b for a railway steel.

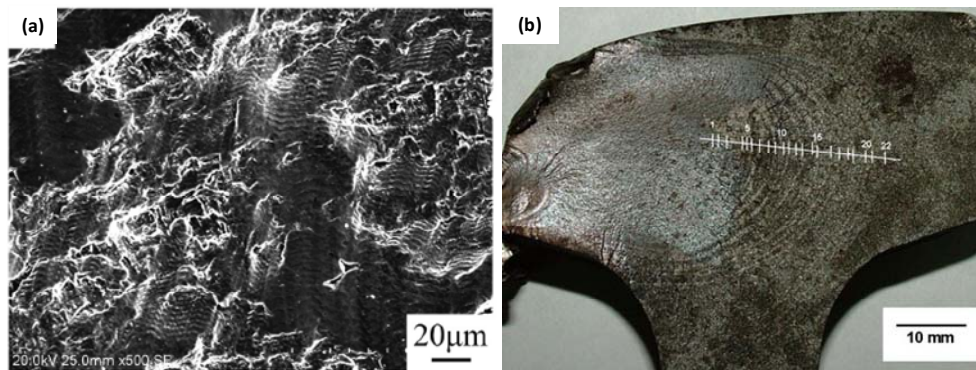


Figure 2.12: Micrograph images of (a) fatigue striations in a 9Cr martensitic steel [Hu *et al.*, 2013] and (b) beach marks in a railway steel [Source: *Transportation Safety Board of Canada*].

Cracking in components can be either transgranular, intergranular or combined, as illustrated in Figure 2.13. During fatigue loading, multiple fatigue cracks will typically start at the surface and propagate through the material with continuous loading. However, in 9Cr steels, following the initiation of a fatigue crack at the surface, intergranular crack propagation is the most common type of fatigue crack observed, due to the formation of micro-voids and micro-cracks at secondary phase particles dispersed along boundaries. This is due to the accumulation of dislocations at obstacles such as precipitates and high-angle grain boundaries, as illustrated schematically

2. Background and Literature Review

in Figure 2.14. This accumulation of dislocations generates significant back-stresses and stress concentrations leading to cracks propagating easily along the boundaries [Hu *et al.*, 2014], highlighting the importance of grain boundaries and defects such as precipitates in the failure of 9Cr steels.

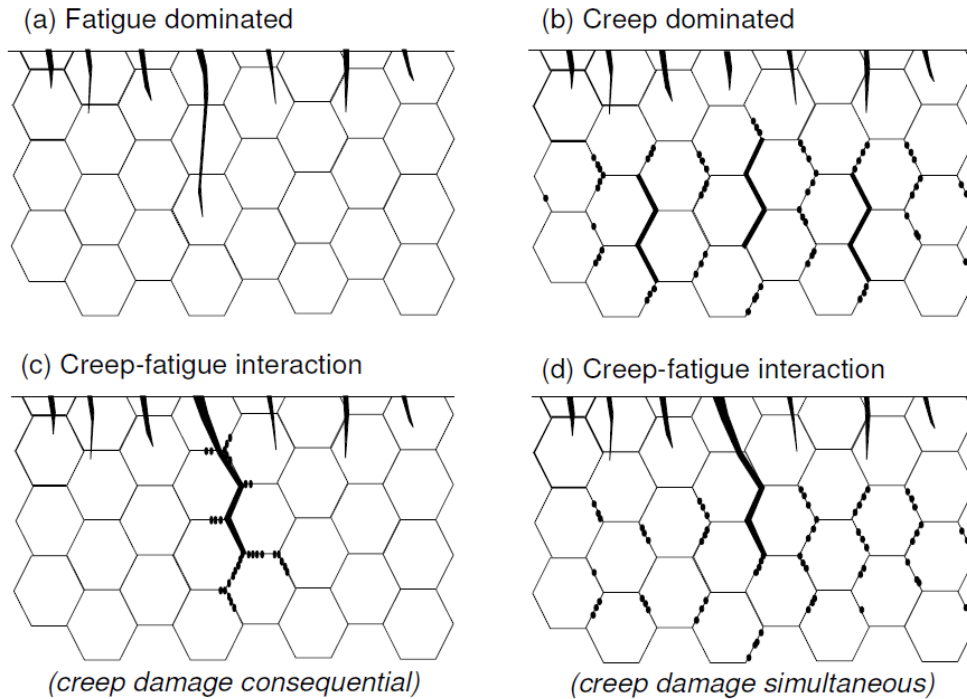


Figure 2.13: Representation of crack propagation in metals during (a) fatigue, (b) creep, (c) creep-fatigue with creep damage consequential and (d) creep-fatigue with creep damage simultaneous [Holdsworth *et al.*, 2007].

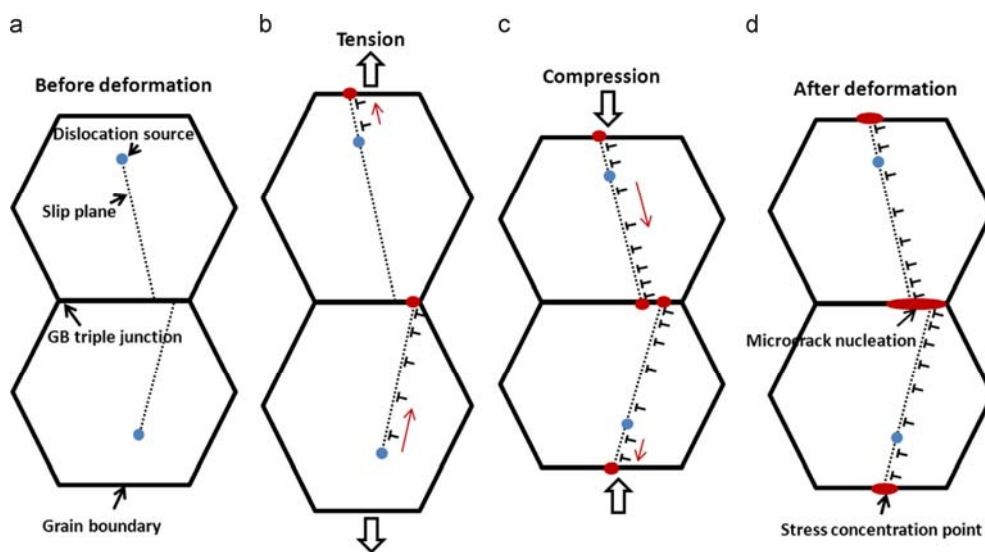


Figure 2.14: Mechanism for dislocation pile-ups and micro-crack formation in a Chinese Low Activation Martensitic (CLAM) 9Cr steel [Hu *et al.*, 2014].

2. Background and Literature Review

In terms of power plant applications, fatigue and interactions involving fatigue may exist in the following capacities:

- a) ***Isothermal fatigue:*** Mechanical load varied at a constant temperature.
- b) ***Thermal fatigue:*** Components are subjected to thermal cycles only.
- c) ***Thermo-mechanical fatigue:*** Both the load and temperature are cycled simultaneously. The thermal cycle can be in-phase (TMF-IP) or out-of-phase (TMF-OP) with the mechanical load. As current power generation transitions from base-load to intermittent mode operation, significant thermal gradients are generated during (i) complex start-up and shut down attemperation cycles, as shown in the measured plant data of Figure 1.2a and (ii) “load following” cycles similar to the data presented in Farragher *et al.* [2013b]. Thus, this flexible operation of power plant has resulted in the requirement to account for TMF of plant components.
- d) ***Fatigue-creep:*** Cyclic loading occurs with varying dwell and constant load periods.
- e) ***Creep-fatigue-corrosion:*** Creep-fatigue loading with oxidation and corrosion of components. This type of loading is most prevalent at the surface of components and can be either fireside (exposure to ash from combustion) or steamside (exposure to high temperature steam) corrosion. For example, the move to biomass co-fired power plants and higher temperature operation leads to the requirement to characterise this potential failure mechanism.

For intermittent mode operation of power plants, cyclic loading is commonly neither stress-controlled (leading to ratchetting) nor strain-controlled (leading to cyclic softening of 9Cr steels). However, due to geometrical constraints imparted on components, strain-controlled loading with dwell or constant load periods possibly represents the most realistic loading scenario, highlighting the requirement and importance of carrying out cyclic-dwell and creep-fatigue strain-controlled experiments. The

2. Background and Literature Review

following sections discuss briefly fatigue testing and the various aspects involved, with a particular focus on fatigue tests carried out on 9Cr steels.

2.3.1. Fatigue testing of 9Cr steels

Although creep testing of 9Cr steels is widespread in the literature, the fatigue testing of 9Cr steels has received limited attention by comparison. Conventional LCF tests have been carried out by Fournier *et al.* [2011], Mannan and Valsan [2006], Nagesha *et al.* [2002; 2012] and Saad and co-workers [2011a; 2011b] on P91 steel and by Giroux [2011] and Saad *et al.* [2013] for P92 steels. Figure 2.15 illustrates a selection of the stress-strain responses for various cycles and the results presented in Figure 2.16 illustrate the cyclic evolution of the various materials. As is evident from Figure 2.15 and Figure 2.16, 9Cr steels are susceptible to cyclic softening and also the Bauschinger effect is clearly visible in Figure 2.15. The strengthening observed is due to the presence of precipitates, solutes and a hierarchical grain microstructure in 9Cr steels. Cyclic softening is as a result of recovery in the material, as discussed in more detail in Section 2.6. TMF tests have been carried out on P91 steel by Mannan and Valsan [2006] and Saad *et al.* [2011a], with a sample of P91 TMF results presented in Figure 2.17, where once again cyclic softening is observed as a primary mechanism of deformation.

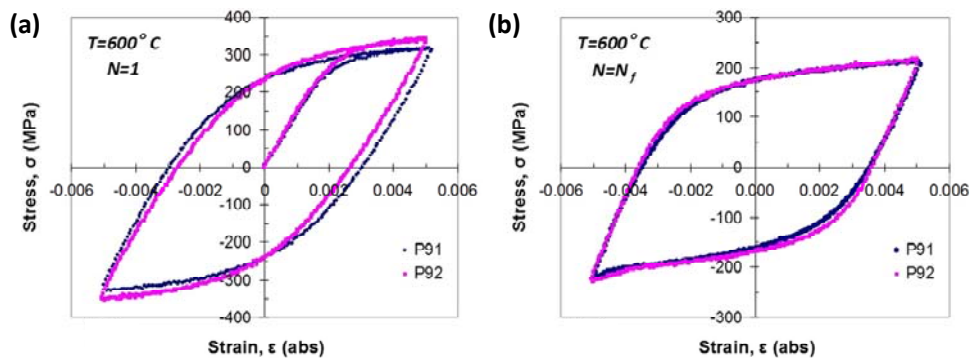


Figure 2.15: Comparison of the measured stress-strain response in P91 and P92 steels for the (a) initial and (b) failure cycle at 600 °C and a strain-rate of 1×10^{-1} %/s [Saad *et al.*, 2013].

2. Background and Literature Review

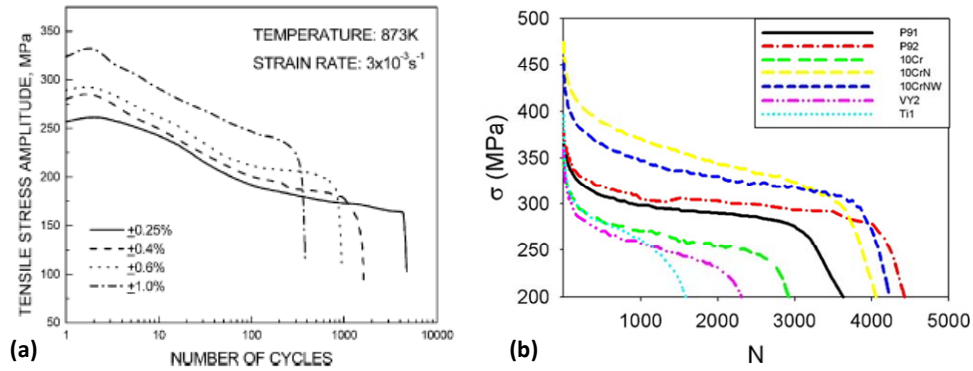


Figure 2.16: Evolution of maximum tensile stress as a function of cycles for (a) P91 steel at 600 °C and applied strain-rate of $3 \times 10^{-1} \text{ %/s}$ [Negesha *et al.*, 2002] and (b) various 9-12Cr steels at 550 °C and applied strain-rate of $2 \times 10^{-1} \text{ %/s}$ [Fournier *et al.*, 2011].

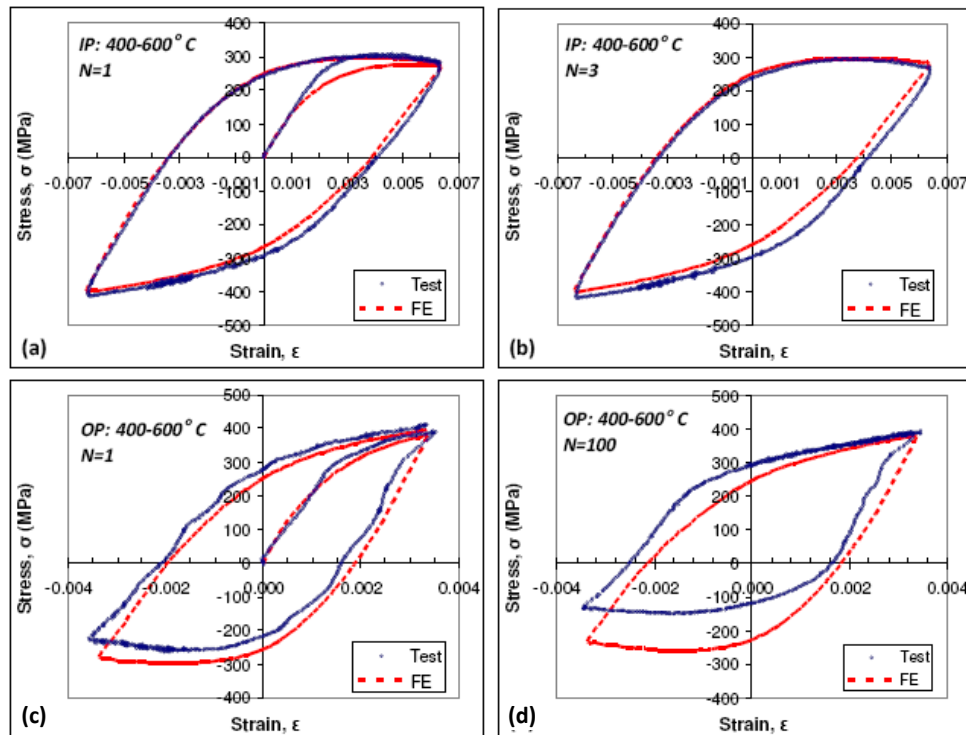


Figure 2.17: Measured and FE predicted TMF behaviour for P91 steel under (a,b) TMF-IP and (c,d) TMF-OP loading conditions for an applied strain-rate of 0.1 %/s [Saad *et al.*, 2011a].

Creep-fatigue (CF) testing has been carried out by Fournier and co-workers [2009a; 2009b; 2010], and the same group has also carried out a program of creep-fatigue-oxidation testing on 9Cr steels [Fournier *et al.*, 2008a; Fournier *et al.*, 2008b; Fournier *et al.*, 2008c]. The constitutive behaviour

2. Background and Literature Review

of such tests is presented in Figure 2.18a, highlighting the cyclic softening in the material. Although the constant stress hold periods are quite short in duration here, the primary effect observed is a considerable reduction in the number of reversals to failure due to the interactions of fatigue and creep, as highlighted in Figure 2.18b. To the author's knowledge, the only HCF tests carried out on 9Cr steels at high temperature are those of Mrozinski and co-workers [2013; 2014].

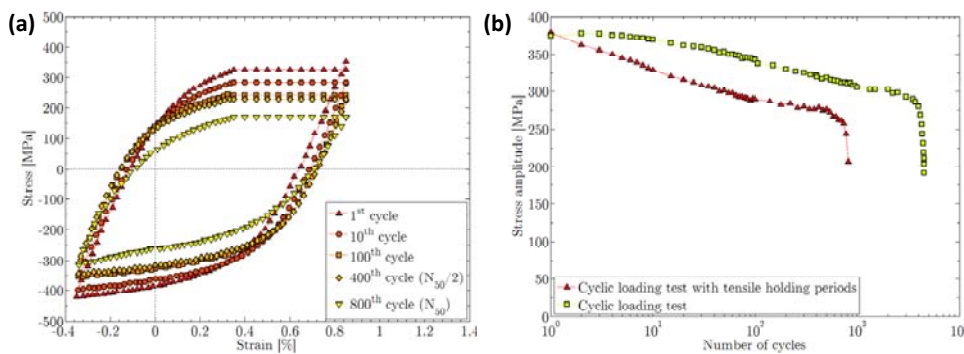


Figure 2.18: Creep-fatigue testing of 9-12Cr steels at 550 °C for (a) cyclic stress-strain response in P92 steel and (b) comparison of creep-fatigue and pure fatigue in P92 steel [Giroux, 2011].

2.3.2. Influence of strain-rate

A strain-rate effect in metals is expected to occur once viscous behaviour becomes important, i.e. for $T > 0.3 T_m$ or $0.4 T_m$. Hence, at temperatures above 400 °C in power plant materials, strain-rate and viscous effects can become important. This effect manifests itself as a decrease in working stress-range for a decreasing strain-rate, as illustrated schematically in Figure 2.19. The results presented in Figure 2.15 are carried out at a constant strain-rate, and hence, omit this important phenomenon. The work of Mannan and Valsan [2006] and Giroux [2011] however, have captured this effect for P91 and P92 steels respectively, as illustrated in Figure 2.20 for example. The measured MSR-stress response for P91 steel, presented on a logarithmic plot in Figure 2.21, highlights the importance of investigating the strain-rate effect in 9Cr steels. There is a requirement to interpolate and extrapolate reliably from higher strain-rate loading conditions (where laboratory tests are normally conducted) to realistic operating conditions at

2. Background and Literature Review

much lower strain-rates. The change in stress-range observed is dominated by time-dependent effects and the evolving microstructural strengthening mechanisms.

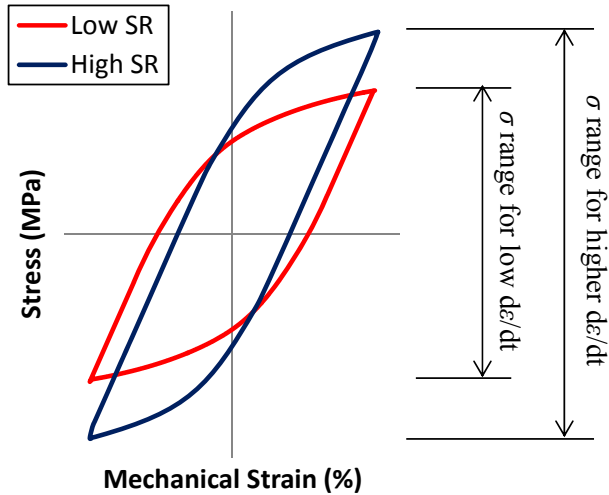


Figure 2.19: Schematic illustration of the effect of strain-rate on resulting stress-range in metals.

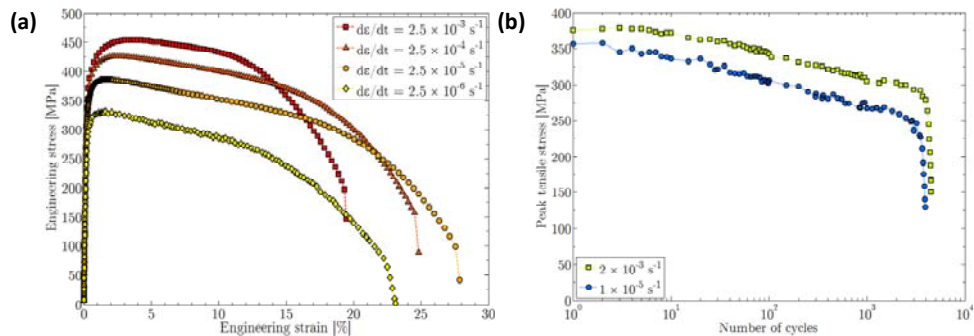


Figure 2.20: Strain-rate effect in P92 steel at 550 °C for (a) monotonic tensile tests, (b) evolution of maximum stress with cycles, carried out at an applied strain of $\pm 0.35\%$ [Giroux, 2011].

2. Background and Literature Review

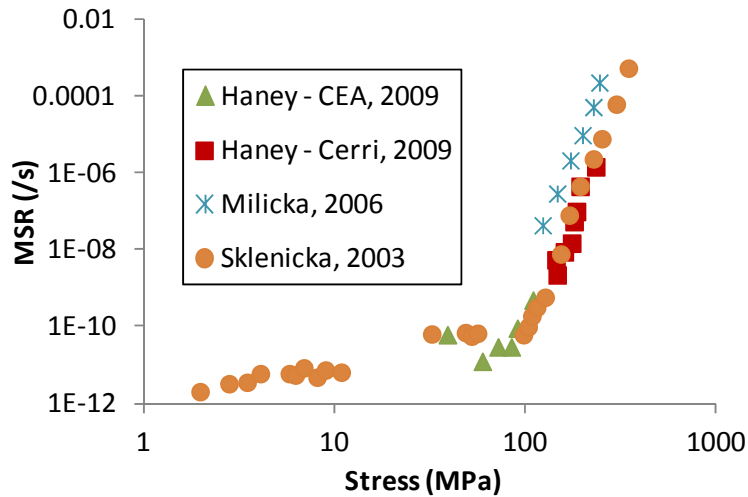


Figure 2.21: Measured minimum creep strain rate (MSR) as a function of applied stress in P91 steel at 600 °C.

As the creep-fatigue-corrosion behaviour of 9Cr steels is strongly dependent on the material microstructure, and more importantly, the evolved material microstructure at a specific point in time, the following sections are devoted to (i) a discussion on the current state-of-the-art material models for cyclic viscoplasticity under high temperature deformation including microstructurally-driven models in Section 2.4, (ii) briefly describing the core strengthening mechanisms in metals (Section 2.5), and (iii) the microstructure and microstructural evolution and degradation of 9Cr steels (Section 2.6).

2.4. Modelling inelastic deformations in materials

Computational modelling of the constitutive behaviour of 9-12Cr steels represents a key part of the design and development of components for next generation power plants. In particular, such models must be capable of accurately predicting the stress and inelastic strain responses to a given loading history, as these quantities represent key variables for both fatigue and creep life prediction.

Inelastic deformations are irreversible deformations in a material and are characterised as either viscoplastic or creep deformations in metals. As

2. Background and Literature Review

illustrated in the deformation mechanisms map of Figure 2.6, elastic behaviour only exists at low temperatures and low stresses, with creep behaviour dominating in metals for high temperature deformation under low applied stress. For a non-negative dissipation potential, Ω , and stresses in excess of the yield stress, viscoplastic behaviour exists, with plasticity a specific case of viscoplastic deformation. The limit of the elastic and creep domain is demarcated by the equipotential surface of $\Omega = 0$, as illustrated in Figure 2.22a, with a viscous or over stress, σ_v generated under viscoplastic deformation. Thus, the total strain, in multi-axial form, is defined as:

$$\boldsymbol{\varepsilon} = \boldsymbol{\varepsilon}^{\text{el}} + \boldsymbol{\varepsilon}^{\text{in}} + \boldsymbol{\varepsilon}^{\text{th}} \quad (2.7)$$

where $\boldsymbol{\varepsilon}^{\text{el}}$, $\boldsymbol{\varepsilon}^{\text{in}}$ and $\boldsymbol{\varepsilon}^{\text{th}}$ are the elastic, inelastic and thermal strain tensors, respectively, with the rate of inelastic deformation simulated using a flow rule. Flow rules are either phenomenological or physically-based, with numerous computational models, with varying benefits, already applied to simulate inelastic deformations in steel alloys. The following section describes a number of material models for simulating inelastic deformations at high temperatures, with a particular focus on applications to 9-12Cr steels.

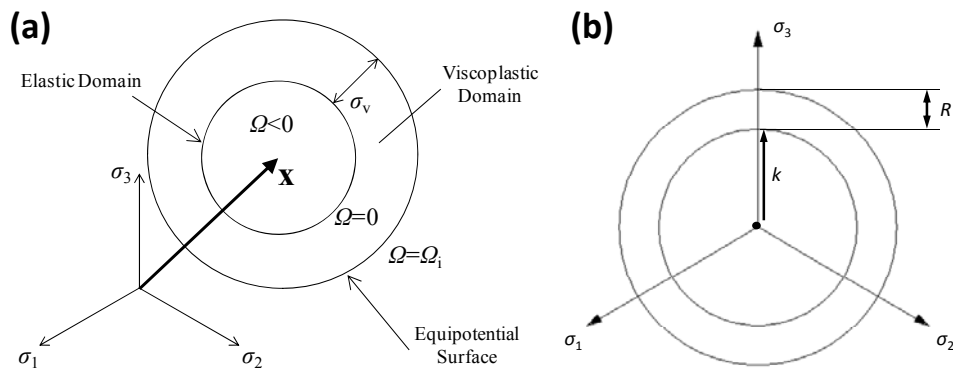


Figure 2.22: Representation of (a) translation and (b) expansion of the equipotential flow surface.

2.4.1. Phenomenological models for high temperature fatigue

The unified cyclic viscoplastic model of Chaboche [Chaboche and Rousselier, 1983a; Chaboche and Rousselier, 1983b] is one of the most

2. Background and Literature Review

commonly used phenomenological models for cyclic viscoplastic deformation in metals. The Chaboche model uses a unified approach to describe both the viscous and plastic behaviour of metals through a power law flow rule, effectively an extension of the power law model of Norton (see Equation (2.3)) to cyclic viscoplasticity. For this model, the constitutive equation defining the accumulated effective plastic strain-rate is defined as:

$$\dot{p} = \left\langle \frac{f}{Z} \right\rangle^n = \left\langle \frac{J_2(\mathbf{s} - \mathbf{x}) - R - k}{Z} \right\rangle^n \quad (2.8)$$

where n is the cyclic viscoplastic exponent, Z is a material constant, \mathbf{s} and \mathbf{x} are the deviatoric stress and back-stress (associated with kinematic hardening) respectively, R is isotropic hardening stress and k is cyclic yield stress. The unified Chaboche model has been successfully applied to steels in the higher strain-rate regime, including 9Cr steels in the work of Koo and co-workers [2007; 2011] and Saad and co-workers [2011a; 2011b], as illustrated in Figure 2.17 for example.

The kinematic back-stress accounts for the Bauschinger effect in materials, i.e. a lower yield stress in compression following a tensile loading and vice versa, and is modelled using a kinematic hardening model. Physically, the back-stress is due to the presence of internal stresses in the material generated at obstacles such as precipitates and grain boundaries. The kinematic back-stress denotes the centre of the elastic domain in 3D stress space as illustrated in Figure 2.22a.

The kinematic hardening variables can be linear or non-linear in nature, with the Prager [1956] and Prager-Ziegler [Ziegler, 1959] models commonly used linear models. However, to predict the constitutive behaviour of 9-12Cr steels, non-linear kinematic hardening (NLKH) models are required. The most commonly used model is the Frederick-Armstrong NLKH model [Frederick and Armstrong, 2007], given by:

$$\dot{\mathbf{x}} = \frac{2}{3} C \dot{\boldsymbol{\varepsilon}}^{in} - \mathbf{x} \dot{p} \quad (2.9)$$

2. Background and Literature Review

where C is the hardening modulus and γ is the non-linear material parameter. Various modifications to this model have been made, including the incorporation of recovery [*Lemaitre and Chaboche, 2000*] and temperature-rate terms [*Chaboche, 2008*]. Other phenomenological NLKH models include the Ziegler [*1959*] and Ohno and Wang [*1993a; 1993b*] models, for example. Either of these models could be incorporated in the Chaboche modelling framework to simulate the NLKH back-stress, e.g. the Ohno and Wang model has been used by Yaguchi and Takahashi [*2005b*] to capture ratchetting behaviour in 9Cr steels, within the constitutive flow rule of Chaboche (Equation (2.8)).

Cyclic hardening in many steels can be approximated as isotropic behaviour, such that the equipotential flow surfaces expand homogeneously in all directions in 3D stress space, as illustrated in Figure 2.22b. This isotropic hardening is incorporated in the Chaboche material model using the isotropic stress, R . The evolution of this variable is a function of plastic deformation and typically modelled using a non-linear isotropic hardening (NLIH) model, e.g. the NLIH model of Chaboche and Rousselier [*1983a; 1983b*]:

$$\dot{R} = b(Q - R)\dot{\rho} \quad (2.10)$$

where Q is the saturated value of isotropic hardening (see Figure 2.23) and b is the isotropic hardening rate exponent.

2. Background and Literature Review

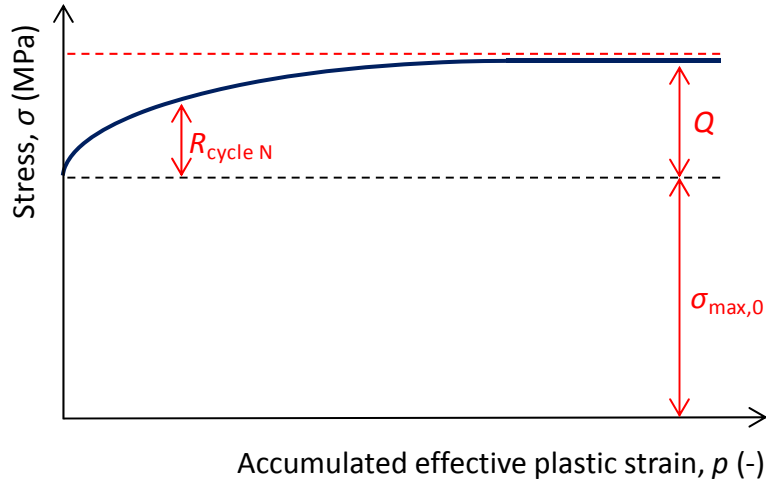


Figure 2.23: Schematic representation of isotropic hardening.

A less commonly-used material model is the two-layer viscoplastic model, developed by Kichenin *et al.* [1996]. Unlike the unified approach of Chaboche, the two-layer viscoplastic model uses decomposed elastic-plastic and elastic-viscous networks, as illustrated in Figure 2.24, such that the total strain is:

$$\boldsymbol{\varepsilon} = \boldsymbol{\varepsilon}^{\text{el}} + (1-F)\boldsymbol{\varepsilon}^{\text{pl}} + F\boldsymbol{\varepsilon}^{\text{cr}} \quad (2.11)$$

where $\boldsymbol{\varepsilon}^{\text{pl}}$ is the plastic strain tensor and the parameter, F , determines the level of the viscous network contribution to the total strain, i.e. the higher the value of the user defined function, F , the greater the viscous component of strain. The parameter, F , is defined as the ratio of the elastic modulus of the viscous network, K_v , to that of the overall elastic modulus, K_v+K_p , such that:

$$F = \frac{K_v}{K_v + K_p} \quad (2.12)$$

where K_p is the modulus of the elastic-plastic network, as per Figure 2.24. The viscous strain is defined using the Norton power law creep model of Equation (2.3).

2. Background and Literature Review

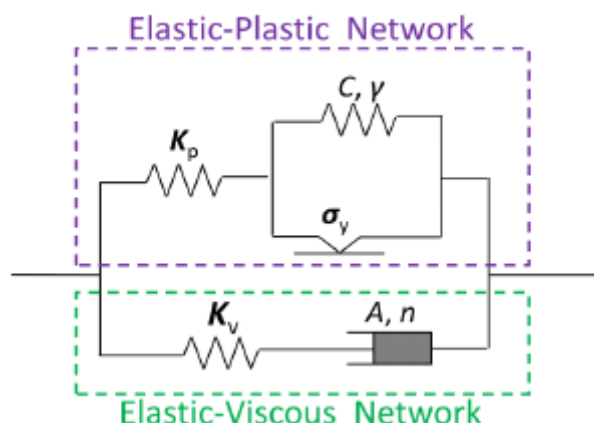


Figure 2.24: Setup for the viscous and plastic networks in the two-layer viscoplastic model [Deshpande, 2009].

The two-layer viscoplastic model of Kichenin *et al.* was adopted by Farragher *et al.* [2013a, 2013b] for TMF simulations of P91 steels, where the two-layer viscoplastic model was calibrated and validated under anisothermal, cyclic loading conditions. Farragher and co-workers have also extended this approach to (i) identify the relevant material parameters to simulate the constitutive behaviour of parent, weld and cross-weld test specimens [Farragher *et al.*, 2014] and (ii) predict the 3D stress state in realistic components, such as the header unit illustrated in Figure 2.25. This 3D modelling methodology uses a sequential thermo-mechanical model firstly to calculate the transient temperature distribution in the header, via conduction and convection, and secondly to calculate the associated transient elastic-plastic-creep cyclic stress-strain response due to varying temperature and pressure conditions. These conditions were representative of measured plant (i) hot and cold start-up and (ii) load trip sample conditions. The predicted stress-strain and strain-time responses for both cases are presented in Figure 2.26. From these results, it is evident that plant components are subjected to asymmetric TMF cycles, with a higher load observed in tension. These numerical simulations of flexible plant operation also exhibit cyclic viscoplastic deformation at intermediate strain-rate values of less than 1×10^{-4} %/s. The largest stresses are also observed at regions of welded connections in the header unit. As the weld and HAZ material properties were omitted from these simulations, the level of

2. Background and Literature Review

viscoplasticity could be higher due to material mismatch and hence, highlighting the potential viscoplasticity experienced by components during flexible operation.

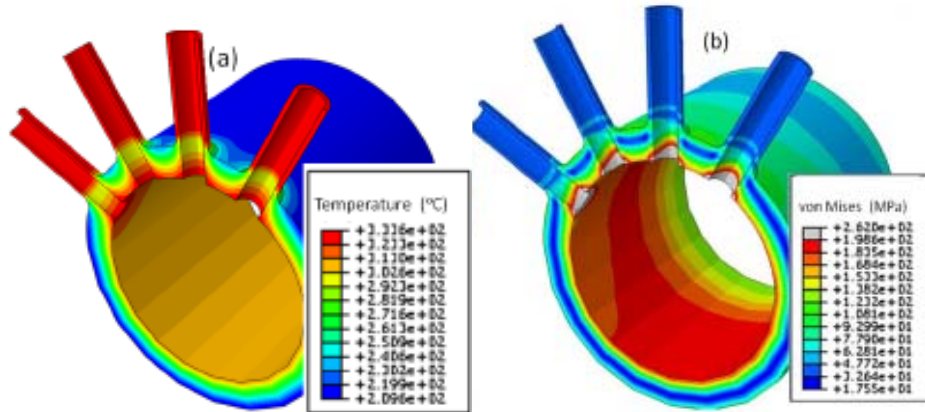


Figure 2.25: Component level modelling of a plant header unit (a) thermal loading and (b) stress contour plot [Farragher, 2013].

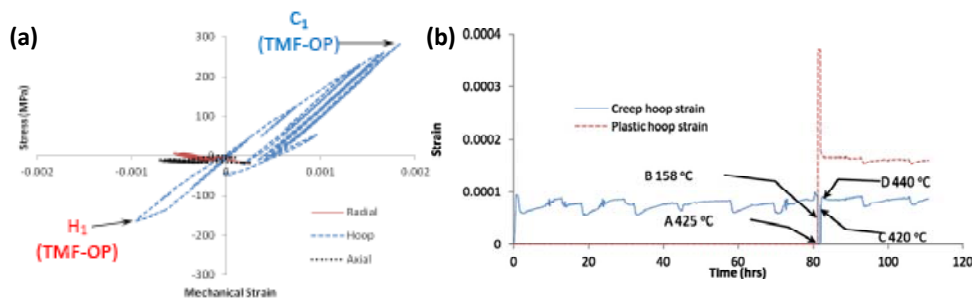


Figure 2.26: FE predicted (a) stress-strain response in the inner bore saddle position of a header unit [Farragher, 2013] and (b) creep and plastic strain histories (hoop) as a function of time following a load trip [Farragher et al., 2013b].

Although the framework for the above models satisfies the first and second laws of thermodynamics, the phenomenological aspect of these models can result in difficulties in identifying a set of unique material parameters with a physical basis. The Chaboche unified cyclic viscoplastic material model has upwards of twelve parameters per temperature to be identified. The use of data fitting methods, such as the genetic algorithm of Mahmoudi and co-workers [2011], for example, can significantly simplify the parameter identification process but may lead to a non-unique set of parameters. This

2. Background and Literature Review

leads to the opportunity for inaccuracies when extrapolating the constitutive behaviour to other loading conditions, resulting in quantitative errors and hence, potentially non-conservative and unsafe results. Thus, to ensure more accurate modelling for realistic loading conditions, this approach requires careful identification of the material parameters and a wide set of validation simulations across a broad range of loading conditions.

Furthermore, such models have only been applied to cyclic viscoplastic deformation at the higher rates typically observed under experimental laboratory conditions to date. However, at intermediate to low strain-rates, the power law exponent, n , transitions from a relatively high value of 3 to 12 to a value of approximately unity. Thus, as this transition region is the regime at which flexible plants operate, caution must be exerted when extending and applying these power law models to viscoplastic deformation under realistic loading conditions.

2.4.2. Simulating inelastic deformations from a physical basis

The parameter identification limitations of the phenomenological approaches discussed above can be overcome by the introduction of models derived from a physical basis. The main approaches used in the literature for incorporating microstructurally driven parameters include (i) continuum damage mechanics (CDM), (ii) dislocation-mechanics frameworks and (iii) micromechanical or crystal plasticity (CP) modelling.

In relation to models for high temperature deformation, the Hayhurst CDM model is used for both 9-12Cr and Cr-Mo-V alloys. This model includes three state variables, namely H for primary creep, Φ for particle coarsening and ω describing tertiary creep. The constitutive law and subsequent evolutionary models for the three state variables are:

$$\dot{\epsilon}_{cr} = \alpha_{cr} \sinh \beta \left(\frac{\sigma(1-H)}{(1-\Phi)(1-\omega)} \right) \quad (2.13a)$$

2. Background and Literature Review

$$\dot{H} = \frac{h}{\sigma} \left(1 - \frac{H}{H^*} \right) \dot{\epsilon}^{cr} \quad (2.13b)$$

$$\dot{\Phi} = \frac{K_c}{3} (1 - \Phi)^4 \quad (2.13c)$$

$$\dot{\omega} = C \dot{\epsilon}^{cr} \quad (2.13d)$$

where α_{cr} and β are the creep constants, h and H^* are primary creep constants, K_c is carbide coarsening rate and C is a cavitation constant. The Hayhurst CDM model has been successfully applied to Cr-Mo-V steels [Perrin and Hayhurst, 1996] and to 9Cr steels by Hyde and co-workers [2006], as illustrated in Figure 2.27 for creep tests under various stresses at 625 °C and 650 °C. The benefit of the Hayhurst CDM model in relation to modelling 9Cr steels is the inclusion of carbide coarsening through the Ostwald ripening based damage term, Φ , and cavitation damage to predict tertiary creep. However, this model does not account for the effect of the hierarchical martensitic lath microstructure and the MX carbonitrides in the lath interiors. The Hayhurst CDM model was improved upon by Oruganti *et al.* [2011], to include the effects of MX carbonitrides. More importantly, the primary creep modelling approach was modified to a more physical approach, incorporating the key effects of the hierarchical microstructure of 9-12Cr steels. Comparisons were made with measured microstructural evolutions of MX particle coarsening, as illustrated in Figure 2.28a. Figure 2.28b illustrates a comparison of the rupture stress for various temperatures, with excellent agreement predicted.

2. Background and Literature Review

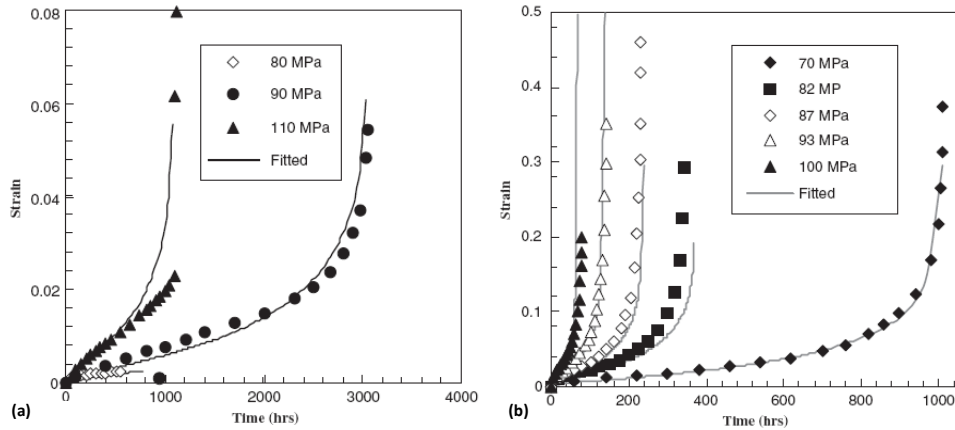


Figure 2.27: Comparison of the Hayhurst CDM model with experimental data for temperatures of (a) 625 °C and (b) 650 °C [Hyde *et al.*, 2006].

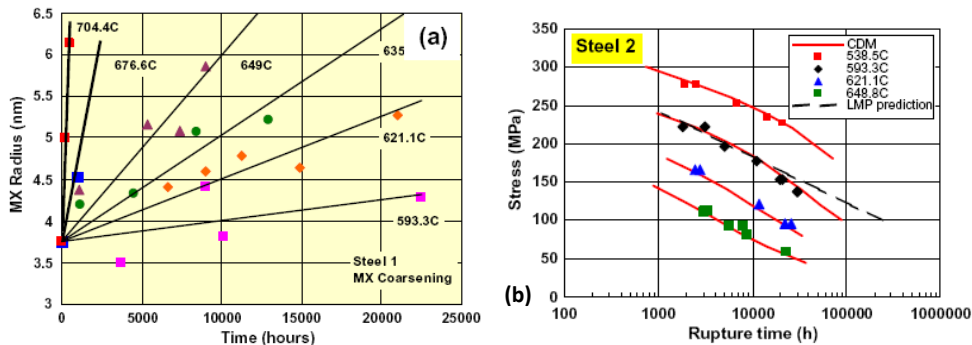


Figure 2.28: Prediction of (a) MX coarsening and (b) rupture stress for 9-12Cr steels [Oruganti *et al.*, 2011].

Although Dyson and co-workers [2000] have included dislocation density within a CDM approach, the concept of dislocation-mechanics offers an attractive method for the evaluation of the constitutive behaviour as the motion of dislocations constitutes inelastic deformation. The dislocation-mechanics approach uses the evolution of dislocation density and the interaction of dislocations with physical models for the key strengthening mechanisms to determine the constitutive behaviour of the material. The dislocation density, ρ , evolves via the growth and annihilation of dislocations, using evolutionary equations such as the Kocks-Mecking model [Kocks and Mecking, 2003; Mecking and Kocks, 1981] to quantify dislocation density evolution:

2. Background and Literature Review

$$\frac{d\rho}{d\varepsilon^{\text{in}}} = M(k_1\sqrt{\rho} - k_2\rho) \quad (2.14)$$

where k_1 and k_2 are material constants to be identified via comparison with measured data. However, the Kocks-Mecking approach does not account for hierarchical microstructures, such as the dislocation network and contribution of the low angle boundary dislocation substructure found in 9-12Cr steels. The approach of Roters and co-workers [2000] incorporates the effects of grain boundaries via a volume fraction approach, where the dislocation density is defined by considering the density of mobile and immobile dislocations:

$$\rho = \rho_m + f_w \rho_w + (1 - f_w) \rho_i \quad (2.15)$$

where f_w is the volume fraction of grain boundaries and ρ_m , ρ_w , and ρ_i are the densities of mobile, cell wall immobile and cell interior immobile dislocations, respectively. The model of Roters and co-workers uses the Orowan equation and the probability of a dislocation annihilation event occurring to evolve dislocation density. Magnusson and Sandström [2007] have successfully applied this approach to 9Cr steels within a Norton-based power law model, focusing on primary creep behaviour. The dislocation-mechanics framework of Roters *et al.* [2000] was adapted to account for contributions from the lath boundaries and lath interiors. The model captured the evolution of various microstructural parameters and a comparison with measured data for constant load conditions is presented in Figure 2.29a.

2. Background and Literature Review

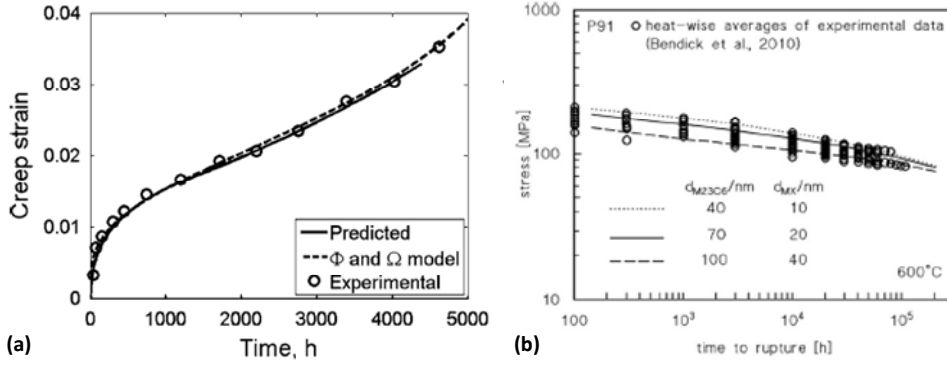


Figure 2.29: Comparison of creep simulations with measured data for (a) creep strain evolution [Magnusson and Sandström, 2007] and (b) stress rupture [Spigarelli, 2013].

Spigarelli [2013] has also implemented a Norton power law-based model for microstructure-based rupture in 9Cr steels. This model used a back-stress to account for the influence of the $M_{23}C_6$ and MX precipitates on the creep behaviour of 9Cr steels, as well as including contributions due to the other key microstructural parameters, including martensitic lath width. The important contribution in the work of Spigarelli relates to the inclusion of the formation of the Laves phase particles (at the expense of solute strengthening mechanism) using computational simulations on the kinetics of Laves phase precipitation in conjunction with a volume fraction approach. The typical correlation achieved with experimental stress rupture data is presented in Figure 2.29b.

The dislocation-mechanics approach is also used extensively in CP modelling. The dislocation-mechanics CP model of Cheong and Busso [2004; 2005], has been successfully adapted from f.c.c. to b.c.c. and modified to incorporate the effects of precipitates and the hierarchical microstructure of 9Cr steels by Li and co-workers [2013b; 2014; 2015]. This model uses the exponential flow rule:

$$\dot{\gamma}^\alpha = \dot{\gamma}_0 \exp\left(-\frac{F}{k_B T} \left\langle 1 - \left\langle \frac{|\tau^\alpha - B^\alpha| - S^\alpha}{\tau_0} \right\rangle^p \right\rangle^q\right) \text{sgn}(\tau^\alpha - B^\alpha) \quad (2.16)$$

2. Background and Literature Review

where F is thermal activation energy, τ_0 is critical shear stress, p , q and $\dot{\gamma}_0$ are constants and τ^α , B^α and S^α are the shear stress, back-stress and slip resistance on slip system α , respectively. In this model, the back-stress, B^α , is quantified using the Frederick-Armstrong NLKH model and the slip resistance term, S^α , accounts for the evolution of dislocation density. Li and co-workers [2013b; 2014; 2015] have successfully developed a CP multi-scale modelling methodology for the hierarchical microstructure of P91 steel, using a measured microstructure model to simulate the block level and a periodic unit cell model to simulate the martensitic lath microstructure. The CP simulations at the martensitic lath scale model the effects of $M_{23}C_6$ precipitates at lath boundaries, with a smaller precipitate radius giving a stronger material for the same volume fraction of $M_{23}C_6$ precipitates. A stronger material is also predicted for decreasing martensitic lath width using this model. Both the block level model from the measured microstructure (using an EBSD scan of P91 steel) and the martensitic lath level models are predicted to give similar monotonic stress-strain response at the macro-scale and both models show excellent comparison with experimental data.

As mentioned above, one of the other benefits of the CP approach is the ability to simulate measured microstructures of 9Cr steels [Golden *et al.*, 2014] and to incorporate length scale effects, e.g. using a strain gradient approach similar to that of Sweeney and co-workers [2014] for a CoCr alloy. The strain-gradient model of Sweeney *et al.* is based on the dislocation-mechanics flow rule developed by Dunne and co-workers [2007], where the plastic slip-rate on the slip system α is defined as:

$$\dot{\gamma}^\alpha = \rho_{SSD} b^2 v \exp\left(-\frac{\Delta H}{k_B T}\right) \sinh\left(\frac{(\tau^\alpha - \tau_c - R)\dot{\gamma}_0 b^2}{k_B T \sqrt{\rho_{SSD} + \rho_{GND}}}\right) \quad (2.17)$$

where ρ_{SSD} and ρ_{GND} are the densities of statistically stored and geometrically necessary dislocations, v is attack frequency, ΔH is Helmholtz free energy, τ_c is critical resolved shear stress and R is an isotropic hardening parameter. The strain gradient approach has also been incorporated in the recent work of Li *et al.* [2014, 2015] for CP simulations

2. Background and Literature Review

of 9Cr steels. The hyperbolic sine material model of Dunne and others would also allow for a smooth transition from dislocation to diffusion mechanisms, e.g. as per data similar to that of Figure 2.21, resulting in less extrapolation errors when simulating lower strain-rates. A similar benefit is observed using the hyperbolic sine model of Hayhurst [*Vakili-Tahami et al., 2005*].

However, there are temporal and geometric limitations associated with the CP modelling methodology. Owing to computational expense, it is only feasible to simulate a small number of cycles and a very limited volume of material, with a typical representative volume element on the order of microns compared to metres corresponding to realistic components. Thus, there exists the requirement for multi-scale modelling methodologies to, on the one hand simulate realistic geometries of plant components under representative timescales, whilst also accounting for microstructural evolution and degradation during deformation. Bardel and co-workers [*2015*] have recently developed a microstructure-sensitive macro-scale model for a 6061 aluminium alloy, with the constitutive equation defined as:

$$\dot{p} = \frac{\text{sgn}(\xi)E\dot{\epsilon}}{\left(E + \frac{\dot{R}}{\dot{p}} + \text{sgn}(\xi) \left[\frac{\dot{X}_G}{\dot{p}} + \frac{\dot{X}_{ppt}}{\dot{p}} \right] \right)} \quad (2.18)$$

where R is an isotropic stress incorporating the contribution of dislocation density and solutes, X_G is the back-stress due to dislocation pile-up at boundaries, X_{ppt} is the precipitate back-stress and $\xi = \sigma - X_G - X_{ppt}$ is the effective stress. The back-stress accounts for strengthening due to precipitates and dislocation pile-up formation at the grain boundaries, and the evolving dislocation density enables the viscoplastic domain to be updated as a function of time. Evolutionary equations are developed here to incorporate and advance the microstructure in the material model.

Due to the complex nature of the hierarchical microstructure, only limited modelling from a physical basis has been carried out for cyclic viscoplasticity of 9-12Cr steels to date. Sauzay and co-workers [*2005; 2008*]

2. Background and Literature Review

have developed a physically-based macro-scale model for cyclic softening of 9-12Cr steels, based on the evolution of the density of low-angle boundary dislocations as a function of cycles. Although this group have carried out micromechanical modelling incorporating terms for dislocation bowing and subgrain growth within a dislocation-mechanics framework [*Giordiana et al., 2012; Giroux, 2011*], no complete model accounting for the evolution of the hierarchical microstructure of 9-12Cr steels, inclusive of precipitate and solute strengthening mechanisms, has been developed to date for the efficient simulation of microstructural evolution at the macro-scale.

A further argument for the development of a multi-scale modelling framework for 9-12Cr steels relates to the simulation of multi-material welded connections. The welding process results in the formation of a narrow heat affected zone (HAZ) region between the weld metal and parent material. As it is difficult to carry out experimental characterisation of the HAZ region independently (with the goal of identifying relevant material constants), the concept of a microstructure-sensitive material model and associated multi-scale modelling framework lends itself well to the prediction of the constitutive behaviour of the heterogeneous HAZ microstructure.

2.5. Strengthening mechanisms in steel alloys

Metals have a crystalline structure made up of ordered repeating units which are typically body-centred cubic (b.c.c.) or face-centred cubic (f.c.c.), as illustrated in Figure 2.30. There are 48 slip systems in b.c.c. materials, yielding more ductile behaviour than f.c.c. systems, where there are 12 slip systems and hence fewer paths for the motion of mobile dislocations and hence, plastic deformation. The post heat treatment crystalline structure of 9-12Cr steels is b.c.c. Plastic deformation in crystalline materials is manifested in the form of plastic slip, i.e. sliding of atoms along the crystallographic or slip plane as illustrated in Figure 2.30c. Plastic slip occurs along the most densely packed crystallographic plane in the closest-

2. Background and Literature Review

packed direction, as highlighted in Figure 2.30a and Figure 2.30b for b.c.c. and f.c.c. crystals respectively. As the slip planes in b.c.c. materials are not as close packed as f.c.c. crystals, b.c.c. materials typically have a higher critical shear stress.

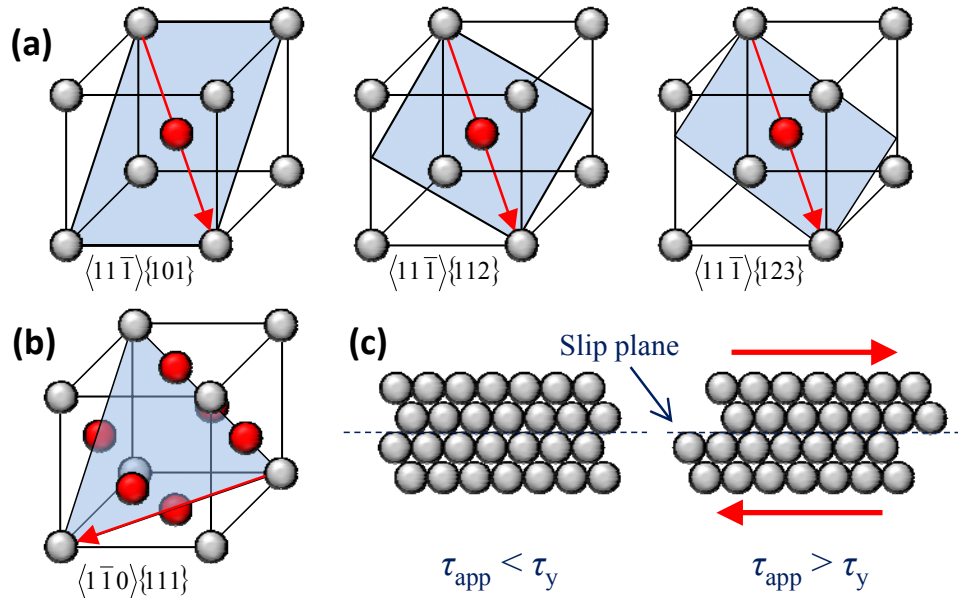


Figure 2.30: Schematic representation of (a) a body-centred cubic (b.c.c.) crystal structure, (b) a face-centred cubic (f.c.c.) structure and (c) plastic slip occurring in a crystalline structure once the applied shear stress exceeds a critical value.

Although an ordered crystalline structure exists in metals, flaws and crystallographic defects are dispersed throughout the microstructure. The primary flaws in materials include (i) intrinsic (vacancies and interstitial atoms) or extrinsic (solute and impurities) point defects, (ii) line defects, i.e. dislocations, (iii) planar defects such as grain boundaries and stacking faults (defect typically in closely-packed crystal structures (f.c.c. or h.c.p.) where the sequence of layers is non-uniform, for example i.e. a twin boundary is an example of a stacking fault) and (iv) bulk defects such as voids, inclusions and precipitates. These crystallographic defects can be detrimental to fatigue and creep life as they are potential sites for crack initiation, propagation and hence, failure. However, they can also be advantageous by providing strengthening in materials and modifying the flow stress. The flow stress, i.e. the stress required to maintain plastic deformation, is defined as:

2. Background and Literature Review

$$\tau_f = \tau^a + \tau^*(\dot{\gamma}^{pl}, T) \quad (2.19)$$

where τ^a is the athermal component and $\tau^*(\dot{\gamma}^{pl}, T)$ is the strain-rate and temperature-dependent component of flow stress. This flow stress is also dependent on the various strengthening mechanisms present in the material. The following sections describe the effect of different strengthening mechanisms on the flow stress in metals. As plastic slip is controlled by the movement of dislocations, potential strengthening mechanisms are discussed primarily in terms of their interactions with dislocations and their ability to retard the motion of mobile dislocations.

2.5.1. Dislocation strengthening

Dislocations are either of edge, screw or mixed type and are split into two primary categories, (i) mobile dislocations and (ii) immobile dislocations. Mobile dislocations are effectively the carriers of plastic deformation and represent the propagation of plastic slip through a material. Orowan's equation [Orowan, 1940] describes the relationship between plastic slip, $\dot{\gamma}^{pl}$, and dislocation density, ρ :

$$\dot{\gamma}^{pl} = \rho b v \quad (2.20)$$

where b is the magnitude of Burger's vector and v is dislocation velocity. Immobile dislocations, on the other hand, are effectively trapped dislocations, such as dislocation pile-ups at grain boundaries or dislocation entanglements in the microstructure, for example, leading to mechanisms which resist plastic slip and hence, strengthen materials. The contribution of dislocation entanglements to the material strengthening can be described in terms of the Taylor hardening equation [Taylor, 1938], which relates the flow stress to dislocation density and is defined as follows:

$$\tau_f = \tau_0 + \alpha_1 \mu b \sqrt{\rho} \quad (2.21)$$

where μ is shear modulus, τ_0 is the friction stress and α_1 is a material parameter, typically with a value between 0.2 and 0.5. The friction stress is

2. Background and Literature Review

the stress required to overcome lattice resistance (intrinsic strength of the material due to the bonds between atoms) to dislocation motion. This parameter can be affected by the presence of solid solution strengthening mechanisms, for example.

2.5.2. Precipitate strengthening

The inclusion of solutes within a chemical composition can form (i) a homogeneous solid solution, where dispersed solutes form either substitutional atoms or interstitials within the crystal lattice (see Section 2.5.3) or (ii) secondary phase particles (or precipitates). The latter are new compounds typically formed locally in the microstructure during tempering at lower temperatures or quenching (second phase is soluble at the higher heat treatment temperature, with less solubility at the lower tempering temperature [*Dieter, 1986*]). Both can lead to increased strengthening by restricting the motion of mobile dislocations and hence, retarding plastic slip.

Second phase particles can be coherent or incoherent. Coherent particles are normally quite small and are a continuation of the lattice structure. They are susceptible to particle shearing, as a dislocation cuts through or ‘shears’ the particle. An increased particle strengthening effect exists for larger precipitate radii. When secondary phase particles are larger (or overaged), the precipitates retard the motion of the mobile dislocations, leading to a bowing out mechanism. Once the mobile dislocation reaches the precipitate, the dislocation starts to bow out away from the pinning positions at the obstacles, leading to the formation of Orowan loops. The strengthening produced by the Orowan bowing mechanism can be defined using the following relationship [*Orowan, 1948*]:

$$\tau_{\text{Or}} = \frac{\mu b}{\lambda} \quad (2.22)$$

where λ is interparticle spacing. Hence, the Orowan stress reduces for increasing particle spacing, i.e. it is easier for a dislocation to ‘bow’ through the increased dimension, λ . As the precipitate radius increases, the

2. Background and Literature Review

precipitate strengthening mechanism decreases, i.e. the interparticle spacing, λ , is directly proportional to precipitate radius.

2.5.3. Solid-solution strengthening

Solid-solution strengthening in metals is due to the inclusion of impurities in the microstructure and exists in two forms, (i) substitutional solid solution, where the solute takes up a lattice position and (ii) interstitial solid solution, where the solutes take up interstitial positions in the crystal. The type of solid-solution strengthening obtained is dependent on the solute size and both of these mechanisms are highlighted in Figure 2.31.

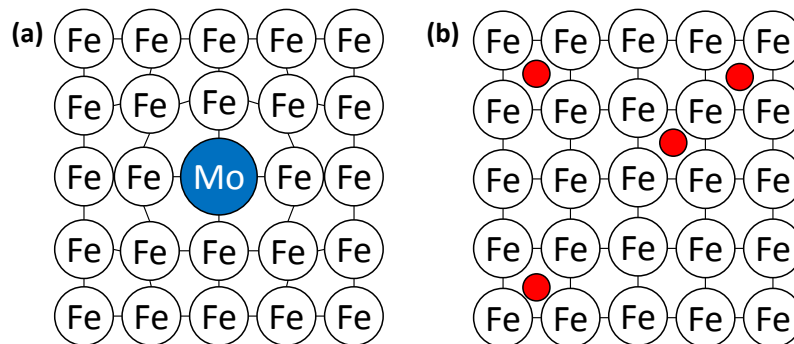


Figure 2.31: Schematic representation of (a) substitutional and (b) interstitial solid solution strengthening in metals. The blue circles represent substitutional atoms and the red circles represent interstitial atoms.

The inclusion of solutes contributes to the material (i) yield stress and (ii) strengthening mechanisms in steel alloys and both are a function of solute atomic concentration, c . In substitutional solid solution strengthening, the solutes take up lattice positions in the crystal lattice, forcing the neighbouring lattice atoms to push out and hence, generate a stress. In turn, the slip plane is now coarser, making it more difficult for dislocations to move, and hence, increasing the resistance to plastic deformation. Thus, for a solute strengthened material, the yield stress can be rewritten as:

$$\tau_y = \tau_0 + B\sqrt{c} \quad (2.23)$$

2. Background and Literature Review

where B is a material constant. The presence of solutes in the material can also lead to a bowing type strengthening mechanism. In a similar manner to the strengthening mechanism of a pinned mobile dislocation bowing out at a precipitate, solutes can provide strengthening based on spacing [Dieter, 1986]:

$$\lambda = \frac{a}{c^{1/3}} \quad (2.24)$$

where a is interatomic spacing. Hence, the resulting stress can be computed using an approach similar to Equation (2.22).

2.5.4. Grain boundary strengthening

Grain boundaries provide strengthening as dislocations pile-up at regions where there is a large angle of misorientation, i.e. the grain boundary acts as an obstacle to mobile dislocation motion. High-angle grain boundaries (HAGBs) are boundaries considered to have an angle of misorientation of 15° or greater between adjacent grains. HAGBs can retard the motion of mobile dislocations due to the high level of disorder at the boundary, resulting in dislocation pile-ups. A dislocation immobilised at a HAGB can become mobile again if the force per unit length of boundary exerted on the dislocation, F , exceeds a critical value, F_{GB} . The force per unit length exerted on a HAGB by a single dislocation is $F = \tau b$, where τ is the applied stress. However, as more dislocations begin to pile-up, the force per unit length exerted by the dislocation pile-up is a function of the number of dislocations piled-up, n_g , such that $F = n_g \tau b$. As a larger number of dislocations can pile-up in a material with a larger grain size, remobilisation of dislocations trapped at grain boundaries occurs more easily, leading to a lower yield stress. This is the Hall-Petch effect [Hall, 1951; Petch, 1953], where the yield strength is inversely proportional to the square root of grain size as there are more boundaries to impede the motion of dislocations. The Hall-Petch relationship is defined as follows:

2. Background and Literature Review

$$\tau_y = \tau_0 + k_y d^{-1/2} \quad (2.25)$$

where k_y is a material constant and d is grain size.

2.6. Microstructure of 9-12Cr steels

Unlike conventional metals and steel alloys, 9-12Cr martensitic-ferritic steels have a hierarchical microstructure, as illustrated schematically in Figure 2.32. During the austenitisation stage of a two stage austenitisation-tempering heat treatment process, austenitic grains are formed with a mean angle of misorientation between adjacent grains of approximately 60° , with a typical dimension in the range of 20 to 150 μm [Das *et al.*, 2009]. Following heat treatment, martensitic transformation takes place during rapid cooling to temperatures below 300 $^\circ\text{C}$, leading to a hierarchical microstructure consisting of prior austenite grains (PAGs), packets and blocks, all of which have high-angle boundaries. Blocks are regions demarcated by an angle of misorientation of approximately 45° between neighbouring blocks and with a typical dimension of approximately 3 to 4 μm [Sauzay *et al.*, 2005].

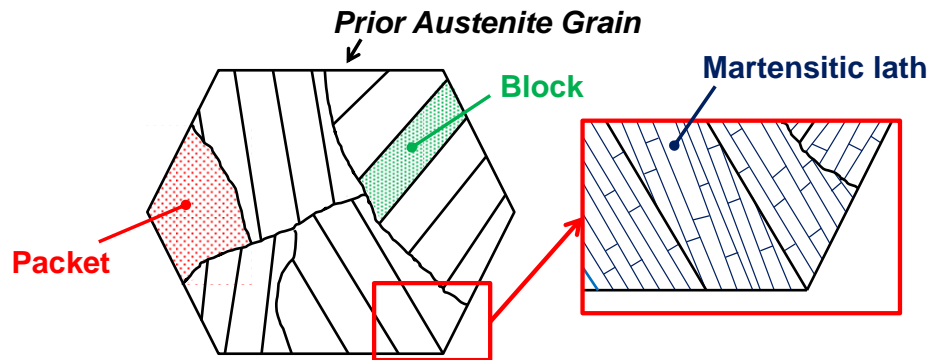


Figure 2.32: Schematic representation of the hierarchical microstructure in 9-12Cr steels.

Martensite forms in 9Cr steels during the rapid cooling phase following austenitisation, resulting in a material with high hardness and high strength [Krauss, 1999]. The martensite can form either martensitic laths or plate martensite as illustrated in the micrographs of Figure 2.33. The type of

2. Background and Literature Review

martensite that forms is a function of the carbon content in the material, as illustrated in Figure 2.34. 9-12Cr steels are characterised by a martensitic lath substructure with a high density of dislocations. Martensitic laths are low-angle boundary (LAB) regions separated by walls of LAB dislocations. In 9Cr steels, martensitic laths have a typical width in the region of 0.3 to 1.0 μm [Abe, 2008; Giroux, 2011; Saad *et al.*, 2011b; Sauzay *et al.*, 2005; Sauzay *et al.*, 2008]. However, if the austenitisation temperature is too low, a subgrain substructure exists in place of the lath martensite in 9Cr steels containing no boron [Das *et al.*, 2013a], leading to a reduction in creep strength of the material. Following martensitic transformation, a tempering process is undertaken, leading to the precipitation of M_{23}C_6 carbides dispersed along boundaries and MX carbonitrides within the martensitic lath interiors. The structure of 9-12Cr steels is further strengthened by solutes, in particular Mo and W solutes.

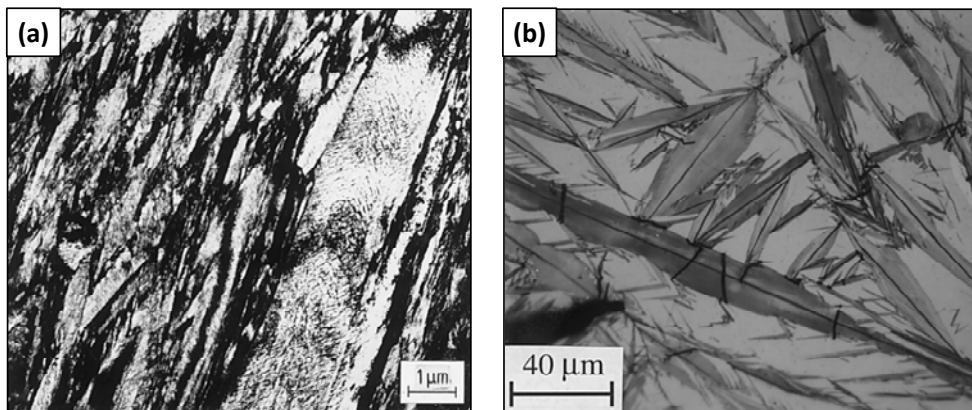


Figure 2.33: Micrographs of (a) lath martensite and (b) plate-like martensite [Krauss, 1999].

2. Background and Literature Review

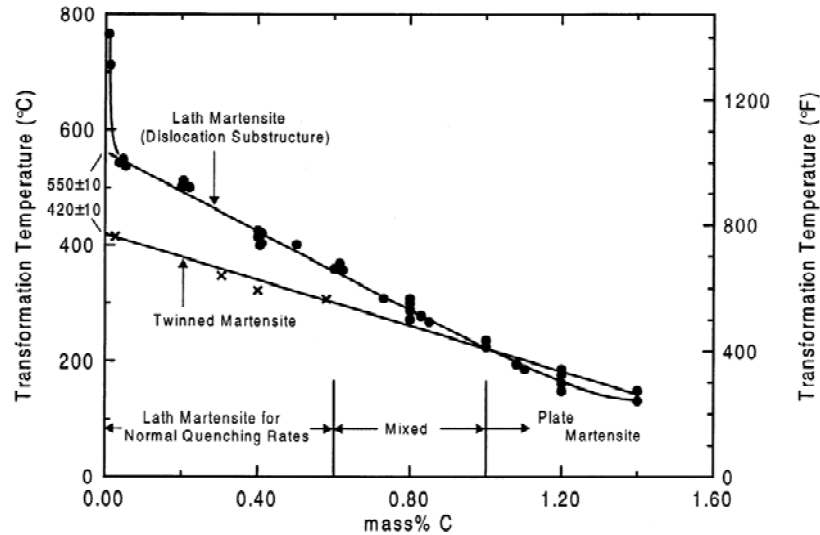


Figure 2.34: Martensitic transformation temperature as a function of carbon content [Marder and Krauss, 1967].

2.6.1. Chemical composition and effect of element content

The chemical compositions of various 9Cr steels are presented in Table 2.1. P91, P92 and MarBN are grades of 9Cr steels with alloying elements including molybdenum, nitrogen, vanadium and cobalt. The primary difference between P91 and P92 steel relates to the addition of tungsten in P92. Increased tungsten, the addition of boron and cobalt and decreased nitrogen content represent the key difference between MarBN and P92 steels. The various alloying elements in 9-12Cr steels are included predominantly to (i) improve oxidation and corrosion resistance, (ii) increase creep rupture strength and (iii) allow a stable precipitate-strengthened, martensitic lath microstructure form during heat treatment. The following section describes the primary function of the various alloying elements in 9-12Cr steels.

2. Background and Literature Review

Table 2.1: Chemical composition of various 9Cr steels by wt.%. The P91 steel composition is from Saad [2012] and P92 and MarBN is taken from Abe [2008]. The balance is made up of Fe.

	Al	B*	C	Co	Cr	Mn	Mo	N	Nb	P	Si	V	W
P91	0.007	-	0.12	-	8.60	-	1.02	0.06	0.07	0.017	0.34	0.24	0.03
P92	-	0.002	0.09	-	8.72	0.47	0.45	0.050*	0.06	-	0.16	0.21	1.87
MarBN (Min)	-	0.005	0.074	2.91	8.77	0.48	-	0.001*	0.046	-	0.30	0.18	2.85
MarBN (Max)	-	0.018	0.081	3.10	9.08	0.51	-	0.065*	0.055	-	0.31	0.20	3.13

*Denotes by mass (%) as opposed to by weight(%)

Chromium and silicon: Cr is a ferrite stabiliser providing oxidation resistance [Dawson, 2012; Klueh, 2004; Maruyama et al., 2001; Masuyama, 2001] in 9-12Cr steels, with 12Cr steels hence offering more (fireside and steamside) oxidation protection than 9Cr steels [Viswanathan et al., 2005]. However, in terms of creep strength, as illustrated in Figure 2.35a, 9 % chromium is identified as the optimum Cr content as it yields the highest creep rupture strength of the 2Cr to 15Cr steels [Abe, 2008; Miki et al., 2002], while maintaining a sufficiently low enough ductile-to-brittle transition temperature and limiting δ -ferrite formation (15Cr-2W steels are found to have 60 % δ -ferrite [Abe et al. 2008]). The formation of δ -ferrite precludes the formation of carbides, martensitic laths and subgrains and causes reduced dislocation density [Abe et al. 2008], thus lowering the creep-fatigue life of the material.

Chromium also plays a pivotal role in the formation of precipitates during tempering. Cr interacts with carbon to form Cr_{23}C_6 precipitates (the dominant M_{23}C_6 precipitate type in 9-12Cr steels), which are dispersed along HAGBs and LABs. Furthermore, in steels with nitrogen present (i.e. 9-12Cr steels), Cr_2N precipitates may also form during heat treatment [Dawson, 2012; Klueh, 2004]. However, due to the unstable nature of this precipitate under high temperature loading, the Cr_2N precipitates are replaced by more stable MX precipitates [Götz and Blum, 2003] during tempering.

Si is also a ferrite stabiliser, included in 9-12Cr steels to provide oxidation resistance [Huntz et al. 2003, Maruyama et al., 2001; Yang et al., 2008].

2. Background and Literature Review

However, Si decreases toughness via increased Laves phase precipitation [Agamennone *et al.*, 2006; Guan *et al.*, 1980; Masuyama, 2001].

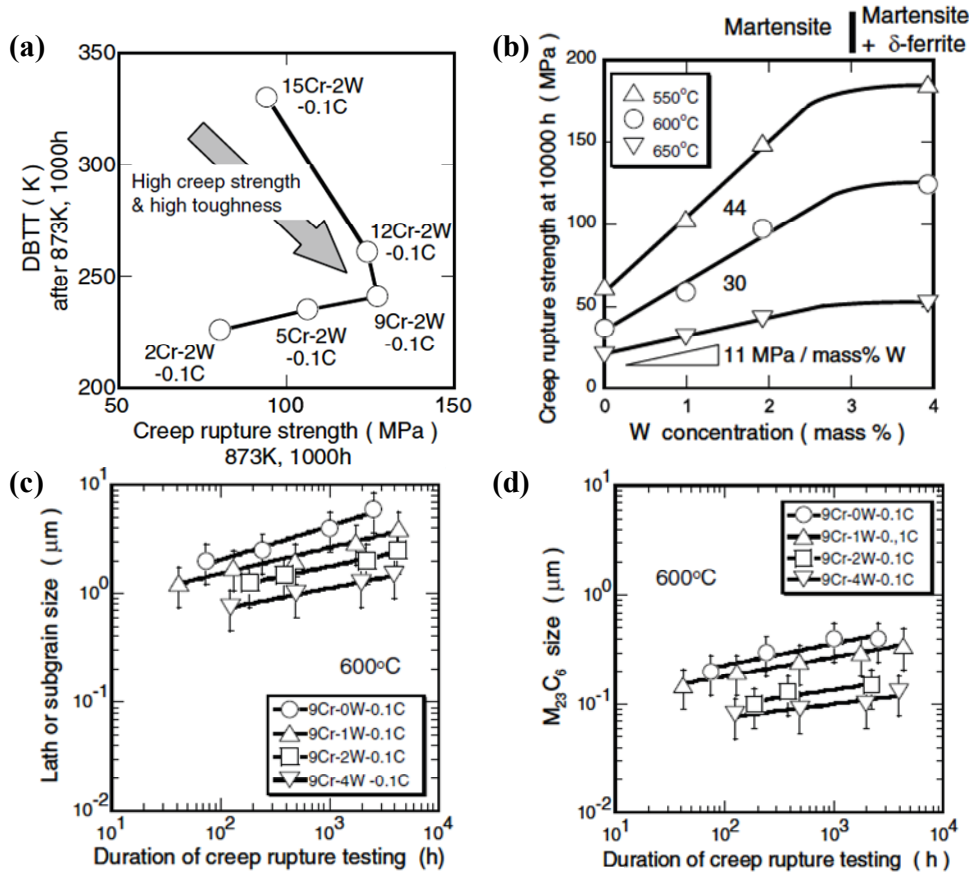


Figure 2.35: Effect of (a) %Cr on creep rupture strength, (b) %W on the creep rupture strength and (c) %W on martensitic lath width evolution and (d) %W on $M_{23}C_6$ precipitate size evolution with creep loading [Abe, 2008].

Molybdenum and tungsten: The primary purpose for including molybdenum and tungsten is (i) to enable the formation of solid solution strengthening mechanisms in 9-12Cr steels and (ii) promote the precipitation of $M_{23}C_6$ (i.e. $Mo_{23}C_6$ and $W_{23}C_6$) particles. The $M_{23}C_6$ carbides are dispersed along grain and lath boundaries, and hence, the inclusion of Mo and W in 9-12Cr steels leads to a reduced martensitic lath width (see Figure 2.35c) – increasing the low-angle boundary strengthening, which is proportional to the inverse of martensitic lath width. However, it has been found that Mo increases the rate of coarsening of $M_{23}C_6$ precipitates, whereas, as shown in Figure 2.35d, W is found to retard the growth of $M_{23}C_6$ precipitates [Maruyama *et al.*, 2001]. The coarsening of

2. Background and Literature Review

$M_{23}C_6$ carbides is a key microstructural degradation mechanism in 9-12Cr steels and hence, thermally stable $M_{23}C_6$ precipitates are highly desirable in 9-12Cr steels.

During long-term creep, Laves phase particles (Fe_2Mo and Fe_2W particles) are known to form at the expense of the solid solution strengthening mechanism [Hald, 2008]. These precipitates form at a relatively large spacing [Abe, 2008] and their contribution to the creep strength of the material is still under investigation. Tungsten is also found to slow down recovery and Laves phase formation in 9-12Cr steels [Klueh, 2004]. However, the level of Mo and W in 9-12Cr steels must be controlled to ensure that excess δ -ferrite does not form [Klueh, 2004]. Above 3% W, 9Cr steels transform from 100% tempered martensite to tempered martensite with δ -ferrite (the level of δ -ferrite increasing as the %W increases) [Abe, 2008]. As precipitates are not present in δ -ferrite, it is imperative that this important strengthening mechanism is maintained. Figure 2.36 illustrates the effect of varying the Mo and W content in 12Cr steels. From Figure 2.36a, there is a limit to the amount of Mo which is beneficial to creep rupture strength and the combined level of Mo+W must be controlled to ensure optimum creep strength. Increasing the W content towards 3 % is found to greatly improve the creep rupture strength. However, the ductility of the material is affected as the W content is increased (see Figure 2.36b). The presence of Mo and W also lowers the M_s point (martensitic transformation temperature) and increases the A_1 temperature (lower critical temperature – below this point, austenite does not exist) [Maruyama *et al.*, 2001].

2. Background and Literature Review

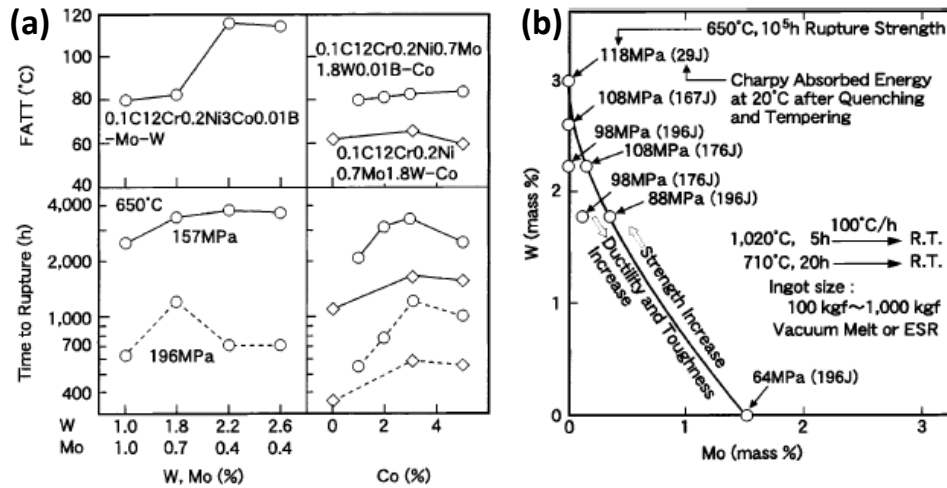


Figure 2.36: Effect of varying the composition of Mo and W on the creep rupture strength of 12Cr steels [Masuyama, 2001].

Carbon and nitrogen: C and N are soluble elements in austenite formation and precipitate out during the tempering process to form secondary phase $M_{23}C_6$ and MX precipitates. Thus, the presence of the C and N alloying elements are extremely important in providing a precipitate strengthening mechanism in 9-12Cr steels. Figure 2.37 illustrates the effect of including precipitates and solutes on the MSR for ferritic and bainite steels. The work of Abe *et al.* [2007a] has also concluded that excess addition of nitrogen can result in MX particle coarsening and the promotion of Z-phase particles at the expense of MX precipitates. This work also concluded that the addition of small amounts of titanium to form TiC particles can have a beneficial impact on the creep life by retarding lath recovery.

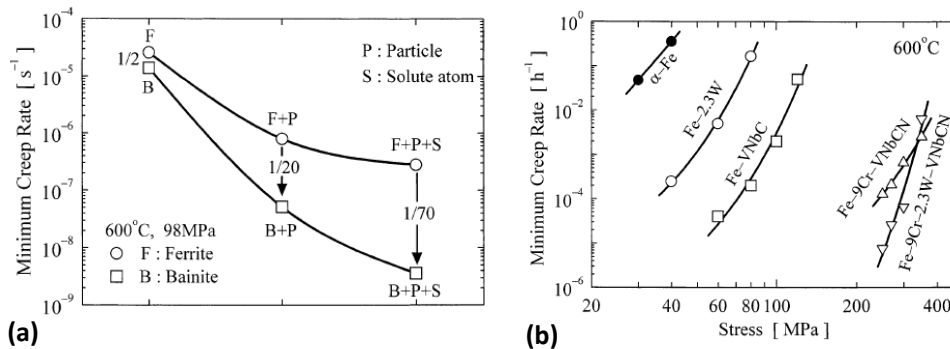


Figure 2.37: Effect of including (a) precipitates (+P) and solutes (+S) on bainite (B) and ferrite (F) steels and (b) V-Nb-C elements in ferritic steels [Maruyama *et al.*, 2001].

2. Background and Literature Review

Vanadium and niobium: V and Nb play a key role in forming the nano-scale MX particles (primarily VN and NbC particles but other elements including titanium and tantalum may also be present), providing a very stable precipitate strengthening mechanism at high temperatures. The typical dimension of these precipitates is in the 10 to 40 nm diameter region [Abe, 2008; Ennis and Czyska-Filemonowicz, 2002; Panait et al., 2010b], with the Nb particles spherical in shape and the VN precipitates plate-like particles. Figure 2.37b illustrates the beneficial effect of including V and Nb precipitates on the creep performance of various steels at a temperature of 600 °C and Figure 2.38 highlights the effect of various combinations of V and Nb compositions on the creep rupture strength in a 12Cr steel. However, large amounts of Nb are to be avoided as they promote the precipitation of Z-phase particles [Dawson, 2012]. The Z-phase particles are complex Cr(Nb,V)N particles which form at the expense of the thermally stable MX precipitates and their precipitation is found to reduce the creep strength of the material [Abe, 2008].

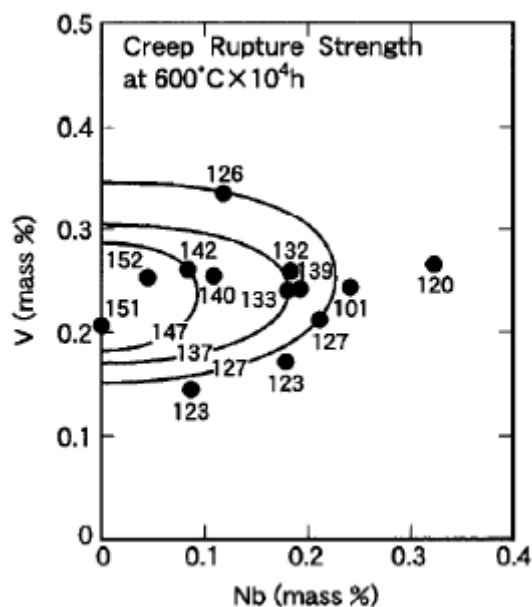


Figure 2.38: The effects of varying V and Nb composition on the creep rupture strength of 12Cr steel at a temperature of 600 °C [Masuyama, 2001].

Cobalt, copper, manganese, and nickel: Co, Cu and Ni are all elements which aid austenite formation and hence, inhibit δ -ferrite formation

2. Background and Literature Review

[*Masuyama, 2001; Oñoro, 2006*] in a similar manner to carbon and nitrogen. Co, Cu and Ni ensure that the material is fully austenitic following the austenitisation process to allow complete martensitic transformation during cooling. Ni (and Mn to a lesser extent) can accelerate precipitate coarsening [*Klueh, 2004*], and hence reduce creep rupture strength [*Maruyama et al., 2001; Viswanathan and Bakker, 2001*] but Ni and Co are beneficial to material toughness [*Klueh, 2004*]. Although Mn can improve toughness [*Masuyama, 2001*] and material ductility by mitigating sulphur enrichment of grain boundaries [*Dawson, 2012*] whilst also providing a small solute strengthening mechanism, the Mn content (as well as the Si content) must be minimised to improve creep strength [*Maruyama et al., 2001; Masuyama, 2001*]. As both Mn and Ni are austenite stabilisers [*Dawson, 2012*], excessive Mn+Ni (> 1 wt.%) can lead to retained austenite during welding [*Santella et al., 2001*] and hence, reducing the ferrite-austenite ($\alpha \leftrightarrow \gamma$) transition temperature and narrowing the post weld heat treatment (PWHT) window of operation [*Swindeman et al., 2004*].

Boron: Boron is added in small amounts to 9-12Cr steels to retard precipitate coarsening of the $M_{23}C_6$ precipitates and hence, maintain the martensitic lath structure during creep deformation [*Abe et al., 2007b; Abe et al., 2008; Hofer et al., 2000a*]. Boron is also found to interact with MX precipitates and Laves phase particles [*Hofer et al., 2000b*]. However, boron may reduce the impact toughness of the material [*Maruyama et al., 2001*].

2.6.2. Heat treatment

The heat treatment process for 9-12Cr steels is extremely important to ensure that full martensitic transformation occurs and the level of δ -ferrite is minimised to less than 8 % [*Brett, 2014*]. The heat treatment is a two-stage process involving austenitisation followed by tempering, as illustrated schematically in Figure 2.39. The initial austenitisation stage is carried out at temperatures high enough for austenite to form, e.g. 900 °C to 1400 °C as illustrated in the phase transformation maps of Figure 2.40, a material with an equi-axed grain structure. Rapid cooling (which must be carefully

2. Background and Literature Review

controlled for large components) to temperatures below 400 °C (see Figure 2.40b) yields martensitic transformation and the formation of a hierarchical microstructure with a very high density of dislocations. $M_{23}C_6$ particles, initially in the material, are replaced with needle-like M_3C precipitates, as well as Nb(C,N) particles [Ennis and Czyska-Filemonowicz, 2002].

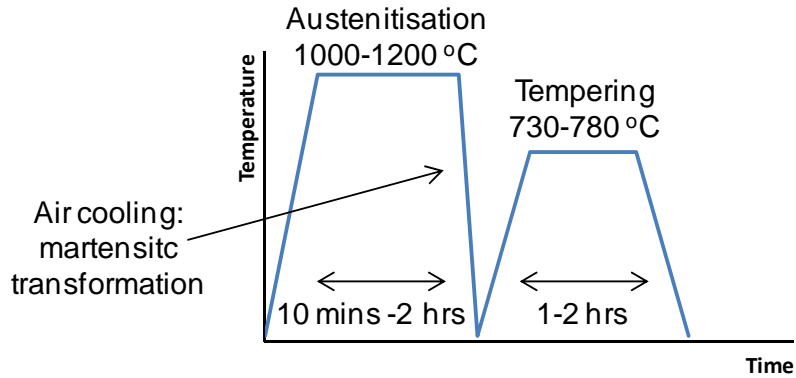


Figure 2.39: Heat treatment process in 9-12Cr steels.

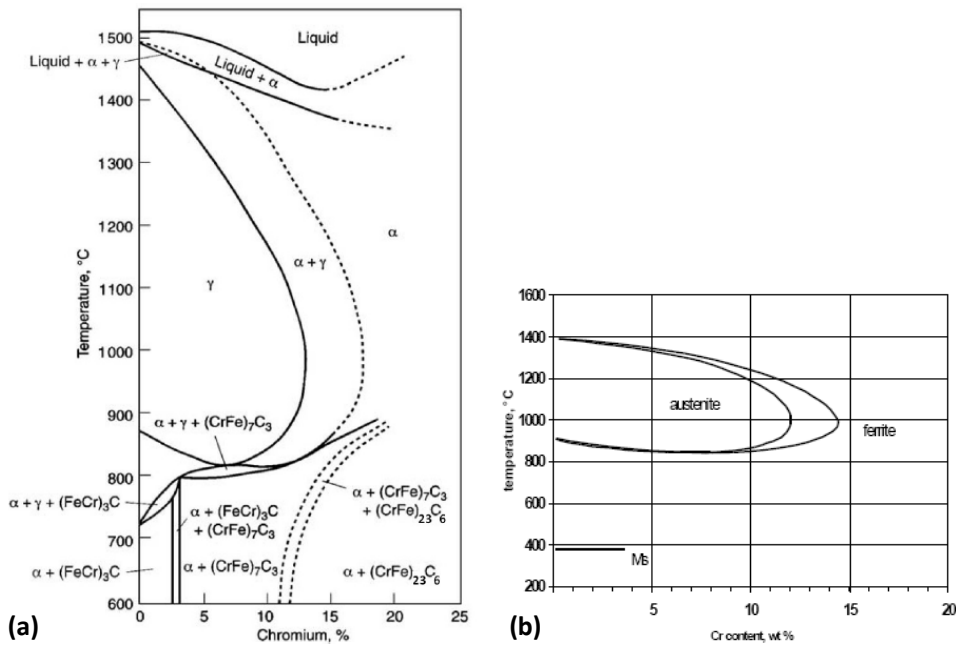


Figure 2.40: Phase transformation maps for (a) steels containing 0.1% C [Pickering, 1997] and (b) martensitic transformation temperatures [Ennis and Czyska-Filemonowicz, 2002].

Figure 2.41 illustrates the effect of austenitising temperature on the size of austenite grains and martensitic laths formed in P92 steel, with an increasing

2. Background and Literature Review

austenitisation temperature resulting in an increased martensitic lath width. This differs to the martensitic structure formed in an Fe-0.2C-Mn(-V) low carbon alloy, from the work of Morito and co-workers [2005], who observed that decreasing the prior austenite grain size significantly reduced the packet and block dimensions, but observed little effect with respect to martensitic lath width.

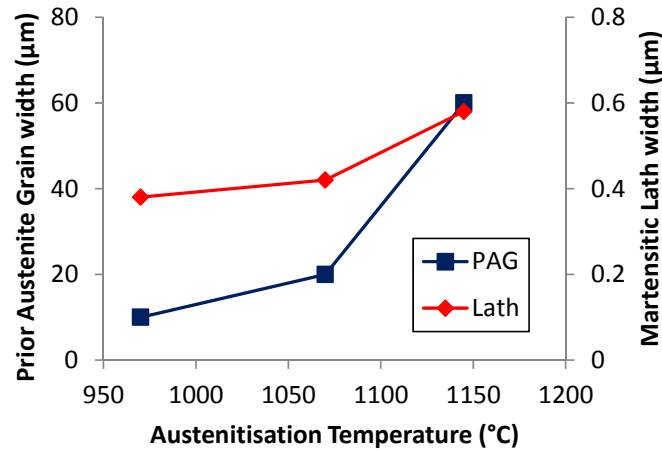


Figure 2.41: Variation of prior austenite grain and martensitic lath width as a function of austenitisation temperature for P92 steel (data from the work of Ennis and Czyrska-Filemonowicz [2002]).

Lath martensite is a brittle material with a high dislocation density and thermally-unstable M_3C precipitates. Hence, to improve ductility and promote the precipitation of more stable particles, 9-12Cr steels undergo a tempering process, at a lower temperature, typically in the 700 °C to 850 °C temperature range. This tempering process promotes (b.c.c.) ferrite formation. As shown in Figure 2.42, a higher tempering temperature causes a large reduction in hardness and dislocation density; the observed decreases are dependent on tempering temperature and tempering time. Recovery during tempering lowers the dislocation density and also forms dislocation networks [Ennis and Czyrska-Filemonowicz, 2002]. Excess tempering can lead to the formation of more equi-axed subgrains in place of martensitic laths [Sawada *et al.*, 2003], as discussed in more detail in Section 2.6.4.2.

Tempering also results in the conversion of M_3C precipitates into more stable carbide and carbonitrides, which are dispersed along boundaries and

2. Background and Literature Review

within the martensitic lath interiors. $M_{23}C_6$ precipitates form along high angle grain boundaries and are also dispersed along the martensitic lath and subgrain boundaries, with Nb(C,N) particles (spherical in shape) and VN nitrides forming in the martensitic lath interiors [Ennis and Czyska-Filemonowicz, 2002; Panait et al., 2010a; Panait et al., 2010b].

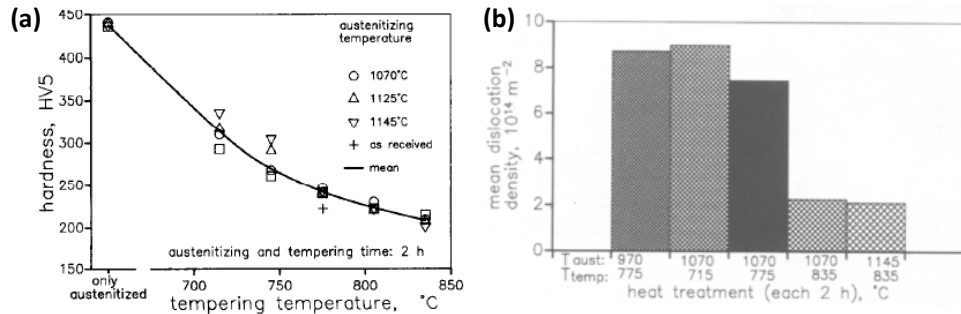


Figure 2.42: Effect of (a) austenitisation temperature on the material hardness for a 2 hr austenitisation process followed by a 2 hr tempering process at 775 °C and (b) comparison of various heat treatment processes on dislocation density [Ennis et al., 1997].

The work of Aghajani *et al.* [2009b] investigated the effect of post austenitisation cooling rates on the microstructural evolution and creep performance of T24 steel. In this study, air-cooling and water quenching techniques were compared, with a reduced rupture life observed for the air-cooled specimens under short-term creep loading conditions and no obvious effect observed for long-term creep behaviour. This difference is related to the material microstructure and the ability of the water quenched specimen to retain its fine martensite structure following long-term creep deformation, illustrating the importance of (i) the creep strength obtained from the martensitic lath structure and (ii) the requirement for a stable microstructure during long-term creep deformation.

This requirement for long-term higher temperature creep strength and microstructural stability has led to the development of the MarBN grade of 9-12Cr steels (9Cr-3W-3Co-V-Nb steels). MarBN is a 9Cr steel with boron added to improve creep strength via the formation of more thermally stable $M_{23}(\text{CB})_6$ carbides along boundaries in place of the more conventional $M_{23}C_6$ carbides present in P91 and P92 steels [Li et al., 2013a]. However, to

2. Background and Literature Review

ensure that unstable BN precipitates do not form, the nitrogen content must be controlled. Hence, this reduction leads to a decrease in the dispersion of the fine MX particles in the martensitic lath interiors, precipitates which are stable under long-term creep [Abe, 2004] and improve the precipitate strengthening, leading to improved creep strength. Abe and co-workers [Abe, 2008; Sakuraya et al., 2006] have suggested limiting the level of nitrogen to less than 100 ppm to help reduce the formation of BN particles. However, this is quite difficult to achieve for larger castings [Li et al., 2013a] and hence, this process has limited benefit for realistic development of components. To overcome this limitation, the IMPACT¹ project have developed a heat treatment procedure, based on ThermoCalc predictions and experimental investigations, which eliminates the formation of BN precipitates by austenitising the material at temperatures of 1175 °C to 1200 °C for periods of 1 to 7 hours [Li et al., 2013a]. This high austenitisation temperature also ensures that any BN precipitates which form during manufacture of the pre heat-treated material are eradicated. The work of Abe [2004] also highlights the need to minimise carbon content to promote the formation of MX particles in place of excess formation of $M_{23}C_6$ precipitates along boundaries. This is beneficial as MX particles are much more thermally stable than $M_{23}C_6$ carbides [Klueh, 2004] and minimising the number of inclusions along boundaries will also limit the potential number of sites for voids to form. The benefits of introducing boron on the creep performance of MarBN over conventional 9Cr steels are summarised by the schematic representations presented in Figure 2.43.

¹ The IMPACT project was a TSB funded project involving project partners from Loughborough University, The Open University, NUI Galway, University of Limerick, E.ON New Build and Technology, Alstom, Doosan Power, Goodwin Steel Castings, National Physical Laboratory and Tata Steel. The industry funded IMPEL project is the follow-up project to continue the development of MarBN.

2. Background and Literature Review

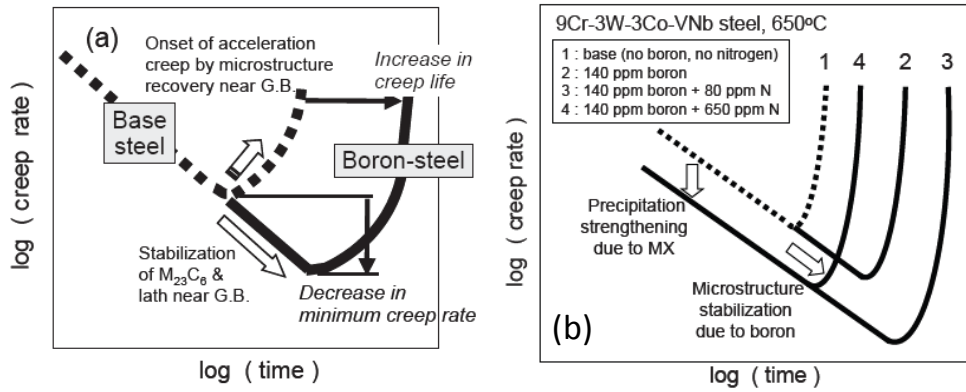


Figure 2.43: Schematic representation of the effect of including (a) boron and (b) additional boron and nitrogen on the creep performance of 9Cr steels [Abe, 2011a].

MarBN steel has a much larger prior austenite grain size [Albert *et al.*, 2005] when compared to P91 and P92 steels as a result of the higher austenitisation temperature. This leads to improved creep performance as there are a reduced number of sites for voids to form along grain boundaries. MarBN also has an increased level of tungsten when compared to P91 and P92 steels, leading to greater solute and precipitate strengthening effects. The work of Albert *et al.* [2005] also illustrated that little carbide coarsening was observed, the fine grain heat affected zone (FG-HAZ) region was absent in a welded connection and no Type IV cracking was observed for 9Cr-3W-3Co-NbV steels with 90 to 130 ppm boron included and tested at 923 K in the 140 to 180 MPa stress range.

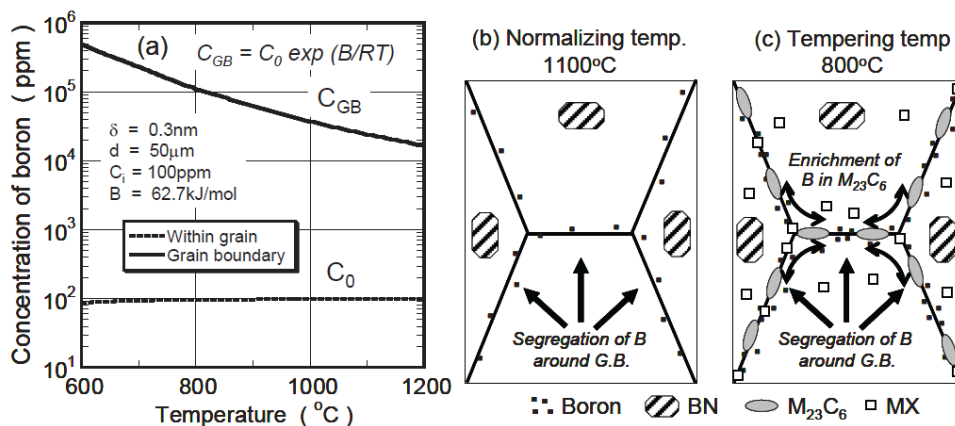


Figure 2.44: Schematic representation of the mechanism of boron enrichment of grain boundaries in MarBN materials [Abe, 2011a].

2. Background and Literature Review

To date, a large amount of work has been carried out to assess the creep behaviour of MarBN, with significant improvements over the current state-of-the-art materials already achieved. However, for the material to be successful under realistic plant operating conditions, further investigation is required. The material needs to be tested under long-term creep loading conditions at lower stresses (<100 MPa) and the performance of the material under cyclic loading conditions must be assessed as plant move towards more flexible operation. Chapter 3 of this thesis investigates the cyclic performance of MarBN and presents, for the first time, high temperature fatigue results.

2.6.3. Cracking of welded connections

Failures in power plant components are commonly related to welded connections, which are multi-material regions with heterogeneous microstructures. A welded connection can be split into parent material (PM), weld metal (WM) and heat affected zone (HAZ), with the various types of failures illustrated schematically in Figure 2.45. The most common type of failures for 9-12Cr steels are Type IV cracks, at the interface between the HAZ and PM. Images of Type IV cracks are presented in Figure 2.46a. The HAZ, which is considerably softer than the parent material, is made up of three distinct regions, namely the coarse-grain region (CG-HAZ) at the interface with the WM, a fine-grained region (FG-HAZ) and the intercritical HAZ (IC-HAZ) region at the interface between the HAZ and PM (see Figure 2.46b). Type IV failures occur in the IC-HAZ region and are primarily related to the microstructure, which does not have the hierarchical structure of the parent material (PM), as shown in Figure 2.46c.

2. Background and Literature Review

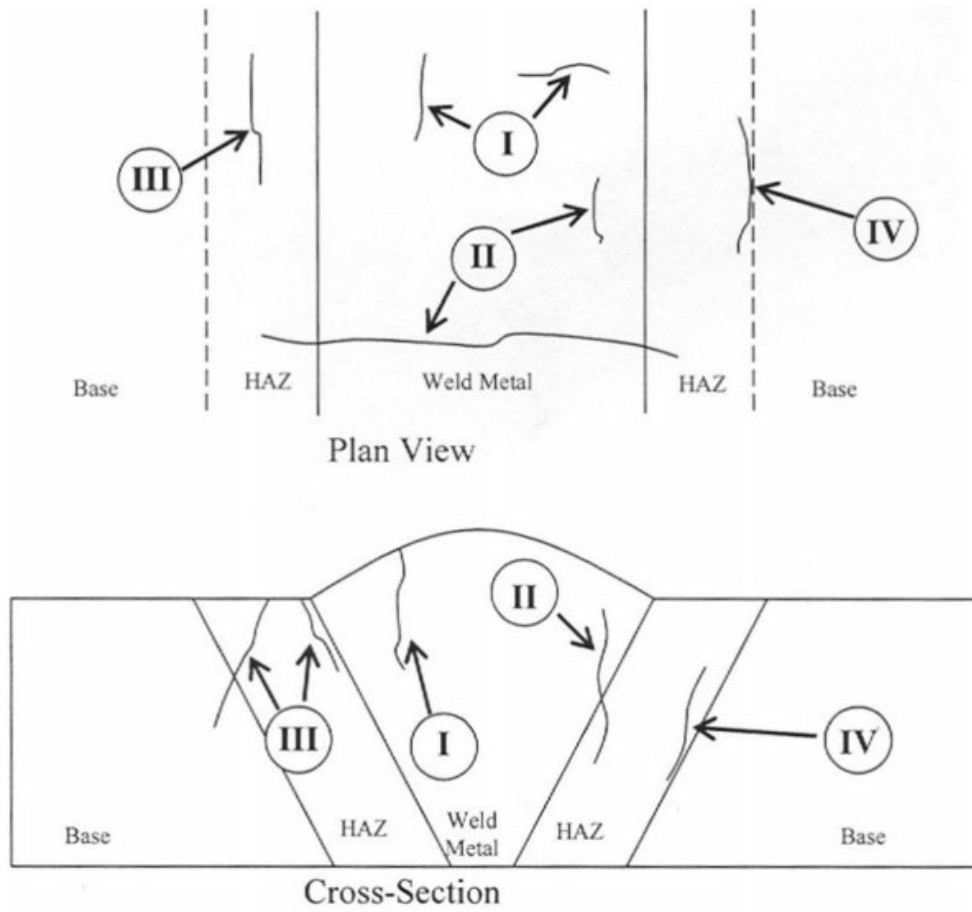


Figure 2.45: Types of failures in welded components [Abson and Rothwell, 2013].

2. Background and Literature Review

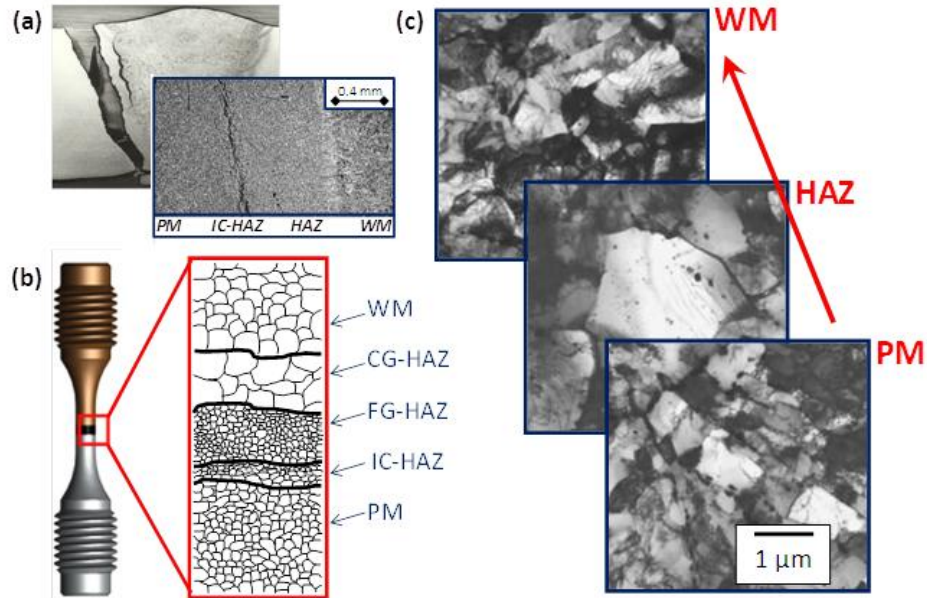


Figure 2.46: Welded connections in 9-12Cr steels: (a) Type IV failure in the IC-HAZ region, (b) schematic representation of a welded connection and cross-weld specimen and (c) TEM images of the different regions in a welded connection [Watanabe *et al.*, 2006]

Figure 2.47 presents an EBSD scan of the microstructure of (i) P92 steel and (ii) 9Cr-3W steel with 90 ppm boron addition for base and HAZ materials. Although the prior austenite grain size in the base materials are quite similar (and relatively similar hierarchical microstructure), significant differences exist in the HAZ regions. The addition of 90 ppm boron has led to a significantly modified HAZ microstructure. The new HAZ is not fine-grained and has a hierarchical microstructure akin to that of parent metal. This hierarchical microstructure results in higher weld creep strength, as illustrated in Figure 2.48, and prevention of Type IV cracking.

2. Background and Literature Review

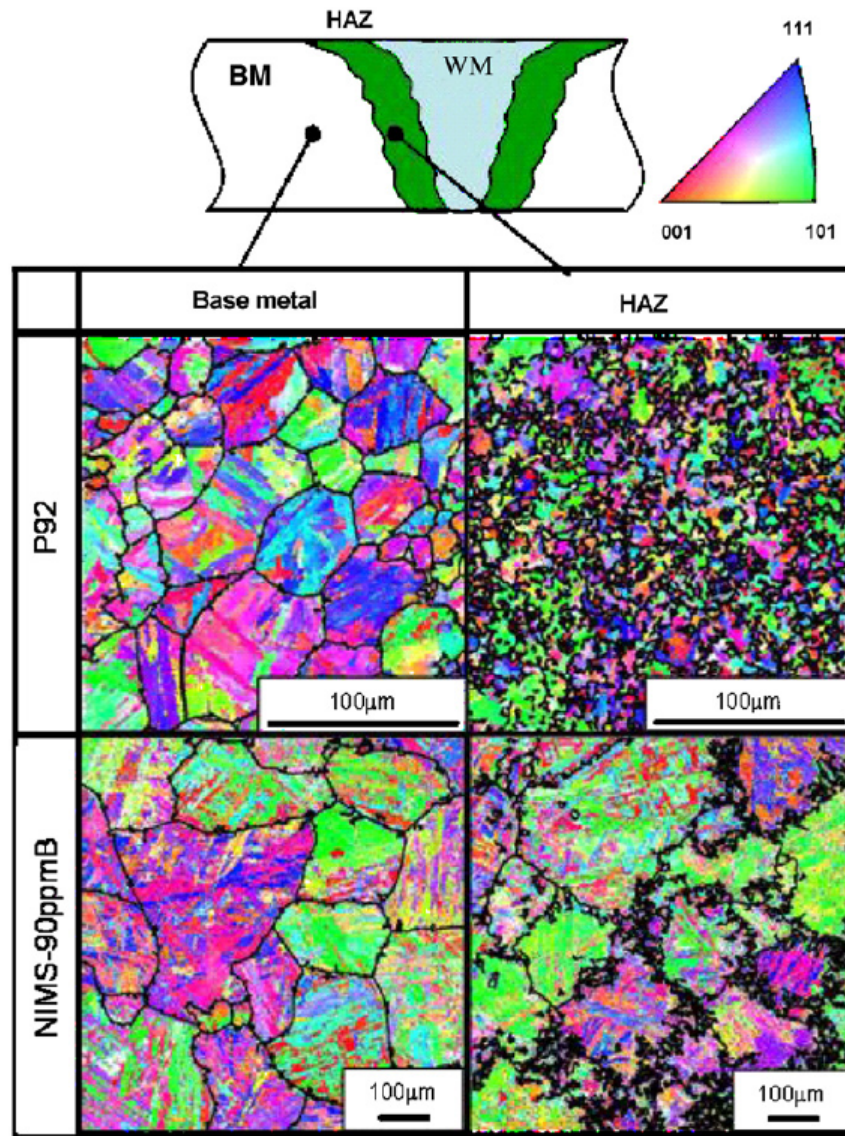


Figure 2.47: EBSD image of the microstructure of base metal and HAZ material in P92 and NIMS-90ppmB (9Cr-3W steel with 90 ppm boron addition) [Abe *et al.*, 2007b].

2. Background and Literature Review

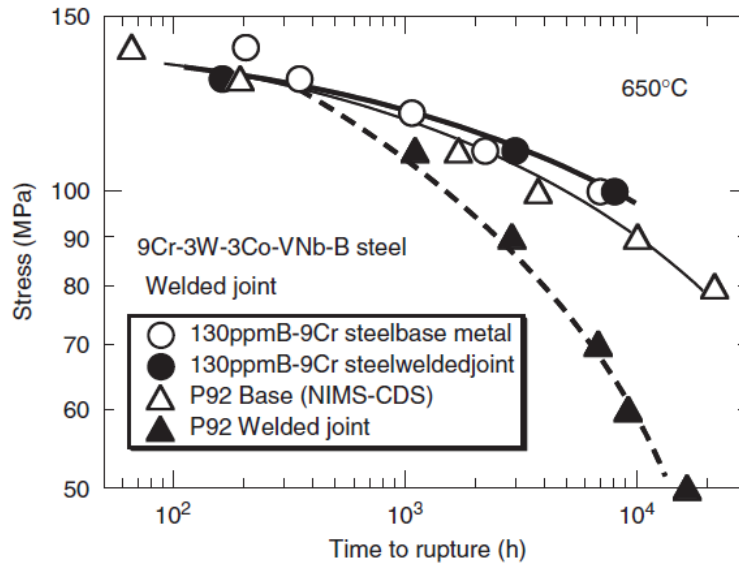


Figure 2.48: Comparison of the time to rupture of welded P92 steel and 9Cr-3W steel with 130 ppm addition of boron at a temperature of 650 °C [Abe *et al.*, 2007b].

2.6.4. Microstructural evolution in 9-12Cr steels

The long-term high-temperature stability of the precipitate-strengthened hierarchical microstructure in 9-12Cr steels is essential in preventing premature failure of power plant components. The following sections discuss the evolution of the key strengthening mechanisms of precipitates, solid solution strengthening, martensitic lath structure and dislocation density evolution.

2.6.4.1. Precipitate and solute strengthening in 9-12Cr steels

In the initial microstructure of 9-12Cr steels, $M_{23}C_6$ and MX precipitates, as well as Mo solutes (and W solutes for P92 and MarBN steels) are the primary interstitial and substitutional obstacles present to enable strengthening. Under cyclic viscoplasticity and creep loading, the mechanism for hardening via these obstacles has been identified by Sauzay and co-workers [2005; 2008] and also Panait and co-workers [2010a; 2010b] as bowing out of mobile dislocations pinned at obstacles. As plastic strain (viscoplastic strain for high temperature loading) accumulates, the force on the mobile dislocation pinned at its ends increases and the

2. Background and Literature Review

dislocation starts to bow out. This bowing out mechanism is depicted in Figure 2.49 from TEM studies for both fatigue and creep loading conditions. Under fatigue loading, the pinning mechanism results in a back-stress which is responsible for the Bauschinger effect and under creep, the pinning mechanism produces the back-stress necessary for hardening primarily observed during primary creep.

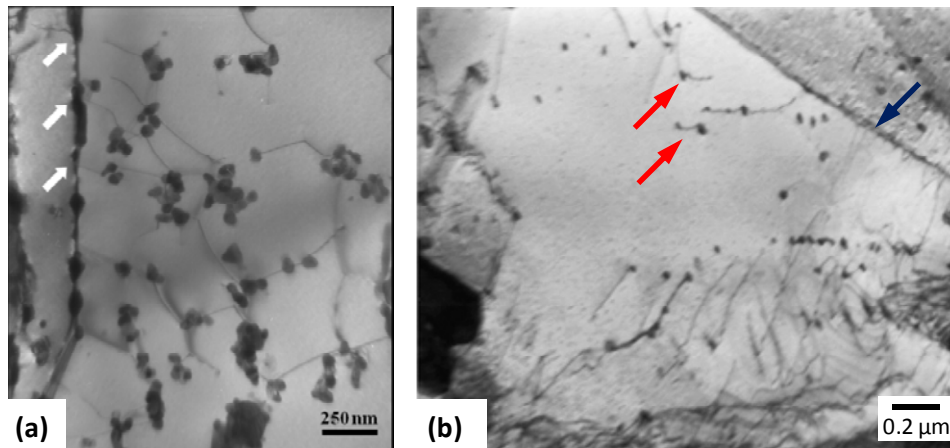


Figure 2.49: Micrographs of martensitic lath interiors in (a) P92 steel [Giroux, 2011] and (b) P91 steel [Panait et al., 2010b]. The red arrows point to dislocations pinned at MX precipitates and white arrows point to lath boundaries.

The stability of these strengthening mechanisms is dependent on the coarsening of the precipitates. Prolonged high temperature exposure results in particle coarsening and precipitation of new secondary phases. The work of Abe [2008], Hald and Korcakova [2003], Panait and co-workers [2010a; 2010b], and Ghassemi-Armaki and co-workers [2009; 2011; 2013] have measured the increase in mean diameter of $M_{23}C_6$ and MX particles with creep loading, e.g. as shown in Figure 2.50 for various Cr concentrations and the increase in particle spacing with creep aging time. For high temperature operation, the dominant mechanism of particle coarsening is the thermodynamically driven Ostwald ripening process. According to the Ostwald ripening process, the requirement to lower the overall energy of the system results in smaller particles, with a higher surface energy, detaching and diffusing through the solution to combine with larger particles, leading to a reduction of surface energy. Thus, the mean particle radius increases

2. Background and Literature Review

with an approximately constant volume fraction of particles. The increase in particle spacing via Ostwald ripening can be described using the well-known kinetic equation derived by Lifshitz and Slyozov [1961], which describes the evolution of the mean precipitate diameter, d_i :

$$d_i^3 = d_{i,0}^3 + K_i t \quad (2.26)$$

where $d_{i,0}$ is the initial mean diameter, t is time and K_i is the coarsening rate of a precipitate of type i and defined as [Lifshitz and Slyozov, 1961]:

$$K_i = \frac{8\gamma C_\infty v^2 D}{9RT} \quad (2.27)$$

where γ is surface energy, C_∞ is particle solubility, v is molar volume and D is the diffusion coefficient. Typical values of the coarsening rates, K_i , are presented by Spigarelli [2013a] for 9-12Cr steels, for example. As Ostwald ripening is a rate (and temperature) dependent process, particle coarsening is of primary concern to creep loading and hence, under fatigue loading conditions, it is assumed that only minimal coarsening occurs. The effect of particle coarsening on precipitate spacing due to long-term creep loading in 9-12Cr steels is presented in Figure 2.50, resulting in a decrease of the precipitate strengthening mechanism and hence, an overall decrease in strength.

2. Background and Literature Review

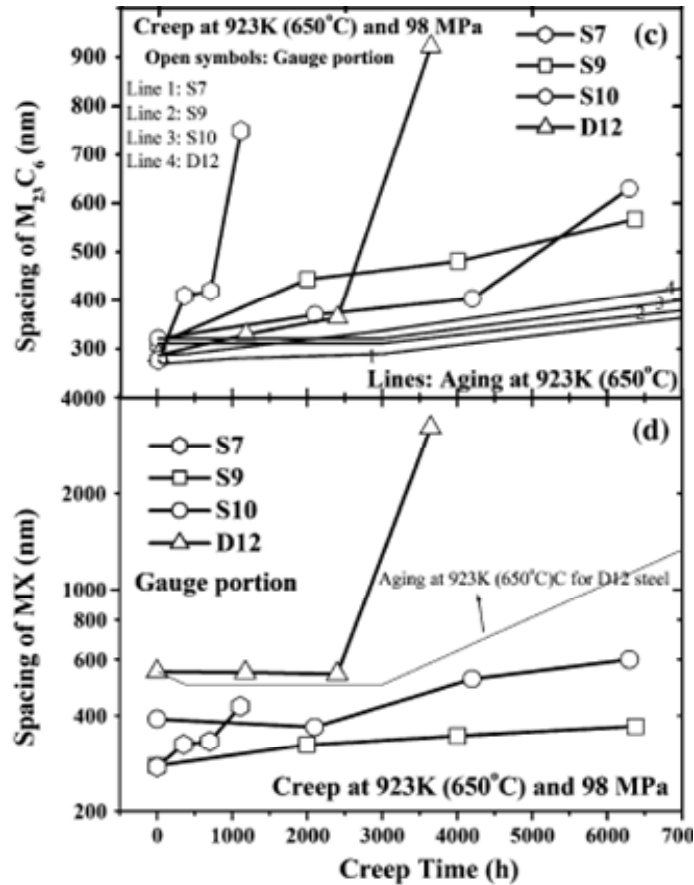


Figure 2.50: Effect of creep loading time on the spacing of $M_{23}C_6$ and MX precipitates [Ghassemi-Armaki *et al.*, 2011].

One of the major benefits of MarBN steels is related to the stability of $M_{23}C_6$ precipitates. The addition of boron atoms produces $M_{23}(CB)_6$ precipitates. These precipitates are much more stable during high temperature loading [Abe *et al.*, 2008; Li *et al.*, 2013a] and hence, result in increased strength [Abe *et al.*, 2008] as the martensitic laths and LAB dislocation substructure is less susceptible to deformation via migration of martensitic lath boundaries [Sawada *et al.*, 2003; Yan *et al.*, 2013] (see description below).

The Ostwald ripening law of Equation (2.26) describes the temperature- and time-dependent coarsening of precipitates only, and is valid for long-term coarsening of precipitates under thermal aging. However, as measured in the work of Hu and co-workers [2014], coarsening of precipitates under fatigue in 9-12Cr steels can also occur. This work investigated the effect of fatigue

2. Background and Literature Review

loading on the microstructure of the China Low Activation Martensitic (CLAM) steel and observed an increase in $M_{23}C_6$ size following short-term LCF tests. The mechanism for the increased coarsening rate is strain-dependent coarsening related to the diffusion term of Equation (2.27), with a significant increase in the diffusion coefficient for dislocation diffusion (viscoplastic-strain dependent diffusion) when compared to lattice diffusion [Taneike *et al.*, 2001]. The work of Taneike and co-workers [2001] also led to the development of a modified Ostwald ripening model to include strain-dependent precipitate coarsening:

$$d_i^3 - d_{i,0}^3 = C_\infty(a_1t + a_2\varepsilon) \quad (2.28)$$

where a_1 and a_2 are constants related to diffusion, similar to that of Equation (2.27). The coarsening of precipitates, either via Ostwald ripening or strain-dependent, results in a decrease in the strengthening provided by the precipitates as the mean spacing between particles is increased. Hence, the Orowan stress is decreased as the ability of the obstacles to impede the motion of mobile dislocations is reduced. Long-term, high temperature exposure also leads to the formation of new secondary phase particles, namely Laves phase and Z-phase particles. The formation of these new precipitates occurs at the expense of other mechanisms of strengthening, as discussed briefly in the following sections.

During long-term thermal aging, Laves phase particles form in 9-12Cr steels at the expense of the solid-solution strengthening mechanism. The formation of these large Fe_2Mo and Fe_2W particles, with a mean diameter in the range of 200 to 800 nm [Panait *et al.*, 2010a], occurs due to long-term high temperature exposure and affect the strengthening available due to two mechanisms. Firstly, as the volume fraction of Laves phase particles increases, precipitate strengthening increases due to the Orowan mechanism. However, after a period of time, the newly formed precipitates will start to coarsen, resulting in a decrease of the strengthening obtained, as illustrated schematically by the blue line in Figure 2.51. This initial dynamic increase of strengthening contributes to the long primary creep phase in 9-12Cr steels [Abe, 2015]. The second mechanism is the decrease in solid-

2. Background and Literature Review

solution strengthening as the Mo and W solutes are consumed to form the Laves phase particles, as highlighted by the red line in Figure 2.51.

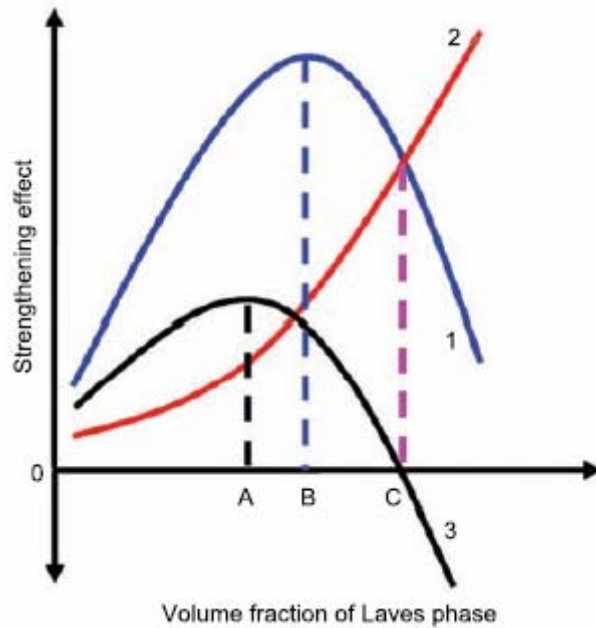


Figure 2.51: Effect of volume fraction of Laves phase on strengthening in 10Cr steel [Hu *et al.*, 2011]. The blue line represents creep strengthening due to Laves phase formation, red line represents decrease in creep rupture strength owing to Laves phase formation at the expense of solutes and the black line represents the overall effect of Laves phase formation.

The second particle type to precipitate during long-term thermal aging are the complex modified Z-phase precipitates, precipitates of the type Cr(Nb,V)N. Due to their structure, modified Z-phase particles consume smaller MX type precipitates following long-term thermal aging. The precipitation of Z-Phase particles is detrimental to the structural integrity of welded connections [Abe, 2008]. The overall evolution of mean precipitate diameters in a 10Cr steel is summarised in Figure 2.52, with the coarsening and precipitation of new secondary phases adversely affecting the performance of 9-12Cr steels under fatigue and creep deformation.

2. Background and Literature Review

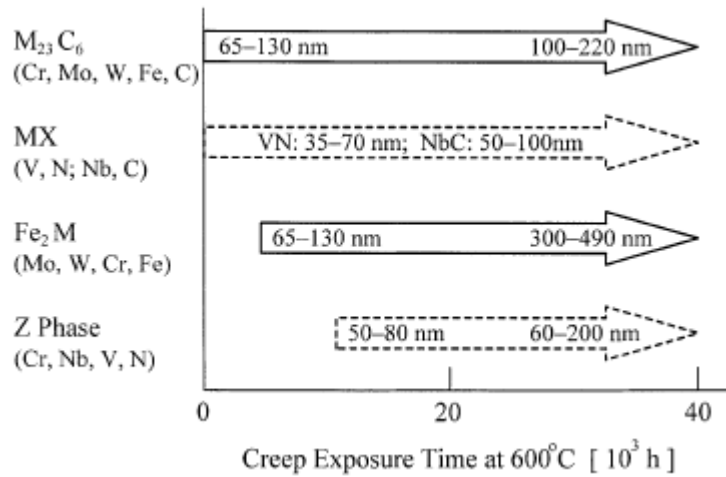


Figure 2.52: Evolution of mean precipitate diameters and formation of new secondary phases in 10Cr-1W-1Mo-VNb steel [Maruyama *et al.*, 2001].

2.6.4.2. Martensitic lath growth and subgrain formation

During creep loading, martensitic laths do not coarsen, but their respective boundaries can migrate [Sawada *et al.*, 2003; Yan *et al.*, 2013] and new dislocation networks can form [Keller *et al.*, 2010], resulting in the establishment of more equi-axed subgrain structures. This martensitic lath to subgrain transformation occurs throughout the three stages of creep deformation and predominately during the tertiary phase of creep [Abe, 2008; Abe, 2011b], under the accumulation of creep strain and evolution of dislocation density, resulting in a transformation of the martensitic lath microstructure to a more equi-axed subgrain microstructure. Panait and co-workers [Panait *et al.*, 2010b] have shown that pure thermal aging (at a temperature of 600 °C), via analysis of the heads of crept specimens, results in minimal martensitic lath coarsening. Figure 2.53 compares the effects of thermal aging and load-dependent martensitic lath (subgrain) evolution via comparison of lath width distribution in the specimen head (thermally aged only) with the distribution on the gauge length (crept material). As is evident from the distributions shown in Figure 2.53, thermal aging at 600 °C has little effect on lath evolution and hence, it can be concluded that lath coarsening is primarily dominated by inelastic deformation. Figure 2.53 also shows the initial and final measured distribution of martensitic lath width in a P91 steel, which was subjected to a creep load of 80 MPa for 113,000 hrs.

2. Background and Literature Review

The insignificant dependence of martensitic lath evolution on thermal aging is related to the thermal stability of martensitic laths [Sawada *et al.*, 2003], which are reinforced by the presence of $M_{23}C_6$ precipitates dispersed along LABs. It is the coarsening of these $M_{23}C_6$ carbides with time which results in the migration of the LABs [Ennis and Czyska-Filemonowicz, 2002], illustrating the importance of minimising the coarsening of $M_{23}C_6$ carbides during long-term creep deformation. The transformation of martensite lath boundaries into more equi-axed subgrains is as a result of this migration mechanism [Panait *et al.*, 2010b; Orlova *et al.*, 1998].

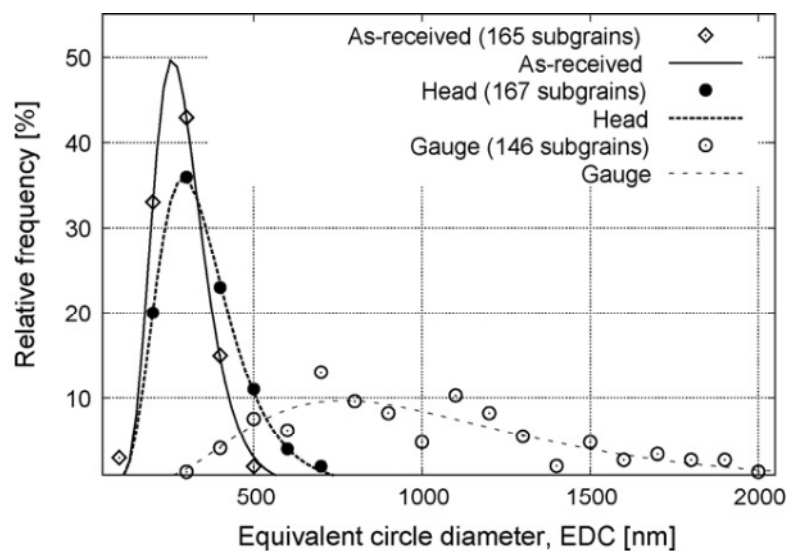


Figure 2.53: Comparison of the initial and final martensitic lath-subgrain width in crept P91 steel [Panait *et al.*, 2010b]. The specimen was crept at 80 MPa for 113,000 hrs at 600 °C.

However, under fatigue loading, martensitic laths widen through the loss of the LAB dislocation substructure [Fournier *et al.*, 2005; Giroux, 2011; Sauzay *et al.*, 2005; Sauzay *et al.*, 2008]. Martensitic laths are defined as regions bounded with LAB dislocations, as illustrated in Figure 2.54 from the work of Hu and co-workers [2013] on CLAM steel. Hence, as discussed by Sauzay and co-workers [2005], the loss of this LAB dislocation substructure occurs due to a glide mechanism, in which mobile dislocations interact with LAB dislocations resulting in the annihilation of the two dislocations. It should also be noted that, while not the primary mechanism

2. Background and Literature Review

for widening of martensitic laths under creep loading, LAB dislocation annihilation should also be considered.

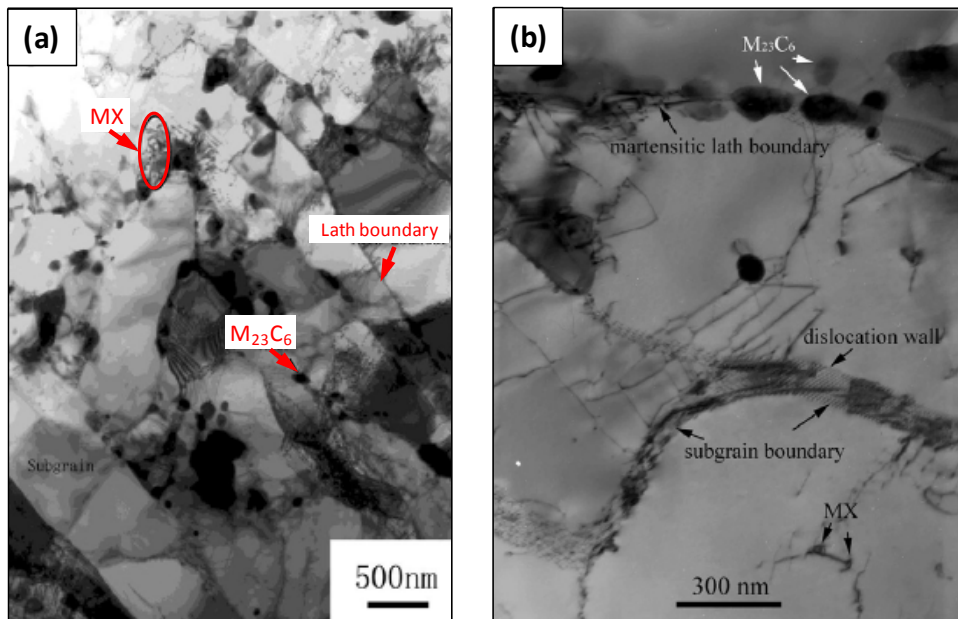


Figure 2.54: Martensitic lath and LAB dislocation microstructure of 9-12Cr steels for (a) the overall martensitic lath structure with $M_{23}C_6$ precipitates dispersed along boundaries and MX particles within the lath interiors and (b) the LAB dislocation substructure with $M_{23}C_6$ carbides dispersed along lath boundaries for a CLAM steel [Hu *et al.*, 2013].

As the density of LAB dislocations decreases, $M_{23}C_6$ carbides, which were originally dispersed along the LABs, are left behind in the lath interiors as a lath interior strengthening mechanism (along with MX particles and Mo and W solutes). This trait of 9-12Cr steels has been identified by Giroux [2011] and Sauzay *et al.* [2008], as is evident in Figure 2.55. The overall effect of the loss of the LAB dislocation substructure is (i) a decrease in mobile dislocation density, (ii) widening of martensitic laths (via the merging of two adjacent laths as their LAB interface disappears) and (iii) reduced strength [Dubey *et al.*, 2005]. Hold periods, i.e. during stress relaxation dwell tests, have also been shown to increase the rate of softening in 9-12Cr materials [Dubey *et al.*, 2005].

2. Background and Literature Review

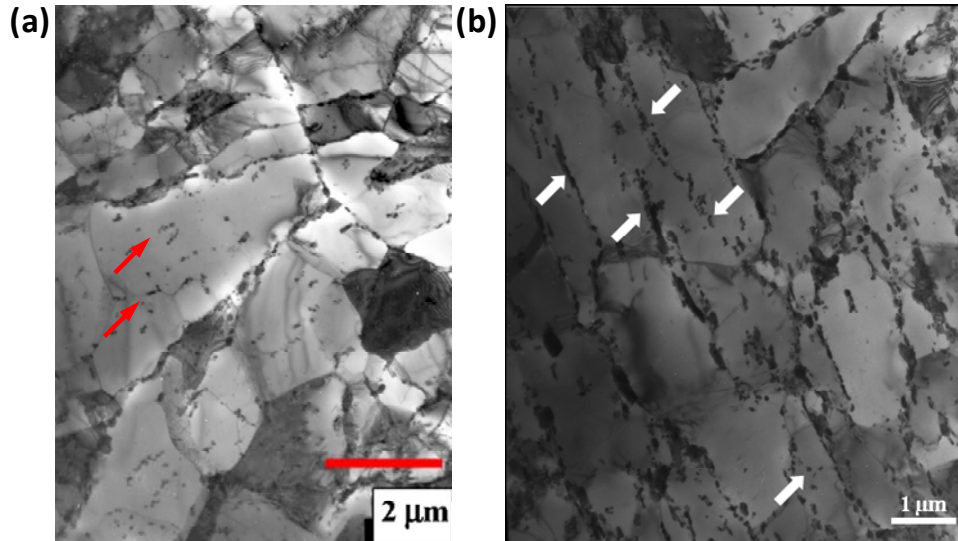


Figure 2.55: TEM images of the martensitic lath microstructure following cyclic deformation in (a) P91 steel [Sauzay *et al.*, 2008] and (b) P92 steel [Giroux, 2011]. The arrows point to $M_{23}C_6$ precipitates, which were originally aligned along martensitic lath boundaries, and now form part of the lath interiors.

The widening of laths, either via migration of boundaries, martensitic lath to subgrain transformation and subsequent subgrain coarsening or loss of LAB dislocations, results in a reduction of the strength of the material. Primarily, this results in a decrease in the yield stress of 9-12Cr steels, as typified by the following equation [Nes, 1998; Pedersen *et al.*, 1981]:

$$\sigma_y = \frac{\alpha_2 M b \mu}{w} \quad (2.29)$$

where α_2 is a material constant, M is Taylor factor, μ is shear modulus, b is magnitude of the Burger's vector and w is martensitic lath width. Typical values for initial martensitic lath widths and final lath width (loading dependent) for 9-12Cr steels are given in the literature [Giroux, 2011; Hyde *et al.*, 2012; Panait *et al.*, 2010b; Sauzay *et al.*, 2008; Sawada *et al.*, 1999]. The limiting martensitic lath width is the width of the block boundary [Sauzay *et al.*, 2005]. The evolution of martensitic lath width under fatigue loading has been measured via TEM from tests repeated at fractions of the failure life for (i) P91 steel [Hyde *et al.*, 2012] and (ii) P92 steel [Giroux, 2011] at temperatures of 600 °C and 550 °C respectively. The results of these tests, which were conducted at an applied strain-rate of 0.1 %/s and

2. Background and Literature Review

strain-range of $\pm 0.5\%$ for P91 steel and a strain-rate of $0.001\%/s$ and strain-range of $\pm 0.35\%$ for P92 steel are summarised in Figure 2.56. Also included in Figure 2.56 is a data point (green point) corresponding to the martensitic lath width at failure for P92 steel tested at a strain-rate of $0.2\%/s$ and strain-range of $\pm 0.35\%$ [Giroux, 2011]. This result illustrates the effect of strain-rate on cyclic martensitic lath evolution of P92 steel at $550\text{ }^\circ\text{C}$, with increased LAB dislocation annihilation occurring at lower strain-rates.

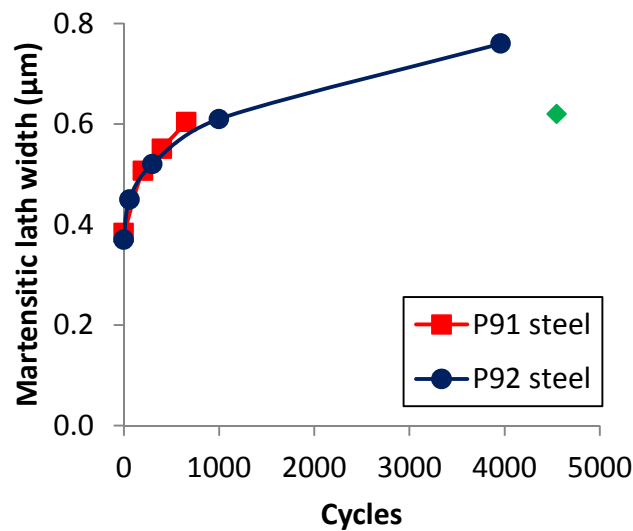


Figure 2.56: Measured martensitic lath evolution in P91 steel [Hyde *et al.*, 2012] and P92 steel [Giroux, 2011] under high temperature fatigue deformation. The green data point corresponds to the post-test measured martensitic lath width in P92 steel at a strain-rate of $0.2\%/s$.

2.6.4.3. Evolution of dislocation density

The initial dislocation density of 9-12Cr steels, which is extremely high compared to stainless steels that cyclically harden, for example, is typically somewhere in the range of $1.5 \times 10^{14}\text{ m}^{-2}$ [Sauzay *et al.*, 2005; Sauzay *et al.*, 2008] to $7.5 \times 10^{14}\text{ m}^{-2}$ [Ennis and Czyrska-Filemonowicz, 2002]. The overall dislocation density is made up of both mobile and immobile dislocations, where mobile dislocations are the carriers of inelastic deformation and immobile dislocations contribute to hardening based on the Taylor hardening equation. The immobile dislocations can be further split into

2. Background and Literature Review

dislocations at HAGBs, LABs and within the martensitic lath interiors. The dislocations at the LABs are as a result of the heat treatment process and form a dislocation substructure resulting in martensitic laths, as illustrated in Figure 2.57. The initial density of dislocations within the martensitic lath interiors is quite low [Magnusson and Sandström, 2007], with some laths void of dislocations [Pešička et al., 2003].

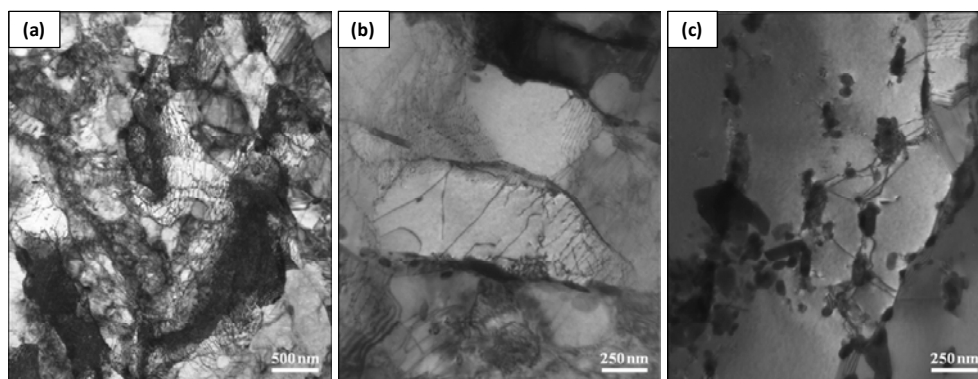


Figure 2.57: TEM images of the P92 dislocation substructure in martensitic laths for (a) ‘as-received’, (b) fractured specimen after 4552 cycles at 550 °C, a strain-rate of 0.2 %/s and strain-range of ± 0.35 % and (c) fractured specimen after 3960 cycles at 550 °C, a strain-rate of 0.001 %/s and strain-range of ± 0.35 % [Giroux, 2011].

It has been shown experimentally [Ennis and Czyska-Filemonowicz, 2002; Pešička et al., 2003] that the initially high density of dislocations decreases during both LCF and creep loading, as illustrated in Figure 2.58 for creep loading. During deformation, dislocations can become trapped at boundaries and precipitates and dislocations can also multiply at sources, e.g. Frank-Read sources. However, due to the accumulation of inelastic deformation, mutual annihilation of dislocations occurs when two dislocations of opposite Burger's vector meet, resulting in a decrease in dislocation density.

For fatigue loading the decrease in overall dislocation density represents a loss of the martensitic lath structure due to LAB dislocation annihilation. As discussed by Sauzay and co-workers [2005; 2008], this is the primary mechanism for recovery and hence, cyclic softening in 9-12Cr steels. The result of LAB dislocation annihilation is effectively an increase in effective martensitic lath width and hence, a reduction in strength. This recovery of

2. Background and Literature Review

martensitic lath width also has a significant impact on creep strain, which is approximately proportional to w^3 during tertiary creep [Abe, 2015].

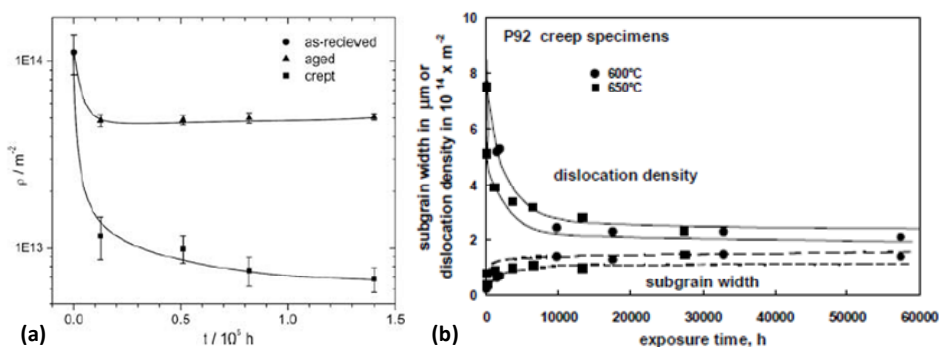


Figure 2.58: Evolution of dislocation density during creep loading in (a) P91 steel under creep and thermal aging [Pešička *et al.*, 2010] and (b) in P92 steel under creep loading [Ennis and Czyrska-Filemonowicz, 2002].

Due to this evolution of dislocation density and associated interactions with LABs, HAGBs and precipitates in 9-12Cr steels, dislocation density represents a key microstructural variable for the evolution of 9-12Cr steels. It is due to these interactions with the various strengthening mechanisms which constitutes the requirement to simulate the evolution of all of these strengthening mechanisms within a material model and the inclusion of only one of these strengthening mechanisms will not suffice to accurately predict the constitutive behaviour of 9-12Cr steels. Furthermore, as discussed by Cheng *et al.* [2003] and Kato *et al.* [2008] and illustrated in Figure 2.59, the deformation of steels may be divided into four distinct groups, dependent on grain size. For smaller grain sizes ('Nano-1', grain size: $d < 10$ nm), dislocation-based plasticity does not occur as the process is defined in terms of either grain-boundary sliding (GBS) or Coble creep. It is under these conditions that the inverse Hall-Petch effect is observed. As you move up the scales (i.e., 'Nano-2' to 'Ultrafine'; $10 \text{ nm} < d < 500 \text{ nm}$), dislocation-mechanics start to become important, but only at grain boundaries. For example, in 'Nano-2', twinning causes grains to be sheared resulting in stacking faults being left behind and for 'Ultrafine', nucleation of lattice dislocations occurs at grain boundaries, resulting in grain shearing [Kato *et al.*, 2008]. Finally, the largest scale (denoted 'Traditional' in Figure 2.59) is

2. Background and Literature Review

related to conventional steels and for grain sizes greater than ~ 500 nm, the effects of both grain boundary and grain interior dislocation sources must be considered for plastic deformation. 9-12Cr steels fall under this regime and hence, both cell interior and cell wall dislocation-mechanics must be considered when adapting a dislocation-based modelling methodology.

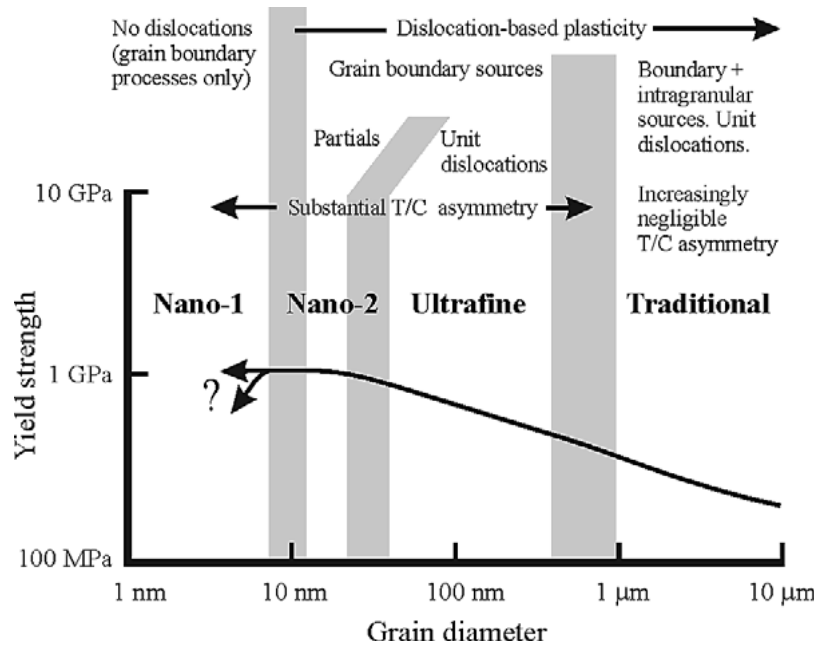


Figure 2.59: Deformation mechanisms map for FCC crystals highlighting the effect of grain size and dislocation-mechanics on the deformation of steels [Cheng *et al.*, 2003].

2.7. Summary and conclusions

The literature on the high temperature performance of 9-12Cr steels is undoubtedly quite extensive, with a sizeable proportion of this literature dedicated to the characterisation of creep behaviour and identification of the mechanisms of creep deformation in such materials. Accompanying this characterisation are numerous models for creep and fatigue deformation in candidate materials, including the 9-12Cr family of steels. However, the recent transition to flexible operation of power plant components has emphasised shortcomings in the literature at present, particularly in relation to modelling of fatigue loading conditions under high temperature deformation in 9-12Cr steels. The following highlights these shortcomings

2. Background and Literature Review

and outlines how this thesis will address these specific gaps in the current literature.

A significant amount of work has been carried out to date on determination of the microstructure of 'as-received' 9-12Cr steels, revealing a hierarchical microstructure strengthened by precipitates and solutes, and to a lesser extent, characterisation of the heterogeneous microstructure of welded connections. The associated microstructural evolution under inelastic deformations (creep and fatigue loading, for example) is known to be extremely complex. Due to these complexities, the development of a multi-scale microstructure-sensitive modelling framework is required to successfully simulate inelastic deformation under next generation loading conditions and to predict fatigue-creep life in power plant components manufactured from such materials. The materials design tool proposed in Figure 1.8 outlines the fundamental requirements to incorporate such effects within a multi-scale methodology, namely:

- Consideration of the chemical composition, heat treatment and initial material microstructure,
- Determination of key strengthening mechanisms via experimental analysis and microscopy and subsequent modelling at the micromechanical and macro-scale levels,
- Adaptation of material models to heterogeneous microstructures such as welded connections and application to diverse loading conditions including fatigue, creep and corrosion loading conditions,
- Multi-axial implementation of the macro-scale model for use with commercial finite element codes for component level simulations and multi-axial failure prediction,
- Application of the material model and life assessment methodology to realistic loading conditions at the component level.

Within this multi-scale modelling methodology, the successful development of a microstructure-sensitive material model for 9-12Cr steels at the macro-

2. Background and Literature Review

scale is paramount to linking the nano- and micro-scale strengthening mechanisms with the large-scale components in realistic plant. The development of such a model will overcome temporal and geometric constraints associated with micromechanical modelling to enable efficient and effective modelling of realistic plant components.

As different loading conditions can result in significantly different constitutive behaviour and microstructural degradation, there is a need to develop a microstructure-sensitive model, with provisions to include parameters and evolutionary equations for (i) $M_{23}C_6$ carbides, MX carbonitrides and Laves phase particles, (ii) Mo and W solutes, (iii) martensitic laths and HAGBs and (iv) dislocation density. This will facilitate accurate simulation of the observations during fatigue and creep deformation. To date, no complete model exists at the macro-scale which can account for the effects of the key microstructural parameters discussed above. Thus, building on the current literature for 9-12Cr steels, this gap will be bridged by the development of a dislocation-mechanics modelling framework for the evolution of the strengthening mechanisms under fatigue and, fatigue-creep in 9-12Cr steels.

As power plants transition to flexible operation, characterisation and numerical modelling of the fatigue, and in particular, TMF behaviour of candidate materials represents a relatively new but important requirement for plant designers. Thus, to aid the development of fatigue models and to broaden the knowledge of fatigue behaviour in 9-12Cr steels, the relatively limited bank of fatigue test data will be extended here via the completion of isothermal fatigue, TMF and stress relaxation experiments across a broad range of strain-rates and strain-ranges on (i) ex-service P91 steel and (ii) MarBN.

MarBN is a 9Cr alloy currently in development with the potential to operate at higher temperatures and hence, improve plant efficiencies and reduce CO₂ emissions. In this early stage of the material development process, only the short-term creep behaviour of this material has been characterised, with some excellent initial results observed in terms of creep strength compared

2. Background and Literature Review

to the current state-of-the-art materials. However, if this material is to prove successful for operation in high temperature plant operating under next generation loading conditions, characterisation of the fatigue behaviour of this new material is crucial. Thus, for the first time, a program of high temperature low cycle fatigue tests will be carried out on a cast MarBN product to qualitatively assess the potential capability of this material for flexible plant operation. The test program will be carried out across a broad range of strain-rates and strain-ranges, with comparisons made to the current state-of-the-art materials, namely P91 and P92 steel.

Due to the strain-rate effect observed at higher operating temperatures, and the significant difference between experimental and realistic strain-rates, there exists a requirement to develop a multi-axial modelling framework with variable strain-rate sensitivity. The development of such a framework is carried out here in conjunction with the construction of a UMAT user material subroutine to allow successful implementation of the material model within the commercial finite element code Abaqus. This fatigue framework will incorporate back-stress and cyclic softening variables which can be simulated using phenomenological or physically-based evolutionary laws.

From a phenomenological viewpoint, the development of such a modelling framework offers a simpler approach to predict the constitutive behaviour of the material, with a set of material parameters identified from experimental data. A step-by-step approach, with particular emphasis on the identification of strain-rate independent material parameters, is developed in the present work, with rigorous validation against experimental data across a broad range of loading conditions carried out.

3. High Temperature Experimental Testing of 9Cr steels

3.1. Introduction

This chapter presents the results of high temperature experimental testing of 9Cr steels. The primary focus of this work is the investigation of (i) high temperature fatigue and (ii) thermo-mechanical fatigue (TMF) of candidate materials. A detailed understanding of the fatigue behaviour of candidate materials is required during the design process to accommodate flexible operation of modern and next generation power plants.

Although a high factor of safety exists in power plant components, the recent transition to flexible operation results in cyclic loading must be accounted for when designing plant components. To this end, a series of high temperature low cycle fatigue (HTLCF) tests are conducted in the 20 °C to 625 °C temperature range and presented in Section 3.4. The effect of strain-rate, which is important for (i) material model calibration to extrapolate from experimental testing conditions at higher strain-rates to realistic power plant behaviour at low strain-rates and (ii) to understand variable strain-rate flexible plant operation [Farragher *et al.*, 2013a; Farragher *et al.*, 2013b], is also investigated in this study via strain-rate testing in the 0.1 %/s to 0.0005 %/s range.

HTLCF tests are required to (i) characterise the fatigue performance of 9Cr steels and (ii) successfully calibrate and validate potential material models for component level modelling. However, a program of TMF tests is required to capture the effects of the candidate materials under more representative loading conditions. Section 3.5 shows that thermo-mechanical loading has a considerable effect on the constitutive behaviour of 9Cr steels and shows a significant effect on fatigue life in Section 3.7. Hence, the extensive TMF test program presented in this chapter highlights the requirement to (i) understand and (ii) characterise the LCF and TMF behaviour of 9Cr steels.

3. High Temperature Experimental Testing of 9Cr Steels

To improve efficiency and reduce CO₂ emissions, next generation power plant will also be required to operate at higher temperatures and pressures. However, the key limiting factor to increased plant operating temperatures relates to material performance. Considering that the current state-of-the-art materials are limited to operation at temperatures of 600 °C or less, there exists a need for the development of materials with enhanced high temperature performance. MarBN, is a new 9Cr steel with enhanced high temperature creep performance, whilst maintaining the benefits of conventional 9Cr steels including (i) a reduced coefficient of thermal expansion, (ii) high creep strength and (iii) reduced cost in comparison with nickel-based superalloys. Although MarBN has exhibited excellent creep performance at high temperature, with an anticipated safe plant operation temperature of at least 625 °C, the high temperature fatigue performance of MarBN must also be characterised if it is to be considered a viable option for achieving increased efficiency and reduced emissions in future power stations operating under increasingly more flexible operation. Section 3.6 presents, for the first time, such a characterisation of a cast MarBN material under HTLCF loading conditions.

Chemical composition and material heat treatment play an important role in the performance of the material vis-à-vis (i) high temperature creep, (ii) fatigue and (iii) oxidation and corrosion behaviour, as well as interactions of these. The composition and heat treatment of each of the materials tested is discussed in Section 3.3 and their effect on the resulting precipitate-strengthened hierarchical microstructure of 9Cr steels is studied briefly in Section 3.7 and discussed throughout Chapter 3. A comparison of the constitutive behaviour for a range of different 9Cr steels, with variations in composition, fabrication and heat treatment, is also presented in Section 3.7.

The following section describes the test facilities at NUI Galway and University of Nottingham for high temperature fatigue testing and the experimental test procedure for HTLCF and TMF testing of 9Cr steels.

3. High Temperature Experimental Testing of 9Cr Steels

3.2. High temperature experimental programs

To characterise the fatigue performance of (i) P91 steel and (ii) MarBN material, a comprehensive test program has been developed for each material. These test programs include characterising the (i) strain-rate, (ii) strain-range, (iii) temperature and (iv) TMF behaviour of P91 steel and MarBN, with all of the tests conducted under strain-controlled loading conditions.

The ex-service P91 steel (ES-P91) used in this study is a 9Cr martensitic steel extracted from a superheater outlet header in Lough Ree power station (Ireland). The material, provided by ESB Energy International, was subjected to 35,168 hrs of service under subcritical loading conditions. The material was removed from service for operational reasons and was only subjected to operation at temperatures below 485 °C (normal operating conditions for Lough Ree power station is in the 460 to 485 °C temperature range) [Farragher, 2013]. However, as discussed by Farragher [2013], the material was exposed to 65 start-up (and shut-down) cycles (similar to Figure 1.2a) in total, with approximately equal numbers of cold, warm and hot start-up cycles. Such flexible operation is anticipated to have resulted in some microstructural degradation. Upon the extraction of the header unit, specimen blanks were extracted for test specimen manufacture.

The test program for ES-P91 steel consists of three phases. Phase 1 is an isothermal high temperature low cycle fatigue (HTLCF) test program including fully reversed and dwell tests at temperatures of 20 °C, 400 °C, 500 °C, 550 °C, 600 °C and 625 °C. Phase 2 is a TMF test program in the 400 to 600 °C temperature, with the complete test program for ES-P91 steel is summarised in Table 3.1. Due to time constraints associated with slow strain-rate testing, the strain-rates in this program are predominantly higher than those observed in realistic plant [Farragher et al., 2013b; Nabarro, 2002]. Thus, a number of tests were included in the test program at an intermediate strain-rate of 5×10^{-4} %/s to ensure potential cyclic viscoplastic material models could be validated at more realistic strain-rates for flexible

3. High Temperature Experimental Testing of 9Cr Steels

operation of power plants. Phase 3 is a program of weld material (WM) and cross weld (CW) tests as discussed in detail in Farragher [2013].

Table 3.1: Ex-service P91 steel HTLCF and TMF test programs.

Test Type	Specimen Type	Temperature (°C)	Strain-range (%)	Strain-rate (%/s)	Waveform
HTLCF ¹	PM	20, 400, 500, and 600	±0.5	0.1	R _ε = -1 (Triangular)
			±0.5	0.033	
			±0.4	0.033	
			±0.3	0.033	
			±0.5	0.025	
HTLCF	PM	400, 500, 550, 600 and 625	±0.3	5×10 ⁻⁴	R _ε = -1 (Triangular)
Cyclic dwell (Relaxation) ₁	PM	20, 400, 500 and 600	±0.5	0.1	120 s hold period
TMF-IP, TMF-OP	PM	400 to 600	±0.5 ±0.4	0.033, 0.025 0.033	R _ε = -1 (Triangular)
TMF-IP, TMF-OP	PM	400 to 600	+0.5/-0.2 +0.4/-0.1	0.033, 0.025	Asymmetric
TMF – Dwell	PM	400 to 600	±0.5	0.033, 0.025	120 s hold period

The MarBN material was acquired via NUI Galway’s ongoing collaboration with the IMPACT project. The material received by NUI Galway as part of the IMPACT project consisted of two cast plates of MarBN material, with the nominal dimensions illustrated in Figure 3.1. As expected, due to location in the melt, the casting quality at various locations in the plates may vary somewhat. The three regions depicted in Figure 3.2 are (i) primary material (highest quality material shaded in red), (ii) secondary material (region shaded in blue with material possibly of slightly inferior quality) and (iii) low quality material (denoted by the green shaded regions). Some low quality material has been employed for specimen manufacture to maximise the material available for testing. However, attention is focused on the primary and secondary grade material for testing. The test program for MarBN, which represents the first such testing to be conducted on a 9Cr-3W-3Co-V-Nb steel, is carried out at a temperature of 600 °C under the conditions listed in Table 3.2.

¹ Tests conducted as part of T.P. Farragher thesis [Farragher, 2013], within the SFI METCAM project.

3. High Temperature Experimental Testing of 9Cr Steels

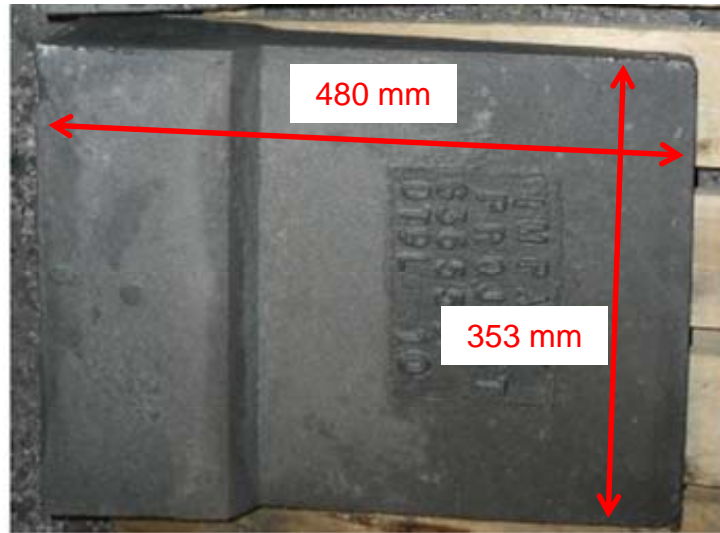


Figure 3.1: Photograph of one of the cast MarBN plates at NUI Galway.

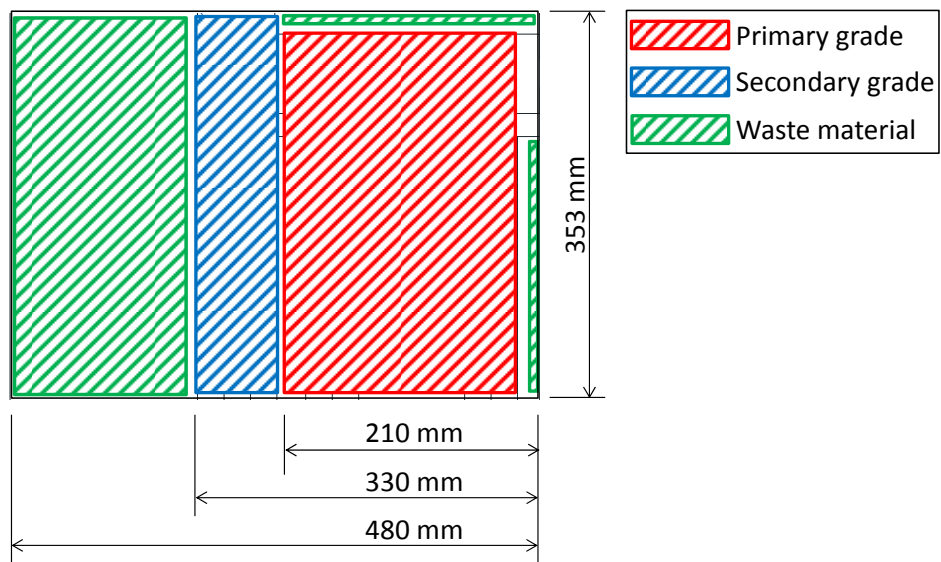


Figure 3.2: Schematic representation of the various regions of the cast MarBN plates.

3. High Temperature Experimental Testing of 9Cr Steels

Table 3.2: Cast MarBN HTLCF test program

Test Type	Specimen Type	Temperature (°C)	Strain-range (%)	Strain-rate (%/s)	Waveform
HTLCF	PM	600	±0.5	0.1	$R_{\epsilon} = -1$ (Triangular)
			±0.5	0.033	
			±0.4	0.033	
			±0.3	0.033	
			±0.5	0.01	
			±0.4	0.01	
			±0.3	0.01	
Cyclic dwell (Relaxation)	PM	600	±0.5	0.1	1 hr hold period

The strain-controlled high temperature fatigue tests were conducted at two different test facilities. Firstly, the TMF test rig at the University of Nottingham (UoN) was predominately utilised to characterise the high temperature fatigue behaviour of the ES-P91 steel parent material (PM). This rig is an INSTRON 8862 TMF test rig, capable of use for isothermal (HTLCF) and anisothermal (TMF) tests. The TMF test rig, illustrated in Figure 3.3, uses a radio frequency induction coil with forced air cooling to accurately control the specimen temperature to within ± 10 °C during testing [Hyde *et al.*, 2010]. To maintain temperature control and follow a triangular temperature waveform under TMF conditions, hollow specimens are required as per the drawing of Figure 3.4 (for isothermal testing, the hollow centre is not required).

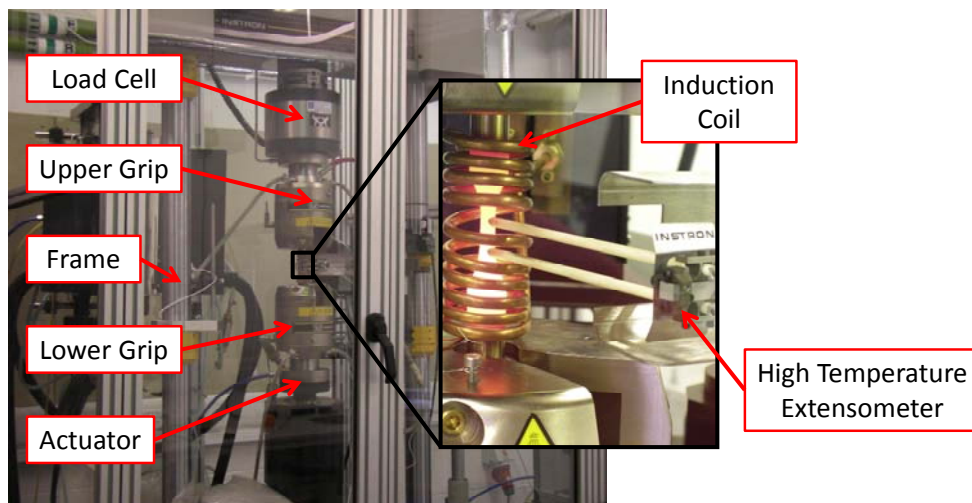


Figure 3.3: INSTRON 8862 TMF test rig at the University of Nottingham [Farragher, 2013; Hyde *et al.*, 2010].

3. High Temperature Experimental Testing of 9Cr Steels

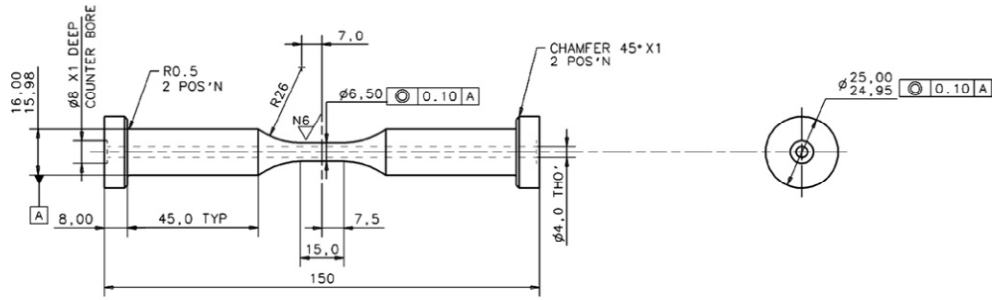


Figure 3.4: Hollow specimen geometry (all dimensions in mm) for the UoN TMF test rig [Hyde *et al.*, 2010].

All WM and CW ES-P91 steel tests, as well as supplementary testing of ES-P91 PM specimens are carried out on the HTLCF test rig at NUI Galway. The HTLCF test rig at NUI Galway is an INSTRON 8800 test rig capable of conducting stress- and strain-controlled fatigue tests at various R -ratios, dwell tests, creep and creep-fatigue tests. The NUI Galway HTLCF test rig has a hydraulic driven actuator and uses a chamber furnace and high temperature pullrods to enable testing up to temperatures of 1000 °C. Figure 3.5 depicts the main components of the INSTRON 8800 at NUI Galway and due to the high temperature pullrod configuration, threaded specimens are required as illustrated in the drawing of Figure 3.6.

3. High Temperature Experimental Testing of 9Cr Steels

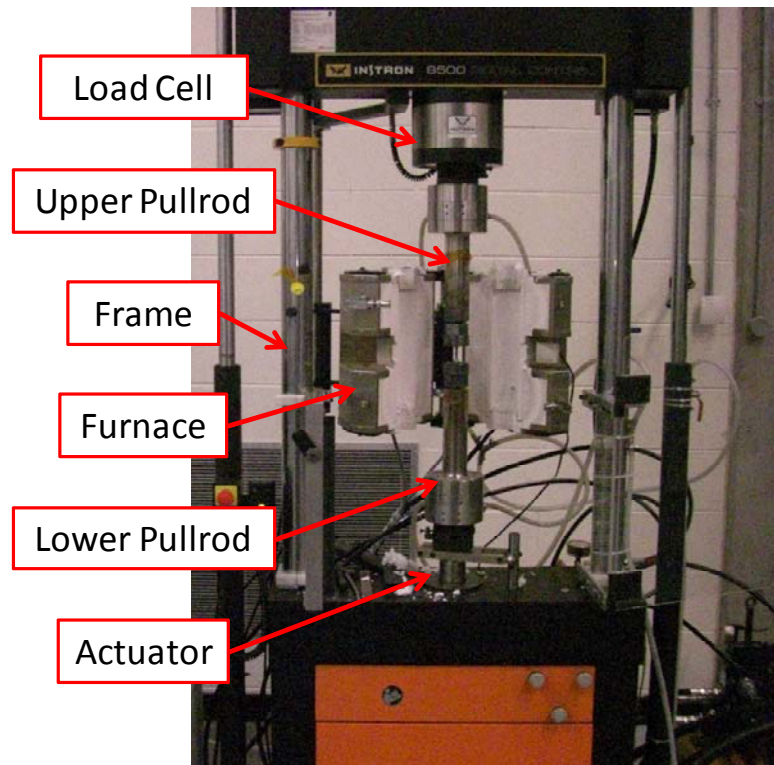


Figure 3.5: HTLCF testing facility at NUI Galway.

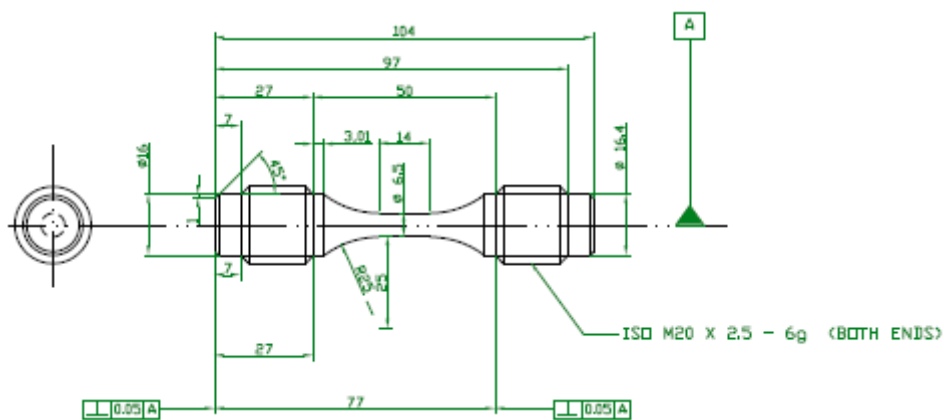


Figure 3.6: Typical geometry (all dimensions in mm) of HTLCF specimen for the NUI Galway test rig [Farragher, 2013].

The specimens for HTLCF testing were manufactured (i) by Takumi Precision Engineering (Co. Limerick, Ireland) for the UoN test rig and (ii) in-house within Mechanical Engineering for the NUI Galway test rig. To compare the respective performances of the two test rigs, repeat tests were conducted, with little difference observed in constitutive behaviour between both test rigs [Farragher, 2013]. For both test rigs (NUI Galway and UoN),

3. High Temperature Experimental Testing of 9Cr Steels

thermal calibration of the test material is required. At NUI Galway, this is achieved via a (HTLCF) specimen with blind holes drilled at various locations along the specimen into which thermocouples are inserted. The desired temperature is then set for the furnace and the actual material temperature measured at the thermocouples. The process is repeated for different materials and specimen geometries; e.g. at NUI Galway, calibration was carried out for (a) a notched ES-P91 specimen and (b) plain cast MarBN specimen as presented in Figure 3.7. A more detailed description of the testing procedures at NUI Galway and UoN can be found elsewhere [Farragher, 2013; Saad, 2012].

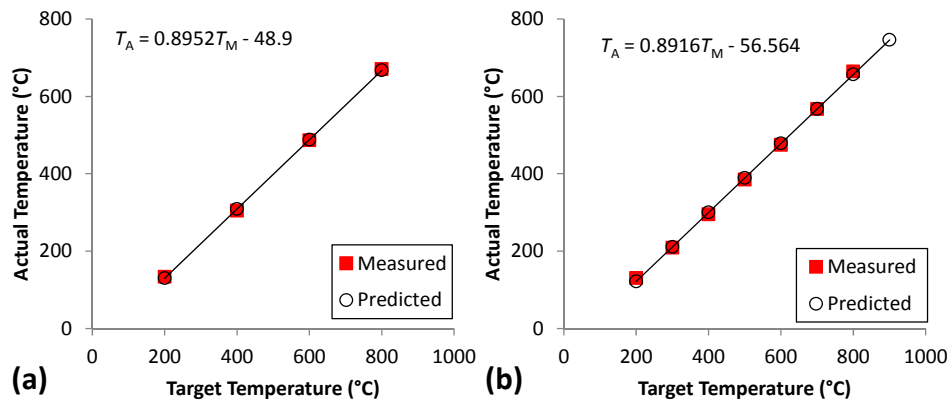


Figure 3.7: Thermal calibration for (a) ES-P91 notched specimen geometry and (b) MarBN plain specimen geometry.

3.3. Chemical Composition and heat treatment

As discussed in Chapter 2, the microstructure of 9-12Cr steels is critical to the high temperature performance of the material. This complex solute and precipitate-strengthened hierarchical microstructure is achieved via careful consideration and design of (i) the chemical composition and (ii) heat treatment.

The chemical composition of the ES-P91 steel prior to service in Lough Ree power station is presented in Table 3.3, coupled with a comparison to an ‘as-received’ P91 steel (AR-P91) from the literature [Saad, 2012]. The ES-P91 steel was fabricated via a rolling process and underwent a typical 9Cr martensitic steel two-stage heat treatment process of normalisation for 0.5

3. High Temperature Experimental Testing of 9Cr Steels

hrs at 1050 °C, followed by tempering at 765 °C for 1 hr [Farragher, 2013]. By comparison, the AR-P91 steel was normalised at 1060 °C for 45 minutes and tempered at 760 °C for 2 hours. Although the chemical compositions and the heat treatment temperatures are quite similar, the longer normalising and tempering times for AR-P91 steel could lead to (i) coarser prior austenite grains and martensitic laths and (ii) slightly increased precipitate diameters.

Table 3.3: Chemical composition of P91 steels in wt%. ES-P91 and AR-P91 steels denote ‘ex-service’ and ‘as-received’ respectively, with the AR-P91 data obtained from [Saad, 2012]. The balance is made up of Fe.

	Al	C	Cr	Mn	Mo	N	Nb	Ni	P	S	Si	V	W
ES-P91	0.007	0.10	8.48	0.42	0.94	0.058	0.07	0.19	0.013	-	0.26	0.204	-
AR-P91	0.007	0.12	8.60	-	1.02	0.06	0.07	-	0.017	<0.002	0.34	0.24	0.03

The chemical composition and heat treatment for the cast MarBN material are the proprietary information of the IMPACT consortium and hence, cannot be disclosed. For the purpose of comparison with P91 steels, a typical chemical composition for MarBN [Abe et al., 2008] is presented in Table 2.1, which has similarities to the IMPACT cast MarBN product. As MarBN is a modified form of P92, a typical P92 steel chemical composition is also included for comparison. When compared with P91 and P92 steels, MarBN has increased tungsten content, reduced molybdenum and carbon and includes boron and cobalt. The inclusion of cobalt in a 9Cr martensitic steel is known to inhibit the production of δ -ferrite [Masuyama, 2001] and also improve material toughness [Kluh, 2004]. The nitrogen content must be carefully controlled to minimise the formation of unstable BN precipitates, which (i) subtract from boron enrichment of grain boundaries to stabilise $M_{23}C_6$ precipitates and (ii) reduce MX precipitate strengthening. Abe and co-workers [2008] suggested a chemical composition with less than 100 ppm nitrogen to ensure BN precipitates do not form for heat treatments with normalisation temperatures of 1080 to 1150 °C for 1 hour, followed tempering at temperatures of 770 to 800 °C for 1 to 4 hours. Hence, MarBN is a material with a reduced nitrogen content, which on the one hand will reduce the strengthening owing to the presence of MX

3. High Temperature Experimental Testing of 9Cr Steels

precipitates but will ensure that segregation of boron at grain boundaries occurs, resulting in the maintenance of a hierarchical martensitic lath microstructure following PWHT [Abe *et al.*, 2007b; Abe *et al.*, 2010; Tabuchi *et al.*, 2004]. However, the heat treatment of cast MarBN in this study follows the approach developed by Li and co-workers [Li *et al.*, 2013a] as part of work conducted within the IMPACT project. In this work, the normalisation temperature is set at 1200 °C and the normalisation time increased (confidential), with a longer tempering cycle. This approach ensures that BN precipitates do not form and the significantly reduced nitrogen content of Abe and co-workers [Abe *et al.*, 2008] can be relaxed slightly (although not to the same extent as in ES-P91 steel), hence, resulting in improved nitride (MX) strengthening.

Figure 3.8 schematically illustrates the various stages in the heat treatment processes and the difference between the heat treatments applied to ES-P91 and MarBN steels used in this study. The normalisation process induces the formation of an austenite microstructure, with the increased normalisation temperature and time increasing the size of the austenite grain structure. Following normalisation, air cooling to temperatures below 300 °C yields a martensitic transformation (for the small specimen blanks with dimensions of 24 mm × 24 mm × 240 mm, air cooling is rapid enough and sufficient for martensitic transformation to occur). This results in the formation of martensitic laths with a high dislocation density. Finally, the tempering process takes place, which has two primary functions, (i) precipitation of the MX nitrides and $M_{23}C_6$ carbides and (ii) further reduction of the extremely high dislocation density. Further increased temperatures and hold times for the tempering process would increase the martensitic lath width and leads to the formation of more equi-axed subgrains [Sawada *et al.*, 2003], resulting in a coarsened precipitate structure (for the same initial chemical composition and normalisation stages).

3. High Temperature Experimental Testing of 9Cr Steels

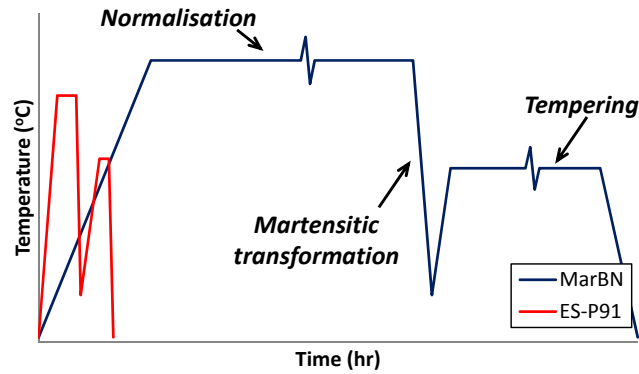


Figure 3.8: Schematic representation (not to scale) comparing the heat treatment of ES-P91 steel with that of cast MarBN, including normalisation, martensitic transformation and tempering.

3.4. High temperature fatigue of ex-service P91 steel

This section presents the results of the HTLCF test program for ES-P91 steel, including characterisation of the effects of temperature, strain-rate and strain-range, under strain-controlled conditions. The results of isothermal dwell (stress relaxation) tests, with a hold period at the maximum tensile strain, are also included. Figure 3.9 illustrates the typical cycle for each of these tests.

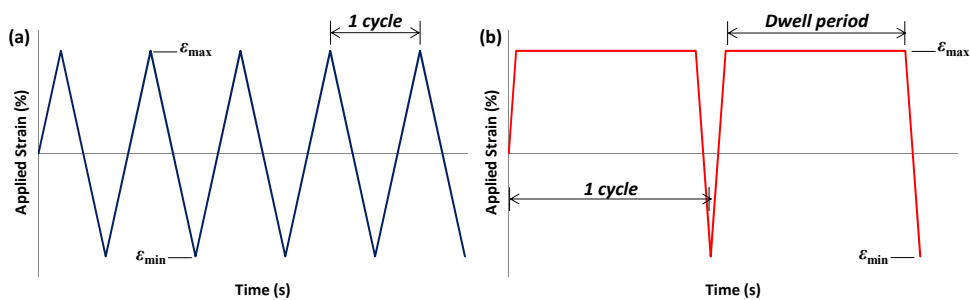


Figure 3.9: Schematic representation of a (a) fully reversed HTLCF test and (b) dwell test.

3.4.1. Effect of temperature on P91 steel

As power plants move to flexible operation and subsequently, (i) more frequent start-up cycles and (ii) part-load operation, one of the most important phenomena to characterise and understand is the effect of

3. High Temperature Experimental Testing of 9Cr Steels

temperature on the material performance. For ES-P91 steel, this effect is presented in Figure 3.10, where as expected, the material strength is decreased with increasing temperature. The ES-P91 steel has a stress range of 1142 MPa at room temperature compared with 686 MPa at 600 °C (1.0 % strain range, 0.033 %/s strain-rate). This 40 % reduction in strength is also accompanied by a considerable reduction in material stiffness. As discussed briefly in Chapter 2, the temperature-dependence of Young's modulus is crucial in predicting the hardening induced by the various strengthening mechanisms, including precipitate and martensitic lath strengthening.

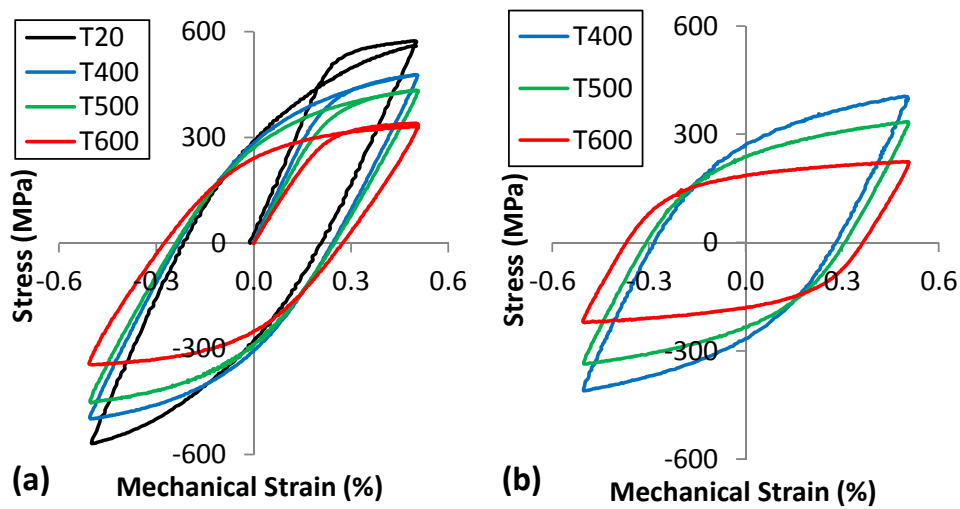


Figure 3.10: Effect of temperature on the measured stress-strain performance of ES-P91 steel for (a) initial cycle and (b) half-life cycle under an applied strain-rate of 0.033 %/s and strain-range ± 0.5 %.

A considerable reduction in yield stress is also observed, as illustrated in Figure 3.11. This decrease in yield stress is concomitant with the decrease in material stiffness for increasing temperatures. Furthermore, the non-linearity in the variation of the measured elastic material parameters of yield stress and Young's modulus illustrates the requirement to conduct testing at multiple temperatures to provide more accurate simulations of complex start-up cycles, similar to those presented in Figure 1.2a.

3. High Temperature Experimental Testing of 9Cr Steels

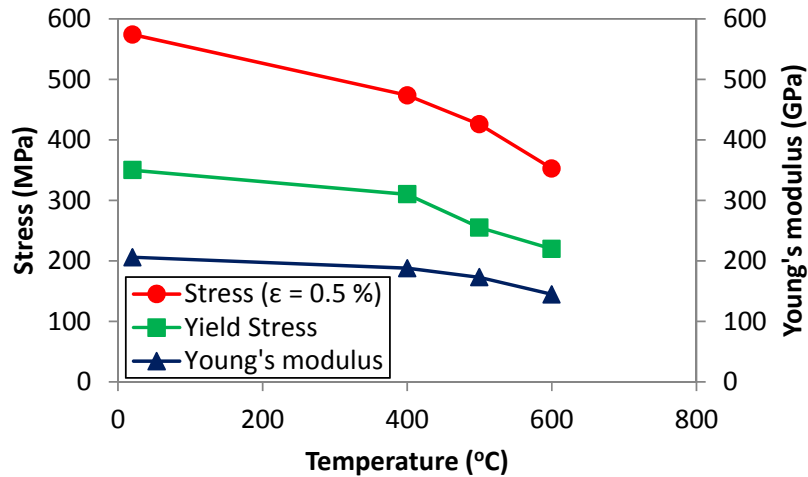


Figure 3.11: Temperature dependence of yield stress and Young's modulus in ES-P91 steel.

Temperature has an even more significant effect on the primary mechanisms of deformation and the performance of the strengthening mechanisms. Although the shear modulus is an important parameter for quantifying the variation in the primary strengthening mechanisms, e.g. strengthening due to interparticle spacing, λ , can be defined by an Orowan stress of the form $\tau_{Or} = \mu b / \lambda$ (where μ is shear modulus and b is the magnitude of Burger's vector), there is clear evidence of viscous effects on the measured stress-strain response at temperatures in excess of 600 °C. This is most clearly represented by the reduction in overall strength (shown here in Figure 3.11 in terms of the tensile stress at an applied strain of 0.5 %). Thus, the effect of temperature on yield stress from 400°C to 500 °C and from 500 °C to 600 °C is less than the effect on maximum stress at 0.5 % strain. This difference can, at least partially, be explained by viscous effects emanating in the test results at temperatures of 600 °C and greater. This effect also leads to rate-dependent behaviour in the material, as discussed in more detail in Section 3.4.4. There is also a much more significant reduction in the hardening modulus at 600 °C, as evidenced by the shape of the stress-strain curve at each temperature, e.g. at 400 °C and 500 °C, the stress-strain response hardens at a much higher rate (increased slope) than at 600 °C. At 600 °C,

3. High Temperature Experimental Testing of 9Cr Steels

the stress-strain response appears to reach a plateau at a relatively low strain, indicative of a low hardening modulus.

3.4.2. High temperature fatigue tests at varying strain-ranges

The effect of strain-range is presented in Figure 3.12 for temperatures of 400, 500 and 600 °C. These results, presented for applied strain-ranges of $\pm 0.3\%$, $\pm 0.4\%$ and $\pm 0.5\%$, illustrate (i) considerable cyclic softening, (ii) non-Masing behaviour and (iii) kinematic hardening with a Bauschinger effect. Cyclic softening is evident via the significant decrease in stress range as the cycles increase. This effect is discussed in more detail in Section 3.4.3.

3. High Temperature Experimental Testing of 9Cr Steels

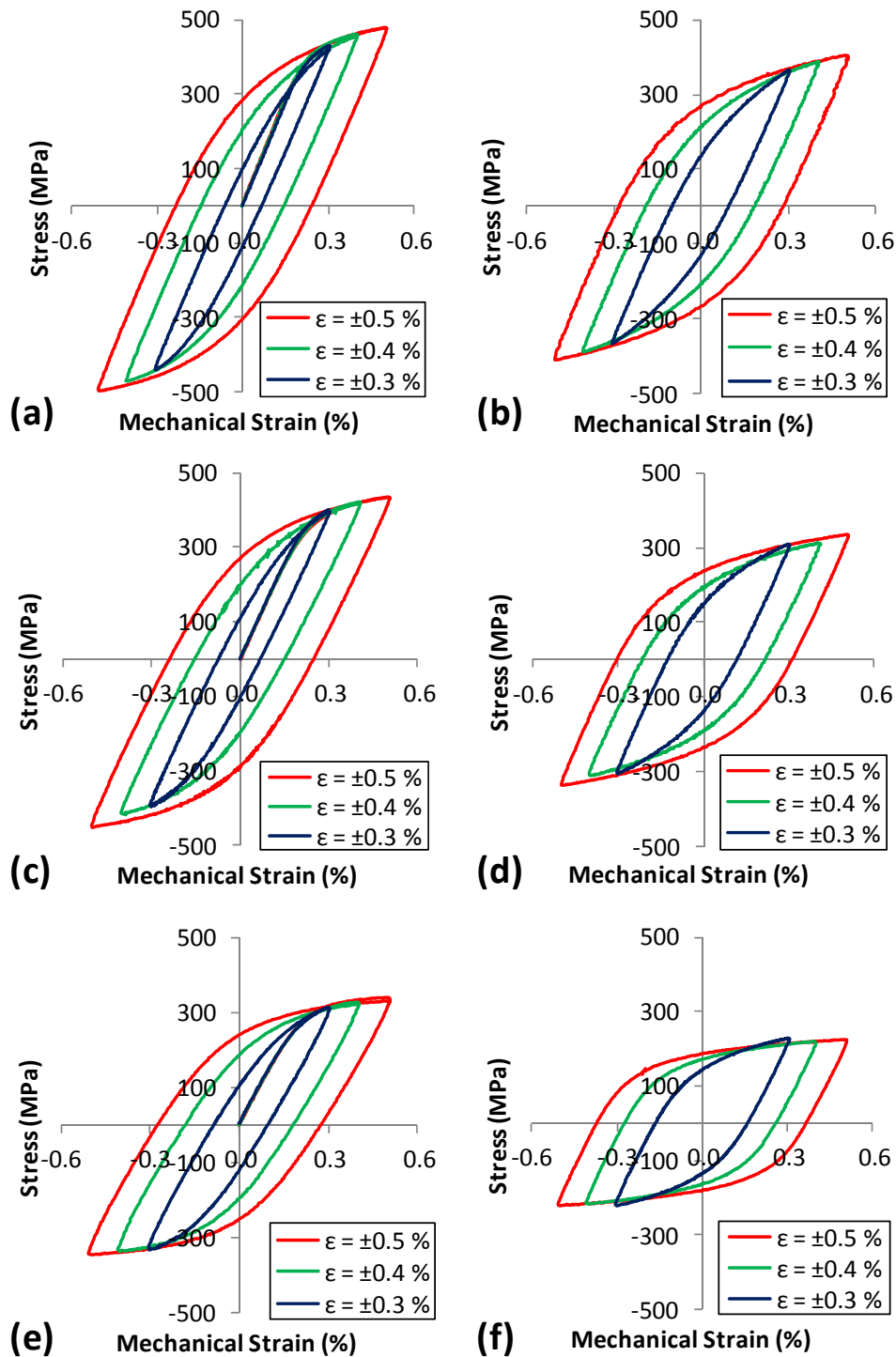


Figure 3.12: Stress-strain response for a strain-rate of 0.033 %/s and (a) initial cycle at 400 °C, (b) half-life cycle at 400 °C, (c) initial cycle at 500 °C, (d) half-life cycle at 500 °C, (e) initial cycle at 600 °C, and (f) half-life cycle at 600 °C for various applied strain-ranges.

Masing behaviour occurs if the shape of the stress-strain loop for LCF at different strain-ranges coincides, geometrically, with twice the value of the

3. High Temperature Experimental Testing of 9Cr Steels

stress response ($2\sigma_{\text{mono}}$) for a monotonic test, as illustrated in the schematic of Figure 3.13. As is evident from Figure 3.14, the ES-P91 steel tested here undergoes non-Masing behaviour at low applied strain-ranges, i.e. the stress-strain response at an applied strain-range of $\pm 0.3\%$ is not coincident with the result at the higher applied strain-range of $\pm 0.5\%$. This is even more evident at $600\text{ }^{\circ}\text{C}$. From Plumtree and Abdel-Raouf [1998], non-Masing behaviour is expected to occur in materials which form dislocation cell substructures, e.g. the low-angle boundary dislocation substructures in 9Cr steels, explaining the existence of such behaviour in the ES-P91 steel. Non-Masing behaviour is representative of microstructural evolution and degradation during cyclic deformation in metals.

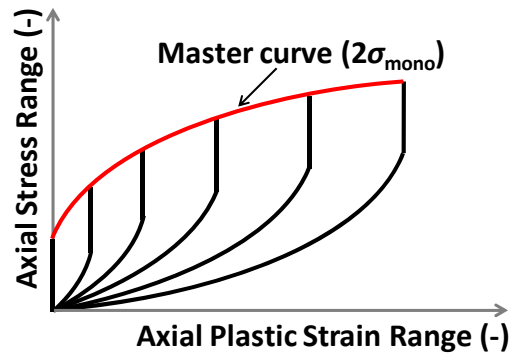


Figure 3.13: Schematic representation of Masing behaviour in metals.

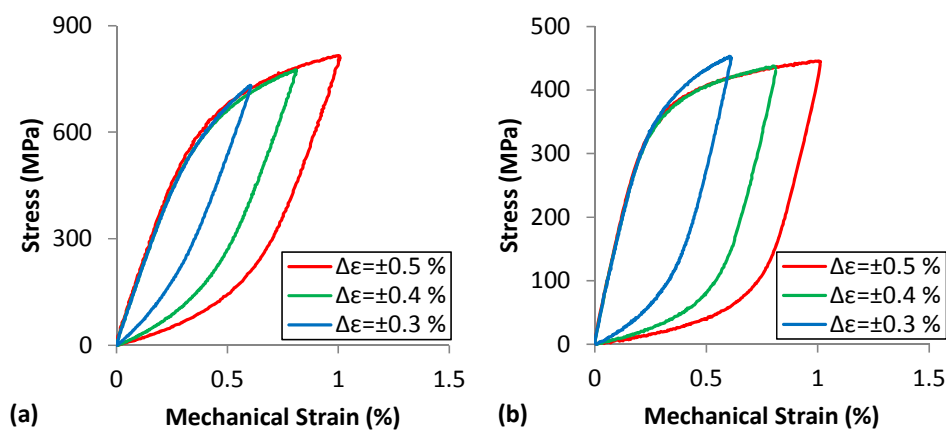


Figure 3.14: Non-Masing behaviour at low strains in ES-P91 steel at temperatures of (a) $400\text{ }^{\circ}\text{C}$ and (b) $600\text{ }^{\circ}\text{C}$.

3.4.3. Cyclic softening behaviour

The primary deformation mechanism of concern to power plant operators under flexible loading conditions should be the cyclic softening observed in the 9Cr steels. Cyclic softening is the cycle-on-cycle reduction in strength of the material, resulting in a decrease in material creep strength. From the results of Figure 3.10 and Figure 3.12, it is evident that the ES-P91 steel studied in this section undergoes considerable cyclic softening, as noted by the reduction in overall stress range with increasing cycles.

Figure 3.15 presents the reduction in maximum tensile stress as a function of cycles at temperatures of 400 °C, 500 °C and 600 °C, illustrating the evolutionary decay in maximum stress. Figure 3.16 plots the cyclic softening stress (the difference between the maximum stress observed following the monotonic loading and the maximum tensile stress of the current cycle, $R = \sigma_{max,0} - \sigma_{max}$) against the accumulated effective plastic strain (sum of absolute plastic strain accumulated for all cycles, $p = 2\Delta\epsilon^{pl}N$). This result illustrates the level of cyclic softening observed in ES-P91 steel and the temperature-dependence on the rate of softening. At a temperature of 600 °C, a significantly higher (initial) rate of cyclic softening is observed when compared with other temperatures, illustrating the need to accurately characterise and understand, the effect of cyclic softening across different loading conditions.

3. High Temperature Experimental Testing of 9Cr Steels

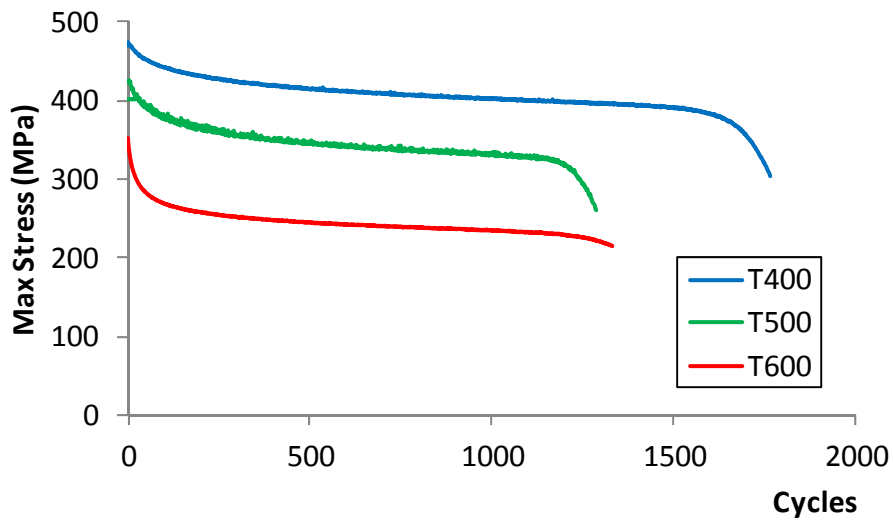


Figure 3.15: Evolution of maximum tensile stress for ES-P91 tested at a strain-rate of 0.1 %/s and applied strain-range of ± 0.5 % for temperatures of 400 °C, 500 °C and 600 °C.

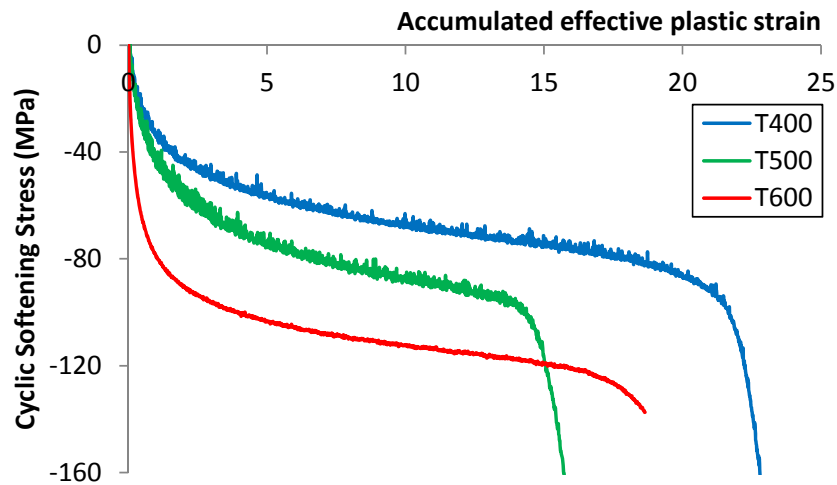


Figure 3.16: Effect of temperature on measured cyclic softening in ES-P91 steel for a strain-rate of 0.1 %/s and applied strain-range of ± 0.5 %.

The effects of varying the loading conditions under isothermal conditions (at temperatures of 400 °C and 600 °C) are illustrated in Figure 3.17. From these results, it can be concluded that the observed cyclic softening behaviour is predominately a function of temperature and accumulated plastic strain (occurring at the onset of plastic deformation), but is also dependent on strain-rate and strain-range.

3. High Temperature Experimental Testing of 9Cr Steels

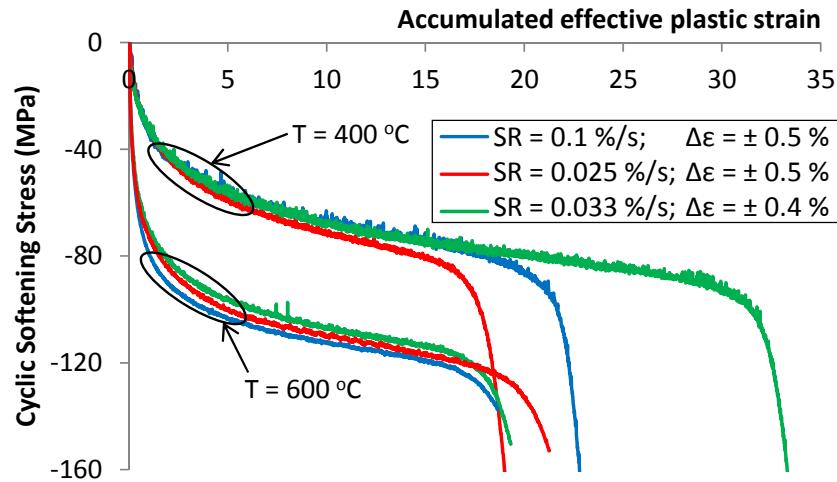


Figure 3.17: Variation of cyclic softening stress with various loading conditions in ES-P91 steel at temperatures of 400 °C and 600 °C.

Cyclic softening is the result of microstructural evolution (degradation) of the material and is a function of (i) plastic strain, (ii) temperature, (iii) chemical composition and (iv) initial microstructure and heat treatment. As discussed by Sauzay and co-workers [2005; 2008], cyclic softening is predominately related to the deformation of the hierarchical microstructure, dominated by a loss of the martensitic lath microstructure. As plastic deformation occurs, mobile dislocations interact with LABs, resulting in LAB dislocation annihilation and a widening of the martensitic lath microstructure. Hence, if plastic deformation occurs, 9Cr steels are susceptible to softening, accompanied by a loss of a primary creep strengthening mechanism in the form of the martensitic lath microstructure.

It should also be noted that the cyclic softening stress plot of Figure 3.15 incorporates two dominant effects, (i) cyclic softening (effectively recovery of the martensitic lath structure) and (ii) fatigue crack propagation. The cycle at which a fatigue crack initiation occurs is not determined in the present work, as repeat tests to various fractions of life, for example, would be required at high temperatures to identify this. However, under the assumption that recovery and the propagation of fatigue cracks are the primary mechanisms responsible for the behaviour observed in Figure 3.15, the cyclic softening-accumulated effective plastic strain plots can be

3. High Temperature Experimental Testing of 9Cr Steels

represented in terms of three specific regions of microstructural deformation, as illustrated schematically in Figure 3.18. The first of these regions is the primary softening region, in which there is a rapid decrease in LAB dislocation density and significant widening of the martensitic laths. This stage is followed by fatigue crack initiation, effectively a transition region in which recovery is still occurring in conjunction with fatigue crack propagation. This is discussed in more detail in Section 3.7. The final stage is failure in which the fatigue crack grows rapidly (and in an unstable manner), eventually leading to a brittle fracture of the remaining load bearing material. Due to the presence of flaws and microstructure inhomogeneities, different numbers of cycles to failure (and subsequent differences in accumulated effective plastic strain at failure) as illustrated in Figure 3.16, are to be expected.

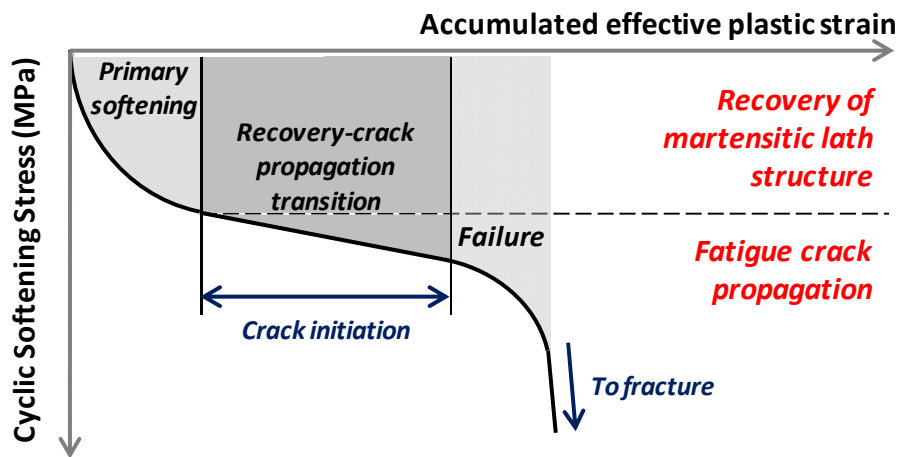


Figure 3.18: Schematic representation of cyclic softening behaviour and dominant mechanisms in 9-12Cr steels.

3.4.4. The strain-rate effect in ex-service P91 steel

In metallic materials, viscous, and hence, strain-rate effects become important at temperatures of approximately 0.3 to 0.4 T_m (where T_m is the absolute melting temperature). With T_m greater than 1500 °C in 9Cr steels [Yaghi *et al.*, 2005], it is expected that viscous behaviour occurs at temperatures above 450 °C. Thus, the effect of strain-rate is investigated here at temperatures of 400 °C and greater. Figure 3.19 illustrates the results

3. High Temperature Experimental Testing of 9Cr Steels

of strain-rate (0.1 %/s to 0.025 %/s) for temperatures of 400 °C, 500 °C and 600 °C. As is evident from these results, no strain-rate effect exists for the initial and half-life cycles at 400 °C, whilst a minimal strain-rate effect can be observed at 500 °C. However, at 600 °C, a considerable strain-rate effect is observed over a relatively small range of strain-rates (less than an order of magnitude). Hence, it can be concluded here that viscous effects become important at temperatures greater than 500 °C. The introduction of viscous effects in this range is also concurrent with the observed drop off in performance of P91 steel at temperatures in and around 600 °C.

3. High Temperature Experimental Testing of 9Cr Steels

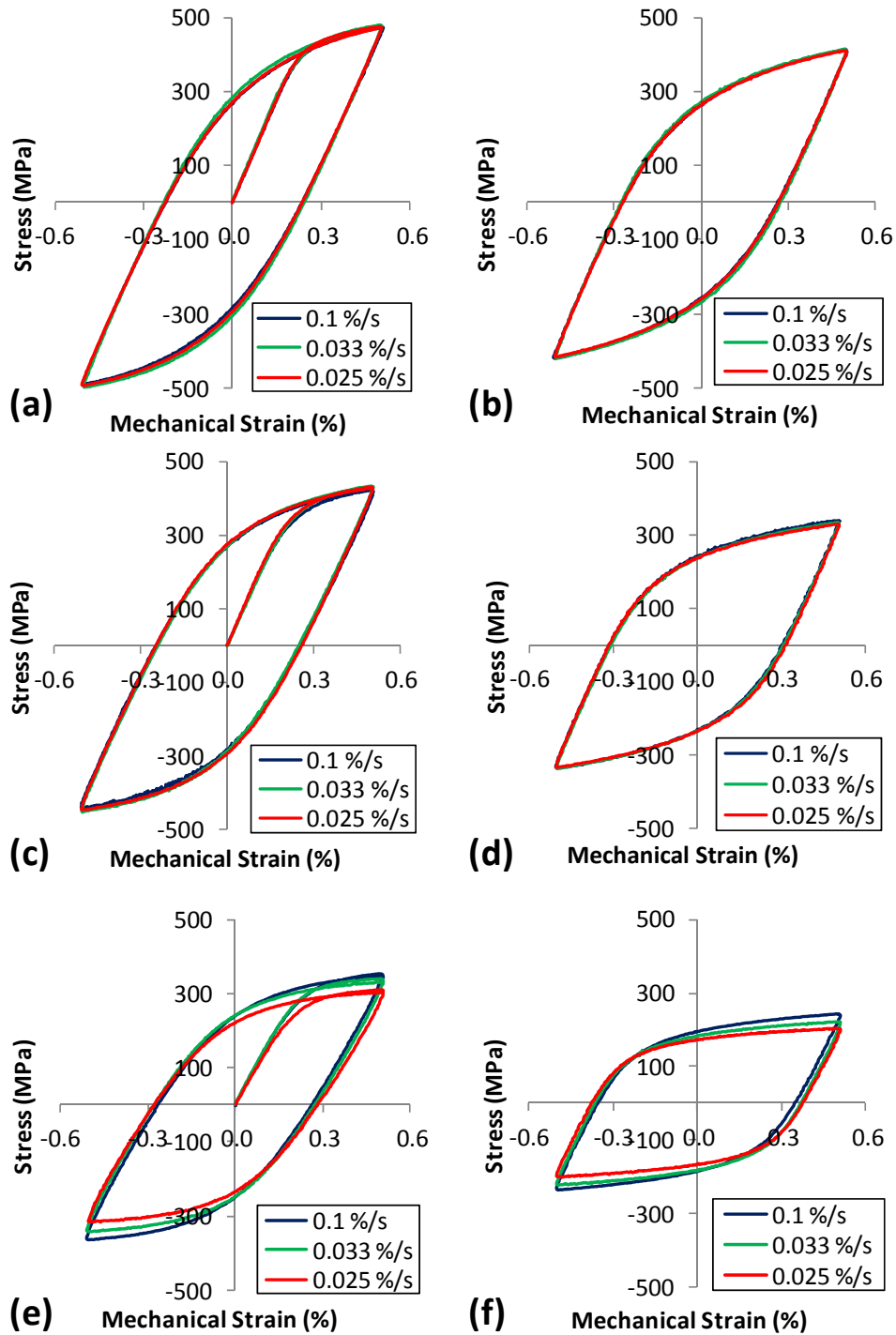


Figure 3.19: Measured stress-strain behaviour for various strain rates at temperatures of (a) and (b) 400 °C, (c) and (d) 500 °C and (e) and (f) 600 °C for an applied strain-range of ± 0.5 % at the initial and half life cycles.

As power plants move to more flexible operation, it is necessary to characterise the performance of candidate materials across a broad range of strain-rates. To avoid lengthy experimental times, high temperature fatigue

3. High Temperature Experimental Testing of 9Cr Steels

experiments are conventionally conducted at higher strain-rates (typically in the range of 1.0 %/s to 1.0×10^{-2} %/s [Fournier et al., 2009a; Fournier et al., 2011; Koo and Kwon, 2011; Koo and Lee, 2007; Saad, 2012; Saad et al., 2011a; Saad et al., 2011b]), well above the realistic plant loading conditions (strain-rates of 1.0×10^{-4} %/s [Farragher, 2013; Farragher et al., 2013b] to 1.0×10^{-10} %/s [Nabarro, 2002], as illustrated in Figure 3.20). Cyclic viscoplastic material models are calibrated and validated at these higher experimental strain-rates, before application to realistic loading conditions. At lower strain-rates (and low stresses), the mechanism of deformation is diffusional creep [Hertzberg, 1996] and hence, fatigue mechanisms of deformation are not considered to be dominant. However, in between this range, there exists an important range of strain-rates, defined in Figure 3.20 as ‘intermediate’ strain-rates, for which viscous dependent fatigue loading is potentially important. To examine any potential strain-rate effects from the higher to intermediate strain-rate regimes, high temperature fatigue tests are carried out at a strain-rate of 5.0×10^{-4} %/s. The results of testing at these intermediate strain-rates at 600 °C (where the tests were stopped after 250 cycles due to the lengthy test times but enough cycles to observe the primary cyclic softening stage) are presented in Figure 3.21, with a comparison with the higher strain-rate tests also included.

3. High Temperature Experimental Testing of 9Cr Steels

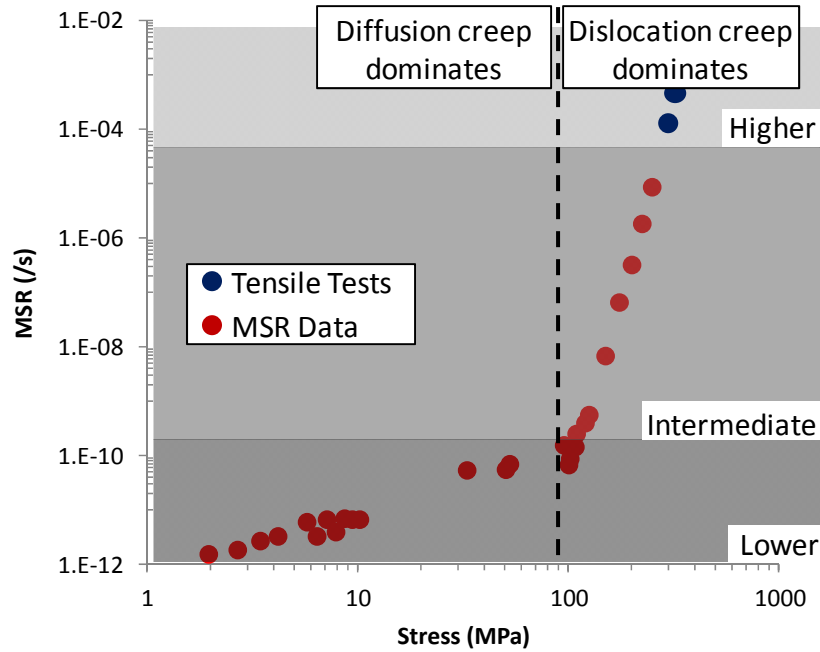


Figure 3.20: MSR data obtained from creep tests [Sklenička *et al.*, 2003] and UTS data from monotonic testing [Golden *et al.*, 2015] at a given strain-rate for a temperature of 600 °C.

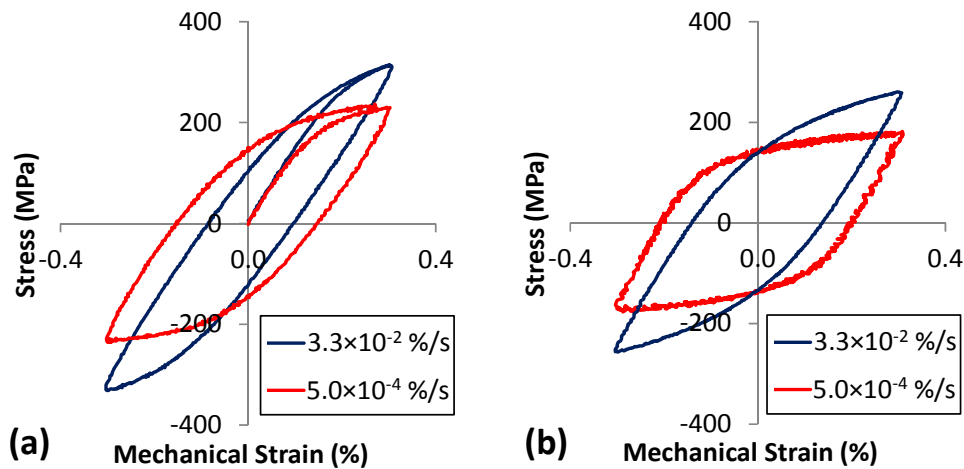


Figure 3.21: Comparison of the experimentally measured stress-strain response for ex-service P91 steel at strain-rates of 0.033 %/s and 0.0005 %/s for the (a) initial and (b) 250th cycles at a temperature of 600 °C and applied strain-range of ± 0.3 %.

The difference in stress-range observed during strain-rate dependent loading at 600 °C in Figure 3.21 can be related to the minimum strain-rate data presented in Figure 3.20. For the first cycle in Figure 3.21a, the difference in maximum stress at a strain of 0.3 % is 84 MPa; a value which relates well

3. High Temperature Experimental Testing of 9Cr Steels

with the data presented in Figure 3.20, where the difference in stress between the strain-rates of 0.033 %/s and 5×10^{-4} %/s is approximately 94 MPa (obtained by fitting a Norton power law function to the data to enable easier interpretation of the experimental data). Hence, it can be concluded that the difference in observed constitutive behaviour is solely related to the viscous behaviour of the material, illustrating the need to include and accurately predict viscous effects in any subsequent material model. The effect of temperature on the constitutive behaviour at the intermediate strain-rate is presented in Figure 3.22a, with the softening behaviour presented in Figure 3.22b. As illustrated in Figure 3.22b, some initial hardening is observed at the higher temperatures of 600 °C and 625 °C. It is possible that this behaviour is the result of an initial increase in dislocation strengthening via dislocation pile-up and entanglement, e.g. analogous to primary creep hardening. However, the reason for this behaviour requires further investigation via repeat testing to ensure that this result is not a test anomaly associated with testing at such low rates.

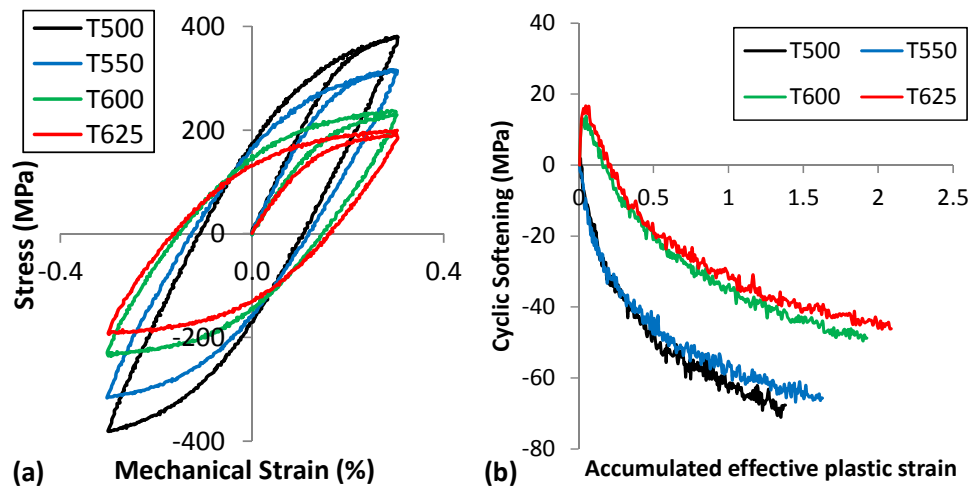


Figure 3.22: Effect of temperature for ES-P91 steel for an intermediate strain-rate of 5×10^{-4} %/s and applied strain-range of ± 0.3 % for (a) the initial cycle stress-strain response and (b) the observed cyclic softening during the first 250 cycles.

Furthermore, as alluded to in Section 3.4.1, the presence of viscous effects on the material behaviour results in a stress-strain loop shape change. At temperatures where viscous effects become important, the hardening modulus is a function of strain-rate, where a high modulus exists for higher

3. High Temperature Experimental Testing of 9Cr Steels

strain-rates, reducing considerably as the strain-rate decreases, causing near elastic perfectly plasticity behaviour at low strain values. This phenomenon is illustrated in Figure 3.21, and is more evident as fatigue cycles accumulate.

3.4.5. Stress relaxation behaviour in 9Cr steels

Dwell tests are carried out to (i) allow calibration of models for viscous effects under high temperature fatigue deformation and (ii) quantify the effect of hold (dwell) periods on the fatigue life of the material. The stress relaxation behaviour of ES-P91 is determined via strain-controlled fatigue testing with a dwell period included at maximum tensile stress, as illustrated in Figure 3.9b. For the ES-P91 steel material, the dwell period is 120 s at an applied strain of 0.5 %. Dwell tests have been completed at temperatures of 400 °C, 500 °C and 600 °C. The results of the dwell tests are presented in Figure 3.23. As the time increases, viscoplastic strain accumulates and the stress reduces, since the total strain is constant and elastic strain relaxes with decreasing stress. From Figure 3.23, as the temperature increases, more stress relaxation is observed as the viscoplastic strain accumulates at a higher rate at 600 °C when compared with the results at 400 °C. These results once again highlight potential issues for plant components operating at temperatures in excess of 500 °C, where rate effects and viscous behaviour become increasingly important.

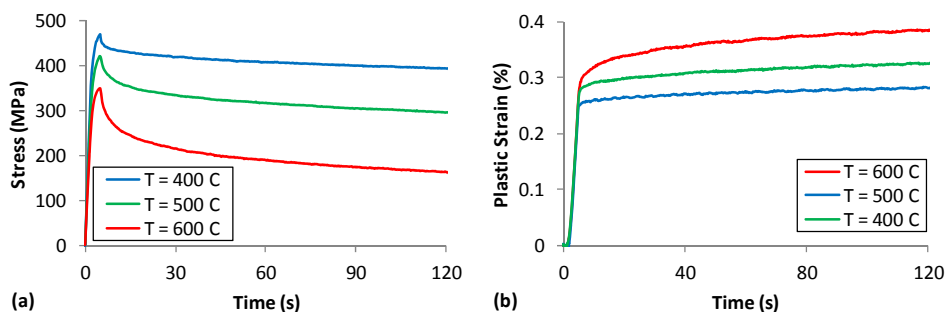


Figure 3.23: Measured (a) stress relaxation and (b) plastic strain evolution during a tensile dwell period at a constant applied strain of 0.5 %.

3. High Temperature Experimental Testing of 9Cr Steels

The results of fatigue tests with a dwell period of 120 s are compared with HTLCF experiments carried out under the same nominal test conditions ($\pm 0.5\%$ strain-range, 0.1% /s strain-rate) are presented in Figure 3.24. This result shows that the dwell period (predominantly) reduces fatigue life, as expected due to the increased time at higher applied strain. More importantly, this result highlights an increased rate of softening for cycles involving dwell periods, further highlighting the importance of cyclic deformation and its associated microstructural degradation on the performance of 9Cr steels.

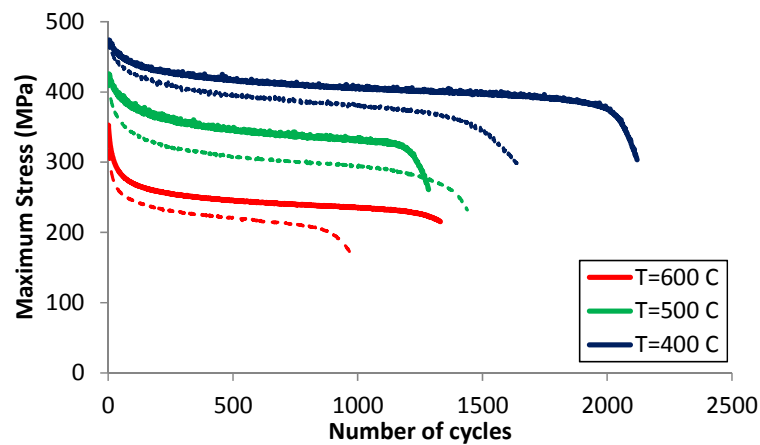


Figure 3.24: Comparison of measured maximum stress as a function of cycles for HTLCF (solid lines) and 120 s dwell test (points) for ES-P91 steel under a strain-range of $\pm 0.5\%$ and strain-rate of 0.1% /s.

3.5. Thermo-mechanical fatigue testing

TMF experiments were undertaken on the test rig at the University of Nottingham. The test program includes both in-phase (TMF-IP) and out-of-phase (TMF-OP) experiments on the ES-P91 steel (parent material), with typical waveforms for TMF-IP and TMF-OP tests shown schematically in Figure 3.25. The test matrix is presented in Table 3.1 and this program includes fully reversed ($R_e = -1$) and asymmetric ($R_e \neq -1$) strain-controlled tests in the $400\text{ }^{\circ}\text{C}$ to $600\text{ }^{\circ}\text{C}$ temperature range. The purpose of conducting asymmetric tests, where the applied strain is higher in tension and lower in compression, is to test under loading conditions more representative of modern plant, as illustrated by the work of Farragher [2013].

3. High Temperature Experimental Testing of 9Cr Steels

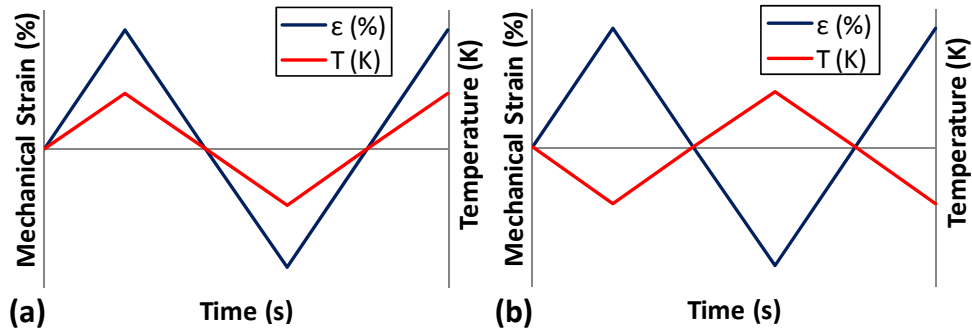


Figure 3.25: Mechanical strain-temperature loading conditions for (a) in-phase (TMF-IP) and (b) out-of-phase (TMF-OP) TMF testing.

The results of the fully reversed tests are presented first. Figure 3.26 illustrates the comparison of TMF-IP and TMF-OP test results with isothermal fatigue behaviour at temperatures of 400 °C and 600 °C, with the stress-mechanical strain TMF loops effectively bounded by isothermal fatigue behaviour at temperatures of 400 °C and 600 °C.

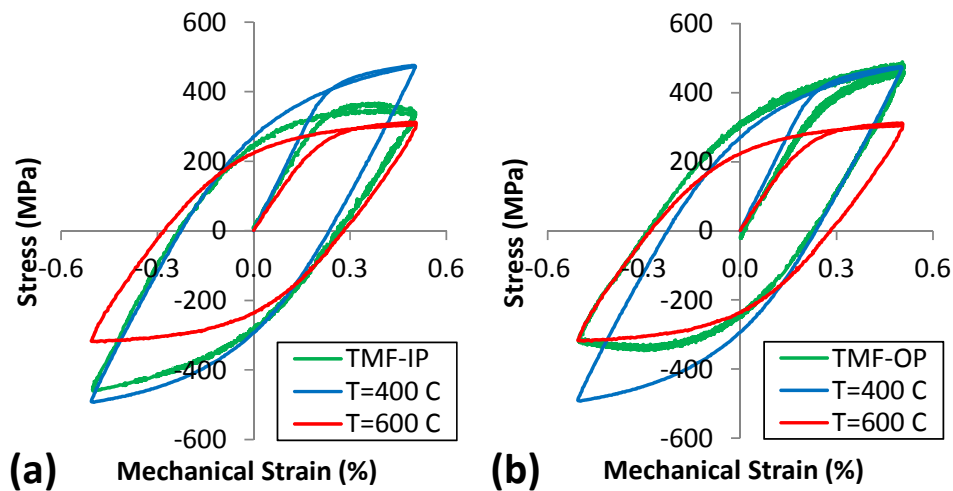


Figure 3.26: Comparison of (a) TMF-IP and (b) TMF-OP experiments for the initial cycle in the 400 to 600 °C temperature range with the IF tests at 400 and 600 °C. The strain-rate is 0.025 %/s and mechanical strain-range is ± 0.5 %.

The TMF data illustrates the typical characteristics of temperature-dependent behaviour. For TMF-IP loading, e.g. see Figure 3.27, where the maximum mechanical strain coincides with the maximum loading temperature, a significant amount of plasticity is observed for maximum

3. High Temperature Experimental Testing of 9Cr Steels

loading as is evident by a widening of the stress-strain loop during tensile loading. In contrast, for compressive loading, where the minimum strain coincides with minimum temperature, the material is subjected to more moderate loading conditions and the material begins to recover some of its strength. This recovery of strength is observed in terms of a continued hardening of the material during the compressive loading (the material stress-strain response moves towards a specific maximum compressive stress before elastic unloading), with narrowing of the loop in compression.

However, for TMF-OP loading, e.g. see Figure 3.28, the maximum strain occurs when the temperature is a minimum, and vice versa. The thermal component of loading is less severe in tension for the same mechanical strain and as a result, the maximum tensile stress is increased. Thus, when compared with TMF-IP, the loops are narrower in tension and wider in compression, highlighting the contributions of thermal and mechanical strains.

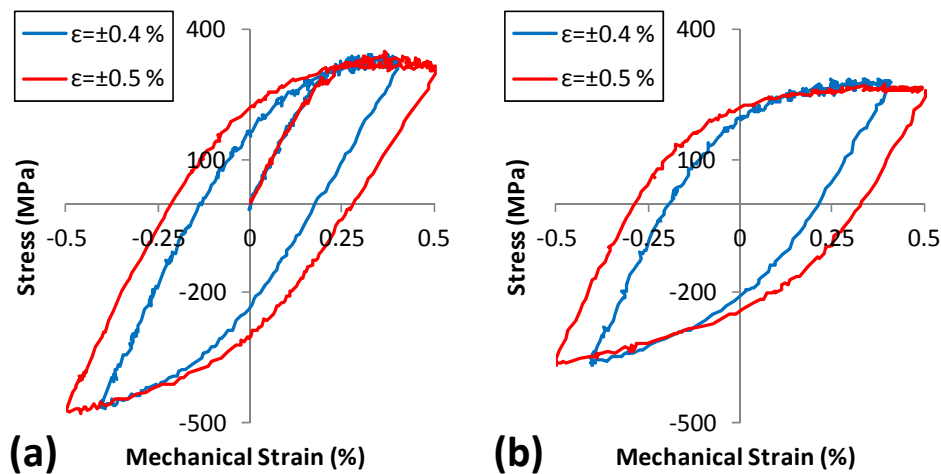


Figure 3.27: Experimentally observed mechanical strain-range effect for (a) the initial and (b) 100th cycles for a strain-rate of 0.033 %/s and TMF-IP loading in the 400 to 600 °C temperature range.

3. High Temperature Experimental Testing of 9Cr Steels

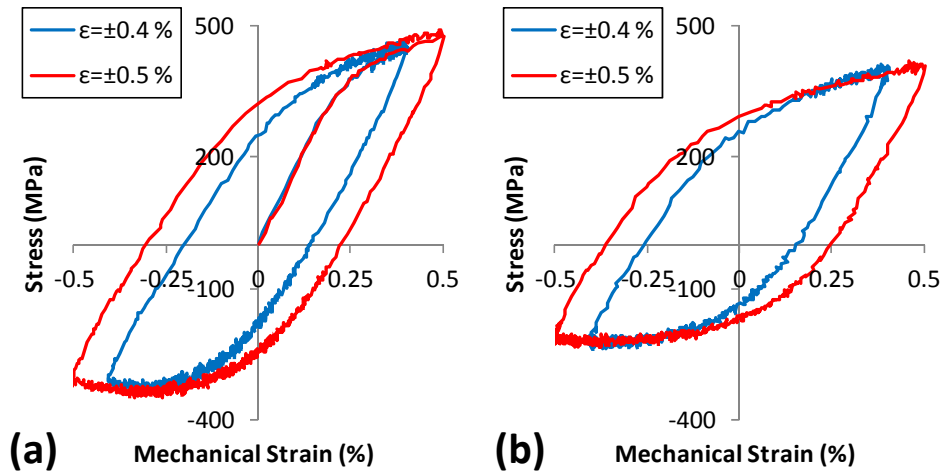


Figure 3.28: Experimentally observed mechanical strain-range effect for (a) the initial and (b) 100th cycles for a strain-rate of 0.033 %/s and TMF-OP loading in the 400 to 600 °C temperature range.

Figure 3.27 and Figure 3.28 also present the effect of applied strain-range on the constitutive behaviour, with cyclic softening evident for all test conditions. The cyclic softening under TMF-IP and TMF-OP are compared in Figure 3.29, with similar softening behaviour to that of isothermal fatigue (IF) testing conditions. Due to a higher maximum tensile stress under TMF-OP, coupled with an increased average loading condition throughout a full cycle, and hence, increased plastic strain, TMF-OP loading conditions result in a much lower fatigue life when compared with TMF-IP data, as discussed in Section 3.7.

3. High Temperature Experimental Testing of 9Cr Steels

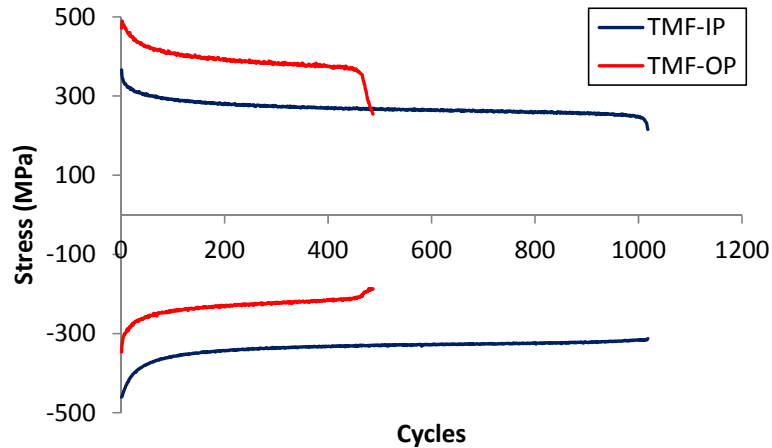


Figure 3.29: Measured maximum and minimum stresses in ex-service P91 steel for TMF-IP and TMF-OP loading under an applied strain-rate of 0.025 %/s and strain-range of ± 0.5 % in the 400 to 600 °C temperature range.

The effect of asymmetric strain-ranges, which are more representative of plant operating conditions, are presented in Figure 3.30 and Figure 3.31 for two different strain-ranges, with considerable cyclic softening also observed. The cyclic evolution of maximum and minimum stresses for an applied strain-range of +0.5 %, -0.2 % are presented in Figure 3.32, with comparisons to symmetric test data at higher and lower total applied strain-ranges. These results indicate that there is not a significant effect of asymmetric loading on fatigue life. However, further symmetric TMF tests at a total applied strain-range of 0.7 % would provide more detail of the role of maximum applied stress on the fatigue life of 9Cr steels under TMF.

3. High Temperature Experimental Testing of 9Cr Steels

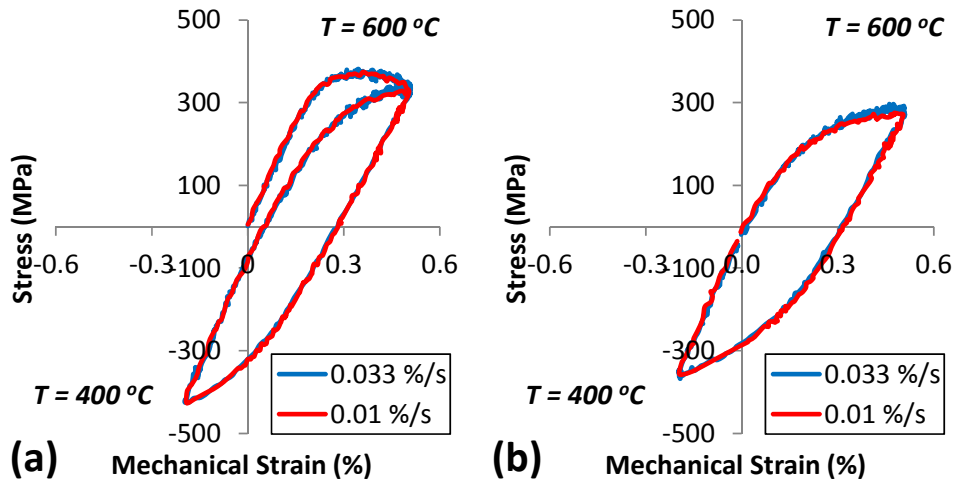


Figure 3.30: TMF-IP behaviour of ES-P91 under an asymmetric applied strain of -0.2 % and +0.5 % for the (a) initial and (b) 100th cycle in the 400 to 600 °C temperature range.

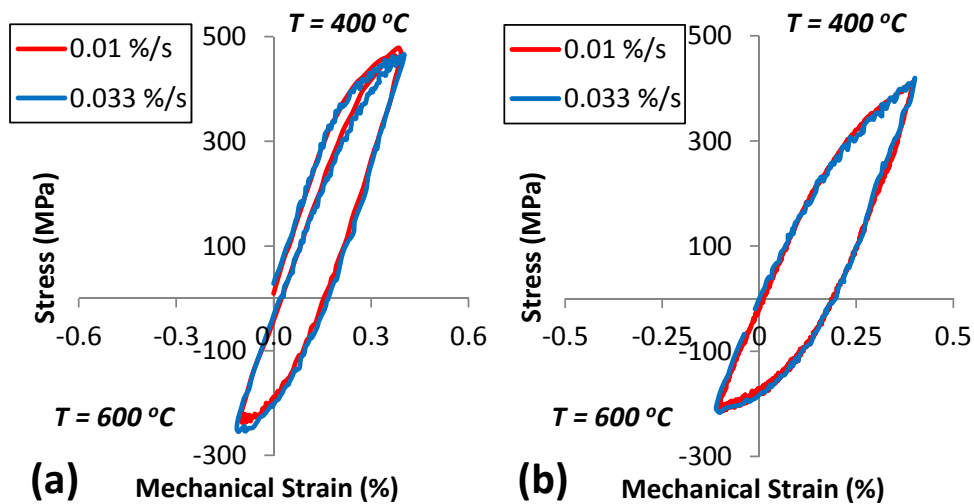


Figure 3.31: TMF-OP behaviour of ES-P91 under an asymmetric applied strain of -0.1 % and +0.4 % for the (a) initial and (b) 100th cycle in the 400 to 600 °C temperature range.

3. High Temperature Experimental Testing of 9Cr Steels

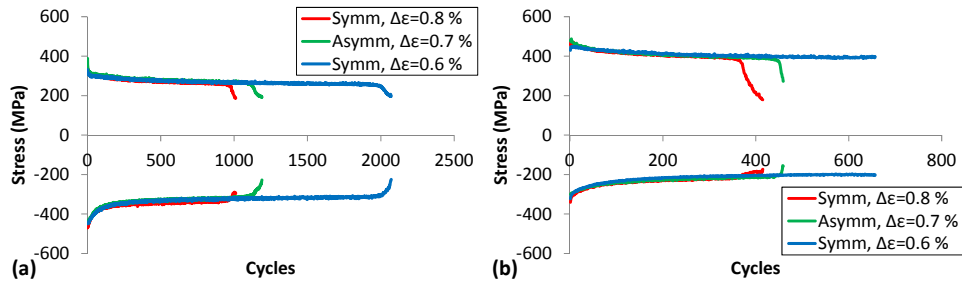


Figure 3.32: Evolution of maximum tensile and compressive stresses for symmetric (Symm) and asymmetric (Asymm) of ES-P91 steel for (a) TMF-IP and (b) TMF-OP tests at a strain-rate of 0.033 %/s in the 400 to 600 °C temperature range. The asymmetric tests have an applied strain of +0.5 %, -0.2 %.

In the results of Figure 3.30 and Figure 3.31, a small strain-rate effect is observed at the higher temperature end of the test, consistent with the strain-rate effect observed for the IF constitutive behaviour in Figure 3.19. The stress-mechanical strain response under symmetric loading for two different strain-rates (0.033 %/s and 0.025 %/s) is presented in Figure 3.33. A subtle strain-rate effect is observed for the TMF-OP case, with an inverse strain-rate effect observed, inconsistent with IF previous results, for the TMF-IP case. Thus, a small and inconclusive strain-rate effect is observed in relation to constitutive behaviour in ES-P91 steel, for the narrow range of strain-rates investigated here. However, for safe plant operation under higher temperatures and flexible loading, there exists a requirement to (i) characterise and predict the strain-rate effect in 9Cr steels under thermo-mechanical loading and (ii) carry out further TMF testing of 9Cr steels at lower, more representative strain-rates.

3. High Temperature Experimental Testing of 9Cr Steels

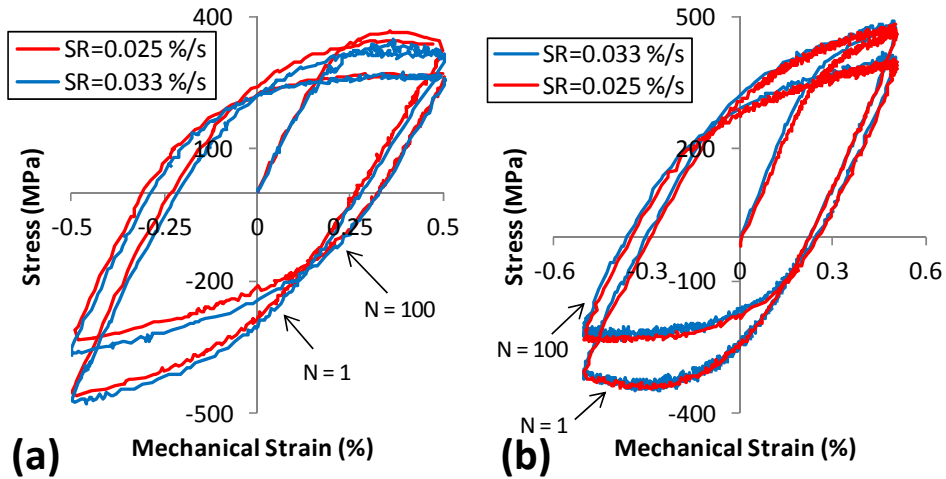


Figure 3.33: Experimental strain-rate effects for (a) TMF-IP and (b) TMF-OP loading under an applied mechanical strain-range of ± 0.5 % and a temperature range of 400 to 600 °C.

3.6. High temperature fatigue testing of MarBN

The high temperature fatigue test program of MarBN is summarised in Table 3.2 and incorporates HTLCF testing across multiple strain-ranges and strain-rates. For this first phase of LCF testing on MarBN, all tests were conducted at 600 °C, using specimens obtained predominantly from the secondary grade material.

Similar to ES-P91, the MarBN material exhibited considerable cyclic softening for all test conditions, as illustrated in Figure 3.34 and Figure 3.35. Figure 3.35 also illustrates the measured effect of strain-range on the constitutive response of MarBN, with non-Masing behaviour also observed. The effect of strain-rate on the monotonic constitutive behaviour is presented in Figure 3.36, where a considerable strain-rate effect is observed across three orders of magnitude.

3. High Temperature Experimental Testing of 9Cr Steels

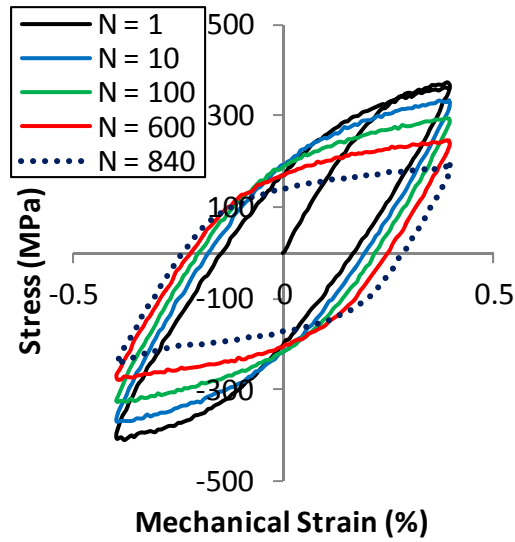


Figure 3.34: Cyclic stress-strain behaviour of MarBN for a strain-rate of 0.01 %/s and applied strain-range of $\pm 0.4\%$.

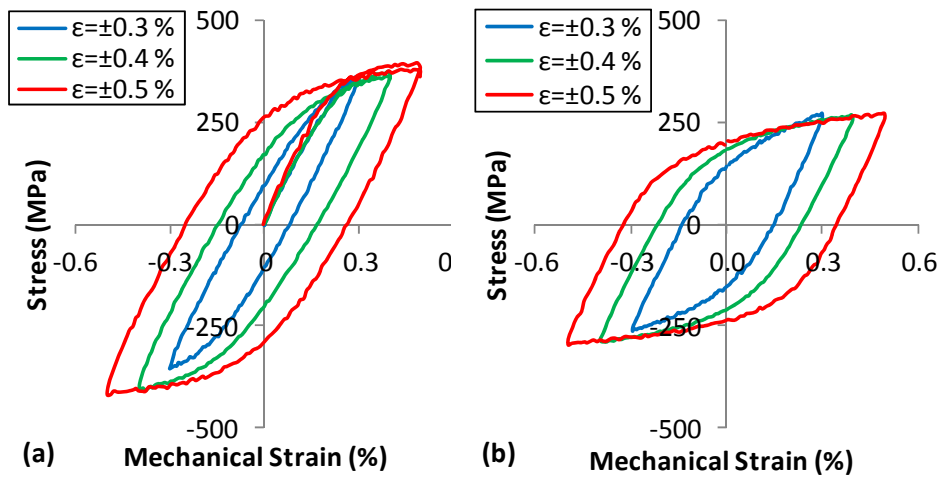


Figure 3.35: Measured stress-strain response of MarBN for the (a) initial cycle and (b) half-life at an applied strain-rate of 0.01 %/s at 600 °C.

3. High Temperature Experimental Testing of 9Cr Steels

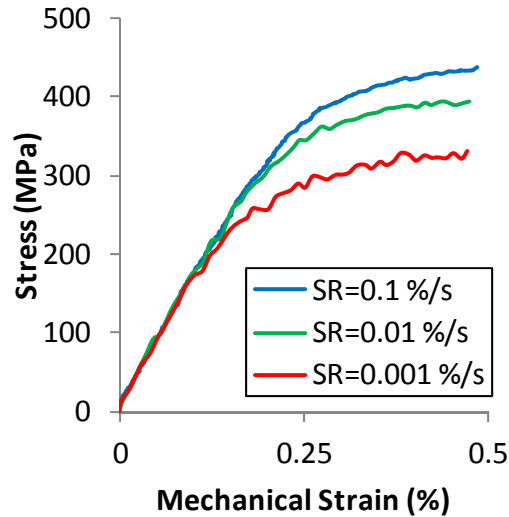


Figure 3.36: Measured tensile stress-strain behaviour of cast MarBN steel across various strain-rates at 600 °C.

Stress relaxation testing of MarBN is also conducted. However, to ensure more representative power plant loading conditions are tested, the dwell period is increased from 120 s (for ES-P91 steel testing) to a 1 hr dwell period. This increased dwell period will (i) allow more accurate representation of the relaxation behaviour as a function of time and (ii) quantify the effect of more realistic dwell periods on the fatigue life. Figure 3.37 illustrates the measured stress time response for MarBN with a 1 hr tensile dwell period at 0.5 % strain.

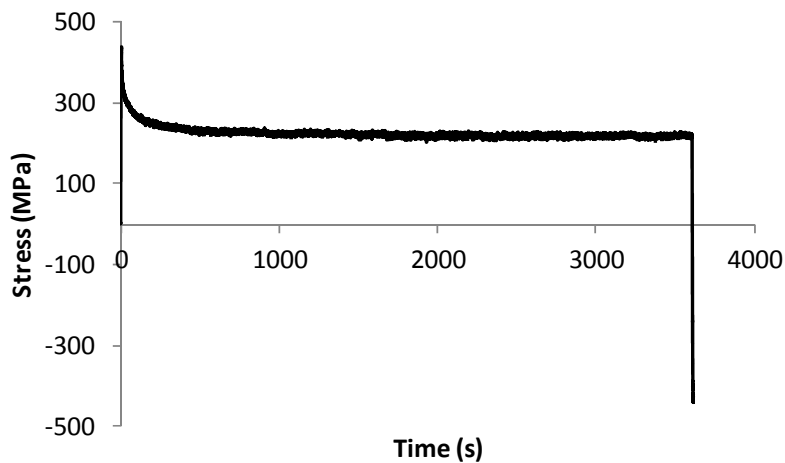


Figure 3.37: Measured stress relaxation data for a 1 hr tensile dwell at 0.5 % strain in cast MarBN at 600 °C.

3. High Temperature Experimental Testing of 9Cr Steels

3.7. High temperature fatigue life of 9Cr steels

This section analyses the high temperature fatigue life results of 9Cr steels. Comparisons are made between different 9Cr steels to assess (i) the effect of service history, (ii) chemical composition and (iii) material heat treatment. This section also includes microstructural analysis carried out on 9Cr steels as part of the SFI METCAM project.

3.7.1. Failure of 9Cr steels under high temperature fatigue

Due to the sensitive nature of the high temperature extensometer and owing to the large amount of energy dissipated during failure, the HTLCF and TMF test specimens were not fractured during the experiments. Instead, a 20 % drop in load relative to the load at 150 cycles is set as the criterion for failure. It is assumed here that the number of fatigue cycles occurring following this point is quite small as the fatigue cracks in the test specimens have sufficiently reduced the load bearing capability of the specimen. A typical dominant fatigue crack, following the 20 % load drop failure criterion, in a non-fractured specimen is presented in Figure 3.38. Fatigue testing of 9Cr steels also leads to significant secondary fatigue cracking, as illustrated in Figure 3.39. In all tests carried out on ES-P91, fatigue cracking from the specimen surface was observed to be the dominant mode of failure. In cast MarBN, fatigue striations were observed along the internal fracture surface in tested specimens [*O'Hara et al., 2015*] alongside cracking from the specimen surface. It is suggested here that some of these striations originated at flaws such as inclusions within the material, leading to internal fatigue cracking and rapid failure. The effect of such inclusions is discussed in more detail below.

3. High Temperature Experimental Testing of 9Cr Steels

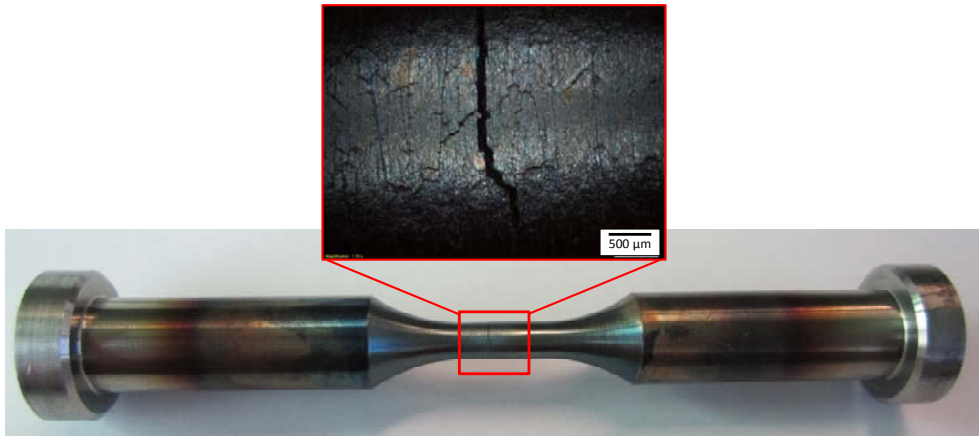


Figure 3.38: Image of failed ES-P91 steel specimen and optical micrograph (inset) of dominant fatigue crack.

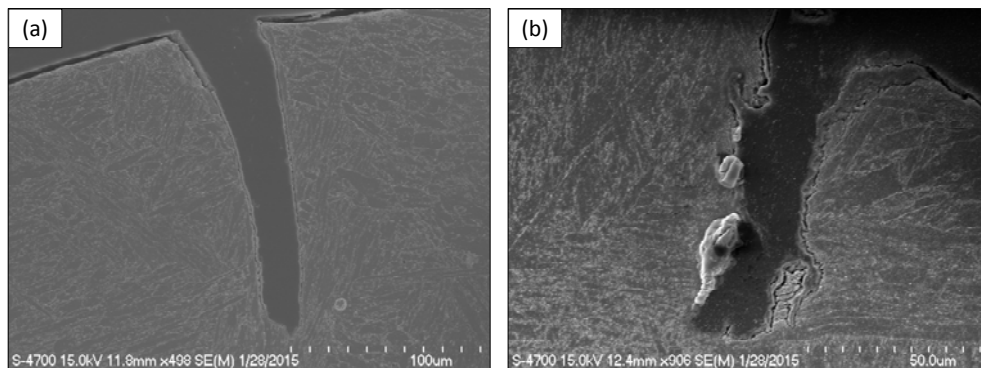


Figure 3.39: SEM images of secondary fatigue cracks in 9Cr steels.

The number of reversals to failure for ES-P91 steel is presented in Figure 3.40 for the various applied strain-ranges, with a comparison to results of an 'as-received' P91 steel (AR-P91) from the literature [Saad, 2013]. As is evident from this result, the ES-P91 steel has a marginally improved fatigue life, with lower fatigue life observed for higher temperatures. This difference is attributed to variations in chemical composition and heat treatment, as discussed in more detail in Section 3.7.4.

3. High Temperature Experimental Testing of 9Cr Steels

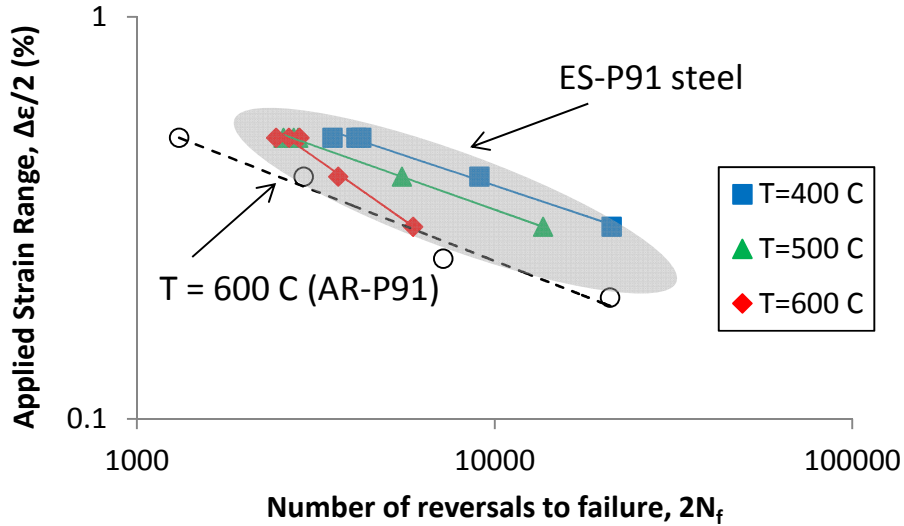


Figure 3.40: Number of reversals to failure as a function of applied strain-range in ES-P91 steel for different temperatures. A comparison with AR-P91 from the literature [Saad, 2013] is also included.

Figure 3.41 plots the HTLCF test data in terms of plastic strain-range, $\Delta\epsilon^{pl}/2$, for identification of the Coffin-Manson (C-M) material parameters. The data points of Figure 3.41 for different temperatures effectively collapse onto a single line when $\Delta\epsilon^{pl}/2$ is used. The C-M relationship [Coffin, 1954; Manson, 1954] is defined as:

$$\frac{\Delta\epsilon^{pl}}{2} = \epsilon'_f (2N_f)^c \quad (3.1)$$

where N_f is the number of cycles to failure, ϵ'_f is the fatigue ductility coefficient and c is the fatigue ductility exponent. The identified C-M material parameters for ES-P91 steel and cast MarBN at an applied strain-rate of 0.033 %/s are presented in Table 3.4. The HTLCF life data for MarBN is presented in Figure 3.42. Figure 3.42 also highlights the effect of strain-rate on fatigue life via comparison of (i) total strain-range and (ii) plastic strain-range as a function of cycles for MarBN at 600 °C.

3. High Temperature Experimental Testing of 9Cr Steels

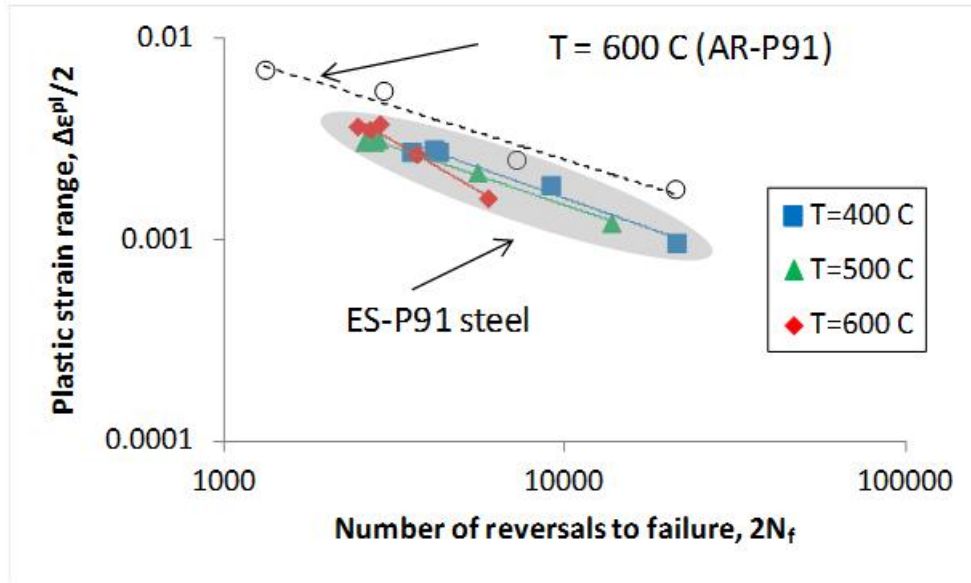


Figure 3.41: Coffin-Manson representation of the IF test data for ES-P91 steel, including a comparison with an 'as-received' P91 steel (AR-P91) from the literature [Saad, 2013].

Table 3.4: Identified Coffin-Manson constants for ES-P91 steel and cast MarBN at an applied strain-rate of 0.033 %/s.

Material	400 °C		500 °C		600 °C	
	ϵ_f'	C	ϵ_f'	c	ϵ_f'	c
ES-P91	0.4036	-0.5714	0.2857	-0.6003	8.6131	-0.9861
Cast MarBN	-	-	-	-	5.4602	-0.934

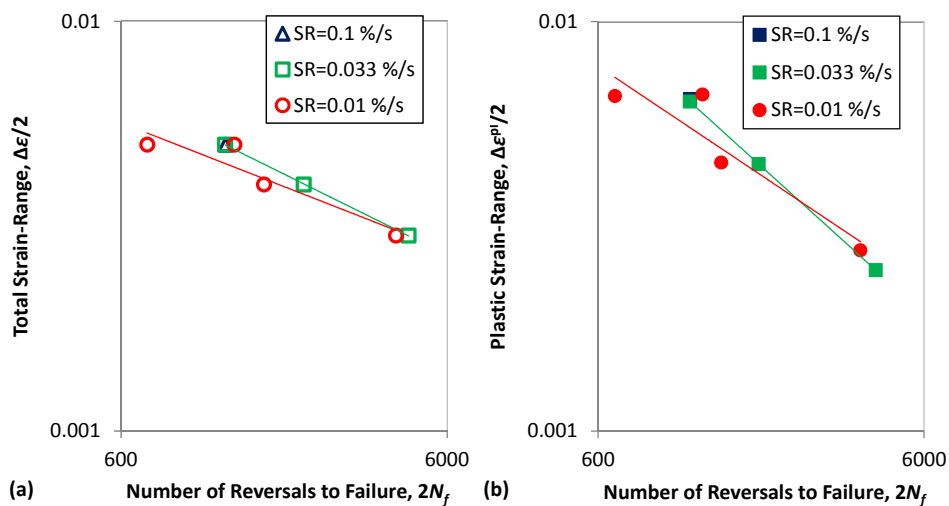


Figure 3.42: MarBN number of reversals to failure, $2N_f$, as a function of (a) total applied strain range and (b) plastic strain-range for various strain-rates at 600 °C.

3. High Temperature Experimental Testing of 9Cr Steels

The effect of thermo-mechanical loading on the fatigue performance of ES-P91 steel is illustrated in Figure 3.43, including a comparison with the isothermal fatigue (IF) data. As can be seen, the effects of thermal cycling lead to a significant reduction in fatigue life. The most severe case relates to that of TMF-OP loading. As the mechanical strain and temperature are out-of-phase, the material is subjected to a maximum tensile stress at minimum temperature and minimum strain a maximum temperature. This is essentially due to the material reaching a higher maximum stress at the lower temperature (under strain control) and giving a harder response (since maximum tensile stress is a key parameter for crack initiation). This result illustrates the requirement to (i) characterise the TMF-OP behaviour of candidate materials and (ii) develop a material model to successfully predict the effects of thermal cycling and subsequent effects on the structural integrity of plant components via finite element methods.

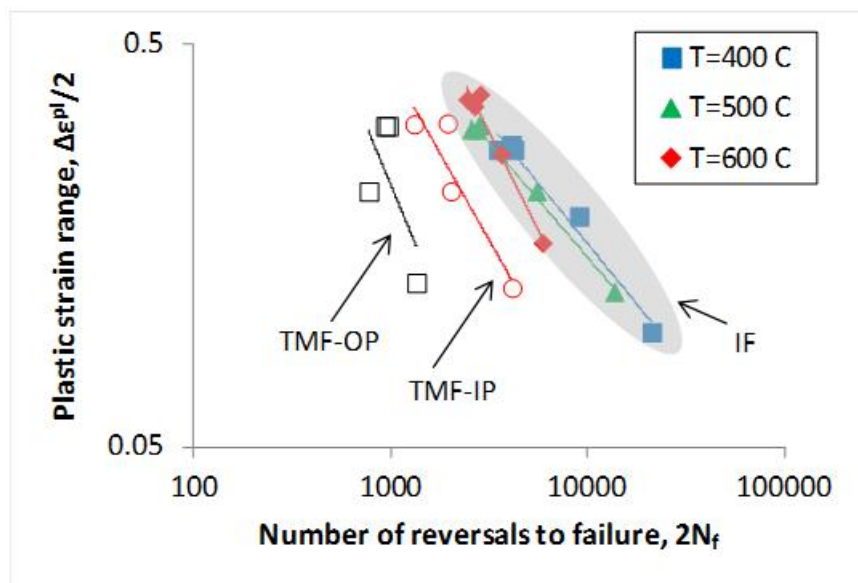


Figure 3.43: Comparison of the number of reversals to failure as a function of plastic strain-range at the half-life for IF, TMF-IP and TMF-OP test data.

3.7.2. Microstructural analysis

The microstructure of ES-P91 steel is presented in Figure 3.44, illustrating the high angle grain boundary structures of prior austenite grains (PAGs), packets and blocks, with identified dimensions of approximately 30 μm , 10

3. High Temperature Experimental Testing of 9Cr Steels

μm and $4 \mu\text{m}$ respectively. These values are consistent with previous observations in the literature [*Das et al., 2013b; Sauzay et al., 2005; Sauzay et al., 2008*]. Figure 3.45 is an electron backscatter diffraction (EBSD) image of the microstructure of ES-P91 steel. From this result, a mean martensitic lath width of approximately $0.5 \mu\text{m}$ is estimated via consideration of the measured distance between angles of misorientation along a line of interest. Angles of misorientation of approximately 45° correspond to PAG boundaries, while angles of approximately 60° are representative of a block structure. Angles of misorientation less than 5° are indicative of martensitic laths.

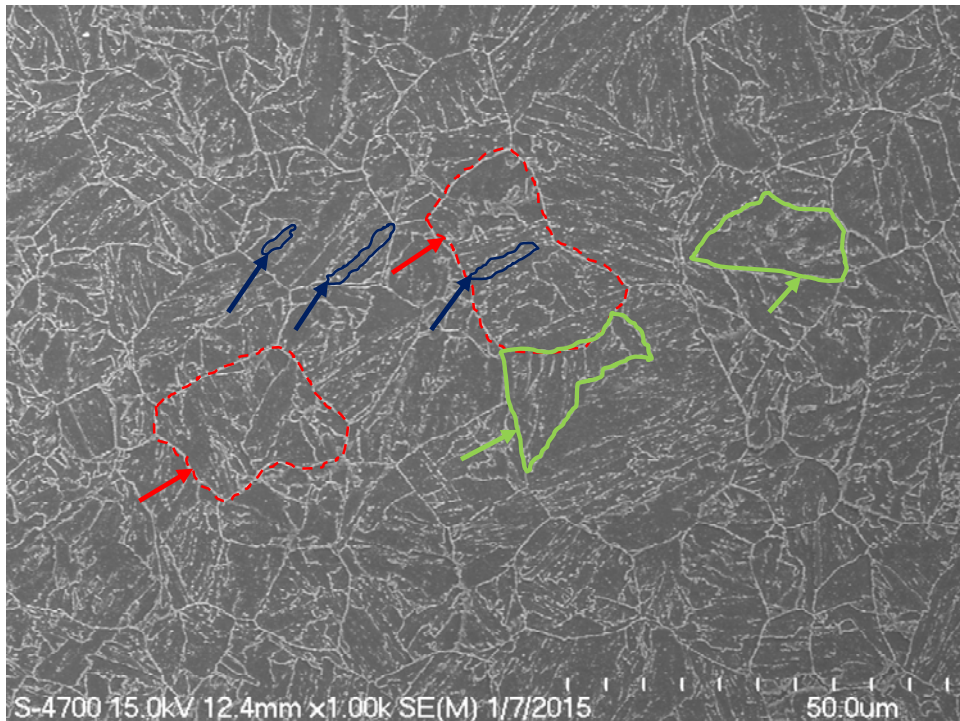


Figure 3.44: SEM image of the microstructure of tested ES-P91 steel. The red arrows point to prior austenite grains, the green arrows point to packets and the blue arrows represent block structures.

3. High Temperature Experimental Testing of 9Cr Steels

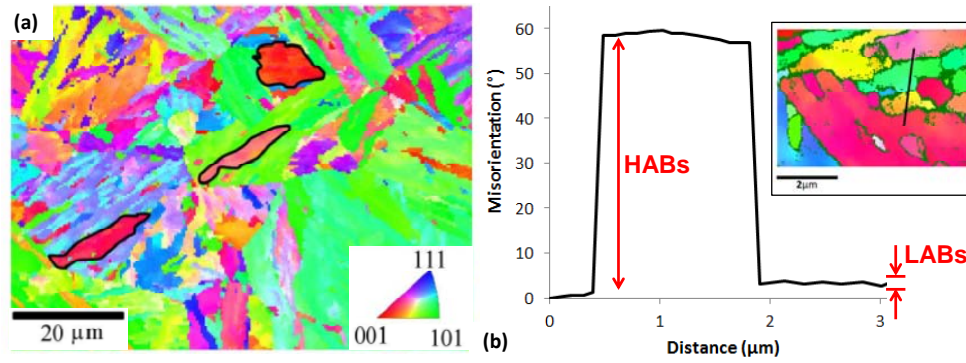


Figure 3.45: EBSD scan of ES-P91 steel microstructure for (a) Euler angle plot highlighting block structures and (b) angles of misorientation generated along a line of interest. *Image courtesy of Brian Golden, University of Limerick (SFI METCAM project).*

Figure 3.46 is an optical micrograph of the cast MarBN microstructure, highlighting (i) PAGs, (ii) block structures and (iii) flaws such as casting defects and inclusions. From this image, and the comparison of the SEM images in Figure 3.47, it is clear that the cast MarBN has a significantly coarser microstructure than ES-P91 steel. Due to the manufacture process and heat treatment (higher temperatures and longer times) for cast MarBN, this result is expected when comparing a rolled (ES-P91 steel) and a cast material (MarBN). The clear hierarchical microstructure observed in the rolled ES-P91 steel is also replaced by a more complex cast microstructure, which is also a hierarchical martensitic structure, but inclusive of columnar grains and the formation of a dendritic structure at some locations. Using a similar EBSD approach as used above (described in more detail elsewhere [Golden, 2015]), the mean martensitic width of cast MarBN is estimated to be 0.63 μm.

3. High Temperature Experimental Testing of 9Cr Steels

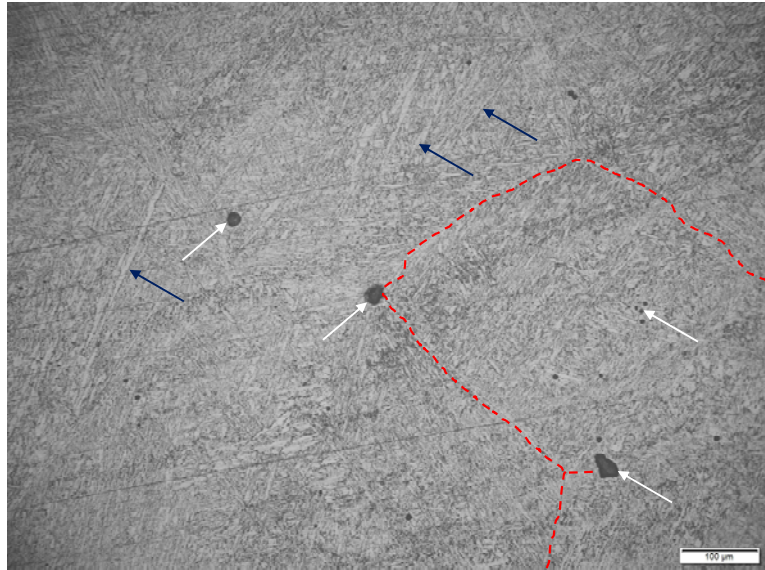


Figure 3.46: Optical micrograph of cast MarBN tested at a strain-rate of 0.033 %/s and applied strain-range of ± 0.5 %. The red line delineates a prior austenite grain boundary, the blue arrows point to block structures and the white arrows point to casting defects.

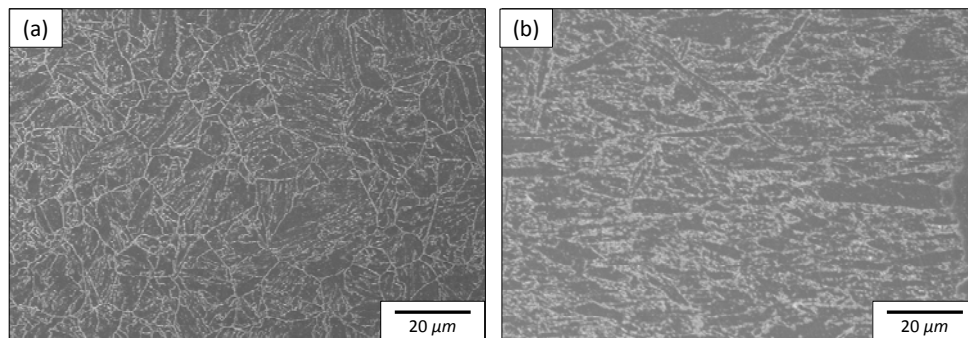


Figure 3.47: SEM comparison of tested (a) ES-P91 steel and (b) cast MarBN steel at 600 °C.

Figure 3.46 also highlights the existence of microstructural flaws such as casting defects, and inclusions (pockets of the melt material which solidify more rapidly than their surrounding regions and maintain this structure following heat treatment) in the cast microstructure. Typical images of the primary casting defects and inclusions observed during the SEM study are presented in Figure 3.48, defects which are quite common for cast materials.

3. High Temperature Experimental Testing of 9Cr Steels

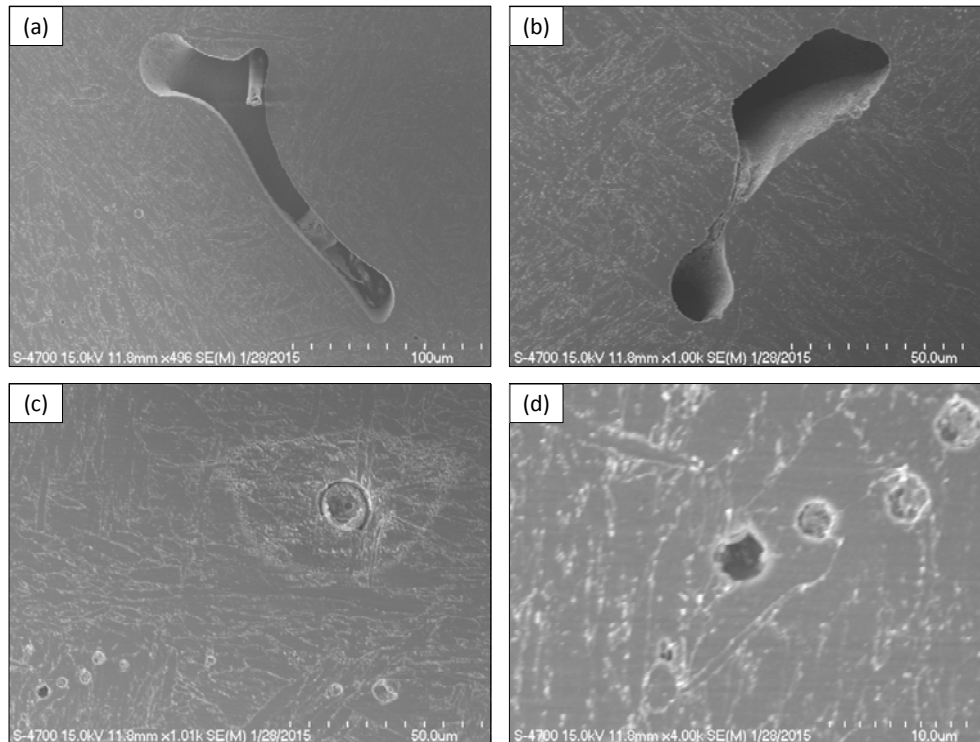


Figure 3.48: SEM images of microstructural defects in cast MarBN including (a) and (b) casting defects and (c) and (d) inclusions following testing at a strain-rate of 0.1 %/s and applied strain-range of ± 0.5 % at a temperature of 600 °C.

3.7.3. Fatigue scatter

The presence of flaws, such as voids, inclusions, casting defects and precipitates for example, can have a significant effect on crack initiation, crack propagation and ultimately, failure. Thus, for fatigue testing, scatter in the number of reversals to failure can be significant, illustrating the need to carry out multiple repeat tests.

Repeat tests have been carried out on ES-P91, with the results illustrated in Figure 3.49, comparing the constitutive behaviour for the initial cycle and the evolution of the maximum stress as a function of cycles. For HTLCF, fatigue lives within a factor of 2 would not be unexpected. This is due to microstructural differences between specimens and the role of impurities and defects (such as precipitates and inclusions) on fatigue crack initiation and growth in metals. From the result of Figure 3.49, the constitutive behaviour and cyclic softening produce almost identical results and it can be concluded that all test results lie within a fatigue scatter band of less than 2.

3. High Temperature Experimental Testing of 9Cr Steels

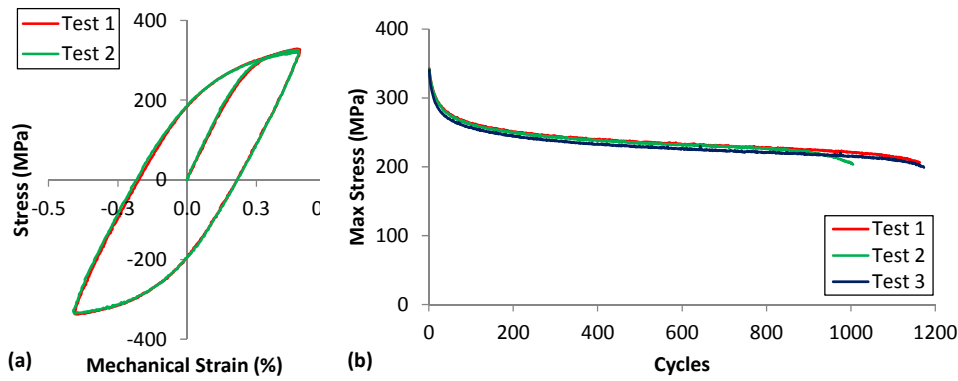


Figure 3.49: Measured stress-strain response for ES-P91 steel repeat tests at 600 °C, strain-rate of 0.033 %/s and an applied strain-range of (a) ± 0.4 %, and (b) ± 0.5 %.

The test results presented to date for the cast MarBN material have been carried out on the secondary grade material from the cast plates, as denoted in Figure 3.2. Figure 3.50 compares the material behaviour for repeat testing, using primary grade material in this case, at a strain-rate of 0.01 %/s and an applied strain-range of ± 0.5 %. As is evident from Figure 3.50a, the constitutive behaviour is similar for primary and secondary grade material. However, as illustrated in Figure 3.50b, a significant difference in fatigue life is observed (685 cycles, primary, versus 385 cycles, secondary). Following completion of the high temperature fatigue test program of MarBN at 600 °C, a study into the area fraction of voids and flaws in the cast MarBN material was conducted [O'Hara *et al.*, 2015]. The results of this study determined that quite small void area fractions of 0.43 % and 0.53 % are present for the primary and secondary grade material, respectively. Furthermore, no fatigue cracks were observed emanating from any of the cast flaws (casting defects or inclusions) during the SEM analysis (e.g. see Figure 3.48). Although this result lies within the upper and lower scatter bounds with respect to fatigue scatter, due to the existence of flaws in the cast material, it is concluded here that further testing and microstructural analysis is required to investigate whether or not casting defects may accelerate fatigue crack growth in the secondary grade material.

3. High Temperature Experimental Testing of 9Cr Steels

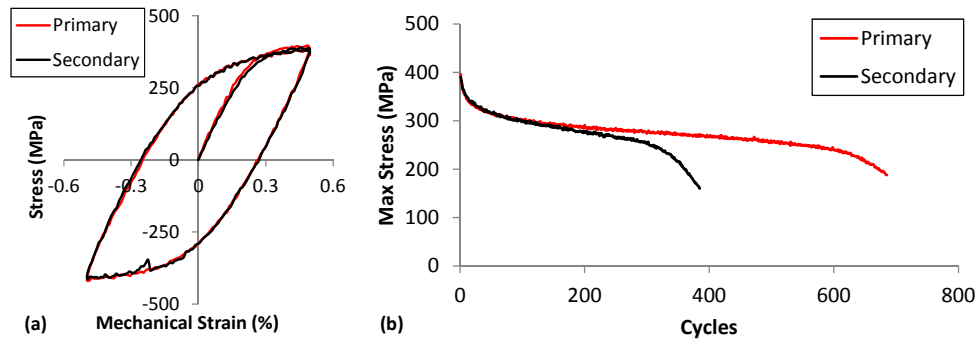


Figure 3.50: Comparison of primary and secondary grade cast MarBN materials tested at a strain-rate of 0.1 %/s and applied strain-range of 0.5 % for (a) constitutive behaviour, (b) and (b) cyclic evolution.

3.7.4. High temperature fatigue comparison of 9Cr steels

In this section, comparisons of the stress-strain behaviour of various 9Cr steels under high temperature fatigue are presented to investigate the effect of (i) chemical composition, (ii) heat treatment and (iii) fabrication process (rolled versus cast material) on the constitutive stress-strain response of the material under cyclic deformation. Comparisons are made with experimental data from the literature. The respective chemical compositions of the various materials are contained in Table 3.3 and Table 3.5, with the respective heat treatments presented in Table 3.6.

Table 3.5: Chemical composition of 9Cr steels in wt.%. The CST-P91 data is from Mroziński *et al.* [2014] and AR-P91 and AR-P92 from Saad [2012]. The balance is made up of Fe.

	Al	B	C	Cr	Mn	Mo	N	Nb	P	S	Si	V	W
CST-P91	-	-	0.12	8.22	0.47	0.90	0.040	0.070	0.014	0.004	0.31	0.12	-
AR-P91	0.007	-	0.12	8.60	-	1.02	0.060	0.070	0.017	<0.002	0.34	0.24	0.03
AR-P92	0.019	0.0034	0.10	8.62	-	0.33	0.047	0.076	0.015	0.002	0.45	0.21	1.86

Table 3.6: Heat treatment of 9Cr steels in wt.%. The CST-P91 data is from Mroziński and Golański [2013] and AR-P91 and AR-P92 from Saad [2012].

	Normalisation		Tempering	
	Temperature	Time	Temperature	Time
CST-P91	1040 °C	12.0 hr	760 °C	8.0 hr
AR-P91	1060 °C	0.75 hr	760 °C	2.0 hr
AR-P92	1070 °C	0.75 hr	780 °C	1.8 hr

Figure 3.51 compares the initial cycle stress-strain response of ES-P91 steel, AR-P91 steel and ‘as received’ P92 (AR-P92) steel data at 600 °C. It is

3. High Temperature Experimental Testing of 9Cr Steels

evident that ES-P91 steel is the strongest. Similarly, Figure 3.52 shows that MarBN is stronger than ES-P91 and P92 steels, and also has an increased Young's modulus.

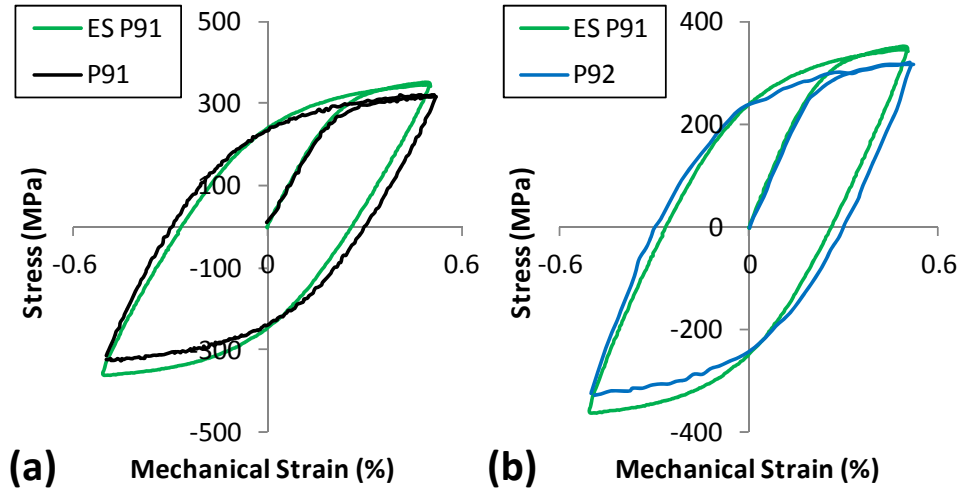


Figure 3.51: Comparison of the stress-strain response of ES-P91 steel with (a) ‘as received’ P91 steel [Saad et al., 2011a] and (b) P92 steel [Saad et al., 2013] at a temperature of 600 °C, strain-rate of 0.1 %/s and applied strain-range of 0.5 %.

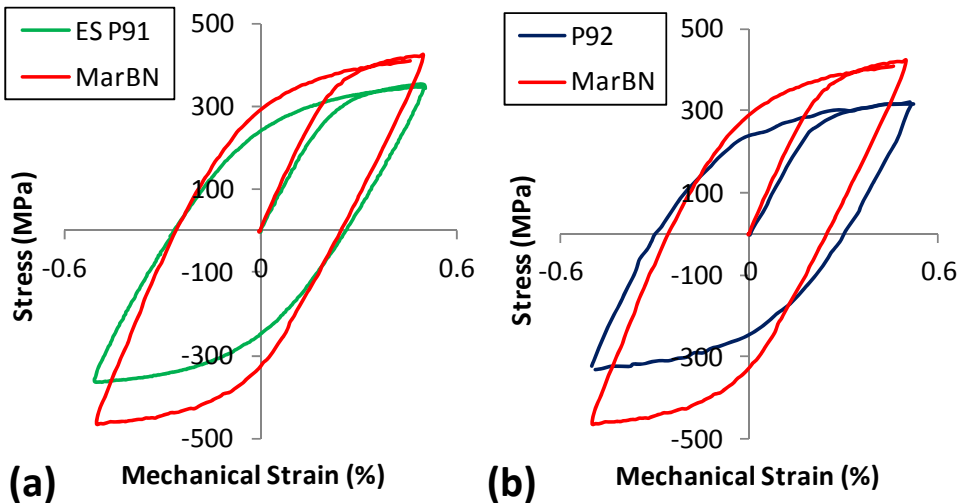


Figure 3.52: Comparison of cast MarBN with (a) ES-P91 steels and (b) P92 steel [Saad et al., 2013], for a strain-rate of 0.1 %/s and applied strain-range of ± 0.5 % at 600 °C.

Figure 3.53 shows a comparison of the HTLCF strain-rate life data from different cast and rolled P91 materials. Figure 3.53a compares the number of reversals to failure obtained at temperatures of 400 °C and 500 °C for

3. High Temperature Experimental Testing of 9Cr Steels

rolled ES-P91 steel and CST-P91 steel [Mroziński and Golański., 2013]. Although the ES-P91 steel is at a lower strain-rate of 0.033 %/s (compared to 0.1 %/s for CST-P91), the fatigue life of ES-P91 exceeds that of CST-P91 for all cases and temperatures (in a similar manner to 600 °C). This result highlights the reduced fatigue performance associated with cast materials compared with rolled materials.

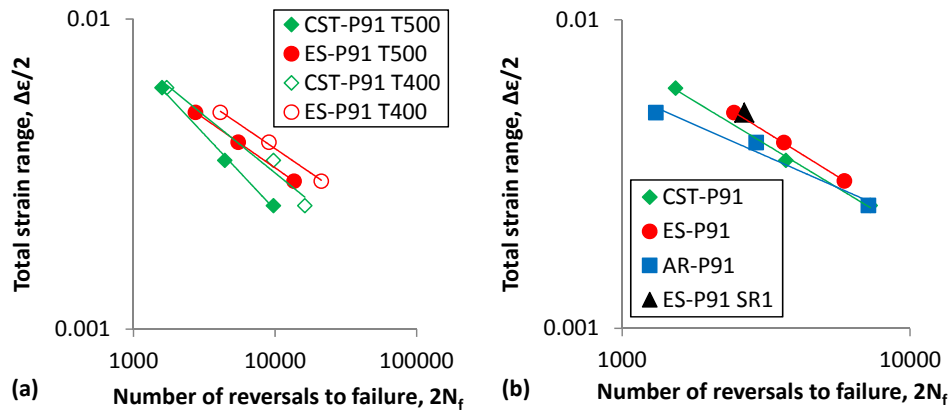


Figure 3.53: Comparison of LCF strain-life response for different P91 steels at (a) 400 °C and 500 °C, and (b) 600 °C.

At high temperature, the fatigue life of rolled P91 (AR-P91, data from [Saad *et al.*, 2012]) and CST-P91 at 600 °C are quite similar, as illustrated in Figure 3.53b. The data for AR-P91 and CST-P91 steels are obtained at a strain-rate of 0.1 %/s and applied strain-range of ± 0.5 %, the same conditions as the ES-P91 SR-1 case. From Figure 3.53, it is evident that the fatigue performance of the rolled ES-P91 steel exceeds that of the CST-P91 steel. The result of Figure 3.53a also incorporates a strain-rate effect, with the ES-P91 data collated at a lower strain-rate of 0.033 %/s. Thus, it can be concluded that this result illustrates little effect of the 35,168 hrs service life under subcritical loading on the fatigue life of ES-P91. However, it must be noted that slight chemical composition differences between rolled and cast P91 steel do exist, as well as a different heat treatment, highlighting the requirement for a much more in-depth study on the effect of heat treatment on the fatigue performance of 9Cr steels.

3. High Temperature Experimental Testing of 9Cr Steels

Table 3.7 shows the effect of casting on the mechanical properties of 9Cr steels. The ultimate tensile strength (UTS) for rolled ES-P91 steel at both 20 °C and 600 °C is significantly higher (approximately 20 %) than cast P91.

Table 3.7: Young's modulus (E) and ultimate tensile strength (UTS) in ES-P91 and CST-P91 steel.

	20 °C		600 °C	
	E (GPa)	UTS (MPa)	E (GPa)	UTS (MPa)
ES-P91 [<i>Golden et al., 2015</i>]	206	683	144	417
CST-P91 [<i>Mroziński et al., 2014</i>]	207	432	150	338

A comparison of the cyclic evolution of maximum stress observed at 600 °C in 9Cr steels is presented in Figure 3.54a (strain-range $\pm 0.5\%$, strain-rate 0.1 %/s). As is evident from this result, cast MarBN has an increased rate of cyclic softening compared to the P91 steels, as presented in Figure 3.54b. It is concluded here that this increased rate of softening is as a result of the coarser initial martensitic lath structure in the cast MarBN material (with the AR-P91 steel having the lowest rate of softening and the smallest initial martensitic lath width). Figure 3.54 also illustrates a slightly increased fatigue life for cast MarBN when compared with the AR-P91 steel under the same loading conditions. However, the cast MarBN has a significantly higher yield strength ($\sim 25\%$) than P91 steels, as illustrated in Figure 3.55. This is primarily attributed here to the inclusion of 3 wt.% W in MarBN, providing enhanced solid-solution strengthening.

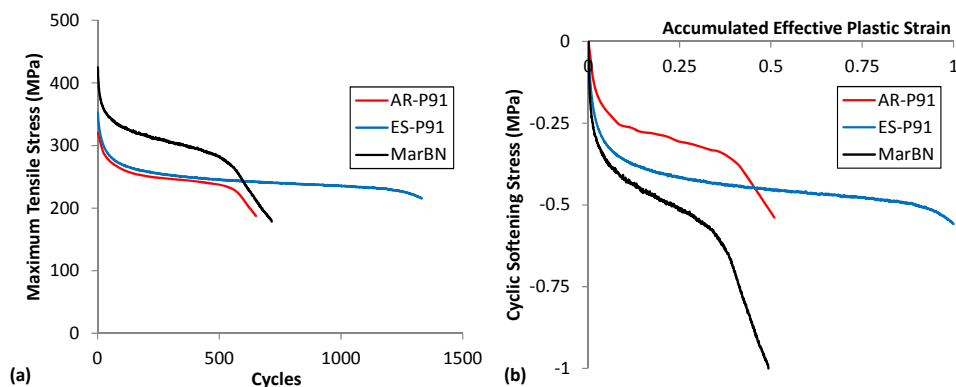


Figure 3.54: Comparison of the cyclic evolution of 9Cr steels for (a) maximum tensile stress versus cycles and (b) cyclic softening as a function of accumulated effective plastic strain. The AR-P91 data is obtained from the literature [*Saad, 2012*].

3. High Temperature Experimental Testing of 9Cr Steels

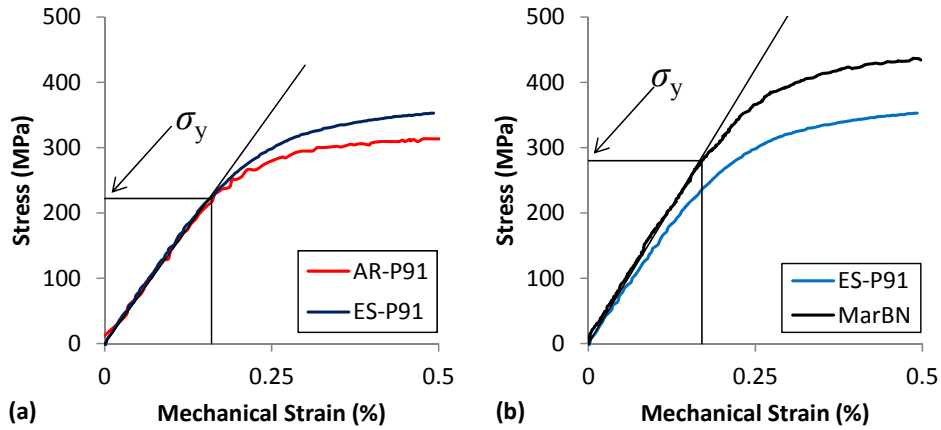


Figure 3.55: Comparison of monotonic stress-strain behaviour for (a) AR-P91 [Saad, 2012] and ES-P91 and (b) ES-P91 and cast MarBN.

Figure 3.56 illustrates a comparison of the number of reversals to failure for various 9Cr steels at 600 °C. The ES-P91 steel and cast MarBN results are obtained at an applied strain-rate of 0.033 %/s in comparison with a higher applied strain-rate of 0.1 %/s for the AR-P91 and AR-P92 materials of Saad [2012]. The rolled ES-P91 steel illustrates superior fatigue performance when compared with ‘as-received’ P91 and P92 steels and also, the MarBN material. However, the MarBN material, a cast product designed for high creep strength, demonstrates a fatigue life performance at least equivalent to AR-P91 steel, when tested at a lower strain-rate. As these test results were obtained using the secondary grade MarBN material, Figure 3.56 coupled with the superior creep performance discussed by Abe *et al.* [2008], illustrate the potential of MarBN to deliver excellent high temperature creep-fatigue performance in realistic plant components.

3. High Temperature Experimental Testing of 9Cr Steels

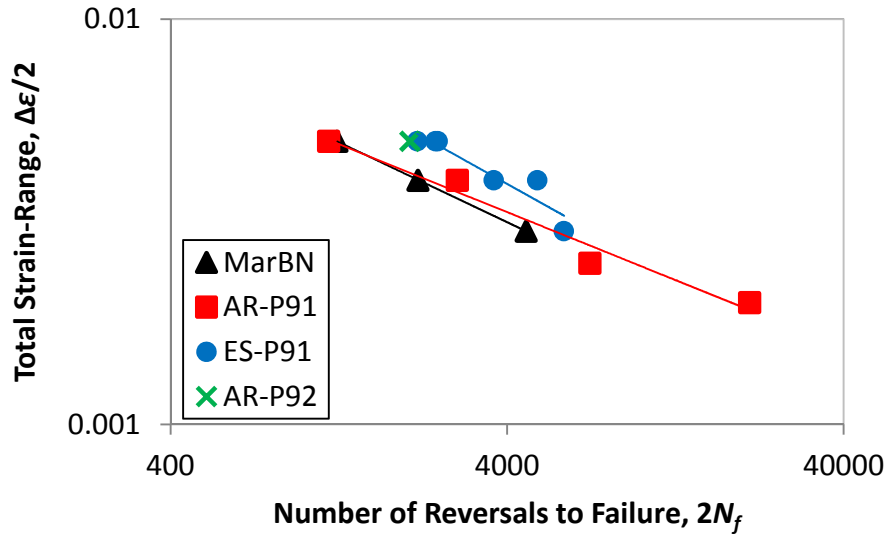


Figure 3.56: Comparison of the number of reversals to failure as a function of applied strain range for 9Cr steels at 600 °C. The AR-P91 and AR-P92 data are 'as-received' P91 and P92 steel data from [Saad, 2012].

3.8. Discussion

3.8.1. HTLCF and TMF test results

The results of the HTLCF test program show a considerable strain-rate effect at temperatures above 500 °C and a negligible effect at 500 °C and below, as illustrated in Figure 3.21. A strain-range effect, including non-Masing behaviour, is also observed across the $\pm 0.3\%$ to $\pm 0.5\%$ applied strain-ranges, as illustrated in Figure 3.14. From Figure 3.10, temperature is also found to have a significant effect on the isothermal stress-strain response, with considerable variations in Young's modulus (206 GPa at 20 °C reducing to 124 GPa at 625 °C). This large drop in Young's modulus (and related drop in shear modulus, μ) has a substantial effect on (i) the material yield strength and (ii) the strengthening obtained from mechanisms such as precipitates (Orowan stress, $\tau_{Or} = \mu b / \lambda$) and immobile dislocations (Taylor hardening, $\tau_p = \alpha_1 \mu b \sqrt{\rho}$, where α_1 is a material constant and ρ is dislocation density) in the material microstructure. As highlighted in the results of Figure 3.21 and Figure 3.36, in particular, the strain-rate effect is

3. High Temperature Experimental Testing of 9Cr Steels

also a key variable for which each material must be characterised. For ES-P91 and MarBN, there is a clear shift in the level of strengthening associated with varying the strain-rate at a temperature of 600 °C due to the effect of a viscous stress, but is not present in P91 at temperatures of 500 °C and below, where viscous effects are no longer considered to be as important. Furthermore, as the tests typically conducted under laboratory conditions are carried out at higher strain-rates compared with typical plant loading conditions, a clear understanding and complete characterisation of the strain-rate behaviour of the material is required if such tests are to be applied during design of realistic plant components.

The TMF test program highlights the clear requirement for (i) the completion of such a test program to illustrate the substantial effect of thermal cycling on the fatigue performance of 9Cr steels and (ii) the development of a material model which can accurately predict such effects. The constitutive behaviour during TMF-IP and TMF-OP largely follows that of the isothermal fatigue loading condition, as presented in Figure 3.26. However, there exists a considerable reduction in fatigue life, as illustrated in Figure 3.43, particular for the TMF-OP loading condition. For TMF-IP loading, the reduction in fatigue life can be explained by the existence of an additional thermal strain at maximum tensile or compressive loading. For TMF-OP loading, the culmination of (i) a higher maximum tensile stress and (ii) the additional thermal strain results in the material being subjected to higher loading and more plastic deformation.

3.8.2. Effect of chemical composition

Figure 3.51a compares the constitutive behaviour of ES-P91 and AR-P91 steels. Both sets of tests were conducted on the same test rig at the University of Nottingham. The ES-P91 steel was in operation for 35,168 hrs under subcritical loading conditions in Lough Ree power station, Ireland (at temperatures of less than 520 °C), with 65 start-up (and shut-down) cycles, prior to commencement of the HTLCF and TMF test programs. Thus, it is assumed that due to the number of start-up and shut-down cycles, the

3. High Temperature Experimental Testing of 9Cr Steels

material may have softened over the duration of its service, resulting in an expected reduction of (i) strength and (ii) fatigue life. These cycles could also have resulted in some microstructural degradation, leading to martensitic lath widening, for example. However, as is evident from Figure 3.51 and Figure 3.53b, the ES-P91 steel appears to have increased strength and fatigue properties when compared to AR-P91 steel. Although the differences in fatigue life could just be fatigue scatter, as discussed in Section 3.7.3, variations in chemical composition and heat treatment could also play a pivotal role in the variation of strength and fatigue performance.

From Table 3.3, the two P91 steels compared in this chapter have very similar chemical compositions. The primary difference in chemical composition relates to the presence of 0.42 wt.% Mn in the ES-P91 steel. As Mn is known to provide a small solute strengthening mechanism [Dawson, 2012] and contribute to carbide strengthening in the form of $Mn_{23}C_6$ precipitates dispersed along boundaries [Silwal *et al.*, 2013], the inclusion of manganese could contribute to the observed difference in material strength. The other primary difference between the ES-P91 and AR-P91 steels relates to the presence of 0.19 wt.% Ni in the ES-P91 steel, with it widely accepted that nickel improves material ductility [Roland *et al.*, 2006]. The slight increases in C, Cr, Mo, N and V in the AR-P91 steel would only suggest increases in material strength via increased precipitate and solute strengthening mechanisms; however, the presence of additional precipitates could act as sites for fatigue crack initiation due to the presence of stress concentrations around such obstacles. Hence, it is assumed here that these small variations may not have a large effect on constitutive behaviour but may play a pivotal role in fatigue crack initiation.

The other notable difference between ES-P91 and AR-P91 steels relates to the material heat treatment. The temperatures at which normalisation and tempering were carried out are quite similar (1050 °C and 765 °C respectively for ES-P91 and 1060 °C and 760 °C for AR-P91 steel). However, there are variations in the heat treatment times. The increased normalisation time for AR-P91 (0.5 hrs and 1 hrs for ES-P91 compared with 0.75 hrs and 2 hrs for AR-P91 steel) suggests that AR-P91 has (i) an

3. High Temperature Experimental Testing of 9Cr Steels

increased prior austenite grain size, (ii) slightly coarsened $M_{23}C_6$ and MX precipitates via the Ostwald ripening process, (iii) decreased dislocation density and (iv) increased initial martensitic lath width [Ennis and Czynska-Filemonowicz, 2002], compared to the ES-P91 steel. It is argued here that the net result of the different heat treatment for AR-P91 steel is (i) decreased strength and (ii) enhanced microstructural degradation, which can contribute to premature failure.

3.8.3. Potential of MarBN for next generation power plant

From Figure 3.52, a significant difference in constitutive behaviour is evident when comparing MarBN with ES-P91 steel and P92 steel, with MarBN also illustrating a slightly decreased LCF life compared to ES-P91 steel and P92 steel data (see Figure 3.56). The reduced LCF life when comparing ES-P91 steel and cast MarBN can, at least partially, be explained by the necessity to load the specimens to a higher stress to achieve a given strain and coupled with the cast nature of the MarBN material.

However, this first phase of HTLCF tests on cast MarBN material demonstrates a clear increase in cyclic stress range when compared to P91 steel. This increased stress-range can be attributed to (i) the inclusion of 3 wt.% tungsten in MarBN, and (ii) boron enrichment of grain boundaries. The inclusion of tungsten leads to an enhanced solute strengthening mechanism and also contributes to $M_{23}C_6$ carbide strengthening ($W_{23}C_6$ carbides). Maruyama *et al.* [2001] have found that tungsten also retards the growth of $M_{23}C_6$ precipitates, resulting in a finer distribution of precipitates along boundaries. This gives an increased precipitate strengthening mechanism, i.e. increased Orowan back-stress due to decreased $M_{23}C_6$ precipitate spacing. The increase in material strength, and increased yield strength compared to P91 observed during the initial cycle in cast MarBN, is quite similar to that of P92 (with 1.8 wt.% W) when compared with P91 (without W), and hence, it is concluded that the increase in yield strength is primarily due to the inclusion of tungsten when compared with P91 steel.

3. High Temperature Experimental Testing of 9Cr Steels

The introduction of boron also helps improve the precipitate strengthening of $M_{23}C_6$ carbides along boundaries. Boron-enriched boundaries result in more thermally stable $M_{23}(CB)_6$ carbides and hence, less carbide coarsening via the Ostwald ripening process during (i) tempering and (ii) long-term creep deformation. Although beneficial for creep loading, under pure fatigue loading conditions at high temperature, the inclusion of additional boron has little effect as precipitate coarsening is not of concern once the heat treatment process is complete.

From the work of Abe and co-workers [2008], it should also be noted that increasing the nitrogen content can significantly improve the creep strength of MarBN, with a maximum bound of approximately 95 ppm due to the formation of BN precipitates. Normalising at higher temperatures, as done in the current work, reduces the risk of BN precipitates forming [Li *et al.*, 2013a], enabling an increased range of nitrogen to be included in the chemical composition. Hence, it is anticipated here that the cast MarBN has increased strengthening owing to the presence of an increased dispersion of fine MX particles compared to other MarBN materials in the literature [Abe *et al.*, 2008]. Boron and nitrogen can also contribute to solid solution strengthening within the matrix if BN precipitates do not form [Abe *et al.*, 2008]. However, the nitrogen content of the cast MarBN tested here does not equate to that of the P91 steels tested, and hence, should have less VN nitride strengthening. Furthermore, there is an inherent loss of grain boundary strengthening as the PAG structure is significantly coarser due to the higher normalising temperatures (as illustrated in Figure 3.46) and there is a reduction in Mo solid solution strengthening as the molybdenum content is significantly reduced. This further highlights the benefits of including (i) 3 wt.% tungsten and (ii) boron enrichment of the grain boundaries in terms of the increased strengthening gained and observed improved creep performance in cast MarBN.

3.8.4. Cyclic softening behaviour

From Figure 3.17, it can be concluded that cyclic softening is both a function of temperature and the accumulated effective plastic strain-rate. As discussed by Sauzay *et al.* [2005; 2008], a loss of the martensitic lath substructure via a decrease of LAB dislocations is the primary mechanism responsible for cyclic softening, resulting in a loss of the overall density of dislocations. Thus, it is assumed here that the consumption of mobile dislocations, which are effectively the carriers of plastic deformation, is responsible for the reduction in strength owing to cyclic softening. Furthermore, an increased rate of cyclic softening is observed in the cast MarBN when compared with the ES-P91 steel, with AR-P91 steel demonstrating the lowest rate of softening (see Figure 3.54). It is suggested here that the increased rate of softening observed in MarBN is primarily due to the initial lath microstructure, i.e. MarBN has a measured initial lath width of 0.63 μm compared to 0.383 μm for AR-P91 [Hyde *et al.*, 2012]. The coarse lath structure in cast MarBN, coupled with a much coarser high angle grain boundary structure (i.e. coarsened prior austenite grains, packets and blocks, due to (i) the harsh heat treatment and (ii) cast nature of the MarBN material) will have fewer boundaries to impede the motion of plastic deformation and hence, result in an increased rate of cyclic softening. For flexible operation of plant, this cyclic softening will result in a significant reduction in creep strength. As little temperature-dependent martensitic lath growth occurs at temperatures of 600 °C or less [Panait *et al.*, 2010b], the temperature-dependence of cyclic softening stress observed in Figure 3.17 is attributed here predominantly to the temperature-dependent yield stress and more fundamentally, the temperature-dependence of stiffness, as discussed in Section 3.4.1 above.

3.8.5. Failure of 9Cr steels

As expected, failure is a function of temperature, strain-rate and applied strain-range. The fatigue life of the specimen is decreased for increasing temperature and strain-range and decreasing strain-rate. Test specimen

3. High Temperature Experimental Testing of 9Cr Steels

failure is also a function of the initial material microstructure. As is typical with cast structures, the resulting microstructure following manufacture for the cast MarBN is much coarser than a rolled equivalent. Thus, the reduced life when compared to the rolled ES-P91 steel observed in Figure 3.56, for example, is expected. This is similar to the work of Williams and Fatemi [2007], who concluded that cast iron used for crankshafts under high temperature fatigue has a fatigue life reduction by up to a factor of six when compared to a forged steel equivalent and further highlighted in Figure 3.53 for cast versus rolled P91 steel. Hence, there exists a need to characterise the fatigue performance of an equivalent rolled MarBN material, as a material with a finer distribution of $M_{23}C_6$ precipitates along boundaries (due to boron enrichment of boundaries) coupled with further refinements in initial martensitic lath width, has the potential for enhanced performance under creep-fatigue loading, along with clear benefits to mitigate Type IV cracking as discussed in detail by Abe *et al.* [2007b; 2010] and Tabuchi *et al.* [2004].

Although all of the test results presented lie within the bounds of expected fatigue scatter, the variations in chemical composition and heat treatments cannot be neglected when considering failure in 9Cr steels. For example, reduced fatigue performance would be expected for materials with coarser grain structures. This larger grain size is desirable for improved creep resistance with a reduction in potential creep void initiation and nucleation sites. However, the loss of a fine microstructure promotes fatigue crack propagation as there are less boundary regions to arrest fatigue crack growth. It is thought that this coarser microstructure in the cast MarBN could contribute to the reduction in fatigue life observed when compared with ES-P91 steel. The presence of inclusions and casting defects in cast MarBN, as illustrated in Figure 3.48, can also have an effect on failure in the cast material. With fatigue striations observed at inclusions in cast MarBN [O'Hara *et al.*, 2015], it is concluded here that such defects potentially have an effect on the fatigue life.

The changes in processing conditions (compared to other 9Cr steels) on the creep-fatigue performance of MarBN must also be investigated. During the

3. High Temperature Experimental Testing of 9Cr Steels

manufacture of MarBN components, careful heat treatment processes [Li *et al.*, 2013a] and controlled levels of nitrogen [Abe, 2008; Sakuraya *et al.*, 2006] are required to prevent the production of unstable BN precipitates when introducing boron to 9Cr steels. This process results in significant improvements in the creep strength of the material [Abe *et al.*, 2008]. However, further work needs to be done to quantify the effect of (i) significantly modified heat treatments and (ii) reduced nitrogen content on the fatigue and creep-fatigue performance of such materials. It is anticipated that this initial study of the high temperature fatigue performance of MarBN provides the first step in determining such effects on the fatigue and subsequently, creep-fatigue life of 9Cr-3W-3Co-V-Nb steels.

However, this coarser microstructure, inclusive of casting defects, does not explain the significant difference in observed fatigue life and variations in cyclic softening rates when comparing ES-P91 and AR-P91 steel. These variations are most likely caused by two primary factors, (i) the increased cyclic plastic strain-range in the ES-P91 steel and (ii) variations in chemical composition. As illustrated in Figure 3.57, the plastic strain-range in the ES-P91 steel is considerably higher than that of AR-P91 steel. As cyclic softening is a function of martensitic lath width, the increased plastic deformation for strain-controlled loading conditions in the ES-P91 steel leads to more low-angle boundary dislocation annihilation and hence, more cyclic softening. Furthermore, the initial martensitic lath width and hence, resulting rate of cyclic softening, is slightly increased in ES-P91 compared with the AR-P91 steel. It is concluded here that the service history, inclusive of 65 start-up cycles, could have resulted in some primary softening and hence, slightly increased the martensitic lath width prior to testing.

From the result of Figure 3.54, this increased rate of cyclic softening does not appear to have a substantial effect on fatigue life. It is thought here that this is predominately related to chemical composition. In terms of microstructure, the additional composition of precipitating elements in AR-P91, such as C, Cr, N and V, can result in more locations for stress concentrations to form and hence, increasing the potential for fatigue crack initiation. Furthermore, the inclusion of 0.19 % Ni in the ES-P91 steel can

3. High Temperature Experimental Testing of 9Cr Steels

improve material ductility and hence, can be beneficial in terms of improving fatigue life [Roland *et al.*, 2006], possibly contributing to the increased fatigue life observed here.

Beyond the possibility of fatigue scatter pointing to the variations in fatigue life, it is concluded that small variations in chemical composition, coupled with fewer sites for crack initiation, play a significant role in fatigue performance of 9Cr steels. Therefore, for example, the possible benefits of including nickel and manganese within the chemical composition require further analysis. The normalising and tempering times can also have a significant bearing on the initial microstructure and subsequent fatigue performance of the 9Cr steels and should be investigated in future work.

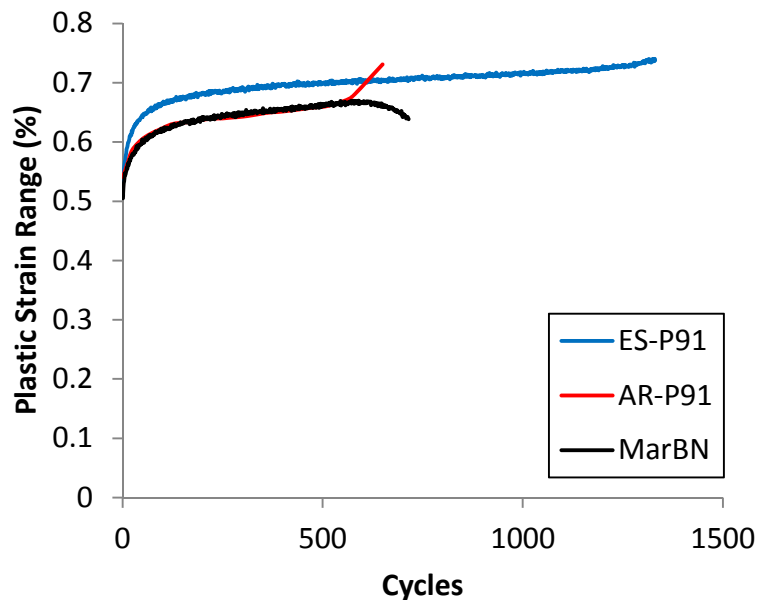


Figure 3.57: Measured plastic strain range as a function of cycles in 9Cr steels.

Finally, the results of this experimental study highlight a key element when designing with precipitate and solute strengthened materials within a complex hierarchical microstructure. When considering the performance of such materials under creep, fatigue, oxidation or interactions of creep, fatigue and oxidation, a single strengthening contribution cannot be considered on its own, i.e. precipitate strengthening is not solely responsible for the inherent strength in 9Cr steels, as $M_{23}C_6$ precipitates are also

3. High Temperature Experimental Testing of 9Cr Steels

important in terms of the martensitic lath substructure produced. Hence, any material model derived from a physical basis must account for interactions of all the mechanisms mentioned above. Chapters 6 and 7 attempt to take a first step towards the development of such a model, building on a phenomenological hyperbolic sine flow rule framework developed in Chapter 4.

3.9. Conclusions

Characterisation of the high temperature fatigue behaviour of two 9Cr steels, (i) ex-service P91 steel and (ii) MarBN, is presented in this chapter. An assessment of the performance of 9Cr steels across various strain-rates, strain-ranges and temperatures has been completed, via low cycle fatigue and stress relaxation testing. The key conclusions of this chapter are:

- At temperatures of 500 °C and less, strain-rate effects are found to be negligible. However, strain-rate effects exist in 9Cr steels at temperatures above 500 °C, resulting in a significant decrease in stress-range with decreasing strain-rate. The decrease in stress-range is directly related to viscous effects in the material. Furthermore, strengthening is observed to be strain-rate dependent once viscous effects become important and the hardening modulus becomes a function of strain-rate.
- Thermo-mechanical loading is found to have a substantial effect on low cycle fatigue life, with out-of-phase loading representing the lowest fatigue life.
- Considerable cyclic softening is observed for all tests conducted on 9Cr steels. The rate of cyclic softening increases with increasing temperature and is dependent on (i) strain-rate and (ii) applied strain-range. Cyclic softening is concluded to be a function of initial martensitic lath width.
- Temperature is found to play a pivotal role in the mechanical performance of 9Cr steels. A 20 GPa reduction in Young's modulus

3. High Temperature Experimental Testing of 9Cr Steels

is observed from 20 °C to 400 °C, with the same reduction observed from 600 °C to 625 °C, highlighting the sensitive nature of operating at temperatures in excess of 550 °C.

- The inclusion of 3 wt.% tungsten and cobalt, coupled with boron enrichment of grain boundaries in MarBN is concluded to result in a significant increase in yield and tensile strength compared to the P91 steels.
- The cast MarBN product is found to have similar fatigue life as existing 9Cr grade materials, with enhanced strength compared to P91 and P92 steels. Coupled with superior creep performance compared to other 9Cr steels, as presented in the literature, this initial fatigue testing illustrates the potential of MarBN as a candidate material for higher temperature flexible operating conditions.

The following chapter develops a hyperbolic sine unified cyclic viscoplastic material model for 9Cr steels. A step-by-step parameter identification procedure is also developed, including calibration and validation of the material model against (i) ‘as received’ P91 steel data from the literature, (ii) ex-service P91 steel and (iii) cast MarBN.

4. A Unified Cyclic Viscoplastic Modelling Framework for Strain-Rate Dependent Materials

4.1. Introduction

This chapter presents a continuum level unified cyclic viscoplastic material modelling framework to simulate the behaviour of 9-12Cr steels under high temperature fatigue, including implementation in a user material subroutine for 3D applications and the development of a step-by-step parameter identification methodology. This hyperbolic sine framework is the basis for (i) the phenomenological modelling conducted in Chapter 5 and (ii) the microstructure-sensitive modelling methodologies presented in Chapters 6 and 7. The continuum level modelling methodology is derived from a thermodynamic framework, presented in detail in Appendix A, and based on state variables for strain and temperature, with careful choice of internal variables to ensure that cyclic plasticity effects are simulated.

To capture cyclic plasticity and viscous effects within one model, a unified approach similar to the Chaboche model [*Chaboche and Rousselier, 1983a; Chaboche and Rousselier, 1983b*] is required. The Chaboche unified cyclic viscoplastic material model has previously been used to simulate the behaviour of 9-12Cr steels under HTLCF [*Koo and Kwon, 2011; Saad et al., 2011*]. However, to ensure that the modelling methodology can capture strain-rate effects, as determined experimentally in Chapter 3, a hyperbolic sine unified cyclic viscoplastic material model is developed in the current chapter. The benefit of such an approach over the existing power law methodologies is the ability to allow a smooth transition from the high stress and strain-rate regimes, at which experiments are normally conducted, to low stress and strain-rate regimes typically observed under flexible plant operating conditions, resulting in a strain-rate sensitive modelling methodology. Yielding and viscoplastic loading are defined in terms of a dissipation potential, as derived from the thermodynamic framework and presented in Section 4.4.

4. A Unified Cyclic Viscoplastic Modelling Framework for Strain-Rate Dependent Materials

Previous work [*Dubey et al., 2005; Farragher et al., 2014; Fournier et al., 2009a; Fournier et al., 2009b; Saad et al., 2011*] shows that 9-12Cr steels undergo considerable cyclic softening due to a loss of the low-angle boundary structure [*Sauzay et al., 2005; Sauzay et al., 2008*]. Cyclic softening is also observed in the experiments conducted here on (i) ex-service P91 steel and (ii) MarBN, a new 9-12Cr with additional boron and nitrogen for increased creep strength, as presented in Chapter 3. Section 4.3 presents a modified version of the Chaboche isotropic hardening model [*Lemaitre and Chaboche, 2000*] to predict the cyclic softening behaviour of 9-12Cr steels, with a negative saturation value to ensure softening behaviour is captured [*Saad et al., 2011*]. In Section 4.3.3, non-linear kinematic back-stress terms are incorporated in the model to account for the Bauschinger effect and strain hardening within a given cycle.

To enable 3D simulations of realistic geometries to be conducted, such as the branched header model presented by Farragher and co-workers [*Farragher et al, 2013a*], the above multi-axial material model is implemented within a UMAT user material subroutine for use with the commercial finite element (FE) code Abaqus. An implicit integration method for determination of the iterative increment in accumulated effective plastic strain is developed to enable more efficient simulations with reduced timestep size compared with explicit integration methods. This implicit integration scheme, which uses the radial return method, is derived in Section 4.4. The UMAT user material subroutine is calibrated and validated against experimental data in Section 4.6 and applied to some multi-axial loading conditions in Chapter 5. One of the requirements for the user material subroutine is that the stiffness matrix be evaluated for every time increment and described in the form of the material Jacobian. Although, the elastic stiffness matrix will eventually converge to the correct result, the consistent tangent stiffness matrix for the continuum level model is developed, and presented in Section 4.4.1, to ensure that more efficient computational simulations are conducted.

4. A Unified Cyclic Viscoplastic Modelling Framework for Strain-Rate Dependent Materials

The hyperbolic sine unified cyclic viscoplastic material model requires 14 temperature-dependent material parameters, which can be separated into (i) the elastic material parameters, (ii) cyclic softening material parameters, (iii) non-linear back-stress parameters and (iv) cyclic viscoplastic material parameters. Although complex multi-objective functions, such as genetic algorithms [Mahmoudi *et al.*, 2011] and neural networks [Huber and Tsakmakis, 2001], can be implemented to identify a number of material parameters rapidly, such approaches are susceptible to a lack of physical correspondence of the identified set of parameters, due to the complexity of the physical phenomena being represented and the non-uniqueness of the solution. Consequently, the approach adopted here is to use a direct step-by-step methodology, via a least squares fitting procedure, to identify material parameters via specific mechanistic (physical) correspondence and representation of the experimentally-observed phenomena.

The multi-axial unified cyclic viscoplasticity material model and parameter identification methodology are calibrated and validated via comparison with experimental data for (i) 'as-received' P91 steel data from the literature, (ii) ex-service P91 test data as presented in Chapter 3 and (iii) for the first time, application of a cyclic viscoplasticity model to a MarBN material. Firstly, the material parameters are identified using the calibration regime conditions only, selected here as the (i) fully reversed strain-controlled ($R_\epsilon = -1$) fatigue tests conducted at an applied strain-rate of 0.1 %/s and applied strain-range of ± 0.5 % and (ii) a dwell test yielding stress relaxation data from a 120 s hold period at the maximum tensile stress location. Following application of the step-by-step material identification process, a standalone uniaxial FORTRAN 95 code is implemented to compare the predicted stress-strain data with experimental data, giving an excellent fit for all three cases under the calibration loading conditions. Validation of the material model and the accuracy of the identified material parameters are investigated in Section 4.6 via application of the UMAT user material subroutine to a range of loading conditions encompassing different strain-rates, strain-ranges and temperatures from the experiments of Chapter 3 and

4. A Unified Cyclic Viscoplastic Modelling Framework for Strain-Rate Dependent Materials

data presented in the literature [*Fournier et al., 2011; Koo and Kwon, 2011; Saad et al., 2011; Takahashi, 2008*].

4.2. Benefits of a hyperbolic sine modelling framework

9-12Cr martensitic steels exhibit a linear stress strain-rate relationship at low stress regimes and strain-rates, and an exponential relationship at higher stresses [*Haney et al., 2009; Klueh, 2004*], as illustrated by the measured data of Figure 4.1. This behaviour is consistent with most steels, where the linear relationship at low stresses represents diffusion-based creep, with dislocation-creep dominated behaviour occurring at higher stresses [*Hertzberg, 1996*]. Figure 4.1 also includes a representation of the typical broad range of stress regimes and strain-rates of modern and next generation flexible operating plant [*Farragher et al., 2013b; Nabarro, 2002*]. Thus, it is clear that a single power law exponent is not sufficient to model the complete stress regime of typical power plant components. However, the use of a hyperbolic sine formulation in place of the more conventional power law model enables more accurate modelling of the key mechanisms of deformation, i.e. the dominant creep process for a given load. Furthermore, most high temperature testing takes place at higher strain-rates (especially for fatigue and TMF), due to the need for reasonable test durations. This leads to the requirement for reliable interpolation and extrapolation beyond a limited range of experimental data [*Vakili-Tahami et al., 2005*].

4. A Unified Cyclic Viscoplastic Modelling Framework for Strain-Rate Dependent Materials

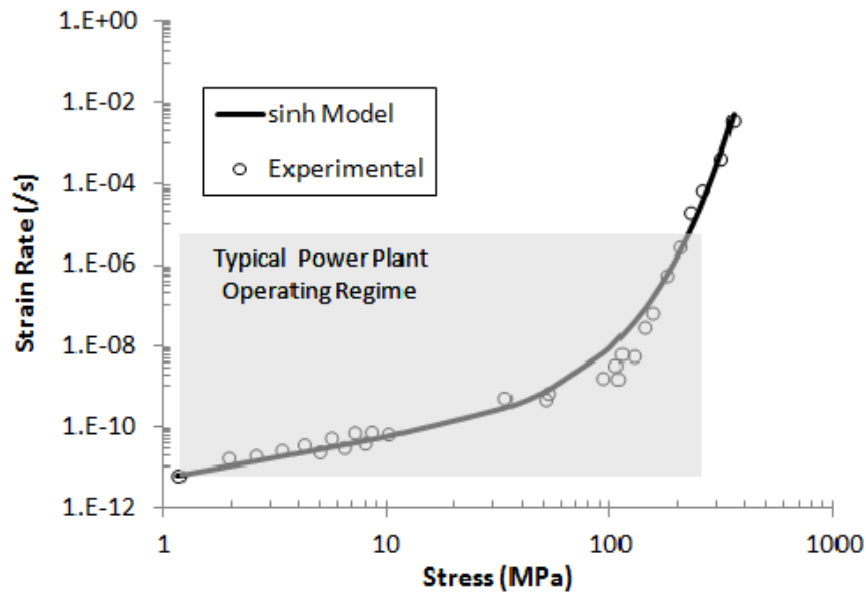


Figure 4.1: Comparison of the hyperbolic sine material model with experimental data for a 9Cr steel [Sklenička *et al.*, 2003], illustrating the extrapolation capability of the model.

Figure 2.6 depicts a generic deformation-mechanism map of a typical steel, which illustrates the range of different creep processes that a candidate material endures with varying stress and temperature. At low stress regimes, deformation is controlled by diffusion based creep and dislocation creep dominates as the stress increases [Dieter, 1986; Esposito and Bonora, 2011; Hertzberg, 1996; Poirier, 2005]. This conforms well with the work of Shrestha *et al.* [2012], who concluded that P91 steel exhibits diffusion based Nabarro-Herring creep, with an exponent of unity at low stress regimes and displays power law creep, with an exponent of up to twelve for the higher stress regimes. As illustrated in Figure 4.2, the hyperbolic sine model permits a smooth transition from one phenomenon to another, enabling the hyperbolic sine material model to simulate the steady-state strain-rate behaviour of the dominant creep mechanism and capture the full strain-rate regime observed in modern plant.

4. A Unified Cyclic Viscoplastic Modelling Framework for Strain-Rate Dependent Materials

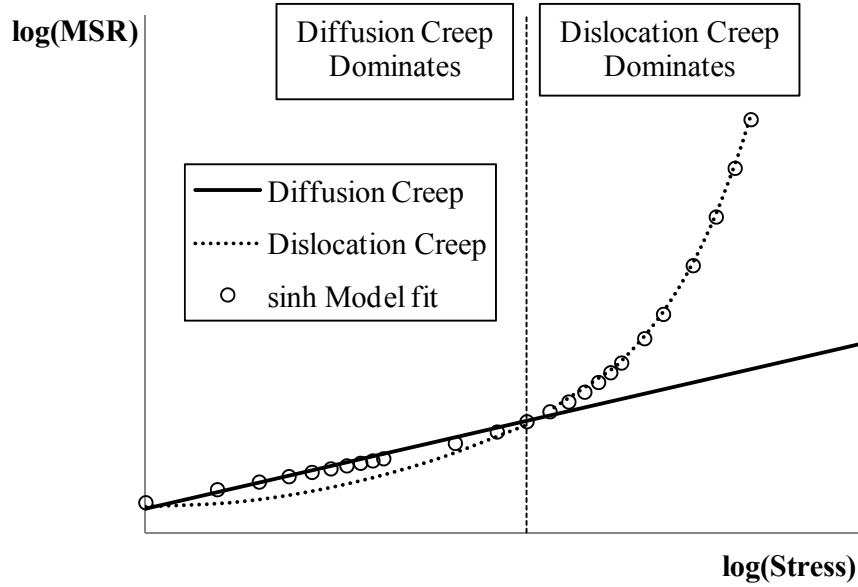


Figure 4.2: Typical stress strain-rate behaviour of the mechanisms of deformation for P91 steel and a hyperbolic sine fit to the dominant creep process.

4.3. A strain-rate sensitive unified cyclic viscoplastic model

In the present study, the well-established unified Chaboche model [Chaboche and Rousselier, 1983a; Chaboche and Rousselier, 1983b] is modified to allow variable strain-rate sensitivity for application to a wide range of strain-rates with a high degree of accuracy. This is achieved by replacing the power law function with a hyperbolic sine function in the constitutive equation defining the accumulated effective plastic strain-rate as follows:

$$\dot{p} = \alpha \sinh(\beta f) \quad (4.1)$$

where α and β are temperature-dependent cyclic viscoplastic material parameters and the function f defines the elastic domain if $f < 0$ and evaluates the viscous stress or overstress, σ_v , if $f \geq 0$. The viscous stress accounts for deviations beyond the elastic domain within 3D stress space, as highlighted in Figure 2.22a. This viscous stress represents the current equipotential surface and f is defined as [Lemaitre and Chaboche, 2000]:

4. A Unified Cyclic Viscoplastic Modelling Framework for Strain-Rate Dependent Materials

$$f = J_2(\mathbf{s} - \mathbf{x}) - R - k \quad \text{if } f < 0 \quad (4.2a)$$

$$f = \sigma_v = J_2(\mathbf{s} - \mathbf{x}) - R - k \quad \text{if } f \geq 0 \quad (4.2b)$$

where \mathbf{s} is the deviatoric stress tensor, \mathbf{x} is deviatoric back-stress tensor, R defines isotropic hardening (see Figure 2.22b), k is temperature-dependent initial cyclic yield stress and $J_2(\mathbf{s} - \mathbf{x})$ corresponds to the von Mises equivalent stress.

4.3.1. Model development

Within the constitutive model, it is assumed that the material is isotropic and only small strain deformations occur (i.e. infinitesimal deformation kinematics), such that classical additive decomposition of the increment in strain tensor, $\Delta\boldsymbol{\varepsilon}$, gives:

$$\Delta\boldsymbol{\varepsilon} = \Delta\boldsymbol{\varepsilon}^{\text{el}} + \Delta\boldsymbol{\varepsilon}^{\text{pl}} + \Delta\boldsymbol{\varepsilon}^{\text{th}} \quad (4.3)$$

where $\Delta\boldsymbol{\varepsilon}^{\text{pl}}$ is the incremental change in plastic strain tensor and $\Delta\boldsymbol{\varepsilon}^{\text{th}}$ corresponds to the incremental change of the thermal strain tensor. The increment in stress tensor, $\Delta\boldsymbol{\sigma}$, is evaluated using the multi-axial form of Hooke's law, which is defined with respect to the elastic strain as:

$$\Delta\boldsymbol{\sigma} = \boldsymbol{\Lambda} : (\Delta\boldsymbol{\varepsilon} - \Delta\boldsymbol{\varepsilon}^{\text{pl}} - \Delta\boldsymbol{\varepsilon}^{\text{th}}) \quad (4.4)$$

where $\boldsymbol{\Lambda}$ is the elasticity tensor. Equation (4.4) for Hooke's law can be written in terms of an elastic predictor and viscoplastic correction term as:

$$\Delta\boldsymbol{\sigma} = 2\mu(\Delta\boldsymbol{\varepsilon} - \Delta\boldsymbol{\varepsilon}^{\text{th}}) + \lambda\text{Tr}(\Delta\boldsymbol{\varepsilon} - \Delta\boldsymbol{\varepsilon}^{\text{th}})\mathbf{I} - 2\mu\Delta\boldsymbol{\varepsilon}^{\text{pl}} \quad (4.5)$$

where \mathbf{I} is the identity matrix and μ and λ are Lamé's constants. The first two terms on the right hand side correspond to the elastic predictor and the final term corresponds to the plastic correction term. The increment in plastic strain is determined using the flow rule:

$$\dot{\boldsymbol{\varepsilon}}^{\text{pl}} = \dot{p}\mathbf{n} \quad (4.6)$$

4. A Unified Cyclic Viscoplastic Modelling Framework for Strain-Rate Dependent Materials

where \mathbf{n} is the tensor normal to the yield surface (e.g. see Figure 4.3) and defined as [Dunne and Petrinic, 2007; Chaboche, 2008]:

$$\mathbf{n} = \frac{3}{2} \frac{\mathbf{s} - \mathbf{x}}{\sigma_e} = \frac{3}{2} \frac{\mathbf{s}^{\text{tr}} - \mathbf{x}_t}{\sigma_e^{\text{tr}}} \quad (4.7)$$

where \mathbf{s}^{tr} , and \mathbf{x}_t are the deviatoric trial stress and deviatoric kinematic hardening back-stress from the previous timestep, respectively. In Equation (4.7), σ_e and σ_e^{tr} are the equivalent and trial equivalent stresses respectively, defined as:

$$\sigma_e = \left[\frac{3}{2} (\mathbf{s} - \mathbf{x}) : (\mathbf{s} - \mathbf{x}) \right]^{1/2} \quad (4.8a)$$

$$\sigma_e^{\text{tr}} = \left[\frac{3}{2} (\mathbf{s}^{\text{tr}} - \mathbf{x}_t) : (\mathbf{s}^{\text{tr}} - \mathbf{x}_t) \right]^{1/2} \quad (4.8b)$$

For the material model considered here, the dissipation potential is obtained retrospectively such that it satisfies the hyperbolic sine constitutive model defined in Equation (4.1), as follows:

$$\Omega(f) = \frac{\alpha}{\beta} \cosh(\beta f) \text{sgn}(f) \quad (4.9)$$

As α and β are positive values, the $\text{sgn}(f)$ function ensures that the dissipation potential can account for load reversal, such that:

$$\text{sgn}(f) = \begin{cases} -1 & \text{if } f < 0 \\ 0 & \text{if } f = 0 \\ 1 & \text{if } f > 0 \end{cases}$$

The following sections outline the hardening models for (i) isotropic hardening leading to the prediction of the cyclic softening behaviour and (ii) the nonlinear kinematic back-stress.

4. A Unified Cyclic Viscoplastic Modelling Framework for Strain-Rate Dependent Materials

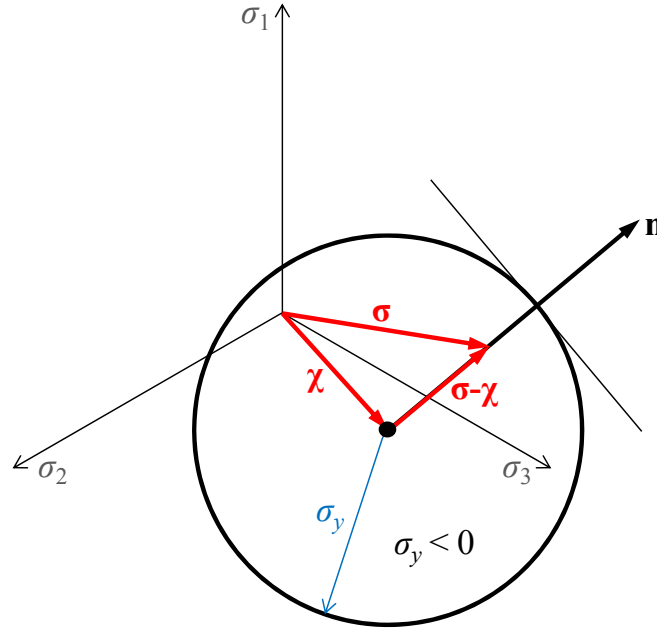


Figure 4.3: Schematic representation of the tensor normal to the yield surface in 3D stress space.

4.3.2. Cyclic softening

Isotropic hardening is simulated using the non-linear evolutionary equation of Chaboche [Chaboche and Rousselier, 1983a; Chaboche and Rousselier, 1983b]. However, to account for thermo-mechanical deformations, a temperature-dependent term is included in the evolutionary equation for R , such that temperature-dependent isotropic hardening is given by [Zhang et al., 2002]:

$$\dot{R}_i = b_i(Q_i - R_i)\dot{p} + \left(\frac{1}{b_i} \frac{\partial b_i}{\partial T} + \frac{1}{Q_i} \frac{\partial Q_i}{\partial T} \right) R_i \dot{T} \quad (4.10)$$

where Q_i is the saturated value of the isotropic hardening term (see Figure 2.23), b_i is the isotropic hardening rate exponent and $i = 1, 2$. Unlike most conventional steels, 9-12Cr steels cyclically soften with increasing number of cycles due to (i) a high initial dislocation density which decreases with cyclic deformation and (ii) the martensitic lath structure. Thus, from this point on, the isotropic hardening behaviour will be defined as cyclic softening. This cyclic softening behaviour is captured using a negative value of the saturated isotropic hardening term, Q_i , [Saad et al., 2011] in Equation

4. A Unified Cyclic Viscoplastic Modelling Framework for Strain-Rate Dependent Materials

(4.10). Figure 4.4 shows the cyclic evolution of the isotropic term, R , as a function of the accumulated effective plastic strain, p , from which it can be seen that the softening evolution can be separated into primary, secondary and failure regions and that no clear saturation point is achieved. The inclusion of a second cyclic softening term (where the first term describes the primary region and the additional term denotes the secondary softening region) improves the correlation with the experimentally observed cyclic softening, where the saturated value, $Q = Q_1 + Q_2$, is taken to be the cyclic softening value prior to the onset of the failure region. The isotropic term, R , then becomes:

$$R = R_1 + R_2 \quad (4.11)$$

with the R_1 term representing primary cyclic softening and R_2 representing the cyclic softening produced during the secondary stage of softening. The tertiary stage can be related to fatigue damage and is neglected in the current framework.

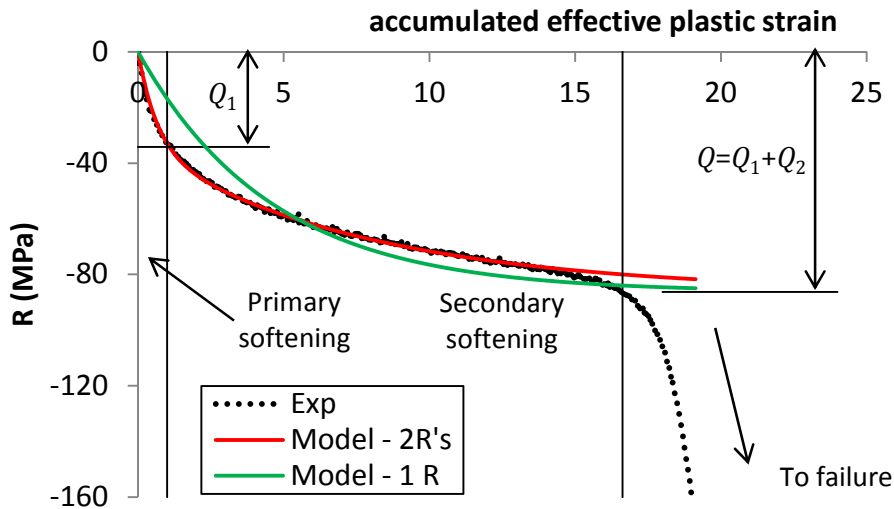


Figure 4.4: Comparison of the isotropic stress model with the experimentally measured P91 steel softening data for a strain-rate of 0.1 %/s and strain-range of ± 0.5 %, at a temperature of 500 °C.

4. A Unified Cyclic Viscoplastic Modelling Framework for Strain-Rate Dependent Materials

4.3.3. Kinematic hardening

The centre of the elastic domain in 3D stress space is defined by the back-stress tensor, χ (e.g. see Figure 4.3). This back-stress tensor accounts for the strain hardening mechanisms in 9-12Cr steels due to dislocation pile-ups at high angle boundaries and the Orowan pinning mechanism at obstacles such as precipitates. For the present formulation, the back-stress tensor is defined as a sum of the individual back-stress terms, such that:

$$\chi = \sum_{i=1}^2 \chi_i \quad (4.12)$$

In Equation (4.12), χ_1 represents the kinematic hardening produced during the initial stages of strain hardening and χ_2 accounts for the kinematic hardening due to the later stages of strain hardening. The evolution of the back-stress components is described by the Armstrong-Frederick kinematic hardening model [*Frederick and Armstrong, 2007*], with the inclusion of a temperature-rate term [*Chaboche, 2008*]:

$$\dot{\chi}_i = \frac{2}{3} C_i \dot{\epsilon}^{\text{pl}} - \gamma_i \chi_i \dot{p} + \frac{1}{C_i} \frac{\partial C_i}{\partial T} \chi_i \dot{T} \quad (4.13)$$

where C_i is the hardening modulus and γ_i is the non-linear kinematic hardening parameter. The three terms in Equation (4.13) correspond to (i) a linear kinematic hardening term, (ii) a recall term to account for the fading memory effect of the deformation path and (iii) a temperature-rate term respectively. There is no temperature-rate term associated with the recall term as it is time and rate-independent [*Lemaitre and Chaboche, 2000*]. The Armstrong-Frederick kinematic back-stress is deviatoric by nature, due to the incompressibility condition, such that the deviatoric back-stress tensor, χ , is equal to the back-stress tensor, χ .

4.4. Implementation of the model within the FE method

The hyperbolic sine unified cyclic viscoplastic material model of Section 4.3 is implemented as is in a UMAT user material subroutine for use with the commercial FE code Abaqus. Within this material model, the increment

4. A Unified Cyclic Viscoplastic Modelling Framework for Strain-Rate Dependent Materials

in effective plastic strain is obtained using an implicit integration scheme. A flowchart depicting the main processes within the UMAT is shown in Figure 4.5.

In order to update all the required quantities in terms of the increment in effective plastic strain-rate, the equivalent stress, σ_e , is defined as a function of the trial stress and the increment in effective plastic strain-rate as:

$$\sigma_e = \sigma_e^{\text{tr}} - 3\mu\Delta p \quad (4.14)$$

where μ is the shear modulus, Δp is the increment in effective plastic strain and σ_e^{tr} is the equivalent trial stress. Thus, the constitutive equation for the increment in effective accumulated plastic strain-rate, given in Equation (4.1), may be rewritten as:

$$\dot{p} = \phi(\Delta p, \chi, R) = \alpha \sinh \beta (\sigma_e^{\text{tr}} - 3\mu\Delta p - R - k) \quad (4.15)$$

where ϕ is the accumulated effective plastic strain-rate for the previous iteration of the current timestep increment (i.e. $\phi = \Delta p^k / \Delta t$ where K is the previous iteration in the implicit integration scheme as illustrated in Figure 4.5). Rearranging and writing the incremental difference of Equation (4.15) in a form suitable for a Newton-Raphson iterative method yields [Dunne and Petrinic, 2007]:

$$\phi(\Delta p, \chi, R) = \Delta p - \phi(\Delta p, \chi, R)\Delta t = 0 \quad (4.16)$$

Applying the Newton-Raphson iterative method then results in:

$$\phi + \frac{\partial \phi}{\partial \Delta p} d\Delta p + \frac{\partial \phi}{\partial \chi} : d\chi + \frac{\partial \phi}{\partial R} dR = 0 \quad (4.17)$$

Writing the partial derivatives of Equation (4.17) in terms of ϕ gives:

$$\phi + \left(1 - \frac{\partial \phi}{\partial \Delta p} \Delta t\right) d\Delta p - \frac{\partial \phi}{\partial \chi} \Delta t : d\chi - \frac{\partial \phi}{\partial R} \Delta t dR = 0 \quad (4.18)$$

Thus, evaluating the partial derivatives and rearranging Equation (4.18) yields the iterative increment in effective plastic strain, $d\Delta p$:

4. A Unified Cyclic Viscoplastic Modelling Framework for Strain-Rate Dependent Materials

$$d\Delta p = \frac{\left[\phi - \frac{\Delta p}{\Delta t} - \sum_{i=1}^2 \left(\mathbf{n} : \boldsymbol{\chi}_i \frac{1}{C_i} \frac{\partial C_i}{\partial T} - \left(\frac{1}{b_i} \frac{\partial b_i}{\partial T} + \frac{1}{Q_i} \frac{\partial Q_i}{\partial T} \right) R_i \right) Z dT \right]}{\left[\frac{1}{\Delta t} + 3\mu Z + Z \left(\sum_{i=1}^2 (C_i - \mathbf{n} : \boldsymbol{\chi}_i \gamma_i + b_i (Q_i - R_i)) \right) \right]} \quad (4.19)$$

where

$$Z = \alpha \beta \cosh \beta (\sigma_e^{\text{tr}} - 3\mu \Delta p - R - k) \quad (4.20)$$

and the increment in effective plastic strain is:

$$\Delta p = \Delta p + d\Delta p \quad (4.21)$$

Equation (4.21) is updated until convergence is obtained. The tolerance within the present study is set at 1×10^{-10} and convergence is checked against the numerator of Equation (4.19).

To ensure that unloading occurs elastically within the material model, the following conditions represent viscoplastic behaviour in 3D stress space:

$$\Omega \geq 0 \text{ and } (\partial \Omega / \partial \boldsymbol{\sigma}) : \dot{\boldsymbol{\sigma}} \quad (4.22)$$

The increment in plastic strain is determined using the flow rule of Equation (4.6), with the increment in stress calculated using Hooke's law, Equation (4.4). The material model is also implemented for uniaxial loading conditions in a strain-driven FORTRAN 95 standalone computer program as a material parameter calibration tool and to validate the UMAT implementation.

4. A Unified Cyclic Viscoplastic Modelling Framework for Strain-Rate Dependent Materials

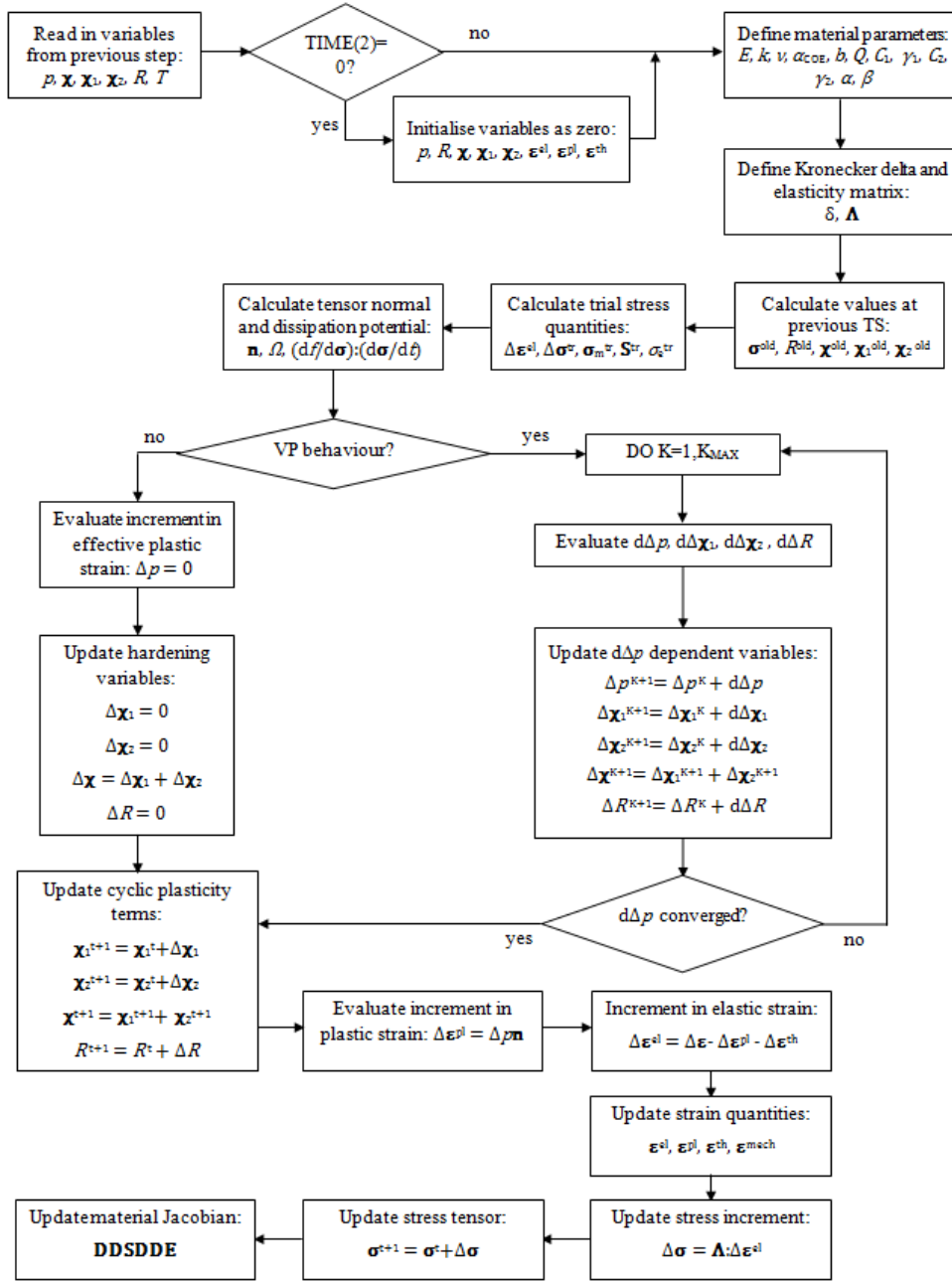


Figure 4.5: Flowchart describing the major processes in the UMAT user material subroutine.

4. A Unified Cyclic Viscoplastic Modelling Framework for Strain-Rate Dependent Materials

4.4.1. Material Jacobian and the consistent tangent stiffness matrix

The UMAT user material subroutine requires the material Jacobian to be provided at every increment for which the UMAT is called. The material Jacobian relates the differential increment in stress, $\delta\boldsymbol{\sigma}$, to the differential increment in total strain, $\delta\boldsymbol{\varepsilon}$, such that the form required in Abaqus is:

$$\mathbf{D} = \frac{\partial \delta \boldsymbol{\sigma}}{\partial \delta \boldsymbol{\varepsilon}} \quad (4.23)$$

For axisymmetric loading conditions, the material Jacobian is:

$$\mathbf{D} = \begin{pmatrix} \frac{\partial \delta \sigma_{11}}{\partial \delta \varepsilon_{11}} & \frac{\partial \delta \sigma_{11}}{\partial \delta \varepsilon_{22}} & \frac{\partial \delta \sigma_{11}}{\partial \delta \varepsilon_{33}} & \frac{\partial \delta \sigma_{11}}{\partial \delta \gamma_{12}} \\ \frac{\partial \delta \sigma_{22}}{\partial \delta \varepsilon_{11}} & \frac{\partial \delta \sigma_{22}}{\partial \delta \varepsilon_{22}} & \frac{\partial \delta \sigma_{22}}{\partial \delta \varepsilon_{33}} & \frac{\partial \delta \sigma_{22}}{\partial \delta \gamma_{12}} \\ \frac{\partial \delta \sigma_{33}}{\partial \delta \varepsilon_{11}} & \frac{\partial \delta \sigma_{33}}{\partial \delta \varepsilon_{22}} & \frac{\partial \delta \sigma_{33}}{\partial \delta \varepsilon_{33}} & \frac{\partial \delta \sigma_{33}}{\partial \delta \gamma_{12}} \\ \frac{\partial \delta \sigma_{12}}{\partial \delta \varepsilon_{11}} & \frac{\partial \delta \sigma_{12}}{\partial \delta \varepsilon_{22}} & \frac{\partial \delta \sigma_{12}}{\partial \delta \varepsilon_{33}} & \frac{\partial \delta \sigma_{12}}{\partial \delta \gamma_{12}} \end{pmatrix} \quad (4.24)$$

Although the standard elasticity matrix, $\boldsymbol{\Lambda}$, will always result in a converged solution, it is not the optimum value for the material Jacobian. To ensure more efficient computational simulations by achieving a converged solution in fewer increments, the material Jacobian is provided in the form of the consistent tangent stiffness matrix. The consistent tangent stiffness matrix describes the differential change in stress tensor in terms of a differential change in strain tensor (i.e. it is the stiffness of a given system as a result of an infinitesimal change in system loading conditions) and is determined for every iteration the UMAT user material subroutine is called. The following section describes the derivation of the consistent tangent stiffness matrix for the material model described in Section 4.3.

The normal tensor of Equation (4.7) can be rearranged as:

$$\mathbf{s} = \frac{\sigma_e}{\sigma_e^{\text{tr}}} (\mathbf{s}^{\text{tr}} - \mathbf{x}_t) + \mathbf{x} \quad (4.25)$$

4. A Unified Cyclic Viscoplastic Modelling Framework for Strain-Rate Dependent Materials

Using the product rule ($\delta uv = u\delta v + v\delta u$) and applying the differential operator yields:

$$\delta \mathbf{s} = \frac{\sigma_e}{\sigma_e^{\text{tr}}} \delta \mathbf{s}^{\text{tr}} + \mathbf{s}^{\text{tr}} \delta \left(\frac{\sigma_e}{\sigma_e^{\text{tr}}} \right) - \frac{\sigma_e}{\sigma_e^{\text{tr}}} \delta \mathbf{x}_t - \mathbf{x}_t \delta \left(\frac{\sigma_e}{\sigma_e^{\text{tr}}} \right) + \delta \mathbf{x} \quad (4.26)$$

Noting that \mathbf{x}_t is a constant for the current iteration and hence, $\delta \mathbf{x}_t = 0$. Using the quotient rule, the differential increment in deviatoric stress is:

$$\delta \mathbf{s} = \frac{\sigma_e}{\sigma_e^{\text{tr}}} \delta \mathbf{s}^{\text{tr}} + (\mathbf{s}^{\text{tr}} - \mathbf{x}_t) \left(\frac{\sigma_e^{\text{tr}} \delta \sigma_e - \sigma_e \delta \sigma_e^{\text{tr}}}{[\sigma_e^{\text{tr}}]^2} \right) + \delta \mathbf{x} \quad (4.27)$$

Taking the differential of the equivalent and trial equivalent stresses (Equation (4.8)) yields:

$$\delta \sigma_e = \frac{1}{2} \left[\frac{2}{3} (\mathbf{s} - \mathbf{x}) : (\mathbf{s} - \mathbf{x}) \right]^{-1/2} 2 \frac{3}{2} (\mathbf{s} - \mathbf{x}) : \delta (\mathbf{s} - \mathbf{x}) = \mathbf{n} : \delta (\mathbf{s} - \mathbf{x}) \quad (4.28a)$$

$$\delta \sigma_e^{\text{tr}} = \frac{1}{2} \left[\frac{2}{3} (\mathbf{s}^{\text{tr}} - \mathbf{x}_t) : (\mathbf{s}^{\text{tr}} - \mathbf{x}_t) \right]^{-1/2} 2 \frac{3}{2} (\mathbf{s}^{\text{tr}} - \mathbf{x}_t) : \delta (\mathbf{s}^{\text{tr}} - \mathbf{x}_t) = \mathbf{n} : \delta \mathbf{s}^{\text{tr}} \quad (4.28b)$$

The elastic-plastic correction form of the differential increment in deviatoric stress is:

$$\delta \mathbf{s} = \delta \mathbf{s}^{\text{tr}} - 2\mu \delta p \mathbf{n} \quad (4.29)$$

where μ is shear modulus and δp is the differential increment in effective plastic strain-rate, such that the differential increment in deviatoric stress becomes:

$$\delta \mathbf{s} = \frac{\sigma_e}{\sigma_e^{\text{tr}}} \delta \mathbf{s}^{\text{tr}} + \delta \mathbf{x} + (\mathbf{s}^{\text{tr}} - \mathbf{x}_t) \left(\frac{1}{\sigma_e^{\text{tr}}} \mathbf{n} : \delta \mathbf{s}^{\text{tr}} - \frac{1}{\sigma_e^{\text{tr}}} \mathbf{n} : 2\mu \delta p \mathbf{n} - \frac{1}{\sigma_e^{\text{tr}}} \mathbf{n} : \delta \mathbf{x} - \frac{\sigma_e}{[\sigma_e^{\text{tr}}]^2} \mathbf{n} : \delta \mathbf{s}^{\text{tr}} \right) \quad (4.30)$$

The evolution of the kinematic back-stress is described here by the Armstrong-Frederick model of Equation (4.13). The differential form of the evolution of kinematic back-stress is:

4. A Unified Cyclic Viscoplastic Modelling Framework for Strain-Rate Dependent Materials

$$\delta\chi_i = \frac{2}{3} C_i \delta p \mathbf{n} - \gamma_i \chi_i \delta \Delta p + \frac{1}{C_i} \frac{\partial C_i}{\partial T} \chi_i \delta T \quad (4.31)$$

As the temperature-rate term is independent of strain, these terms go to zero when evaluating the consistent tangent stiffness matrix. With $\mathbf{n} : \mathbf{n} = 3/2$, the differential increment in deviatoric stress is:

$$\begin{aligned} \delta \mathbf{s} = & \frac{\sigma_e}{\sigma_e^{\text{tr}}} \delta \mathbf{s}^{\text{tr}} + \sum_{i=1}^2 \left(\frac{2}{3} C_i \delta p \mathbf{n} - \gamma_i \chi_i \delta p \right) \\ & + \left(\mathbf{s}^{\text{tr}} - \mathbf{x}_i \right) \left(\frac{1}{\sigma_e^{\text{tr}}} \mathbf{n} : \delta \mathbf{s}^{\text{tr}} - \frac{1}{\sigma_e^{\text{tr}}} \mathbf{n} : 2\mu \delta p \mathbf{n} - \frac{1}{\sigma_e^{\text{tr}}} \mathbf{n} : \delta \mathbf{x} - \frac{\sigma_e}{[\sigma_e^{\text{tr}}]^2} \mathbf{n} : \delta \mathbf{s}^{\text{tr}} \right) \end{aligned} \quad (4.32)$$

The differential increment in effective plastic strain-rate is determined using an implicit integration scheme via the Newton-Raphson method. Equation (4.15) can be written in differential form as:

$$\delta \Delta p = (\delta \phi(\boldsymbol{\sigma}) : \delta \boldsymbol{\sigma} + \delta \phi(\boldsymbol{\chi}) : \delta \boldsymbol{\chi} + \delta \phi(R) : \delta R) \quad (4.33)$$

And the differential form of the isotropic stress model of Equation (4.10) is:

$$\delta R_i = b_i (Q_i - R_i) \delta p + \left(\frac{1}{b_i} \frac{\partial b_i}{\partial T} + \frac{1}{Q_i} \frac{\partial Q_i}{\partial T} \right) R_i \delta T \quad (4.34)$$

where the temperature-rate term is independent of strain and hence, goes to zero when evaluating the consistent tangent stiffness matrix. Using the relationship of Equation (4.29), the differential stress term is $\delta \boldsymbol{\sigma} = \delta \boldsymbol{\sigma}^{\text{tr}} - 2\mu \delta p \mathbf{n}$. Substitution of this relationship into Equation (4.33) and rearranging yields the differential increment in effective plastic strain-rate:

$$\delta p = \frac{\delta \phi(\boldsymbol{\sigma}) : \delta \boldsymbol{\sigma}^{\text{tr}}}{\left[\frac{1}{\Delta t} + \delta \phi(\boldsymbol{\sigma}) : 2\mu \mathbf{n} - \sum_{i=1}^2 \left(\delta \phi(\boldsymbol{\chi}) : \frac{2}{3} C_i \mathbf{n} - \delta \phi(\boldsymbol{\chi}) : \gamma_i \chi_i - \delta \phi(R) b_i (Q_i - R_i) \right) \right]} \quad (4.35)$$

where the partial derivatives are determined from the constitutive equation for the accumulated effective plastic strain-rate (Equation 4.15):

4. A Unified Cyclic Viscoplastic Modelling Framework for Strain-Rate Dependent Materials

$$\delta\phi(\boldsymbol{\sigma}) = \frac{\delta\phi}{\delta\boldsymbol{\sigma}} = \frac{\delta\phi}{\delta\sigma_e^{\text{tr}}} \frac{\delta\sigma_e^{\text{tr}}}{\delta\boldsymbol{\sigma}} = Y\mathbf{n} \quad (4.36a)$$

$$\delta\phi(\boldsymbol{\chi}) = \frac{\delta\phi}{\delta\boldsymbol{\chi}} = \frac{\delta\phi}{\delta\sigma_e^{\text{tr}}} \frac{\delta\sigma_e^{\text{tr}}}{\delta\boldsymbol{\chi}} = -Y\mathbf{n} \quad (4.36b)$$

$$\delta\phi(R) = \frac{\delta\phi}{\delta R} = \frac{\delta\phi}{\delta\sigma_e^{\text{tr}}} \frac{\delta\sigma_e^{\text{tr}}}{\delta R} = -Y \quad (4.36c)$$

where $Y = -\alpha\beta\cosh\beta(\sigma_e^{\text{tr}} - 3\mu\Delta p - R - k)$. The differential increment in accumulated effective plastic strain-rate is thus:

$$\delta p = \frac{Y\mathbf{n} : \delta\boldsymbol{\sigma}^{\text{tr}}}{\left[\frac{1}{\Delta t} + 3\mu Y - \sum_{i=1}^2 (YC_i - Y\mathbf{n} : \gamma_i \boldsymbol{\chi}_i - Yb_i(Q_i - R_i)) \right]} = \frac{Y\mathbf{n} : \delta\boldsymbol{\sigma}^{\text{tr}}}{\Gamma} \quad (4.37)$$

As the differential deviatoric trial stress, $\delta\mathbf{s}^{\text{tr}}$, can be related to the differential strain tensor, $\delta\boldsymbol{\epsilon}$, as:

$$\delta\mathbf{s}^{\text{tr}} = 2\mu\delta\boldsymbol{\epsilon} = 2\mu\delta\boldsymbol{\epsilon} - \frac{2}{3}\mu(\delta\boldsymbol{\epsilon} : \mathbf{I})\mathbf{I} \quad (4.38)$$

where $\boldsymbol{\epsilon}$ is the deviatoric strain tensor. The differential trial stress is:

$$\delta\boldsymbol{\sigma}^{\text{tr}} = \delta\mathbf{s}^{\text{tr}} + \frac{1}{3}(\delta\boldsymbol{\sigma}^{\text{tr}} : \mathbf{I})\mathbf{I} = \delta\mathbf{s}^{\text{tr}} - \frac{\chi_t}{2\sigma_e^{\text{tr}}}(\delta\boldsymbol{\sigma}^{\text{tr}} : \mathbf{I})\mathbf{I} \quad (4.39)$$

The second term of Equation (4.39) goes to zero when differentiated with respect to the differential strain. The deviatoric stress is defined as:

$$\delta\mathbf{s} = \delta\boldsymbol{\sigma} - K\mathbf{II} : \delta\boldsymbol{\epsilon} \quad (4.40)$$

where $K = E/(3(1-2\nu))$ is the bulk modulus. Thus, Equation (4.32) can be rewritten in terms of the differential deviatoric stress tensor as:

4. A Unified Cyclic Viscoplastic Modelling Framework for Strain-Rate Dependent Materials

$$\begin{aligned}
\delta\boldsymbol{\sigma} = & \frac{\sigma_e}{\sigma_e^{\text{tr}}} \left(2\mu\delta\boldsymbol{\varepsilon} + \left(K - \frac{2}{3}\mu \right) (\delta\boldsymbol{\varepsilon} : \mathbf{I})\mathbf{I} \right) \\
& + \sum_{i=1}^2 \left[\left(\frac{2}{3} C_i \mathbf{n} - \gamma_i \boldsymbol{\chi}_i \right) \frac{Y}{G} \mathbf{n} : \mu \left(2\delta\boldsymbol{\varepsilon} - \frac{2}{3} (\delta\boldsymbol{\varepsilon} : \mathbf{I})\mathbf{I} \right) \right] \\
& + \frac{(\mathbf{s}^{\text{tr}} - \mathbf{x}_t)}{\sigma_e^{\text{tr}}} \left[1 - \frac{\sigma_e}{\sigma_e^{\text{tr}}} - \left(3\mu + \sum_{i=1}^2 (C_i - \mathbf{n} : \gamma_i \boldsymbol{\chi}_i) \right) \frac{Y}{G} \right] \mathbf{n} : \mu \left(2\delta\boldsymbol{\varepsilon} - \frac{2}{3} (\delta\boldsymbol{\varepsilon} : \mathbf{I})\mathbf{I} \right)
\end{aligned} \tag{4.41}$$

The material Jacobian, \mathbf{D} , is determined by differentiating $\delta\boldsymbol{\sigma}$ in Equation (4.41) with respect to $\delta\boldsymbol{\varepsilon}$. For elastic loading conditions, it can be shown that the material Jacobian reduces to the elastic stiffness matrix, $\boldsymbol{\Lambda}$:

$$\mathbf{D} = \frac{\partial\delta\boldsymbol{\sigma}}{\partial\delta\boldsymbol{\varepsilon}} = \boldsymbol{\Lambda} = \begin{pmatrix} 2\mu + \lambda & \lambda & \lambda & 0 \\ \lambda & 2\mu + \lambda & \lambda & 0 \\ \lambda & \lambda & 2\mu + \lambda & 0 \\ 0 & 0 & 0 & \mu \end{pmatrix} \tag{4.42}$$

where μ and λ are Lamé's constants $\mu = E/(2(1+\nu))$ and $\lambda = E\nu/((1+\nu)(1-2\nu))$.

The components of the material Jacobian for elastic-viscoplastic deformation are presented in Appendix B.

4.5. Material parameter identification process

The required material parameters are identified using a step-by-step procedure, in which the elastic material parameters of Young's modulus, E , Poisson's ratio, ν , and initial cyclic yield stress, k , must be identified first. Next, the isotropic hardening constants, Q_i and b_i , are identified from cyclic softening data derived from experiments, followed by the kinematic constants, C_i and γ_i , identified using the approach of Zhan [2004]. Finally, the cyclic viscoplastic material parameters are identified using a newly developed analytical model for stress relaxation. Figure 4.6 summarises the main processes of this step-by-step methodology for identifying the material parameters for the hyperbolic sine unified cyclic viscoplastic model. The material parameters are calibrated from experimental data using the standalone uniaxial code, with the complete set of constitutive equations for the material model presented in uniaxial form in Table 4.1. The following

4. A Unified Cyclic Viscoplastic Modelling Framework for Strain-Rate Dependent Materials

section describes the step-by-step parameter identification methodology in detail.

Table 4.1: Complete set of evolution equations, in uniaxial form, for the hyperbolic sine unified cyclic viscoplasticity material model.

Hooke's law:	$\Delta\sigma = E\Delta\varepsilon^{\text{el}} = E(\Delta\varepsilon - \Delta\varepsilon^{\text{pl}})$
Flow rule:	$\dot{\varepsilon}^{\text{pl}} = \alpha \sinh \beta (\sigma - \chi - R - k) \text{sgn}(\sigma - \chi)$
Constitutive Equation:	$\dot{p} = \dot{\varepsilon}^{\text{pl}} $
Kinematic back-stress:	$\dot{\chi}_i = C_i \dot{\varepsilon}^{\text{in}} - \gamma_i \chi_i \dot{p} + \frac{1}{C_i} \frac{\partial C_i}{\partial T} \chi_i \dot{T}$
Cyclic softening:	$\dot{R}_i = b_i (Q_i - R_i) \dot{p} + \left(\frac{1}{b_i} \frac{\partial b_i}{\partial T} + \frac{1}{Q_i} \frac{\partial Q_i}{\partial T} \right) R_i \dot{T}$

4. A Unified Cyclic Viscoplastic Modelling Framework for Strain-Rate Dependent Materials

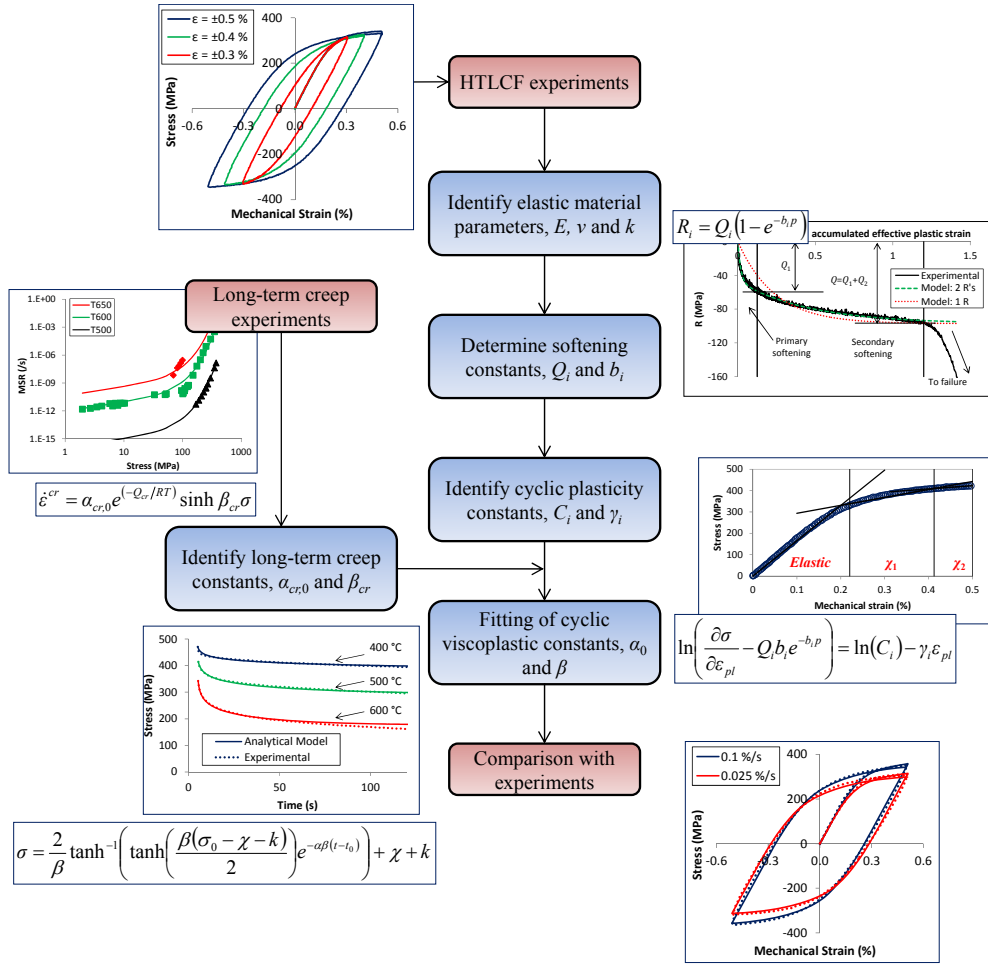


Figure 4.6: Flowchart illustrating the main processes of the material parameter identification process for the hyperbolic sine unified cyclic viscoplastic material model.

4.5.1. Elastic material parameters

The temperature-dependent Young's modulus is identified from the slope of the linear portion of the monotonic test data (the first quarter loop of the initial cycle). Furthermore, from the experiments presented in Chapter 3, no cyclic degradation of Young's modulus is observed, as shown in Figure 4.7, prior to the onset of failure. Thus, it can be concluded that the value of Young's modulus is independent of any fatigue damage which occurs during the primary and secondary stages of cyclic deformation.

4. A Unified Cyclic Viscoplastic Modelling Framework for Strain-Rate Dependent Materials

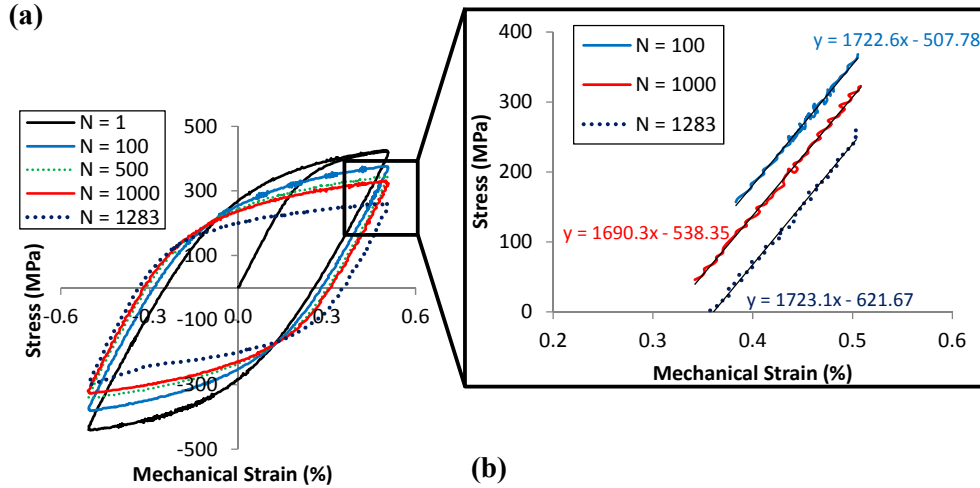


Figure 4.7: Cyclic evolution of the stress-strain response of ex-service P91 steel at a temperature of 500 °C and strain-rate of 0.1 %/s, illustrating (a) the stress-strain response for various cycles and (b) the effect of increasing cycles on Young's modulus.

Poisson's ratio is assumed to have a constant value of 0.3 throughout this study and the coefficient of thermal expansion is taken from the literature for P91 steel. However, the values for the coefficient of thermal expansion presented in the ASME Boiler and Pressure Vessel Codes [ASME, 1998] are compared and validated against the experiments conducted in Chapter 3, via analysis of the thermal strains resulting from specimen heat up. As the extensometer is balanced initially (and the specimen is mounted with approximately zero applied load), the initial strain, ε_0 , is approximately zero. However, due to thermal expansion, a thermal strain, ε^{th} , is imparted on the specimen during heat up of the specimen. This thermal strain is defined as:

$$\varepsilon - \varepsilon_0 = \Delta\varepsilon^{\text{th}} = \alpha_{\text{coe}} \Delta T \quad (4.43)$$

Hence, the coefficient of thermal expansion can be estimated by rearranging Equation (4.43) and using measured data for thermal strain. The values obtained during experiments illustrated good agreement with the literature values of the ASME Boiler and Pressure Vessel Codes [ASME, 1998].

The value of the initial cyclic yield stress, k , is obtained by plotting stress versus plastic strain and identifying $2k$ as the magnitude of the linear

4. A Unified Cyclic Viscoplastic Modelling Framework for Strain-Rate Dependent Materials

(vertical) portion of stress following load reversal during the initial cycle, as highlighted in Figure 4.8.

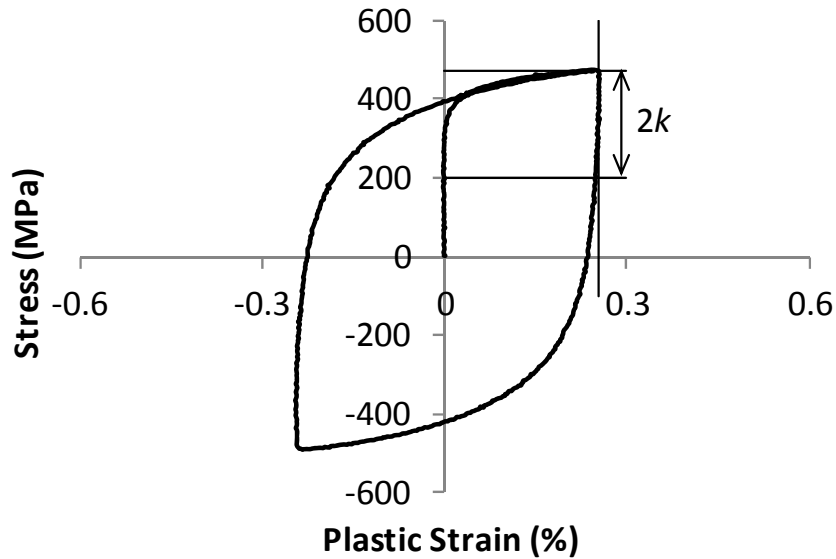


Figure 4.8: Identification of the initial cyclic yield stress value at a temperature of 400 °C.

4.5.2. Cyclic softening material constants

Once the elastic constants have been determined, the isotropic hardening parameters, Q_i and b_i can be estimated. This is achieved by determining the cyclic softening stress, $R = \sigma_{0,\max} - \sigma_{\max}$, from experimental data as illustrated in Figure 4.4 for the case of cyclic softening. Firstly a value of Q (normally an asymptotic, saturated value of R for cyclically hardening materials) is obtained from the experimental data by plotting R against the accumulated effective plastic strain, $p = 2N|\epsilon^{pl}|$. As 9Cr steels cyclically soften and the experimental data does not exhibit a clear softening saturation plateau, the value of Q is taken to be the cyclic softening stress value just prior to the onset of failure, as shown in Figure 4.4. Splitting the experimental data into its primary, secondary and failure softening regions enables the values of Q_i to be determined, such that:

$$Q = Q_1 + Q_2 \quad (4.44)$$

4. A Unified Cyclic Viscoplastic Modelling Framework for Strain-Rate Dependent Materials

where Q_1 is the value of isotropic softening at the transition to the secondary softening regime. The values of b_i , which describe the rate of decay of R_i , are then fitted to the experimental data using a least squares approach. The least squares optimisation function to be minimised is:

$$F(x_k) = \sum_{j=1}^m (R^{\text{thr}}(x_k) - R^{\text{exp}})^2 \quad (4.45)$$

where x_k represents the material parameters to be optimised and the superscripts ‘*thr*’ and ‘*exp*’ denote theoretical and experimental values of the cyclic softening stress, respectively. To identify the rate of decay constants b_i , the theoretical cyclic softening stress, R^{thr} , is determined by integrating the evolution law for cyclic softening (Equation (4.10)) with respect to time. As the material parameters are identified from strain-controlled isothermal fatigue tests, the temperature-rate term of Equation (4.10) is set to zero. Thus, the isotropic stress is:

$$R_i = Q_i (1 - e^{-b_i p}) \quad \text{where } i = 1, 2 \quad (4.46)$$

Hence, the total theoretical cyclic softening stress is:

$$R^{\text{thr}} = \sum_{i=1}^2 R_i = \sum_{i=1}^2 Q_i (1 - e^{-b_i p}) \quad (4.47)$$

Using the least squares optimisation procedure, the constants describing the rate of decay during cyclic softening, b_i , can be determined using the *data solver* software built into Microsoft Excel. Figure 4.4 also illustrates the benefit of the inclusion of an additional non-linear isotropic stress parameter, with the second softening term resulting in a greatly improved isotropic stress evolution prediction when compared with the experimental data.

4.5.3. Back-stress material parameters

The non-linear kinematic back-stress (in uniaxial form), χ , consists of two Armstrong-Frederick [*Frederick and Armstrong, 2007*] terms defining the

4. A Unified Cyclic Viscoplastic Modelling Framework for Strain-Rate Dependent Materials

initial and later stages of strain hardening respectively, such that $\chi = \chi_1 + \chi_2$. The parameter fitting method outlined in Lemaitre and Chaboche [2000] will not permit the identification of the constants for more than one non-linear back-stress term. Hence, the method developed by Zhan [2004] is adopted here and extended to suit the current framework. Assuming that the temperature is constant for the parameter identification process and that the plastic strain-rate, $\dot{\varepsilon}^{\text{pl}}$, equals the accumulated equivalent plastic strain-rate, \dot{p} , for monotonic loading, integration of Equation (4.13) with respect to time yields:

$$\chi_i = \frac{C_i}{\gamma_i} (1 - e^{-\gamma_i p}) \quad \text{where } i = 1, 2 \quad (4.48)$$

The viscous stress, σ_v , is defined as the value of the function, f , if it is greater than or equal to zero. For monotonic loading the kinematic back-stress, χ , is less than the uniaxial applied stress, σ , for monotonic loading, such that the uniaxial applied stress can be rewritten using Equation (4.2) as:

$$\sigma = \chi + R + k + \sigma_v = \chi_1 + \chi_2 + R_1 + R_2 + k + \sigma_v \quad (4.49)$$

As χ_1 defines the hardening directly after the elastic portion of loading, the value of the kinematic back-stress is $\chi = \chi_{1,\text{max}} = C_1/\gamma_1$ at the onset of the secondary hardening region. Thus, for loading in the secondary hardening region, Equation (4.49) can be rewritten as:

$$\sigma = \frac{C_1}{\gamma_1} + \frac{C_2}{\gamma_2} (1 - e^{-\gamma_2 p}) + R_1 + R_2 + k + \sigma_v \quad (4.50)$$

Under the assumption that $p = \varepsilon^{\text{pl}}$ and the terms C_1/γ_1 , C_2/γ_2 , k and $\sigma_v = \beta^{-1} \sinh^{-1}(\dot{p}/a)$ are constants with respect to plastic strain, differentiating Equation (4.50) with respect to the plastic strain, ε^{pl} , yields the following expression:

$$\frac{\partial \sigma}{\partial \varepsilon^{\text{pl}}} = C_2 e^{-\gamma_2 p} + \frac{\partial R_1}{\partial \varepsilon^{\text{pl}}} + \frac{\partial R_2}{\partial \varepsilon^{\text{pl}}} \quad (4.51)$$

4. A Unified Cyclic Viscoplastic Modelling Framework for Strain-Rate Dependent Materials

Taking the natural logarithm of Equation (4.51), yields an equation which can be used for determining the unknown constants C_2 and γ_2 via a linear fit to experimental data of the form:

$$\ln\left(\frac{\partial\sigma}{\partial\varepsilon^{\text{pl}}} - \frac{\partial R_1}{\partial\varepsilon^{\text{pl}}} - \frac{\partial R_2}{\partial\varepsilon^{\text{pl}}}\right) = \ln(C_2) - \gamma_2\varepsilon^{\text{pl}} \quad (4.52)$$

where the constant γ_2 is the slope and $\ln(C_2)$ is the intercept obtained when plotting the plastic strain, ε^{pl} , versus the left hand side (LHS) of Equation (4.52). The terms $\partial R_1/\partial\varepsilon^{\text{pl}}$ and $\partial R_2/\partial\varepsilon^{\text{pl}}$ are easily defined by differentiating Equation (4.46) with respect to plastic strain, ε^{pl} :

$$\frac{\partial R_i}{\partial\varepsilon^{\text{pl}}} = Q_i b_i e^{-b_i p} \quad \text{where } i = 1, 2 \quad (4.53)$$

However, to fully define the relationship of Equation (4.52), the term $\partial\sigma/\partial\varepsilon^{\text{pl}}$ must first be determined. Using the chain rule, $\partial\sigma/\partial\varepsilon^{\text{pl}}$ can be written as:

$$\frac{\partial\sigma}{\partial\varepsilon^{\text{pl}}} \approx \frac{d\sigma}{d\varepsilon} \frac{d\varepsilon}{dt} \frac{dt}{d\varepsilon^{\text{pl}}} = \frac{d\sigma}{d\varepsilon} \dot{\varepsilon} \frac{1}{\dot{\varepsilon}^{\text{pl}}} \quad (4.54)$$

The plastic strain-rate is defined as:

$$\dot{\varepsilon}^{\text{pl}} = \dot{\varepsilon} - \dot{\varepsilon}^{\text{el}} = \dot{\varepsilon} - \frac{\dot{\sigma}}{E} = \dot{\varepsilon} \left(1 - \frac{1}{E} \frac{d\sigma}{d\varepsilon}\right) \quad (4.55)$$

Such that equation (4.54) becomes:

$$\frac{\partial\sigma}{\partial\varepsilon^{\text{pl}}} = \left(\frac{d\sigma}{d\varepsilon}\right) \left/ \left(1 - \frac{1}{E} \frac{d\sigma}{d\varepsilon}\right)\right. \quad (4.56)$$

Following the approach of Hyde *et al.* [2010] and Zhan [2004], the term $d\sigma/d\varepsilon$ can be determined using the Ramberg-Osgood equation:

$$\frac{\varepsilon}{\varepsilon_0} = \frac{\sigma}{\sigma_0} + \left(\frac{\sigma}{\sigma_0}\right)^n \quad (4.57)$$

4. A Unified Cyclic Viscoplastic Modelling Framework for Strain-Rate Dependent Materials

As $E = \sigma_0 / \varepsilon_0$, differentiating with respect to the total strain, ε , and rearranging yields:

$$\frac{d\sigma}{d\varepsilon} = \frac{E}{\left(1 + n \left(\frac{\sigma}{\sigma_0}\right)^{n-1}\right)} \quad (4.58)$$

The constants for the Ramberg-Osgood equation are determined by taking the logarithm of both sides of Equation (4.57):

$$\log(E\varepsilon - \sigma) = n \log(\sigma) - (n-1) \log(\sigma_0) \quad (4.59)$$

and plotting $\log(\sigma)$ versus $\log(E\varepsilon - \sigma)$ allows the constants n and σ_0 to be determined as the slope and intercept respectively. Figure 4.9 illustrates the plots for the identification of the Ramberg-Osgood parameters across a range of temperatures. Table 4.2 shows the identified constants for ex-service P91 steel at temperatures of 400 °C, 500 °C and 600 °C.

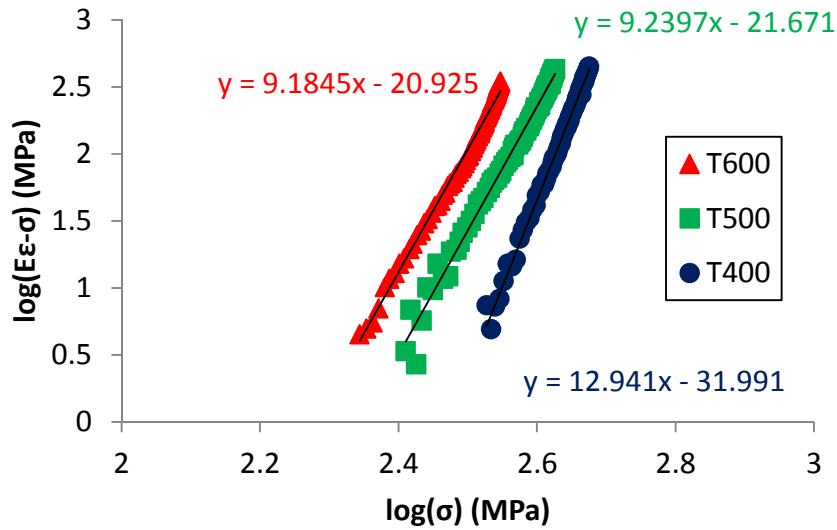


Figure 4.9: Identification of the Ramberg-Osgood constants for ex-service P91 steel at temperatures of 400 °C, 500 °C and 600 °C.

4. A Unified Cyclic Viscoplastic Modelling Framework for Strain-Rate Dependent Materials

Table 4.2: Identified Ramberg-Osgood constants for ex-service P91 steel.

T (°C)	σ_0 (MPa)	n (-)
400	477.627	12.941
500	426.650	9.240
600	360.298	9.185

The kinematic back-stress constants are determined from Equation (4.52) by plotting ε^{pl} versus $\ln\left(\frac{\partial\sigma}{\partial\varepsilon^{\text{pl}}} - \frac{\partial R_1}{\partial\varepsilon^{\text{pl}}} - \frac{\partial R_2}{\partial\varepsilon^{\text{pl}}}\right)$. Finally, the kinematic hardening constants related to the initial stages of hardening (C_1, γ_1) can be determined from Equation (4.49), assuming k and σ_v are constant. Differentiating with respect to plastic strain, ε^{pl} , and rearranging yields:

$$\ln\left(\frac{\partial\sigma}{\partial\varepsilon^{\text{pl}}} - \frac{\partial\chi_2}{\partial\varepsilon^{\text{pl}}} - \frac{\partial R_1}{\partial\varepsilon^{\text{pl}}} - \frac{\partial R_2}{\partial\varepsilon^{\text{pl}}}\right) = \ln(C_1) - \gamma_1\varepsilon^{\text{pl}} \quad (4.60)$$

Similar to above, C_1 and γ_1 can then be determined as the intercept and slope, respectively, from plots of ε^{pl} versus $\ln\left(\frac{\partial\sigma}{\partial\varepsilon^{\text{pl}}} - \frac{\partial\chi_2}{\partial\varepsilon^{\text{pl}}} - \frac{\partial R_1}{\partial\varepsilon^{\text{pl}}} - \frac{\partial R_2}{\partial\varepsilon^{\text{pl}}}\right)$.

4.5.4. Identification of cyclic viscoplasticity parameters

The cyclic viscoplastic material parameters α and β , of Equation (4.1), are intrinsically linked to the viscous (creep) behaviour of the material, and should ideally be obtained from long-term creep data, similar to the experimental data of Figure 4.10. Plotting stress against strain-rate on a log-log axis for the creep loading case enable curve fitting to the data using the following expression for the minimum creep rate:

$$\dot{\varepsilon}^{\text{cr}} = \alpha_{\text{cr}} \sinh\beta_{\text{cr}}\sigma \quad (4.61)$$

where α_{CR} and β_{CR} are the secondary creep constants and σ is the uniaxial stress. Figure 4.10 illustrates the excellent correlation achieved with the experimental data of Haney *et al.* [2009] and Klueh [2004], using Equation

4. A Unified Cyclic Viscoplastic Modelling Framework for Strain-Rate Dependent Materials

(4.61), further highlighting the importance and capability of the hyperbolic sine constitutive equation.

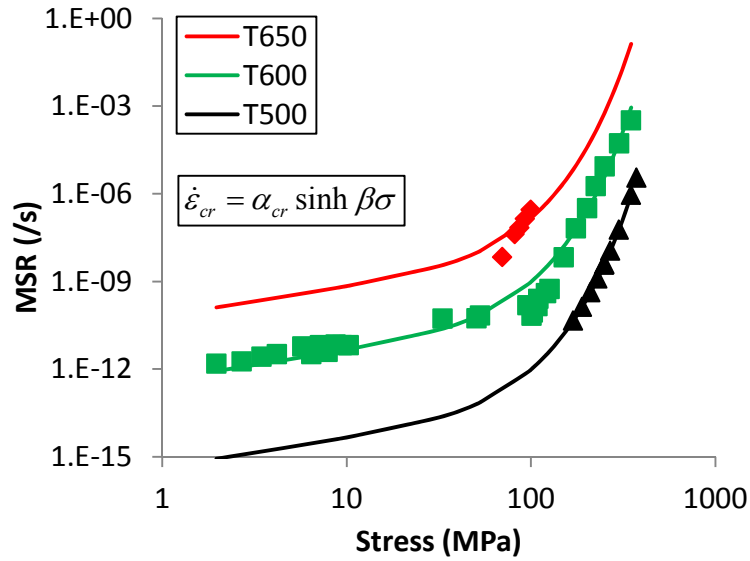


Figure 4.10: Identification of the cyclic viscoplastic material constant, β , from minimum strain-rate (MSR) data from the creep tests of Hyde *et al.*, [2006] at 650 °C, Sklenička *et al.* [2003] at 600 °C and Haney *et al.* [2009] at 500 °C. The symbols represent the experimental data and the lines represent the correlation obtained using the hyperbolic sine steady-state creep constitutive equation.

However, the conditions present in modern plant operating under increased flexibility and the unified nature of the current material model dictates that the effects of rate-independent cyclic plasticity must also be accounted for through the use of cyclic viscoplastic material parameters, namely α and β of Equation (4.1). Hence, the values of α_{CR} and β_{CR} need to be adjusted to fit the isothermal fatigue test data and the experimental stress relaxation results. This process uses the constants obtained from the long-term creep data as a starting position. A relationship between the viscoplastic parameters in a pure creep loading condition (α_{CR} and β_{CR}) and the cyclic (short-term) viscoplastic material parameters (α and β) has been identified to allow the value of β to be obtained from creep data. This relationship is:

$$\beta = \beta_{cr} \quad (4.62)$$

so that α may be scaled as:

4. A Unified Cyclic Viscoplastic Modelling Framework for Strain-Rate Dependent Materials

$$\alpha = \frac{\alpha_{cr} \sinh \beta \sigma}{\sinh \beta f} = A \alpha_{cr} \quad (4.63)$$

where A is termed the cyclic viscoplastic scaling factor. As Equation (4.63) includes the cyclic plasticity terms, χ and R via the function f , the value of α is identified here from stress relaxation tests, using the theoretical approach given below, supplemented by the standalone uniaxial code implemented in FORTRAN 95. For an isothermal, uniaxial loading conditions, the total strain rate, $\dot{\epsilon}$, is defined as:

$$\dot{\epsilon} = \dot{\epsilon}^{el} + \dot{\epsilon}^{pl} \quad (4.64)$$

In a stress relaxation test with a tensile dwell period, once the initial displacement has been applied and the hold period has begun, the displacement, and hence, the strain are held constant from a time t_0 as shown in Figure 4.11. Thus, the total strain-rate, $\dot{\epsilon}$, is zero and rearranging Equation (4.64) yields:

$$\dot{\epsilon}^{el} = -\dot{\epsilon}^{pl} \quad (4.65)$$

Using Hooke's law, the elastic strain-rate is defined as:

$$\dot{\epsilon}^{el} = \frac{\dot{\sigma}}{E} \quad (4.66)$$

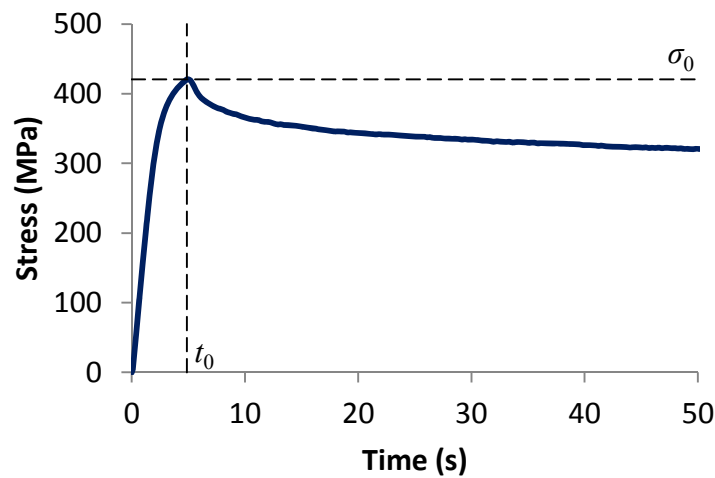


Figure 4.11: Representation of the initial tensile dwell period stress, σ_0 , and initial dwell time, t_0 .

4. A Unified Cyclic Viscoplastic Modelling Framework for Strain-Rate Dependent Materials

For a tensile hold period, the plastic strain-rate is determined using the hyperbolic sine constitutive equation for the effective accumulated plastic strain-rate:

$$\dot{\varepsilon}^{\text{pl}} = \alpha \sinh \beta (|\sigma - \chi| - R - k) \quad (4.67)$$

Thus, using Equations (4.66) and (4.67) in Equation (4.65) and rearranging yields:

$$\frac{d\sigma}{\sinh \beta (|\sigma - \chi| - R - k)} = -\alpha E dt \quad (4.68)$$

Integrating equation (4.68) yields:

$$\int_{\sigma_0}^{\sigma} \frac{d\sigma}{\sinh \beta (|\sigma - \chi| - R - k)} = -\int_{t_0}^t \alpha E dt \quad (4.69a)$$

$$\int_{\sigma_0}^{\sigma} \text{csch} [\beta (|\sigma - \chi| - R - k)] d\sigma = -\alpha E (t - t_0) \quad (4.69b)$$

$$\frac{1}{\beta} \ln \left| \tanh \left(\frac{\beta (|\sigma - \chi| - R - k)}{2} \right) \right|_{\sigma_0}^{\sigma} = -\alpha E (t - t_0) \quad (4.69c)$$

For a tensile dwell period, it is assumed that the uniaxial stress, σ , is positive throughout the region of concern in the stress relaxation curve, such that Equation (4.69c) becomes:

$$\ln \left| \frac{\tanh \beta (|\sigma - \chi| - R - k)/2}{\tanh \beta (|\sigma_0 - \chi| - R - k)/2} \right| = -\alpha \beta E (t - t_0) \quad (4.70)$$

Taking the exponential of both sides yields:

$$\left| \tanh \frac{\beta (|\sigma - \chi| - R - k)}{2} \right| = \left| \tanh \frac{\beta (|\sigma_0 - \chi| - R - k)}{2} \right| e^{-\alpha \beta E (t - t_0)} \quad (4.71)$$

4. A Unified Cyclic Viscoplastic Modelling Framework for Strain-Rate Dependent Materials

Thus, an analytical model for the theoretical stress which describes the uniaxial stress, σ , as a function of time for the tensile hold period during a stress relaxation test is given by:

$$\sigma = \frac{2}{\beta} \tanh^{-1} \left[\left(\tanh \frac{\beta(\sigma_0 - \chi - R - k)}{2} \right) e^{-\alpha\beta E(t-t_0)} \right] + \chi + R + k \quad (4.72)$$

Equation (4.72) is implemented with Equations (4.46) and (4.48) to define R and χ as a function of time, respectively, where the values σ_0 and t_0 are defined from experimental data, as presented in Figure 4.11. By comparing this equation to the measured stress relaxation test data, the value of α can be identified. In Equation (4.72), the initial decay rate is predominately controlled by β and the level of stress obtained increases with decreasing values of α and/or β . To optimise the cyclic viscoplastic material parameter, α , the least squares optimisation approach of Equation (4.45) is adopted using Microsoft Excel to minimise the difference between the experimentally observed and theoretically determined dwell stress values.

4.6. Validation of material model against experimental data

The following section implements the step-by-step parameter identification procedure described above for (i) ‘as-received’ P91 steel from the literature, (ii) ex-service P91 steel and (iii) MarBN, in conjunction with validation via comparison of model predictions with experimental test data obtained under different conditions. In all cases, calibration is conducted at a strain-rate of 0.1 %/s under an applied strain-range of ± 0.5 %. Validation of the material model is conducted at strain-ranges and strain-rates different to the calibration regime to (i) ensure that the identified material parameters are optimised for a broad range of loading conditions and (ii) investigate the ability of the material model to simulate more representative flexible plant operating conditions, with a particular emphasis on capturing the strain-rate effect.

4. A Unified Cyclic Viscoplastic Modelling Framework for Strain-Rate Dependent Materials

4.6.1. Modelling of 'as received' P91 under HTLCF and TMF

To validate the initial implementation of the FORTRAN 95 standalone uniaxial code and UMAT user material subroutine, the unified cyclic viscoplasticity model is applied to various 'as received' P91 steels from the literature [*Fournier et al. 2011; Koo and Kwon, 2011; Saad et al., 2011*]. Firstly, the required material parameters are calibrated using the approach of Section 4.5.

4.6.1.1. Model calibration for 'as received' P91 steel

Young's modulus is calibrated from the initial monotonic portion of the cyclic test data and the values of the coefficient of thermal expansion are taken from published ASME data [*ASME, 1998*], with an assumed linear dependence on temperature in the 400 °C to 600 °C temperature range. Poisson's ratio, ν , is taken to have a constant value of 0.3 throughout the simulations. The resulting identified elastic material parameters for 'as received' P91 steel are presented in Table 4.3.

Table 4.3: Elastic material parameters for 'as received' P91 steel.

Temperature (°C)	Young's Modulus (GPa)	Thermal Expansion (1/°C) [<i>ASME, 1998</i>]
400	184	12.95×10^{-6}
500	180	13.31×10^{-6}
600	142	13.59×10^{-6}

The isotropic and kinematic hardening evolution equations are similar to those used by Saad *et al.* [*2011*], except for the additional anisothermal terms of the present model. Hence, the hardening parameters have been adopted from the latter, with algebraic manipulation to suit the specific formulation used here. The resulting cyclic plasticity parameters for the 400 °C to 600 °C temperature range are presented in Table 4.4. Note that, in the work of Saad *et al.* [*2011*], only a single cyclic softening term is used, such that $R=R_1$.

4. A Unified Cyclic Viscoplastic Modelling Framework for Strain-Rate Dependent Materials

Table 4.4: Cyclic plasticity material parameters for 'as received' P91 steel [Saad *et al.*, 2011].

T (°C)	Q (MPa)	b	C₁ (MPa)	γ₁	C₂ (MPa)	γ₂	k (MPa)
400	-55.0	0.45	352500.0	2350.0	48600.00	405.0	96
500	-60.0	0.60	215872.6	2191.6	48235.29	460.7	90
600	-75.4	1.00	106860.0	2055.0	31159.90	463.0	43

The cyclic viscoplastic material parameters, identified here for 'as received' P91 steel from the test relaxation test data of Koo and Kwon [2011] are given in Table 4.5 for temperatures of 400 °C, 500 °C and 600 °C.

Table 4.5: Identified cyclic viscoplastic material parameters for 'as received' P91 steel.

Temperature (°C)	α (s⁻¹)	β (MPa⁻¹)
400	1.4×10 ⁻⁶	0.07
500	8.0×10 ⁻⁷	0.064
600	1.0×10 ⁻⁷	0.055

The calibration process is carried out here based on data at 400 °C, 500 °C and 600 °C and a cyclic strain-rate of 0.1 %/s. For the temperatures listed above, the results of this calibration process are shown in Figure 4.12 to Figure 4.15. Figure 4.12 depicts the calibrated fit obtained with the stress relaxation data of Koo and Kwon, [2011] at temperatures of 500 °C and 600 °C respectively. Figure 4.13 illustrates the correlation achieved with the cyclic data of Saad *et al.* [2011] at 400 °C and a strain-rate of 0.1 %/s for the initial and stabilised cycles, i.e. capturing the evolution (softening) of the cyclic responses. Figure 4.14 and Figure 4.15 show the calibration results at 500 °C and 600 °C respectively, where an excellent fit with the experimental data (also including cyclic softening) is obtained.

4. A Unified Cyclic Viscoplastic Modelling Framework for Strain-Rate Dependent Materials

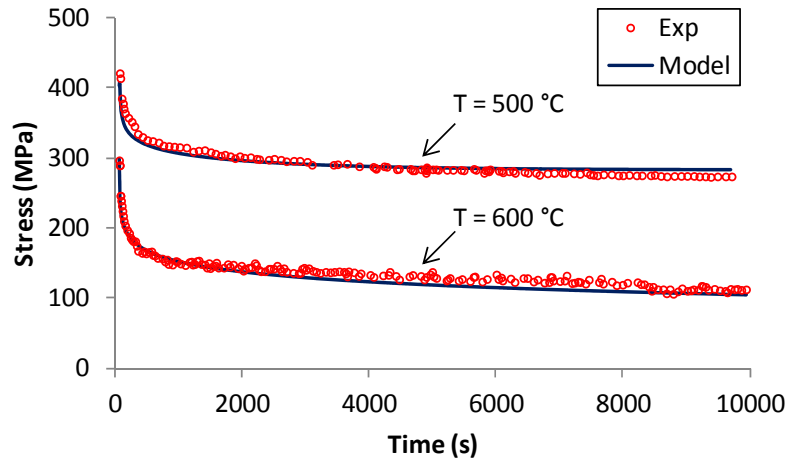


Figure 4.12: Calibration of the cyclic viscoplasticity material parameters for 'as received' P91 steel from stress relaxation tests of Koo and Kwon [2011], at temperatures of (a) 500 °C and (b) 600 °C.

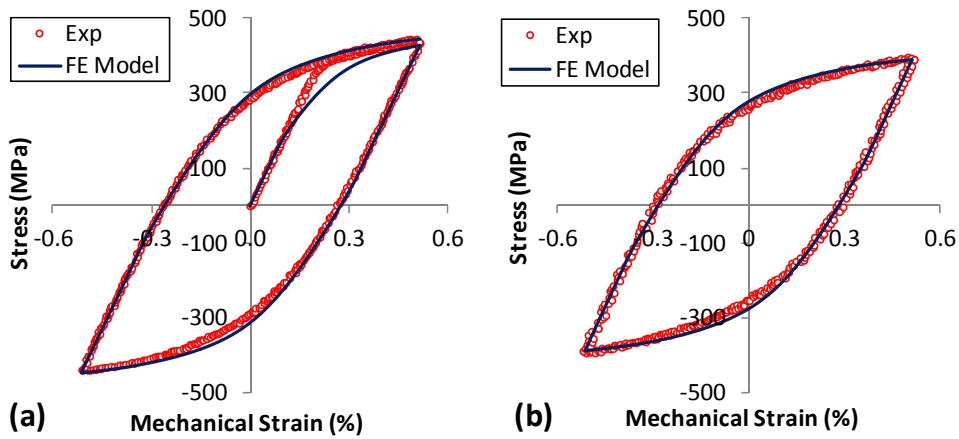


Figure 4.13: Calibration of material parameters from measured evolving stress data of Saad *et al.* [2011] at 400 °C and a strain-rate of 0.1 %/s for (a) the initial cycle and (b) after 800 cycles.

4. A Unified Cyclic Viscoplastic Modelling Framework for Strain-Rate Dependent Materials

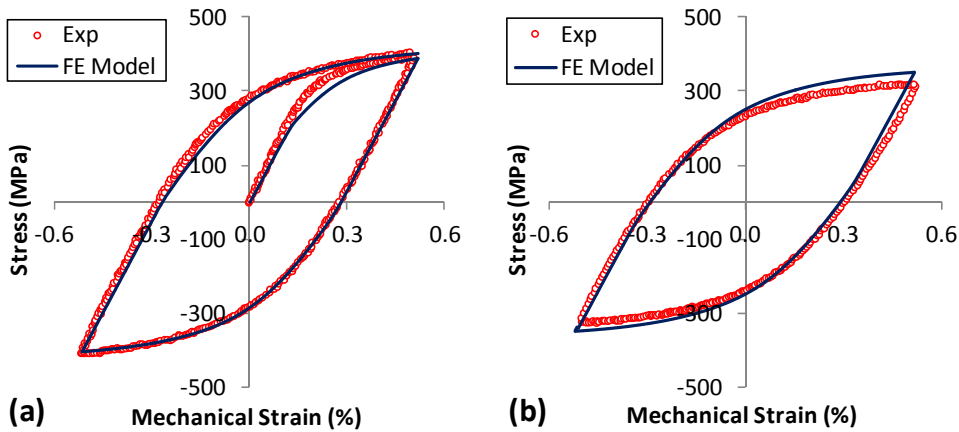


Figure 4.14: Calibration of material parameters from measured evolving stress data of Saad *et al.* [2011] at 500 °C and a strain-rate of 0.1 %/s for (a) the initial cycle and (b) after 800 cycles.

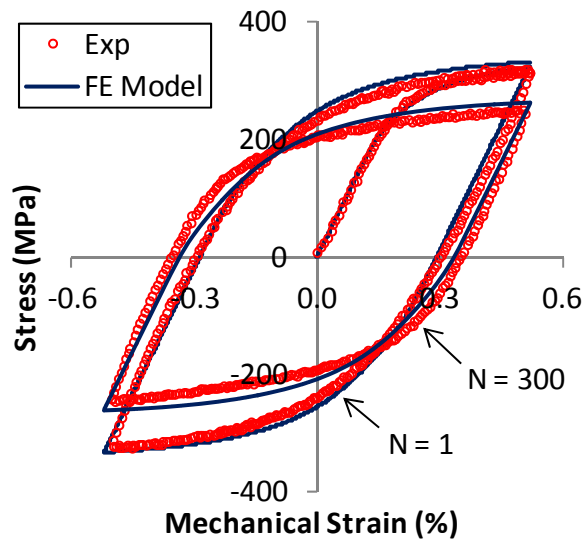


Figure 4.15: Calibration of material parameters from experimental data of Saad *et al.* [2011] at 600 °C and a strain-rate of 0.1 %/s for the initial and 300th cycles.

4.6.1.2. Validation against HTLCF experimental data

To analyse the performance of the material model, validation is conducted against a range of experimental data intermediate to or outside of the range of the calibration test conditions presented above. Hence, application of the model to other temperatures and strain-rates constitutes validation with respect to temperature and strain-rate sensitivity via interpolation and extrapolation. The validation model setup employs an axisymmetric FE

4. A Unified Cyclic Viscoplastic Modelling Framework for Strain-Rate Dependent Materials

implementation of a test specimen gauge length. As an initial step in the validation process, it was first established that the standalone uniaxial code and the UMAT implementation gave identical results for uniaxial loading conditions. The model results presented below are those of the UMAT and the loading conditions applied to the FE model are based on the isothermal fatigue experiments conducted by Fournier *et al.* [2011], Koo and Kwon [2011], Saad *et al.* [2011] and the TMF data of Saad *et al.* [2011], as summarised in Table 4.6. Within the present study, piece-wise linear interpolation is used to account for the variation of the material parameters as a function of temperature.

Table 4.6: Isothermal fatigue experimental test conditions.

Source	Strain-Rate (%/s)	Strain Range (%)
Fournier <i>et al.</i> [2011]	1.00	±0.35
Saad <i>et al.</i> [2011]	0.10	±0.50
Koo and Kwon [2011]	0.01	±0.60

To assess the strain-rate sensitivity of the material model (and the strain-rate independence of the material parameters), the predicted FE results are compared with stress relaxation tests conducted at a variety of different loading conditions, temperatures and hold times on 'as received' P91 steel. The experimental results are obtained from data available in the literature (Saad *et al.* [2011] and Takahashi [2008]) for temperatures of 500 °C and 550 °C. Validation is obtained by comparison with two different hold times of 120 s and 3500 s, which are simulated at the displacements corresponding to the maximum stress in Figure 4.16. The results in Figure 4.16 illustrate excellent agreement with the experimental data for the range of conditions simulated.

4. A Unified Cyclic Viscoplastic Modelling Framework for Strain-Rate Dependent Materials

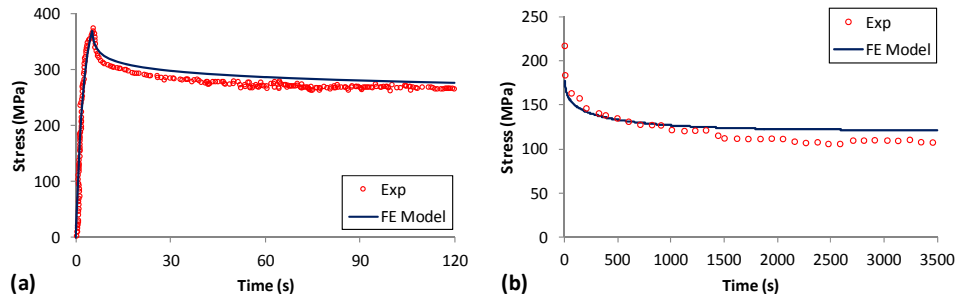


Figure 4.16: Comparison of predicted FE results with experimental stress relaxation data at (a) a temperature of 500 °C for 120 s (Saad *et al.* [2011]) and (b) a temperature of 550 °C for 3500 s (Takahashi [2008]).

For cyclic loading under isothermal conditions, the performance of the material model was compared with experimental data at temperatures of 500 °C and 550 °C. The material model was validated at strain-rates of 1.0 %/s to 0.01 %/s, which lie above and below the strain-rate used for calibration, with strain ranges of ± 0.35 % to ± 0.6 %, respectively. Validation is achieved by comparison with experimental data available from two different sources in the literature (Fournier *et al.* [2011] and Koo and Kwon [2011]). Figure 4.17 illustrates the result obtained at a temperature of 500 °C for the initial and stabilised cycles, where good correlation is obtained with the test data. Figure 4.18 and Figure 4.19 demonstrate the interpolation performance of the material model with respect to temperature and strain-rate. The results show excellent correlation with the test data.

4. A Unified Cyclic Viscoplastic Modelling Framework for Strain-Rate Dependent Materials

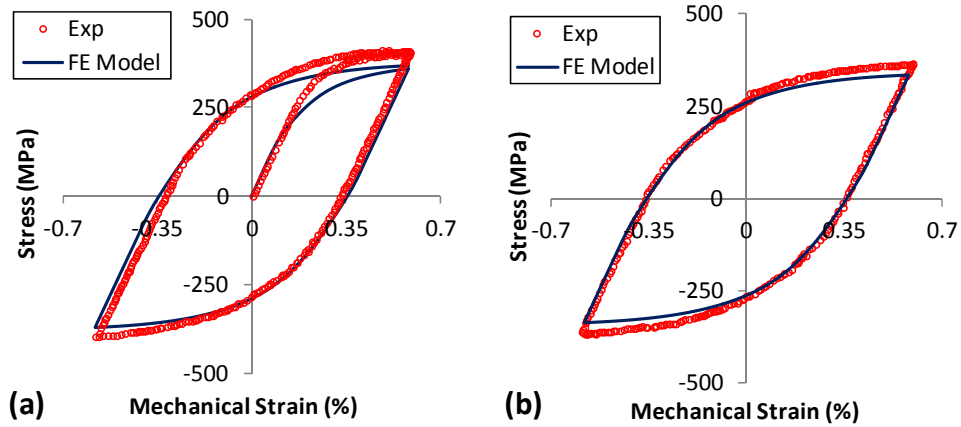


Figure 4.17: Comparison of FE-predicted and measured evolving stress-strain data [Koo and Kwon, 2011] at 500 °C and a strain-rate of 0.01 %/s for (a) the initial cycle and (b) after 130 cycles.

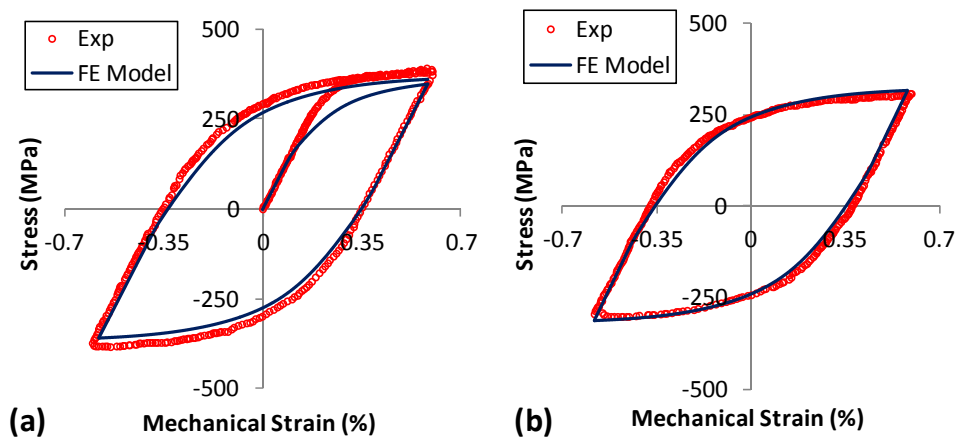


Figure 4.18: Comparison of FE-predicted and measured evolving stress-strain data [Koo and Kwon, 2011] at 550 °C and a strain-rate of 0.01 %/s for (a) the initial cycle and (b) after 103 cycles.

4. A Unified Cyclic Viscoplastic Modelling Framework for Strain-Rate Dependent Materials

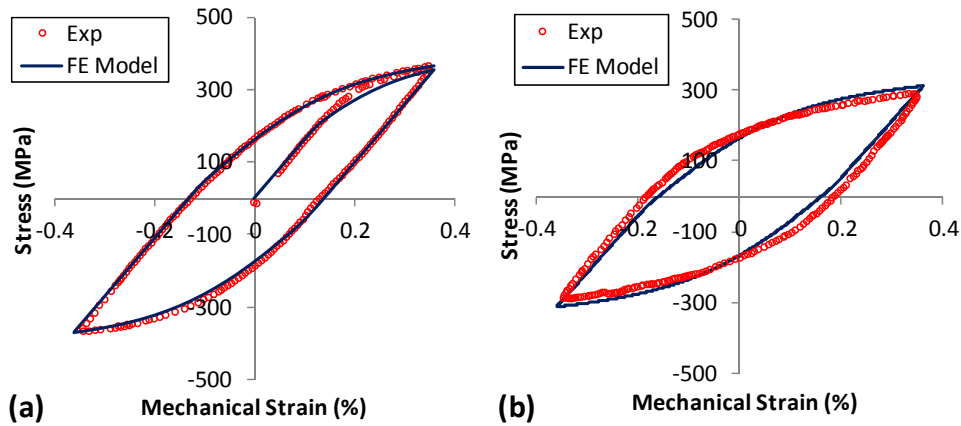


Figure 4.19: Comparison of FE predicted and measured evolving stress-strain data [Fournier *et al.*, 2011] at 550 °C and a strain-rate of 1.0 %/s for (a) the initial cycle and (b) after 2000 cycles.

4.6.1.3. Modelling TMF deformation in 'as received' P91 steel

Anisothermal loading conditions are also simulated to validate the model against TMF tests from Saad *et al.* [2011], within the 400 °C to 600 °C temperature range. Both in-phase and out-of-phase TMF loading conditions are simulated, as depicted in the schematic of Figure 3.25. For in-phase loading, Figure 4.20 shows the excellent correlation achieved with TMF test data for the 400 °C to 500 °C case and Figure 4.21 also illustrates good correlation for the out-of-phase case. The results of the 400 °C to 600 °C in-phase loading simulations are shown in Figure 4.22, where good correlation with the experimental data is again obtained.

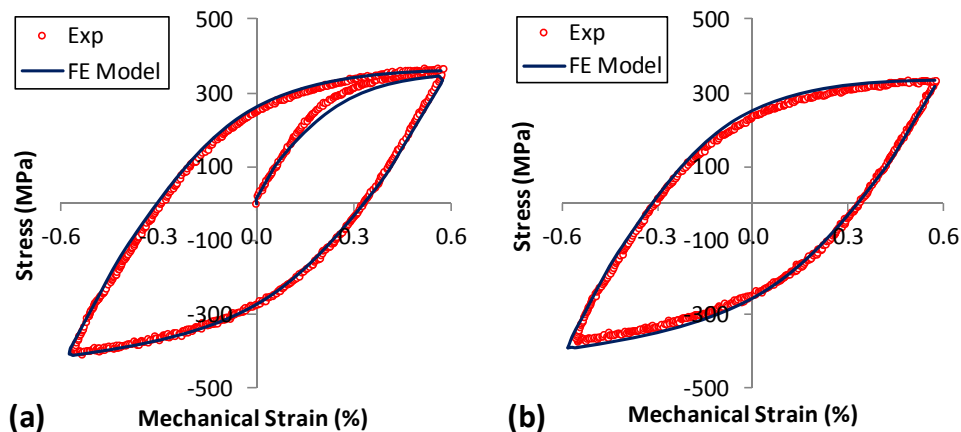


Figure 4.20: Comparison of FE-predicted and measured [Saad *et al.*, 2011] hysteresis loops for 400-500 °C, TMF-IP loading for (a) the initial cycle and (b) after 100 cycles.

4. A Unified Cyclic Viscoplastic Modelling Framework for Strain-Rate Dependent Materials

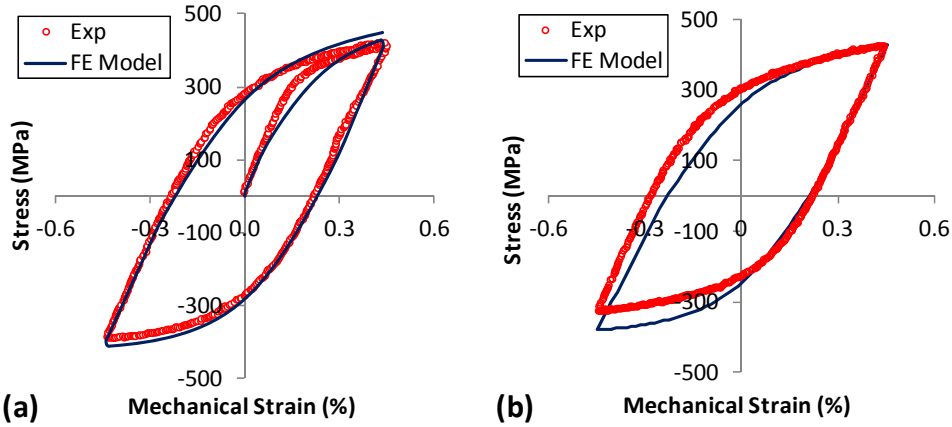


Figure 4.21: Comparison of FE predicted and measured [Saad *et al.*, 2011] hysteresis loops for 400-500 °C, TMF-OP loading for (a) the initial cycle and (b) after 100 cycles.

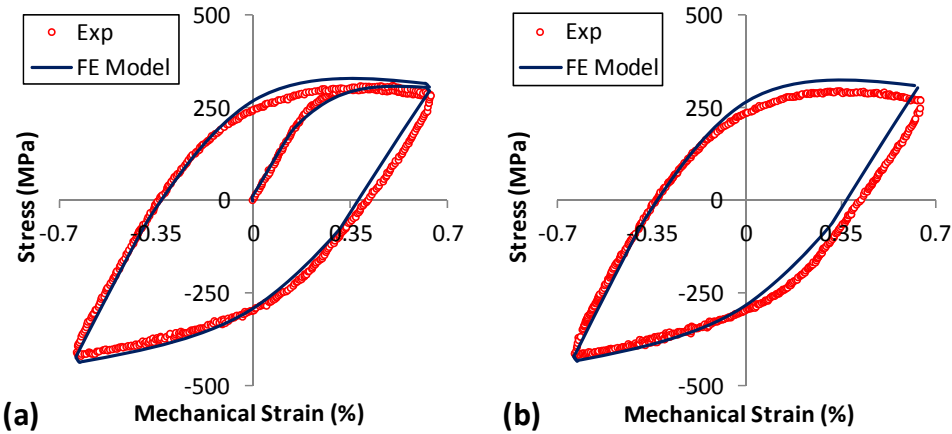


Figure 4.22: Comparison of FE predicted and measured [Saad *et al.*, 2011] hysteresis loops for 400-600 °C, TMF-IP loading for (a) the initial cycle and (b) after 3 cycles.

4.6.2. Application of material model to ex-service P91 steel

This section details the application of the step-by-step parameter identification methodology of Section 4.5 to the HTLCF test program on ex-service P91 steel presented in Chapter 3.

4.6.2.1. Identification of parameters for ex-service P91

Young's modulus is identified by applying Hooke's law ($\sigma = E\varepsilon^{\text{el}}$) to the linear portion of the initial loop (monotonic region) under the calibration

4. A Unified Cyclic Viscoplastic Modelling Framework for Strain-Rate Dependent Materials

conditions of an applied strain-range of $\pm 0.5\%$ and strain-rate of $0.1\%/s$. Young's modulus is estimated as the slope of the elastic region during the first cycle, as shown in Figure 4.23(a, c, e).

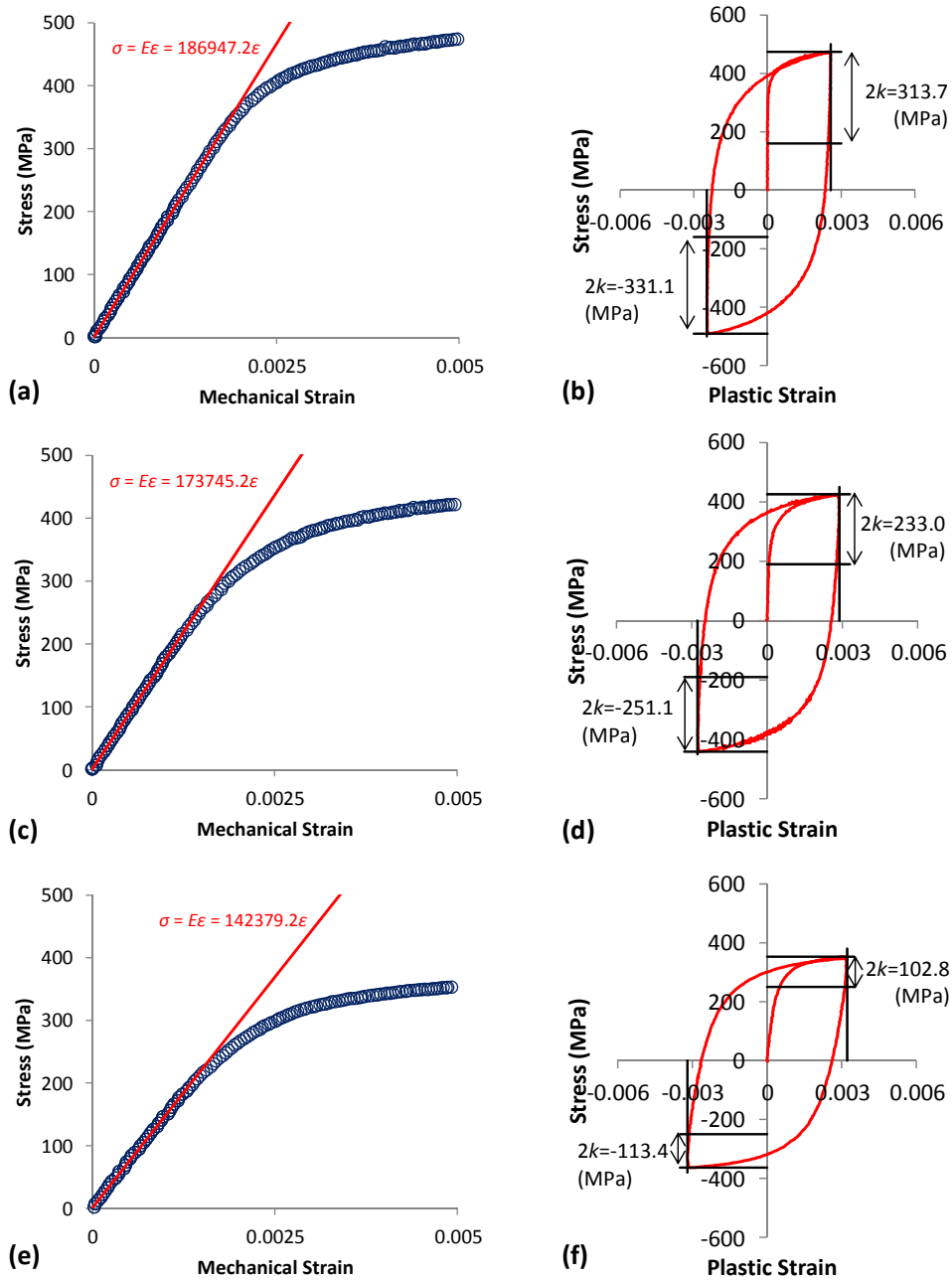


Figure 4.23: Identification of Young's modulus, E , and initial cyclic yield stress, k , at (a & b) $400\text{ }^{\circ}\text{C}$, (c & d) $500\text{ }^{\circ}\text{C}$ and (e & f) $600\text{ }^{\circ}\text{C}$.

The temperature-dependent initial cyclic yield stress is defined as half the distance of the linear vertical region when plotting plastic strain versus stress. The initial cyclic yield stress, k , is taken as the average of the linear

4. A Unified Cyclic Viscoplastic Modelling Framework for Strain-Rate Dependent Materials

regions following tensile and compressive load reversals as identified from the initial cycle. The plastic strain, ϵ^{pl} , at any point in the cycle is identified using the measured total strain, ϵ_{exp} , and the measured stress, σ_{exp} , such that $\epsilon^{pl} = \epsilon_{exp} - \sigma_{exp}/E$. Hence, the initial cyclic stress values, k , are defined from the correlation presented in Figure 4.23(b, d, f) for temperatures of 400 °C, 500 °C and 600 °C. The identified elastic material parameters are presented in Table 4.7 for ex-service P91 steel.

The cyclic softening material parameters are identified by determining the experimental cyclic softening stress, R^{exp} , as defined in Section 4.5.2. From this experimental data, the primary, secondary and failure softening regions are identified. This allows the saturation values, Q_1 and Q_2 , to be identified, as illustrated in Figure 4.4. The material parameters defining the rate of decay of cyclic softening, b_i , are obtained by fitting Equation (4.46) to the data and optimised using the least squares optimisation function of Equation (4.45). Table 4.7 presents the identified material parameters. The correlation achieved with experimental data using the analytical model of Equation (4.46) is shown in Figure 4.24.

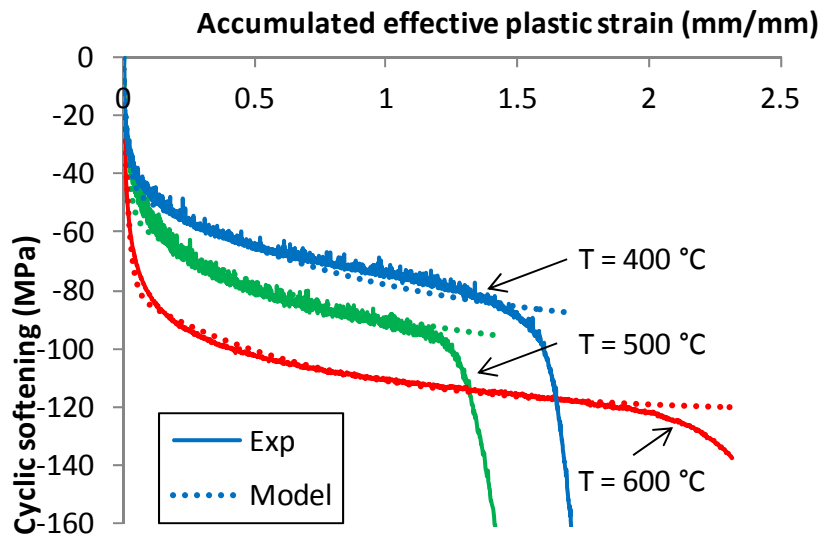


Figure 4.24: Identification of cyclic softening material parameters at temperatures of 400 °C, 500 °C and 600 °C

4. A Unified Cyclic Viscoplastic Modelling Framework for Strain-Rate Dependent Materials

Using the material parameter identification process outlined in Section 4.5.3, the four NLKH material parameters are identified via application of the procedure to monotonic data. Firstly, the Ramberg-Osgood material parameters are identified as highlighted in Figure 4.9 and presented in Table 4.2 for temperatures of 400 °C, 500 °C and 600 °C. The monotonic test data is then split into (i) elastic behaviour, (ii) short-range NLKH back-stress (χ_1 region) and (ii) long-range NLKH back-stress (χ_2 region), as illustrated in Figure 4.25. The long-range NLKH back-stress region is defined as the region of low hardening as the material stress-response starts to stabilise (plateau region of Figure 4.25). Thus, the hardening modulus, C_2 , is quite low in this region.

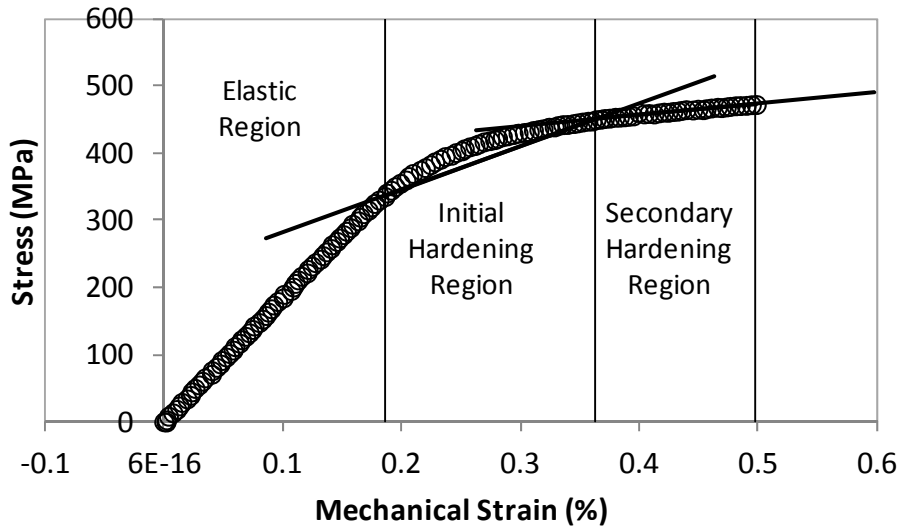


Figure 4.25: Various regions of hardening for monotonic loading.

The NLKH material parameters, C_2 and γ_2 , are identified by plotting Equation (4.52) and fitting a straight line as illustrated in Figure 4.26 for a temperature of 400 °C. In a similar manner, Equation (4.60) is used to identify the constants C_1 and γ_1 , as illustrated in Figure 4.27. The complete set of identified NLKH material parameters for ex-service P91 steel are presented in Table 4.7.

4. A Unified Cyclic Viscoplastic Modelling Framework for Strain-Rate Dependent Materials

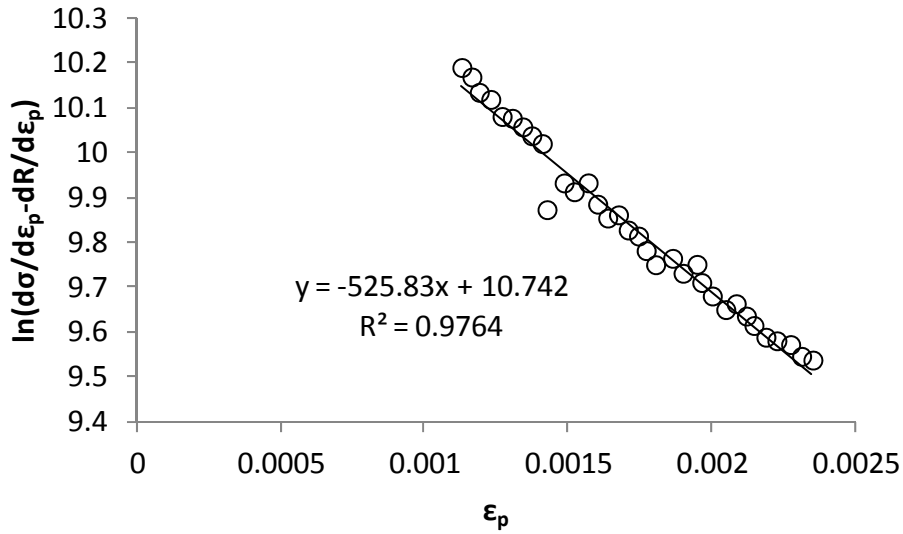


Figure 4.26: Identification of the secondary hardening material parameters, C_2 and γ_2 , for ex-service P91 steel at a temperature of 400 °C.

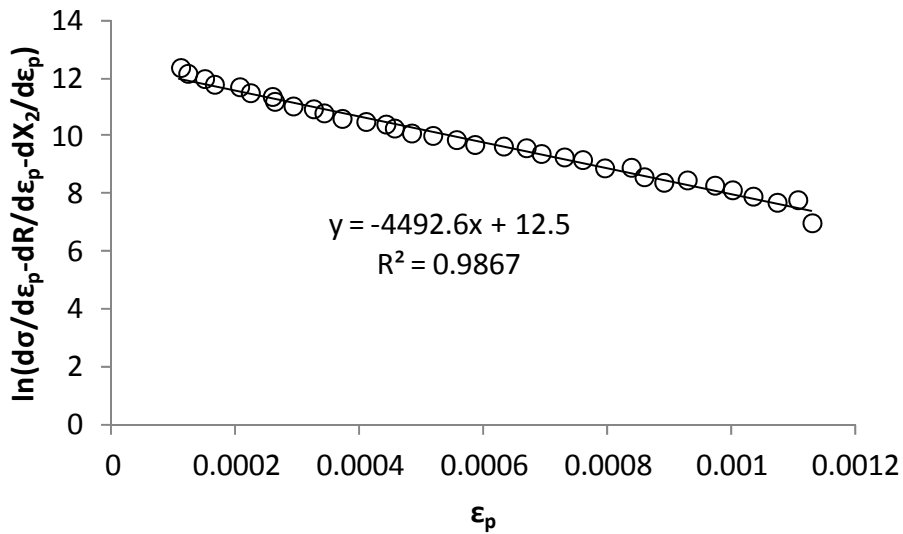


Figure 4.27: Identification of the initial hardening region material parameters, C_1 and γ_1 , for ex-service P91 steel at a temperature of 400 °C

The cyclic viscoplastic material parameters, α and β , are identified using the analytical model for stress relaxation behaviour derived in Equation (4.72). The time, t_0 , and stress, σ_0 , at the start of the hold period are identified from stress relaxation test data, as illustrated in Figure 4.11. The cyclic viscoplastic material parameters, α and β , are then determined via

4. A Unified Cyclic Viscoplastic Modelling Framework for Strain-Rate Dependent Materials

comparison with experimental data, where the least squares fitting procedure is implemented to identify an optimised set of material parameters. The typical results achieved using the analytical material model are illustrated in Figure 4.28 for temperatures of 400 °C, 500 °C and 600 °C. The identified material parameters are presented in Table 4.7.

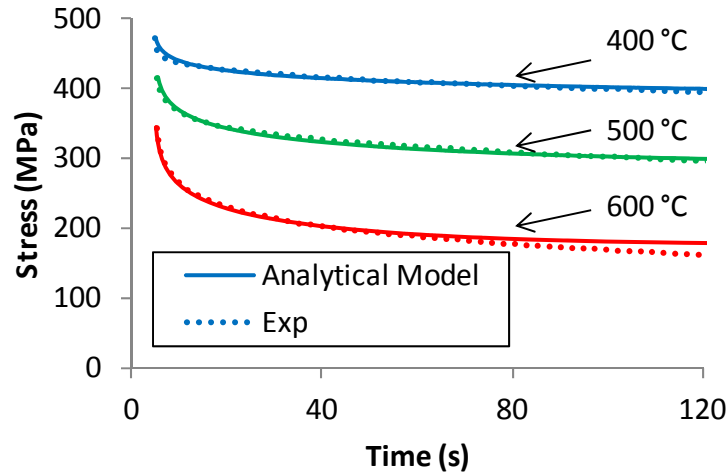


Figure 4.28: Identification of the cyclic viscoplastic material parameters, α and β , from stress relaxation data using the analytical model at temperatures of 400 °C, 500 °C and 600 °C.

Table 4.7: Identified material parameters for ex-service P91 steel.

Parameter	400 °C	500 °C	600 °C
E (MPa)	183623	173074	144741
k (MPa)	161.19	121.04	54.04
Q_1 (MPa)	-34.19	-46.67	-72.90
b_1 (-)	1.52	2.00	3.02
Q_2 (MPa)	-52.11	-52.11	-52.11
b_2 (-)	0.13	0.13	0.13
C_1 (MPa)	373248.61	304370.20	275130.28
γ_1 (-)	3076.85	3422.52	3397.2
C_2 (MPa)	65186.00	48484.52	38101.16
γ_2 (-)	339.451	406.73	626.64
α (1/s)	8.0×10^{-7}	8.0×10^{-7}	9.0×10^{-7}
β (1/MPa)	0.1	0.055	0.055

4. A Unified Cyclic Viscoplastic Modelling Framework for Strain-Rate Dependent Materials

The predicted stress-strain response for the calibration regime of an applied strain-rate of 0.1 %/s and applied strain-range of ± 0.5 % is presented in Figure 4.29. The results, which are obtained using the standalone uniaxial code, illustrate good agreement with the experimental data across a range of temperatures. In Figure 4.30, the calibrated material model is applied to stress relaxation loading using the UMAT user material subroutine. For both the monotonic and stress relaxation conditions simulated, the material model exhibits excellent agreement with the experimental data. Similarly, in Figure 4.31, a comparison of the FE predicted plastic strain with experimental data is presented, where good agreement with the experimental data is achieved.

4. A Unified Cyclic Viscoplastic Modelling Framework for Strain-Rate Dependent Materials

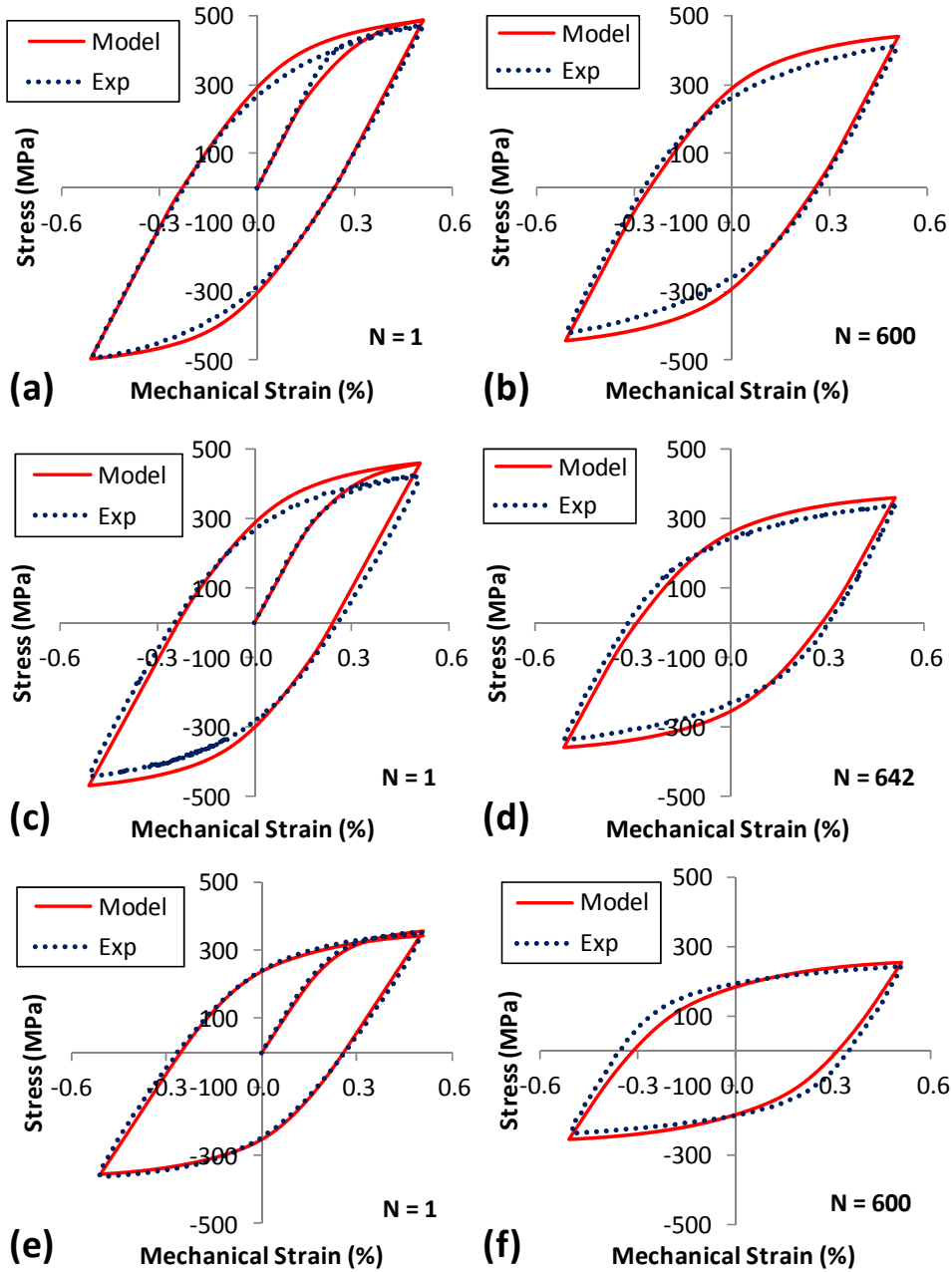


Figure 4.29: Comparison of the predicted stress-strain response with measured data for the calibration regime of an applied strain-rate of 0.1 %/s and applied strain-range of ± 0.5 % for (a) initial cycle at 400 °C, (b) 642nd cycle at 400 °C, (c) initial cycle at 500 °C, (d) 600th cycle at 500 °C, (e) initial cycle at 600 °C and (f) 600th cycle at 600 °C.

4. A Unified Cyclic Viscoplastic Modelling Framework for Strain-Rate Dependent Materials

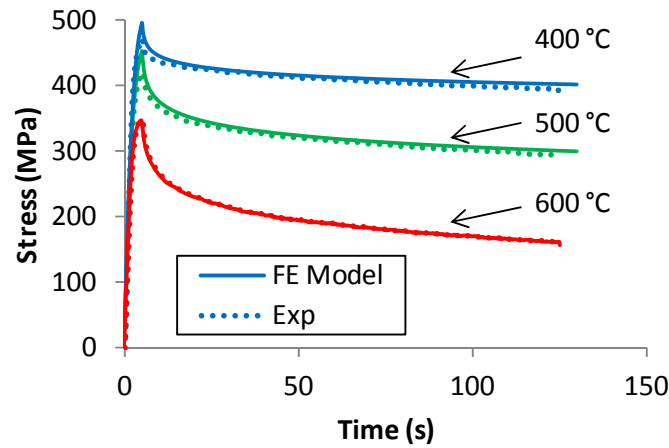


Figure 4.30: Comparison of the FE predicted and experimentally measured monotonic and stress relaxation response at temperatures of 400 °C, 500 °C and 600 °C.

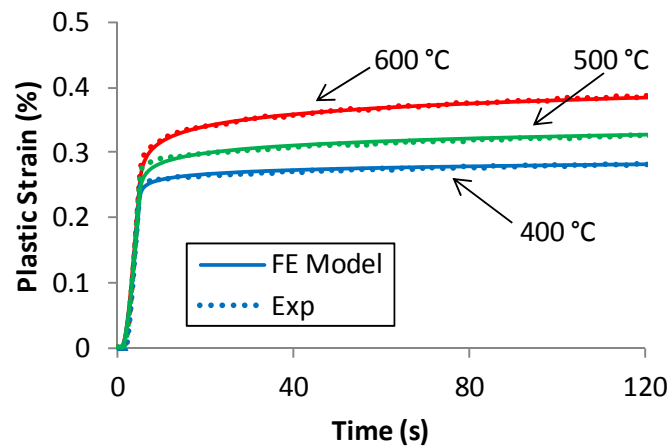


Figure 4.31: Comparison of the FE predicted and experimentally measured plastic strain during monotonic and stress relaxation loading for temperatures of 400 °C, 500 °C and 600 °C.

4.6.2.2. Strain-range validation for ex-service P91 steel

As the strain-ranges typically observed in conventional power plant components [Farragher *et al.*, 2013a; Farragher *et al.*, 2013b] are smaller than those of the tests (for practical reasons) and due to the presence of strain-range amplification at geometric discontinuities, the material model and related material parameter identification must be capable of operating across a broad range of strain-ranges. Figure 4.32 illustrates the ability of the material model to accurately predict the correct strain-range behaviour for the initial and half-life cycles when strain-ranges of $\pm 0.3\%$, $\pm 0.4\%$ and

4. A Unified Cyclic Viscoplastic Modelling Framework for Strain-Rate Dependent Materials

$\pm 0.5\%$ are applied at various temperatures, illustrating the ability of the material model to capture the cyclic softening behaviour across a range of strain-ranges. The stress-strain responses of Figure 4.32 are also conducted at a strain-rate of $0.033\%/s$, a strain-rate alternative to that of calibration.

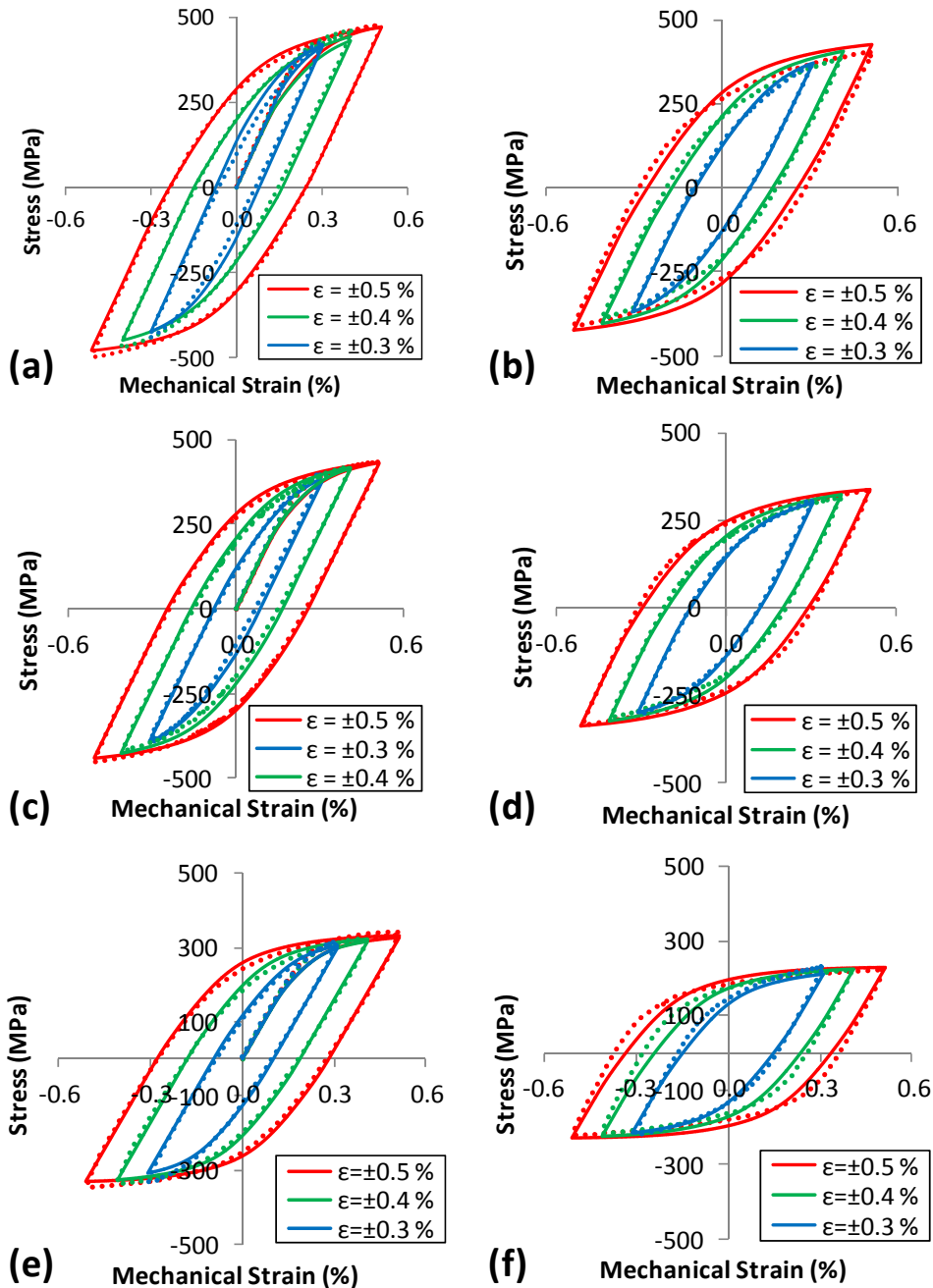


Figure 4.32: Comparison of the FE predicted and experimentally measured stress-strain response for an applied strain-rate of $0.033\%/s$ and varying strain-range for (a) initial cycle at 400 °C , (b) half-life at 400 °C , (c) initial cycle at 500 °C , (d) half-life at 500 °C , (e) initial cycle at 600 °C and (f) half-life at 600 °C . The solid lines represent the FE model prediction and the dotted lines represent experimental data.

4. A Unified Cyclic Viscoplastic Modelling Framework for Strain-Rate Dependent Materials

4.6.2.3. Prediction of cyclic softening

One of the main phenomena observed in 9-12Cr steels during fatigue loading is cyclic softening, as illustrated in Chapter 3. As power plants move to more flexible operation, heavy wall 9-12Cr steel components such as header units will be subjected to increased fatigue loading and hence, cyclic softening. This will result in a significant decrease in the creep strength of the material [Dubey et al., 2005; Fournier et al., 2009a; Fournier et al., 2009b] and reduced component life. Hence, to successfully capture the constitutive behaviour of the material, accurate prediction of cyclic softening is required. Figure 4.33 and Figure 4.34 illustrate the ability of the material model to capture the stress-strain response at different cycles for various strain-rates and strain-ranges, at temperatures of 400 °C, 500 °C and 600 °C. The stress-strain response in Figure 4.35 shows the effect of temperature variation on stress-strain response and the ability of the material model to predict the softening observed.

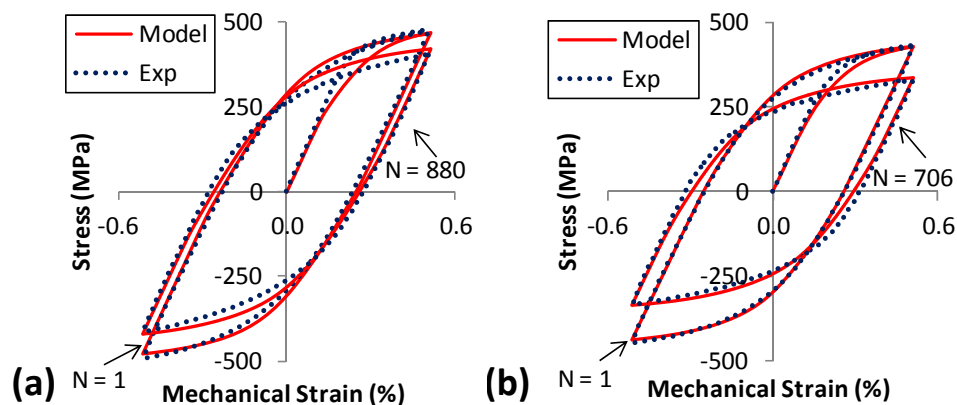


Figure 4.33: FE predicted and experimentally observed stress-strain response at a strain-rate of 0.25 %/s and ± 0.5 % applied strain-range at temperatures of (a) 400 °C for the initial and 880th cycles and (b) 500 °C for the initial and 706th cycles.

4. A Unified Cyclic Viscoplastic Modelling Framework for Strain-Rate Dependent Materials

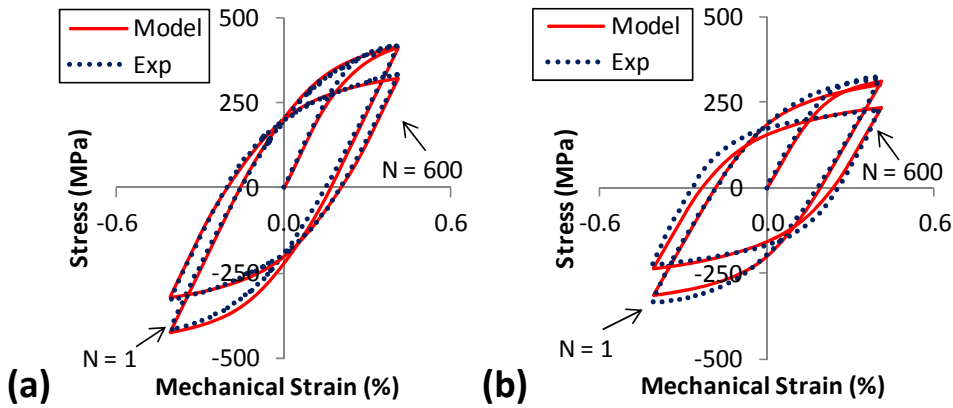


Figure 4.34: FE predicted and experimentally observed stress-strain response following an applied strain-rate of 0.033 %/s and applied strain-range of ± 0.4 % for the initial and 600th loop at a temperature of (a) 500 °C and (b) 600 °C.

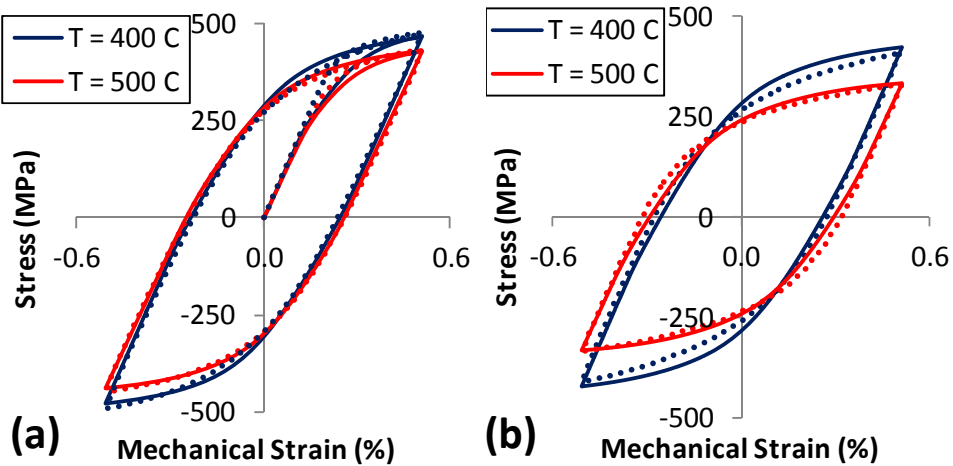


Figure 4.35: Comparison of the FE predicted (solid line) and experimentally measured (dotted line) stress-strain response at temperatures of 400 °C and 500 °C for (a) the initial cycle and (b) the half-life at an applied strain-rate of 0.025 %/s.

4.6.2.4. Capturing strain-rate effects in ex-service P91 steel

As power generation moves to more flexible operation, one of the key requirements for any material model is its ability to predict strain-rate effects accurately, with the observed thermal gradients during start-up [Farragher et al., 2013a; Farragher et al., 2013b] leading to variable strain-rate loading. To validate the performance of the hyperbolic sine formulation across a range of strain-rates, the model is applied to (i) stress relaxation

4. A Unified Cyclic Viscoplastic Modelling Framework for Strain-Rate Dependent Materials

loading conditions and (ii) a broad range of strain-rates. This broad range of strain-rates includes intermediate strain-rate values of 5×10^{-4} %/s to higher strain-rate values in the typical experimental regime of 0.1 %/s to 0.01 %/s. The lower strain-rates, in the order of 1×10^{-7} to 1×10^{-10} %/s, typically constitute pure creep loading (i.e. where creep diffusion and migration of vacancies are the primary mechanisms of deformation [Hertzberg, 1996; Nabarro, 2002] in place of dislocation glide and climb mechanisms under flexible loading conditions [Ashby and Jones, 2012] as shown in Figure 4.36) and hence, are beyond the scope of the regime of the unified cyclic viscoplastic material model.

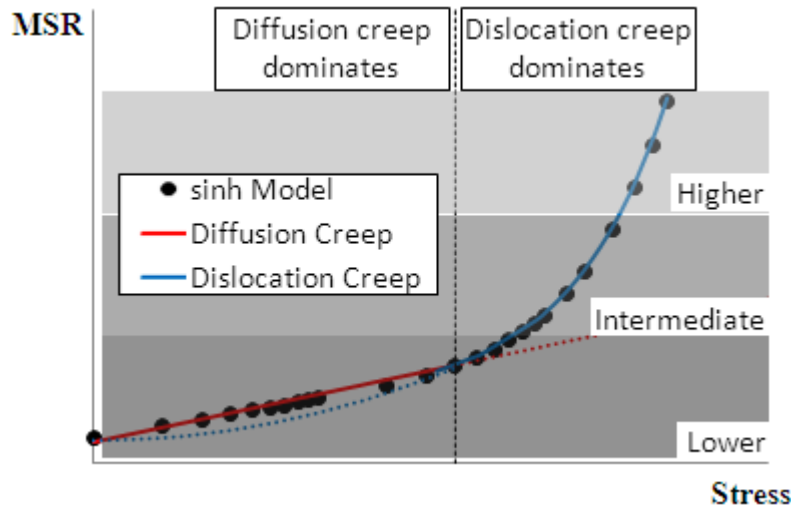


Figure 4.36: Deformation mechanisms and strain-rate regimes in 9-12Cr steels.

As discussed in Chapter 3, a large strain-rate effect is observed at 600 °C with little or no such effect observed at 500 °C and less. To capture this effect, careful choice of the cyclic viscoplastic material parameters, (α and β), is required, via the use of Equation (4.72) in conjunction with long-term creep data. Figure 4.30 and Figure 4.31 illustrate the ability of the hyperbolic sine formulation to predict the stress relaxation behaviour (via comparison with measured stress and plastic-strain responses), showing excellent agreement with the experimental data across a range of temperatures. Figure 4.37 illustrates the accuracy of agreement achieved for

4. A Unified Cyclic Viscoplastic Modelling Framework for Strain-Rate Dependent Materials

HTLCF loading conditions at varying strain-rates, demonstrating the capability of the model to predict the strain-rate effect.

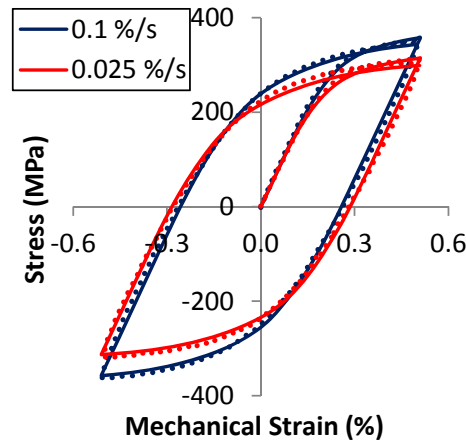


Figure 4.37: Comparison of the FE predicted and experimentally measured stress-strain response for the initial cycle at a temperature of 600 °C and applied strain-range of ± 0.5 %.

4.6.3. Application of the material model to MarBN

The material model is also applied to cast MarBN under the test conditions of Table 3.2 to (i) calibrate, and (ii) validate, the parameter identification methodology and hyperbolic sine modelling framework for alternative materials. As with 'as received' and ex-service P91 steel, calibration of cast MarBN is strictly conducted under a strain-rate of 0.1 %/s at an applied strain-range of ± 0.5 %, following the material parameter identification process of Section 4.5. Figure 4.38 illustrates the identification of the cyclic softening material parameters, b_i and Q_i for MarBN, as well as highlighting the benefit of including a second cyclic softening term. Figure 4.39 illustrates the identification of the NLKH material parameters using Equation (4.52) and Equation (4.60).

4. A Unified Cyclic Viscoplastic Modelling Framework for Strain-Rate Dependent Materials

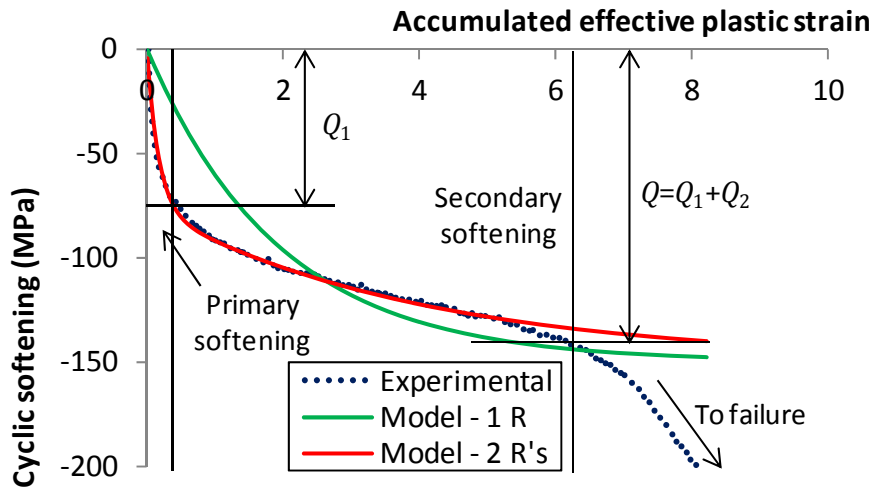


Figure 4.38: Identification of the cast MarBN cyclic softening material parameters at 600 °C.

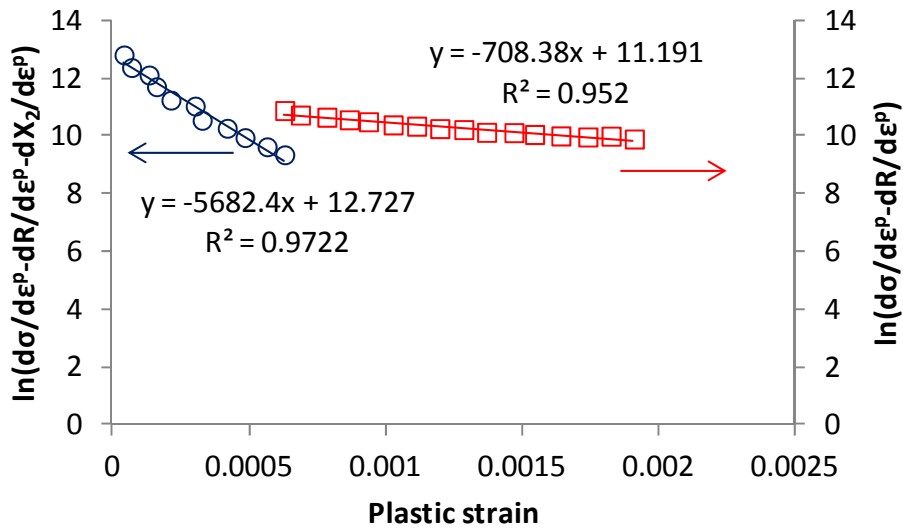


Figure 4.39: Identification of the NLKH material parameters for cast MarBN at 600 °C.

For P91 steel, as presented in Section 4.6.1 and Section 4.6.2, the cyclic viscoplastic material parameter, β , was identified from long-term minimum creep-rate data. However, as MarBN steel is still in the early stages of development, such long-term creep data is not available at present. Hence, β for MarBN is identified via comparison with (i) stress relaxation data and (ii) values obtained for P91 steel data. Figure 4.40 compares the stress

4. A Unified Cyclic Viscoplastic Modelling Framework for Strain-Rate Dependent Materials

relaxation behaviour (normalised against the value at the start of the dwell period) of ex-service P91 steel and cast MarBN. At a temperature of 600 °C, stress relaxation occurs at an increased rate in ex-service P91 steel. Hence, from Equation (4.72), a lower value of the cyclic viscoplastic parameter, β , is required to capture the lower values of stress relaxation during a tensile hold period in cast MarBN. Figure 4.41 compares the fit obtained with stress relaxation data during the identification procedure, where the material parameter, α , is identified from Equation (4.72) using a least squares fitting procedure.

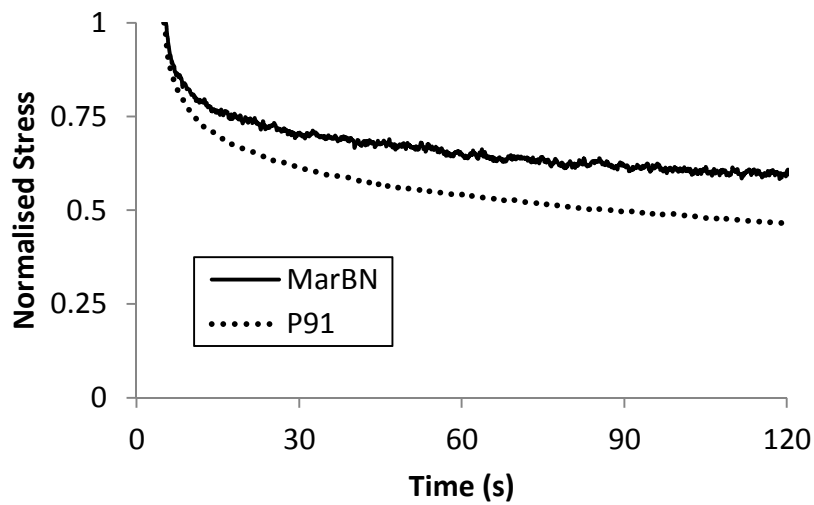


Figure 4.40: Comparison of the measured stress relaxation behaviour in ex-service P91 steel and cast MarBN at a temperature of 600 °C.

4. A Unified Cyclic Viscoplastic Modelling Framework for Strain-Rate Dependent Materials

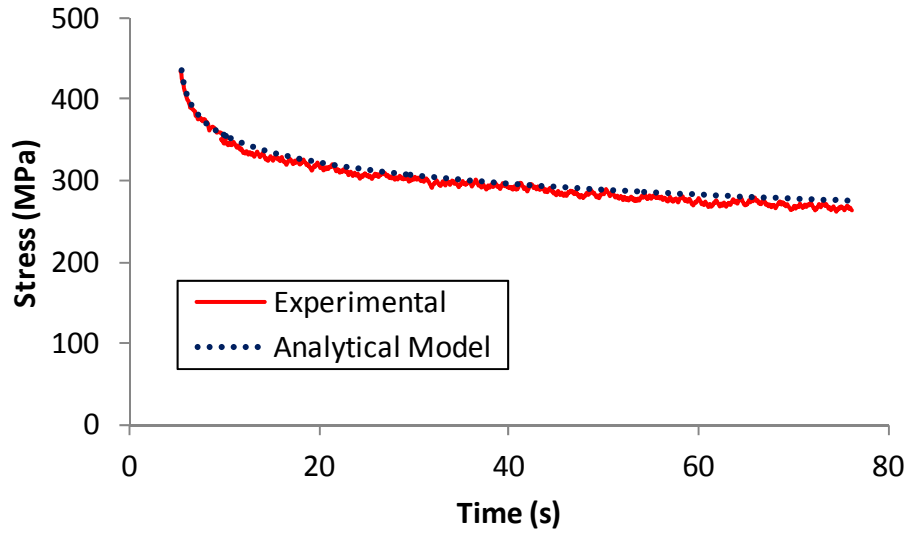


Figure 4.41: Identification of the cast MarBN cyclic viscoplastic material parameters using the analytical model for stress relaxation at a temperature of 600 °C.

Table 4.8 presents the complete set of identified material parameters for cast MarBN at 600 °C and Figure 4.42 illustrates the accuracy of agreement achieved for the initial monotonic response and subsequent stress relaxation behaviour under the calibration conditions. Following calibration, the material model and identified material parameters are validated against experimental data under alternative strain-rates and strain-ranges to investigate the performance of the material model across varying loading conditions, as presented below.

Table 4.8: Identified material parameters for cast MarBN at 600 °C.

Parameter	Value	Parameter	Value
E (GPa)	162	C_1 (MPa)	295966
k (MPa)	100	γ_1 (-)	5488.1
Q_1 (MPa)	-76.14	C_2 (MPa)	61574.3
b_1 (-)	5.90	γ_2 (-)	601.4
Q_2 (MPa)	-73.81	α (/s)	2×10^{-6}
b_2 (-)	0.25	β (/MPa)	0.031

4. A Unified Cyclic Viscoplastic Modelling Framework for Strain-Rate Dependent Materials

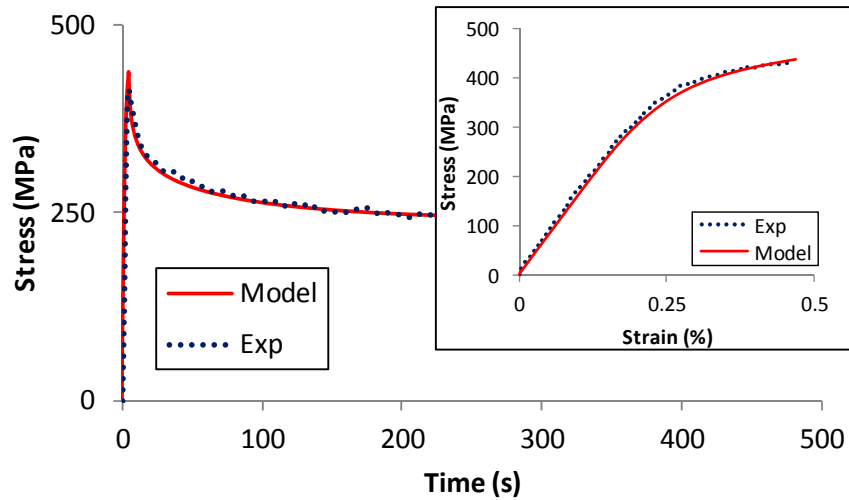


Figure 4.42: Comparison of the correlation achieved with experimental data under the calibration regime for stress relaxation and the monotonic stress-strain response (inset) at 600 °C.

Further validation of the performance of the material model is achieved via comparison with test data at different strain-ranges and strain-rates for MarBN at 600 °C. Figure 4.43 illustrates the prediction of the material model across different strain-ranges. Figure 4.44 highlights the prediction of the model for the strain-rate effect for initial and half-life cycles. These results also highlight the importance of using the hyperbolic sine flow rule in conjunction with the cyclic viscoplastic material parameter identification method developed in Section 4.5. The accuracy of agreement achieved when predicting the cyclic softening behaviour during the first 400 cycles is presented in Figure 4.45 for a strain-rate of 0.01 %/s at an applied strain-range of ± 0.5 %. Figure 4.45 also includes a comparison of the evolution of plastic strain-range with the experimentally measured values under the same conditions.

4. A Unified Cyclic Viscoplastic Modelling Framework for Strain-Rate Dependent Materials

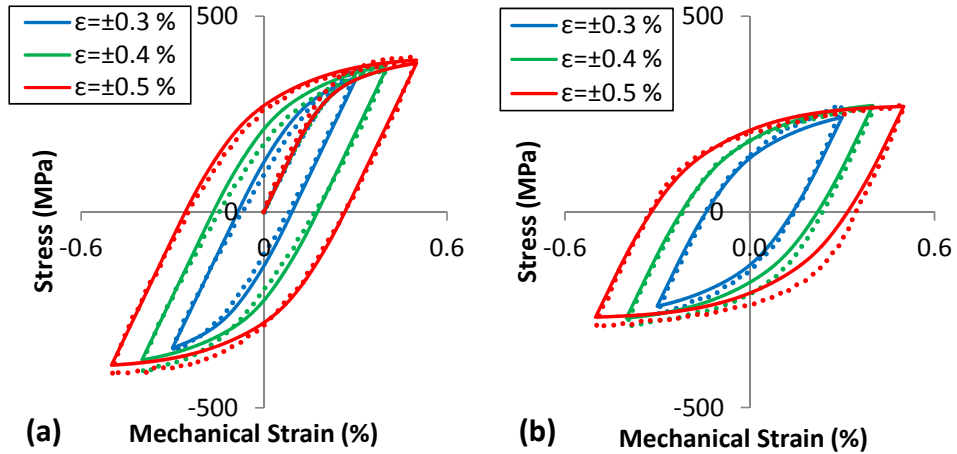


Figure 4.43: Comparison of the FE predicted (solid line) and experimentally observed (dotted line) stress-strain response at temperatures in cast MarBN steel for (a) the initial loop and (b) the half-life cycle at an applied strain-rate of 0.01 %/s.

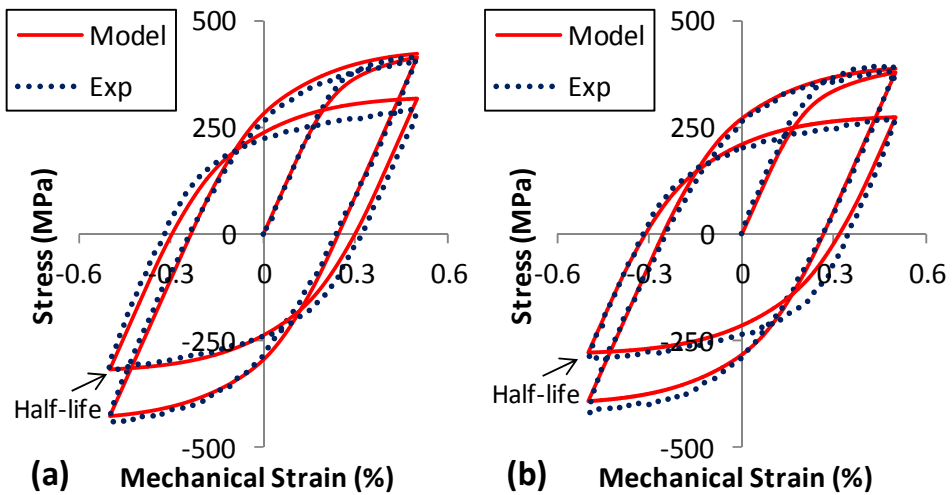


Figure 4.44: Measured (dotted lines) and predicted (solid line) stress-strain response for the initial and half-life cycles in cast MarBN at 600 °C for an applied strain-range of $\pm 0.5\%$ at strain-rates of (a) 0.033 %/s and (b) 0.01 %/s.

4. A Unified Cyclic Viscoplastic Modelling Framework for Strain-Rate Dependent Materials

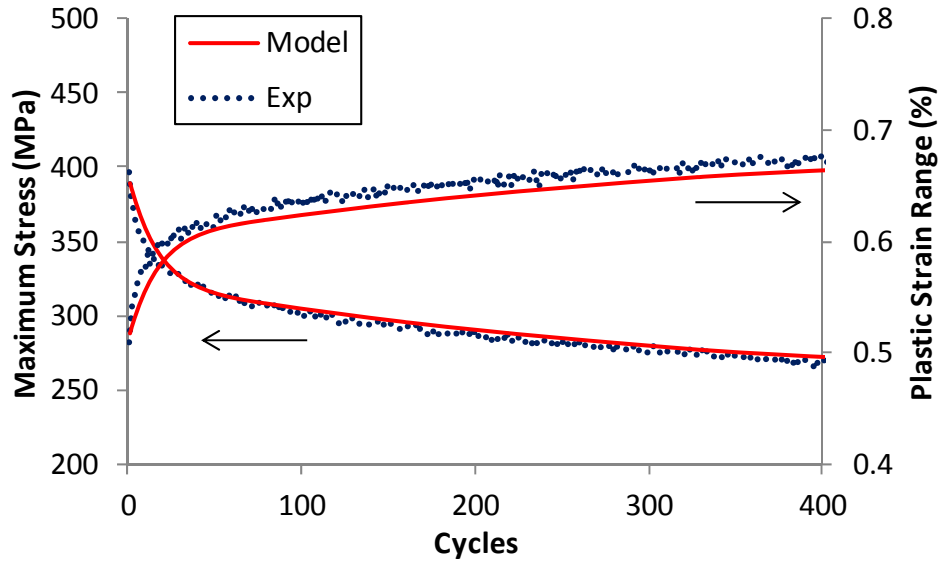


Figure 4.45: Comparison of the maximum stress and plastic strain-range evolution with cycles in cast MarBN at 600 °C, a strain-rate of 0.01 %/s and applied strain-range of ± 0.5 %.

4.7. Life prediction

Life prediction is carried out using the Coffin-Manson life prediction methodology [Coffin, 1954; Manson, 1953] of Equation (3.1) and represents a measure of the ability of the material model to accurately predict the correct plastic strain-range. The Coffin-Manson material parameters were presented in Table 3.4 and Figure 4.46 presents a comparison between the predicted number of cycles to failure and the experimentally observed values. The predicted results are shown to agree with the test data to within a factor of 1.15.

4. A Unified Cyclic Viscoplastic Modelling Framework for Strain-Rate Dependent Materials

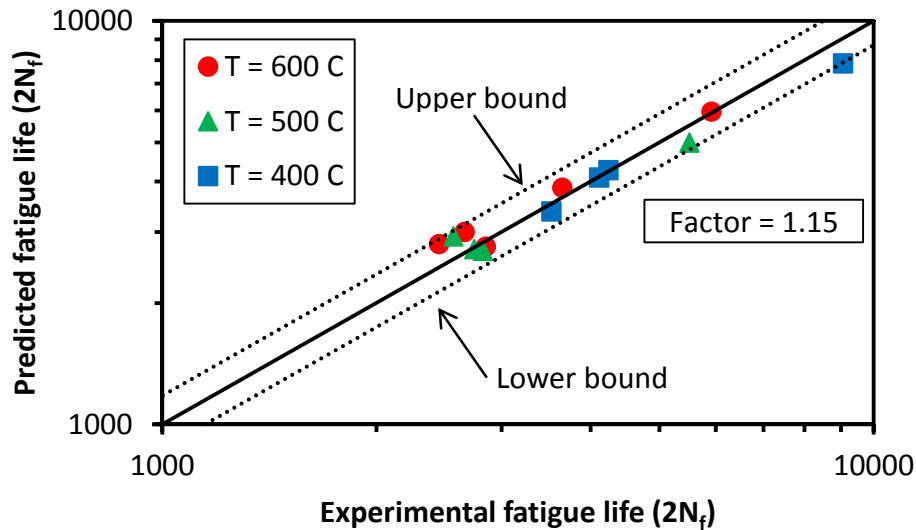


Figure 4.46: Comparison of Coffin-Manson predicted number of cycles to failure with the number of cycles to failure obtained from HTLCF tests.

4.8. Discussion

This chapter presents an improved (hyperbolic sine) unified cyclic viscoplastic material model capable of capturing the complex high temperature material behaviour of 9-12Cr steels under cyclic loading conditions. The material model is implemented in a UMAT user material subroutine for use with the commercial finite element code Abaqus and the model is successfully validated for a range of uniaxial loading conditions. The benefit of using the hyperbolic sine material model is its ability to capture the measured strain-rate sensitivity of stress, as illustrated in Figure 4.10, and hence enables the identification of material parameters which are independent of strain-rate. This contrasts with the more conventional (Chaboche) power law unified cyclic viscoplastic model [Chaboche and Rousselier, 1983a; Chaboche and Rousselier, 1983b; Hyde et al., 2010; Koo and Kwon, 2011; Lemaitre and Chaboche, 2000; Saad et al., 2011], which is limited to a narrow range of strain-rates via the constraint of constant strain-rate sensitivity.

A parameter identification methodology, coupled with uniaxial calibration and validation for the hyperbolic sine unified cyclic viscoplastic material model is also developed and applied in this chapter. The identification of the

4. A Unified Cyclic Viscoplastic Modelling Framework for Strain-Rate Dependent Materials

fourteen material parameters is conducted via a step-by-step procedure, where the elastic material parameters are identified first, followed by the cyclic softening parameters and NLKH material constants from a single isothermal fatigue test. Finally, the cyclic viscoplastic material parameters are identified from stress relaxation test data to enable strain-rate effects to be predicted. This validated methodology is both efficient and economically beneficial as only two tests are required per temperature to identify a valid set of material parameters. Compared to other parameter identification methods [*Lemaitre and Chaboche, 2000*], this methodology allows more model validation to be conducted, for a similar experimental program.

Initially, the possibility of identifying the material parameters using more complex identification methods, i.e. using genetic algorithms [*Mahmoudi et al., 2011*], was investigated. However, this approach can lead to inaccuracies in the values of material constants identified, resulting in the omission of strain-rate independent material constants, for instance. Such approaches have the potential to play an important role in the optimisation of material parameters if, and only if, this optimisation is conducted via careful selection of an initial set of material parameters, e.g. the process of Figure 4.6. For the material parameters identified here, this new procedure effectively allows for a unique set of constants to be determined for a given material and temperature, enabling increased confidence when interpolating and extrapolating to alternative loading conditions.

The key step in the identification of a set of strain-rate sensitive material parameters relates to the determination of the cyclic viscoplastic material parameters, α and β . These parameters could be identified via correlation with the cyclic stress-strain data across multiple strain-rates. However, such an approach would require additional material data to conduct a full calibration and validation program. For the intermediate to low strain-rates required for simulating realistic plant loading conditions, this would be a costly and time-consuming process. Hence, the approach of identifying the cyclic viscoplastic material parameters from the dwell period of stress relaxation tests is more efficient and effective. For the hyperbolic sine

4. A Unified Cyclic Viscoplastic Modelling Framework for Strain-Rate Dependent Materials

formulation, the analytical model for stress as a function of time during a dwell period is derived in Section 4.5.4. Application of the fitting procedure in Section 4.5 highlights the requirement for careful choice of the cyclic viscoplastic material parameters. A satisfactory correlation can be achieved with the stress relaxation test data and a selection of strain-rates. However, the proposed methodology of identifying the viscous parameter, β , from minimum creep strain-rate (MSR) data alleviates this problem and a simple least squares fitting procedure can be used in conjunction with Equation (4.72) to identify a strain-rate independent value for α . The identification of pure creep material parameters, α_{CR} and β_{CR} , and the subsequent determination of a scaled value of the cyclic viscoplastic parameter α , represents a significant step towards reconciling long- and short-term creep data and is the key step to capturing the strain-rate effect. As presented in Section 4.6, identification of the viscous parameter, β , is relatively straight forward, provided the relevant creep data is available.

The NLKH parameter identification methodology presented here is an extension of the method derived in Zhan [2004] as successfully applied to 316 stainless steel and P91 steel in Hyde *et al.* [2010] and Saad *et al.* [2011], respectively. The benefit of this approach, over the commonly used method of Chaboche [Lemaitre and Chaboche, 2000], is the ability to define NLKH material parameters for multiple back-stress terms. Furthermore, the Zhan method only requires calibration from a single experiment compared to the Chaboche method [Lemaitre and Chaboche, 2000], which requires test data across multiple strain-ranges. Zhan also presented results for the identification of the NLKH material parameters from (i) the initial monotonic stress-strain curve and (ii) stabilised stress-strain response. In the present study, only calibration from the monotonic test data (initial monotonic region of the first cycle), is conducted. Implementing the second approach of Zhan may provide slight enhancements to the choice of material parameters, but the quality of fits achieved in Figure 4.33 to Figure 4.35, for example, proved more than satisfactory.

4. A Unified Cyclic Viscoplastic Modelling Framework for Strain-Rate Dependent Materials

As discussed in Sweeney *et al.* [2015], the identification of the Armstrong-Frederick NLKH back-stress material parameters can be achieved by first fitting long-term parameters to tensile test data (tested to ultimate tensile strength or greater) and then fitting a second set of NLKH parameters to smaller strain ranges to capture short-range NLKH material behaviour. In the present work, a similar approach is employed, restricted to the initial and later stages of kinematic hardening within the LCF test data, as in the work of Saad *et al.* [2011]. As power plant components are subjected to plastic strains much less than those observed during HTLCF testing at a strain range of $\pm 0.5\%$ [Farragher, 2013; Farragher *et al.*, 2013a; Farragher *et al.*, 2013b], the identification of NLKH material parameters from this range is more than adequate for future component level applications of the present modelling framework. For the purpose of comparison with test data, and as a more general recommendation, material parameter identification should be conducted at strain-ranges equal to or greater than the typical application to ensure that identified material parameters are applicable to the full test regime.

The choice of the isotropic hardening model described in Equation (4.10), coupled with a negative Q value, as highlighted in Saad *et al.* [2011], allows for the cyclic softening behaviour of martensitic steels to be modelled, with reductions of up to 22 % measured in the maximum stress per cycle by Saad and co-workers [2011]. The inclusion of a second non-linear cyclic softening term in Sections 4.6.2 and 4.6.3, compared to the results presented in Section 4.6.1, leads to a significant improvement in the prediction of the cyclic softening behaviour. These improved results are presented in Figure 4.4 and Figure 4.38 and highlight the requirement for the inclusion of an adequate number of softening terms, i.e. two terms required for 9-12Cr steels, to predict cyclic softening. Although the softening parameters are relatively easy to determine, precise identification of these parameters is required for modelling of realistic plant conditions, as the softening behaviour reduces the creep strength of the material. This degradation in material performance, in turn, adversely affects plant life.

4. A Unified Cyclic Viscoplastic Modelling Framework for Strain-Rate Dependent Materials

At a temperature of 600 °C, the value of $k + Q$ can become negative, resulting in a negative yield surface. Future work should consider including a constraint in the material parameter identification methodology to ensure that $k + Q > 0$. However, with the present constitutive model, it may be difficult to achieve a satisfactory fit to experimental data for both HTLCF and stress relaxation behaviour. Thus, alternative methods, such as the stress partition method [Cottrell, 1953; Keller *et al.*, 2010; Lu *et al.*, 2015] should also be considered. An alternative method to this is the concept of a physically-based macro-scale model, as presented in Chapter 6 and Chapter 7. These models ensure a more realistic value of the cyclic yield stress is obtained and also have the capability to account for key microstructural mechanisms, including the evolution of the spacing of precipitates. The $M_{23}C_6$ and MX particles in 9Cr steels provide a kinematic back-stress and as these particles coarsen under thermal- and strain-dependent loading [Hu *et al.*, 2013; Taneike, 2001], a decrease in maximum (kinematic hardening) stress may occur. In the current approach, such microstructural evolution is not accounted for and may lead to an over prediction of the level of softening in the material model, and hence, excessive isotropic softening.

Lemaitre and Chaboche [2000] discuss the inclusion of a recovery term in the context of stainless steel and a similar term is presented for aluminium alloys in Felfeli *et al.* [2015]. Similar consideration was given in the current work. However, during cyclic deformation, the high-angle boundary quantities, i.e. blocks, packets and prior austenite grains, do not coarsen [Touboul *et al.*, 2012] and the work of Sauzay and co-workers [Sauzay *et al.*, 2005; Sauzay *et al.*, 2008], has identified low-angle boundary annihilation as the mechanism for martensitic lath growth in 9-12Cr steels. Thus, the apparent recovery in 9-12Cr steels can be related to the loss of low-angle boundaries. For this reason, no recovery term is included in the current NLKH modelling framework, as cyclic softening (due to loss of low-angle boundaries) is adequately predicted using the current model, as presented in the results of Figure 4.33 to Figure 4.35. The inclusion of such a term would unnecessarily include additional material parameters. Furthermore, Sauzay and co-workers [Sauzay *et al.*, 2005; Sauzay *et al.*,

4. A Unified Cyclic Viscoplastic Modelling Framework for Strain-Rate Dependent Materials

2008] proposed a suitable model to account for low-angle boundary annihilation. A similar model is derived and extended in Chapters 6 and 7.

The results of the validation process illustrate that the material model can be used to predict the constitutive behaviour of high Cr steels across a broad range of strain-rates and strain ranges. This ability is typified by Figure 4.16, which portrays the relaxation behaviour of 'as received' P91 steel, obtaining excellent agreement with the experimental data at 500 °C and a reasonable fit with the experimental data at the intermediate temperature of 550 °C. The results depicted in Figure 4.17 to Figure 4.19 show that the material model is capable of reproducing the isothermal cyclic constitutive behaviour for the test conditions of Koo and Kwon [2011] and Fournier et al. [2011], to a high degree of accuracy at strain-rates of 0.01 %/s and 1.0 %/s respectively, which lie outside the range of calibration. Similar results are presented in Figure 4.37 and Figure 4.44 for ex-service P91 steel and cast MarBN, respectively. These results show that the hyperbolic sine unified cyclic viscoplasticity model can accurately capture the strain-rate effect observed in high Cr steels under high temperature loading, to facilitate accurate interpolation and extrapolation from the limited range of experimental data typically available. This is important for simulating, and hence, designing for the requirements of flexible operating conditions of modern [Farragher et al., 2013a; Farragher et al., 2013b] and next generation plant.

From Figure 4.20 to Figure 4.22, the FE predicted results show excellent correlation with the TMF test data of Saad et al. [2011], particularly for the initial cycles and in-phase loading conditions. The slight over-prediction of the stress range, by approximately 5 % for out-of-phase TMF, in the 400 °C to 500 °C temperature range, is attributed to non-optimised material parameters, including the coefficient of thermal expansion, and the use of a piece-wise linear interpolation scheme. The opportunity exists for the development of more complex global optimisation techniques, such as presented by Gong et al. [2010], Huber and Tsakmakis, [2001] and Mahmoudi et al. [2011], which may be used to obtain more precise material

4. A Unified Cyclic Viscoplastic Modelling Framework for Strain-Rate Dependent Materials

parameters. The inclusion of an Arrhenius type function, following Nagode *et al.* [2011], Henshall *et al.* [1996] and Miller [1987], may give further improvements and simplification in the interpolation of material parameters as a function of temperature. Furthermore, the impact of the inclusion of temperature-rate terms in Equations (4.10) and (4.13) is found to have a beneficial impact for the conditions simulated here.

The increased stress range in cast MarBN when compared to ex-service P91 steel (approximately 120 MPa) is predominantly captured in the current model via (i) an increased initial cyclic yield stress value of 100 MPa compared with 55 MPa for ex-service P91 steel and (ii) an increased initial hardening modulus, C_1 , of 295 GPa compared with 275 GPa for ex-service P91 steel. Although the increased initial cyclic yield stress observed in the coarser cast MarBN does not appear to follow the Hall-Petch relationship, this is attributed here to other strengthening mechanisms, such as the solute strengthening due to the inclusion of tungsten and cobalt, contributing to the increased yield stress and hence, increased initial cyclic yield stress, k . The increased NLKH contribution is analogous to the increased Orowan back-stress attributed to the reduced precipitate spacing obtained by boron enrichment of grain boundaries in the cast MarBN and possibly the presence of additional $W_{23}C_6$ carbides.

The predicted number of cycles to failure presented in Figure 4.46, which all lie within 15 % of the values obtained experimentally, illustrates the ability of the current material model to replicate the plastic strain-ranges produced in HTLCF experiments. As plastic strain-range is a primary variable for most life prediction methods and coupled with the extrapolation capability of the hyperbolic sine formulation, it is argued that the accurate life prediction produced at the specimen level will provide confidence when applying this material model to realistic plant geometries and loading conditions, e.g. similar to Farragher *et al.* [2013a]. This accuracy of agreement is paramount to precise life assessment of power plant components subjected to TMF and determination of remaining life of current power plant components.

4. A Unified Cyclic Viscoplastic Modelling Framework for Strain-Rate Dependent Materials

4.9. Conclusions

This chapter presents the development and multi-axial implementation of a novel hyperbolic sine unified cyclic viscoplastic material model and step-by-step methodology for the determination of the fourteen material parameters in the hyperbolic sine model. This approach enables the hyperbolic sine material model to predict (i) strain-range behaviour, (ii) strain-rate effects and (iii) cyclic softening across a range of different temperatures. The key novel contributions of this study are as follows:

- An improved unified cyclic viscoplasticity model, via a hyperbolic sine flow rule with cyclic evolution of nonlinear isotropic and kinematic hardening, to achieve significantly improved strain-rate sensitivity for high temperature fatigue applications. This is important for life prediction of modern power plant under significantly more flexible operation modes.
- Multi-axial implementation of the material model in a UMAT user subroutine, incorporating cyclic evolution of isotropic and kinematic hardening and creep effects under anisothermal loading conditions, using an implicit integration scheme.
- The step-by-step parameter identification methodology enables the fourteen material parameters to be determined without the need for complex parameter identification methodologies, such as genetic algorithms.
- The development of an analytical model for the determination of the cyclic viscoplastic material parameters allows the strain-rate behaviour of 9-12Cr steels to be predicted. As power plants transition to flexible operation, this ability to predict the strain-rate effect represents a key requirement for simulating next generation power plant components.
- Calibration and validation of the hyperbolic sine unified cyclic viscoplastic material model is conducted for (i) 'as received' P91 steel, (ii) ex-service P91 steel and (iii) cast MarBN. Validation is performed across a range of strain-ranges, strain-rates and

4. A Unified Cyclic Viscoplastic Modelling Framework for Strain-Rate Dependent Materials

temperatures to evaluate the performance of the model across a broad range loading of conditions. This represents the first application of a viscoplastic material model to fatigue of 9Cr-3W-3Co-NbV (MarBN) steels.

- The incorporation of two non-linear kinematic back-stress terms is found to be adequate for the prediction of the kinematic behaviour observed in 9-12Cr steels. More terms could easily be included, but at the expense of identifying additional material parameters.
- The inclusion of a second non-linear cyclic softening term allows significant improvements to be achieved in the prediction of the primary cyclic softening region over a material model with a single cyclic softening term.
- The results illustrate the ability of the model to capture the strain-rate effect of 9-12Cr steels. The identification of the viscous material parameters using the analytical model for stress relaxation in combination with the longer-term creep behaviour of P91 steels is found to be critical in accurately capturing strain-rate effects.
- The modelling of TMF test conditions via temperature-rate terms in the evolution equations of the hardening variables and temperature-dependent material parameters, identified from isothermal test data for 'as received' P91 power plant material.
- The results of the implementation of the Coffin-Manson fatigue life prediction demonstrated excellent agreement with the experimentally observed values. The results all lie within 15 % of the experiments, illustrating the ability of hyperbolic sine formulation developed here to accurately predict the plastic strain-range observed under fatigue loading.

The next chapter presents applications of the hyperbolic sine unified cyclic viscoplastic material model to thermo-mechanical fatigue and multi-axial loading conditions. Chapter 5 validates the hyperbolic sine UMAT user material subroutine for multi-axial loading conditions via comparison with notched specimen testing. The material model is also applied to a variety of different loading conditions to assess the ability of the multi-axial material

4. A Unified Cyclic Viscoplastic Modelling Framework for Strain-Rate Dependent Materials

model to predict strain-rate effects across a range of temperatures and strain-ranges.

5. Application of a Unified Cyclic Viscoplastic Material Model to Thermo-mechanical and Multi-Axial Fatigue

5.1. Introduction

Applications of the unified cyclic viscoplastic material model developed in Chapter 4 are presented in this chapter. TMF, notched specimen (NS) modelling and thin-walled tubing simulations are performed to investigate the robustness and ability of the hyperbolic sine material model across a broad range of loading conditions.

The prediction of TMF behaviour represents a key loading scenario for modern and next generation power plants as intermittent mode operation comes online. As illustrated in Chapter 3, TMF loading has a significant effect on the life of 9Cr steels and hence, power plants under flexible operation. Section 5.2 focuses on simulating the constitutive behaviour of ES-P91 steel using the hyperbolic sine unified cyclic viscoplastic material model of Chapter 4.

Section 5.3 presents numerical simulations of test specimens with notches of varying radii included to investigate multi-axial predictions made using the hyperbolic sine configuration. This section provides multi-axial validation of the numerical modelling methodology developed in Chapter 4 via life prediction using the approach of Coffin-Manson [*Coffin, 1954; Manson, 1953*] and comparison with NS tests carried out on ES-P91 steel. Further analysis using the hyperbolic sine formulation is carried out via comparison with an equivalent Chaboche power law unified cyclic viscoplastic material model [*Chaboche and Rousselier, 1983a; Chaboche and Rousselier, 1983b*]. The constitutive behaviour of the AR-P91 steel [*Saad et al., 2011a*] and fatigue life is predicted using both models, highlighting the potential benefits of using the hyperbolic sine formulation.

The material model is also applied to a thin-walled tube in Section 5.4, which is representative of piping systems in a power plant. The material model is applied in the calibrated regime of 400 to 600 °C. Two simplified

5. Application of a Unified Cyclic Viscoplastic Material Model to Thermo-mechanical and Multi-Axial Fatigue

pressure-temperature cycles are simulated in this study, (i) a low pressure regime illustrative of subcritical plant operation and (ii) a high pressure loading to simulate typical pressures observed in an ultra-supercritical power plant. Ratchetting is predicted in some cases and failure is predicted using a ratcheting life assessment methodology [Mohd Tobi *et al.*, 2009; Zhang *et al.*, 2011].

5.2. Simulating thermo-mechanical fatigue in ex-service P91

To provide further validation of the UMAT user material subroutine and the step-by-step material parameter identification methodology developed in Chapter 4, TMF simulations are carried out on the ES-P91 specimens as per the TMF test conditions presented in Chapter 3. As these tests are conducted under anisothermal conditions at different strain-rates to that of calibration, this validation represents verification of the model's ability to predict (i) strain-rate effects and (ii) capture the effects of thermal transients, such as those presented in Figure 1.2a.

Figure 5.1 illustrates the comparison of the FE predicted stress-strain response for the initial and 300th hysteresis loops at two different strain-rates in the 400 °C to 600 °C temperature range for TMF-IP loading conditions. Initially, the model achieves an excellent fit with the measured data. However, the correlation achieved for the 300th loop in all cases is inferior to that of the initial cycle. A similar result is achieved for the out-of-phase (TMF-OP) case in the same temperature range and applied strain-rates, as presented in Figure 5.2. The poorer fit obtained for the lower temperature regions of the loops at the later cycles is indicative of non-optimised cyclic softening material constants. It is anticipated that further refinement of these parameters would achieve a better fit.

5. Application of a Unified Cyclic Viscoplastic Material Model to Thermo-mechanical and Multi-Axial Fatigue

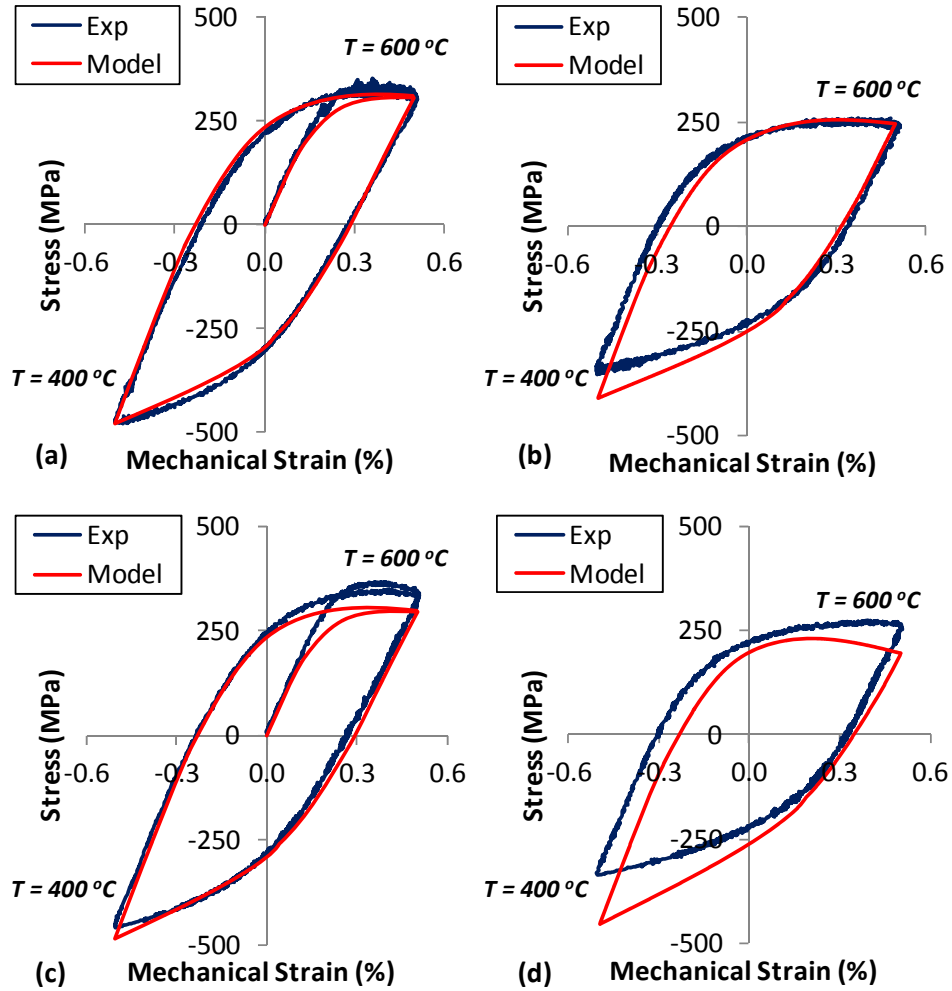


Figure 5.1: Effect of strain-rate on TMF-IP behaviour for (a) initial cycle at an applied strain-rate of 0.033 %/s, (b) the 300th cycle at 0.033 %/s, (c) initial cycle at 0.025 %/s and (d) 300th cycle at 0.025 %/s in the 400 °C to 600 °C temperature range.

5. Application of a Unified Cyclic Viscoplastic Material Model to Thermo-mechanical and Multi-Axial Fatigue

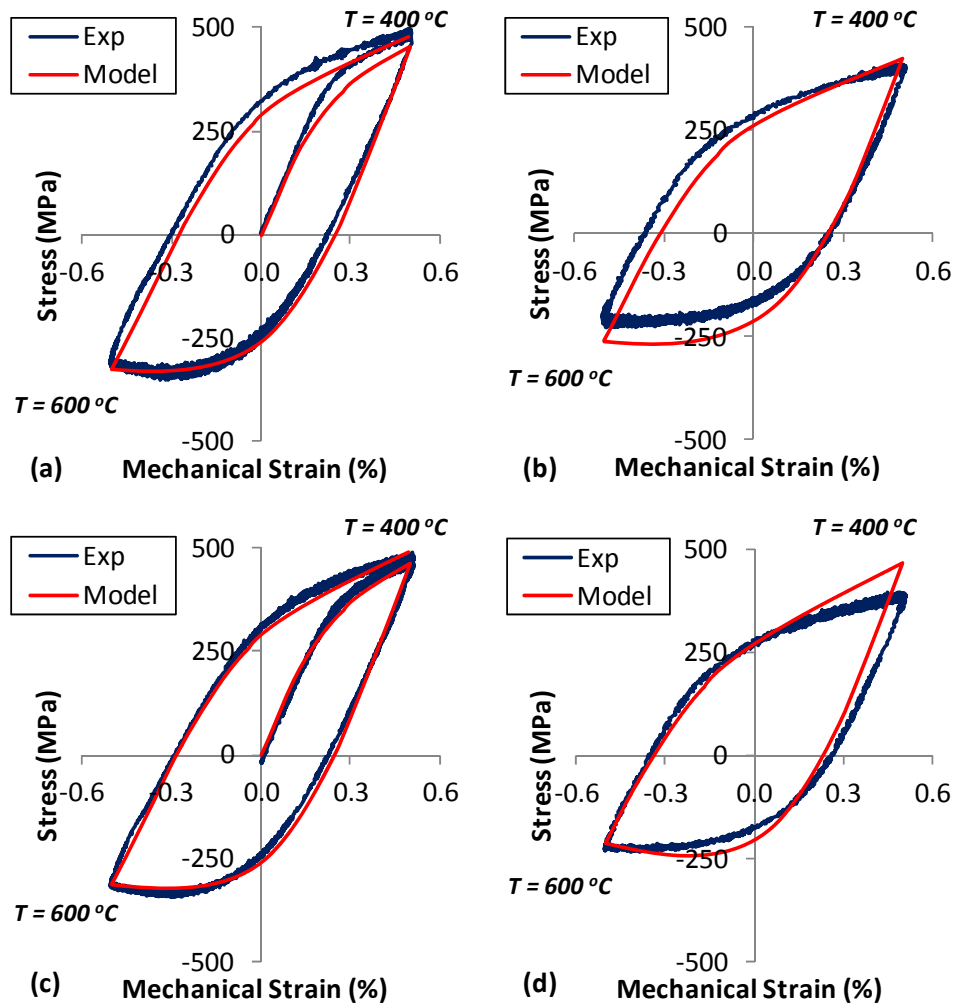


Figure 5.2: Effect of strain-rate on TMF-OP behaviour for (a) initial cycle at an applied strain-rate of 0.033 %/s, (b) the 150th cycle at 0.033 %/s, (c) initial cycle at 0.025 %/s and (d) 150th cycle at 0.025 %/s in the 400 °C to 600 °C temperature range.

Figure 5.3 highlights the ability of the material model to operate across various strain-ranges. These results correspond to different strain-rates to those used for calibration. Once again, an excellent correlation is achieved for the high temperature portion of the curve throughout. However, the issue of non-optimised cyclic softening parameters is evident from the results presented.

5. Application of a Unified Cyclic Viscoplastic Material Model to Thermo-mechanical and Multi-Axial Fatigue

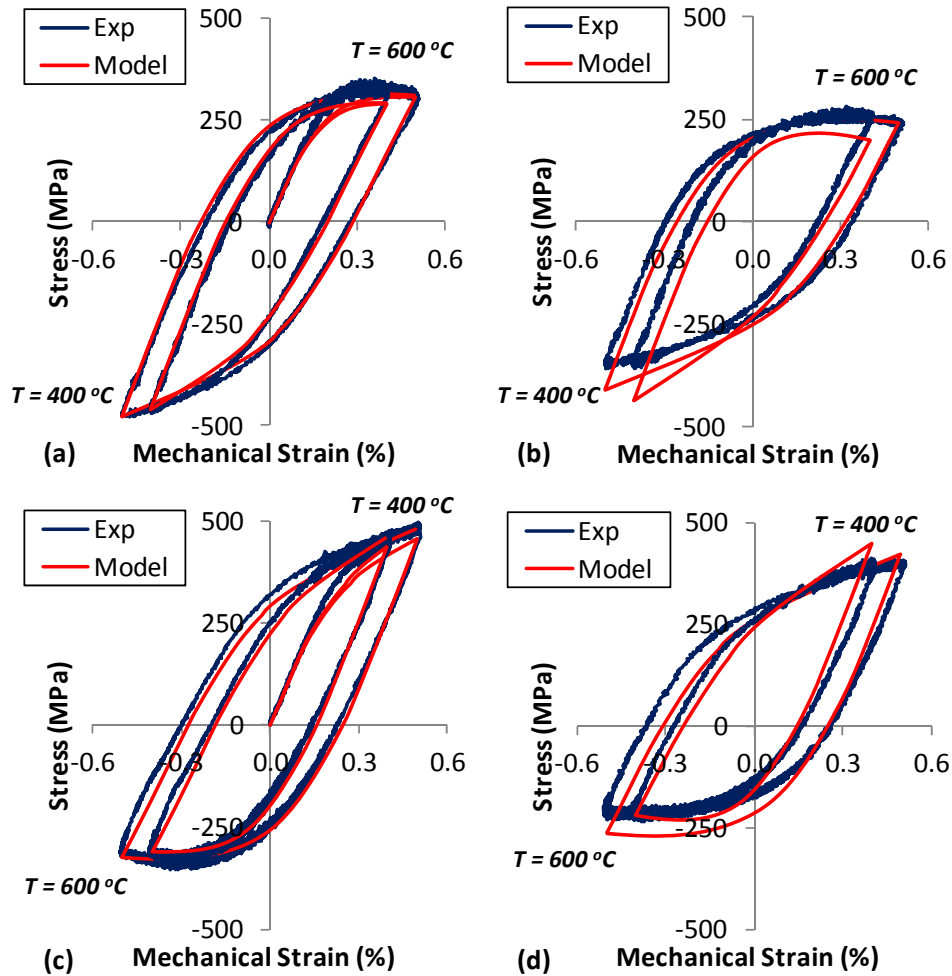


Figure 5.3: Comparison of the measured and predicted stress-strain response for an applied strain-rate of 0.033 %/s and varying strain-range for (a) TMF-IP initial cycle, (b) TMF-IP 280th cycle, (c) TMF-OP initial cycle and (d) TMF-OP 150th cycle in the 400 °C to 600 °C temperature range.

5.3. Multi-axial modelling of notched specimens

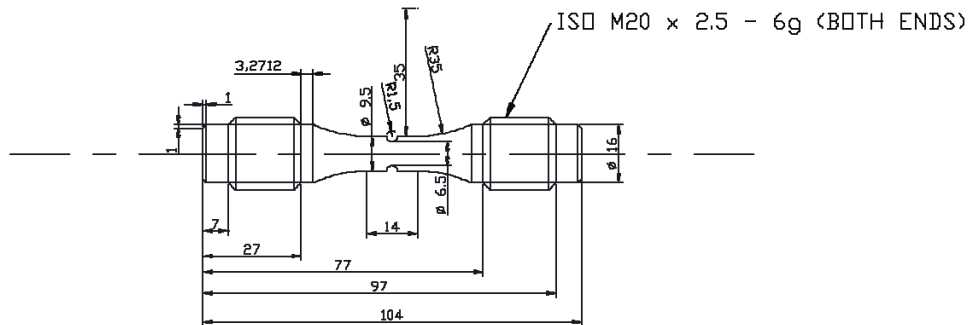
Multi-axial loading conditions are investigated in the form of simulating test specimens with a notch included. In this work, two cases are considered, (i) simulations of the test specimen of Figure 3.6 with a notch radius of 0.5 mm included and (ii) numerical modelling of NS tests carried out on ES-P91 steel. Firstly, the results of the NS experiments are presented.

5.3.1. Notched specimen experiments

NS tests were carried out on the ES-P91 steel as a first step in the multi-axial validation of the UMAT user material subroutine. The NS design is

5. Application of a Unified Cyclic Viscoplastic Material Model to Thermo-mechanical and Multi-Axial Fatigue

based on the specimen presented by Kupkovits and Neu [2010] and also on the now expired ASTM Standard Test Method for Sharp-Notch Tension Testing with Cylindrical Specimens [ASTM E602-03]. The final specimen design is presented in Figure 5.4.



ALL DIMENSIONS IN MILLIMETRES

Figure 5.4: Geometry of the NUI Galway notched specimen design for HTLCF loading.

Due to the limited availability of ES-P91 test material, only a single test result is presented here, with future work planned to obtain similar results using P91 from a different source and also other materials such as 316 stainless steel. Figure 5.5a presents the force-displacement response for the various cycles in the test carried out under a nominal applied strain-range of $\pm 0.2\%$ and applied strain-rate of $0.1\%/s$ at $500\text{ }^\circ\text{C}$. Due to the inhomogeneous stress state in the NS, a measured stress-strain response is not available. The small area within the force-displacement hysteresis loops indicates the existence of localised (notch) plasticity. The evolution of maximum force as a function of cycles is presented in Figure 5.5b, where as expected, considerable cyclic softening is evident. A comparison with corresponding smooth specimen (SS) result at an applied strain-range of $\pm 0.5\%$ is also included in Figure 5.5b. The increased LCF life (failure is taken here to correspond to a 20% load drop after the first 150 cycles) in the NS is possibly due to the local applied strain in the notch region being less than the $\pm 0.5\%$ applied to the SS.

5. Application of a Unified Cyclic Viscoplastic Material Model to Thermo-mechanical and Multi-Axial Fatigue

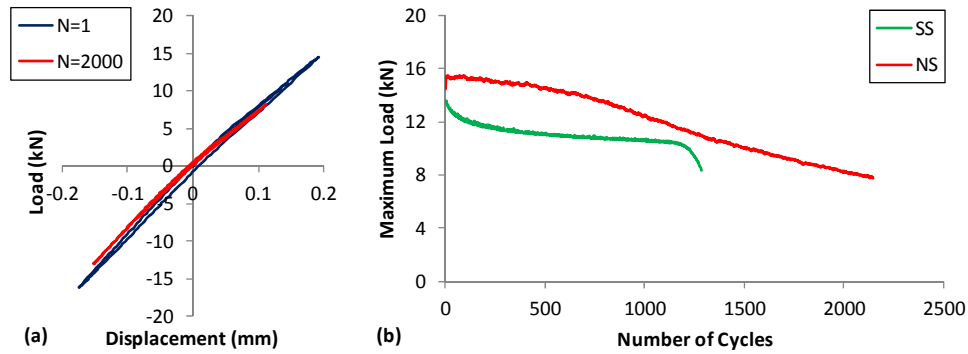


Figure 5.5: Measured (a) force-displacement response and (b) evolution of maximum load as a function of cycles for a notched specimen test carried out at 500 °C under a nominal applied strain-rate of 0.1 %/s and nominal applied strain-range of ± 0.2 %.

5.3.2. Application of material model to notched geometry

Firstly, a NS geometry was analysed based on the smooth fatigue test specimen (Figure 3.6). A notch of radius 0.5 mm was introduced at the midpoint of the gauge length (see Figure 5.6). The specimen has an axial stress concentration factor of 2.9, where the nominal stress is based on the stress remote from the notch root. Figure 5.7 depicts the stress ranges covered by the uniaxial and notch test specimens at 600 °C, along with the correlation achieved by the hyperbolic sine model to the experimental data of Kloc *et al.* [1998] and Sklenička *et al.* [2003]. The comparison with the minimum creep-rate data of Figure 5.7 illustrates the ability of the material model to operate across a broad range of strain-rates and hence, reliable extrapolation from accelerated laboratory test conditions to typical strain-rates corresponding to modern plant conditions [Farragher *et al.*, 2013a; Farragher *et al.*, 2013b; Nabarro, 2002].

5. Application of a Unified Cyclic Viscoplastic Material Model to Thermo-mechanical and Multi-Axial Fatigue

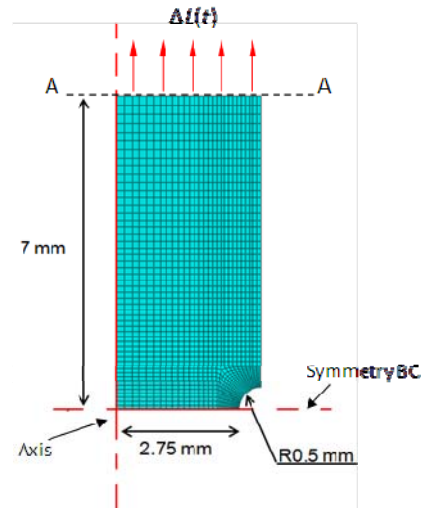


Figure 5.6: The notched specimen gauge length, axisymmetric FE mesh and symmetrical boundary conditions.

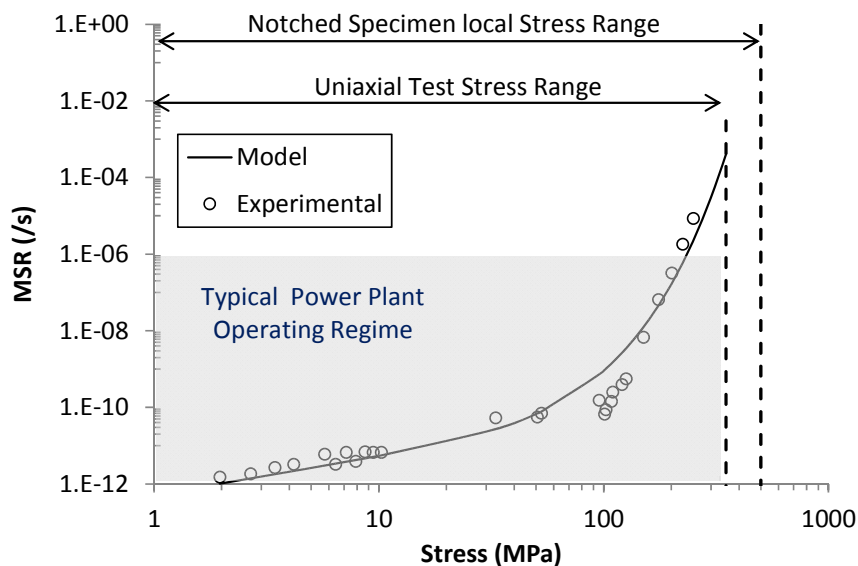


Figure 5.7: Comparison of the hyperbolic sine material model with the experimental data of [Kloc *et al.*, 1998; Sklenička *et al.*, 2003], illustrating the uniaxial test range and the simulated NS range.

A nominal strain-rate of 0.1 %/s and a nominal strain-range of $\pm 0.5\%$ (see Figure 5.8) is applied to the NS. The nominal strain here is the average strain applied to the gauge length of the specimen of Figure 5.6, which corresponds to the applied displacement divided by the gauge length. The nominal stress is the total load across the unnotched section of the gauge length, i.e. remote from the notch section of Figure 5.6, e.g. section A-A.

5. Application of a Unified Cyclic Viscoplastic Material Model to Thermo-mechanical and Multi-Axial Fatigue

Figure 5.9 shows a comparison of the predicted responses for the initial and 50th cycles for the smooth (SS) and notch specimen (central axis and notch root), at 600 °C. The results presented in Figure 5.9 illustrate the effect of the notch on local stress-strain range.

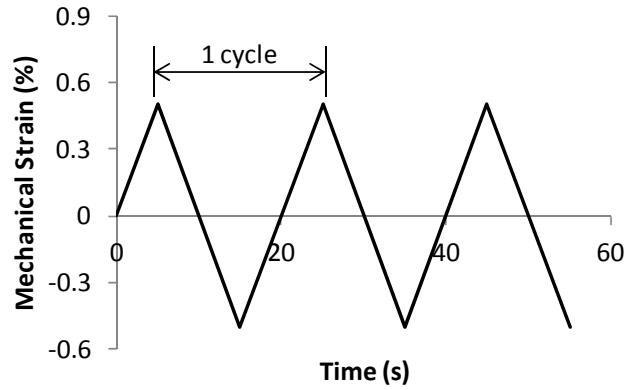


Figure 5.8: Strain-controlled loading conditions for a nominal strain-rate of 0.1 %/s and nominal strain-range of $\pm 0.5\%$.

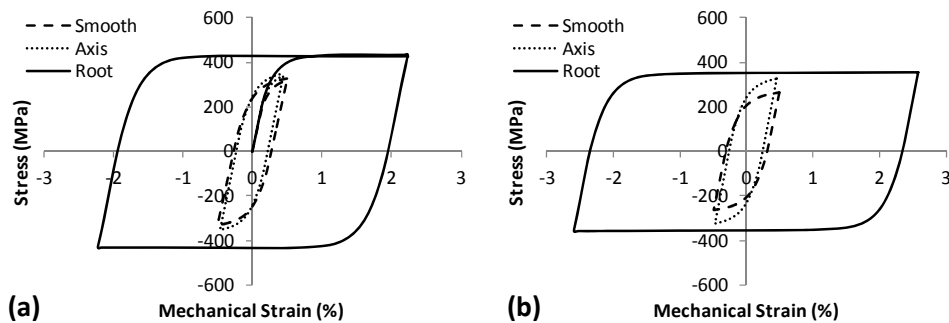


Figure 5.9: Axial stress-strain response for the (a) initial cycle and (b) 50th cycle at a temperature of 600 °C with a nominal strain-range of $\pm 0.5\%$ and nominal strain-rate of 0.1 %/s.

In multi-axial creep and plastic failure, triaxiality, and hence hydrostatic stress, represent key parameters for failure [Zhao *et al.*, 2012]. The hydrostatic stress is the average of the three normal stress components, i.e:

$$\sigma_k = \frac{1}{3}(\sigma_{11} + \sigma_{22} + \sigma_{33}) \quad (5.1)$$

Figure 5.10 illustrates the predicted distributions of hydrostatic stress (a) and axial plastic strain range (b) with radial position from the central axis to the notch root. The hydrostatic stress is dominated by the axial stress and in

5. Application of a Unified Cyclic Viscoplastic Material Model to Thermo-mechanical and Multi-Axial Fatigue

the initial elastic regime ($\sigma < \sigma_y$), the highest stress is observed at the notch root. Under viscoplastic behaviour, yielding and the maximum plastic strain are predicted at the notch root. As the loading increases, the maximum hydrostatic stress redistributes away from the notch root. The hydrostatic stress reduces to an almost constant value towards the centre of the specimen. This result is consistent with the work of Flavenot and Skalli [1989] and Zhang *et al.* [2012]. As the cycles increase, the stress from an initial peak distribution ($N=1$), reduces due to the cyclic softening behaviour of P91 steel [Saad *et al.*, 2011a; Fournier *et al.*, 2009b], as illustrated in Figure 5.9 and Figure 5.10. The high localisation of the stress relatively close to the notch root (see Figure 5.10a) is concomitant with a high localisation of plastic strain in the zone surrounding the notch root as highlighted in Figure 5.10b. However, away from the notch root, a significant portion of the specimen has a strain value slightly lower than the nominal applied strain of $\pm 0.5\%$. Initially the maximum von Mises stress is predicted at the notch root, but with increased time is predicted to redistribute circumferentially around the notch to a region labelled 'A' in Figure 5.11. Figure 5.11 also illustrates the predicted redistribution of von Mises stress in terms of the FE contour plots at times of 2 s and 505 s respectively. This redistribution of von Mises stress around the notch root is related to the time-dependent behaviour of the model (in a similar manner to creep stress redistribution, as presented in [Eggeler and Wiesner, 1993], for example). For conventional J_2 plasticity, this redistribution of von Mises stress is not observed, as presented in Figure 5.12 for (i) J_2 plasticity, (ii) the Chaboche, power law unified cyclic viscoplasticity model and (iii) the hyperbolic sine unified cyclic viscoplasticity model. The J_2 plasticity model is the combined non-linear kinematic and isotropic hardening model built into the commercial FE code, Abaqus. Furthermore, the location of maximum principal stress is also found to be consistent with the location of failure in the notched specimen tests, as discussed in more detail in Section 5.3.3 below.

5. Application of a Unified Cyclic Viscoplastic Material Model to Thermo-mechanical and Multi-Axial Fatigue

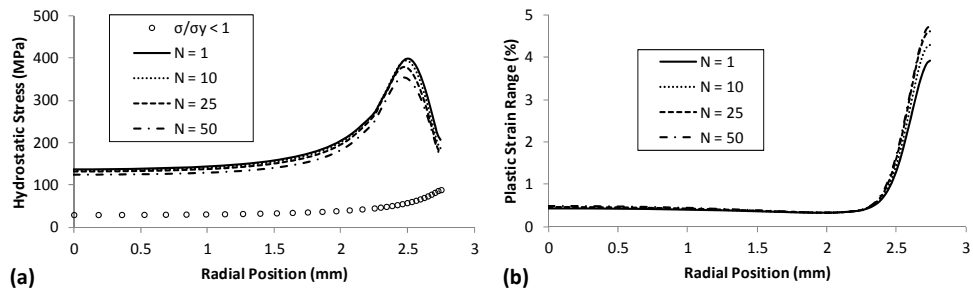


Figure 5.10: FE-predicted variation of (a) hydrostatic stress and (b) axial plastic strain-range with radial position for various cycles, illustrating the effect of stress redistribution and cyclic softening of P91 steel.

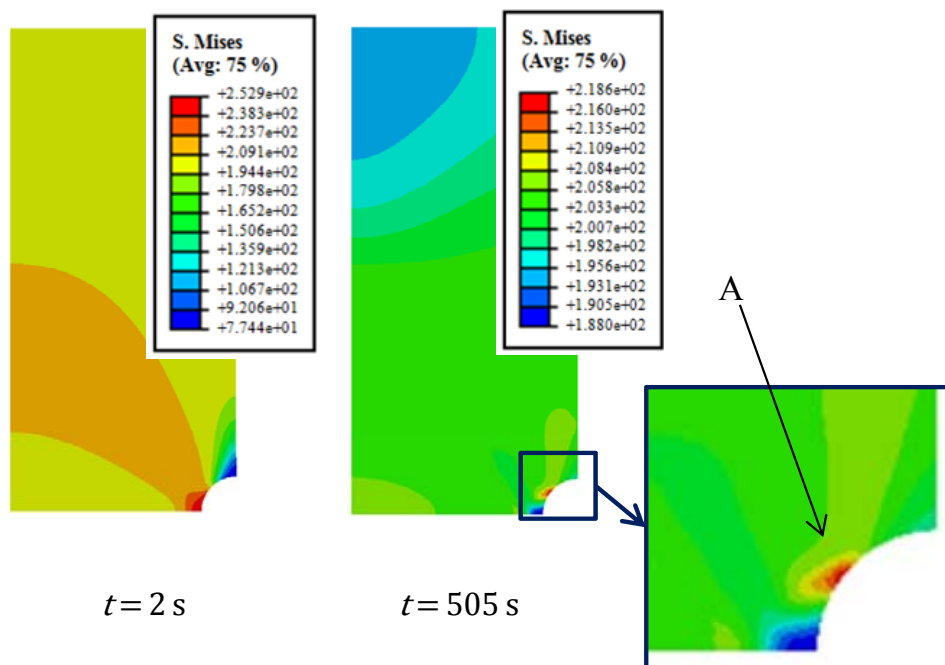


Figure 5.11: FE-predicted von Mises contour plots produced by the hyperbolic sine material model at 2 s ($N < 1$) and 505 s ($N = 25$), under strain-controlled HTLCF loading conditions.

5. Application of a Unified Cyclic Viscoplastic Material Model to Thermo-mechanical and Multi-Axial Fatigue

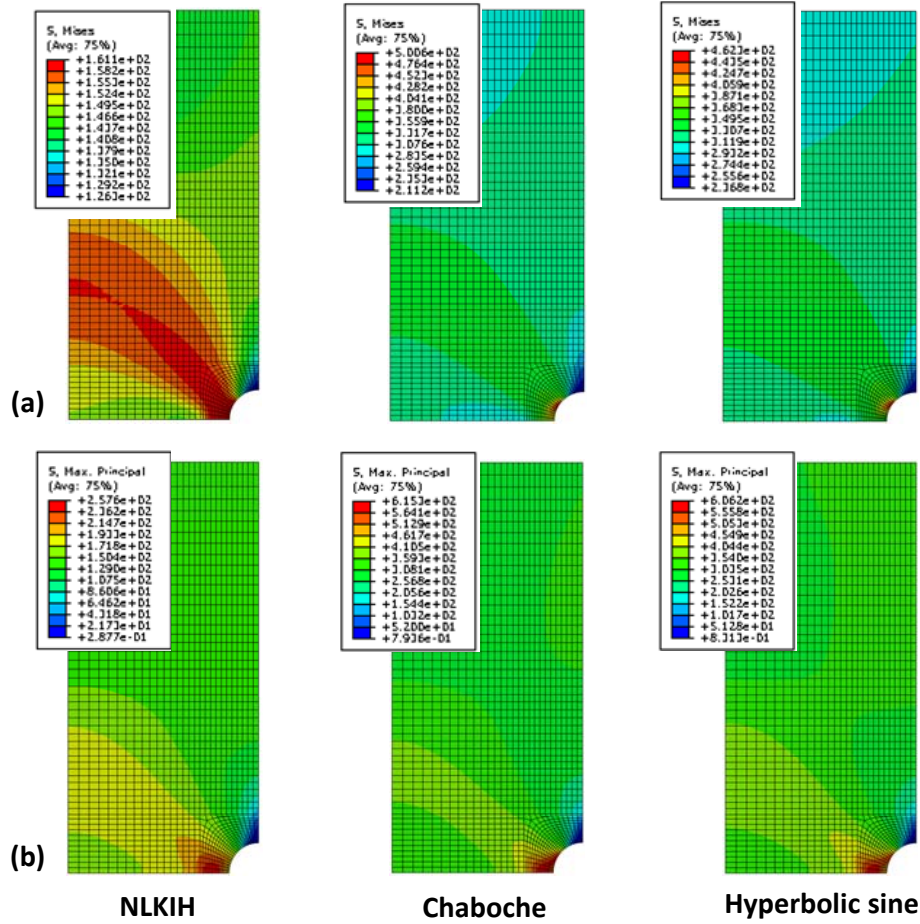


Figure 5.12: Contour plots of FE predicted (a) von Mises stress and (b) maximum principal stress using the NLKIH, Chaboche and hyperbolic sine models. The results correspond to a time of 5 s.

As the FE predictions illustrate, the inclusion of a stress concentration in the form of a notch has a considerable effect on the performance of P91 steel. This is predicted to cause a significant reduction in life based on a C-M prediction. From the HTLCF experiments conducted by Saad *et al.* [2011a; 2011b] and subsequent identification of the Coffin-Manson constants for P91 steel in Saad *et al.* [2011b], ϵ_f' has a value of 0.225 and c is -0.577 at 600 °C.

Table 5.1 contains the C-M predictions for the SS and NS cases, illustrating the influence of the stress concentration on the predicted life in both cases. The predicted results for the SS case, via comparison with fatigue life data of Saad [2012], are within 12 % of the experimentally observed values. The

5. Application of a Unified Cyclic Viscoplastic Material Model to Thermo-mechanical and Multi-Axial Fatigue

result of the C-M prediction is based on the value of highest axial plastic strain range. Future work will investigate a critical plane approach to identify the plane of maximum plastic strain-range and account for the multi-axial effects of the inclusion of a notch.

Table 5.1: C-M life prediction at 600 °C for the smooth and notched specimens.

Model	Test Case	
	Smooth specimen	Notched specimen
Hyperbolic sine	728	25
Power law	743	35
Experimental [Saad, 2012]	656	-

Table 5.1 also presents a comparison between the hyperbolic sine model and widely used Chaboche unified power law model [Chaboche and Rousselier, 1983a; Chaboche and Rousselier, 1983b], described using the model of Equation (2.8). The Chaboche model is implemented using the constants identified by Saad *et al.* [2011a]. In Figure 5.13a, the stress-strain response produced by both models for the initial loop at the position labelled ‘axis’ in Figure 5.6 are presented; almost identical results are obtained. At this position, the material response is close to the nominal loading conditions and thus, the excellent comparison in Figure 5.13a is expected as this is close to the regime of calibration in both cases. Figure 5.13b presents predicted responses at the notch root. The effect of the stress concentration is observed to cause a considerable difference between the two models. The power law model predicts a significantly lower plastic strain-range, leading to a 28 % higher predicted life, as shown in Table 5.1. Referring to Figure 5.13, the hyperbolic sine model is correlated with experimental data across the full range of test data, giving confidence for extrapolation. The power law model is a linear approximation to a relatively small range of test data and should only be used within that calibrated range of strain and strain-rate. Hence, for this application to the notch root or similar stress (and hence strain-rate) concentrations in realistic applications, it is argued that the hyperbolic sine model is more suitable. A closely related issue is that of extrapolation from common laboratory test conditions (typically

5. Application of a Unified Cyclic Viscoplastic Material Model to Thermo-mechanical and Multi-Axial Fatigue

comparatively high strain-rate) to realistic (much slower strain-rate) conditions. It is likewise argued here, based on Figure 5.13 and the results presented, that the present (hyperbolic sine) model is more suitable and reliable for this purpose.

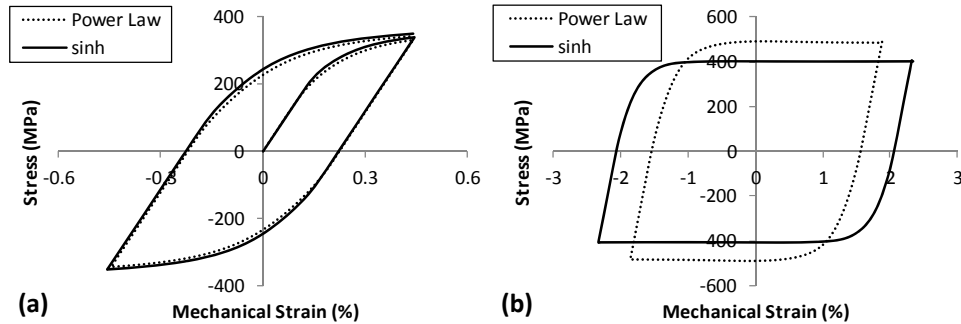


Figure 5.13: FE predicted stress-strain response produced by both the hyperbolic sine and power law material models at (a) the axis of symmetry for the initial loop and (b) at the notch root for the 50th cycle.

5.3.3. Multi-axial validation of the UMAT subroutine

The UMAT subroutine is validated for multi-axial loading conditions via comparison with the notched specimen tests presented in Section 5.3.1. As stress and strain at the notch tip were not measured during the experiments, a measure of validation is presented here based on comparison of predicted and measured numbers of cycles to failure. The logic here is that successful prediction of local plastic strain will lead to successful prediction of cycles to failure. In the present study, this is achieved by application of the Coffin-Manson (C-M) relationship [*Coffin, 1954; Manson, 1953*], presented in Equation (3.1). The Coffin-Manson material parameters for P91 steel and ES-P91 steel are presented in Table 3.4.

Simulations of the NS fatigue tests were conducted at 500 °C and under nominal (remote) loading conditions of a strain-rate of 0.1 %/s and applied nominal strain-range of ± 0.2 %. The FE mesh is presented in Figure 5.14, along with the assumed loading and boundary conditions. Coffin-Manson finite element life prediction is made here using the maximum viscoplastic strain in the axial (loading) direction. The predicted C-M results for the notched specimen, along with uniaxial HTCLF results are presented in

5. Application of a Unified Cyclic Viscoplastic Material Model to Thermo-mechanical and Multi-Axial Fatigue

Figure 5.15, where the results all lie within 20 % of the experimentally-observed values. This gives confidence in the applicability of the hyperbolic sine UMAT subroutine to multi-axial (notched) conditions, albeit in conjunction (here), necessarily, with the C-M relationship.

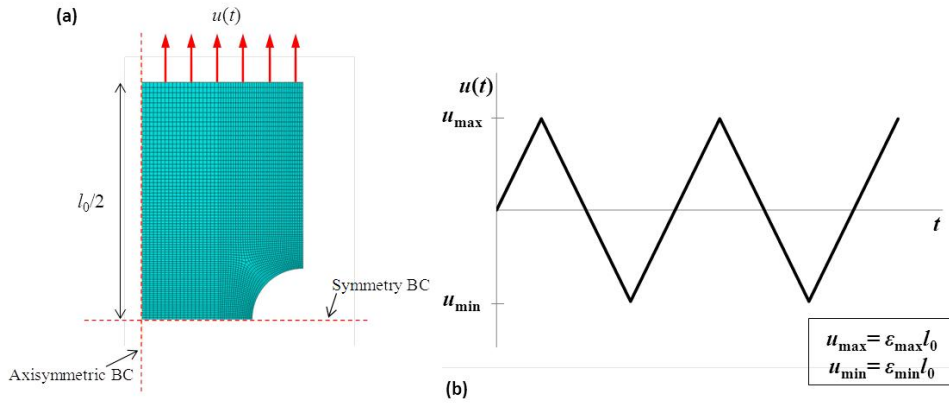


Figure 5.14: FE model (a) mesh and boundary conditions and (b) loading conditions for the notched geometry for multi-axial validation of the UMAT subroutine.

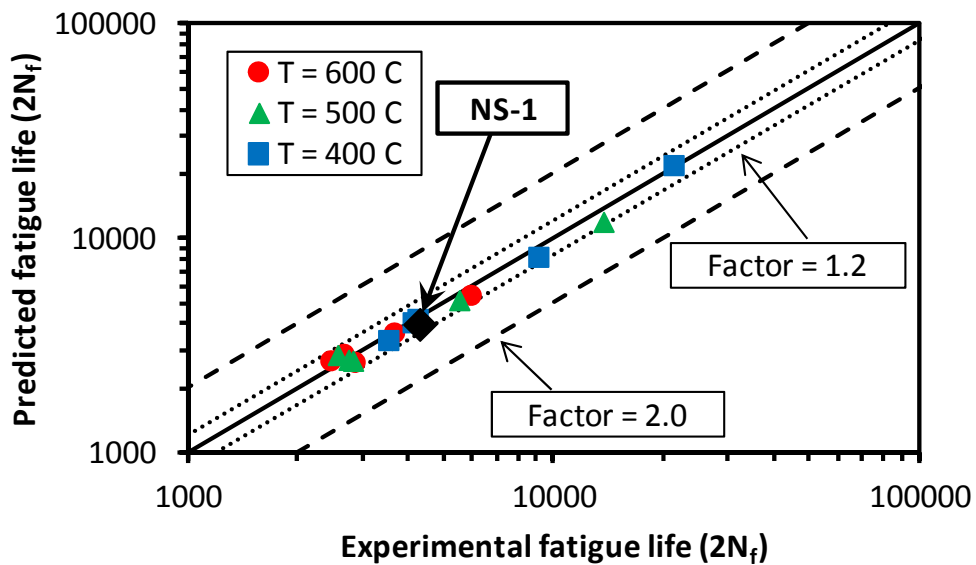


Figure 5.15: C-M predicted and experimentally observed fatigue life for ES-P91 including comparison of the NS result.

The location of failure in the notched specimen is also investigated. Through optical microscopy, the location of the primary fatigue crack was determined and compared to the FE predicted location in Figure 5.16. The

5. Application of a Unified Cyclic Viscoplastic Material Model to Thermo-mechanical and Multi-Axial Fatigue

measured and predicted crack location is seen to be slightly away (at location C in Figure 5.16) from the minimum ligament segment (transverse plane of symmetry, |AB|). The FE model assumes that the location of maximum viscoplastic strain is the location of the primary fatigue crack, further illustrating the ability of the UMAT user material subroutine to predict multi-axial loading effects.

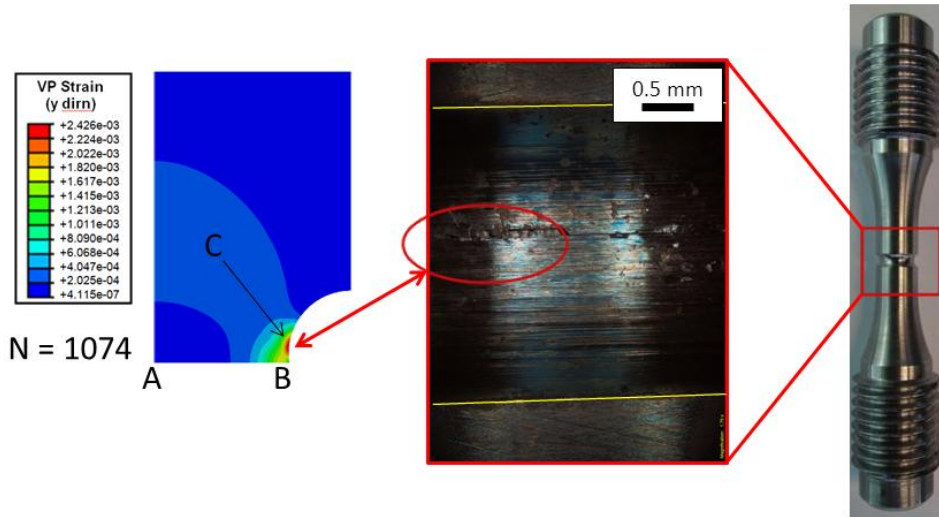


Figure 5.16: Comparison of the FE-predicted location of maximum viscoplastic strain at the 1074th cycle and location of experimental failure observed using optical microscope.

The maximum von Mises stress for the 1074th cycle is also observed at location C in Figure 5.17, just ahead of the notch tip in the notch root region. This result is expected due to the use of a time-dependent flow rule (viscoplasticity induced stress redistribution) and also as the notch tip starts to yield first and hence, the plasticity produces a lower stress when compared to the region just ahead of the notch tip. Furthermore, the location of the maximum equivalent stress in Figure 5.17 are consistent with the location of failure in the tested specimen of Figure 5.16.

5. Application of a Unified Cyclic Viscoplastic Material Model to Thermo-mechanical and Multi-Axial Fatigue

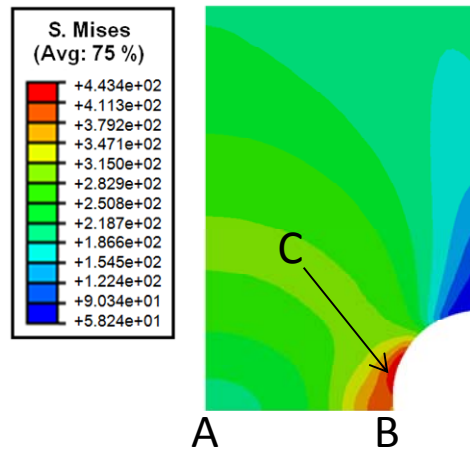


Figure 5.17: FE-predicted equivalent stress distribution in the notched specimen geometry for the 1074th cycle at 500 °C.

The elastic-plastic stress concentration factor (SCF) for this geometry, calculated as the maximum von Mises stress relative to the remote nominal applied stress is 2.38. For a typical tube, with a nominal hoop stress of 77 MPa to 122 MPa (internal pressures 17 MPa, subcritical operation, or 27 MPa, ultra-supercritical plant operation, respectively) with a SCF of 2.38, a discontinuity or branched connection will produce stress concentrations and viscoplasticity, leading to creep-fatigue deformation.

5.4. Modelling of thin-walled tubes

The material model is applied to the case of a thin-walled pipe with uniform temperature across the pipe wall, with geometry as in Figure 5.18, subjected to pressurised TMF loading conditions as per Figure 5.19. Two different cyclic ($R=0$) operating pressures are considered, a low pressure (LP) case of 17 MPa and a high pressure (HP) case of 25 MPa. The former is representative of current (subcritical) plant operating conditions and the latter of future ultra-supercritical (USC) conditions. The calculated hoop stress-strain relationships for the two maximum cycling pressures are illustrated in Figure 5.20.

5. Application of a Unified Cyclic Viscoplastic Material Model to Thermo-mechanical and Multi-Axial Fatigue

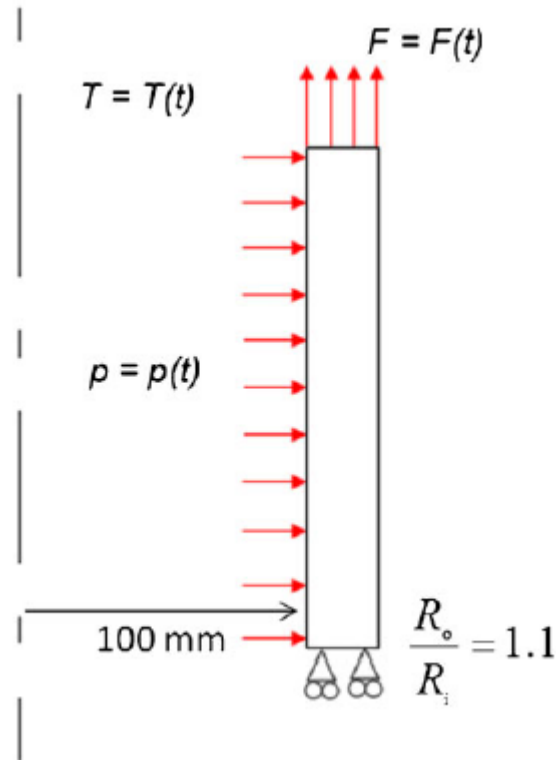


Figure 5.18: FE model setup for the axisymmetric thin-walled pipe geometry.

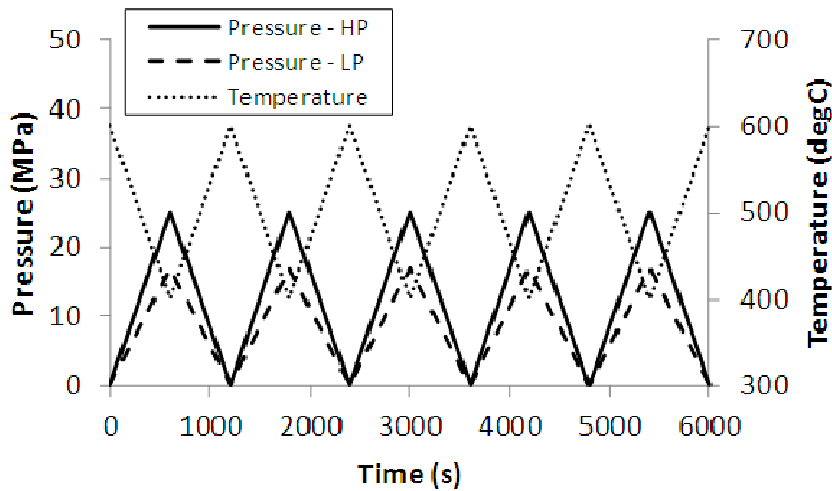


Figure 5.19: TMF-OP loading conditions for the pressure and temperature cycle corresponding to a temperature rate of 0.33 °C/s.

In both cases, ratchetting is predicted initially, with significantly more severe values of ratchet strain predicted for the HP case. For the LP case, the predicted effect of ratchetting reduces to plastic shakedown as the cycles increase. However, as depicted in Figure 5.21, the effect of ratchetting

5. Application of a Unified Cyclic Viscoplastic Material Model to Thermo-mechanical and Multi-Axial Fatigue

increases with the number of cycles due to the increased operating pressure for the HP case and this illustrates the need to account for the potential of ratchetting as a failure mechanism in thin-walled tubes as plant operating pressures increase. The number of cycles to ratchetting failure, N_r , may be estimated by the following equation [Mohd Tobi et al., 2009; Zhang et al., 2011]:

$$N_r = \frac{\varepsilon_c}{\sum_{i=1}^{N_r} \Delta \varepsilon_r} = \frac{\varepsilon_c}{\sum_{i=1}^{N_r} \sqrt{\frac{2}{3} \Delta \varepsilon_{ij}^r \Delta \varepsilon_{ij}^r}} \quad (5.2)$$

where ε_c is a critical strain, typically taken to be the material ductility, $\Delta \varepsilon_r$ is an equivalent ratchet strain in a cycle and $\Delta \varepsilon_{ij}^r$ are the increments in ratchet strain components. Assuming a material ductility of 4 % [Klueh and Vitek, 1989], application of Equation (5.2) predicts 240 cycles (~4 yrs) to failure by ratchetting for the HP case. These results highlight potential issues in moving to higher pressures, e.g. USC loading conditions, and the need to conduct life analysis of plant components under increased pressure loading and realistic temperature-pressure histories [Farragher et al., 2013a; Farragher et al., 2013b]. It is also noted that future work should assess the ability of alternative non-linear kinematic hardening (NLKH) models to predict the effects of ratchetting accurately, as the Armstrong-Frederick NLKH model is known to over-predict ratchet strain [Yaguchi and Takahashi, 2005b].

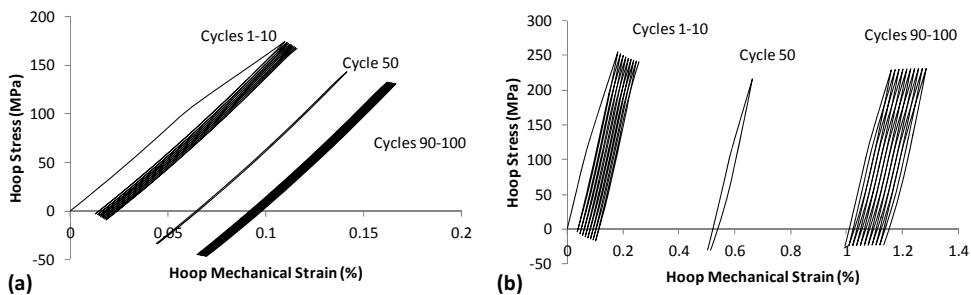


Figure 5.20: FE-predicted hoop stress-strain response for TMF-OP loading in the 400–600 °C temperature range and cycling pressure for (a) HP and (b) LP loading conditions.

5. Application of a Unified Cyclic Viscoplastic Material Model to Thermo-mechanical and Multi-Axial Fatigue

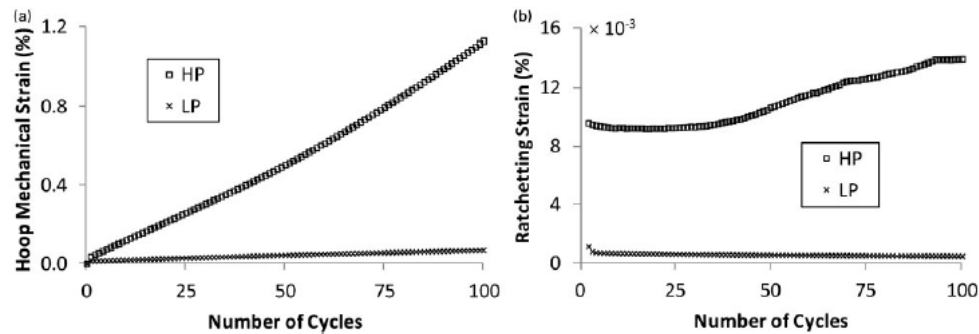


Figure 5.21: FE-predicted (a) hoop mechanical strain and (b) hoop ratchet strain, plotted as a function of the number of cycles illustrating the effect of ratchetting observed for the conditions outlined in Figure 5.19.

5.5. Discussion

The results in Figure 5.16 and Figure 5.17 illustrate the ability of the UMAT user material subroutine developed in Chapter 4 to predict the constitutive behaviour of multi-axial behaviour of materials. This is achieved here via the comparison of fatigue life using the Coffin-Manson LCF life prediction model [Coffin, 1954; Manson, 1953] and comparing the location of maximum plastic strain with that of macroscopic cracking. These results illustrate an initial validation of the multi-axial capabilities of the developed model. In future work, it is planned to carry out digital image correlation (DIC) of notched specimens under fatigue loading to further validate the ability of the constitutive model to predict the correct strain-field via comparison with the strain contour plot produced by the DIC and the strain contour plot from FE modelling.

The contribution of triaxial stress is quantified in Figure 5.10a via consideration of the hydrostatic stress (triaxial stress is proportional to the ratio of hydrostatic stress to von Mises equivalent stress). For multi-axial loading conditions, stress triaxiality is well known to play an important role in the failure of materials under plastic and creep deformation via a reduction in material ductility locally at a point. Triaxiality can therefore lead to cleavage fracture as the stress increases locally or by promoting the formation of microvoids in the material at existing inclusions. As loading continues, these microvoids coalesce resulting in ductile fracture of the material, as per the model of Rice and Tracey [1969]. In 9Cr steels,

5. Application of a Unified Cyclic Viscoplastic Material Model to Thermo-mechanical and Multi-Axial Fatigue

inclusions such as $M_{23}C_6$ precipitates dispersed along boundaries are potential sites for microvoid formation under triaxial stress states. Thus, in terms of life prediction, stress triaxiality can play an important role in crack initiation and must therefore be considered in any multi-axial life prediction model. This is the subject of ongoing work by [Li *et al.*, 2015] and illustrates the requirement to consider the effect of microstructure when predicting (i) the constitutive behaviour and (ii) failure of power plant components. Hence, the development of a multi-scale modelling framework for 9Cr steels is discussed in Chapters 6 and 7, including the development of a microstructure-sensitive modelling framework at the continuum level.

The ability of the hyperbolic sine and Chaboche power law flow rules to predict strain-rate effects are presented in Figure 5.13 for multi-axial loading conditions. The results of this section highlight the requirement for reliable extrapolation to strain-rates alternative to those for which calibration was carried out. For the case of power plant applications, this represents a key requirement as power plants typically operate at low-to-intermediate strain-rates during flexible operation of power plants [Farragher, 2014], and this extrapolation capability is crucial to the successful development of a material model. The ability of the hyperbolic sine formulation to reliably extrapolate from experimental loading conditions to realistic operating conditions is highlighted in Figure 5.7 and is assessed in Chapter 7 for the intermediate strain-rate tests carried out on the ES-P91 steel in Chapter 3. Furthermore, the results presented in Figure 5.1 and Figure 5.2 illustrate the ability of the hyperbolic sine material model to capture the strain-rate effect under TMF loading conditions, albeit over a relatively narrow range, at strain-rates alternative to those for which calibration is carried out.

The final multi-axial loading case considered here is the case of simulating thermo-mechanical loading of a thin-walled piping geometry. Considerable ratchetting was predicted by the FE model for higher operating pressures, values which equate to that of USC plant operation. Although the thermal load is relatively representative of realistic plant conditions (the rate of temperature change was estimated from the thermal transients of Figure

5. Application of a Unified Cyclic Viscoplastic Material Model to Thermo-mechanical and Multi-Axial Fatigue

1.2a), it must be noted that the mechanical loading cycle here is quite severe, leading to harsher loading conditions. However, the result does highlight possible issues and a potential mode of failure for thin-walled tubing with more complex geometries in USC power plant components.

Furthermore, the choice of NLKH material model can have an important role in the predicted material response. In the present framework, the NLKH Frederick-Armstrong model [Frederick and Armstrong, 2007] is used to provide the back-stress. For uniaxial, strain-controlled loading conditions, this model provides excellent results. Although the Frederick-Armstrong NLKH model is implemented in Chapters 4 and 5 of this thesis, moving to multi-axial loading conditions, some important limitations of the Frederick-Armstrong NLKH model must be understood and accounted for. Firstly, Ziegler [1959] noted that the Prager NLKH model [Prager, 1956] (Frederick-Armstrong model without the recall term) provides the correct behaviour for 1D uniaxial loading conditions – for 1D loading conditions, the Prager and Ziegler models revert to the same equation. However, for 2D and 3D cases, there exists a deficiency in the Frederick-Armstrong NLKH model. Secondly, the Frederick-Armstrong NLKH model is not capable of predicting the effects of ratcheting to the same degree of accuracy as other models, such as the Ohno and Wang model [Abdel-Karim and Ohno, 2000; Ohno and Wang, 1993a; Ohno and Wang, 1993b; Ohno and Abdel-Karim, 2000], for instance. Yaguchi and Takahashi discuss this limitation in detail elsewhere [Yaguchi and Takahashi, 2005b], concluding that the Frederick-Armstrong NLKH model tends to over-predict the effects of ratcheting. To corroborate this assumption, the current material model should be compared with ratcheting loading tests, e.g. such as the tests performed by Yaguchi and Takahashi [2005a] or Farragher [2013] for the ES-P91 steel tested in Chapter 3, and modifications to the current framework should be incorporated to account for such behaviour. Finally, the kinematic back-stress in 9-12Cr steels is due to the presence of a variety of microstructural strengthening mechanisms, including (i) solid solution strengthening, (ii) $M_{23}C_6$ and MX precipitate strengthening and (iii) dislocation strengthening due to the presence of dislocation pile-ups at high-angle boundaries. As

5. Application of a Unified Cyclic Viscoplastic Material Model to Thermo-mechanical and Multi-Axial Fatigue

these strengthening mechanisms contribute different forms of back-stress under different loading conditions, and also evolve as the microstructure degrades, the ideal model for kinematic back-stress should account for each of these strengthening mechanisms. The development of such a model is one of the objectives of Chapters 6 and 7.

5.6. Conclusions

The UMAT user material subroutine developed in Chapter 4 is applied here to numerous different loading applications for variable strain-rate sensitivity during high temperature fatigue of P91 steel, including (i) comparison with thermo-mechanical fatigue test results, (ii) notched specimens and (iii) a thermo-mechanically pressurised thin-walled pipe. The study concludes that:

- The hyperbolic sine material model has the ability to operate across a large stress and strain-rate regime, as typically observed under realistic loading and geometry conditions, and with the ability to allow reliable extrapolation from high-rate laboratory test conditions to low-rate plant conditions.
- When applying material models to conditions outside the regime of calibration, care must be exercised to ensure reliable results. The present novel constitutive model predicted a notch (Coffin-Manson) fatigue life of 28 % less than the power-law model, for almost equal smooth specimen lives. The power law is considered to be unsafe for this example case.
- For pressurised TMF loading of thin-walled pipes, ratchetting is predicted to be a candidate mode of failure, with increased pressure predicted to significantly increase the ratchet rate and strain, and hence reduce component life.

6. A dislocation-based model for high temperature cyclic deformation of 9-12Cr steels

6.1. Introduction

This chapter is concerned with the development of a dislocation-mechanics modelling methodology for 9-12Cr ferritic-martensitic steels under high temperature loading conditions. The motivations for the development of such a model are:

- To provide a mechanistic link between crystal plasticity modelling at the micromechanical level (e.g. [Li *et al.*, 2013b; Golden *et al.*, 2014]) and microstructurally informed-modelling at the component level.
- To enable more accurate simulation of the complex interactions between the physical strengthening mechanisms and the primary mechanisms of deformation for 9-12 Cr steels.
- To facilitate development of a continuum level material model to allow the complex heterogeneous behaviour of welded connections to be predicted during high temperature thermo-mechanical deformation.

6.2. Strengthening mechanisms of 9-12Cr steels

The microstructure of 9-12Cr steels is a complex precipitate and solute strengthened martensitic microstructure, designed for high creep strength at high temperatures and formed due to careful consideration of the heat treatment process. The primary strengthening mechanisms of 9-12Cr steels are illustrated in Figure 6.1.

6. A dislocation-based model for high temperature cyclic deformation of 9-12Cr steels

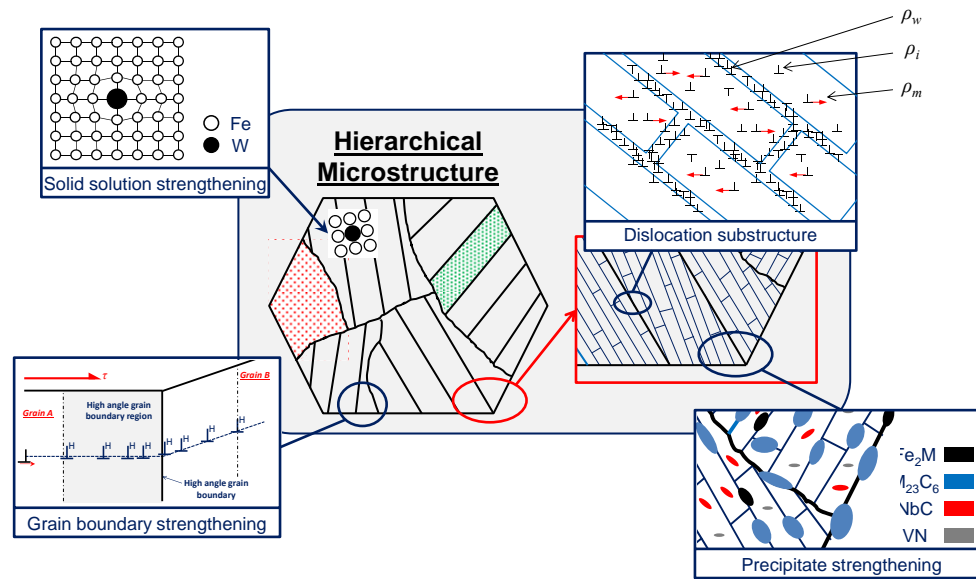


Figure 6.1: Strengthening mechanisms in 9-12Cr steels.

The microstructure is hierarchical in nature, consisting of prior austenite grains (PAGs), packets and blocks, all of which are high angle grain boundaries (HAGBs). The dimension of prior austenite grains, which form during the austenitisation phase of heat treatment, is in the range of 20 to 150 μm [Das *et al.*, 2009] and have an angle of misorientation of 60° between neighbouring grains. Blocks are defined as regions with a typical dimension of 3 to 4 μm [Sauzay *et al.*, 2005] and an angle of misorientation of approximately 45° between adjacent blocks. The HAGBs in 9-12Cr steels increase strength via dislocation interactions, whereby mobile dislocations approach the HAGBs and the high level of disorder at the boundary will cause dislocations to pile-up and hence, retard plastic deformation.

Dislocation substructures of low-angle boundary (LAB) martensitic laths are located within the block structures, with typical martensitic lath widths in the range of 0.3 to 1 μm [Abe, 2008; Giroux, 2011; Saad *et al.*, 2011b; Sauzay *et al.*, 2005; Sauzay *et al.*, 2008] and angles of misorientation of less than 5° . The LABs provide strengthening by impeding the motion of mobile dislocations and the maintenance of a high yield stress. As the smallest grain dimension in 9-12Cr steels, martensitic laths play a key role in the

6. A dislocation-based model for high temperature cyclic deformation of 9-12Cr steels

dislocation behaviour, as well as controlling the cyclic softening microstructural degradation mechanism.

Solid solution strengthening in 9-12Cr steels exists predominantly in the form of molybdenum and tungsten solutes. Due to the large atomic size of these particles, Mo and W provide substitutional solid-solution strengthening as illustrated schematically in Figure 6.1, where Mo or W atoms take the place of Fe atoms in the lattice structure, thereby increasing the yield strength of the material by retarding the motion of mobile dislocations. Similarly, the inclusions of Mo and W in the chemical composition are known to contribute to the high creep strength of 9Cr steels [Hald, 2008]. Other elements such as carbon and nitrogen can provide solid-solution strengthening in interstitial form [Abe *et al.*, 2008], thereby increasing the creep strength of the material.

In the initial microstructure, two main precipitate types are present; (i) $M_{23}C_6$ carbides dispersed along grain and martensitic lath boundaries and (ii) MX type particles within the martensitic lath interiors. $M_{23}C_6$ carbides, where M can represent Fe, Cr, Mo or W, are a key strengthening mechanism for 9Cr steels, with thermally stable precipitates being required to maintain a high creep strength (e.g. Mo is found to provide accelerated $M_{23}C_6$ carbide coarsening, with W known to retard the growth of $M_{23}C_6$ carbides [Maruyama *et al.*, 2001]). $M_{23}C_6$ carbides initially have a mean diameter in the region of 65 to 130 nm [Maruyama *et al.*, 2001], with a volume fraction of approximately 2 % [Abe, 2008]. The nano-scale MX particles, primarily present in the form of VN and NbC particles, are thermally stable particles with a typical diameter of 10 to 40 nm [Abe, 2008; Ennis and Czyska-Filemonowicz, 2002; Panait *et al.*, 2010b]. The mechanism for hardening via these precipitates has been identified by Sauzay and co-workers [Giroux, 2011; Sauzay *et al.*, 2005; Sauzay *et al.*, 2008] and Panait *et al.* [2010a; 2010b] as bowing out of mobile dislocations pinned at obstacles, for both high temperature cyclic and creep deformation respectively, as depicted in the TEM images of Figure 2.49. Thus, it is concluded that the mean precipitate radius in the tempered microstructure is too large for particle

6. A dislocation-based model for high temperature cyclic deformation of 9-12Cr steels

shearing to occur, resulting in higher strengthening for smaller precipitate diameters, as illustrated in Figure 6.2.

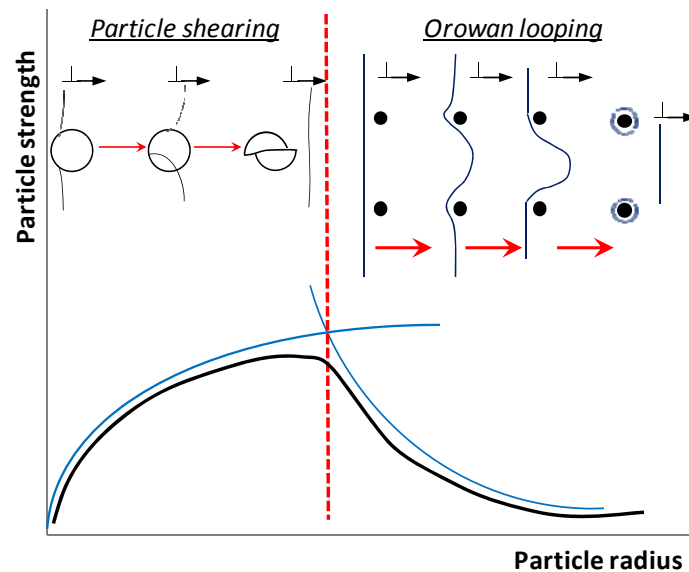


Figure 6.2: Schematic representation of a dislocation interacting with precipitates in the form of particle shearing and the production of Orowan loops.

During long-term, high temperature creep exposure, both Laves phase (Fe_2Mo and Fe_2W) and complex Z-phase $\text{Cr}(\text{Nb},\text{V})\text{N}$ precipitation occurs. Laves phase precipitates form at the expense of the Mo and W solid-solution strengthening mechanism. Although the Laves phase particles provide an initial pinning mechanism, they coarsen to diminish their contribution to the overall strength of 9Cr steels [Hu *et al.*, 2011]. The Z-phase particles form at the expense of the thermally stable MX precipitates and their precipitation is found to reduce the creep strength of the material [Abe, 2008]. Thus, the instantaneous spacing of precipitates and concentration of solutes represent key microstructural parameters for 9-12Cr steels.

6.2.1. Cyclic softening

One of the key contributions to a loss of strength in 9-12Cr steels under fatigue, TMF and fatigue-creep loading conditions is cyclic softening [Sauzay *et al.*, 2005], which typically occurs in materials with a high initial

6. A dislocation-based model for high temperature cyclic deformation of 9-12Cr steels

dislocation density. The significant measured effects of cyclic softening on the material stress-strain response are presented and discussed in Chapter 3 for the ES-P91 steel of the present study. The work of Sauzay *et al.* [2005; 2008] concluded that the physical mechanisms behind cyclic softening in 9-12Cr steels are: (i) a loss in overall dislocation density, (ii) a loss of the LAB dislocations eventually resulting in a disappearance of the LAB and a decrease in the angle of misorientation between LABs, (iii) a subsequent coarsening of the martensitic lath microstructure and (iv) precipitate coarsening at higher temperatures. Due to the presence of $M_{23}C_6$ precipitates along boundaries, it is assumed that HAGBs (PAGs, packets and blocks) do not coarsen due to cyclic deformation. Coarsening of LABs is attributed here to the mechanism of LAB annihilation in which the angle of misorientation reduces to zero. As Sauzay and co-workers [2008] have illustrated for lath coarsening, the $M_{23}C_6$ precipitates, which were originally present on LABs, remain behind after the LAB has disappeared and form part of the coarsened lath interior.

6.3. Dislocation-based material model

The material model is defined in terms of a number of micro-structural variables describing the main strengthening and cyclic softening mechanisms, within the hyperbolic sine flow rule framework developed in Chapter 4. The increment in stress, $\Delta\sigma$, presented in uniaxial form here, is defined using Hooke's law:

$$\Delta\sigma = E\Delta\varepsilon^{el} = E(\Delta\varepsilon - \Delta\varepsilon^{pl}) \quad (6.1)$$

where E is Young's modulus and $\Delta\varepsilon^{el}$, $\Delta\varepsilon$ and $\Delta\varepsilon^{pl}$ are the increments in elastic, total and viscoplastic strain, respectively. To enable more accurate extrapolation from the strain-rates conducted in laboratory experiments to the strain-rates typically observed in realistic plant, a hyperbolic sine material model is used to simulate strain-rate sensitivity and strain-rate independence of the material parameters. Thus, the flow rule for the increment in viscoplastic strain is defined using the following equation set:

6. A dislocation-based model for high temperature cyclic deformation of 9-12Cr steels

$$\dot{\varepsilon}^{pl} = \alpha \sinh(\beta f) \text{sgn}(\sigma - \sigma_b)$$

$$f = |\sigma - \sigma_b| - \sigma_y \quad (6.2)$$

$$\dot{\rho} = |\dot{\varepsilon}^{pl}|$$

where f is the viscous stress for $f \geq 0$ and defines the elastic domain for $f < 0$, $\dot{\rho}$ is the accumulated effective viscoplastic strain-rate, α and β are the cyclic viscoplastic material parameters, σ is stress, σ_b is the back-stress, which accounts for the strengthening mechanisms in 9-12Cr steels, and σ_y is the cyclic yield stress, which accounts for dislocation-based cyclic softening. The main strengthening mechanisms represented in the present model are: (i) precipitate strengthening, σ_p , (ii) dislocation strengthening, σ_d , and (iii) martensitic lath hardening coupled with a back-stress produced by the presence of the dislocation network within a hierarchical grain structure, σ_d . For monotonic loading, the back-stress is defined using a linear superposition of the above mentioned strengthening mechanisms. However, for fully reversed loading, it is also assumed that the presence of the precipitates facilitates the deformation process during reverse loading [Suresh, 1998]. Thus, the evolution of back-stress is defined as:

$$\dot{\sigma}_b = \begin{cases} \dot{\sigma}_p + \dot{\sigma}_d & \text{monotonic loading} \\ 2\dot{\sigma}_p + \dot{\sigma}_d & \text{load reversal} \end{cases} \quad (6.3)$$

where σ_p and σ_d are the back-stresses produced by precipitate hardening and dislocation strengthening, respectively. The evolution of cyclic yield stress, σ_y , is based on the cyclic evolution of mobile dislocation density, $\bar{\rho}$, where the cyclic yield stress is defined as:

$$\sigma_y = M \left(\tau_0 + B\sqrt{c} + \alpha_1 b \mu \sqrt{\bar{\rho}} \right) \quad (6.4)$$

where τ_0 is the friction shear stress accounting for the intrinsic strength (lattice resistance) of the material, B is a material constant, c is concentration of solutes, α_1 is a material parameter, M is the Taylor factor, μ is shear modulus and b is the magnitude of the Burgers vector. For long-

6. A dislocation-based model for high temperature cyclic deformation of 9-12Cr steels

term creep, a solute strengthening model such as that of Gypen and Deruyttere [1977a; 1977b], which accounts for multiple solutes (e.g. Mo and W in 9-12Cr steels) is required. However, due to the short-term nature of the present application, the evolution of the solute strengthening stress with time can be assumed to be negligible as the concentration of solutes does not decrease. Thus, the time evolution of the cyclic yield stress is thus:

$$\dot{\sigma}_y = \frac{\alpha_1 M b \mu}{2 \sqrt{\rho}} \dot{\rho} \quad (6.5)$$

The lattice resistance, τ_0 , does not evolve as a function of time and temperature dependence of the yield stress is accounted for via the temperature-dependent shear modulus, μ . The above material model is implemented in uniaxial form within a standalone computer program. A flowchart of the main processes in this implementation is presented in Figure 6.3.

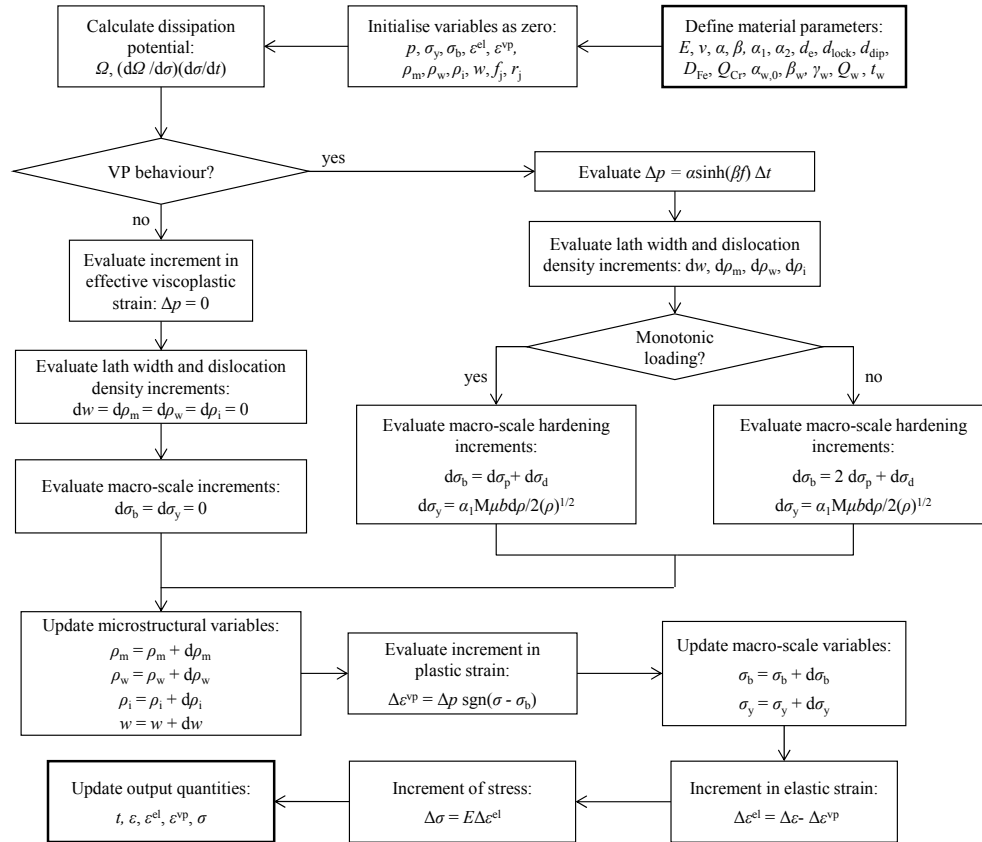


Figure 6.3: Flowchart of the main processes in the uniaxial material model.

6. A dislocation-based model for high temperature cyclic deformation of 9-12Cr steels

6.3.1. Precipitate Hardening

The Fisher-Hart-Pry (FHP) model [Fisher *et al.*, 1953; Hart, 1972] is used to simulate the back-stress caused by the presence of the various precipitates. For small strain monotonic loading and a single precipitate of type j , the precipitate hardening produced is:

$$\sigma_p = \sigma_0 \left[1 + 6 \left(\frac{C\mu}{\sigma_0} \right)^{1/2} f_j^{3/4} \sqrt{p} + 18 \frac{C\mu}{\sigma_0} f_j^{3/2} p \right] \quad (6.6)$$

In Equation (6.6), σ_0 is the Orowan stress, f_j is the volume fraction of precipitate type j and C is a material parameter, defined as [Hart, 1972]:

$$C = 0.509 \left[1 + \frac{\nu}{2(1-\nu)} \right] \quad (6.7)$$

where ν is Poisson's ratio. Thus, differentiating Equation (6.6) with respect to time and adapting the FHP model for cyclic plasticity, the evolution of hardening due to m precipitates is defined as:

$$\dot{\sigma}_p = \sum_{j=1}^m \left[3(\sigma_{0,j} C\mu)^{1/2} f_j^{3/4} \frac{1}{\sqrt{p^{cyc}}} + 18\mu C f_j^{3/2} \right] \dot{p} \operatorname{sgn}(\sigma - \sigma_b) \quad (6.8)$$

where p^{cyc} is the cyclic range of effective viscoplastic strain accumulated during load reversal. The Orowan stress associated with a precipitate of type j is defined as:

$$\sigma_{0,j} = \frac{Mb\mu}{\lambda_j} \quad (6.9)$$

where λ_j is the inter-particle spacing, defined as [Spigarelli, 2013]:

$$\lambda_j = \frac{r_j}{\sqrt{6f_j/\pi}} - 2r_j \sqrt{\frac{2}{3}} \quad (6.10)$$

with r_j as the mean precipitate radius. In the present study, it is assumed that insignificant particle coarsening occurs during high temperature cyclic viscoplasticity, i.e. r_j is assumed to be constant.

6. A dislocation-based model for high temperature cyclic deformation of 9-12Cr steels

6.3.2. Dislocation strengthening and evolution of dislocation density

Dislocation-based work hardening occurs as mobile dislocations interact with immobile dislocations in lath interiors and at lath boundaries. Thus, the contribution to the flow stress from the dislocation network using the approach of Nes [1997] and Ryen [2003], extended to the continuum level using the Taylor factor, is defined as:

$$\sigma_d = \alpha_1 Mb\mu\sqrt{\rho_i} + \alpha_2 Mb\mu\left(\frac{1}{w} + \frac{1}{D}\right) \quad (6.11)$$

where ρ_i is the lath interior immobile dislocation density, α_2 is a material parameter, w is the martensitic lath width and D is PAG size. Assuming that PAGs do not coarsen during short-term cyclic plasticity, the hardening rate due to the dislocation structure is defined as:

$$\dot{\sigma}_d = Mb\mu\left(\alpha_1 \frac{\dot{\rho}_i}{\sqrt{\rho_i}} - \alpha_2 \frac{\dot{w}}{w^2}\right) \quad (6.12)$$

The evolution of dislocation density is defined here in three distinct groups: (i) mobile dislocations, $\bar{\rho}$, (ii) lath interior immobile dislocations, ρ_i , and (iii) lath boundary immobile dislocations, ρ_w , so that the overall dislocation density, ρ , is defined as [Roters *et al.*, 2000]:

$$\rho = \bar{\rho} + (1 - f_w)\rho_i + f_w\rho_w \quad (6.13)$$

where f_w is the volume fraction of the lath boundary regions. As mobile dislocations are the carriers of viscoplastic deformation, the Orowan equation [Orowan, 1940] is used to define mobile dislocation density evolution rate in terms of the rate of deformation:

$$\dot{\bar{\rho}} = \frac{|\dot{\gamma}^{pl}|}{bL_e} \quad (6.14)$$

6. A dislocation-based model for high temperature cyclic deformation of 9-12Cr steels

where $\dot{\gamma}^p$ is the crystallographic viscoplastic slip-rate and L_e is the mean free path travelled by a mobile dislocation before it is annihilated or immobilised. To relate the microscopic viscoplastic slip-rate, $\dot{\gamma}^p$, to the macroscopic accumulated effective plastic strain-rate, \dot{p} , the Taylor model is used [Taylor, 1938]:

$$n|\dot{\gamma}^p| = M\dot{p} \quad (6.15)$$

where n is the number of active slip systems required to define the deformation-rate in the Taylor model. In this model, due to the assumption of incompressibility, only five independent components of viscoplastic strain-rate are required to define the deformation of a polycrystalline material. Hence, the combination of deformation-rates from five slip systems which contribute the lowest energy dissipation must be identified using Taylor's minimum work principle. However, as the macro-scale model presented here is independent of slip system, i.e. the level of deformation per slip system is homogeneous across all slip systems, the contribution of five arbitrary active slip systems (of 48 active slip systems for b.c.c.) will suffice to define the deformation-rate and hence, n is assigned a constant value of 5.

The evolution of mobile dislocation density includes both growth and consumption terms, where the growth of mobile dislocations is determined using the Orowan equation above. Following the work of Cheong and Busso [2004; 2005], the probability of a mobile dislocation consumption event occurring is $P = 0.5A\bar{\rho}$, where A is the critical area for consumption of mobile dislocations. The present study extends the approach of Cheong and Busso [2004; 2005] to the macro-scale and includes consumption of mobile dislocations via the mechanisms discussed in Roters *et al.* [2000]; namely (i) mutual annihilation of two mobile dislocations, (ii) the formation of immobile locked configurations and (iii) dipole dislocation formation, as well as incorporating LAB annihilation as described in Sauzay *et al.* [2005; 2006]. The critical areas for consumption for each event are illustrated

6. A dislocation-based model for high temperature cyclic deformation of 9-12Cr steels

schematically in Figure 6.4 and the evolution equation for mobile dislocation density is:

$$\dot{\bar{\rho}} = \frac{\dot{p}M}{bn} \left(\frac{1}{L_e} - \bar{\rho} (2d_{dip} + 4d_l(n-1) + d_e) \right) \quad (6.16)$$

where d_e , d_{dip} and d_l are the critical distances for loss of mobile dislocations due to annihilation, dipole formation and locked configurations, respectively. The mean free path is defined as:

$$L_e = \frac{w}{\kappa} \quad (6.17)$$

where κ is a material parameter. The evolution of lath interior immobile dislocations accounts for the loss of mobile dislocations due to the formation of immobile locked configurations, with the density of lath interior immobile dislocations decreasing via a dislocation climb process. Thus, the evolution equation for ρ_i is defined as [*Magnusson and Sandström, 2007*]:

$$\dot{\rho}_i = \frac{\dot{p}M}{bn} 4d_l(n-1)\bar{\rho} - m_{cl}\mu b^2 \rho_i^2 \quad (6.18)$$

where m_{cl} is the climb mobility rate of dislocations. From the Taylor hardening equation, $\sigma_w = \alpha_1 Mb\mu\sqrt{\rho_w}$, and Equation (6.11), the density of immobile dislocations at lath walls is:

$$\rho_w = \left(\frac{\alpha_2}{\alpha_1} \frac{1}{w} \right)^2 \quad (6.19)$$

with a subsequent rate evolution given by:

$$\dot{\rho}_w = -2 \left(\frac{\alpha_2}{\alpha_1} \right)^2 \frac{\dot{w}}{w^3} \quad (6.20)$$

6. A dislocation-based model for high temperature cyclic deformation of 9-12Cr steels

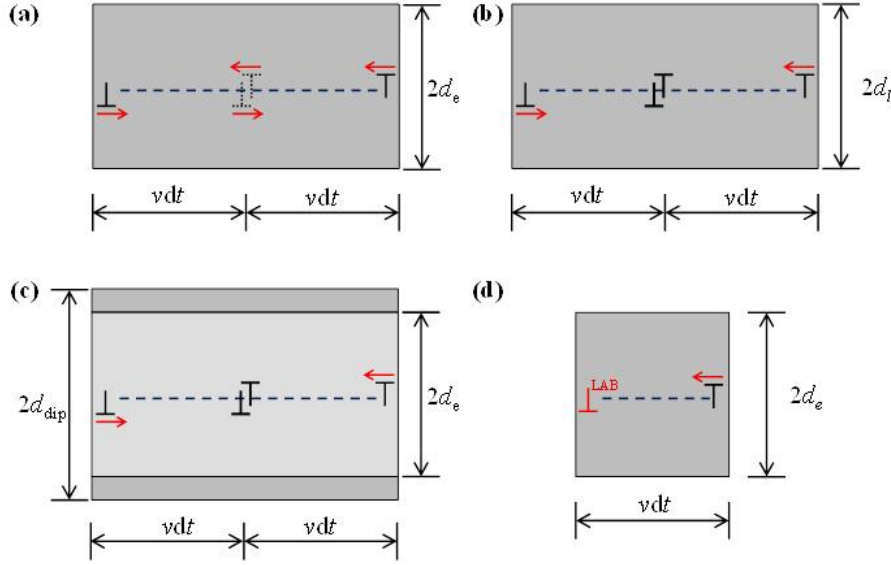


Figure 6.4: Critical areas (shaded regions) for (a) mutual annihilation of two mobile dislocations, (b) formation of an immobile locked configuration, (c) formation of a dipole configuration and (d) LAB dislocation annihilation.

6.3.3. Evolution of the lath microstructure

The growth of martensitic laths is assumed here to consist of two mechanisms, a static term defining time-dependent growth due to high temperature and a dynamic component accounting for the dependence on applied plastic strain [Lin and Dunne, 2001]. This model has been adapted to include an Arrhenius temperature-dependent function describing the static grain growth term:

$$\dot{w} = \left(\alpha_{w,0} \exp\left(\frac{-Q_w}{RT}\right) + \beta_w \dot{p} \right) w^{-\gamma_w} \quad (6.21)$$

where γ_w is a material parameter, $\alpha_{w,0}$ is a static lath growth model parameter, Q_w is activation energy, \bar{R} is the universal gas constant and β_w is a dynamic lath growth material parameter.

6.4. Results

The newly developed continuum level material model is applied to HTLCF experiments on ex-service P91 steel from Chapter 3. Firstly, the necessary

6. A dislocation-based model for high temperature cyclic deformation of 9-12Cr steels

material parameters are identified using a step-by-step procedure involving a combination of physically measured parameters and comparison with experimental test data. Calibration is then carried out via comparison with experimental data at an applied strain-rate of 0.1 %/s and applied strain-range of ± 0.5 %. The material model is finally validated against test data at other conditions and the effects of some key microstructural parameters are investigated.

6.4.1. Parameter identification

The step-by-step procedure for the identification of the material parameters is illustrated in Figure 6.5. The material parameters within this study may be split into three distinct groups, namely: (i) elastic material parameters, viz. Young's modulus, E , shear modulus, μ , Poisson's ratio, ν , and initial yield stress, $\sigma_{y,0}$, (ii) the cyclic viscoplasticity material parameters, α and β , and (iii) the microstructural material parameters, related to the evolution of dislocation density, coarsening of the lath structure and precipitate hardening.

6. A dislocation-based model for high temperature cyclic deformation of 9-12Cr steels

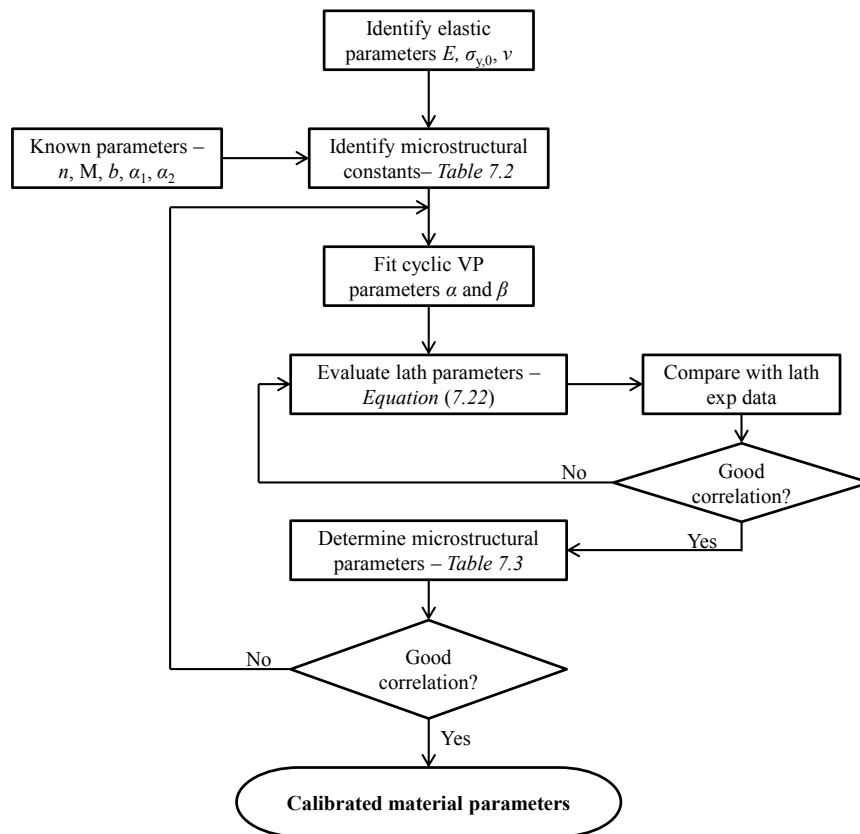


Figure 6.5: Flowchart for parameter identification method used in the present study.

The elastic material parameters are easily identified from monotonic test data and are presented in Table 6.1. Although Poisson's ratio is a temperature-dependent parameter, for simplicity a constant value of 0.3 is used throughout the present study. The cyclic viscoplasticity material parameters, α and β , are obtained from stress relaxation data. The identified cyclic elasto-viscoplastic material parameters for temperatures of 400 °C, 500°C and 600°C are presented in Table 6.1.

As 9-12Cr steels are b.c.c. crystals, the magnitude of Burgers vector is 0.248 nm and the Taylor factor is 2.9. The specific microstructural material parameters related to (i) precipitates, (ii) dislocation densities and (iii) evolution of the martensitic laths are defined below. The microstructural material constants employed here are listed in Table 6.1. The initial mean radii for the $M_{23}C_6$, VN and NbC precipitates have been obtained from measurements using TEM [Maruyama et al., 2001]. Similarly the initial volume fractions of a given precipitate were estimated using thermo-kinetic

6. A dislocation-based model for high temperature cyclic deformation of 9-12Cr steels

simulations calibrated against experimental data [Srinivas Prasad *et al.*, 2012].

From the heat treatment process, 9-12Cr steels have an initially high overall dislocation density, with a range of values from $1.6 \times 10^{14} \text{ m}^{-2}$ to $7.5 \times 10^{14} \text{ m}^{-2}$ identified in the literature using TEM, e.g. as per the work of Sauzay *et al.* [2008] or Ennis and Czyrska-Filemonowicz [2003]. Thus, the initial dislocation density is set at $4.5 \times 10^{14} \text{ m}^{-2}$. The overall dislocation density of the 'as-received' material is approximately 10 % greater than that at the lath walls [Peřička *et al.*, 2003], such that the initial lath boundary immobile dislocation density, $\rho_{w,0}$, is $0.9\rho_0$. The initial lath interior immobile dislocation density is assigned a low value of $1 \times 10^{11} \text{ m}^{-2}$ [Magnusson and Sandström, 2007]. The critical distance for a dipole dislocation to form is assigned a constant value of $7b$. The volume fraction at the lath boundaries is defined as [Collini and Bonardi, 2013]:

$$f_w = 1 - \left(1 - \frac{t_w}{w}\right)^3 \approx \frac{3t_w}{w} \quad (6.22)$$

where t_w is the cell wall thickness and is assigned a constant value of $100b$ [Magnusson and Sandström, 2007]. To account for the effect of the Mo interstitial atoms reducing the climb mobility rate, m_{cl} is defined as [Magnusson and Sandström, 2007]:

$$m_{cl} = k_{sol} \frac{D_{Fe} b}{k_b T} \quad (6.23)$$

where k_{sol} is a solute atom constant with a value of 0.05 [Magnusson and Sandström, 2007], k_b is the Boltzmann constant and D_{Fe} is the diffusion coefficient for iron, defined as:

$$D_{Fe} = D_{Fe,0} e^{-Q_{CR}/\bar{R}T} \quad (6.24)$$

where Q_{CR} is the activation energy for creep. The lath material parameters are obtained by fitting the lath evolution model to creep data [Orlová, 1998]. Figure 6.6 presents the correlation achieved with experimental data

6. A dislocation-based model for high temperature cyclic deformation of 9-12Cr steels

during the calibration procedure for the identification of the lath growth parameters $\alpha_{w,0}$, β_w and γ_w .

6. A dislocation-based model for high temperature cyclic deformation of 9-12Cr steels

Table 6.1: Material parameters for ex-service P91 steel.

Parameter	T (°C)	Value	Source	
Elastic material parameters				
E	400	183.6 GPa		
	500	173.1 GPa		
	600	144.7 GPa		
ν	N/A	0.3		
$\sigma_{y,0}$	400	255 MPa		
	500	228 MPa		
	600	196 MPa		
Material constants (b.c.c.)				
M	N/A	2.9		
b	N/A	0.248 nm		
α_1	N/A	0.235		
α_2	N/A	3.0		
n	N/A	5		
Precipitate material parameters				
r_{M23C6}	N/A	45 nm	[Srinivas Prasad et al., 2012]	
r_{NbC}	N/A	25 nm		
r_{VN}	N/A	20 nm		
f_{M23C6}	N/A	1.9 %	[Maruyama et al., 2001]	
f_{NbC}	N/A	0.1 %		
f_{VN}	N/A	0.4 %		
Martensitic lath material parameters				
$\alpha_{w,0}$	N/A	1.0×10^{-18}	[Oruganti et al., 2011] [Sauzay et al., 2008]	
β_w	N/A	2.05×10^{-9}		
γ_w	N/A	2.002		
Q_w	N/A	303 kJ/mol		
w_0	N/A	0.7 μ m		
Dislocation density material parameters				
$\bar{\rho}_0$	N/A	$4.5 \times 10^{14} \text{ m}^{-2}$	[Magnusson and Sandström, 2007] [Pešička et al., 2003] [Magnusson and Sandström, 2007] [Essmann and Mughrabi, 1979] [Ashby and Jones, 2012] [Magnusson and Sandström, 2007] [Oruganti et al., 2011]:	
$\rho_{i,0}$	N/A	$1.0 \times 10^{11} \text{ m}^{-2}$		
$\rho_{w,0}$	N/A	$0.9 \rho_0$		
t_w	N/A	$100b$		
d_{dip}	N/A	$7b$		
d_e	N/A	$6b$		
d_l	N/A	b		
$D_{Fe,0}$	N/A	$1.6 \times 10^{-4} \text{ m}^2/\text{s}$		
k_{sol}	N/A	0.05		
κ	N/A	1.45		
Q_{CR}	N/A	400 kJ/mol		
Cyclic viscoplastic material parameters				
α	400	8.0×10^{-6}		
	500	4.0×10^{-6}		
	600	4.2×10^{-5}		
β	N/A	0.05 MPa^{-1}		

6. A dislocation-based model for high temperature cyclic deformation of 9-12Cr steels

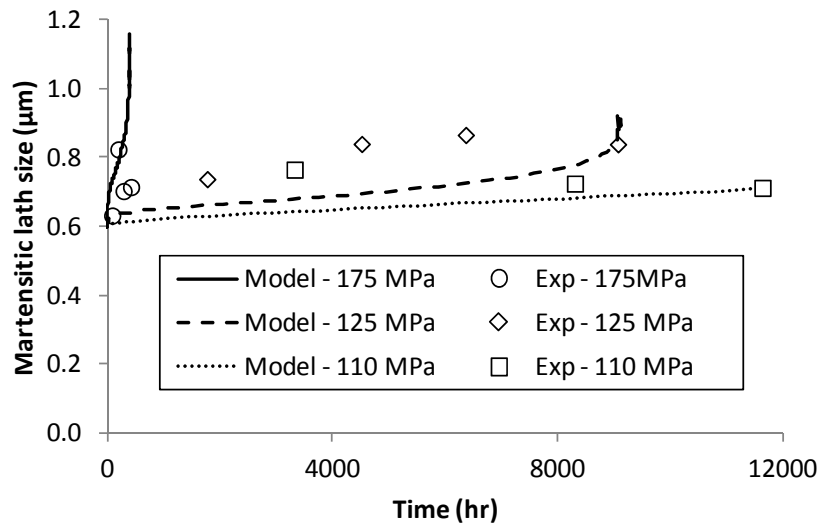


Figure 6.6: Identification of the martensitic lath growth material parameters from the material data of Orlová [1998].

6.4.2. Calibration of micro-structural parameters

The material model is calibrated against high temperature cyclic viscoplasticity experiments conducted at a strain-rate of 0.1 %/s. Figure 6.7 illustrates the typical correlation achieved with the experimental data for the initial and 600th cycles under the calibration regime at temperatures of 400 °C, 500 °C and 600 °C respectively. From the results of Figure 6.7a to Figure 6.7c, it is evident that the material undergoes significant cyclic softening, which is captured by the model. This capability of the model is verified in Figure 6.7d, which compares the maximum stress from the model with the experimental data. Clearly, good agreement with the data is achieved for the calibration conditions of a strain-rate of 0.1 %/s and a strain-range of ± 0.5 %. Table 6.1 shows the resulting set of micro-structural parameters identified through the calibration process.

6. A dislocation-based model for high temperature cyclic deformation of 9-12Cr steels

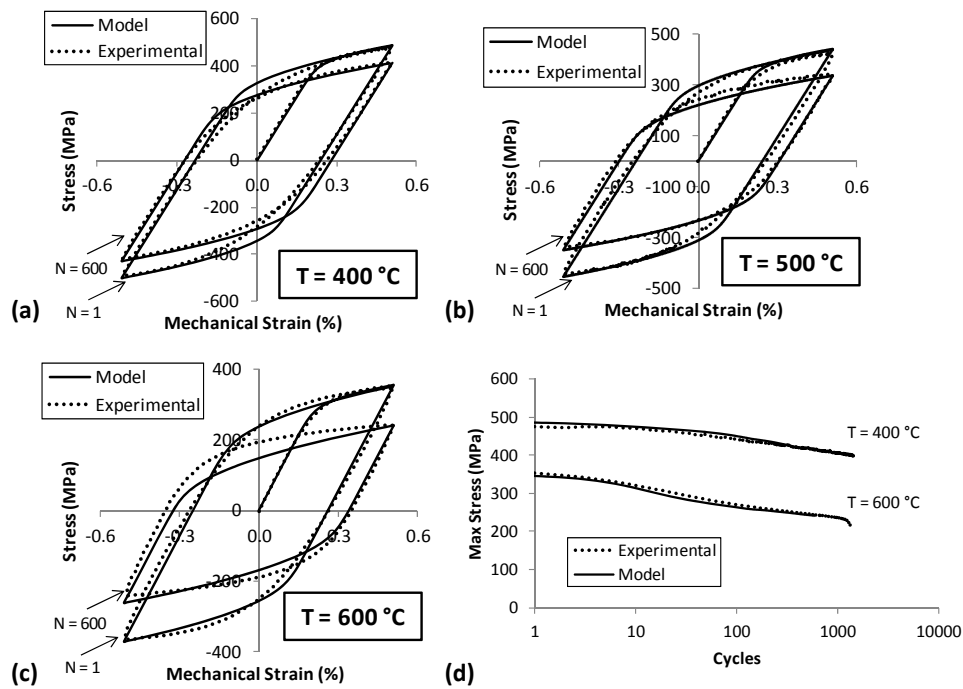


Figure 6.7: Comparison of the calibrated model against measured stress-strain response for the 1st and 600th cycles at a strain-rate of 0.1 %/s at (a) 400 °C, (b) 500 °C, (c) 600 °C and (d) the evolution of maximum stress with cycles for temperatures of 400 °C and 600 °C.

6.4.3. Validation against high temperature fatigue data

Validation of the performance of the model for extrapolation with respect to strain-rate, for example, is achieved via comparison with high temperature cyclic viscoplasticity data at the strain-rate of 0.025 %/s, across a range of temperatures. Figure 6.8a to Figure 6.8c depict the correlation achieved with the experimental data at temperatures of 400 °C, 500 °C and 600 °C and a strain-rate of 0.025 %/s for the initial and 600th cycles. Figure 6.8d demonstrates the capability of the model to predict the softening behaviour of 9-12Cr steels outside the range of calibration. For the 400 °C case, the model captures the material behaviour reasonably well but over predicts cyclic softening.

6. A dislocation-based model for high temperature cyclic deformation of 9-12Cr steels

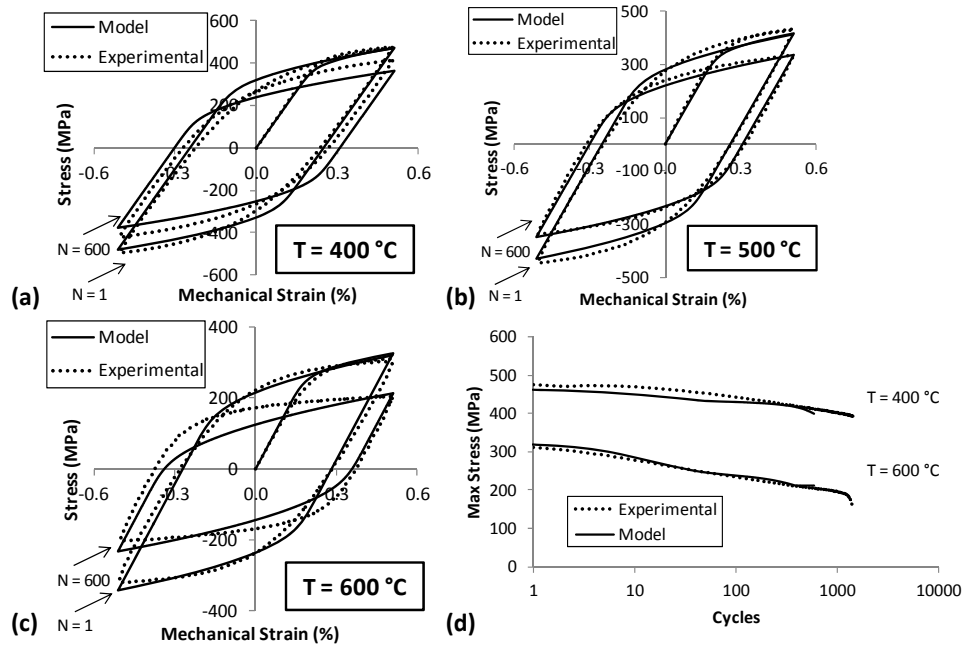


Figure 6.8: Validation of the material model against measured stress-strain response for the 1st and 600th cycles at a strain-rate of 0.025 %/s and temperature of (a) 400 °C, (b) 500 °C, (c) 600 °C and (d) the evolution of maximum stress with cycles for temperatures of 400 °C and 600 °C.

The effect of extrapolating the material model to strain-rates which are more representative of those observed in modern plant is presented in Figure 6.9. These results compare the predicted stress-range for strain-rates of 0.1 %/s and 0.0001 %/s respectively. Although the lower strain-rate is still larger than values typically observed in base-load operating plant [Nabarro, 2002], this result predicts a decrease of 70 MPa in stress-range; this is a significant loss in cyclic strength, e.g. see Figure 3.20. This illustrates the need for an ability to accurately extrapolate from laboratory test conditions (typically higher loading rates) to those observed in realistic loading conditions (typically much lower).

6. A dislocation-based model for high temperature cyclic deformation of 9-12Cr steels

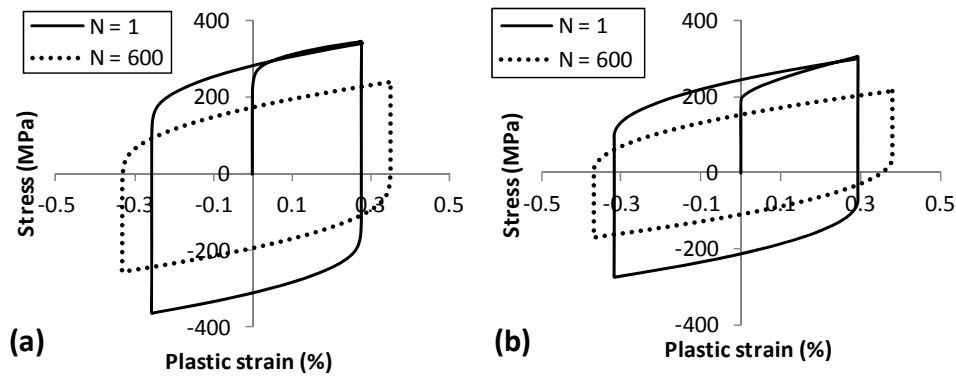


Figure 6.9: Model prediction of the stress-strain response at 600 °C at strain-rates of (a) 0.1 %/s and (b) 0.0001 %/s.

6.4.4. Effects of micro-structural parameters

The effects of two primary micro-structural variables, namely (i) the initial precipitate radii ($M_{23}C_6$ and MX particles) and (ii) initial lath width, on predicted plastic strain-range is investigated. Five initial precipitate radii, above and below typical values (e.g. see Maruyama *et al.* [2001]) are considered. Figure 6.10 illustrates the effect of increasing the initial precipitate radius on the stress-strain response for a stabilised loop. Larger particles are predicted to give a weaker material, as the particle spacing is increased, viz. Equation (6.10), and assuming constant f_j . For example, increasing r_j from 15 nm to 90 nm causes a 19.5 % reduction in cyclic strength for $M_{23}C_6$ precipitates. Hence, the capability of the pinning mechanism provided by the $M_{23}C_6$ precipitates is reduced. Figure 6.11 summaries the results of simulations on the effect of varying the initial precipitate radii. As is evident from Figure 6.11, the predicted effect MX precipitate size is less significant than for $M_{23}C_6$ precipitates.

6. A dislocation-based model for high temperature cyclic deformation of 9-12Cr steels

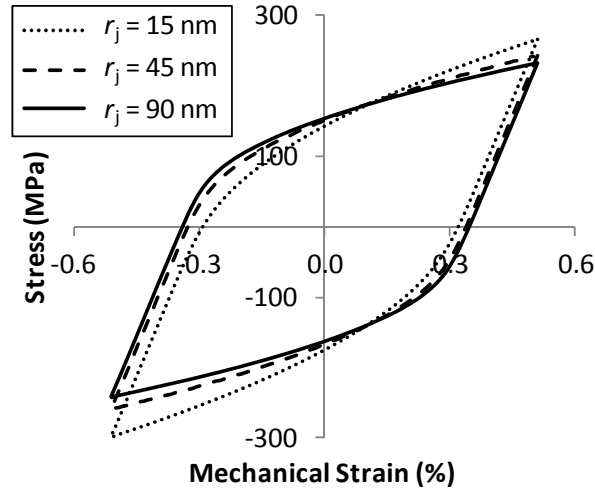


Figure 6.10: Predicted effect of $M_{23}C_6$ particle radius (r_j) on stress-strain response at 600 °C for a strain-rate of 0.1 %/s for the 600th cycle.

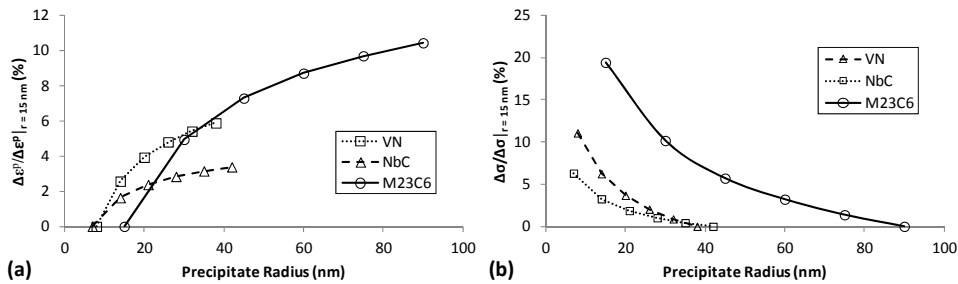


Figure 6.11: Predicted effect of varying the mean initial precipitate radius of the MX and $M_{23}C_6$ particles (relative to the values at a radius of 15 nm) on (a) the plastic strain range and (b) the stress range at a temperature of 600 °C, strain-range of 0.5 % and a strain-rate of 0.1 %/s.

Figure 6.12 shows the effect of initial lath width, w , on the stress-strain response at 400 °C and 600 °C, respectively, for the 600th cycle, where the initial dislocation density is defined using Equation (6.19). A significant effect of up to 21 % on cyclic strength (stress range) is predicted at the lower temperature of 400 °C. At 600 °C, the effect of stress range and plastic strain range is significantly less for the 600th cycle. Figure 6.13 shows the effect of temperature and lath width on the predicted plastic strain-range. Below 500 °C, an intrinsic size effect is predicted, where the presence of more LABs of smaller dimensions inhibits cyclic plasticity and

6. A dislocation-based model for high temperature cyclic deformation of 9-12Cr steels

increases cyclic strength. However, at temperatures above 500 °C, initial lath width is predicted to have a negligible effect.

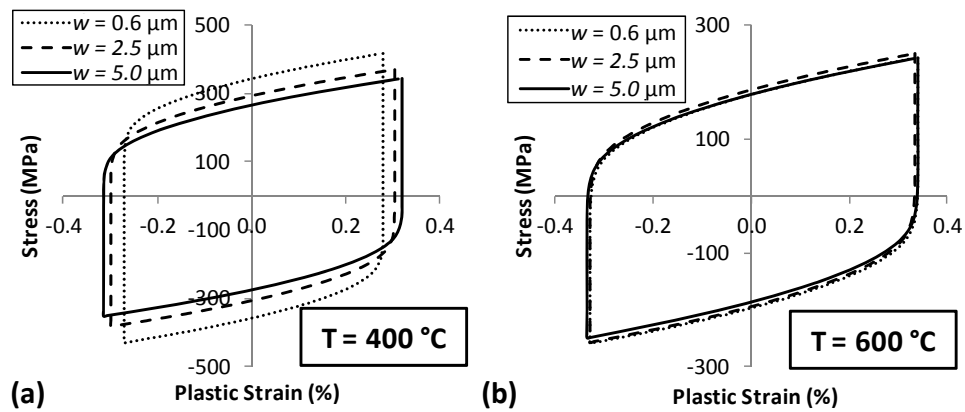


Figure 6.12: Comparison of the predicted stress-strain responses for various initial martensitic lath sizes at (a) 400 °C and (b) 600 °C for a strain-range off $\pm 0.5\%$ and a strain-rate of 0.1 %/s for the 600th cycle.

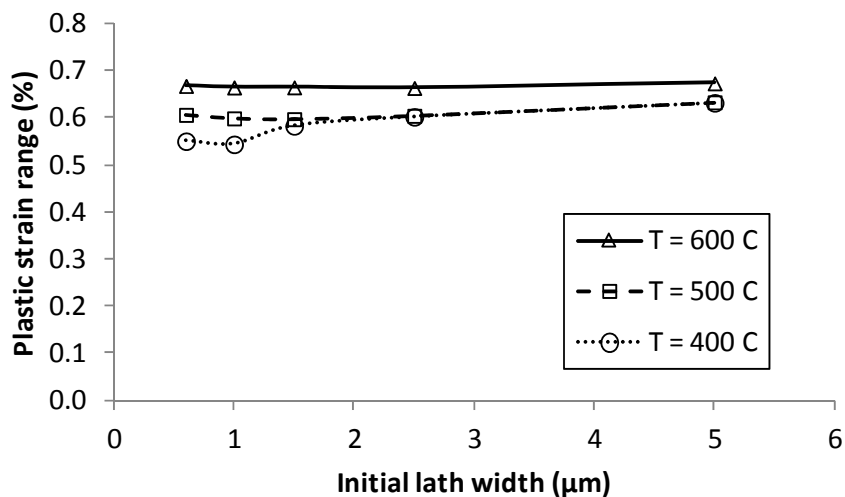


Figure 6.13: Predicted effect of various initial mean martensitic lath dimensions on the plastic strain-range produced for 400 °C, 500 °C and 600 °C for the 600th cycle.

6.5. Discussion

The present model simulates the mean effect of precipitate strengthening and dislocation-based cyclic softening. The measured history of hardening has been reasonably well predicted for a range of loading conditions and temperatures, as presented in Figure 6.7 for the calibration loading

6. A dislocation-based model for high temperature cyclic deformation of 9-12Cr steels

conditions and in Figure 6.8 for the validation regime. The back-stress produced is dependent on the stress exerted by (i) the various nano-scale precipitates and their effectiveness in pinning dislocation motion and maintaining a lath hardening structure, e.g. see Kostka *et al.* [2007] and (ii) dislocation hardening due to the presence of immobile dislocations. The model predicts the effectiveness of smaller precipitate size in increasing the (cyclic) strength and reducing the resultant cyclic plastic strain-range across all temperatures. As Figure 6.10 illustrates, the effect of the precipitate radius on the predicted stress-strain response is pivotal for the larger and more abundant $M_{23}C_6$ carbides dispersed along LABs, with a minimal size effect observed for the MX precipitates. Figure 6.11 predicts that a factor of 6 increase in $M_{23}C_6$ precipitate size causes a 10 % increase in plastic strain-range and a 19.5 % decrease in (cyclic) strength. This highlights the importance of ensuring a minimum $M_{23}C_6$ particle radius from tempering. The predicted effect of an increase of NbC particle size is not as important, giving only a 4 % change in plastic strain-range. However, it should also be noted that an initial diameter of 20 nm for $M_{23}C_6$ precipitates is less than half the minimum values typically observed in realistic components at the commencement of service and hence, the predictions made here represent an extreme case. Furthermore, for the initial diameters considered here, it is worth noting that Figure 6.11 shows a larger volume fraction effect than particle radius effect as the VN particles, with a higher volume fraction, are predicted to have a greater effect on plastic strain-range than the NbC precipitates.

Figure 6.13 indicates an optimum initial lath width of less than 1 μm for the current material. This result is consistent with an intrinsic size effect, i.e. a smaller grain size decreases the predicted plastic strain-range and increases the strength at the lower temperature. The results from Chapter 3 illustrate a negligible strain-rate effect at 500 °C, but a significant effect at 600 °C. As presented in Figure 6.13, at the higher temperature, where rate-dependency and creep effects are important, it is predicted that the benefit of smaller lath width is mitigated. This prediction is similar to the findings of Kassner and co-workers [Doherty *et al.*, 1997; Kassner, 1993; Kassner, 2004], who have

6. A dislocation-based model for high temperature cyclic deformation of 9-12Cr steels

shown experimentally that the flow stress of aluminium alloys under high temperature creep loading is independent of initial subgrain size. However, this effect is attributed here to the lath evolution model of Equation (6.21) which simulates the effects of temperature-induced static lath growth, combined with a lath width size effect. This results in an interaction between (static) lath growth and the lath size effect, such that at higher temperatures, the evolution of lath width overrides (i.e. saturation occurs) the lath size effect after 600 cycles at 600 °C. This is due to the laths coarsening (and saturation of size increase occurring) much more rapidly than at 400 °C. Furthermore, the predicted lath width at 600 °C is 3.8 μm after 600 cycles (for $w_0 = 0.6 \mu\text{m}$), a value which is consistent with the measured final TEM values of 3 to 4 μm for a block structure in P91 steel at a lower temperature of 550 °C [*Sauzay et al., 2005*]. Thus, this result at 600 °C illustrates that the coarsened lath width is approaching the dimension of the HAGB blocks (approximately 4 μm); the latter do not cyclically coarsen. In comparison, a lath width of 1 μm is predicted for the 400 °C case after 600 cycles. This shortcoming (static lath growth and over-prediction of martensitic lath width) illustrates that the current model for martensitic lath growth does not accurately predict the mechanism of LAB deformation and martensitic lath growth (and subsequent effects with respect to dislocation density evolution) in 9-12Cr steels. Hence, improvements to the LAB dislocation density evolution model of Equation (6.19) are required.

Although the general (qualitative) trends of the latter investigations into the effects of varying the precipitate radii and lath width microstructural parameters can perhaps be deduced from individual equations, the significance of the present work is the quantitative prediction on stress-strain hysteresis (cyclic plasticity) response, which is not possible without solving the complete system of non-linear equations, including the viscoplastic flow-rule equation.

Chapter 7 will address the limitations of the present framework via significant enhancements to the evolution of dislocation density. In particular, a novel approach to simulating low-angle boundary dislocation annihilation, the key mechanism of deformation during cyclic deformation

6. A dislocation-based model for high temperature cyclic deformation of 9-12Cr steels

of 9Cr martensitic steels, is developed. Further modifications to the model include (i) simulation of both edge and screw dislocations, (ii) simulation of the formation of dislocation pile-ups at HAGBs and (iii) inclusion of a dislocation bowing model for $M_{23}C_6$ and MX precipitate strengthening. These modifications will significantly reduce the number of fitted material parameters, yielding a microstructure-sensitive model which is more representative of the primary mechanisms of deformation under high temperature fatigue.

6.6. Conclusions

The key outcomes and conclusions of this chapter are:

- Initial development of a microstructure-sensitive modelling framework for the simulation of cyclic viscoplasticity in 9-12Cr steels via the incorporation of the key microstructural variables of martensitic lath width, dislocation density and the $M_{23}C_6$ and MX precipitates.
- A dislocation-based cyclic softening model is developed to account for the main mechanisms of cyclic deformation, including (i) decrease in overall dislocation density, (ii) loss of low angle boundary dislocations and (iii) a coarsening of the lath microstructure and precipitates. The model captures the experimentally observed phenomena across a range of strain-rates and strain-ranges.
- Hardening effects, produced by the main strengthening mechanisms in 9-12Cr steels, are modelled through the inclusion of evolution equations defining precipitate strengthening.
- Using the present framework, $M_{23}C_6$ precipitates are predicted to dominate in terms of effect on the plastic strain-range and cyclic strength and hence, life, relative to other precipitate types (e.g. MX precipitates).
- At low temperatures, a lath size effect on plastic strain-range was predicted, i.e. a smaller lath width gave a lower plastic strain-range.

6. A dislocation-based model for high temperature cyclic deformation of 9-12Cr steels

However, at the higher temperatures, lath growth is accelerated and the model predicts more rapid saturation of lath width and hence, cyclic softening. Thus, the initial lath width is predicted to have little effect on the plastic strain range at 600 °C.

7. An improved dislocation-mechanics model for microstructural evolution and degradation in 9-12Cr steels

7.1. Introduction

This chapter describes a number of modifications and significant improvements to the dislocation-mechanics framework of Chapter 6, with the objective of (i) simulating the key mechanisms of deformation, (ii) reducing the number of fitted material constants in the model and (iii) identification of material parameters from a physical basis via microstructural studies. These enhancements include:

1. Simulation of the LAB dislocation annihilation process via the development of a LAB model for the martensitic lath geometry and LAB dislocation density. This model uses the microstructural variables for martensitic lath width, angle of misorientation and lath shape to define the evolution of the martensitic lath microstructure.
2. Extension of the dislocation-mechanics approach to incorporate edge and screw dislocations. The volume fraction approach of Chapter 6 is also extended to include dislocations at HAGBs.
3. Inclusion of a kinematic back-stress to simulate dislocation pile-up formation at HAGBs. This back-stress accounts for the effect of the block structure in 9Cr steels.
4. The FHP model of Chapter 6 is replaced by a dislocation bowing model to provide precipitate strengthening. A volume fraction approach is used to account for $M_{23}C_6$ carbides dispersed along boundaries and MX carbonitrides within the martensitic lath interiors, with the back-stress defined as a function of the mean precipitate spacing.

The following section outlines the improved dislocation-mechanics modelling framework for simulating the constitutive behaviour of alloys

7. An improved dislocation-mechanics model for microstructural evolution and degradation in 9-12Cr steels

with a precipitate and solute strengthened hierarchical microstructure. The concept is based on a multi-scale dislocation-mechanics modelling methodology and uses mean values and evolution of a set of key microstructural variables representing the primary strengthening mechanisms in 9-12Cr steels. The proposed model is intended for simulating the constitutive behaviour and associated microstructural degradation under general high temperature deformation, including cyclic plasticity and creep effects. The present study focuses on the cyclic plasticity (LCF) aspect, although some creep results are also presented at the end of this chapter.

7.2. A dislocation-mechanics framework for 9Cr steels

The dislocation-mechanics material model is developed based on a set of key microstructural variables, chosen based on the discussion of Section 6.2 and the important role they play in cyclic plasticity and creep deformation. This framework is predicated on the evolution and degradation of the material microstructure during cyclic plasticity or creep. The inelastic strain-rate, is defined to be a function of the set of key microstructural variables, such that:

$$\dot{\epsilon}^{in} = f(d_g, w, \lambda, c, \rho) \quad (7.1)$$

where d_g is block width, w is martensitic lath width, λ is precipitate spacing, c is the concentration of solutes and ρ is dislocation density.

The framework defining the constitutive behaviour of the material is based on the unified cyclic viscoplastic constitutive model of Chapter 4. The hyperbolic sine formulation is extended here to incorporate the microstructural variables describing the primary strengthening and degradation mechanisms. In the proposed framework, it is defined that the inelastic deformation consists only of creep if the effective stress, σ_e , is less than the yield value for viscoplastic deformation, σ_y . For an effective stress value above σ_y , the deformation is defined to consist also of viscoplasticity. Thus, the yield criterion for viscoplastic deformation is:

7. An improved dislocation-mechanics model for microstructural evolution and degradation in 9-12Cr steels

$$\sigma_e = |\sigma - \sigma_b| < \sigma_y(\varepsilon^{in}) \quad \text{Elastic-creep deformation} \quad (7.2)$$

$$\sigma_e = |\sigma - \sigma_b| \geq \sigma_y(\varepsilon^{in}) \quad \text{Viscoplastic deformation}$$

where σ is stress and σ_b is back-stress. The yield stress, σ_y , evolves as a function of inelastic deformation, as discussed below. The rate of inelastic deformation is defined using a hyperbolic sine flow rule to allow reliable extrapolation from the higher strain-rates, at which laboratory tests are normally conducted, to the intermediate and lower strain-rates, at which power plant typically operate [Farragher, 2013; Nabarro, 2002]. Thus, the flow rule defining the inelastic deformations for cyclic plasticity (LCF), based on the yielding criteria is:

$$\dot{\varepsilon}^{in} = \alpha \sinh \beta (|\sigma - \sigma_b| - \sigma_y) \text{sgn}(\sigma - \sigma_b) \quad (7.3)$$

where α and β are the cyclic viscoplastic material constants. The kinematic back-stress is incorporated to capture the Bauschinger effect and the primary creep behaviour during long-term constant load deformation. These effects are due to an alteration of the local (microscopic) stress distribution within the polycrystalline microstructure, as a result of (i) bowing out of dislocations pinned at obstacles and (ii) dislocation pile-up formation at HAGBs, such that the kinematic back-stress is:

$$\sigma_b = \sigma_p + \sigma_g \quad (7.4)$$

where σ_p is the contribution of obstacles such as precipitates and solutes to the Orowan pinning mechanism back-stress and σ_g is the back-stress due to dislocation pile-ups at HAGBs. From the discussion of strengthening mechanisms in Chapter 2, the yield stress is a function of the lattice resistance, solid solution strengthening and dislocation network, and is defined here as:

$$\sigma_y = M(\tau_0 + \tau_{sol} + \tau_d) \quad (7.5)$$

7. An improved dislocation-mechanics model for microstructural evolution and degradation in 9-12Cr steels

where M is the Taylor factor (2.9 for b.c.c. materials), τ_0 is the friction shear stress accounting for the intrinsic strength (lattice resistance) of the material, and τ_{sol} is the contribution of the solutes to the yield strength. The contribution of the density of dislocations to the yield strength, τ_d , is quantified using the Taylor equation, such that the yield strength can be defined as:

$$\sigma_y = M \left(\tau_0 + B\sqrt{c} + \alpha_1 \mu b \sqrt{\bar{\rho}} \right) \quad (7.6)$$

where α_1 and B are material constants, μ is shear modulus and $\bar{\rho}$ is mobile dislocation density. As τ_0 is a constant and Mo is assumed to be the sole contributor to solid-solution strengthening in P91 steels, the rate form of Equation (7.6) is:

$$\dot{\sigma}_y = M \left(B \frac{\dot{c}}{\sqrt{c}} + \frac{\alpha_1 \mu b}{\sqrt{\bar{\rho}}} \dot{\bar{\rho}} \right) \quad (7.7)$$

The material model described here is implemented in a uniaxial standalone computer program with Figure 7.1 highlighting the main processes in the code.

7. An improved dislocation-mechanics model for microstructural evolution and degradation in 9-12Cr steels

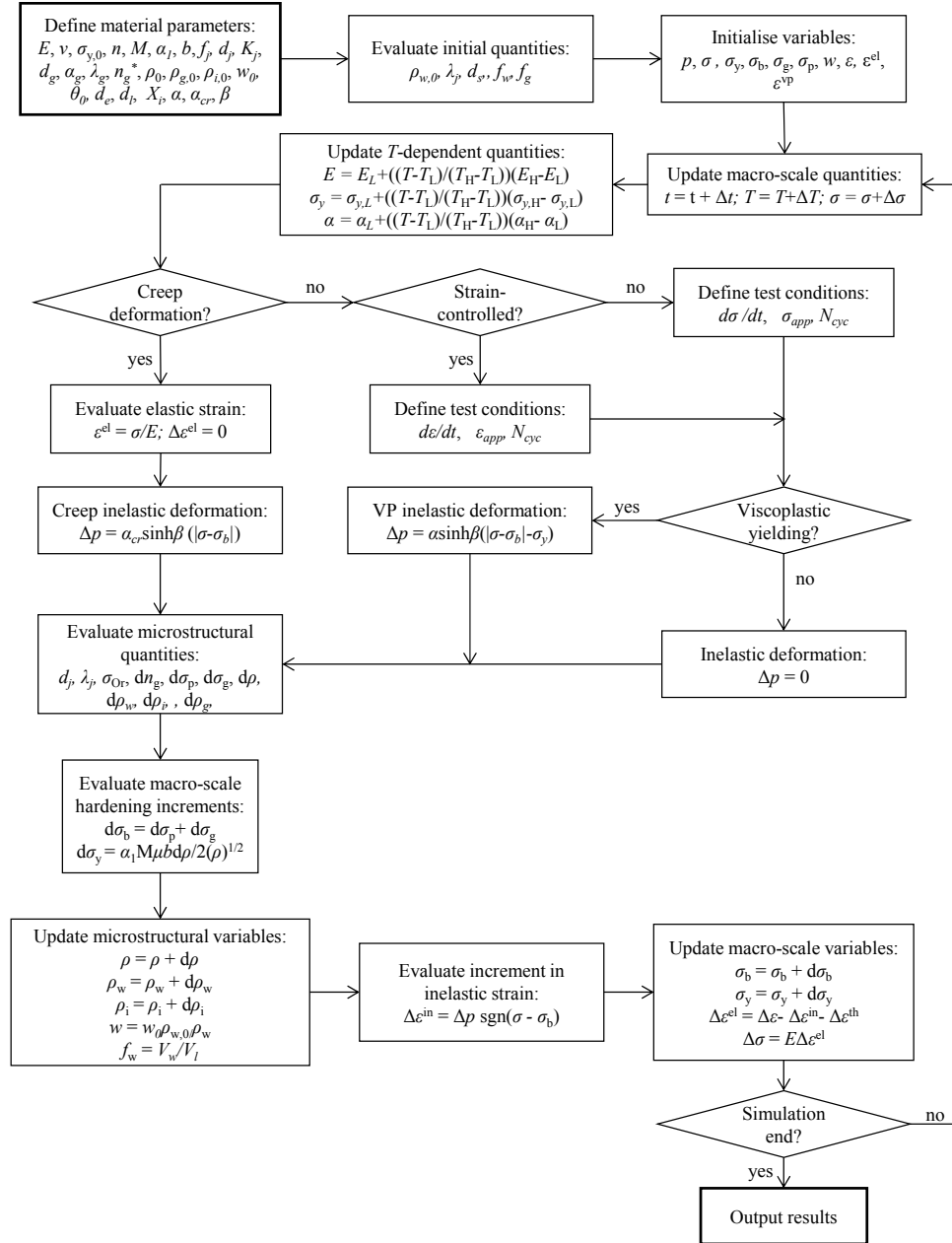


Figure 7.1: Flowchart representing the main processes in the uniaxial model.

7.2.1. Precipitate hardening in 9-12Cr steels

Based on microstructural deformations studies, e.g. the TEM images of Figure 2.49, the controlling mechanism for interactions of mobile dislocations and precipitates in 9-12Cr steels has been identified as the Orowan mechanism [Giroux, 2011; Panait et al., 2010b]. A pinned dislocation bows out from its original position under viscoplastic deformation, as illustrated schematically in Figure 7.2, resulting in a back-

7. An improved dislocation-mechanics model for microstructural evolution and degradation in 9-12Cr steels

stress which is inversely proportional to the spacing of precipitates, λ . This back-stress occurs at (i) $M_{23}C_6$ carbides dispersed along grain boundaries and (ii) MX particles within the martensitic lath interiors. The formation of Laves phase particles following long-term, high temperature exposure also yields a similar strengthening mechanism [Spigarelli, 2013]; the Laves phase precipitate strengthening is a function of (i) long-term thermal stability of the Laves phase precipitates and (ii) the radii and volume fraction of such precipitates.

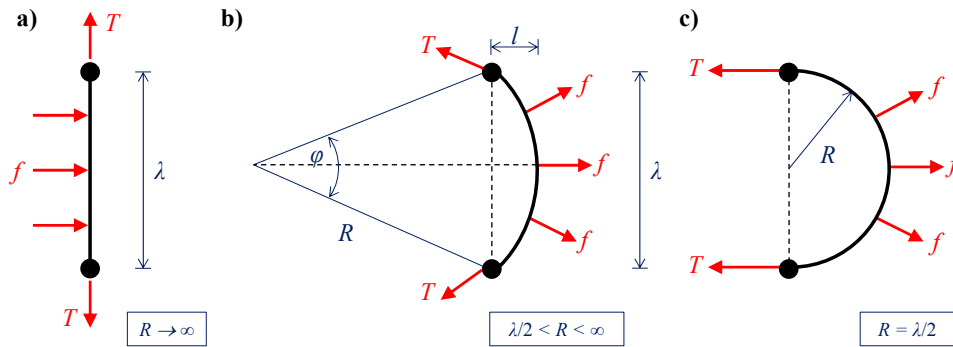


Figure 7.2: Process of a dislocation, pinned at two precipitates, bowing out under an applied force, f , for (a) the initial configuration, (b) the dislocation bowed out at a radius of curvature, R , and (c) at the point of detachment at a radius of curvature of $\lambda/2$

In the initial microstructure of 9Cr steels, the arrangement of precipitates can be defined as MX particles in the martensitic lath interiors and $M_{23}C_6$ carbides dispersed along both HAGBs and LABs. Thus, using a volume fraction approach, the rate change in precipitate strengthening is defined as:

$$\dot{\sigma}_p = (f_w + f_g)\dot{\sigma}_{M_{23}C_6} + (1 - f_w - f_g)\dot{\sigma}_{MX} \quad (7.8)$$

where f_w and f_g are the volume fractions of the LABs and HAGBs, respectively, and $\sigma_{M_{23}C_6}$ and σ_{MX} are the back-stresses associated with the $M_{23}C_6$ and MX precipitates. The micromechanical model developed by Giroux and co-workers [Giordiana et al., 2012; Giroux, 2011], for a single dislocation bowing out whilst pinned at two obstacles, is adopted and modified here to account for precipitate strengthening from $M_{23}C_6$ carbides and MX particles. During this process, a dislocation is subjected to an

7. An improved dislocation-mechanics model for microstructural evolution and degradation in 9-12Cr steels

applied force F and the resulting plastic slip, γ^{in} , is defined by the Orowan equation:

$$\gamma^{in} = \bar{\rho} b l \quad (7.9)$$

where l is the distance by which the dislocation has bowed out (see Figure 7.2). The dimension, l , is defined as the swept area, A , divided by the spacing of obstacles, λ , such that the plastic slip is [*Giordiana et al., 2012; Giroux, 2011*]:

$$\gamma^{in} = \bar{\rho} b \frac{A}{\lambda} = \frac{\bar{\rho} b}{\lambda} \left[R^2 \arctan \left(4 \frac{R^2}{\lambda^2} - 1 \right)^{\frac{1}{2}} - \frac{\lambda}{4} (4R^2 - \lambda^2)^{\frac{1}{2}} \right] \quad (7.10)$$

where R is the radius of curvature. As all points along the dislocation are in a state of equilibrium between the applied force, $F = \tau b$, and the dislocation line tension, $T = \mu b^2 / 2$, the radius of curvature is:

$$R = \frac{T}{F} = \frac{\mu b}{2\tau} \quad (7.11)$$

where τ is the resultant back-stress at the micromechanical level. The minimum value of the radius of curvature is $R = \lambda/2$, the point where the dislocation detaches from the pinning obstacles as illustrated in Figure 7.2c. Thus, the maximum value of the back-stress, τ , is the Orowan stress:

$$\tau_{\max} = \frac{\mu b}{\lambda} \quad (7.12)$$

Thus, rewriting Equation (7.10) and generalising the equation for a precipitate of type i gives the plastic slip as:

$$\gamma^{in} = \frac{\bar{\rho} b \lambda_i}{4} \left[\frac{\tau_{i,\max}^2}{\tau_i^2} \arctan \left(\frac{\tau_{i,\max}^2}{\tau_i^2} - 1 \right)^{\frac{1}{2}} - \left(\frac{\tau_{i,\max}^2}{\tau_i^2} - 1 \right)^{\frac{1}{2}} \right] \quad (7.13)$$

7. An improved dislocation-mechanics model for microstructural evolution and degradation in 9-12Cr steels

The Taylor model is used to relate the microscopic shear strain-rate, $\dot{\gamma}^{in}$, to the accumulative effective plastic strain-rate, \dot{p} , at the macro-scale [Taylor, 1938]:

$$n|\dot{\gamma}^{in}| = M\dot{p} \quad (7.14)$$

where n is the number of active slip systems required to define deformation in the Taylor model. Thus, under the assumption that the mobile dislocation density, $\bar{\rho}$, and the precipitate spacing, λ_i , are constant for an infinitesimal change in back-stress, differentiating Equation (7.13) with respect to time and introducing the Taylor model gives the rate change in back-stress at the macro-scale as:

$$\dot{\sigma}_i = \frac{2}{\bar{\rho}b\lambda_i} \frac{|\sigma_i^3|}{\sigma_{i,max}^2} \frac{\dot{p}M}{n} \left[\left(\frac{\sigma_{i,max}^2}{\sigma_i^2} - 1 \right)^{\frac{1}{2}} - \arctan \left(\frac{\sigma_{i,max}^2}{\sigma_i^2} - 1 \right)^{\frac{1}{2}} \right]^{-1} \quad (7.15)$$

The model of Equation (7.15) exhibits finite limits at $\sigma_i = 0$ and $\sigma_i = \sigma_{i,max}$ [Giroux, 2011]:

$$\lim_{\sigma_i \rightarrow 0} (\dot{\sigma}_i) = \frac{6M\mu}{\bar{\rho}\lambda_i^2} \frac{\dot{p}M}{n} \quad (7.16a)$$

$$\lim_{\sigma_i \rightarrow \sigma_{i,max}} (\dot{\sigma}_i) = \lim_{\sigma_i \rightarrow -\sigma_{i,max}} (\dot{\sigma}_i) = 0 \quad (7.16b)$$

7.2.2. Back-stress at high angle grain boundaries

Unlike LABs, HAGBs are capable of hindering the motion of mobile dislocations [Zhang and Wang, 2000]. This is achieved by the ability of such boundaries to impede the motion of mobile dislocations as a result of the high angle of misorientation and variation of the crystal lattice structure between neighbouring grains. As the material undergoes viscoplastic slip, mobile dislocations will pile-up at disordered regions along grain boundaries of the crystalline structure, as illustrated schematically in Figure

7. An improved dislocation-mechanics model for microstructural evolution and degradation in 9-12Cr steels

7.3. The motion of mobile dislocations and hence, viscoplastic slip, is then retarded due to the difficulty in overcoming the angle of misorientation and disordered structure at grain boundaries. This results in a localised back-stress which enables the dislocations to move through the matrix material more easily upon load reversal, and hence, allows viscoplastic deformation to occur at lower values of stress.

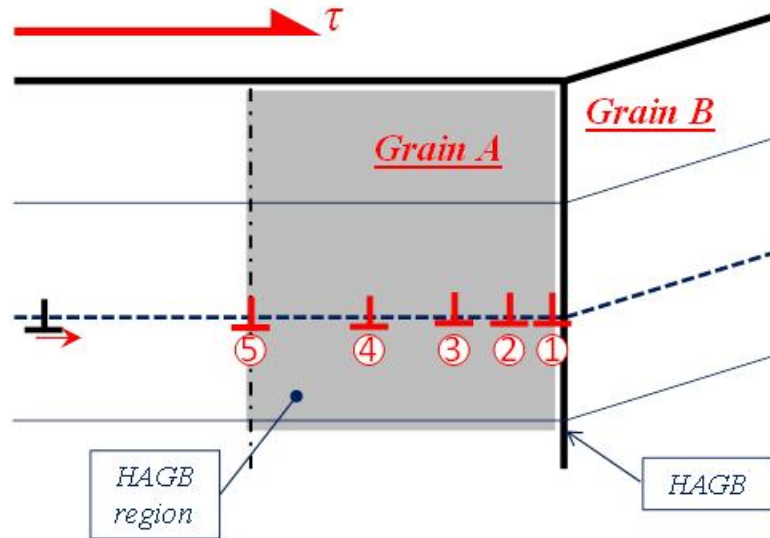


Figure 7.3: Mechanism of dislocation pile-up formation at a high angle boundary.

The back-stress, σ_g , at the HAGBs is [Ashby and Jones, 2012]:

$$\sigma_g = \frac{Mb\mu}{\alpha_g d_g} n_g \quad (7.17)$$

where α_g is a material constant and n_g is the number of dislocations in the pile-up. The mean block size, d_g , is used to represent the mean distance between HAGBs. Hence:

$$\dot{\sigma}_g = \frac{Mb\mu}{\alpha_g} \left(\frac{d_g \dot{n}_g - n_g \dot{d}_g}{d_g^2} \right) \quad (7.18)$$

As dislocations of opposite sign will interact at grain boundaries, not all dislocations at the boundaries are available to contribute to the back-stress

7. An improved dislocation-mechanics model for microstructural evolution and degradation in 9-12Cr steels

presented in Equation (7.18). Following Sinclair *et al.* [2006], the probability that a dislocation contributes to grain boundary strengthening is:

$$P_g = 1 - \frac{n_g}{n_g^*} \quad (7.19)$$

where n_g^* is the number of sites at the boundary available for dislocations to form a dislocation pile-up. Thus, the modified Sinclair model for cyclic deformation (Bardel and co-workers [2015]) is implemented to define the rate change of n_g :

$$\dot{n}_g = \frac{M\lambda_g}{b} \left(1 - \frac{n_g}{n_g^* \text{sgn}(\dot{\epsilon}^{in})} \right) \dot{\epsilon}^{in} \quad (7.20)$$

where λ_g is the mean spacing between slip lines and the quantity λ_g/b is the number of dislocations required, geometrically, to generate deformation. The number of sites available for dislocations to pile-up, n_g^* , should be a function of (i) grain size, d_g , and (ii) the applied strain. However, for simplicity, n_g^* is set as a constant value. For high temperature cyclic loading, the block size can be taken as a constant [Touboul *et al.*, 2012], such that the back-stress evolution due to dislocation pile-up formation is:

$$\dot{\sigma}_g = \frac{Mb\mu}{\alpha_g d_g} \dot{n}_g \quad (7.21)$$

For long-term creep deformation, in contrast, degradation of the HAGB structure must be simulated. As this microstructural degradation is both strain- and temperature-dependent, the block growth model is:

$$\dot{d}_g = (\eta_1 + \eta_2 \dot{\epsilon}^{cr}) d_g^{-\zeta} \quad (7.22)$$

where η_1 is the static HAGB growth parameter, η_2 is strain-dependent grain growth parameter and ζ is a material constant.

7. An improved dislocation-mechanics model for microstructural evolution and degradation in 9-12Cr steels

7.2.3. A model for dislocation density evolution

The overall density of dislocations, ρ , consists of mobile dislocation density, $\bar{\rho}$, and immobile dislocation densities along LABs, HAGBs and within martensitic lath interiors, ρ_w , ρ_g , and ρ_i , respectively, such that the overall density of dislocations is:

$$\rho = \bar{\rho} + f_w \rho_w + f_g \rho_g + (1 - f_w - f_g) \rho_i \quad (7.23)$$

The density of dislocations varies as a function of time due to growth, annihilation and immobilisation processes, such that the rate change of the various dislocation density terms can be defined using evolutionary models of the form [Roters *et al.*, 2000]:

$$\dot{\bar{\rho}} = \dot{\bar{\rho}}^+ - \dot{\bar{\rho}}^- \quad (7.24)$$

The first term on the right hand side represents growth (accumulation) and the second term represents consumption (annihilation and immobilisation). The density of mobile dislocations is:

$$\bar{\rho} = \bar{\rho}_e + \bar{\rho}_s \quad (7.25)$$

where the subscripts *e* and *s* represent edge and screw types respectively. The growth of mobile dislocations is assumed to occur due to a Frank-Read source [Frank and Read, 1950; Frank, 1980] (Figure 7.4a). These dislocations are formed from existing dislocations due to plastic slip and the complex mixed dislocation is modelled here based on the assumption that the Frank-Read source is considered to be made up of edge parts, with a Burgers vector perpendicular to the dislocation line direction and screw parts, characterised by a Burgers vector parallel to the dislocation line direction, as illustrated in Figure 7.4b. The Orowan equation is used to model the growth of mobile dislocations, with the assumption that half are of type edge and half are of type screw:

7. An improved dislocation-mechanics model for microstructural evolution and degradation in 9-12Cr steels

$$\dot{\rho}_e^+ = \dot{\rho}_s^+ = \frac{2}{bL_{eff}} \frac{\dot{p}M}{n} \quad (7.26)$$

where L_{eff} is the active slip length, the mean free path travelled by a dislocation before it is annihilated or immobilised. For materials with a LAB dislocation substructure, the active slip length is a function of the martensitic lath width, w [Plumtree and Abdel-Raouf, 1998].

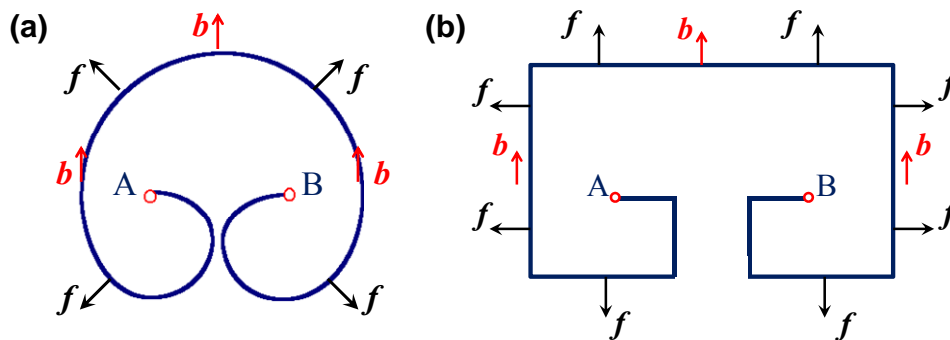


Figure 7.4: Multiplication of mobile dislocations from (a) a Frank-Read source and (b) simplified model of a Frank-Read source using edge and screw components.

The consumption of mobile dislocations occurs due to (i) mutual annihilation of two mobile dislocations, (ii) LAB dislocation annihilation, (iii) formation of locked dislocation configurations and (iv) dipole dislocation formation.

Spontaneous mutual annihilation of two mobile dislocations will occur if two edge (or screw) mobile dislocations of opposite sign and anti-parallel Burgers vector are present within a critical area for annihilation. Following a similar approach to the work of Roters *et al.* [2000] and Hosseini *et al.* [2011], two mobile dislocation of opposite Burgers vector will move a total distance of $2vdt$ towards each other during a time increment, dt , as illustrated in Figure 6.4a before being annihilated. Mutual annihilation of these two mobile dislocations will occur if both dislocations lie within a critical distance for annihilation, d_e for edge (or d_s for screw) dislocations. Thus, under the assumption that half of the mobile dislocations are positive and half are negative, the probability that relevant dislocations for an

7. An improved dislocation-mechanics model for microstructural evolution and degradation in 9-12Cr steels

annihilation event are present within the critical area of interest is [Cheong and Busso, 2004; Cheong et al., 2005; Hosseini et al., 2011]:

$$dP_k = \frac{1}{2} A_k \bar{\rho}_k = \frac{1}{2} 4d_k v dt \bar{\rho}_k \quad (7.27)$$

where the subscript k can be e or s and the dislocation velocity, v , is defined using the Orowan equation [Orowan, 1940]. The annihilation event consumes two mobile edge (or screw) dislocations. Thus, the reduction rate of mobile edge (or screw) dislocations due to mutual annihilation is:

$$\dot{\bar{\rho}}_k = 4d_k \frac{\dot{\rho} M \bar{\rho}_k^2}{bn \bar{\rho}} \quad (7.28)$$

The critical distance for annihilation of edge dislocations is set at a constant value of $6b$ [Sauzay et al., 2005; Sauzay et al., 2008] and the critical distance for annihilation of two mobile screw dislocations is given by the following expression [Essmann and Mughrabi, 1979]:

$$d_s = \frac{\mu b}{2\pi\tau_{crss}} \quad (7.29)$$

where τ_{crss} is the critically resolved shear stress, assumed here to be

$$\tau_{crss} = \alpha_1 \mu b \sqrt{\bar{\rho}}.$$

The mechanism for LAB dislocation annihilation occurs under a similar mechanism to that of mutual annihilation. However, as LAB dislocations are immobile, only one edge (or screw) mobile dislocation will travel a distance of $v dt$ to interact with the LAB dislocation within the critical annihilation distance d_e for edge (or d_s for screw) dislocations, as illustrated in Figure 6.4d. Thus, LAB dislocation annihilation occurs when a mobile dislocation of anti-parallel Burger's vector is present within a critical area for annihilation and as only one edge (or screw) mobile dislocation is annihilated during each event, the contributions to a reduction of mobile dislocation density due to LAB annihilation is:

7. An improved dislocation-mechanics model for microstructural evolution and degradation in 9-12Cr steels

$$\frac{\dot{\bar{\rho}}_k}{\bar{\rho}_k} = d_k \frac{\dot{p}M}{bn} \frac{\bar{\rho}_k \rho_{k,w}}{\bar{\rho}} \quad (7.30)$$

where the inclusion of the parameter defining the volume fraction of LABs, f_w , ensures that such an event only occurs at LABs. There is also a concomitant loss of LAB dislocations, assumed here to be the only mechanism for loss of the LAB structure under high temperature fatigue deformation.

Locked dislocation configurations can form due to the processes highlighted in Figure 7.5, leading to the immobilisation of dislocations. The number of active slip systems and the processes are described below:

- Two edge (or screw) mobile dislocations interact with the immobilisation of two edge (or screw) mobile dislocations. As edge-edge (or screw-screw) immobilisation of dislocations cannot take place on the same slip system, the number of active slip systems in this process is $(n-1)/n$ [Hosseini and Kazeminezhad, 2011].
- One edge (or screw) mobile dislocation interacts with one screw (or edge) mobile dislocation leading to the immobilisation of one edge and one screw mobile dislocation. This process can occur on all slip systems.
- One edge (or screw) mobile dislocation interacts with one edge (or screw) immobile dislocation, leading to dislocation entanglement and an immobilisation of the edge (or screw) mobile dislocation.
- One edge (or screw) mobile dislocation interacts with one screw (or edge) immobile dislocation leading to the immobilisation of one edge (or screw) mobile dislocation.

Thus, the loss of mobile dislocations due to dislocation lock formation is:

$$\frac{\dot{\bar{\rho}}_j}{\bar{\rho}_j} = \frac{d_l}{b} \frac{\bar{\rho}_j}{\bar{\rho}} \frac{\dot{p}M}{n} [4(n-1)\bar{\rho}_j + 2\bar{\rho}_k + \rho_j + \rho_k] \quad \text{where } j, k = e, \quad (7.31)$$

s

7. An improved dislocation-mechanics model for microstructural evolution and degradation in 9-12Cr steels

where d_l is the critical distance for locked configurations to form and ρ_e and ρ_s are the density of immobile edge and screw dislocations respectively, defined as:

$$\rho_j = (1 - f_w - f_g)\rho_{i,j} + f_w\rho_{w,j} + f_g\rho_{g,j} \quad \text{where } j = e, s \quad (7.32)$$

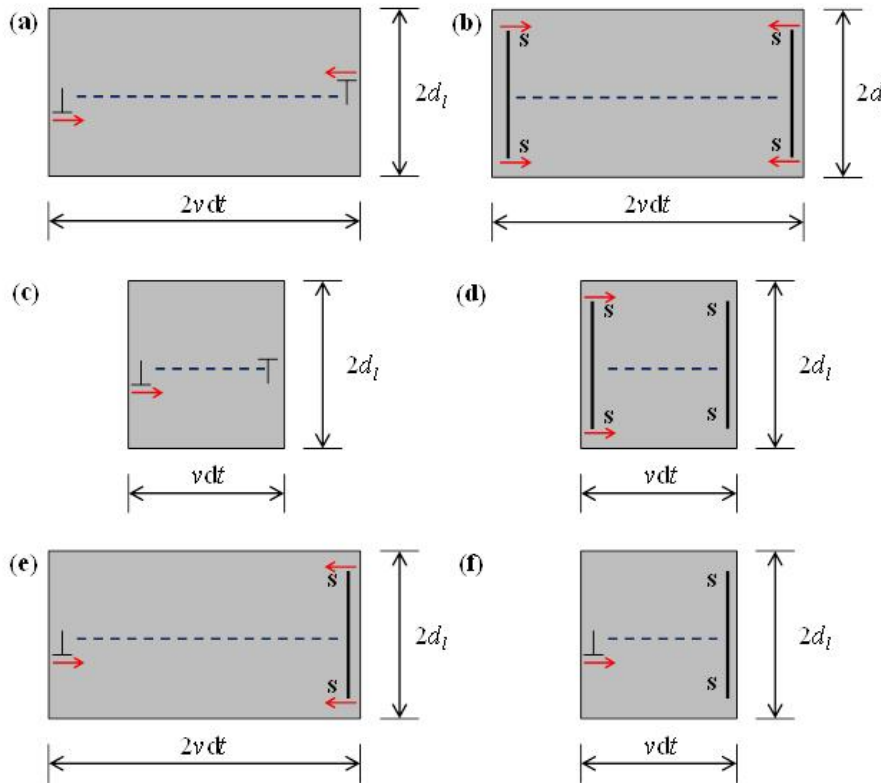


Figure 7.5: Formation of locked configurations for (a) edge-edge, (b) screw-screw, (c) edge-immobile edge, (d) screw-immobile screw, (e) edge-screw and (f) edge-immobile screw.

The final mechanism for loss of mobile dislocations considered in this work is the formation of dipole dislocations. Dipole dislocations are mobile dislocations, but do not accommodate plastic deformation [Hosseini and Kazeminezhad, 2011, Roters et al., 2000] and are only considered to be immobilised upon reaching a HAGB. The formation of a dipole configuration is illustrated in Figure 6.4c for an edge configuration, with the critical distance for dipole generation defined as [Hosseini and Kazeminezhad, 2011, Ma and Roters, 2004; Zaaferani et al., 2008]:

7. An improved dislocation-mechanics model for microstructural evolution and degradation in 9-12Cr steels

$$d_{dip} \approx \frac{\sqrt{3}b\mu}{16\pi(1-\nu)\tau_a^*} \quad (7.33)$$

where τ_a^* is defined using a Taylor dislocation hardening model as $\tau_a^* \approx \alpha_1 b \mu \sqrt{\rho_e + \rho_s}$. A similar model for mutual annihilation can describe the formation of dipole dislocations, such that the rate of reduction in mobile dislocation density is:

$$\frac{\dot{\rho}_{e-dip}}{\bar{\rho}} = 4 \frac{(d_{dip} - d_e)}{b} \frac{\dot{p}M}{n} \frac{\bar{\rho}_e^2}{\bar{\rho}} \quad (7.34)$$

The generation of screw dipole dislocations is possible [Hosseini and Kazeminezhad, 2011] but due to the large value of d_s , the rate of reaction tends to be quite small and hence, their generation can be neglected.

7.2.4. Simulating the martensitic lath microstructure

The martensitic laths are regions separated by walls of LAB dislocations with an angle of misorientation of less than 5° , as illustrated in the TEM images of Figure 7.6a and Figure 7.6b. Due to the small angle of misorientation, LABs cannot retard the motion of mobile dislocations via a dislocation pile-up mechanism, in a similar manner to HAGBs [Zhang and Wang, 2000]. However, LABs do (i) interact and impede the motion of mobile dislocations due to the high number of boundaries [Sonderegger et al., 2007] and (ii) owing to the presence of $M_{23}C_6$ precipitates dispersed along LABs, LABs provide strengthening via the Orowan strengthening mechanism.

7. An improved dislocation-mechanics model for microstructural evolution and degradation in 9-12Cr steels

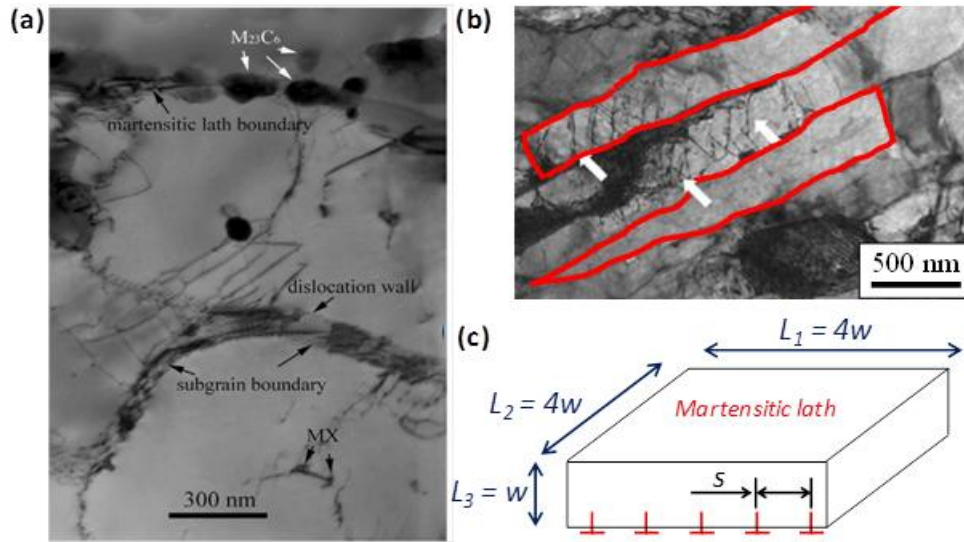


Figure 7.6: Martensitic lath and low-angle boundary dislocation microstructure of 9-12Cr steels for (a) the low-angle boundary dislocation substructure with $M_{23}C_6$ carbides dispersed along martensitic lath boundaries for a CLAM steel [Hu *et al.*, 2013], (b) martensitic lath structure in a P92 steel [Giroux, 2011] and (c) the assumed martensitic lath structure for the material model.

To simulate (i) the kinematic back-stress provided by the $M_{23}C_6$ carbides dispersed along LABs and (ii) the reduction in creep strength as a result of the loss of the martensitic lath structure due to LAB dislocation annihilation, a definition of the structure of a martensitic lath is required. The key parameters defining the structural integrity of a martensitic lath include lath width, shape and the angle of misorientation between the given lath and its neighbouring lath [Sonderegger *et al.*, 2007]. Hence, to simulate the contribution of the martensitic lath structure to the constitutive behaviour of the material, a relationship between the martensitic lath width, shape and LAB angle of misorientation is developed. In the present work, the formulation developed is primarily concerned with pure fatigue deformation and hence, transformation of the martensitic lath structure to a more equiaxed subgrain structure and simultaneous coarsening (the primary mechanism of martensitic lath degradation during creep deformation) is currently not considered in the material model. This deformation mechanism is discussed in more detail in Section 7.3.5.

7. An improved dislocation-mechanics model for microstructural evolution and degradation in 9-12Cr steels

As martensitic laths are regions separated by an array of LAB dislocations, the martensitic lath width will increase as the density of LAB dislocations decreases. Hence, as the cyclic softening behaviour observed in 9Cr steels is primarily due to a loss of the LAB structure [*Fournier et al., 2005; Sauzay et al., 2005; Sauzay et al., 2008*], a subsequent widening of the mean martensitic lath width will occur, such that the martensitic lath width, w , is defined in terms of the fraction of LAB dislocations annihilated [*Giroux, 2011*]:

$$w = \frac{w_0}{1 - \kappa} = \frac{w_0 \rho_{w,0}}{\rho_w} \quad (7.35)$$

where κ is the fraction of annihilated LABs and w_0 and $\rho_{w,0}$ are the initial martensitic lath width and initial LAB dislocation density, respectively. Thus, the widening of martensitic laths during cyclic loading is defined here as martensitic lath coalescence, as the boundary between two adjacent laths does not move, but is annihilated to form a single martensitic lath configuration.

LAB dislocations are made up of both tilt and twist boundaries, arrays of edge and screw dislocations respectively [*Dieter, 1986*], such that:

$$\rho_w = \rho_{w,e} + \rho_{w,s} \quad (7.36)$$

where $\rho_{w,e}$ is the density of edge LAB dislocations and $\rho_{w,s}$ is the density of screw LAB dislocations. From the schematic of Figure 7.7 and the work of Read and Shockley [*1950*], the number of dislocations per metre of boundary, A_w , is:

$$A_w = A_{w,e} + A_{w,s} = \frac{\theta}{b} \quad (7.37)$$

where $A_{w,e}$ and $A_{w,s}$ are the number of LAB dislocations per metre of tilt and twist boundary respectively, and θ is the angle of misorientation between two adjacent LABs. For A_w dislocations per metre of boundary, the spacing between two LAB dislocations, s , is:

7. An improved dislocation-mechanics model for microstructural evolution and degradation in 9-12Cr steels

$$s = \frac{1}{A_w} \quad (7.38)$$

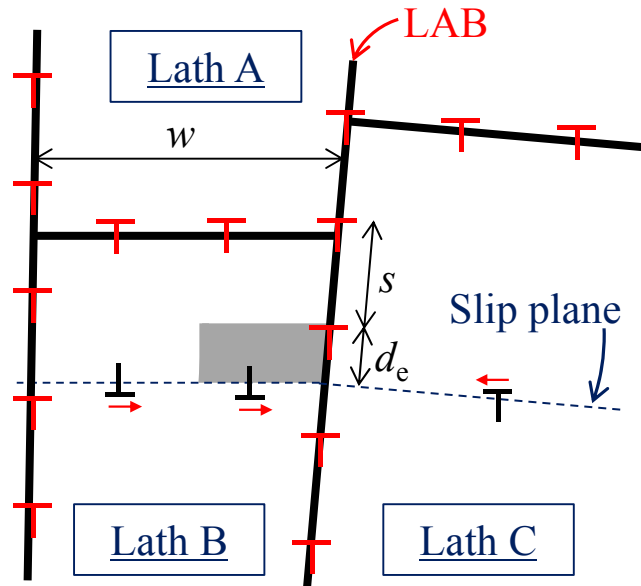


Figure 7.7: Schematic representation of the low-angle boundary structure in martensitic steels.

For a martensitic lath of perimeter length, P_w , the density of LAB dislocations is:

$$\rho_w = \frac{1}{2} \frac{A_w P_w}{A_w} = \frac{1}{2s} \frac{P_w}{A_w} \quad (7.39)$$

where A_w is the area of the LAB regions and the factor $\frac{1}{2}$ ensures that a given LAB is only accounted for once. Equation (7.39) assumes that LABs are a dislocation wide [Riccoult and Kohlstedt, 1983]. To model the LAB regions, a martensitic lath geometry has been developed based on TEM observations and is dependent on the martensitic lath width, w , as shown in Figure 7.8. Using this geometric model, the volume of a martensitic lath is:

$$V_l = L_1 L_2 L_3 = X_1 X_2 X_3 w^3 \quad (7.40)$$

where L_i are the individual lengths which characterise the martensitic lath model in Figure 7.8 (where $i = 1,2,3$) and the constants X_i represent the

7. An improved dislocation-mechanics model for microstructural evolution and degradation in 9-12Cr steels

relationship between the martensitic lath width, w , and the length, L_i , i.e. $L_i = X_i w$. The LAB volume is:

$$V_w = L_1 L_2 L_3 - (L_1 - s_0)(L_2 - s_0)(L_3 - s_0) \quad (7.41)$$

where s_0 is the initial LAB dislocation spacing and thus, the width of a LAB. Hence, the volume fraction of the LAB region is:

$$f_w = \frac{V_w}{V_l} \quad (7.42)$$

Thus, the surface area is defined using the geometry of Figure 7.8 as:

$$A_w = 4s_0 \left(L_1 + L_2 + L_3 - \frac{s_0}{2} \right) = 4s_0 \left(Z w - \frac{s_0}{2} \right) \quad (7.43)$$

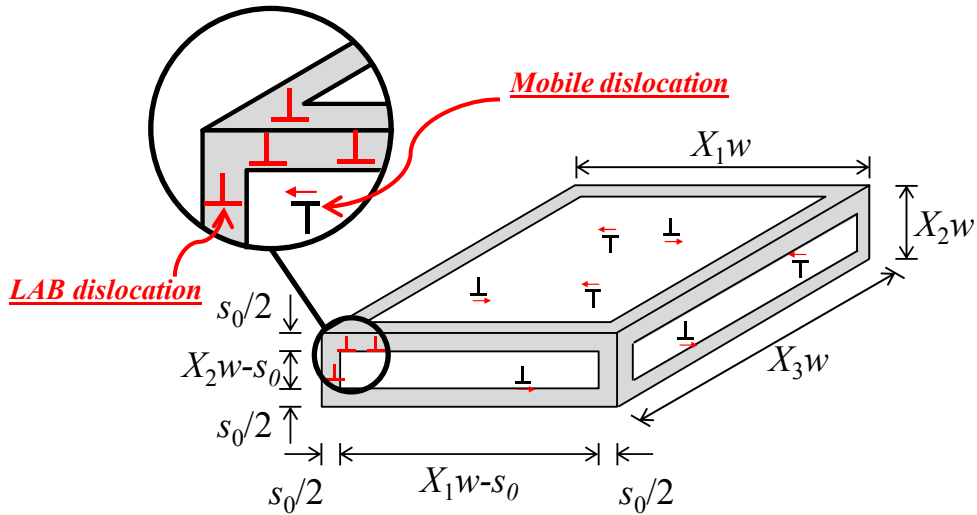


Figure 7.8: Representative model for the LAB microstructure. The shaded regions represent the LAB regions.

As the lath perimeter is $P_w = 4w(X_1 + X_2 + X_3) = 4wZ$, the density of LAB dislocations (Equation (7.39)), becomes:

$$\rho_w = \frac{1}{2s} \frac{wZ}{s_0 \left(wZ - \frac{s_0}{2} \right)} \quad (7.44)$$

From Equation (7.35) and rearranging, gives the LAB spacing as:

7. An improved dislocation-mechanics model for microstructural evolution and degradation in 9-12Cr steels

$$s = \frac{\Gamma}{2s_0\Gamma\rho_w - s_0^2\rho_w^2} \quad (7.45)$$

where $\Gamma = w_0\rho_{w,0}Z$ is a constant dependent on the initial conditions. Then:

$$\dot{s} = -\frac{2s_0\Gamma}{\rho_w^2} \frac{(\Gamma - s_0\rho_w)}{(2s_0\Gamma - s_0^2\rho_w)^2} \dot{\rho}_w \quad (7.46)$$

Equation (7.46) allows the mean angle of misorientation of LABs to be updated incrementally, i.e. as the density of LAB dislocations decreases, the spacing between LAB dislocations continues to increase.

7.3. Results

7.3.1. Material parameter identification

The process of identifying the required material parameters is carried out using a step-by-step procedure. For high temperature cyclic deformation initially, the key steps are (i) elastic, (ii) b.c.c. (iii) precipitate hardening, (iv) HAGB back-stress, (v) dislocation density and (vi) cyclic viscoplastic material parameters. These steps are carried out using a combination of experimental test data and microstructural analysis.

Step 1: The elastic material constants for Young's modulus, E (as illustrated in Chapter 4) and initial cyclic yield stress, $\sigma_{y,0}$, are identified from monotonic test data. Poisson's ratio, ν , is assumed to take a constant value of 0.3 throughout. The shear modulus is defined using Lamé's equation and the elastic material parameters for the ex-service P91 steel are presented in Table 7.1.

Step 2: For b.c.c. materials, the Taylor factor is 2.9, the magnitude of the Burger's vector, b , is 0.248 nm and the material constant, α_1 is 0.4. The number of active slip systems, n , required to define the deformation-rate in the Taylor model is 5.

7. An improved dislocation-mechanics model for microstructural evolution and degradation in 9-12Cr steels

Step 3: For cyclic loading, it is assumed that the precipitate diameter and volume fraction are constant. Furthermore, it is assumed here that the excess Mo, i.e. Mo which does not form solutes contributing to the solid solution strengthening, forms Mo_{23}C_6 carbides dispersed along boundaries. Although the carbides along boundaries are typically dominated by the Cr_{23}C_6 carbides, these precipitates are treated here as one family of precipitate and hence, their spacing is quantified using a mean spacing approach. The model of Spigarelli [2013a] is extended to incorporate the assumption that M_{23}C_6 carbides are dispersed along boundaries and MX carbonitrides are within martensitic lath interiors to define the spacing between particles:

$$\lambda_i = d_i \left(\frac{1}{2} \sqrt{\frac{f\pi}{6f_i}} - \sqrt{\frac{2}{3}} \right) \quad (7.47)$$

where d_i and f_i are the precipitate diameter and volume fraction respectively and i is M_{23}C_6 or MX, with the values taken from measured data [Abe, 2008]. The quantity f is the volume fraction of boundaries for M_{23}C_6 carbides ($f_w + f_g$) and the volume fraction of martensitic lath interiors ($1 - f_w - f_g$) for MX precipitates. Due to the short-term nature of the cyclic tests, Laves phase particles do not form and hence, the concentration of molybdenum solutes, c , remains constant, such that the dc/dt term in Equation (7.7) goes to zero. The precipitate material parameters are presented in Table 7.1.

Step 4: The fourth group of parameters to be identified are the dislocation pile-up material parameters, namely (i) the number of positions available for dislocation pile-ups, n_g^* , (ii) the number of dislocations required for deformation, λ_g/b , and (iii) the grain (block) size parameter, α_g . Assuming that viscous effects can be neglected for temperatures below 500 °C, these parameters are determined by implementing the material model as an elasto-plastic flow rule (as opposed to the elasto-viscoplastic flow rule of Equation (7.6)). The development of the elasto-plastic flow rule is similar to that presented in the precipitate strengthening dislocation-mechanics model of

7. An improved dislocation-mechanics model for microstructural evolution and degradation in 9-12Cr steels

Bardel *et al.* [2015] and the phenomenological approach in Dunne and Petrinic [2005], with the governing flow rule defined as:

$$\dot{p} = \frac{E\dot{\epsilon} \operatorname{sgn}(\sigma - \sigma_b)}{(E + \Psi + (\Omega_g + \Omega_p) \operatorname{sgn}(\sigma - \sigma_b))} \quad (7.48)$$

where Ψ is isotropic hardening modulus and Ω_g and Ω_p are the dislocation pile-up and dislocation bowing kinematic back-stress moduli respectively, defined as:

$$\Psi = \frac{\alpha_1 M b \mu}{2\sqrt{\rho}} \frac{\dot{\rho}}{\dot{p}} \quad (7.49a)$$

$$\Omega_g = \frac{M^2 \lambda_g \mu}{\alpha_g d_g} \left| 1 - \frac{n_g}{n_g^*} \right| \quad (7.49b)$$

$$\Omega_p = \sum_{i=1}^m \left(\frac{2}{\bar{\rho} b \lambda_i} \frac{|\tau_i^3|}{\tau_{i,\max}^2} \frac{M}{n} \left[\left(\frac{\tau_{i,\max}^2}{\tau_i^2} - 1 \right)^{-1/2} - \tan^{-1} \left(\frac{\tau_{i,\max}^2}{\tau_i^2} - 1 \right)^{-1/2} \right]^{-1} \right) \quad (7.49c)$$

Under the assumption that cyclic softening is not important for the initial monotonic phase of loading, the flow rule of equation (7.48) is a function of the kinematic back-stress only. Hence, using the precipitate strengthening spacing constants and initial mobile dislocation density (as described below), the three parameters, n_g^* , λ_g , and α_g , are determined by fitting the constants to test results at 20 °C, 400 °C and 500 °C to ensure that the identified parameters are temperature-independent. The resulting monotonic predicted response with the optimised fit is presented in Figure 7.9 for calibration conditions of applied strain-rate of 0.1 %/s and applied strain-range of ± 0.5 %. The identified material parameters for the formation of dislocation pile-ups at high-angle grain boundaries are presented in Table 7.1.

7. An improved dislocation-mechanics model for microstructural evolution and degradation in 9-12Cr steels

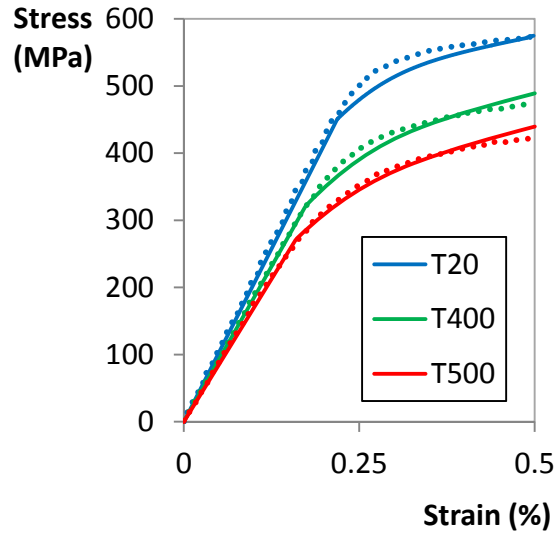


Figure 7.9: Identification of the dislocation pile-up back-stress parameters from monotonic test data at temperatures of 20 °C, 400 °C and 500 °C.

Step 5: The dislocation density evolution material parameters relating to Equations (7.27) to (7.38) are determined using microstructural analysis based on values presented in the literature. The initial mobile dislocation density, $\bar{\rho}$, is set at $1.6 \times 10^{14} \text{ m}^{-2}$, as per the TEM measurements of Sauzay and co-workers [2005; 2008] and the initial density of LAB dislocations is determined based on Equation (7.44) in conjunction with the initial values of mean initial martensitic lath width, w_0 , and mean angle of misorientation, θ_0 . These values are identified from EBSD measurements on ES-P91 steel as discussed in Chapter 3, where the initial values are estimated at $0.5 \text{ }\mu\text{m}$ and 1.6° for w_0 and θ_0 , respectively. Based on the idealised geometry of a martensitic lath structure as shown in Figure 7.6c, with $X_1 = X_2 = 4.0$ and $X_3 = 1.0$, the initial LAB dislocation density, $\rho_{w,0}$, is $9.53 \times 10^{15} \text{ m}^{-2}$, a value which is within the range of 10^{15} to 10^{16} m^{-2} given in the literature [Magnusson and Sandström, 2007]. The mean width of the block configuration is $4.0 \text{ }\mu\text{m}$, from the measured EBSD images of Golden *et al.* [2014], with a block structure model similar to that of the martensitic lath structure of Figure 7.6c, with $X_1 = X_2 = 5$ and $X_3 = 1$. Assuming that the initial density of HAGB dislocations, $\rho_{g,0}$, is set at a value of 10^{16} m^{-2} , the volume fraction of HAGBs is estimated to be 0.1 if the spacing of HAGB

7. An improved dislocation-mechanics model for microstructural evolution and degradation in 9-12Cr steels

dislocations is determined as $s_g = 1/\sqrt{\rho_g}$ and using the identified parameters of Table 7.1. This value is consistent with similar values obtained by Roters and co-workers [2000] for an aluminium alloy, where the volume fraction of the cell wall regions was 0.1. The initial density of cell interior immobile dislocations, $\rho_{i,0}$, is set at $1.0 \times 10^{11} \text{ m}^{-2}$, assuming that the material is initially in a relaxed state [Magnusson and Sandström, 2007]. The critical distance for annihilation of edge dislocations, d_e , is set at a value of $6b$, as determined for copper [Essmann and Mughrabi, 1979] and applied to P91 steel in the work of Sauzay and co-workers [2005; 2008]. It is assumed that there are initially equal densities of edge and screw mobile, LAB and HAGB dislocations. Thus, one fitting parameter is left to be identified, the critical distance for dislocation lock configurations to form, d_l . This value is identified using a best fit to experimental data for cyclic softening. The identified value of d_l is $2b$, a value which lies within the range of values presented in the literature for the critical distance for dislocation lock formation, i.e. from b [Hosseini and Kazeminezhad, 2011] to $6b$ [Roters et al., 2000].

Step 6: The final step involves the identification of the cyclic viscoplastic material parameters, α and β . The value of β is set a constant value of 0.055 MPa^{-1} for P91 steel and the value α is then fitted to stress relaxation test data. The identified temperature-dependent material parameter, α , is presented in Table 7.1 and the correlation achieved with experimental data for the calibration regime is presented in Figure 7.10.

7. An improved dislocation-mechanics model for microstructural evolution and degradation in 9-12Cr steels

Table 7.1: Material constants for ex-service P91 steel.

Parameter	T (°C)	Value	Source
Elastic material parameters			
E	400	183.6 GPa	
	500	173.1 GPa	
	600	144.7 GPa	
μ	400	70.6 GPa	
	500	66.6 GPa	
	600	55.7 GPa	
$\sigma_{y,0}$	400	275 MPa	
	500	200 MPa	
	600	120 MPa	
Material constants (b.c.c.)			
M	N/A	2.9	
b	N/A	0.248 nm	
α_1	N/A	0.4	
n	N/A	5	
Precipitate material parameters			
d_{M23C6}	N/A	50 nm	[Abe, 2008]
f_{M23C6}	N/A	2.0 %	[Abe, 2008]
d_{MX}	N/A	20 nm	[Abe, 2008]
f_{MX}	N/A	0.2 %	[Abe, 2008]
Dislocation pile-up back-stress material parameters			
d_g	N/A	4.0 μm	EBSD
n_g^*	N/A	8.0	
λ_g	N/A	1.0 μm	
a_g	N/A	1.0	
Martensitic lath material parameters			
w_0	N/A	0.5 μm	EBSD
θ_0	N/A	1.6°	EBSD
Dislocation density material parameters			
$\bar{\rho}_0$	N/A	$1.6 \times 10^{14} \text{ m}^{-2}$	[Sauzay et al., 2008]
$\rho_{i,0}$	N/A	$1.0 \times 10^{11} \text{ m}^{-2}$	[Magnusson and Sandström, 2007]
$\rho_{g,0}$	N/A	$1.0 \times 10^{16} \text{ m}^{-2}$	
f_g	N/A	0.1	
d_e	N/A	$6b$ nm	[Essmann and Mughrabi, 1979]
d_l	N/A	$2b$ nm	
Cyclic viscoplastic material parameters			
α	400	$6.0 \times 10^{-6} \text{ s}^{-1}$	
	500	$1.0 \times 10^{-6} \text{ s}^{-1}$	
	600	$8.0 \times 10^{-7} \text{ s}^{-1}$	
β	N/A	0.055 MPa^{-1}	

7. An improved dislocation-mechanics model for microstructural evolution and degradation in 9-12Cr steels

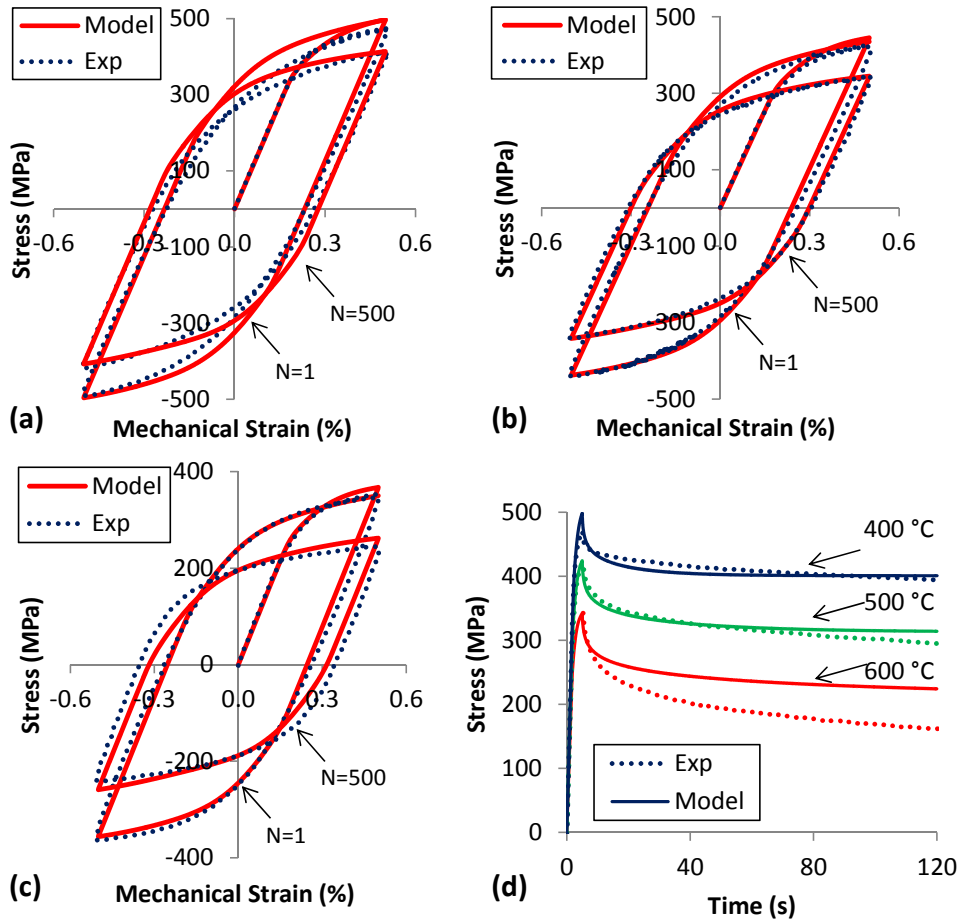


Figure 7.10: Comparison of the experimentally-measured and predicted evolutions of stress-strain response for temperatures of (a) 400 °C, (b) 500 °C, (c) 600 °C and (d) stress relaxation across the three temperatures under calibration conditions of an applied strain-range of $\pm 0.5\%$ and strain-rate of 0.1 %/s.

7.3.2. Validation for 9Cr steel cyclic plasticity

The model is validated against ES-P91 tests for a range of strain-rates and strain-ranges different to the calibration conditions. The results are presented in Figure 7.11 for the initial and softened states across multiple strain ranges, for temperatures of 400 °C and 600 °C.

7. An improved dislocation-mechanics model for microstructural evolution and degradation in 9-12Cr steels

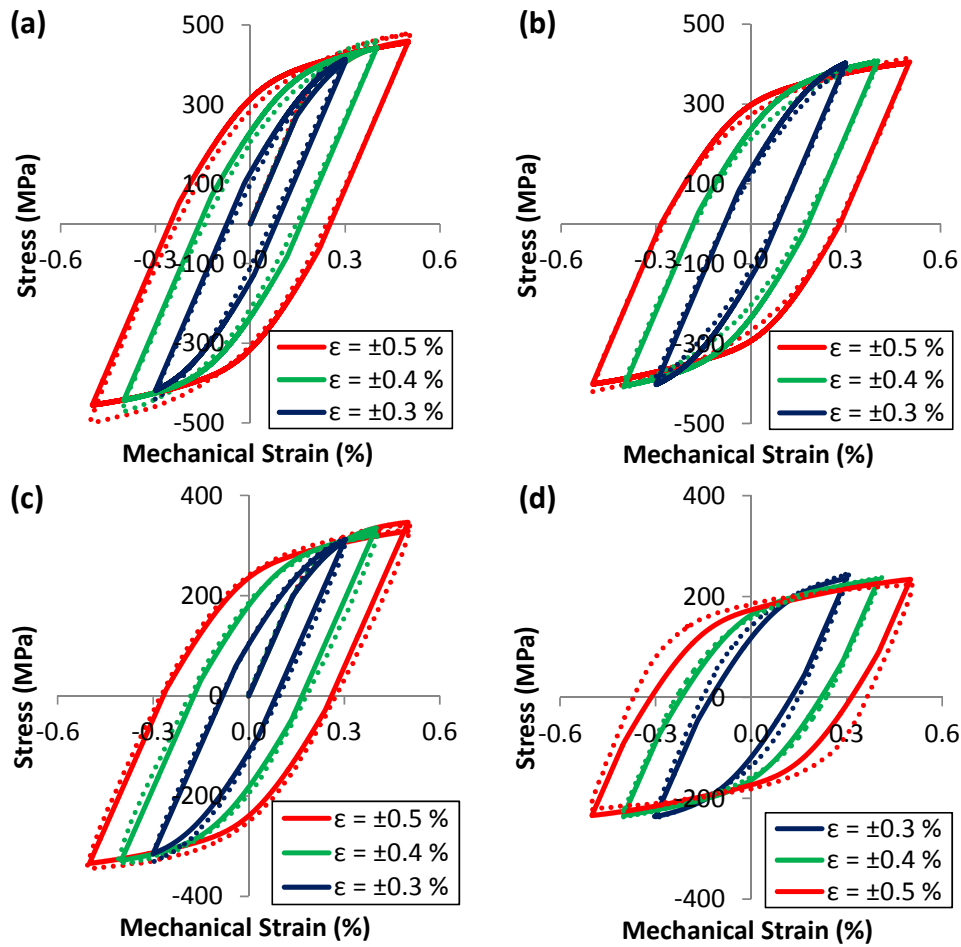


Figure 7.11: Comparison of the measured and predicted stress-strain response for an applied strain-rate of 0.033 %/s for the (a) initial cycle at 400 °C, (b) 600th cycle at 400 °C, (c) initial cycle at 600 °C and (d) 600th cycle at 600 °C across strain-ranges of $\pm 0.3\%$, $\pm 0.4\%$ and $\pm 0.5\%$.

Figure 7.12 compares the predicted stress-strain response at sample strain-rates of 0.1 %/s and 0.0005 %/s for two different strain-ranges, to show the ability of this model to predict both strain-range and strain-rate effects, as well as kinematic back-stress.

7. An improved dislocation-mechanics model for microstructural evolution and degradation in 9-12Cr steels

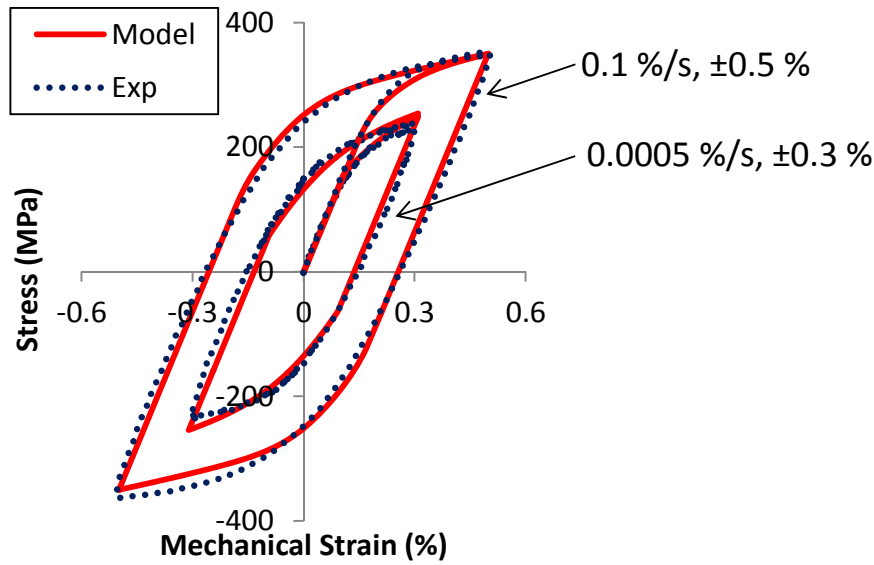


Figure 7.12: Comparison of predicted and measured stress-strain response at 600 °C, for strain-rates of 0.1 %/s and 0.0005 %/s and strain-ranges of ± 0.5 % and ± 0.3 %.

7.3.3. Effect of microstructure on constitutive behaviour

This section investigates the effect of the microstructural parameters on the constitutive behaviour of P91 steel, including the effect of precipitate radii and volume fraction, as well as the effect of initial block size. These microstructural parameters, which are sensitive to the heat treatment process and thermal aging, directly affect the key strengthening mechanisms for both fatigue and creep loading, and hence, play an important role in the high temperature performance of P91 steel. The effects of cyclic loading on the evolution of microstructural parameters, such as martensitic lath width and mobile dislocation density, is also investigated. The microstructural investigations are carried out for the calibration conditions of a strain-rate of 0.1 %/s and a strain-range of ± 0.5 %.

The predicted effect of the initial diameters of MX and $M_{23}C_6$ precipitates on the first hysteresis cycle at 600 °C is shown in Figure 7.13. Smaller precipitates (for a constant volume fraction) are predicted to yield higher strength material, as there are more obstacles to impede the motion of mobile dislocations. This model does not include particle shearing. For the range of precipitates included in this analysis, the MX particles are

7. An improved dislocation-mechanics model for microstructural evolution and degradation in 9-12Cr steels

predicted to have a larger effect on the P91 response, as highlighted in the normalised stress-range predictions of Figure 7.14. The mean spacing between MX precipitates is smaller leading to an increased pinning effect within the martensitic lath interiors.

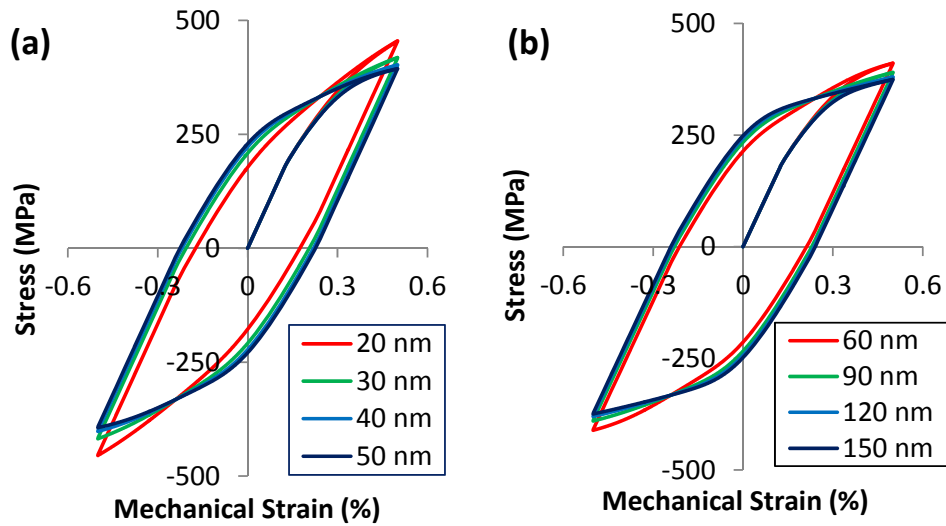


Figure 7.13: Predicted stress-strain response for varying the initial (a) MX and (b) $M_{23}C_6$ precipitate diameter.

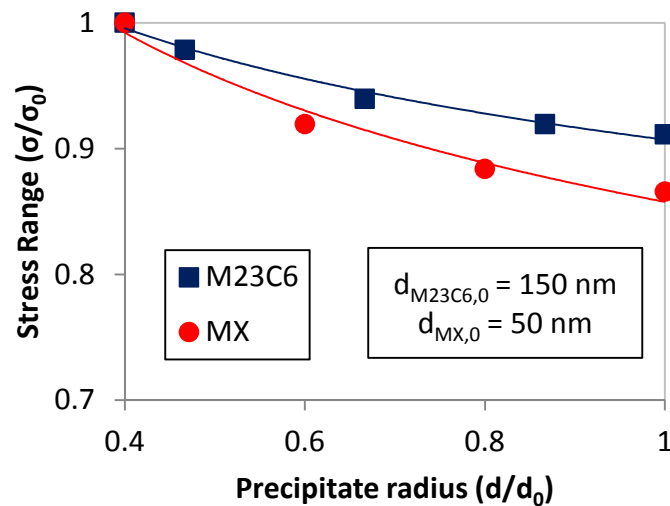


Figure 7.14: Normalised comparison of the effect of MX and $M_{23}C_6$ precipitate diameters on the predicted stress-range. σ_0 is the stress range for the precipitate diameter, $d_{i,0}$.

The initial block size of 9Cr steels is dependent on the heat treatment process; longer hold times and higher temperatures result in a coarser

7. An improved dislocation-mechanics model for microstructural evolution and degradation in 9-12Cr steels

microstructure. In the model presented here, the effect of block size is taken into account via the back-stress for dislocations accumulating at HAGBs (see Equation (7.18)). The model predicts that coarser microstructures give a softer response (reduced stress-range), as illustrated by the result presented in Figure 7.15. The decrease in stress-range for increasing initial block width gives an increased plastic strain-range for the same strain-controlled loading conditions. This, in turn, reduces low cycle fatigue life, assuming material strain-life response is independent of block width, highlighting the requirement to optimise heat treatment prior to use under creep-fatigue loading conditions.

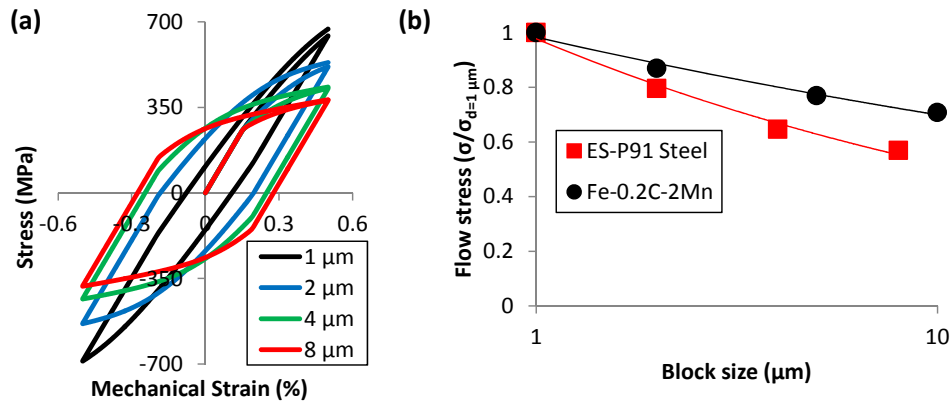


Figure 7.15: (a) Effect of initial block width on the predicted constitutive behaviour of P91 steel and (b) comparison of predicted ES-P91 block size effect with measured data for an Fe-0.2C-2Mn steel [Morito *et al.*, 2006].

The predicted effect of temperature on cyclic evolution of lath width is shown in Figure 7.16a for ES-P91 steel, with only a small effect of temperature predicted. This is expected as thermal aging has been shown to have little effect on the martensitic lath widening [Panait *et al.*, 2010a], and hence, highlighting the importance of plastic deformation on the LAB dislocation annihilation process. However, it must be noted that the cross slip mechanism for immobile dislocations has been omitted from the present study, assuming that dislocation glide is the dominant mechanism for dislocation annihilation. Figure 7.16b highlights the effect of temperature on the dislocation density evolution for temperatures of 400 °C, 500 °C and 600 °C. From this result, a number of observations can be made. Firstly, an

7. An improved dislocation-mechanics model for microstructural evolution and degradation in 9-12Cr steels

overall trend of a loss of mobile dislocations is predicted which is consistent with experimental observations [Giroux, 2011; Sauzay et al., 2005; Sauzay et al., 2008]. The model predicts some initial (anomalous) dislocation hardening for the 400 °C case. This appears to be due to the identification of the critical distance of dislocation lock formation, d_l , and the assumption of constant immobile dislocation density at HAGBs. At lower temperatures, the effects of climb and cross slip are minimised, resulting in a net increase of immobile dislocations and subsequently an increased quantity of mobile dislocations trapped via dislocation entanglement (e.g. dislocation lock formation). Overall, for all three temperatures, a decreasing mobile dislocation density is predicted (indicative of cyclic softening). The initial loss of mobile dislocations for 600 °C (i.e. during cycle 1), appears to be quite large. Once again, this can be linked, at least partially, to the fitting parameter, d_l , and the omission of immobile dislocation density evolution.

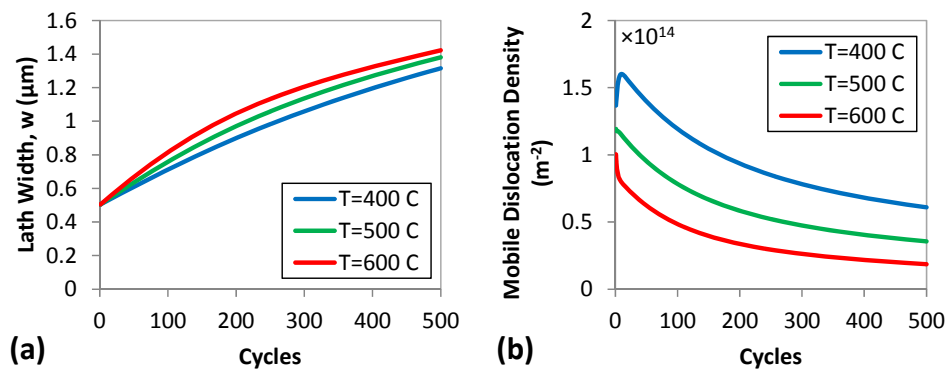


Figure 7.16: Predicted effect of temperature on (a) martensitic lath width and (b) mobile dislocation density with cyclic evolution.

Figure 7.17a shows a comparison of the predicted evolution of martensitic lath width, for two different initial martensitic lath widths, with measured data from the literature [Saad et al., 2011b; Sauzay et al., 2008] for a temperature of 600 °C. Similar martensitic lath growth is predicted for both initial lath widths. The predicted values show significantly more growth than measured data of Saad et al. [2011b]. The latter data was obtained from ‘as-received’ P91, which experienced considerably lower plastic strain accumulation (see Figure 3.57) and the differences in initial microstructure

7. An improved dislocation-mechanics model for microstructural evolution and degradation in 9-12Cr steels

have not been accounted for here, e.g. initial value of dislocation density. The comparison with the measurements by Sazuay *et al.* [2008] of P91 steel tested under cyclic loading (1.0 % applied strain-range) at a temperature of 550 °C give very good agreement. The final value of 1.4 μm predicted here is in very good agreement with the final measured value of 1.5 μm . The evolution of mobile dislocation density is presented in Figure 7.17b; the final predicted value is in agreement with that of Sazuay *et al.* [2008], highlighting the ability of the material model to predict the evolution of mobile dislocation density.

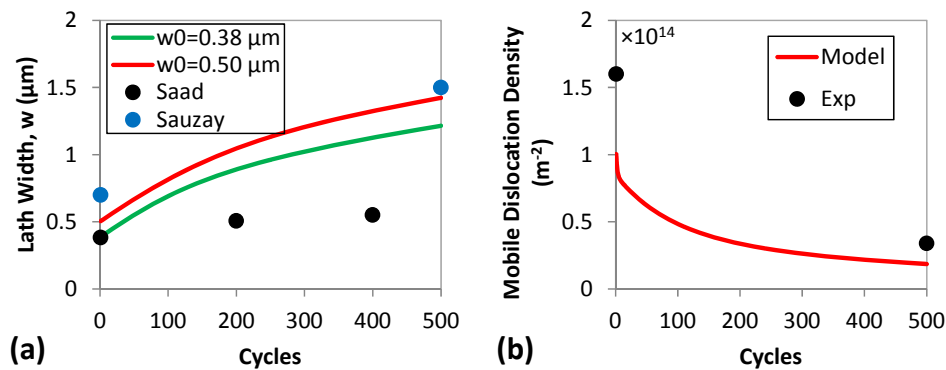


Figure 7.17: Comparison of predicted microstructural evolution with measured data for (a) martensitic lath width (test data of [Saad *et al.*, 2011b; Sazuay *et al.*, 2008]) and (b) mobile dislocation density (data of [Sazuay *et al.*, 2008]).

Figure 7.18 compares the predicted evolution of densities of LAB dislocations and mobile dislocations for increasing numbers of cycles, illustrating a significantly higher density of LAB dislocations. The cyclic evolution of two initial martensitic lath widths is illustrated, with approximately equal densities of LAB dislocations with increasing cycles for both cases (only w_0 and not the accompanying microstructure were modified for this simulation). A considerable reduction in mobile dislocation density is predicted for the coarser lath structure, illustrating the effect of a lack of boundaries for dislocation interactions to occur.

7. An improved dislocation-mechanics model for microstructural evolution and degradation in 9-12Cr steels

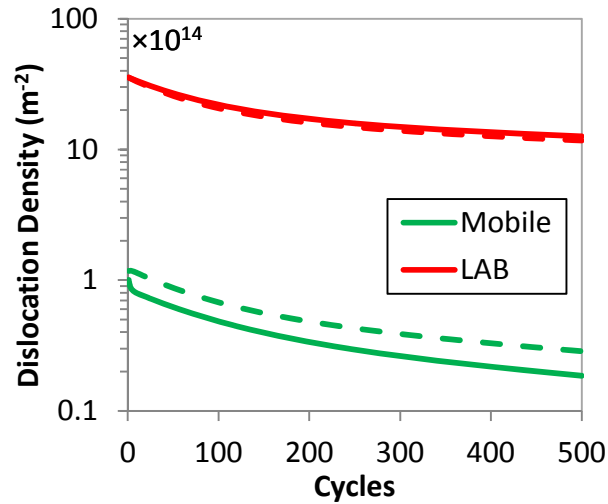


Figure 7.18: Cyclic evolution of mobile dislocation density (mobile) and low-angle boundary dislocation density (LAB) in ES-P91 steel. The solid lines correspond to an initial martensitic lath width of 0.5 μm and dashed to an initial martensitic lath width of 0.383 μm .

Figure 7.19 compares the cyclic evolution of mobile dislocation density with and without the lath structure; highlighting the key role of LAB dislocation annihilation in cyclic softening. Note that the effect of the martensitic lath microstructure on initial yield strength, (recall that $\sigma_{y,0} \sim 10\mu b/w_0$) and the initially high dislocation density associated with a LAB structure is not taken into account. However, the results of Figure 7.19 highlight the ability of the model to simulate cyclic hardening also (e.g. austenitic stainless steels for example).

7. An improved dislocation-mechanics model for microstructural evolution and degradation in 9-12Cr steels

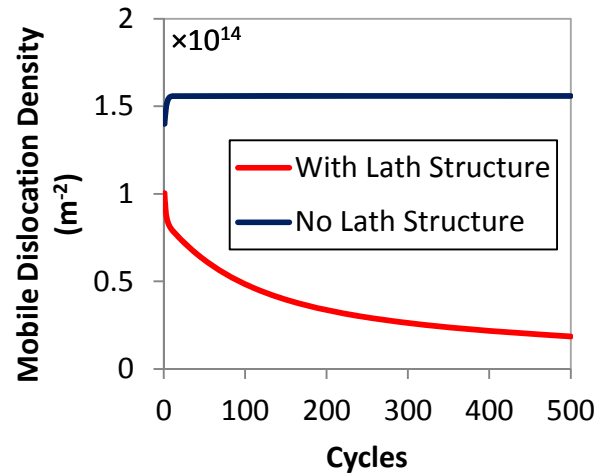


Figure 7.19: Predicted effect of removing the martensitic lath structure.

7.3.4. Initial modelling of creep deformation

Application of the microstructure-sensitive modelling framework to constant load, long-term creep deformation is carried out using stresses in the range of 80 MPa to 125 MPa, at a temperature of 600 °C. This simulation of creep deformation represents a preliminary adaptation of the material model prescribed above, with some modifications to the creep model.

For creep deformation, under the conditions of Equation (7.5), the inelastic strain-rate is:

$$\dot{\epsilon}^{in} = \alpha_{cr} \sinh \beta (|\sigma - \sigma_b|) \text{sgn}(\sigma - \sigma_b) \quad (7.50)$$

The back-stress, σ_b , of Equation (7.50) must account for (i) block growth (as per Equation (7.18)) and (ii) precipitate coarsening. The long-term, high temperature coarsening of precipitates is the key degradation mechanism included here and governed by the Ostwald ripening process, where the mean precipitate diameter is given by:

$$d_i^3 = d_{i,0}^3 + K_i t \quad (7.51)$$

7. An improved dislocation-mechanics model for microstructural evolution and degradation in 9-12Cr steels

with ‘ i ’ denoting either $M_{23}C_6$ or MX precipitates, $d_{i,0}$ is initial precipitate diameter, K_i is coarsening rate and t is time. K_i is fitted to measured data from the literature, with the correlation presented in Figure 7.20 for MX and $M_{23}C_6$ precipitates.

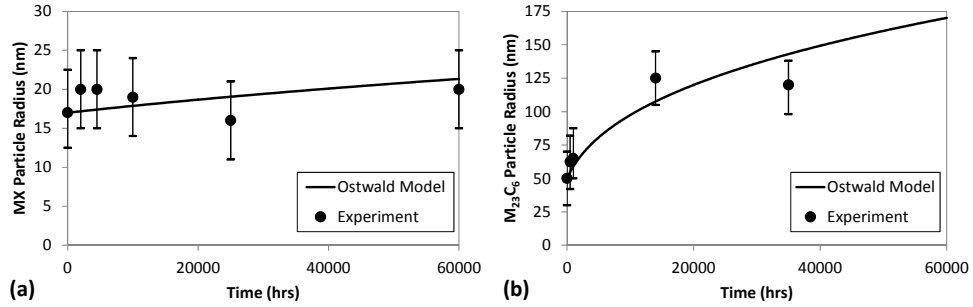


Figure 7.20: Identification of the Ostwald ripening coarsening rates, via comparison with the measured data of Hald and Korcakova [2003], for (a) MX precipitates and (b) $M_{23}C_6$ carbides.

The second adjustment to the cyclic deformation model presented above relates to the evolution of dislocation density. As the current dislocation-mechanics model does not yet account for the transformation of the martensitic lath microstructure to a subgrain structure, the evolution of dislocation density is accounted for via the model of Esposito and Bonora [2012]:

$$\dot{\rho} = \frac{\rho}{\tau_s} \left(1 - \frac{\rho}{\rho_{ss}} \right) \quad (7.52)$$

where τ_s is a constant and ρ_{ss} is the steady-state value of dislocation density.

The final difference between the cyclic and creep models relates to the viscoplastic (creep) constant, α_{cr} . This parameter is identified by consideration of MSR data and the steady state hyperbolic sine creep flow rule ($\dot{\epsilon}_{ss}^{cr} = \alpha_{cr} \sinh \beta \sigma$) is fitted to measured data, as illustrated in Figure 4.10. The identified set of creep constants are presented in Table 7.2.

7. An improved dislocation-mechanics model for microstructural evolution and degradation in 9-12Cr steels

Table 7.2: Creep material constants for P91 steel at 600 °C.

K_{M23C6} (m^3/hr)	K_{MX} (m^3/hr)	ρ_0 (m^{-2})	ρ_{ss} (m^{-2})	τ_s (hr)	α_{cr} (hr^{-1})
5.0×10^{-16}	1.0×10^{-18}	8.0×10^{14}	3.0×10^{14}	1000	0.36×10^{-6}

Figure 7.21 illustrates application of the creep model to P91 steel at 600 °C for applied uniaxial stresses of 80 MPa, 110 MPa and 125 MPa. The comparison of the material model with experimental data demonstrates the potential of a microstructure driven approach to simulating creep deformation. As this is an initial implementation of the material model, some modifications are required to comprehensively account for the evolution of the microstructure and its effect on the resulting creep strains. Potential modifications to enhance the capability of the model are presented in Section 7.3.5.

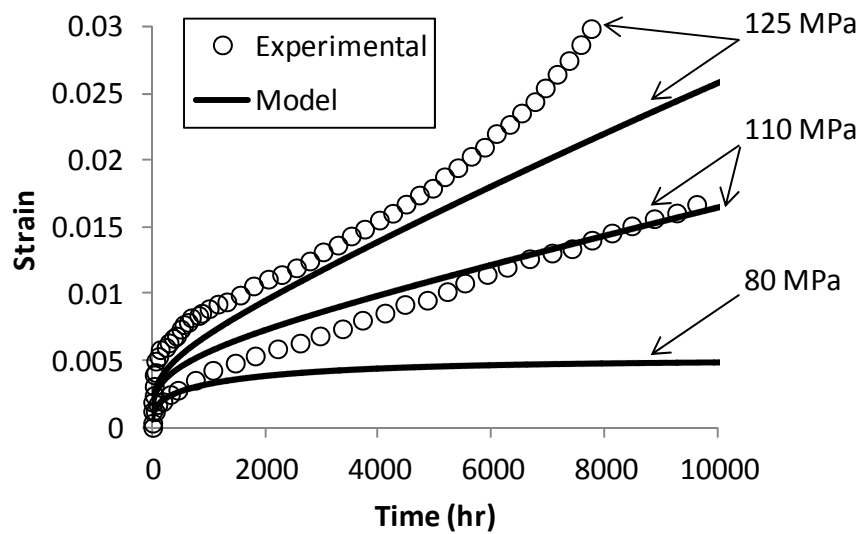


Figure 7.21: Comparison of model predicted and measured [Orlová, 1998] strain for creep deformation at 600 °C.

7.3.5. Limitations of the current model for creep deformation

The cyclic plasticity and creep models demonstrate a new concept for microstructure-sensitive modelling of 9Cr steels. The creep model provides an initial assessment of the capability of the microstructural degradation

7. An improved dislocation-mechanics model for microstructural evolution and degradation in 9-12Cr steels

approach to simulating creep-fatigue deformation in the material. The following highlights the future modifications to be incorporated in the modelling framework to greatly enhance the creep and cyclic plasticity modelling capability.

The present methodology does not incorporate the effect of the time-dependent precipitation of Laves phase particles during long-term creep deformation and the concomitant loss of the solute strengthening. Under the assumption that Laves phase particles form at grain boundaries, as per TEM investigations by Panait *et al.* [2010a], the strengthening owing to these secondary phase particles could be incorporated within the present framework by taking a mean spacing of precipitate value, using an approach similar to Spigarelli [2013]. Although the formation of Laves phase particles does provide a key strengthening mechanism during creep deformation, contributing to the extended primary creep phase observed in 9Cr steels, the loss of the Mo and W solute strengthening mechanism results in (i) decreased creep strength and (ii) a reduced yield stress value, σ_y , via Equation (7.7). Thus, a simultaneous model for the rate of Mo and W depletion (for P92 steels) depletion is required within the present framework.

There is a requirement to measure and subsequently develop a model, for the coarsening of the HAGB microstructure, as well as transformation and coarsening of the martensitic lath microstructure to a more equi-axed subgrain structure during creep deformation.

Finally, the creep deformation only incorporates primary and secondary creep and does not account for the mechanisms of degradation during tertiary creep. In particular, the formation of creep voids, which predominantly tend to form near larger particles such Laves phase precipitates, lead to creep damage in the material, and hence, tertiary creep. The formation of voids could be incorporated using the CDM approach of Hayhurst and co-workers [Perrin and Hayhurst, 1996]. The rapid degradation of the microstructural parameters, such as HAGB deformation [Abe, 2015], during tertiary creep should also be investigated and included

7. An improved dislocation-mechanics model for microstructural evolution and degradation in 9-12Cr steels

within the current formulation to yield more accurate simulations of the tertiary creep deformation.

7.4. Discussion

The material model presented here, coupled with the parameter identification methodology, predicts the constitutive response of the material including salient microstructure variables. A key advantage is that the microstructural parameters are primarily temperature-independent. Furthermore, the hyperbolic sine formulation allows prediction of the strain-rate effect.

During cyclic softening, LAB dislocation annihilation occurs, leading to martensitic lath coalescence and an increase in the mean martensitic lath width (Figure 7.16a and Figure 7.17a). The increased rate of martensitic lath widening in the ES-P91 steel when compared to the AR-P91 steel of Saad and co-workers [2011a; 2012] is expected due to the higher plastic strain-range in the ES-P91 steel (see Chapter 3). The predictions of Figure 7.17 show the ability of the model to capture the effect of initial martensitic lath width on the cyclic dislocation density evolution. This illustrates the importance of (i) chemical composition and (ii) heat treatment on the high temperature constitutive performance of 9Cr steels.

From the present microstructural evolution predictions and comparisons with measured microstructural data from the literature, it is clear that cyclic deformation can have a detrimental effect on structural integrity of P91 and similar materials. In particular, the initial rapid decrease of dislocation density, concomitant with a rapid increase in martensitic lath width, leads to a much coarser microstructure over a relatively small number of cycles. This coarser hierarchical microstructure, with the potential for strain-dependent particle coarsening [Taneike *et al.*, 2001], yields a material with a significantly reduced creep strength. This highlights the requirement for the material microstructure modelling for fatigue-creep and creep-fatigue. It is argued here that the microstructural degradation of 9Cr steels due to LCF loading is the predominant source of fatigue damage for power plant

7. An improved dislocation-mechanics model for microstructural evolution and degradation in 9-12Cr steels

components, even though such components are predominantly subjected to creep loading. However, on the other hand, due to the potential short time to fatigue crack initiation in 9Cr steels [Li *et al.*, 2015], the effects of the formation of micro-cracks at point defects such as $M_{23}C_6$ and MX precipitates cannot be omitted, along with their potential contribution to the coalescence of creep voids along boundaries. This requires the inclusion of HAGBs and dislocation pile-up formation in a microstructure-sensitive macro-scale material model, as dislocation-mechanics plays an important role in micro-crack formation [Hu *et al.*, 2014]. Coupled with the exacerbated microstructural degradation generally associated with TMF conditions, it is anticipated that thermal fatigue (and associated microstructural degradation) is a key consideration for failure of power plant components, including Type IV cracking. Thus, the development of a creep model, using the present set of microstructural parameters, and incorporating new parameters, such as the precipitation of Laves phase particles and creep void formation, represents a key next step in the development of a multi-scale modelling methodology for next generation power plant components under flexible operation.

The ability of the material model to predict the stress-strain response in materials without a hierarchical microstructure (Figure 7.19) is of particular importance for the simulation of welded connections. For 9Cr welded connections, without the inclusion of boron to maintain the hierarchical structure following welding [Albert *et al.*, 2005; Abe *et al.*, 2010], the microstructure of the material is significantly different to that of parent material. Due to the narrow HAZ region in a welded connection (more accurately characterised as coarse-grain, fine-grain and inter-critical HAZ subdivisions of a heterogeneous microstructure), it is difficult to determine phenomenological material parameters, i.e. such as the fourteen parameters required per temperature for the model presented in Chapter 4, across a broad range of temperatures and loading conditions. Hence, a material model based on microstructural parameters measured using EBSD, SEM and TEM offers an attractive solution. The yield stress and Young's modulus can be determined from micro-hardness and nano-indentation

7. An improved dislocation-mechanics model for microstructural evolution and degradation in 9-12Cr steels

testing, leaving only a small number of material parameters to be identified via cross-weld specimen testing.

Compared to the model presented in Chapter 6, this new model represents significant improvements in the definition of (i) martensitic lath widening due to the physical LAB dislocation annihilation process, (ii) an improved model for the bowing out of a dislocation pinned at precipitates, (iii) extension of the dislocation-mechanics framework to include both edge and screw type dislocations, and (iv) the incorporation of HAGB strengthening via a dislocation pile-up mechanism, resulting in a significant reduction in the required number of material parameters and improved prediction of the evolution of key microstructural variables, such as martensitic lath widening. Although this model does not currently account for immobile dislocation-dislocation interactions (e.g. dislocation entanglement leading to increased strengthening), future work will look to incorporate this within the present framework, in conjunction with (i) strain-dependent precipitate coarsening [*Taneike et al., 2001*] and (ii) more physical representation of the cyclic viscoplastic material parameters, as discussed in the work of Dyson [2000].

7.5. Conclusions

This chapter presents an improved modelling methodology for microstructure-sensitive modelling of 9Cr steels compared to the model presented in Chapter 6. In particular, this chapter presents a novel macro-scale modelling methodology for LAB dislocation annihilation and enhanced precipitate and grain boundary strengthening. The main conclusions from this work are:

- Incorporation of key microstructural parameters within a strain-rate sensitive material model. The newly developed model is capable of predicting the strain-rate effect for higher and intermediate strain-rates via the variable strain-rate sensitivity of the hyperbolic sine formulation.

7. An improved dislocation-mechanics model for microstructural evolution and degradation in 9-12Cr steels

- Development of a model for the combined kinematic back-stress due to (i) $M_{23}C_6$ carbide and MX carbonitride precipitate strengthening and (ii) the formation of dislocation pile-ups at high-angle boundaries, with successful application to high temperature low cycle fatigue conditions. The predicted results highlight the requirement for long-term thermal (and strain-dependent) stability of precipitates and the importance of maintaining a minimum block width within the hierarchical microstructure for high temperature cyclic deformation.
- Development of a dislocation-mechanics modelling framework for simulating cyclic softening due to microstructural degradation and a reduction of the initially high mobile dislocation density. The initial martensitic lath width is predicted to control the level of consumption of mobile dislocations.
- Due to the complex nature of the hierarchical microstructure in 9Cr steels, a broad range of strengthening mechanisms must be incorporated to accurately predict the constitutive behaviour. The omission of any one of these strengthening mechanisms is found to yield unsatisfactory results.
- The predicted results highlight the considerable microstructural degradation which occurs in 9Cr materials under cyclic loading. In particular, martensitic lath coalescence due to the loss of the low-angle boundary microstructure is predicted to be severe for initial cycles. This microstructural degradation is anticipated to have a significant effect on the thermo-mechanical performance of such materials.

8. Conclusion and Recommendations

8.1. Conclusions

The investigation into the high temperature fatigue performance of 9Cr steels presented in this research includes (i) the experimental testing of P91 steel and MarBN, (ii) development of a phenomenological user material subroutine and step-by-step parameter identification methodology for the constitutive behaviour of 9Cr steels using a hyperbolic sine unified cyclic viscoplastic material model and (iii) a microstructure-sensitive cyclic viscoplastic model for high temperature fatigue. The key conclusions determined during this research are presented below.

The high temperature low cycle fatigue tests carried out on ex-service P91 steel (ES-P91) in Chapter 4 illustrate considerable cyclic softening and a significant strain-rate effect. Cyclic softening is shown to be a temperature-dependent phenomenon resulting in a material with lower (creep) strength. Comparisons made against 'as-received' P91 steel from the literature, with similar chemical composition and heat treatment, highlight little or no effect of the 35,168 hrs subcritical service history. However, the coarser martensitic lath structure of the ES-P91 prior to fatigue testing indicates that the 65 start-up cycles (flexible plant operation) have possibly softened the material, leading to more rapid cyclic softening.

The strain-rate effect in P91 steel becomes significant at temperatures in excess of 500 °C, resulting in a reduction in stress-range. Decreasing strain-rate also yields a lower number of cycles to failure across the three temperatures tested (e.g. 400 °C, 500 °C and 600 °C). The experimentally observed decrease in stress-range with decreasing strain-rate at 600 °C (e.g. 646 MPa at a higher strain-rate of 0.033 %/s compared with 473 MPa at an intermediate strain-rate of 0.0005 %/s) is consistent with the measured effect of stress on minimum creep strain-rate for constant load tests. This highlights (i) potential complications and limitations with operating 9Cr

8. Conclusion and Recommendations

steels at higher temperatures and (ii) the requirement to account for the strain-rate effect when predicting plant creep-fatigue life. As laboratory experiments are normally carried out at higher strain-rates, reliable extrapolation to the intermediate and lower strain-rates of power plant components is required. Hence, material models, which are normally calibrated at higher strain-rates, must be capable of accurately predicting the constitutive behaviour of materials across a broad range of strain-rates and validated against slower strain-rate tests. The incorporation of variable strain-rate sensitivity in the constitutive model through a hyperbolic sine flow rule represents an important capability of the framework presented. It was shown in Chapter 4 that the hyperbolic sine methodology allows a smooth transition from the higher strain-rate regime to the low strain-rate regime. This formulation has been validated in Chapter 7 for high temperature low cycle fatigue behaviour at strain-rates from 0.1 %/s to 0.0005 %/s.

Thermo-mechanical loading is found to have a potentially detrimental effect on the fatigue life of P91 steel. Through a comprehensive thermo-mechanical fatigue (TMF) test program of ES-P91, across a range of strain-rates and strain-ranges and for in-phase (TMF-IP) and out-of-phase (TMF-OP) loading, the fatigue life of the ES-P91 steel is found to be considerably lower than that of isothermal fatigue tests in the same 400 °C to 600 °C temperature range. In particular, TMF-OP loading, which is more representative of realistic loading conditions, is shown to have a devastating effect on the fatigue life of ES-P91 steel (approximately 50 % of the fatigue life of TMF-IP loading in the 400 °C to 600 °C range and just 30 % of the fatigue life under isothermal loading conditions at 600 °C). This highlights (i) the requirement to characterise the TMF behaviour of candidate materials, (ii) the importance of thermal strains on the structural integrity of plant components and (iii) the significance of being able to simulate the effect of thermal transients on the material deformation.

MarBN, a new 9Cr steel, developed for higher creep strength at higher operating temperatures, has been tested, for the first time, under fatigue

8. Conclusion and Recommendations

loading conditions. This initial phase of fatigue testing represents a key step in the successful development of a candidate material for next generation power plant materials. The cast MarBN product tested here is found to have a superior strength when compared to both P91 and P92 steels. It is concluded that this improved strength is predominantly due to the inclusion of 3 wt.% tungsten, improving the solid-solution strengthening mechanism and the density and performance of $W_{23}C_6$ carbides. Secondly, it is the opinion of the author that the inclusion of a small amount of boron yields more stable $M_{23}C_6$ precipitates and hence, improved precipitate strengthening which contributes to the overall strength of the material. These modifications to the 9Cr steels have been shown here to vastly improve the material strength under fatigue loading conditions and early indications in the literature also anticipate that these changes will yield a material with improved creep performance also.

A key observation relating to microstructure is that the initial martensitic lath width is found to be extremely important for cyclic softening in 9Cr steels. The coarser initial martensitic lath width results in a higher rate of cyclic softening, leading to (i) more rapid microstructural degradation and (ii) a reduction in creep strength. This is due to easier motion of dislocations in the coarser microstructure. The coarser grain size in MarBN may also facilitate increased mobility of dislocations. However, due to the superior strength, MarBN maintains a higher stress-range until the onset of failure, further highlighting the important role played by tungsten for high temperature deformation.

The MarBN material tested here is shown to have a fatigue life comparable with P91 steel. However, it should be noted that the MarBN material is in cast form, leading to the existence of casting defects and gas pores in the microstructure. This has led to the formation of fatigue striations at such inclusions within the test specimen, reducing the fatigue life of the MarBN material. Due to the potential improvements to fatigue life which may be gained from a rolled product and optimised heat treatments, as well as the higher strength at 600 °C, MarBN is predicted to have at least equivalent fatigue performance to that of the current state-of-the-art materials.

8. Conclusion and Recommendations

Combined with (i) a higher creep strength compared with the current power plant materials and (ii) suppression of Type IV cracking via the maintenance of a hierarchical microstructure following welding, MarBN has the potential to be a successful material for future power plant operating under flexible loading and higher temperatures (e.g. ultra-supercritical operation), resulting in more sustainable power generation with reduced emissions.

The results of the high temperature fatigue test program highlight the rapid microstructural degradation under flexible operation and the requirement to account for the evolution of key microstructural variables for potential creep-fatigue-corrosion models. The evolution of the microstructure under cyclic plasticity is also extremely important for realistic creep-fatigue simulations at the component level. The development of a microstructure-sensitive cyclic viscoplasticity model at the macro-scale, involving key microstructural parameters for both creep and fatigue loading such as martensitic lath width, precipitates and dislocation density, represents an important framework for microstructural evolution. Hence, more accurate simulations of the constitutive behaviour of 9Cr steels under creep-fatigue loading can be carried out. The newly developed microstructure-sensitive fatigue model demonstrates excellent performance in the prediction of the constitutive behaviour of ES-P91 steel across a range of temperatures, strain-ranges and strain-rates. The material model is capable of predicting cyclic softening due to a decrease of mobile dislocation density via (i) spontaneous mutual annihilation of dislocations, (ii) low-angle boundary dislocation annihilation, and (iii) the immobilisation of dislocations. The development of a geometrical model relating martensitic lath width, shape and angle of misorientation to low-angle boundary dislocation density is the key step to simulating the cyclic softening phenomenon in a macro-scale material model. The predictions for the evolution of mean martensitic lath width, which occurs here due to low-angle boundary dislocation annihilation and subsequent martensitic lath coalescence, are found to be within acceptable limits for measured data presented in the literature. This successful prediction of martensitic lath width is central to mobile

8. Conclusion and Recommendations

dislocation density evolution and subsequently, prediction of recovery in 9Cr steels.

8.2. Recommendations for Future Work

The work presented here represents a significant first step in the successful development of a materials design tool to aid the manufacture of complex alloys for high temperature creep-fatigue-corrosion loading conditions. Further work is necessary to achieve the overall aim of an advanced materials capability to design and optimise materials for next generation power plant. The following section highlights some of the key steps required to fulfil this aim, with concepts relating to experimental testing, microstructural analysis, manufacture (including chemical composition and heat treatment with thermodynamic modelling) and physically-based multi-scale modelling discussed.

The test program of Chapter 3 presents a characterisation of the high temperature fatigue behaviour of 9Cr steels. However, clearly a more expansive and comprehensive program of tests would be beneficial. For example, a series of creep-fatigue, creep-TMF and creep-fatigue-corrosion tests could be considered to investigate the effect of the interactions of these different key loading conditions on the life of 9Cr steels. These tests would allow validation of more complex constitutive models and life assessments at the component level. There is also a broad range of thermal aging, corrosion and oxidation experiments which can be carried out to investigate and quantify the temperature-dependent mechanisms of deformation, such as precipitate coarsening and oxide layer growth similar to that of O'Hagan *et al.* [2015a].

Coupled with this potential to investigate a wider scope of mechanisms of deformation, there are opportunities to extend upon the microstructural analyses carried out on 9Cr steels to date. This microstructural analysis should focus on (i) characterising the initial microstructure (e.g. for varying composition and heat treatments), (ii) microstructural evolution under creep, fatigue and corrosion loading and (iii) microstructural investigations to

8. Conclusion and Recommendations

determine the mechanisms of failure across a range of test conditions. In particular, more TEM studies are required to provide more detail, in terms of cyclic evolution for example, on (i) the precipitates, (ii) dislocation density and (iii) martensitic laths during high temperature creep-fatigue deformation.

On the basis of the numerical modelling methodology presented here, a number of minor improvements and modifications can be suggested for the microstructure-sensitive fatigue model. Firstly, the volume fraction of $M_{23}C_6$ carbides left behind in the matrix material can be incorporated using the volume fraction of low-angle boundaries annihilated and incorporating the new density of $M_{23}C_6$ precipitates within the martensitic lath interiors to adjust the spacing of cell interior obstacles to account for low-angle boundary dislocation annihilation. The spacing of solutes (Mo and W) should also be included as obstacles to the motion of mobile dislocations, as well as the presence of immobile dislocations. Furthermore, the strain-dependent increase in particle spacing should also be incorporated in the present framework, e.g. as per the model of Taneike and co-workers [2001].

The microstructure-sensitive model presented here for recovery in 9Cr steels is predicated on the evolution of mean martensitic lath width and dislocation-mechanics based on the glide of mobile dislocations only. Thus, there exists an opportunity to incorporate the effects of climb and cross-slip to evolve the density of immobile dislocations. In particular, cross-slip can be quite important for b.c.c. materials at high temperature and inclusion of cross-slip will also account for stacking faults. As the stacking fault energy is quite high in 9Cr steels, and hence, dynamic recovery and not dynamic recrystallization is important, illustrating the need to account for the cross-slip mechanism with respect to screw dislocations. Furthermore, the effect of initial martensitic lath width (via variations in heat treatment and measuring the subsequent evolution of martensitic lath width as a function of cycles) requires further experimental investigation to (i) quantify its effect on the high temperature fatigue performance of 9Cr steels and (ii) provide further validation of the proposed microstructure-sensitive modelling framework. The initially rapid degradation of martensitic lath

8. Conclusion and Recommendations

width also highlights the requirement to carry out creep tests and pre-fatigued creep tests. The pre-fatigued creep test would be at identical conditions to the creep test, but cycled for approximately 20 to 50 cycles prior to the commencement of the creep part. The purpose of this test would be to illustrate the importance of accelerated microstructural degradation on the creep life of hierarchical 9Cr steels.

The modelling approach presented here uses mean values of the microstructural variables, for example, martensitic lath width and angle of misorientation between laths. However, the microstructure of such materials has a distribution of such parameters; these distributions which can be measured using techniques such as EBSD, in the case of the initial angle of misorientation of low-angle boundaries, for example. The distributions can be incorporated by extending the UMAT subroutine of Chapter 4 to incorporate the microstructure-sensitive model, coupled with distributions of microstructural parameters in the material microstructure. The distribution of $M_{23}C_6$ and MX precipitates may yield precipitates which are too small to pin dislocations. For these smaller precipitates, particle shearing may be important and hence, further investigation is required to examine these processes.

The microstructure-sensitive model developed here focused on fatigue (and creep to a lesser extent) loading at high temperature. However, for component level modelling under realistic conditions, it would be beneficial to extend the current framework to incorporate the effect of corrosion deformation. Thermal aging and corrosion testing is the focus of ongoing work at NUI Galway [*O'Hagan et al., 2015a*], in conjunction with material models incorporating the effect of corrosion on creep life of 9Cr steels [*O'Hagan et al., 2015b*]. There also exists the opportunity to account for the loss of strengthening mechanisms, e.g. $M_{23}C_6$ carbide depletion near the surface, due to the corrosion process via volume fraction approaches. Moving forward to realistic operating conditions, this microstructural degradation could play an important role in accurate life assessment of next generation power plant components.

8. Conclusion and Recommendations

The majority of the discussion in this thesis relates to the development of material models at the macro-scale. However, as the proposed concepts are based on physical and micromechanical processes, a multi-scale modelling methodology is required, with the microstructure-sensitive modelling framework at the continuum level representing an efficient method for providing a physical link between the macro-scale deformation of components and the micro- and nano-scale mechanisms of deformation. Thus, there is a necessity to carry out bottom-up modelling using a crystal plasticity framework such as those developed by Li *et al.* [2014], Giroux [2011] or Sweeney *et al.* [2014]. This approach should follow a consistent methodology through all of the scales and, as proposed here, should be based on a dislocation-mechanics methodology. The importance of the crystal plasticity modelling is to ensure that the effects predicted at the macro-scale, e.g. precipitate strengthening, are consistent with that of measured microstructure models at the micromechanical level. Furthermore, due to the complexity of dislocation interaction events, for example at high-angle grain boundaries, and to ensure that the dislocation-mechanics approach is providing realistic simulations, discrete dislocation dynamics and atomistic level modelling can be important in the multi-scale modelling framework.

The current modelling methodology just considers the constitutive behaviour of 9Cr steels. However, in such materials, crack initiation occurs quite early, with the generation of micro-cracks possibly at microstructural defects such as precipitates dispersed along boundaries. The formation of such micro-cracks, which have been observed using SEM, can propagate to form macro-scale cracks leading to a fatigue dominated failure. The development of a dislocation-based failure prediction methodology is the focus of ongoing work, e.g. see Li *et al.* [2015]. The formation of micro-cracks due to fatigue loading at precipitates dispersed along boundaries also has the potential to aid the coalescence of creep voids, promoting creep crack growth in the material, representing a potentially important creep-fatigue damage mechanism.

8. Conclusion and Recommendations

In terms of the phenomenological modelling methodology presented, the development of a plastic strain energy density based failure model represents an appealing prospect for predicting the failure of 9Cr steels subjected to TMF loading conditions. With the predicted constitutive behaviour illustrating good agreement with experimental data, plastic strain energy density methods would allow for the asymmetric nature of TMF hysteresis loops to be accounted for, and hence, enabling more accurate life prediction for (i) TMF tests under experimental conditions and (ii) realistic TMF loading for power plant candidate materials and even other TMF processes such as automotive exhaust systems, for example. Continuum damage mechanics methodologies, e.g. the approach of Perrin and Hayhurst [1996], should also be investigated and extended to creep-fatigue-corrosion deformation in 9Cr steels and other candidate materials.

There also exists a requirement to investigate the manufacturing process of candidate materials, including detailed analysis of the material chemical composition and heat treatment procedure. The simulation of the thermodynamic processes involved using ThermoCalc, for example, can provide invaluable information into the precipitation process during heat treatment. Hence, using a microstructure-sensitive creep-fatigue modelling methodology, an optimised initial material microstructure can be developed for flexible, high temperature operation of power plant components. Of course, a comprehensive test program is also necessary to (i) validate the thermodynamic simulations and (ii) investigate the strengthening mechanisms, mechanisms of microstructural deformation and failure of any potential candidate materials. With respect to welded connections, the post weld heat treatment must also be investigated, as well as the welding process itself. The possibility of carrying out tests on simulated heat affected zone (HAZ) specimens under the conditions mentioned above should also be considered.

Investigations into the effect of microstructure evolution during creep-fatigue loading of welded connections is also important for the prediction of Type IV cracking of power plant components. Although Type IV cracking is a creep-dominated failure mechanism, microstructural degradation during

8. Conclusion and Recommendations

flexible loading can soften the material, reduce creep strength and accelerate the failure of such components. Thus, the development of a microstructure-sensitive creep-fatigue modelling methodology in this research is anticipated to aid numerical life prediction of such components and due to the reduction in creep strength, also highlights the key requirement to account for the evolution of the microstructure under flexible operation.

Appendix A: Thermodynamic Framework

The thermodynamic framework for the hyperbolic sine continuum level model is predominately based on the well established framework for the power law model of Chaboche [*Lemaitre and Chaboche, 2000*]. The thermodynamic framework satisfies both the first and second laws of thermodynamics and the thermodynamic variables related to the hardening terms are obtained through careful choice of internal variables. The conservation of energy is defined as [*Lemaitre and Chaboche, 2000; Maugin, 1992; Othman et al., 1993; Vakili-Tahami et al., 2005*]:

$$\rho \dot{e} = \boldsymbol{\sigma} : \dot{\boldsymbol{\varepsilon}} + r_{\text{vd}} - \text{div } \mathbf{q} \quad (\text{A1})$$

where e is the specific internal energy, r_{vd} is the volumetric density of internal heat production and \mathbf{q} is the heat flux. The second law of thermodynamics is defined as [*Lemaitre and Chaboche, 2000*]:

$$\rho \frac{ds}{dt} + \frac{\text{grad } \mathbf{q}}{T} - \frac{r_{\text{vd}}}{T} \geq 0 \quad (\text{A2})$$

where s is the specific entropy. Combining the first and second laws of thermodynamics and multiplying by $T > 0$ yields:

$$\rho \left(T \frac{ds}{dt} - \frac{de}{dt} \right) + \boldsymbol{\sigma} : \dot{\boldsymbol{\varepsilon}} - \mathbf{q} \cdot \frac{\text{grad } T}{T^2} \geq 0 \quad (\text{A3})$$

The rate form of the specific free energy, Ψ , is given as [*Lemaitre and Chaboche, 2000*]:

$$\dot{\Psi} = \frac{de}{dt} - T \frac{ds}{dt} - s \frac{dT}{dt} \quad (\text{A4})$$

The Clausius-Duhem inequality may then be obtained by rearranging and inserting Equation (A4) into the second law of thermodynamics [*Lemaitre and Chaboche, 2000*]:

$$\boldsymbol{\sigma} : \dot{\boldsymbol{\varepsilon}} - \rho(\dot{\Psi} - s\dot{T}) - \mathbf{q} \cdot \frac{\text{grad } T}{T^2} \geq 0 \quad (\text{A5})$$

Appendix A: Thermodynamic Framework

For the hyperbolic sine material model within the present study, the specific free energy, Ψ , may be decomposed into its elastic and inelastic components as:

$$\Psi = \Psi_{\text{el}}(\boldsymbol{\varepsilon}^{\text{el}}, T) + \Psi_{\text{pl}}(\boldsymbol{\alpha}_i, r_i, T) \quad (\text{A6})$$

where Ψ_{el} represents the elastic specific free energy, $\boldsymbol{\varepsilon}^{\text{el}}$ is the elastic strain tensor, Ψ_{pl} is the inelastic specific free energy, $\boldsymbol{\alpha}_i$ represents the kinematic hardening variables, r_i corresponds to the isotropic hardening variable and $i = 1, 2$. From Equation (A6), the thermodynamic variables related to the hardening terms are given as:

$$R_i = \rho \frac{\partial \Psi}{\partial r_i} \quad (\text{A7})$$

$$\boldsymbol{\chi}_i = \rho \frac{\partial \Psi}{\partial \boldsymbol{\alpha}_i} \quad (\text{A8})$$

To relate the hardening thermodynamic variables to a set of complementary laws, a dissipation potential is required. A Legendre-Fenchel transformation is used to obtain the flux variables as a function of the dual variables, to allow the required complementary laws to be calculated through the evaluation of the increment in effective plastic strain. The flux and dual variables are highlighted in Table A.1 and for the current material model, the dual form of the dissipation potential is:

$$\Omega = \Omega(\boldsymbol{\sigma}, \boldsymbol{\chi}_i, R_i; T, \boldsymbol{\alpha}_i, r_i) \quad (\text{A9})$$

Thus, the resulting complementary laws are of the form:

$$\dot{\boldsymbol{\varepsilon}}^{\text{pl}} = \frac{\partial \Omega}{\partial \boldsymbol{\sigma}} \quad (\text{A10})$$

$$\dot{\boldsymbol{\alpha}}_i = -\frac{\partial \Omega}{\partial \boldsymbol{\chi}_i} \quad (\text{A11})$$

$$\dot{r}_i = -\frac{\partial \Omega}{\partial R_i} \quad (\text{A12})$$

Appendix A: Thermodynamic Framework

The free energy is given by [*Chaboche, 1997; Lemaitre and Chaboche, 2000*]:

$$\rho\Psi = \rho\Psi_{\text{el}} + \sum_{i=1}^2 \frac{1}{3} C_i \boldsymbol{\alpha}_i : \boldsymbol{\alpha}_i + h_i(p) \quad (\text{A13})$$

and the isotropic hardening term, $h_i(p)$, is defined as [*Lemaitre and Chaboche, 2000*]:

$$h_i(p) = Q_i p - \frac{Q_i}{b_i} [1 - \exp(-b_i p)] \quad (\text{A14})$$

Thus, the associated thermodynamic variables (see Equations (A7) and (A8)) may be rewritten as:

$$R_i = \frac{dh_i(p)}{dp} \quad (\text{A15})$$

$$\boldsymbol{\chi}_i = \frac{2}{3} C_i \boldsymbol{\alpha}_i \quad (\text{A16})$$

In this model, it is assumed that the viscoplastic flow is volume preserving and the third invariant is neglected. The dissipation potential is chosen in such a manner that the evolution laws for isotropic and kinematic hardening (described in more detail below), are preserved and the dissipation potential, Ω , is defined as [*Lemaitre and Chaboche, 2000*]:

$$\begin{aligned} \Omega = \Omega \left(J_2(\boldsymbol{\sigma} - \boldsymbol{\chi}) - R - k + \frac{1}{2} \frac{\gamma_i(p)}{C_i} J_2^2(\boldsymbol{\chi}_i) \right. \\ \left. - \frac{2}{9} C_i \gamma_i(p) J_2^2(\boldsymbol{\alpha}_i); T, p \right) \end{aligned} \quad (\text{A17})$$

where γ_i is the temperature-dependent non-linear kinematic hardening material parameter. Thus, the complementary laws may be obtained by differentiating Equation (A9) with respect to the dual variables, such that the complementary laws of Equations (A10) to (A12) become [*Chaboche, 2008; Chaboche et al., 2012; Lemaitre and Chaboche, 2000*]:

$$\dot{\boldsymbol{\varepsilon}}^{\text{pl}} = \frac{\partial \Omega(f)}{\partial \boldsymbol{\sigma}} = \frac{\partial \Omega}{\partial f} \frac{\partial f}{\partial \boldsymbol{\sigma}} = \frac{\partial \Omega}{\partial f} \mathbf{n} \quad (\text{A18})$$

$$\dot{\boldsymbol{\alpha}}_i = -\frac{\partial \Omega(f)}{\partial \boldsymbol{\chi}_i} = \dot{\boldsymbol{\varepsilon}}^{\text{pl}} - \frac{3}{2} \frac{\gamma_i(p)}{C_i} \boldsymbol{\chi}_i \dot{p} \quad (\text{A19})$$

$$\dot{r}_i = -\frac{\partial \Omega(f)}{\partial R_i} \quad (\text{A20})$$

where \mathbf{n} is the tensor normal. Combining Equation (A11) and Equation (A19) allows for the kinematic hardening evolution law described in Equation (4.13) to be obtained and such that the dissipation potential reduces to [*Lemaitre and Chaboche, 2000*]:

$$\Omega = \Omega(J_2(\boldsymbol{\sigma} - \boldsymbol{\chi}) - R - k; T, p) \quad (\text{A21})$$

Table A.1: The dissipation variables within the material model written in terms of the flux and dual variables.

Dissipation Variables	
Flux Variables	Dual Variables
$\dot{\boldsymbol{\varepsilon}}^{\text{pl}}$	$\boldsymbol{\sigma}$
$-\dot{\boldsymbol{\alpha}}_i$	$\boldsymbol{\chi}_i$
$-\dot{r}$	R

Appendix B: Material Jacobian for Viscoplastic Deformation

For an axisymmetric loading conditions, the material Jacobian for the phenomenological hyperbolic sine unified cyclic viscoplastic model of Chapter 4 is:

$$\mathbf{D} = \begin{bmatrix} D_{11} & D_{12} & D_{13} & D_{14} \\ D_{21} & D_{22} & D_{23} & D_{24} \\ D_{31} & D_{32} & D_{33} & D_{34} \\ D_{41} & D_{42} & D_{43} & D_{44} \end{bmatrix} = \begin{pmatrix} \frac{\partial \delta \sigma_{11}}{\partial \delta \varepsilon_{11}} & \frac{\partial \delta \sigma_{11}}{\partial \delta \varepsilon_{22}} & \frac{\partial \delta \sigma_{11}}{\partial \delta \varepsilon_{33}} & \frac{\partial \delta \sigma_{11}}{\partial \delta \gamma_{12}} \\ \frac{\partial \delta \sigma_{22}}{\partial \delta \varepsilon_{11}} & \frac{\partial \delta \sigma_{22}}{\partial \delta \varepsilon_{22}} & \frac{\partial \delta \sigma_{22}}{\partial \delta \varepsilon_{33}} & \frac{\partial \delta \sigma_{22}}{\partial \delta \gamma_{12}} \\ \frac{\partial \delta \sigma_{33}}{\partial \delta \varepsilon_{11}} & \frac{\partial \delta \sigma_{33}}{\partial \delta \varepsilon_{22}} & \frac{\partial \delta \sigma_{33}}{\partial \delta \varepsilon_{33}} & \frac{\partial \delta \sigma_{33}}{\partial \delta \gamma_{12}} \\ \frac{\partial \delta \sigma_{12}}{\partial \delta \varepsilon_{11}} & \frac{\partial \delta \sigma_{12}}{\partial \delta \varepsilon_{22}} & \frac{\partial \delta \sigma_{12}}{\partial \delta \varepsilon_{33}} & \frac{\partial \delta \sigma_{12}}{\partial \delta \gamma_{12}} \end{pmatrix} \quad (\text{B1})$$

with the relationship between the differential increment of the stress tensor, $\delta \boldsymbol{\sigma}$, differential increment of the strain tensor, $\delta \boldsymbol{\varepsilon}$, derived in Section 4.4.1 and defined as:

$$\begin{aligned} \delta \boldsymbol{\sigma} &= \frac{\sigma_e}{\sigma_e^{\text{tr}}} \left(2\mu \delta \boldsymbol{\varepsilon} + \left(K - \frac{2}{3} \mu \right) (\delta \boldsymbol{\varepsilon} : \mathbf{I} \mathbf{I}) \right) \\ &+ \sum_{i=1}^2 \left[\left(\frac{2}{3} C_i \mathbf{n} \cdot \gamma_i \chi_i \right) \frac{Y}{\Gamma} \mathbf{n} : \mu \left(2\delta \boldsymbol{\varepsilon} - \frac{2}{3} (\delta \boldsymbol{\varepsilon} : \mathbf{I} \mathbf{I}) \right) \right] \\ &+ \frac{(\mathbf{s}^{\text{tr}} - \mathbf{x}_t)}{\sigma_e^{\text{tr}}} \left[1 - \frac{\sigma_e}{\sigma_e^{\text{tr}}} - \left(3\mu + \sum_{i=1}^2 (C_i - \mathbf{n} : \gamma_i \chi_i) \right) \frac{Y}{\Gamma} \right] \mathbf{n} : \mu \left(2\delta \boldsymbol{\varepsilon} - \frac{2}{3} (\delta \boldsymbol{\varepsilon} : \mathbf{I} \mathbf{I}) \right) \end{aligned} \quad (\text{B2})$$

Equation (B2) can be rewritten more concisely as:

$$\delta \boldsymbol{\sigma} = Z_1 \delta \boldsymbol{\varepsilon} + Z_2 (\delta \boldsymbol{\varepsilon} : \mathbf{I} \mathbf{I}) + \left[Z_3 \sum_{i=1}^2 \left(\frac{2}{3} C_i \mathbf{n} \cdot \gamma_i \chi_i \right) + Z_4 (\mathbf{s}^{\text{tr}} - \mathbf{x}_t) \right] \mathbf{n} : \left(\delta \boldsymbol{\varepsilon} - \frac{1}{3} (\delta \boldsymbol{\varepsilon} : \mathbf{I} \mathbf{I}) \right) \quad (\text{B3})$$

where:

$$Z_1 = 2\mu \frac{\sigma_e}{\sigma_e^{\text{tr}}} \quad (\text{B4a})$$

$$Z_2 = \frac{\sigma_e}{\sigma_e^{\text{tr}}} \left(K - \frac{2}{3} \mu \right) \quad (\text{B4b})$$

Appendix B: Material Jacobian for Viscoplastic Deformation

$$Z_3 = 2\mu \frac{Y}{\Gamma} \quad (\text{B4c})$$

$$Z_4 = \frac{2\mu}{\sigma_e^{\text{tr}}} \left(1 - \frac{\sigma_e}{\sigma_e^{\text{tr}}} - 3\mu \frac{Y}{\Gamma} - \sum_{i=1}^2 (C_i - \gamma_i \mathbf{n} : \boldsymbol{\chi}_i) \frac{Y}{\Gamma} \right) \quad (\text{B4d})$$

In Equation (B3), the contracted tensor products can be extended as:

$$\mathbf{I} : \boldsymbol{\delta \boldsymbol{\varepsilon}} = \delta \varepsilon_{11} + \delta \varepsilon_{22} + \delta \varepsilon_{33} \quad (\text{B5a})$$

$$\mathbf{n} = \begin{bmatrix} n_{11} \\ n_{22} \\ n_{33} \\ 2n_{12} \end{bmatrix} \quad (\text{B5b})$$

$$\mathbf{n} : \mathbf{I} = n_{11} + n_{22} + n_{33} \quad (\text{B5c})$$

$$\mathbf{n} : \boldsymbol{\delta \boldsymbol{\varepsilon}} = n_{11} \delta \varepsilon_{11} + n_{22} \delta \varepsilon_{22} + n_{33} \delta \varepsilon_{33} + 4n_{12} \delta \varepsilon_{12} \quad (\text{B5d})$$

$$\mathbf{n} : \boldsymbol{\delta \boldsymbol{\chi}} = n_{11} \chi_{11} + n_{22} \chi_{22} + n_{33} \chi_{33} + 2n_{12} \chi_{12} \quad (\text{B5e})$$

For viscoplastic deformation, the individual components of the material Jacobian presented in Equation (B1) are defined in the following sections.

For the $\delta \sigma_{11}$ components:

$$D_{11} = Z_1 + Z_2 + Z_3 \left(n_{11} - \frac{1}{3} (\mathbf{n} : \mathbf{I}) \right) \sum_{i=1}^2 \left(\frac{2}{3} C_i n_{11}^{-\gamma_i} \chi_{i,11} \right) + Z_4 \left(n_{11} - \frac{1}{3} (\mathbf{n} : \mathbf{I}) \right) (s_{11}^r - x_{t,11}) \quad (\text{B6a})$$

$$D_{12} = Z_2 + Z_3 \left[n_{22} - \frac{1}{3} (\mathbf{n} : \mathbf{I}) \right] \sum_{i=1}^2 \left(\frac{2}{3} C_i n_{11}^{-\gamma_i} \chi_{i,11} \right) + Z_4 \left[n_{22} - \frac{1}{3} (\mathbf{n} : \mathbf{I}) \right] (s_{11}^r - x_{t,11}) \quad (\text{B6b})$$

$$D_{13} = Z_2 + Z_3 \left[n_{33} - \frac{1}{3} (\mathbf{n} : \mathbf{I}) \right] \sum_{i=1}^2 \left(\frac{2}{3} C_i n_{11}^{-\gamma_i} \chi_{i,11} \right) + Z_4 \left[n_{33} - \frac{1}{3} (\mathbf{n} : \mathbf{I}) \right] (s_{11}^r - x_{t,11}) \quad (\text{B6c})$$

$$D_{14} = 2n_{12} Z_3 \sum_{i=1}^2 \left(\frac{2}{3} C_i n_{11}^{-\gamma_i} \chi_{i,11} \right) + 2n_{12} Z_4 (s_{11}^r - x_{t,11}) \quad (\text{B6d})$$

For the $\delta \sigma_{22}$ components:

Appendix B: Material Jacobian for Viscoplastic Deformation

$$D_{21} = Z_2 + Z_3 \left[n_{11} - \frac{1}{3}(\mathbf{n} : \mathbf{I}) \right] \sum_{i=1}^2 \left(\frac{2}{3} C_i n_{22} \gamma_i \chi_{i,22} \right) + Z_4 \left[n_{11} - \frac{1}{3}(\mathbf{n} : \mathbf{I}) \right] (s_{22}^{tr} - x_{t,22}) \quad (\text{B7a})$$

$$D_{22} = Z_1 + Z_2 + Z_3 \left[n_{22} - \frac{1}{3}(\mathbf{n} : \mathbf{I}) \right] \sum_{i=1}^2 \left(\frac{2}{3} C_i n_{22} \gamma_i \chi_{i,22} \right) + Z_4 \left[n_{22} - \frac{1}{3}(\mathbf{n} : \mathbf{I}) \right] (s_{22}^{tr} - x_{t,22}) \quad (\text{B7b})$$

$$D_{23} = Z_2 + Z_3 \left[n_{33} - \frac{1}{3}(\mathbf{n} : \mathbf{I}) \right] \sum_{i=1}^2 \left(\frac{2}{3} C_i n_{22} \gamma_i \chi_{i,22} \right) + Z_4 \left[n_{22} - \frac{1}{3}(\mathbf{n} : \mathbf{I}) \right] (s_{22}^{tr} - x_{t,22}) \quad (\text{B7c})$$

$$D_{24} = 2n_{12}Z_3 \sum_{i=1}^2 \left(\frac{2}{3} C_i n_{22} \gamma_i \chi_{i,22} \right) + 2n_{12}Z_4 (s_{22}^{tr} - x_{t,22}) \quad (\text{B7d})$$

For the $\delta\sigma_{33}$ components:

$$D_{31} = Z_2 + Z_3 \left[n_{11} - \frac{1}{3}(\mathbf{n} : \mathbf{I}) \right] \sum_{i=1}^2 \left(\frac{2}{3} C_i n_{33} \gamma_i \chi_{i,33} \right) + Z_4 \left[n_{11} - \frac{1}{3}(\mathbf{n} : \mathbf{I}) \right] (s_{33}^{tr} - x_{t,33}) \quad (\text{B8a})$$

$$D_{32} = Z_2 + Z_3 \left[n_{22} - \frac{1}{3}(\mathbf{n} : \mathbf{I}) \right] \sum_{i=1}^2 \left(\frac{2}{3} C_i n_{33} \gamma_i \chi_{i,33} \right) + Z_4 \left[n_{22} - \frac{1}{3}(\mathbf{n} : \mathbf{I}) \right] (s_{33}^{tr} - x_{t,33}) \quad (\text{B8b})$$

$$D_{33} = Z_1 + Z_2 + Z_3 \left[n_{33} - \frac{1}{3}(\mathbf{n} : \mathbf{I}) \right] \sum_{i=1}^2 \left(\frac{2}{3} C_i n_{33} \gamma_i \chi_{i,33} \right) + Z_4 \left[n_{33} - \frac{1}{3}(\mathbf{n} : \mathbf{I}) \right] (s_{33}^{tr} - x_{t,33}) \quad (\text{B8c})$$

$$D_{34} = 2n_{12}Z_3 \sum_{i=1}^2 \left(\frac{2}{3} C_i n_{33} \gamma_i \chi_{i,33} \right) + 2n_{12}Z_4 (s_{33}^{tr} - x_{t,33}) \quad (\text{B8d})$$

For the $\delta\sigma_{12}$ components:

$$D_{41} = Z_3 \left[n_{11} - \frac{1}{3}(\mathbf{n} : \mathbf{I}) \right] \sum_{i=1}^2 \left(\frac{4}{3} C_i n_{12} \gamma_i \chi_{i,12} \right) + Z_4 \left[n_{11} - \frac{1}{3}(\mathbf{n} : \mathbf{I}) \right] (s_{12}^{tr} - x_{t,12}) \quad (\text{B9a})$$

$$D_{42} = Z_3 \left[n_{22} - \frac{1}{3}(\mathbf{n} : \mathbf{I}) \right] \sum_{i=1}^2 \left(\frac{4}{3} C_i n_{12} \gamma_i \chi_{i,12} \right) + Z_4 \left[n_{22} - \frac{1}{3}(\mathbf{n} : \mathbf{I}) \right] (s_{12}^{tr} - x_{t,12}) \quad (\text{B9b})$$

$$D_{43} = Z_3 \left[n_{33} - \frac{1}{3}(\mathbf{n} : \mathbf{I}) \right] \sum_{i=1}^2 \left(\frac{4}{3} C_i n_{12} \gamma_i \chi_{i,12} \right) + Z_4 \left[n_{33} - \frac{1}{3}(\mathbf{n} : \mathbf{I}) \right] (s_{12}^{tr} - x_{t,12}) \quad (\text{B9c})$$

Appendix B: Material Jacobian for Viscoplastic Deformation

$$D_{44} = \frac{Z_1}{2} + 2n_{12}Z_3 \sum_{i=1}^2 \left(\frac{2}{3} C_i n_{12}^{-\gamma_i} \chi_{i,12} \right) + 2n_{12}Z_4 (s_{12}^{pr} - x_{i,12}) \quad (\text{B9d})$$

Bibliography

- [Abd El-Azim et al., 2013]: Abd El-Azim, M.E., Ibrahim, O.H., El-Desoky, O.E. Long term creep behaviour of welded joints of P91 steel at 650 °C. *Materials Science and Engineering A*, **560** (2013), pp. 678-684.
- [Abdel-Karim and Ohno, 2000]: Abdel-Karim, M., Ohno, N. Kinematic hardening model suitable for ratchetting with steady-state. *International Journal of Plasticity*, **16** (2000), pp. 225-240.
- [Abe, 2004]: Abe, F. Bainitic and martensitic creep-resistant steels. *Current Opinions in Solid State and Materials Science*, **8** (2004), pp. 305-311.
- [Abe, 2008]: Abe, F. Precipitate design for creep strengthening of 9% Cr tempered martensitic steel for ultra-supercritical power plants. *Science and Technology of Advanced Materials*, **9** (2008), pp. 013002 (1-15).
- [Abe, 2011a]: Abe, F. Effect of boron on microstructure and creep strength of advanced ferritic power plant steels. *Procedia Engineering*, **10** (2011), pp. 94-99.
- [Abe, 2011b]: Abe, F. Strengthening mechanisms in creep of advanced ferritic power plant steels based on creep deformation analysis. Weng, Y., Dong, H., Gan, Y. (Eds.) *Advanced Steels: The Recent Scenario in Steel Science and Technology*, Springer, Berlin, pp. 409-422.
- [Abe et al., 2007a]: Abe, F., Taneike, M., Sawada, K. Alloy design of creep resistant 9Cr steel using a dispersion of nano-sized carbonitrides. *International Journal of Pressure Vessels and Piping*, **84** (2007), pp. 3-12.
- [Abe et al., 2007b]: Abe, F., Tabuchi, M., Kondo, M., Tsukamoto, S. Suppression of Type IV fracture and improvement of creep strength of 9Cr steel welded joints by boron addition. *International Journal of Pressure Vessels and Piping*, **84** (2007), pp. 44-52.
- [Abe et al., 2008]: Abe, F., Tabuchi, M., Semba, H., Igarashi, M., Yoshizawa, M., Komai, N., Fujita, A. Feasibility of MARBN steel for application to thick section boiler components in USC power plant at 650 °C. In: Viswanathan, R., Gandy, D., Coleman, K. (Eds.) *Advances in Materials Technology for Fossil Power Plants: Proceedings from the Fifth International Conference*. Electrical Power Research Institute: Palo Alto, CA (2008), pp. 92-106.
- [Abe et al., 2010]: Abe, F., Tabuchi, M., Tsukamoto, S., Shirane, T. Microstructure evolution in HAZ and suppression of Type IV fracture in advanced ferritic power plant steels. *International Journal of Pressure Vessels and Piping*, **87** (2010), pp. 598-604.
- [Abe, 2015]: Abe, F. Correlation between creep deformation parameters and creep life for high-Cr ferritic steels. In: *Creep 2015, 13th International Conference on Creep and Fracture of Engineering Materials and Structures*, May 31st - June 4th, Toulouse, France (2015).
- [Abson and Rothwell, 2013]: Abson, D.J., Rothwell, J.S. Review of type IV cracking of weldments in 9-12%Cr creep strength enhanced ferritic steels.

Bibliography

- International Materials Reviews, **58** (2013), pp. 437-473.
- [Agamennone et al., 2006]: Agamennone, R., Blum, W., Gupta, C., Chakravartty, J.K. Evolution of microstructure and deformation resistance in creep of tempered martensite 9-12%Cr-2%W-5%Co steels. *Acta Materialia*, **54** (2006), pp. 3003-3014.
- [Aghajani et al., 2009a]: Aghajani, A., Somsen, Ch., Eggeler, G. On the effect of long-term creep on the microstructure of a 12% chromium tempered martensite ferritic steel. *Acta Materialia*, **57** (2009), pp. 5093-5106.
- [Aghajani et al., 2009b]: Aghajani, A., Somsen, Ch., Pesicka, J., Bendick, W., Hahn, B., Eggeler, G. Microstructural evolution in T24, a modified 2(1/4)Cr-1Mo steel during creep after different heat treatments. *Materials Science and Engineering A*, **510-511** (2009), pp. 130-135.
- [Albert et al., 2005]: Albert, S.K., Kondo, M., Tabuchi, M., Yin, F., Sawada, K., Abe, F. Improving the creep properties of 9Cr-3W-3Co-NbV steels and their weld joints by the addition of boron. *Metallurgical and Materials Transactions A*, **36** (2005), pp. 333-343.
- [Ashby, 1972]: Ashby, M.F. A first report on deformation-mechanism maps. *Acta Metallurgica*, **20** (1972), pp. 887-897.
- [Ashby and Jones, 2012]: Ashby, M.F., Jones, D.R.H. *Engineering Materials 1: An Introduction to Properties, Applications and Design*. Elsevier Ltd.: Oxford (2012).
- [ASME, 1998]: ASME. Boiler and pressure vessel code. Section II, part D. ASME: New York (1998).
- [ASTM E602-03]: American Society for Testing and Materials (ASTM). Annual book of ASTM standards, vol. 03.01. ASTM International: West Conshohocken, PA (2007).
- [Bardel et al., 2015]: Bardel, D., Perez, M., Nelias, D., Dancette, S., Chaudet, P., Massardier, V. Cyclic behaviour of a 6061 aluminium alloy: Coupling precipitation and elastoplastic modelling. *Acta Materialia*, **83** (2015), pp. 256-268.
- [Basquin, 1910]: Basquin, O.H. The exponential law of endurance tests. *Proc. ASTM*, **10** (1910), pp. 625-630.
- [Brett, 2014]: Brett, S. Scully, S. Personal communication (2014).
- [Chaboche, 1997]: Chaboche, J.L. Thermodynamic formulation of constitutive equations and application of viscoplasticity and viscoelasticity of metals and polymers. *International Journal of Solids and Structures*, **34** (1997), pp. 2239-2254.
- [Chaboche, 2008]: Chaboche, J.L. A review of some plasticity and viscoplasticity constitutive theories. *International Journal of Plasticity*, **24** (2008), pp. 1642-1693.
- [Chaboche and Rousselier, 1983a]: Chaboche, J.L., Rousselier, G. On the plastic and viscoplastic constitutive equations – part I: rules developed with internal variable concept. *Transactions of the ASME Journal of Pressure Vessel Technology*, **105** (1983), pp. 153-158.
- [Chaboche and Rousselier, 1983b]: Chaboche, J.L., Rousselier, G. On the plastic and viscoplastic constitutive equations – part II: Application of internal variable concepts to the 316 stainless steel. *Transactions of the ASME Journal of Pressure Vessel Technology*, **105** (1983), pp. 159-164.
- [Chaboche et al., 2012]: Chaboche, J.L., Kanouté, P., Azzouz, F. Cyclic inelastic constitutive equations and their impact on the fatigue life predictions. *International Journal of Plasticity*, **35** (2012), pp. 44-66.
- [Cheng et al., 2003]: Cheng, S., Spencer, J.A., Milligan, W.W. Strength and tension/compression asymmetry in nanostructured and ultrafine-

Bibliography

- grain metals. *Acta Materialia* **51** (2003) pp. 4505-4518.
- [Cheong and Busso, 2004]: Cheong, K.-S., Busso, E.P. Discrete dislocation density modelling of single phase FCC polycrystalline aggregates. *Acta Materialia*, **52** (2004), pp. 5665-5675.
- [Cheong et al., 2005]: Cheong, K.-S., Busso, E.P., Arsenlis, A. A study of microstructural length scale effects on the behaviour of FCC polycrystals using strain gradient concepts. *International Journal of Plasticity*, **20** (2005), pp. 1797-1814.
- [Coble, 1963]: Coble, R.L. A model for boundary diffusion controlled creep in polycrystalline materials. *Journal of Applied Physics*, **34** (1963), pp. 1679-1682.
- [Coffin, 1954]: A study of the effects of cyclic thermal stresses on a ductile metal. *Transactions of ASME*, **76** (1954), pp. 931-950.
- [Collini and Bonardi, 2013]: Collini, L., Bonardi, A. A micromechanical model of the evolution of stress and strain fields in ultrafine-grained metal structures under tension. *The Journal of Strain Analysis for Engineering Design*, **48** (2013), pp. 91-102.
- [Cottrell, 1953]: Cottrell, A.H. *Dislocations and plastic flow in crystals*. Oxford University Press: Oxford (1953).
- [Das et al., 2009]: Das, C.R., Divya, M., Albert, S.K., Bhaduri, A.K., Murty, B.S. Microstructural evolution in the intercritical heat affected zone of a boron containing modified 9Cr-1Mo steel. *Welding World*, **53** (2009), pp. 511-515.
- [Das et al., 2013a]: Das, C.R., Albert, S.K., Bhaduri, A.K., Murty, B.S. Effect of boron addition and initial heat-treatment temperature on microstructure and mechanical properties of modified 9Cr-1Mo steels under different heat-treatment conditions. *Metallurgical and Materials Transactions A*, **44** (2013), pp. 2171-2186.
- [Das et al., 2013b]: Das, C.R., Albert, S.K., Bhaduri, A.K., Raj, B., Swaminathan, J., Murty, B.S. Improvement in creep resistance of modified 9Cr-1Mo steel weldment by boron addition. *Welding in the World*, **56** (2013), pp. 10-17.
- [Dawson, 2012]: Dawson, K.E. *Dissimilar metal welds*. Ph.D. Thesis, University of Liverpool, UK (2012).
- [Deshpande, 2009]: Deshpande, A.A. *High temperature an-isothermal mechanical analysis of superplastic forming tools*. Ph.D. Thesis, University of Nottingham, UK (2009).
- [Dieter, 1986]: Dieter, G.E. *Mechanical Metallurgy*. McGraw-Hill: New York (1986).
- [Doherty et al., 1997]: Doherty, R.D., Hughes, D.A., Humphreys, F.J., Jonas, J.J., Jensen, D.J., Kassner, M.E., King, W.E., McNelley, T.R., McQueen, H.J., Rollett, A.D. Current issues in recrystallisation: A review. *Materials Science and Engineering A*, **238** (1997), pp. 219-274.
- [Dubey et al., 2005]: Dubey, J.S., Chilukuru, H., Chakravarty, J.K., Schwienheer, M., Scholz, A., Blum, W. Effects of cyclic deformation on subgrain evolution and creep in 9-12% Cr steels. *Materials Science and Engineering A*, **406** (2005), pp. 152-159.
- [Dunne and Petrinic, 2005]: Dunne, F.P.E., Petrinic, N. *Introduction to Computational Plasticity*. Oxford University Press: Oxford (2005).
- [Dunne et al., 2007]: Dunne, F.P.E., Rugg, D., Walker, A. Lengthscale-dependent, elastically anisotropic, physically-based hcp crystal plasticity: Application to cold-dwell fatigue in Ti alloys. *International Journal of Plasticity*, **23** (2007), pp. 1061-1083.
- [Dyson, 2000]: Dyson, B. Use of CDM in materials modelling and component creep life prediction. *Transactions of the ASME Journal of*

Bibliography

- Pressure Vessel Technology, **122** (2000), pp. 281-296.
- [Eggeler and Wiesner, 1993]: Eggeler, G., Wiesner, C. A numerical study of parameters controlling stress redistribution in circular notched specimens during creep. *Journal of Strain Analysis for Engineering Design*, **28** (1993), pp. 13-22.
- [Ennis et al., 1997]: Ennis, P.J., Zielinska-Lipiec, A., Wachter, O., Czyrska-Filemonowicz, A. Microstructural stability and creep rupture strength of the martensitic steel P92 for advanced power plant. *Acta Materialia* **45** (1997) pp. 4901-4907.
- [Ennis and Czyrska-Filemonowicz, 2002]: Ennis, P.J., Czyrska-Filemonowicz, A. Recent advances in creep resistant materials for power plant applications. *Power Plant Operation, Maintenance and Material Issues (OMMI)*, **1** (2002), pp. 1-28.
- [Ennis and Czyrska-Filemonowicz, 2003]: Ennis, P.J., Czyrska-Filemonowicz, A. Recent advances in creep-resistant steels for power plant applications. *Sadhana*, **28** (2003), pp. 709-730.
- [Esposito and Bonora, 2011]: Esposito, L., Bonora, N. A primary creep model for Class M materials. *Materials Science and Engineering A*, **528** (2011), pp. 5496-5501.
- [Essmann and Mughrabi, 1979]: Essmann, U., Mughrabi, H. Annihilation of dislocations during tensile and cyclic deformation and limits of dislocation densities. *Philosophical Magazine A*, **40** (1979), pp. 731-756.
- [Farragher, 2013]: Farragher, T.P. Thermomechanical analysis of P91 power plant components. Ph.D. Thesis, National University of Ireland, Galway (2013).
- [Farragher et al., 2013a]: Farragher, T.P., Scully, S., O'Dowd, N.P., Leen, S.B. Development of life assessment procedures for power plant headers operated under flexible loading scenarios. *International Journal of Fatigue*, **49** (2013), pp. 50-61.
- [Farragher et al., 2013b]: Farragher, T.P., Scully, S., O'Dowd, N.P., Leen, S.B. Thermomechanical analysis of a pressurised pipe under plant conditions. *Transactions of the ASME Journal of Pressure Vessel Technology*, **135** (2013), pp. 011204.
- [Farragher et al., 2014]: Farragher, T.P., Scully, S., O'Dowd, N.P., Hyde, C.J., Leen, S.B. High temperature, low cycle fatigue characterisation of P91 weld and heat affected zone material. *Transactions of the ASME Journal of Pressure Vessel Technology*, **136** (2014), pp. 021403.
- [Felfeli et al., 2015]: Felfeli, M., Azadi, M., Farrahi, G.H. Constitutive modelling of elasto-visco-plastic behaviours in aluminium alloys subjected to cyclic loadings at various strain-rates. *Journal of Strain Analysis*, **50** (2015), pp. 103-124.
- [Fisher et al., 1953]: Fisher, J.C., Hart, E.W., Pry, R.H. The hardening of metal crystals by precipitate particles. *Acta Metallurgica*, **1** (1953), pp. 336-339.
- [Flavenot and Skalli]: Flavenot, J.F., Skalli, N. A critical depth criterion for the evaluation of long life fatigue strength under multiaxial loading and a stress gradient. Brown, M.W., Miller, K.J. (Eds.). *Biaxial and multiaxial fatigue*. Mechanical Engineering Publications: London (1989), pp. 355-365.
- [Fournier et al., 2005]: Fournier, B., Sauzay, M., Mottot, M., Brillet, H., Monnet, I., Pineau, A. Experimentally based modelling of cyclically induced softening in a martensitic steel at high temperature. ECCC Creep Conference, Sept. 12th to 14th, 2005, London, UK.
- [Fournier et al., 2008a]: Fournier, B., Sauzay, M., Caës, C., Noblecourt, M., Mottot, M., Bougault, A., Rabeau, V., Pineau, A. Creep-fatigue-oxidation interactions in a 9Cr-1Mo martensitic steel. Part I: Effect of

Bibliography

- tensile holding period on fatigue lifetime. *International Journal of Fatigue*, **30** (2008), pp. 649-662.
- [Fournier et al., 2008b]: Fournier, B., Sauzay, M., Caës, C., Noblecourt, M., Mottot, M., Bougault, A. Rabeau, V., Pineau, A. Creep-fatigue-oxidation interactions in a 9Cr-1Mo martensitic steel. Part II: Effect of compressive holding period on fatigue lifetime. *International Journal of Fatigue*, **30** (2008), pp. 663-676.
- [Fournier et al., 2008c]: Fournier, B., Sauzay, M., Caës, C., Noblecourt, M., Mottot, M., Bougault, A. Rabeau, V., Pineau, A. Creep-fatigue-oxidation interactions in a 9Cr-1Mo martensitic steel. Part III: Lifetime prediction. *International Journal of Fatigue*, **30** (2008), pp. 1797-1812.
- [Fournier et al., 2009a]: Fournier, B., Sauzay, M., Caës, C., Noblecourt, M., Mottot, M., Allais, L., Tournie, I., Pineau, A. Creep-fatigue interactions in a 9 Pct Cr-1 Pct Mo martensitic steel: Part I. Mechanical test results. *Metallurgical and Materials Transactions A*, **40** 321-329.
- [Fournier et al., 2009b]: Fournier, B., Sauzay, M., Caës, C., Noblecourt, M., Mottot, M., Allais, L., Tournie, I., Pineau, A. Creep-fatigue interactions in a 9 Pct Cr-1 Pct Mo martensitic steel: Part II. Microstructural evolutions. *Metallurgical and Materials Transactions A*, **40** 330-341.
- [Fournier et al., 2010]: Fournier, B., Salvi, M., Dalle, F., De Carlan, Y., Caës, C., Sauzay, M., Pineau, A. Lifetime prediction of 9-12%Cr martensitic steels subjected to creep-fatigue at high temperature. *International Journal of Fatigue*, **32** (2010), pp. 971-978.
- [Fournier et al., 2011]: Fournier, B., Dalle, F., Sauzay, M., Longour, J., Salvi, M., Caës, C., Tournié, I., Giroux, P.-F., Kim, S.-H. Comparison of various 9-12%Cr steels under fatigue and creep-fatigue loadings at high temperature. *Materials Science and Engineering A*, **528** (2011), pp. 6934-6945.
- [Frank and Read, 1950]: Frank, F.C., Read, W.T. Multiplication processes for slow moving dislocations. *Physical Review*, **79** (1950), pp. 722-723.
- [Frank, 1980]: Frank, F.C. The Frank-Read source. *Proceedings of the Royal Society of London Series A – Mathematical, Physical and Engineering Sciences*, **371** (1980) pp. 136-138.
- [Frederick and Armstrong, 2007]: Frederick, C.O., Armstrong, P.J. A mathematical representation of the multiaxial Bauschinger effect. *Materials at High Temperature*, **24** (2007), pp. 1-26.
- [Ghassemi-Armaki et al., 2009]: Ghassemi-Armaki, H., Chen, R.P., Maruyama, K., Yoshizawa, M., Igarashi, M. Static recovery of tempered lath martensite microstructures during long-term aging in 9-12% Cr heat resistant steels. *Materials Letters* **63** (2009) pp. 2423-2425.
- [Ghassemi-Armaki et al., 2011]: Ghassemi-Armaki, H., Chen, R., Maruyama, K., Igarashi, M. Creep behaviour and degradation of subgrain structures pinned by nanoscale precipitates in strength-enhanced 5 to 12 Pct Cr ferritic steels. *Metallurgical and Materials Transactions A* **42** (2011) pp. 3084-3094.
- [Ghassemi-Armaki et al., 2013]: Ghassemi-Armaki, H., Chen, R., Bhat, S., Sadagopan, S., Kumar, S., Bower, A. Microscale calibrated 337hermos337g of the deformation response of low-carbon martensite. *Acta Materialia* **61** (2013) pp. 3640-3652.
- [Giordana et al., 2012]: Giordana, M.F., Giroux, P.-F., Alvarez-Armas, I., Sauzay, M., Armas, A., Kruml, T. Microstructure evolution during cyclic tests on EUROFER 97 at room temperature. TEM observation and modelling. *Materials Science and Engineering A*, **550** (2012), pp. 103-111.

Bibliography

- [Giroux, 2011]: Giroux, P.-F. Experimental study and simulation of cyclic softening of tempered martensite ferritic steels. Ph.D. thesis, l'École Nationale Supérieure des Mines de Paris, 2011.
- [Golden et al., 2014b]: Golden, B.J., Li, D-F., O'Dowd, N.P., Tiernan, P. Microstructural modelling of P91 martensitic steel under uniaxial loading conditions. Transactions of the ASME Journal of Pressure Vessel Technology, **136** (2014), pp. 021404.
- [Golden et al., 2015]: Golden, B.J. University of Limerick, personal communication (2015).
- [Gong et al., 2010]: Gong, Y.P., Hyde, C.J., Sun, W., Hyde, T.H. Determination of material properties in the Chaboche unified viscoplasticity model. Proceedings of the Institution of Mechanical Engineers, Part L: Journal of Materials: Design and Application, **224** (2010), pp. 19-29.
- [Götz and Blum, 2003]: Götz, G., Blum, W. Influence of thermal history on precipitation of hardening phases in tempered martensite 10%Cr steel X12CrMoWVNbN 10-1-1. Materials Science and Engineering A, **348** (2003), pp. 201-207.
- [Guan and Ye, 1980]: Guan, X.M., Ye, H.Q. Intergranular embrittlement caused by the precipitation of M_6C carbide containing silicon. Journal of Materials Science, **15** (1980), pp. 2935-2937.
- [Gypen and Deruyttere, 1977a]: Gypen, L.A., Deruyttere, A. Multi-component solid solution hardening - Part I: Proposed model. Journal of Materials Science, **12** (1977), pp. 1028-1033.
- [Gypen and Deruyttere, 1977b]: Gypen, L.A., Deruyttere, A. Multi-component solid solution hardening - Part II: Agreement with experimental results. Journal of Materials Science, **12** (1977), pp. 1034-1038.
- [Ha et al., 2004]: Ha, J., Tabuchi, M., Hongo, H., Toshimitsu Yokobori Jr, A., Abe, F. Creep crack growth properties for 12CrWCoB rotor steel using circular notched specimens. International Journal of Pressure Vessels and Piping, **81** (2004), pp. 401-407.
- [Hald, 2008]: Hald, J. Microstructure and long-term creep properties of 9-12% Cr steels. International Journal of Pressure Vessels and Piping, **85** (2008), pp. 30-37.
- [Hald and Korcakova, 2003]: Hald, J., Korcakova, L. Precipitate stability in creep resistant ferritic steels - Experimental investigations and modelling. ISIJ International, **43**(2003), pp. 420-427.
- [Hall, 1951]: Hall, E.O. The deformation and aging of mild steel: III Discussion of results. Proceedings of the Royal Society, London, **64** (1951), pp. 747-753.
- [Haney et al., 2009]: Haney, E.M., Dalle, F., Sauzay, M., Vincent, L., Tournié, I., Allais, L., Fournier, B. Macroscopic results of long-term creep on a modified 9Cr-1Mo steel (T91). Materials Science and Engineering A, **510-511** (2009), pp. 99-103.
- [Hart, 1972]: Hart, E.W. Theory of dispersion hardening in metals. Acta Metallurgica, **20** (1972), pp. 275-289.
- [Henshall et al., 1996]: Henshall, G.A., Helling, D.E., Miller, A.K. Improvements in the MATMOD equations for modelling solute effects and yield surface distortion. In: Krausz, A.S., Krausz, K. (Eds.). Unified constitutive laws of plastic deformation. Academic Press: San Diego (1996), pp. 153-228.
- [Herring, 1950]: Herring, C. Diffusional viscosity of polycrystalline solid. Journal of Applied Physics, **21** (1950), pp. 437-445.
- [Hertzberg, 1996]: Hertzberg, R.W. Deformation and fracture mechanics of engineering materials. J. Wiley & Sons: New York (1996).

Bibliography

- [Hofer et al., 2000a]: Hofer, P. Miller, M.K., Babu, S.S., David, S.A., Cerjak, H. Atom probe field ion microscopy investigation of boron containing martensitic 9 pct chromium steel. *Metallurgical and Materials Transactions A*, **31** (2000), pp. 975-984.
- [Hofer et al., 2000b]: Hofer, P., Cerjak, H., Warbichler, P. Quantification of precipitates in a 10%Cr steel using TEM and EFTEM. *Materials Science and Technology*, **16** (2000), pp. 1221-1225.
- [Holdsworth et al, 2007]: Holdsworth, S.R., Mazza, E., Binda, L., Ripamonti, L. Development of thermal fatigue damage in 1CrMoV rotor steel. *Nuclear Engineering and Design*, **237** (2007), pp. 2292-2301.
- [Hosseini and Kazeminezhad, 2011]: Hosseini, E., Kazeminezhad, M. A microstructural model based on dislocation generation and consumption mechanisms through severe plastic deformation. *Computational Materials Science*, **50** (2011), pp. 1123-1135.
- [Hu et al., 2011]: Hu, P., Yan, W., Sha, W., Wang, W., Shan, Y., Kang, K. Microstructure evolution of a 10Cr heat-resistant steel during high temperature creep. *Journal of Material Science and Technology* **27** (2011), pp. 344-351.
- [Hu et al., 2013]: Hu, X., Huang, L., Yan, W., Wang, W., Sha, W., Shan, Y., Yang, K. Evolution of microstructure and changes of mechanical properties of CLAM steel after long-term aging. *Materials Science and Engineering A* **586** (2013) pp. 253-258.
- [Hu et al., 2014]: Hu, X., Huang, L., Yan, W., Wang, W., Sha, W., Shan, Y., Yang, K. Low cycle fatigue properties of CLAM steel at 823 K. *Materials Science and Engineering A*, **613** (2014), pp. 404-413.
- [Huber and Tsakmakis, 2001]: Huber, N., Tsakmakis, C. A neural network tool for identifying the material parameters of a finite deformation viscoplasticity model with static recovery. *Computer Methods in Applied Mechanics and Engineering*, **191** (2001), pp. 353-384.
- [Huntz et al., 2003]: Huntz, A.M. Bague, V., Beauplé, G., Haut, C., Sévérac, C., Lecour, P., Longaygue, X., Ropital, F. Effect of silicon on the oxidation resistance of 9% Cr steels. *Applied Surface Science*, **207** (2003), pp. 255-275.
- [Hyde et al., 2006]: Hyde, T.H., Becker, A.A., Sun, W., Williams, J.A. Finite-element creep damage analyses of P91 pipes. *International Journal of Pressures Vessels and Piping*, **83** (2006), pp. 853-863.
- [Hyde et al., 2010]: Hyde, C.J., Sun, W., Leen, S.B. Cyclic Thermo-mechanical material modelling and testing of 316 stainless steel. *International Journal of Pressure Vessels and Piping*, **87** (2010), pp. 365-372.
- [Hyde et al., 2012]: Hyde, C.J., Sun, W., Hyde, T.H., Saad, A.A. Thermo-mechanical fatigue testing and simulation using a viscoplasticity model for P91 steel. *Computational Materials Science*, **56** (2012), pp. 29-33.
- [Kassner, 1993]: Kassner, M.E. Role of small-angle (subgrain boundary) and large-angle (grain boundary) interfaces on 5- and 3-power-law-creep. *Materials Science and Engineering A*, **166** (1993), pp. 81-88.
- [Kassner, 2004]: Kassner, M.E. Taylor hardening in five-power-law creep of metals and Class M alloys. *Acta Materialia*, **52** (2004), pp. 1-9.
- [Kato et al., 2008]: Kato, M., Fujii, T., Onaka, S. Dislocation bow-out model for yield stress of ultra-fine grained materials. *Materials Transactions* **49** pp. 1278-1283.
- [Keller et al., 2010]: Keller, C., Margulies, M.M., Hadjem-Hamouche, Z., Guillot, I. Influence of the temperature on the tensile behaviour of a modified 9Cr-1Mo T91 martensitic steel. *Materials Science and*

Bibliography

- Engineering A, **527** (2010), pp. 6758-6764.
- [Kichenin et al., 1996]: Kichenin, J., van Dang, K., Boytard, K. Finitie element simulation of a new two-dissipative mechanisms model for bulk medium-density polyethylene. *Journal of Materials Science*, **31** (1996), pp. 1653-1661.
- [Kloc et al., 1998]: Kloc, L., Sklenička, V., Dlouhy, A., Kuchařová, K. Power-law and viscous creep in advanced 9% Cr steel. In: Strang, A., Cawley, J., Greenwood, G.W. (Eds.). *Microstructural stability of creep resistant alloys for high temperature plant applications*. The Institute of Materials: London (1998), pp. 445-455.
- [Klueh, 2004]: Klueh, R.L. Elevated-temperature ferritic and martensitic steels and their application to future nuclear reactors. *Oakridge National Laboratory*, 4 (2004), ORNL/TM-2004/176:200.
- [Klueh and Vitek]: Klueh, R.L., Vitek, J.M. Fluence and helium effects on the tensile properties of ferritic steels at low temperatures. *Journal of Nuclear Materials*, **161** (1989), pp. 13-23.
- [Kocks and Mecking, 2003]: Kocks, U.F., Mecking, H. Physics and phenomenology of strain hardening: the FCC case. *Progress in Materials Science*, **48** (2003), pp. 171-273.
- [Koo and Kwon, 2011]: Koo, G.-H., Kwon, J.-H. Identification of inelastic material parameters for modified 9Cr-1Mo steel applicable to the plastic and viscoplastic constitutive equations. *International Journal of Pressure Vessels and Piping*, **88** (2011), pp. 26-33.
- [Koo and Lee, 2007]: Koo, G.-H., Lee, J.-H. Investigation of ratcheting characteristics of modified 9Cr-1Mo steel by using the Chaboche constitutive model. *International Journal of Pressure Vessels and Piping*, **84** (2007), pp. 284-292.
- [Kostka et al., 2007]: Kostka, A., Tak, K.-G., Hellmig, R.J., Estrin, Y., Eggeler, G. On the contribution of carbides and micrograin boundaries to the creep strength of tempered martensitic ferritic steels. *Acta Materialia*, **55** (2007), pp. 539-550.
- [Krauss, 1999]: Krauss, G. Martensite in steel: strength and structure. *Materials Science and Engineering A*, **273-275** (1999), pp. 40-57.
- [Kupkovits and Neu, 2010]: Kupkovits, R.A., Neu, R.W. Thermomechanical fatigue of a directionally-solidified Ni-base superalloy: smooth and cylindrically-notched specimens. *International Journal of Fatigue*, **32** (2010), pp. 1330-1342.
- [Lemaitre and Chaboche, 2000]: Lemaitre, J., Chaboche, J.L. *Mechanics of Solid Materials*. Cambridge University Press: Cambridge (2000).
- [Li et al., 2013a]: Li, L., MacLachlan, R., Jepson, M.A.E., Thomson, R. Microstructural evolution of boron nitride particles in advanced 9Cr power plant steels. *Metallurgical and Materials Transactions A*, **44** (2013), pp. 3411-3418.
- [Li et al., 2013b]: Li, D.-F., Golden, B.J., O'Dowd, N.P. Modelling of micro-plasticity evolution in crystalline materials. *Proceedings of the ASME 2013 Pressure Vessels and Piping Division Conference*, ASME, Paris, France, 2013.
- [Li et al., 2014]: Li, D.-F., Golden, B.J., O'Dowd, N.P. Multi-scale modelling of mechanical response in a martensitic steel: A micromechanical and length-scale-dependent framework for precipitate hardening. *Acta Materialia*, **80** (2014), pp. 445-456.
- [Li et al., 2015]: Li, D.-F., Barrett, R.A., O'Donoghue, P.E., O'Dowd, N.P., Leen, S.B. A multi-scale crystal plasticity model for cyclic plasticity and low-cycle fatigue in P91 steel at elevated temperature. *International Journal of Plasticity*, (2015) Under Review.
- [Lifshitz and Slyozov, Lifshitz, I.M., Slyozov, V.V. The kinetics of precipitation from

Bibliography

- 1961]: supersaturated solid solutions. *J. Physics and Chemistry of Solids* **19** (1961) pp. 35-50.
- [Lin and Dunne, 2001]: Lin, J., Dunne, F.P.E. Modelling grain growth evolution and necking in superplastic blow-forming. *International Journal of Mechanical Sciences*, **43** (2001), pp. 595-609.
- [Lu et al., 2015]: Lu, J., Sun, W., Becker, A., Saad, A.A. Simulation of the fatigue behaviour of a power plant steel with damage variable. *International Journal of Mechanical Sciences*, **100** (2015), pp. 145-157.
- [Ma and Roters, 2004]: Ma, A., Roters, F. A constitutive model for fcc single crystals based on dislocation densities and its application to uniaxial compression of aluminium single crystals. *Acta Materialia*, **52** (2004), pp. 3603-3612.
- [Magnusson and Sandström, 2007]: Magnusson, H., Sandström, R. Creep strain modelling of 9 to 12 Pct Cr steels based on microstructure evolution. *Metallurgical and materials transactions A*, **38** (2007), pp. 2033-2039.
- [Magnusson and Sandström, 2009]: Magnusson, H., Sandström, R. Influence of aluminium on creep strength of 9-12% Cr steels. *Materials Science and Engineering A*, **527** (2009), pp. 118-125.
- [Mahmoudi et al., 2011]: Mahmoudi, A.H., Pezeshki-Najafabadi, S.M., Badnava, H. Parameter determination of Chaboche kinematic hardening model using a multi objective genetic algorithm. *Computational Materials Science*, **50** (2011), pp. 1114-1122.
- [Mannan and Valsan]: Mannan, S.L., Valsan, M. High-temperature low cycle fatigue, creep-fatigue and thermomechanical fatigue of steels and their welds. *International Journal of Mechanical Sciences*, **48** (2006), pp. 160-175.
- [Manson, 1953]: Manson, S.S. Behaviour of materials under conditions of thermal stress. NACA Report 1170, Lewis Flight Propulsion Laboratory, Cleveland (1954).
- [Marder and Krauss, 1967]: Marder, A.R., Krauss, G. The morphology of martensite in iron-carbon alloys. *Transactions of the American Society of Metals (ASM)*, **60** (1967), pp. 651-660.
- [Maruyama et al., 2001]: Maruyama, K., Sawada, K., Koite, J. Strengthening mechanisms of creep resistant tempered martensitic steel. *ISIJ International*, **41** (2001), pp. 641-653.
- [Masuyama, 2001]: Masuyama, F. History of power plants and progress in heat resistant steels. *ISIJ International* **41** (2001) pp. 612-625.
- [Maugin, 1992]: Maugin, G.A. *The Thermodynamics of Plasticity and Fracture*. Cambridge University Press: Cambridge (1992).
- [Mecking and Kocks, 1981]: Mecking, H., Kocks, U.F. Kinetics of flow and strain-hardening. *Acta Metallurgica*, **29** (1981), pp. 1865-1875.
- [Miki et al., 2002]: Miki, K., Azuma, T., Ishiguro, T., Hashizume, R., Murata, Y., Morinaga, M. Effect of Cr content on the creep strength and microstructural change in high Cr heat resistant steels. *Proceedings of the 7th Liège COST Conference on Materials for Advanced Power Engineering, Sept. 30th to Oct. 2nd, 2002, Liège, Belgium*.
- [Milička and Dobeš, 2006]: Milička, K., Dobeš, F. Small punch creep testing of P91 steel. *International Journal of Pressure Vessels and Piping*, **83** (2006), 625-634.
- [Miller, 1987]: Miller, A.K. The MATMOD equations. In: Miller, A.K. (Ed.). *Unified equations for creep and plasticity*. Elsevier Applied Science: London (1987), pp. 139-220.
- [Mohd Tobi et al., Mohd Tobi, A.L., Ding, J., Bandak, G., Leen, S.B., Shipway, P.H. A study on the interaction between fretting wear and cyclic

Bibliography

- 2011]: plasticity for Ti-6Al-4V. *Wear*, **267** (2009), pp. 270-282.
- [Morito et al., 2005]: Morito, S., Saito, H., Ogawa, T., Furuhashi, T., Maki, T. Effect of austenite grain size on the morphology and crystallography of lath martensite in low carbon steels. *ISIJ International*, **45** (2005), pp. 91-94.
- [Morito et al., 2006]: Morito, S., Yoshida, H., Maki, T., Huang, X. Effect of block size on the strength of lath martensite in low carbon steels. *Materials Science and Engineering A*, **438-440** (2006), pp. 237-240.
- [Mroziński and Golański., 2013]: Mroziński, S., Golański, G. Elevated temperature low cycle fatigue properties of martensitic cast steel. *International Journal of Engineering and Technology*, **13** (2013), pp. 86-91.
- [Mroziński et al., 2014]: Mroziński, S., Golański, G., Zielińska-Lipiec, A. Fatigue resistance of GX12CrMoVNbN9-1 cast steel after ageing process. *Materials Science*, **20** (2014), pp. 396-402.
- [Nabarro, 1948]: Nabarro, F.R.N. Deformation of crystals by the motion of single ions. In: Mott, N.F. (Ed.). *Strength of Solids: Report of a Conference on the Strength of Solids, Bristol 7th – 9th July 1947*. Physical Society: London (1948), pp. 75-90.
- [Nabarro, 2002]: Nabarro, F. Creep at very low rates. *Metallurgical and Materials Transactions A*, **33** (2002), pp. 213-218.
- [Nagesha et al., 2002]: Nagesha, A., Valsan, M., Kannan, R., Bhanu Sankara Rao, K., Mannan, S.L. Influence of temperature on the low cycle fatigue behaviour of a modified 9Cr-1Mo ferritic steel. *International Journal of Fatigue*, **24** (2002), pp. 1285-1293.
- [Nagesha et al., 2012]: Nagesha, A., Kannan, R., Sastry, G.V.S., Sandhya, R., Singh, V., Bhanu Sankara Rao, K. Isothermal and thermomechanical fatigue studies on a modified 9Cr-1Mo ferritic martensitic steel. *Materials Science and Engineering A*, **554** (2012), pp. 95-104.
- [Nagode et al., 2011]: Nagode, A., Kosec, L., Ule, B. Uni-axial and multi-axial creep behaviour of P91-type steel in the temperature range 600-675 °C. *Engineering Failure Analysis*, **18** (2011), pp. 61-67.
- [Nes, 1998]: Nes, E. Modelling of work hardening and stress saturation in FCC metals. *Progress in Materials Science* **41** (1998) pp. 129-193.
- [Norton, 1929]: Norton, F.H. *The Creep of Steel at High Temperature*. McGraw-Hill Book Co.: New York (1929).
- [O'Hagan et al., 2015a]: O'Hagan, C.P., O'Brien, B.J., Griffin, F., Hooper, B., Leen, S.B., Monaghan, R.F.D. Porosity-based corrosion model for alkali halide ash deposits during biomass co-firing. *Energy and Fuels*, **29** (2015), pp. 3082-3095.
- [O'Hagan et al., 2015b]: O'Hagan, C.P., Barrett, R.A., Leen, S.B., Monaghan, R.F.D. Effect of high temperature corrosion on the service life of P91 piping in biomass co-firing. *Transactions of the ASME Journal of Pressure Vessel Technology* (2015) Under Review.
- [O'Hara et al., 2015]: O'Hara, E., Barrett, R.A., O'Donoghue, P.E., Leen, S.B. High temperature low cycle fatigue characterisation of MarBN at 600 °C. *Proceedings of the ASME 2015 Pressure Vessels and Piping Division Conference*, ASME, Boston, MA, 2015.
- [Ohno and Abdel-Karim, 2000]: Ohno, N., Abdel-Karim, M. Uniaxial ratchetting of 316FR steel at room temperature – Part II: constitutive modelling and simulation. *Transactions of the ASME Journal of Engineering Materials and Technology*, **122** (2000), pp. 35-41.
- [Ohno and Wang, 1993a]: Ohno, N., Wang, J.D. Kinematic hardening rules with critical state of dynamic recovery. Part I: formulation and basic features for ratchetting behaviour. *International Journal of Plasticity*, **9** (1993), pp. 375-390.

Bibliography

- [Ohno and Wang, 1993b]: Ohno, N., Wang, J.D. Kinematic hardening rules with critical state of dynamic recovery. Part II: application to experiments of ratchetting behaviour. *International Journal of Plasticity*, **9** (1993), pp. 391-403.
- [Oñoro, 2006]: Oñoro, J. Martensite microstructure of 9-12%Cr steels weld metals. *Journal of Materials Processing Technology*, **180** (2006), pp. 137-142.
- [Orlová et al., 1998]: Orlová, A., Buršík, J., Kuchařová, K., Sklenička, V. Microstructural development during high temperature creep of 9% Cr steel. *Materials Science and Engineering A* **245** (1998) pp. 39-48.
- [Orowan, 1940]: Orowan, E. Problems of plastic gliding. *Proceedings of the Physical Society*, **52** (1940), pp. 8-22.
- [Oruganti et al., 2011]: Oruganti, R., Karadge, M., Swaminathan, S. Damage mechanics-based creep model for 9-10%Cr ferritic steels. *Acta Materialia*, **59** (2011), pp. 2145-2155.
- [Othman et al., 1993]: Othman, A.M., Hayhurst, D.R., Dyson, B.F. Skeletal point stresses in circumferentially notched tension bars undergoing tertiary creep modelled with physically based constitutive equations. *Proceedings: Mathematical and Physical Sciences*, **441** (1993), pp. 343-358.
- [Panait et al., 2010a]: Panait, C.G., Bendick, W., Fuchsmann, A., Gourgues-Lorenzon, A.-F., Besson, J. Study of the microstructure of the Grade 91 steel after more than 100,000 h of creep exposure at 600 °C. *International Journal of Pressure Vessels and Piping*, **87** (2010), pp. 326-335.
- [Panait et al., 2010b]: Panait, C.G., Zielińska-Lipiec, A., Koziel, T., Czyrska-Filemonowicz, A., Gourgues-Lorenzon, A.-F., Bendick, W. Evolution of dislocation density, size of subgrains and MX-type precipitates in a P91 steel during creep and thermal aging at 600 °C for more than 100,000 h. *Materials Science and Engineering A*, **527** (2010), pp. 4062-4069.
- [Pedersen et al., 1981]: Pedersen, O.B., Brown, L.M., Stobbs, W.M. The Bauschinger effect in copper. *Acta Metallurgica* **29** (1981) pp. 1843-1850.
- [Perrin and Hayhurst, 1996]: Perrin, I.J., Hayhurst, D.R. Creep constitutive equations for a 0.5Cr-0.5Mo-0.25V ferritic steel in the temperature range 600-675 °C. *Journal of Strain Analysis*, **31** (1996), pp. 299-314.
- [Pešička et al., 2003]: Pešička, J., Kužel, R., Dronhofer, A., Eggeler, G. The evolution of dislocation density during heat treatment and creep of tempered martensite ferritic steels. *Acta Materialia* **51** (2003) pp. 4847-4862.
- [Pešička et al., 2010]: Pešička, J., Aghajani, A., Somsen, Ch., Hartmaier, A., Eggeler, G. How dislocation substructures evolve during long-term creep of a 12% Cr tempered martensitic ferritic steel. *Scripta Materialia*, **62** (2010), pp. 353-356.
- [Petch, 1953]: Petch, N.J. The cleavage strength of polycrystals. *Journal of the Iron and Steel Institute, London*, **173** (1953), pp. 25-28.
- [Pickering, 1997]: Pickering, F.B. Historical developments and microstructure of high chromium ferritic steels for high temperature applications. In: Strang, A., Gooch, D.J. (Eds.). *Microstructural Development and Stability in High Chromium Ferritic Power Plant Steels*. The Institute of Materials: London (1997), pp. 1-30.
- [Plumtree and Abdel-Raouf, 1998]: Plumtree, A., Abdel-Raouf, H.A. Relationship between cyclic stress-strain response and substructure. In: Rie, K.T., Portella, P.D. (Eds.). *Low cycle fatigue and elasto-plastic behaviour of materials*. Elsevier Science Ltd.: London (1998), pp. 279-284.

Bibliography

- [Poirier, 2005]: Poirier, J.O. Creep of crystals: High temperature deformation processes in metals, ceramics and minerals. Cambridge University Press: Cambridge (2005).
- [Prager, 1956]: Prager, W. A new method of analysing stresses and strains in work-hardening plastic solids. *Journal of Applied Mechanics*, **23** (1956), pp. 493-496.
- [Read and Shockley, 1950]: Read, W.T., Shockley, W. Dislocation models of crystal grain boundaries. *Physical Review*, **73** (1950), pp. 275-289.
- [Reardon, 2011]: Reardon, A.C. *Metallurgy for the Non-Metallurgist*, 2nd Edition. ASM International: Ohio (2011).
- [Ricoult and Kohlstedt, 1983]: Ricoult, D.L., Kohlstedt, D.L. Structural width of low-angle grain boundaries in Olivine. *Physics and Chemistry of Minerals*, **9** (1983) pp. 133-138.
- [Rice and Tracey, 1969]: Rice, J.R., Tracey, D.M. On the ductile enlargement of voids in triaxial stress fields. *Journal of the Mechanics and Physics of Solids*, **17** (1969), pp. 201-217.
- [Roland et al., 2006]: Roland, T., Reirant, D., Lu, K., Lu, J. Fatigue life improvement through surface nanostructuring of stainless steel by means of surface mechanical attrition treatment. *Scripta Materialia*, **54** (2006), pp. 1949-1954.
- [Roters et al., 2000]: Roters, F., Raabe, D., Gottstein, G. Work hardening in heterogeneous alloys – A microstructural approach based on three internal state variables. *Acta Materialia*, **48** (2000), pp. 4181-4189.
- [Ryen, 2003]: Ryen, O. Work hardening and mechanical anisotropy of aluminium sheets and profiles. Ph.D. Thesis, The Norwegian University of Science and Technology (NTNU), Norway (2003).
- [Saad, 2012]: Saad, A.A. Cyclic plasticity and creep of power plant materials. Ph.D Thesis, University of Nottingham, UK (2012).
- [Saad et al., 2011a]: Saad, A.A., Hyde, C.J., Sun, W., Hyde, T.H. Thermal-mechanical fatigue simulation of a P91 steel in a temperature range of 400-600 °C. *Materials at High Temperature*, **28** (2011), pp. 212-218.
- [Saad et al., 2011b]: Saad, A.A., Sun, W., Hyde, T.H., Tanner, D.W.J. Cyclic softening behaviour of a P91 steel under low cycle fatigue at high temperature. *Procedia Engineering*, **10** (2011), pp. 1103-1108.
- [Saad et al., 2013]: Saad, A.A., Hyde, T.H., Sun, W., Hyde, C.J., Tanner, D.W.J. Characterization of viscoplasticity behaviour of P91 and P92 power plant steels. *International Journal of Pressure Vessel and Piping*, **111** (2013), pp. 246-252.
- [Sakuraya et al., 2006]: Sakuraya, K., Okada, H., Abe, F. BN type inclusions formed in high Cr ferritic heat resistant steel. *Energy Materials*, **1** (2006), pp. 158-166.
- [Santella et al., 2001]: Santella, M.L., Swindeman, R.W., Reed, R.W., Tanzosh, J.M. Martensite transformation, microsegregation, and creep strength of 9Cr-1Mo-V steel weld metal. EPRI Conference on 9Cr Materials Fabrication and Joining Technologies, July 10-11, 2001, Myrtle Beach, South Carolina, USA.
- [Sauzay et al., 2005]: Sauzay, M., Brillet, H., Monnet, I, Mottot, M., Barcelo, F., Fournier, B., Pineau, A. Cyclically induced softening due to low-angle boundary annihilation in a martensitic steel. *Materials Science and Engineering A*, **400-401** (2005), pp. 241-244.
- [Sauzay et al., 2008]: Sauzay, M., Fournier, B., Mottot, M., Pineau, A., Monnet, I. Cyclic softening of martensitic steels at high temperature – Experiments and physically based modelling. *Materials Science*

Bibliography

- and Engineering A, **483-484** (2008), pp. 410-414.
- [Sawada et al., 1999]: Sawada, K., Takeda, M., Maruyama, K., Ishii, R., Yamada, M., Nagae, Y., Komine, R. Effect of W on recovery of lath structure during creep of high chromium martensitic steels. *Materials Science and Engineering A*, **267** (1999) pp. 19-25.
- [Sawada et al., 2003]: Sawada, K., Taneike, M., Kimura, K. In situ observation of recovery of lath structure in 9% chromium creep resistant steel. *Materials Science and Technology*, **19** (2003) pp. 739-742.
- [Scully, 2013]: Scully, S. Personal communication (2013).
- [Shrestha et al., 2012]: Shrestha, T., Basirat, M., Charit, I., Potirniche, G.P., Rink, K.K., Sahaym, U. Creep deformation mechanisms in modified 9Cr-1Mo steel. *Journal of Nuclear Materials*, **423** (2012), pp. 110-119.
- [Silwal et al., 2013]: Silwal, B., Li, L., Deceuster, A., Griffiths, B. Effect of postweld heat treatment on the toughness of heat-affected zone for Grade 91 steel. *Welding Research*, **92** (2013), pp. 80-87.
- [Sinclair et al., 2006]: Sinclair, C.W., Poole, W.J., Bréchet, Y. A model for the grain size dependent work hardening of copper. *Scripta Materialia*, **55** (2006), pp. 739-742.
- [Sklenička et al., 2003]: Sklenička, V., Kuchařová, K., Svoboda, M., Kloc, L., Buršík, J., Kroupa, A. Long-term creep behaviour of 9-12%Cr power plant steels. *Materials Characterization*, **51** (2003), pp. 35-48.
- [Sonderegger et al., 2007]: Sonderegger, B., Mitsche, S., Cerjak, H. Martensite laths in creep resistant martensitic 9-12% Cr steels – Calculation and measurement of misorientations. *Materials Characterization*, **58** (2007) pp. 874-882.
- [Spigarelli, 2013]: Spigarelli, S. Microstructure-based assessment of creep rupture strength in 9Cr steels. *Int. J. Pressure Vessel and Piping* **101** (2013) pp. 64-71.
- [Srinivas Prasad et al., 2012]: Srinivas Prasad, B.S., Rajkumar, V.B., Hari Kumar, K.C. Numerical simulation of precipitate evolution in ferritic-martensitic power plant steels. *CALPHAD: Computer Coupling of Phase Diagrams and Thermochemistry*, **36** (2012), pp. 1-7.
- [Stephens et al., 2001]: Stephens, R.I., Fatemi, A., Stephens, R.R., Fuchs, H.O. *Metal Fatigue in Engineering*. Wiley and Sons: New Jersey (2001).
- [Suresh, 1998]: Suresh, S. *Fatigue of Materials*. Cambridge University Press: Cambridge (1998).
- [Sweeney et al., 2014a]: Sweeney, C.A., O'Brien, B., Dunne, F.P.E., McHugh, P.E., Leen, S.B. Strain-gradient modelling of grain size effects on fatigue of CoCr alloy. *Acta Materialia*, **78** (2014), pp. 341-353.
- [Swindeman et al., 2004]: Swindeman, R.W., Santella, M.L., Maziasz, P.J., Roberts, B.W., Coleman, K. Issues with replacing Cr-Mo steels and stainless steels with 9Cr-1Mo-V steel. *International Journal of Pressure Vessels and Piping*, **81** (2004), pp. 507-512.
- [Tabuchi et al., 2004]: Tabuchi, M., Kondo, M., Kubo, K., Albert, S.K. Improvement of Type IV creep cracking resistance of 9Cr heat resisting steels by boron addition. *OMMI*, **3** (2004), pp. 1-11.
- [Takahashi, 2008]: Takahashi, Y. Study on creep-fatigue evaluation procedures for high-chromium steels – part I: test results and life prediction based on measured stress relaxation. *International Journal of Pressure Vessels and Piping*, **85** (2008), pp. 406-422.
- [Taneike, 2001]: Taneike, M., Kondo, M., Morimoto, T. Accelerated coarsening of MX carbonitrides in 12%Cr steels during creep deformation. *ISIJ International*, **41**(2001), pp. S111-S115.
- [Taylor, 1934]: Taylor, G.I. The mechanism of plastic deformation of crystals.

Bibliography

- Part I - Theoretical. Proceedings of the Royal Society, Series A, **145** (1934), pp. 362-387.
- [Taylor, 1938]: Taylor, G.I. Plastic strain in Metals. Journal of the Institute of Metals, **62** (1938), pp. 307-324.
- [Touboul et al., 2012]: Touboul, M., Crépin, J., Rousselier, G., Latourte, F. Identification of local viscoplastic parameters in welds at room temperature and 625 °C by inverse method based on digital image correlation and finite element simulation. 15th International Conference on Experimental Mechanics (ICEM15), 22nd-27th July, 2012; Porto, Portugal.
- [Vakili-Tahami et al., 2005]: Vakili-Tahami, F., Hayhurst, D.R., Wong, H.T. High-temperature creep rupture of low alloy ferritic steel butt-welded pipes subjected to combined internal pressure and end loadings. Philosophical Transactions of the Royal Society A: Mathematical, Physical and Engineering Sciences, **363** (2005), pp. 2629-2661.
- [Viswanathan and Bakker, 2001]: Viswanathan, R., Bakker, W. Materials for ultrasupercritical coal power plants – boiler materials: Part I. Materials Science and Engineering A, **510-511** (2009), pp. 88-94.
- [Viswanathan et al., 2005]: Viswanathan, R., Henry, J.F., Tanzosh, J., Stanko, G., Shingledecker, J., Vitalis, B., Purgert, R. U.S. program on materials technology for ultra-supercritical coal power plants. Journal of Materials Engineering and Performance, **14** (2005), pp. 281-292.
- [Watanabe et al., 2006]: Watanabe, T., Tabuchi, M., Yamazaki, M., Hongo, H., Tanabe, T. Creep damage evaluation of 9Cr-1Mo-V-Nb steel welded joints showing Type IV fracture. Int. J. Pressure Vessels and Piping **83** (2006), pp. 63-71
- [Williams and Fatemi, 2007]: Williams, J., Fatemi, A. Fatigue performance of forged steel and ductile cast iron crankshafts. SAE Technical Paper.
- [Yaghi et al., 2005]: Yaghi, A.H., Hyde, T.H., Becker, A.A., Williams, J.A., Sun, W. Residual stress simulation in welded sections of P91 pipes. Journal of Materials Processing Technology, **167** (2005), pp. 480-487.
- [Yaguchi and Takahashi, 2005a]: Yaguchi, M., Takahashi, Y. Ratchetting of viscoplastic material with cyclic softening – Part I: Experiments on modified 9Cr-1Mo steel. International Journal of Plasticity, **21** (2005), pp. 43-65.
- [Yaguchi and Takahashi, 2005b]: Yaguchi, M., Takahashi, Y. Ratchetting of viscoplastic material with cyclic softening – Part II: Application of constitutive models. International Journal of Plasticity, **21** (2005), pp. 835-860.
- [Yan, et al., 2013]: Yan, W., Wang, W., Shan, Y.-Y., Kang, K. Microstructural stability of 9-12%Cr ferrite/martensite heat-resistant steels. Frontiers of Materials Science **7** (2013) pp. 1-27.
- [Yang et al., 2008]: Yang, Y.-L., Yang, C.-H., Lin, S., Chen, C.-H., Tsai, W.-T. Effects of Si and its content on the scale formation on hot-rolled steel strips. Materials Chemistry and Physics, **112** (2008), pp. 566-571.
- [Zaafarani et al., 2008]: Zaafarani, N., Raabe, D., Roters, F., Zaefferer, S. On the origin of deformation-induced rotation patterns below nanoindentations. Acta Materialia, **56** (2008), pp. 31-42.
- [Zhan, 2004]: Zhan, Z. A study of creep-fatigue interaction in a new Nickel-based superalloy. Ph.D. Thesis, University of Portsmouth, UK (2004).
- [Zhang and Wang, 2000]: Zhang, Z.F., Wang, Z.G. Comparison of fatigue cracking possibility along large- and low-angle grain boundaries.

Bibliography

- Materials Science and Engineering A, **284** (2000), pp. 285-291.
- [Zhang et al., 2002]: Zhang, Z., Delagnes, D., Bernhart, G. Anisothermal cyclic plasticity modelling of martensitic steels. *International Journal of Fatigue*, **24** (2002), pp. 635-648.
- [Zhang et al., 2011]: Zhang, T., McHugh, P.E., Leen, S.B. Computational study on the effect of contact geometry on fretting behaviour. *Wear*, **271** (2011), pp. 1462-1480.
- [Zhang et al., 2012]: Zhang, T., McHugh, P.E., Leen, S.B. Finite element implementation of multiaxial continuum damage mechanics for plain and fretting fatigue. *International Journal of Fatigue*, **44** (2012), pp. 260-272.
- [Zhao et al., 2012]: Zhao, L., Jing, H., Xu, L. An, J., Xiao, G. Numerical investigation of factors affecting creep damage accumulation in ASME P92 steel welded joint. *Materials and Design*, **34** (2012), pp. 566-575.
- [Ziegler, 1959]: Ziegler, H. A modification of Prager's hardening rule. *Applied Mathematics*, **17** (1959), pp. 55-65.